Disclaimer

The contents of this report reflect the views of the authors who are responsible for the facts and accuracy of the data presented herein. The contents do not necessarily reflect the official views or policies of the State of California or the Federal Highway Administration. This report does not constitute a standard, specification or regulation.

Table of Contents

Chapter 4:   Test Details and Results of CFPS1 (Conventional Reinforcement)

Chapter 5:   Test Details and Results of CFPS2 (Headed Reinforcement)

Chapter 6:   Discussion of Results

Chapter 7:   Conclusions and Recommendations

Appendix A: Analytical Tools For Response Of Test Units 241

Appendix B: Design Tools For Pilecap Joints Of Test Units 258

Appendix C: Hysteresis Loops at Loading Phases 2 and 3 269

List of Figures

x

List of Tables

Acknowledgements

ABSTRACT

Seismic performance of CIDH pile supported foundation

by

Inho Ha

In recent years the use of large diameter CIDH pile supported footings to support bridge super structures has become common. The seismic response of bridge super structures supported on such footings relies on a moment-resisting connection between the piles and pilecap.

There are, however, uncertainties about the force transfer mechanism from column to piles in the 4-CIDH(Cast-In-Drilled-Hole)-pile-supported-foundation system. When piles are in the elastic state, the distribution of moment and shear force in the footing and in the piles can be significantly affected by the axial force in the piles, due to the variation of pile bending stiffness with the axial load. Furthermore, the influence of the three-dimensional geometry of the foundation on the shear direction of elastic pile can also affect the magnitude of the bending moment acting on the piles.

Although the foundation system is usually designed to remain elastic during the earthquake, plastic hinging in the piles may not be avoided during a severe earthquake. Recent research on Knee and Tee joints of bridge bents indicates that significant amounts

of joint reinforcement may be necessary in the pilecap joint regions. To investigate these issues, two large-scale models of full Column-Pilecap-Piles assemblages were designed and tested under simulated seismic loading.

The test units were designed according to state-of-the-art seismic design requirements. The first test unit contained conventional reinforcement while the second test unit contained headed reinforcement. Following the observed behavior of the test units, the pilecap force transfer mechanism is further investigated using a simplified foundation model similar to the test units. Consequently, a simple procedure is developed for seismic design of the 4-CIDH pile-supported-footing system.

Chapter 1: Introduction

1.1 Scope of Research

The seismic behavior of the 4-CIDH(Cast-In-Drilled-Hole) pile supported footing systems is the focus of this investigation. In recent years the use of large diameter CIDH-pile-supported-footings (see Figure 1.1-(b)) to support bridge super-structures has become common. Moment-resisting connection between the piles and pilecap are required in order for such structures to sustain seismic loading.
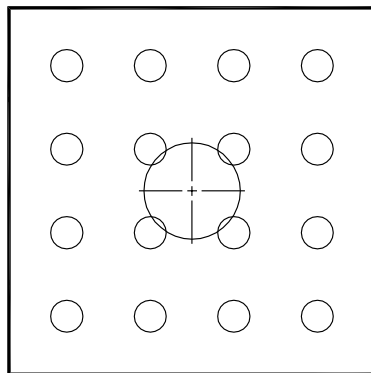
| (a) Multi-driven-pile
supported footing | (b) 4-CIDH-pile
supported footing |
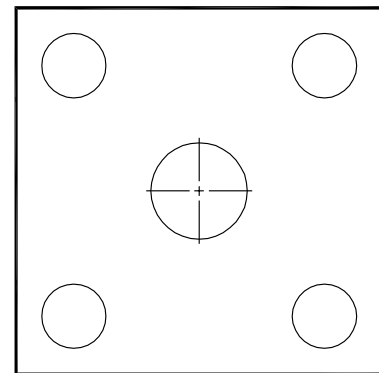
Figure 1.1: Plan view of pile supported foundation alternatives

(a) Equal moment between piles
(conventional analysis)

(b) Unequal moment between piles
(research topic)
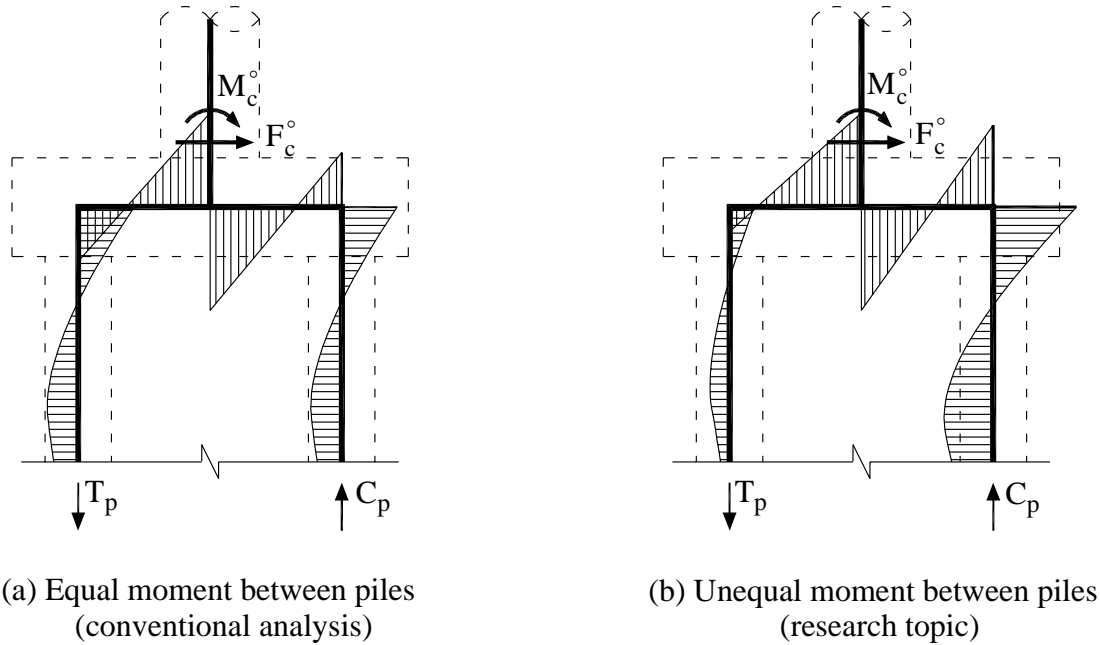
Figure 1.2: Qualitative moment distribution of CIDH pile supported footing

For most pile supported foundations the design philosophy is to force a plastic hinge to occur at the base of the column and to keep the piles elastic during the seismic response. In conventional design, the number of piles is obtained by distributing the column shear force, determined for the plastic hinge flexural overstrength, evenly among piles and the shear design of an individual pile is performed based on evenly distributed shear forces, see Figure 1.2-(a). However, when reinforced concrete piles are in an elastic state, the distribution of moment and shear force in the footing and in the piles can be significantly affected by the axial force in the piles, due to the variation of pile bending stiffness with the axial load, see Figure 1.2-(b). The moment and shear force in the piles are also affected by the rotation of the pilecap caused by the vertical stiffness of pile-soil interaction, and lateral passive soil pressure on the vertical face of the footing

(a) Rotation (b) Translation
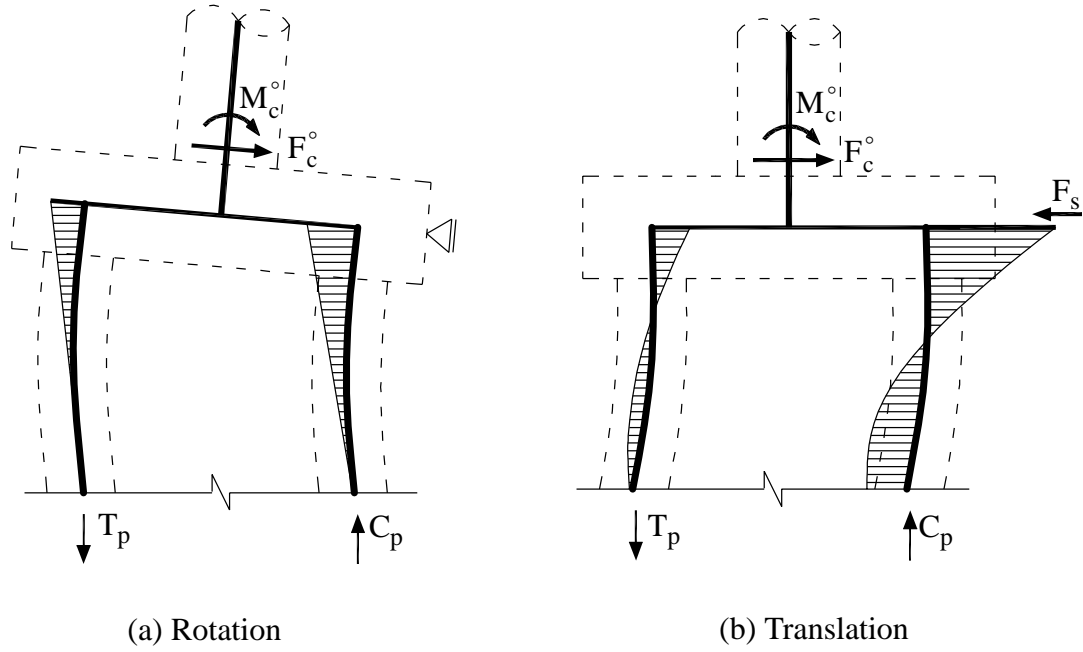
Figure 1.3: Influence of pilecap rotation and translation

as shown in Figure 1.3. Furthermore, the influence of the three dimensional geometry of the foundation on the shear direction of the elastic pile can also affect the magnitude of the bending moment acting on the piles, see Figure 1.4.

Although the foundation system is usually designed to remain elastic during the earthquake, plastic hinging in the piles may not be avoided during severe earthquakes, see Figure 1.5. Therefore, the external strut joint force transfer model and the corresponding joint reinforcement details for the knee and T joints of bridge bents may be used as a design tool for the joint regions of CIDH pile supported footing.

In addition, a factor that deserves attention when building congested cages is the use of headed reinforcement. Headed reinforcement provides better anchorage than
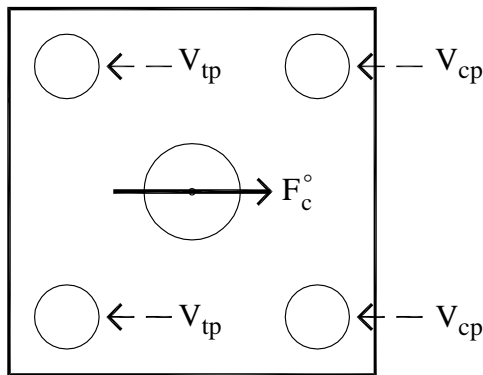
(a) Reaction parallel to lateral load
(conventional analysis)
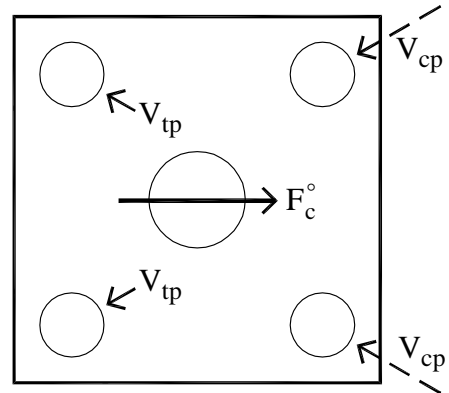
(b) Reaction with angle to lateral load
(research topic)

Figure 1.4: Direction of pile resistance

Column
plastic hinge

⬚ Inverted T joint

⬚ Knee Joint

Potential
Plastic hinge
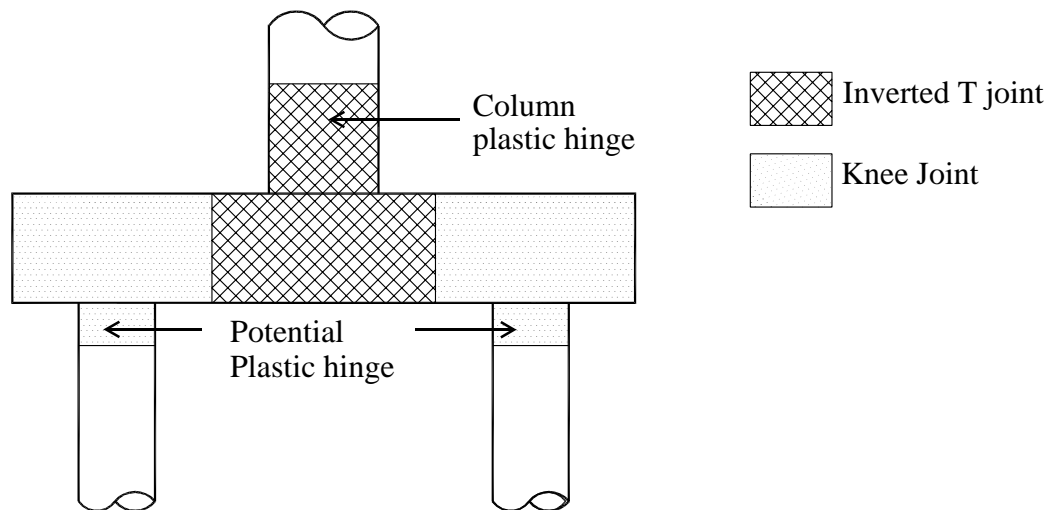
Figure 1.5: Pilecap joints

Figure 1.6: Headed reinforcement at pile/pilecap joint

conventional reinforcement, which should help the moment transfer between the pile and pilecap.

These issues were investigated through comprehensive experimental and analytical research and are presented in this report. The experimental program involved two half-scale seismic tests on full column-footing-pile assemblies. The test units were designed in accordance with the capacity design philosophy with conventional and headed reinforcement, respectively. Joint regions were designed using the external joint strut approach proposed by Priestley et al.[26].

1.2 Format of The Report

Following the introduction presented in this chapter, the analytical study on the axial force effect on the pile shear force distribution is covered in Chapter 2. Linear and non-linear analyses on the soil-structure interaction were carried out for the 2-D skeletal frame, by finite element modeling the piles and the surrounding soil. During the nonlinear pushover analyses, the tangential stiffness, obtained from the moment-curvature curves based on the induced moment and axial force in the element, were used for updating the bending stiffnesses of each pile beam element. The soil was modeled as an array of uncoupled nonlinear spring elements. In the elastic analysis, the bending stiffness for tension and compression piles were made equal and were not updated in the analysis. Likewise, a linear model was used for the soil. The study was done for five different soil properties and three different column heights.

In Chapter 3 the test setup and design of test units are described. Two large-scale 3-D test units, which are composed of a column, a pilecap and four piles, were designed and tested under simulated seismic loading. The first test unit, CFPS1, was designed with a conventional reinforcement while the second unit, CFPS2, was designed to incorporate headed reinforcement. When designing the test units, a state-of-the-art design procedure was adopted. In designing of joints, the external strut joint mechanism was used to improve the joint performance and to reduce the joint reinforcement.

The experimental work on CFPS1(test unit containing conventional reinforcement) and CFPS2(test unit containing headed reinforcement) are summarized in Chapters 4 and 5, respectively. The test results showed that the behavior of test units generally correlated

to the anticipated response based on the simple anlytical predictions. However,it was revealed from the data of instrumentation devices and damage to test units that the actual force transfer mechanism of the four CIDH pile supported footing system was quite different to that assumed in the design of footing as two dimensional portal frame. The pilecap of Unit CFPS1 suffered severe damage, which showed high inelastic strains at the bottom reinforcement although they were supposed to remain elastic. This damage was investigated and the findings were considered in the design of Unit CFPS2. No significant damage occurred to Unit CFPS2. It was also found from the test result of unit CFPS2 that the direction of pile resistance is not parallel to the applied lateral load.

Chapter 6 is dedicated to the discussion of the test results. A pilecap force transfer mechanism is proposed and the principal direction of pile shear force is further investigated. Since the three dimensional geometry of the foundation system influences the shear direction of the elastic pile, a parameter study was performed to investigate the combined effect of axial force and shear force direction of the piles. For the parameter study, a simplified foundation model similar to the test units was adopted and four distinctive parameters were used, which are representative of gravity load, column length, soil property and the relative stiffness of pile.

Based on the discussions, the conclusions of the investigation are presented in Chapter 7 with recommendations and a simple design procedure for seismic design of the 4-CIDH pile supported footing system.

1.3 Terminology and Units

In this report two distinctive lateral loading directions are expressed as "Orthogonal direction loading" and "Diagonal direction loading". "Orthogonal direction loading" means the lateral loading which is parallel to the pilecap sides, and "Diagonal direction loading" means diagonally applied lateral load in pilecap plan view. This is shown in Figure 1.7.

In this report, SI units are exclusively used.
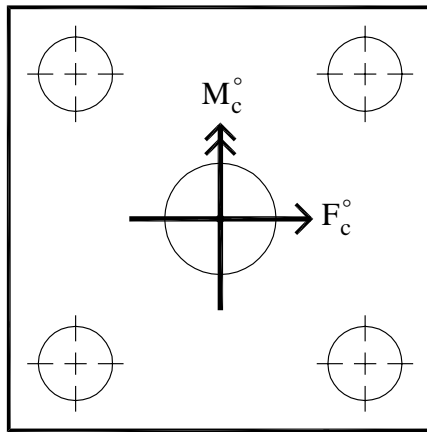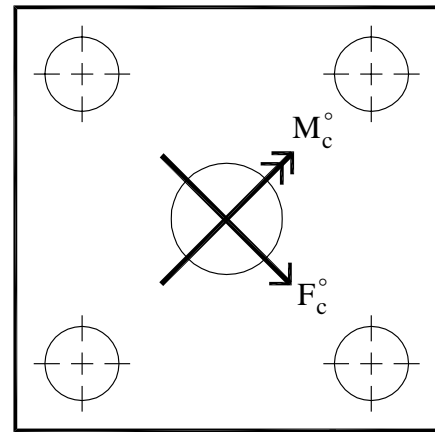
(a) Orthogonal direction loading   (b) Diagonal direction loading

Figure 1.7: Definition of lateral loading direction

Chapter 2 : Axial Force Effects on the Moment Demands in CIDH Pile Groups

2.1 Introduction

The purpose of this study is to assess the influence of axial force on a 4-CIDH-pile-supported foundation systems. Soil-structure interaction analyses were performed using the finite element method by adopting beam and bar elements to model the piles and the surrounding soil, respectively. Elastic and nonlinear pushover analyses were performed. For the elastic analyses, both bending stiffnesses of tension and compression piles are assumed to be the same as is traditionally done. However, during the nonlinear pushover analyses, the bending stiffnesses of each pile beam element were modified with the corresponding tangential stiffness based on the induced moment and axial force in the element. The tangential stiffness was determined from a moment-curvature analysis of the pile section for a given axial force. The soil was modeled as an array of uncoupled spring elements. The study was done for five different soil properties and three different column heights.

2.2 Literature review on soil - pile interaction theoretical approach

Various analytical models have been proposed to investigate the behavior of laterally loaded piles. The first model was that of a transversely loaded thin elastic beam, supported by a series of linear springs acting along the length of the beam[10]. Many

advanced approaches, including modified boundary element analysis[3], and the 3-D finite element method[8] were developed subsequently. Out of all the analytical models described in the literature, the following approaches are briefly reviewed in this section. For the axially loaded floating piles, the Winkler[31] and Gazetas[9] methods are reviewed.

2.2.1 Stiffness of laterally loaded pile-soil interaction

1) Elastic Continuum Method

The elastic continuum method is based on the theory of elasticity and assumes that the soil is an elastic, homogeneous, isotropic half-space with a constant Young's modulus and Poisson's ratio. This method was introduced by Mindlin[17] in 1936. The pile was modeled as a thin, rectangular, vertical strip, with soil pressure constant across the pile width. In 1971, Poulos[23] presented the elastic solution for the problem of a single pile subjected to lateral loading.

For a single pile loaded at the pile head, Poulos[23] presents the following equations to obtain the displacements and rotations at the ground level.

$$u = f_{uv}V + f_{um}M \qquad\qquad (2.1)$$

$$\theta = f_{\theta v}V + f_{\theta m}M \qquad\qquad (2.2)$$

where f_{uv}, f_{um}, $f_{\theta v}$ and $f_{\theta m}$ are flexibility coefficients and V, M are applied horizontal load and moment, respectively. For a long pile, these coefficients depend on the Young's modulii of the pile, E_p, and soil, E_s, respectively, and on the pile diameter, D_p.

The advantage of this approach is its simplicity. Furthermore, the continuity of the soil is taken into account such that stresses and displacements spread outward and diminish with distance from the point of application of a force. However, the elastic continuum approach is limited by several factors. The soil in reality is far from being homogeneous and isotropic. Furthermore, the behavior of the soil under large deflections is highly nonlinear and, accordingly, the assumption that the soil is linear elastic is valid when only the soil is deformed to very small strains.

2) Equivalent Cantilever Approach

Another approach that structural engineers usually use to analyze the responses of laterally loaded pile is the equivalent cantilever method[30]. In this method the soil-pile system is replaced by an equivalent cantilever fully restrained against translation and rotation at the base. The equivalent depth to fixity can be determined by equating the lateral siffness of the soil-pile system to that of an equivalent fixed-base cantilever.

The drawback of this method is that the depth to fixity is determined based on solutions for an elastic pile embedded in elastic soil. This approach needs two distinctive cantilever lengths depending on whether maximum pile top lateral deflections or moments are in question for design because the depth of maximum moment does not occur at the base of the cantilever but at a depth shallower than the equivalent depth to fixity.

3) Winkler method

In 1867 E. Winkler[4] introduced the analysis method of a beam on an elastic foundation under an applied pressure loading. In this approach, the soil is modeled as a bed of independent springs. The uncoupling between the springs results in the mathematical simplicity of the Winkler method. Before 1955, the concept of the Winkler spring model had been adopted to predict the response of laterally loaded pile by assuming that the soil is linearly elastic and the Young's modulus of soil increases with depth.

In the Winkler method the displacement, y, at a given point relates to the contact pressure developed in the soil, p, at that point via the coefficient of horizontal subgrade reaction, k_s, by the expression:

$$p = k_s \cdot y \tag{2.3}$$

Once the relations between p and y along the pile length are constructed or predicted, the response of the pile under lateral load can be obtained by solving the following differential equation. :

$$EI_p \frac{d^4y}{d^4z} + k_s y = V \tag{2.4}$$

where EI_p is the bending stiffness of pile, y is the lateral displacement, z is the depth, k_s is the stiffness of the soil and V is the applied lateral load.

2.2.2 Soil nonlinearity

In reality the relationship between soil pressure, p, and deflection, y, is nonlinear and several approaches have been developed to account for the nonlinearity of soil. One of the common methods is the p-y curve which was first introduced by McClelland and Focht(1956).

A set of p-y curves along the pile is, in the most pure sense, constructed with the data from the full scale testing of the instrumented piles. After the bending moment diagram along the pile is constructed from the measured strain data at a given point, the shear force diagram is obtained by differentiating the moment along the pile. With the soil reactions, obtained by differentiating the shear force diagram, and the deflections, from the double integration of the curvature diagram, a set of p-y curves is constructed.

In 1984 Carter[7] developed a simple method of constructing a p-y curve. The idea of the method is that the nonlinear response of the soil is determined by the initial subgrade coefficient, k_s, and the ultimate lateral pressure, p_{ult}, at which the soil reaches the maximum pressure it can sustain. With these two limits the p-y curve is hyperbolic and is controlled by the power factor, n. Carter's hyperbolic soil model is given by :

$$y = \frac{p}{k_s}\left[\frac{p_{ult}^n}{(p_{ult}^n - p^n)}\right] \tag{2.5}$$

For the value of p_{ult}, Carter proposed the following equation through his finite element analysis work.

$$p_{ult} = 5 \cdot K_p \cdot \sigma' \tag{2.6}$$
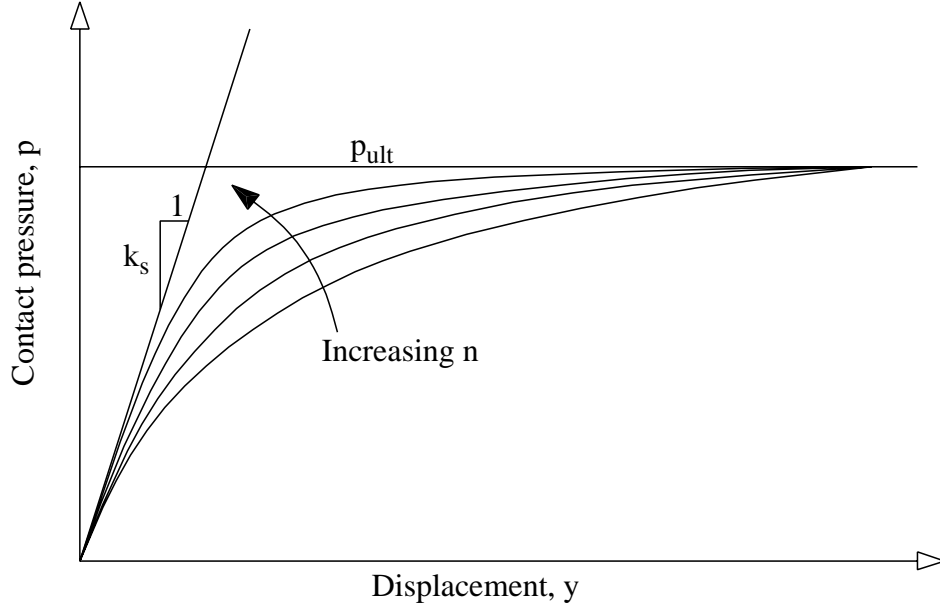
Figure 2.1: Nonlinear p-y curve for the Carter's soil model

In Eq. (2.6), K_p is the coefficient of passive soil pressure, which is given by :

$$K_p = \frac{1 + \sin\phi_s}{1 - \sin\phi_s} \qquad (2.7)$$

where ϕ_s is the friction angle of the soil.

The vertical effective stress, σ', at a depth of z is :

$$\sigma' = \gamma \cdot z \qquad (2.8)$$

where γ is the unit weight of soil.

The tangential subgrade coefficient, k_{st}, can be obtained by differentiating Eq. (2.5) as :

$$k_{st} = \frac{dp}{dy} = \frac{k_s\left[1 - \left(\dfrac{p_s}{p_{ult}}\right)^n\right]^2}{\left[1 + (n-1)\left(\dfrac{p_s}{p_{ult}}\right)^n\right]} \tag{2.9}$$

Carter suggested $n = 1$ for sand, based on the results of comparisons with back analyses from full scale pile tests[7].

2.2.3 Determination of k_s and relationship with E_s

The determination of the subgrade coefficient, k_s, is the major limitation which is associated with all soil models. Unlike k_s, the modulus of elasticity, E_s, is easily obtainable from the published data on soil properties. Furthermore, the ultimate pressure, p_{ult}, can be determined with a good degree of accuracy. Therefore, it is of interest to study the relationship between k_s and E_s as the former is one of three key parameters of Eq. (2.5).

Vesic in 1961 provided the following relationship between the soil Young's modulus, E_s, which is used in the continuum method, and the subgrade modulus, k_h.

$$k_h = \frac{0.65E_s}{(1 - v_s^2)}\left(\frac{E_s D_p^4}{EI_p}\right)^{1/12} \tag{2.10}$$

where v_s is the soil Poisson's ratio, D_p is the pile diameter and EI_p is the flexural rigidity of the pile. For the purpose of practical use of Eq. (2.10), the term, $(E_s D^4/EI_p)^{1/12}$ is simplified to 1.0, since its magnitude generally yields approximately that value[7, 13]. Accordingly, Eq. (2.10) becomes :

$$k_h = \frac{0.65E_s}{1 - v_s^2} \tag{2.11}$$

Bowles[4] suggested Eq. (2.12) which results in the twice of the value of Eq. (2.11) as the modulus of subgrade reaction K_h for the laterally loaded pile. He argued that soil and pile are in contact on both sides of the pile while Eq. (2.11) is derived from the beam on the elastic foundation with soil acting on only one side of the beam. Therefore,

$$k_h = \frac{1.3E_s}{1 - v_s^2} \qquad (2.12)$$

However, the soil does not necessarily contact the entire surface of the pile when it is subjected to the lateral loading inducing large lateral displacement. Therefore, the value of the modulus of subgrade reaction should lie between the value given by Eq. (2.11) and (2.12). Carter[7] and Ling[13] found that when the factor is 1.0, the prediction of the pile is in good agreement with the pile deflection. Hence,

$$k_h = \frac{1.0E_s}{1 - v_s^2} \qquad (2.13)$$

Carter and Ling also accounted for the effect of pile diameter, D_p, on the modulus of subgrade reaction, k_h, and suggested the following equation.

$$k_h = \frac{1.0E_s \cdot D_p}{(1 - v_s^2) \cdot (1.0\text{m})} \qquad (2.14)$$

where E_s is the soil Young's modulus. Ling divided Eq. (2.14) by 1.0 meter to make it dimensionally correct. If $(1 - v_s^2)$ is approximated as 1.0 considering that the Poisson's ratio is small, Eq. (2.14) becomes :

$$k_h = E_s \cdot \frac{D_p}{1.0\text{m}} \qquad (2.15)$$

From the definition of the modulus of subgrade reaction, k_h,

$$k_h = k_s \cdot D_p \tag{2.16}$$

Combining Eqs. (2.15) and (2.16),

$$k_s = \frac{E_s}{1.0m} \tag{2.17}$$

Eq. (2.17) shows that $E_s(FL^{-2})$ and $k_s(FL^{-3})$ are essentially identical quantities except the dimensional difference between the two, resulting from the definition that the modulus of elasticity, E_s, is defined as the ratio of stress to strain, and the coefficient of subgrade reaction, k_s, is defined as the ratio of pressure to displacement. Eq. (2.17) is notable since the coefficient of subgrade reaction, k_s, can be directly calculated from the modulus of elasticity of the soil.

2.2.4 Axially loaded pile - soil interaction

1) Elastic Continuum Method

In 1991, Gazetas[9] presented the static axial stiffness expressions of axially loaded piles, which are embedded in three different types of soil, using the elastic continuum approach. The expressions provided are only for a floating pile. A floating pile is the one in which there is no abrupt change in the properties of the soil at the end of the pile. The equations for the three different soil types are :

- Constant soil modulus at all depth

$$K_v = 1.9 E_s D_p \left(\frac{L}{D_p}\right)^{0.67} \left(\frac{E_p}{E_{sl}}\right)^{-(L/D_p)/(E_p/E_s)} \tag{2.18}$$

17

- Linear increase of soil modulus with depth

$$K_v = 1.8 E_{sL} D_p \left(\frac{L}{D_p}\right)^{0.55} \left(\frac{E_p}{E_{sL}}\right)^{-(L/D_p)/(E_p/E_{sL})} \tag{2.19}$$

where, $E_{sL} = E_{s1} \cdot (L/D_p)$

- Parabolic increase of soil modulus with depth

$$K_v = 1.9 E_{sL} D_p \left(\frac{L}{D_p}\right)^{0.6} \left(\frac{E_p}{E_{sL}}\right)^{-(L/D_p)/(E_p/E_{sL})} \tag{2.20}$$

where, $E_{sL} = E_{s1} \cdot \sqrt{L/D_p}$

In the above equations L and D_p are, respectively, the length and the diameter of the pile ; E_p and E_{sL} are the Young's modulus of pile and soil at the depth of pile length, L, respectively. As was seen in the above equations, the axial stiffness of a floating pile-soil interaction depends not only on its relative compressibility, E_p/E_{sL}, but also on the slenderness ratio, L/D_p.

2) Winkler method

The solution of the axial stiffness of the floating pile was given by R. F. Scott[31] in 1981. Although two different solutions which are for a rigid pile and a compressible pile under axial load were presented, only the solution for the compressible pile embedded in soil with constant Young's modulus is reviewed here. In Figure 2.2-(c), force decrement in the pile occurs along its depth for a given axial load as a result of pile axial flexibility. If the vertical displacement of the pile in the z-direction is set to be *w*, the force in the pile, F_p, is :

(a) Pile under tension load, T_p (b) Linear distribution of Young's modulus with depth   (c) Magnified view of "A"
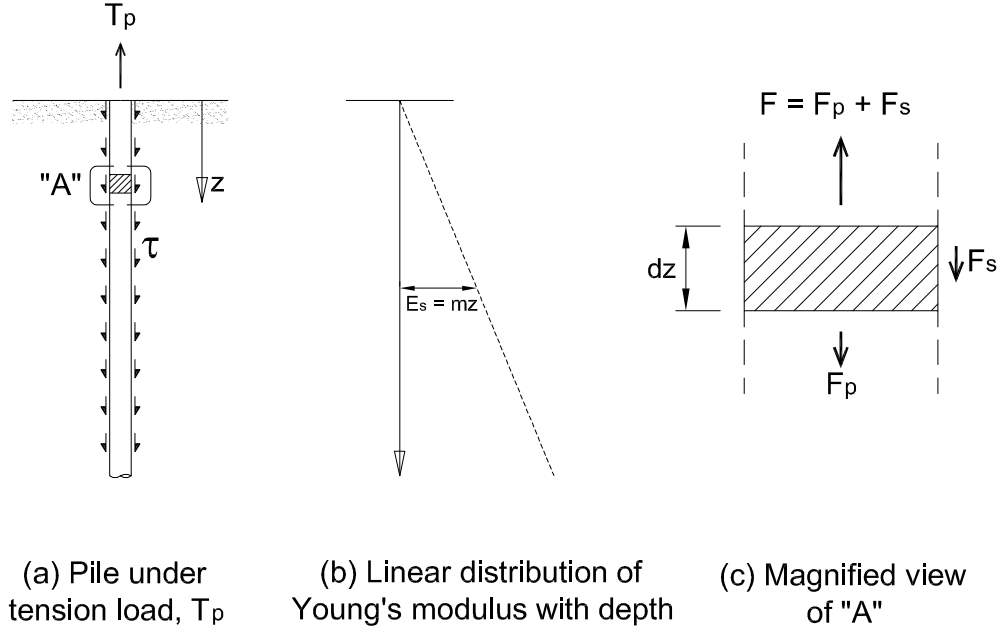
Figure 2.2: Winkler representation of axially loaded tension pile and soil model

$$F_p = \sigma_p A_p = (E_p \varepsilon_p) A_p = E_p A_p \frac{dw}{dz} \tag{2.21}$$

where E_p is the Young's modulus of the pile and A_p is the area of the pile section. The decrement of the force in the tension pile, dF_p, at a distance down of dz, must be taken by the shear force, F_s, acting on the surface area of the pile segment. If the soil spring constant, k_s, is defined as :

$$\tau = k_s w \tag{2.22}$$

where τ is the shearing stress acting on a segmental pile surface area, then the total force due to shear friction on the peripheral surface of the pile segment, F_s, is :

$$F_s = \tau S dz = S k_s w dz \tag{2.23}$$

where S is the pile perimeter. From the equilibrium consideration, :

19

$$F - F_p = dF_p = F_s = Sk_swdz \qquad (2.24)$$

Substituting Eq. (2.21) into Eq. (2.24) yields :

$$_pA_p\frac{dw^2}{dz^2} = Sk_sw \qquad (2.25)$$

Eq. (2.25), describes the behavior of the vertically loaded pile with the appropriate

boundary conditions such as :

$$\varepsilon_p\big|_{z=0} = \frac{dw}{dz}\bigg|_{z=0} = \frac{T_p}{E_pA_p} \qquad (2.26)$$

$$\varepsilon_p\big|_{z=1} = \frac{dw}{dz}\bigg|_{z=1} = 0 \qquad (2.27)$$

where F is the applied force at the top of the pile.

Therefore, the axial stiffness of soil-pile interaction can be obtained along the pile

by dividing the pile force, F_p, by the corresponding pile displacement, w.

2.3 Modeling of soil-pile group interaction analysis

2.3.1 Finite element modeling

To study the response of laterally loaded four-CIDH pile supported foundations

subjected to varying axial force in the piles, linear and nonlinear analyses were

performed in this investigation for the two-dimensional finite elemented skeletal frame

model, which consists of a column, a pilecap and two piles embedded in the ground, as

shown in Figure 2.3. The major considerations in the modeling of soil-foundation

structure interactions are described here.

6786kN
(5% axial load ratio)

Column
Diameter : 2.4m
Length : 6m, 12m, 18m
Rebar : 78-D43(2.5%)
Spiral : D19@80mm
M_y = 53316kNm

6m
12m
18m

M_c°

F_c°

Stiffness degradation
due to strain penetration

K_s

Initial stiffness

1.7m

Stiffness degradation
due to strain penetration

Pilecap
9.0m(b_f) x 9.0m(w_f) x 1.7m(h_f)
$EI_{cap}/EI_{pile} \approx 10$

K_i

K_i

20m

Pile
Diameter : 1.5m
Length : 20m
Rebar : 17-D43(1.4%)
Spiral : D19@80mm
M_y = 11007kNm

K_{vt}

K_{vc}

Figure 2.3: Skeletal model for the nonlinear pushover analysis

21

1) The vertical stiffnesses of the tension(k_{vt}) and of the compression piles(k_{vc}) are considered since the pilecap rigid body rotation depends on the vertical stiffnesses of the piles. For the tension pile the end bearing stiffness is considered as long as the pile is in compression. Once the pile is in tension only the floating pile - soil interaction stiffness is considered. For the compression pile the stiffness from the pile end bearing and friction is considered.

2) The effect of the lateral stiffness of the passive soil on the pilecap bearing face(k_s) is studied because the passive soil pressure on the pilecap is believed to be significant due to its size.

3) The strain penetration of the pile longitudinal bars inside the pilecap is considered. The bending stiffnesses of the discrete pile and column elements, which are inside the pilecap, is affected by strain penetration.

4) For the linear analysis the elastic stiffnesses were used for the elements of structure. The bending stiffnesses between compression and tension piles were identical and constant. The stiffness of soil springs were also linear. However, in the nonlinear analysis the bending stiffnesses of each discrete pile element were updated during each segmental analysis operation according to the moment and the axial force levels induced in a individual pile element. The tangential stiffness of a pile element was obtained from the moment-curvature analysis of the pile section subjected to the updated axial force. A bi-linear soil model is adopted for the analyses. Figure 2.4 shows the variation in bending stiffnesses of tension and compression piles at the end of the analysis, which are normalized by the elastic pile stiffness. Since the vertical
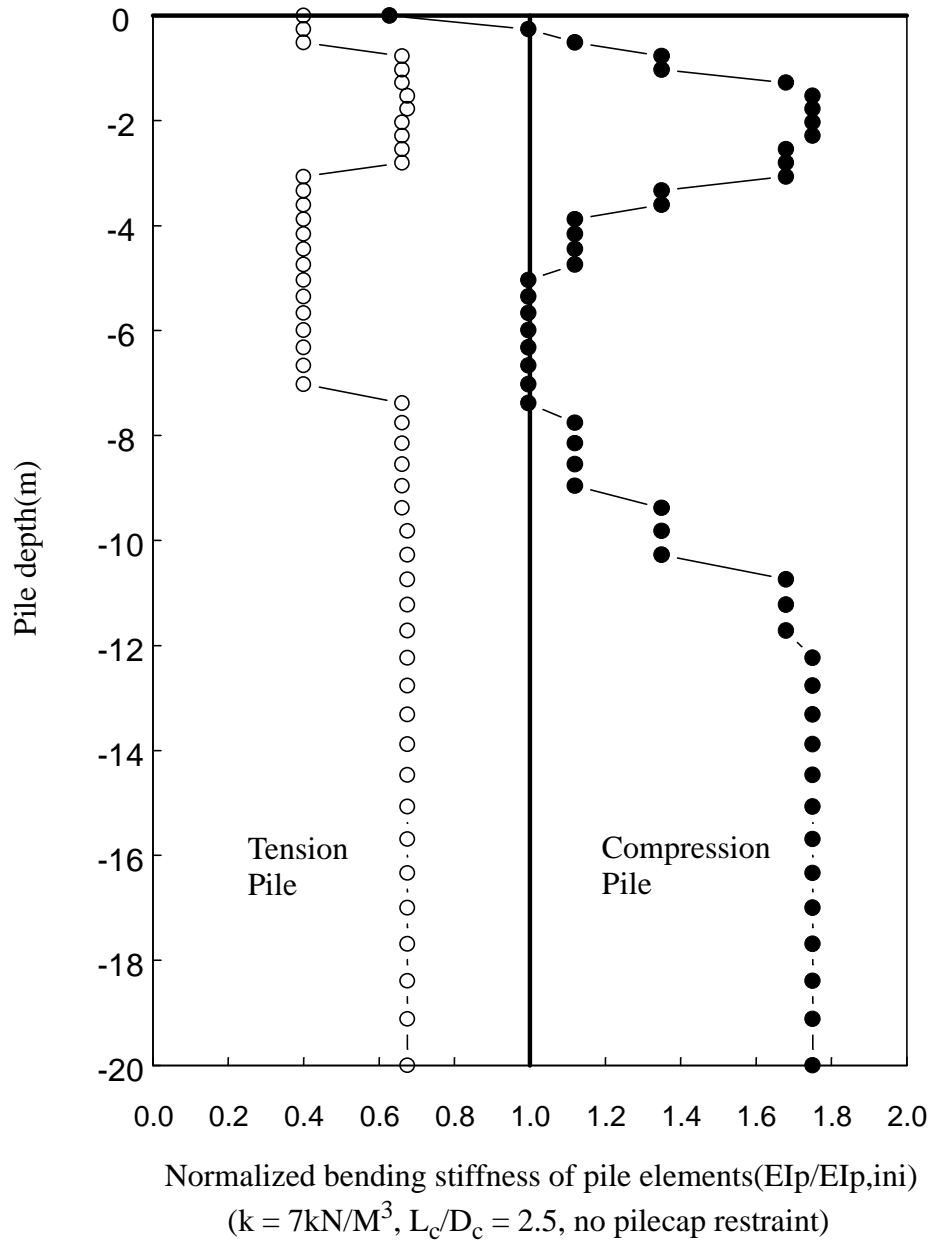
Figure 2.4: Variation of pile stiffnesses with depth due to axial force and moment
(at the end of the analysis)

soil-pile interaction stiffness was modeled as a lumped springs at the base of each pile, axial force along the entire length of each pile was constant. In reality, the distributed vertical soil-pile interaction causes the axial force to vary along the length of the pile. The axial force induced at the pile base changed the bending stiffness of the pile as shown in Figure 2.4. However, the change in stiffness does not affect the behavior of the structure because there is no moment demand at the base of the piles and the axial force developed above the inflection point of the pile is almost same between the distributed and the lumped spring models.

Because the pilecap is supported by four CIDH piles in reality, the stiffness of each compression and tension pile of the model corresponds to twice the stiffness of an individual pile.

2.3.2 Soil resistance model

1) Lateral stiffness of the soil - pile interaction

The soil around the pile was modeled using a series of uncoupled spring elements. In this study, the Winkler model is used. This approach allows for modeling soil types which vary with depth and exhibit nonlinearities.

Since the soil which is chosen for the parameter study is sand, the modulus of subgrade reaction, k_h, increases linearly with depth, z. Therefore, the individual soil spring stiffness, $k_i(z)$, using the Winker method, can be calculated based on the following expression :

$$k_i(z) \,=\, k_h(z) \cdot \Delta z \tag{2.28}$$

where $k_h(z)$ is the horizontal modulus of the subgrade reaction at depth, z, and Δz is the spring spacing.

Carter found that the subgrade reaction modulus, $k_h(z)$, for a pile with diameter D_p can be obtained from a known quantity, $k_h^*(z)$ for D_p^* as :

$$k_h(z) \; = \; k_h^*(z) \cdot \frac{D_p}{D_p^*} \qquad\qquad (2.29)$$

Therefore, from Eqs. (2.28), (2.29), the individual soil spring stiffness, $k_i(z)$, is :

$$k_i(z) \; = \; k_{h1}^* \cdot z \cdot \frac{D_p}{D_p^*} \cdot \Delta z \qquad\qquad (2.30)$$

where k_{h1}^* is the increasing rate of subgrade reaction modulus with depth, z.

2) Vertical stiffnesses of the soil - pile interaction

The springs for the vertical stiffness of soil-pile interaction were calculated using Eq. (2.19) and attached to pile ends. Although the vertical springs act as lumped springs at the end of the piles, the difference to the distributed springs is negligible.

2.4 Results of Analyses

The results of the analyses are presented in Figures 2.6 - 2.37. The definition of the different moments referred to in the text are given in Figure 2.5. Because the analyses were done for the in-plane skeletal frame, the results show only the effect of axial force in the piles on the distribution of the moments between the compression and tension piles. In the real pile supported foundation system, pile moments will be greater than
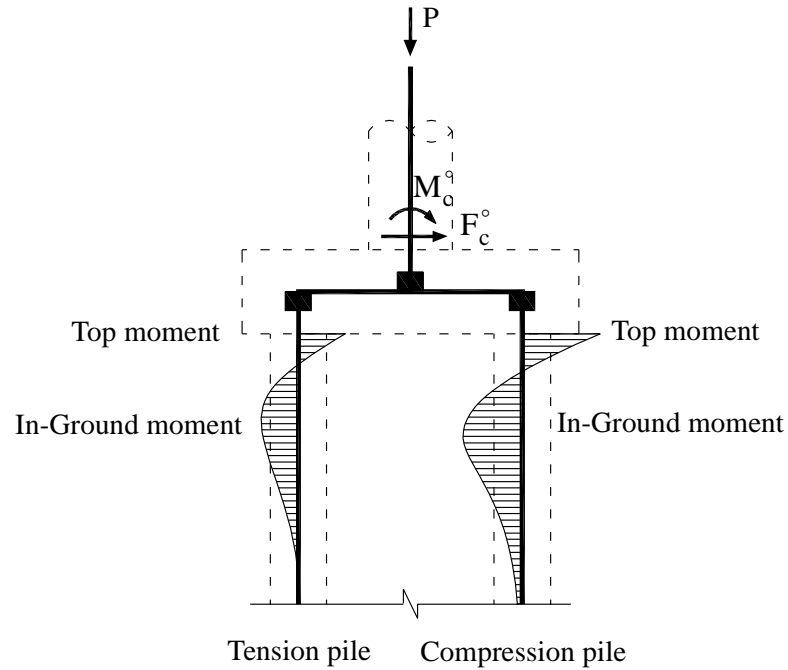
Figure 2.5: Pile maximum moment locations

those of the two-dimensional analysis due to the three dimensional effect of the foundation. This aspect is discussed in detail in Chapter 6.

2.4.1 Uneven force distribution between compression and tension piles

The linear analysis based on the same stiffness for tension and compression piles yields that the magnitudes of the moment and shear between the compression and tension piles are almost the same although there is a small difference due to the presence of gravity load. However, it is clearly seen that significant differences in the moment and shear does occur in nonlinear analysis that used tangential stiffness of pile moment-curvature curve. The main reason for this is the variation of flexural stiffness in the piles as the axial load varies at each load increment. The tension pile softens due to axial

tension in the piles, while the compression piles becomes stiffer and attract more moment than the tension piles. Figures 2.30 - 2.33 show that the compression pile moment is more sensitive to axial load than the tension moments. Axial load has, however, a similar effect on the shear force for both tension and compression piles.

2.4.2 Effect of pilecap passive soil pressure on pile moments

For both the linear and nonlinear analyses, the pile moment and shear force are largely dependent on the degree of restraint provided by the pilecap. The decrease of the pile moment and shear force, due to the passive soil pressure on the pilecap, is significant when compared to the cases without pilecap restraint. In Figures 2.30-2.31, the influence of pilecap passive soil pressure on the pile moment is observed in the form of a moment reversal at the top of the pile embedded in dense sand and supporting a long column. Nonlinear analysis shows a notable reversal of pile top moment in the compression pile.

Figure 2.38 also shows that there is a significant contribution of passive soil pressure on the pilecap vertical face that reduces the shear force demand on pile group. The effect of pilecap restraint is closely related to the soil properties. In soft sand which corresponds to 7 MPa/m of subgrade coefficient, k_s, in Figure 2.38, the decrease in the pile group shear force due to pilecap passive soil restraint is 17% - 28%. However, in dense sand which is represented by 60 MPa/m of subgrade coefficient, ks, the pile group shear force reduced to 35% - 55% of total applied shear force due to the pilecap restraint.

In addition, the influence of the pilecap passive soil pressure on the shear force of pile group also depends on the nondimensional column length, L_c/D_c. The column length is an indicator of relative influences of column moment and shear force on the system

behavior. The degree of dependency on the column length becomes significant in denser soil. This is clearly shown in 2.38.

Because linear soil p-y curves are used for the linear analysis and bi-linear soil p-y curves for the nonlinear analysis, there is almost no difference in the effects of pilecap restraint between linear and nonlinear analyses when soil has not yielded. However, once the pilecap passive soil has yielded, the difference between linear and nonlinear analyses is obvious. This is shown in Figure 2.38 for the case of $L_c/D_c = 2.5$ and $k_s = 7$ MPa/m.

2.4.3 Sensitivity of pile forces on variables

Figures 2.30 - 2.33 shows the variation of pile moments with the soil stiffness. As the stiffness of soil increases, the magnitude of the pile moment is reduced since the relative lateral displacement of the piles are decreased. The decrease of the pile top moments with increasing soil stiffness is highly nonlinear although the rate of decrease reduces as soil becomes stiffer. The influence of soil property on pile moment is greater at the top of the piles than in the ground. Furthermore, the maximum In-Ground moment develops at shallower depth as soil gets stiffer and, accordingly, the inflection point of the pile also becomes shallower. This is shown in Figures 2.6-2.29. In the piles embedded in stiffer soil, the reversal of the pile moment direction occurs as shown in Figures 2.26, 2.27, 2.30 and 2.31.

However, the shear force of the pile is not as sensitive to the soil property as pile moment. From Figures 2.34 - 2.37, it is known that, without pilecap restraint, the shear force of the piles is almost constant regardless of soil property. But, with pilecap passive soil pressure, the pile shear force with pilecap restraint lessens significantly as soil

becomes stiffer. This can be seen clearly in Figure 2.38. The pile moment and shear

forces are also highly dependent on the column length. The pile forces increases

parabolically as column length decreases as shown in Figures 2.30 - 2.37.
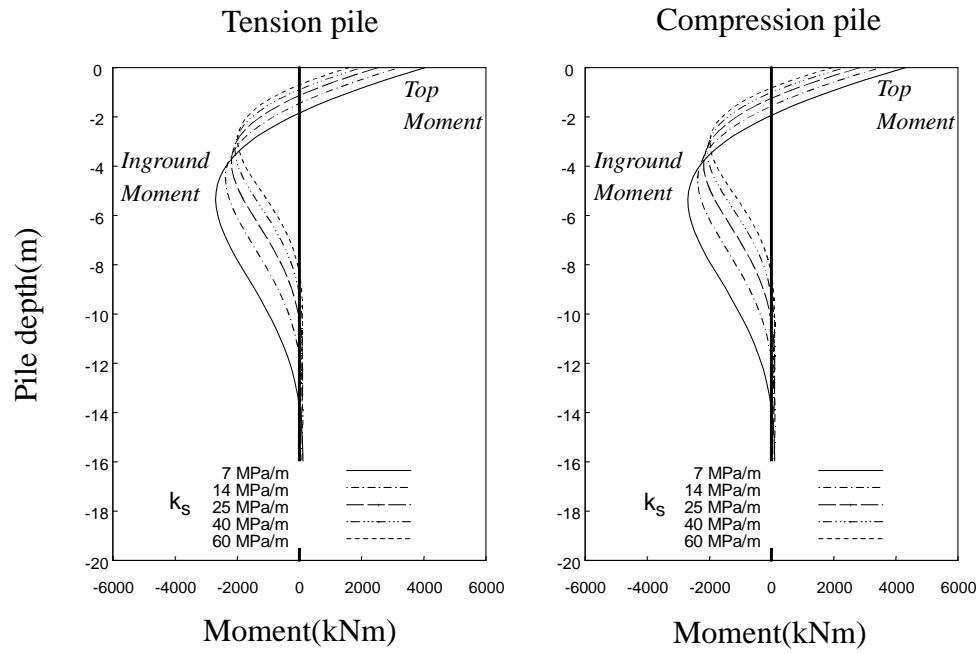
Figure 2.6: Pile moment of linear analysis(L_c/D_c = 2.5, no pilecap restraint)
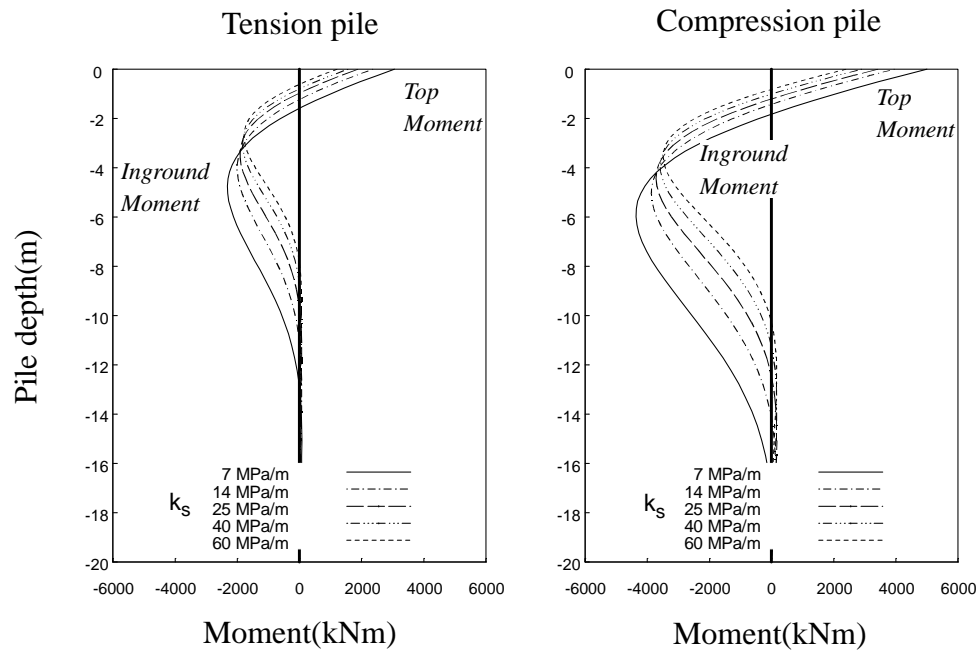
Figure 2.7: Pile moment of nonlinear analysis(L_c/D_c = 2.5, no pilecap restraint)

Tension pile

Compression pile
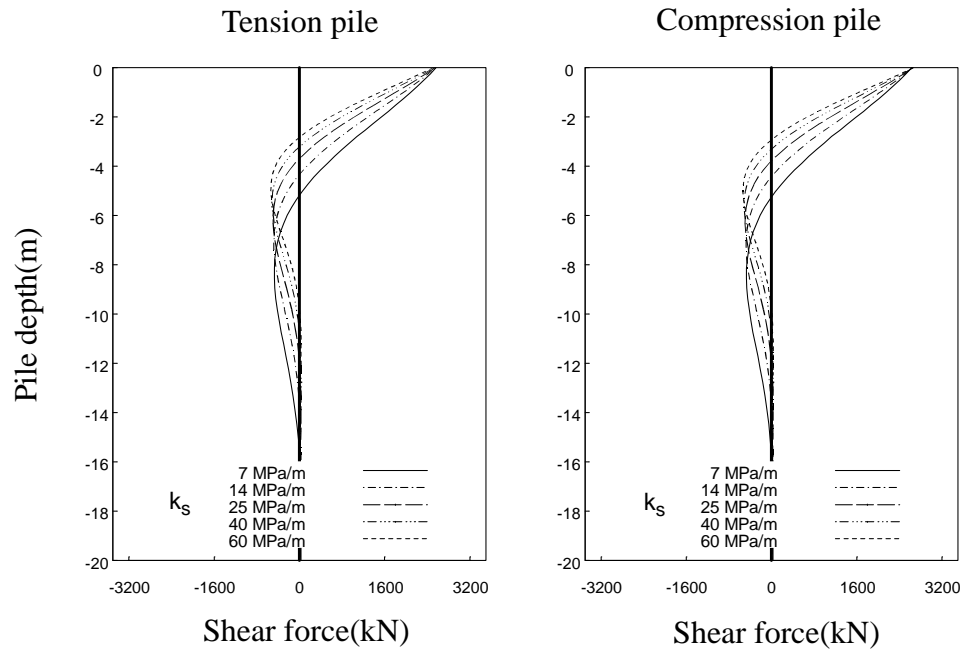
Figure 2.8: Pile shear force of linear analysis($L_c/D_c = 2.5$, no pilecap restraint)

Tension pile

Compression pile
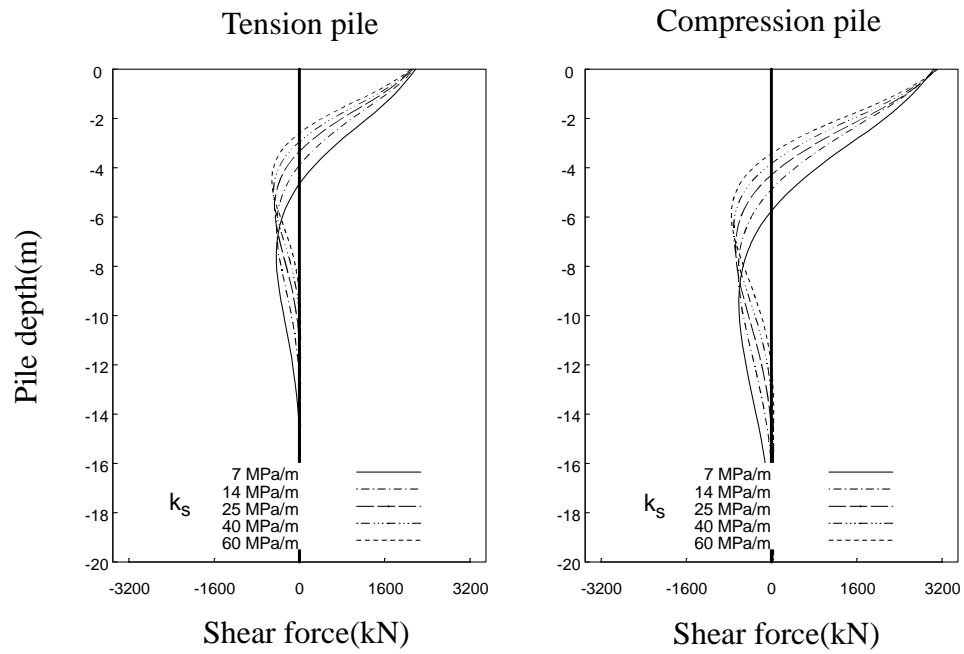
Figure 2.9: Pile shear force of nonlinear analysis($L_c/D_c = 2.5$, no pilecap restraint)
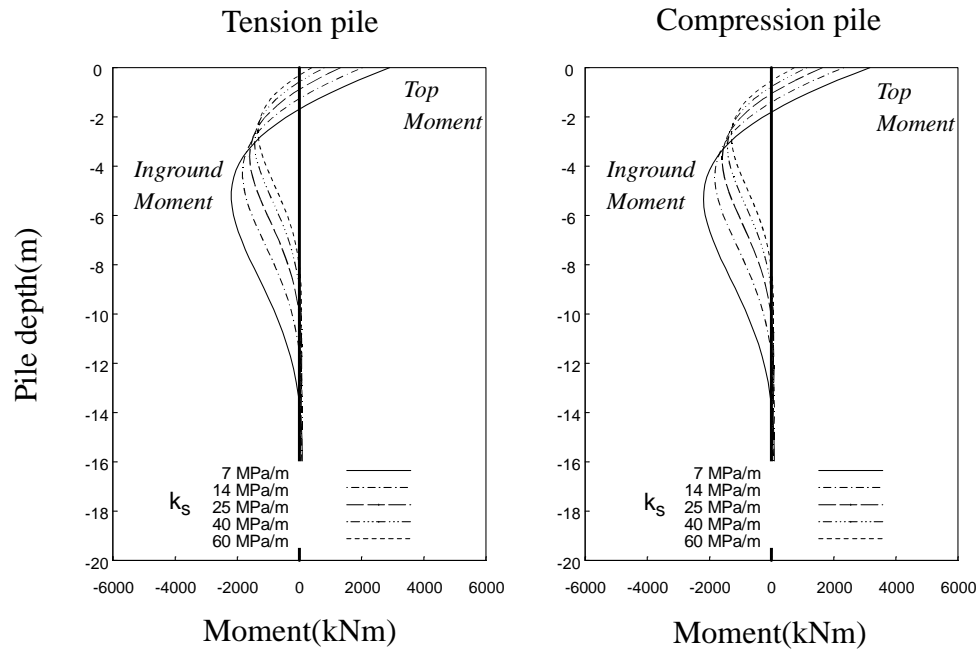
Figure 2.10: Pile moment of linear analysis($L_c/D_c = 2.5$, pilecap restraint)
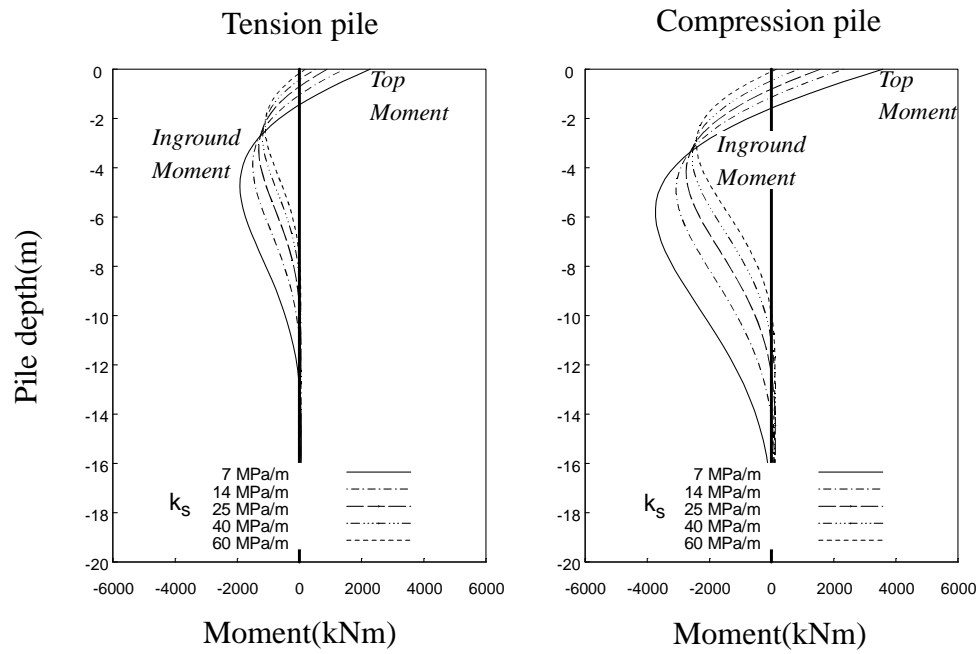
Figure 2.11: Pile moment of nonlinear analysis($L_c/D_c = 2.5$, pilecap restraint)
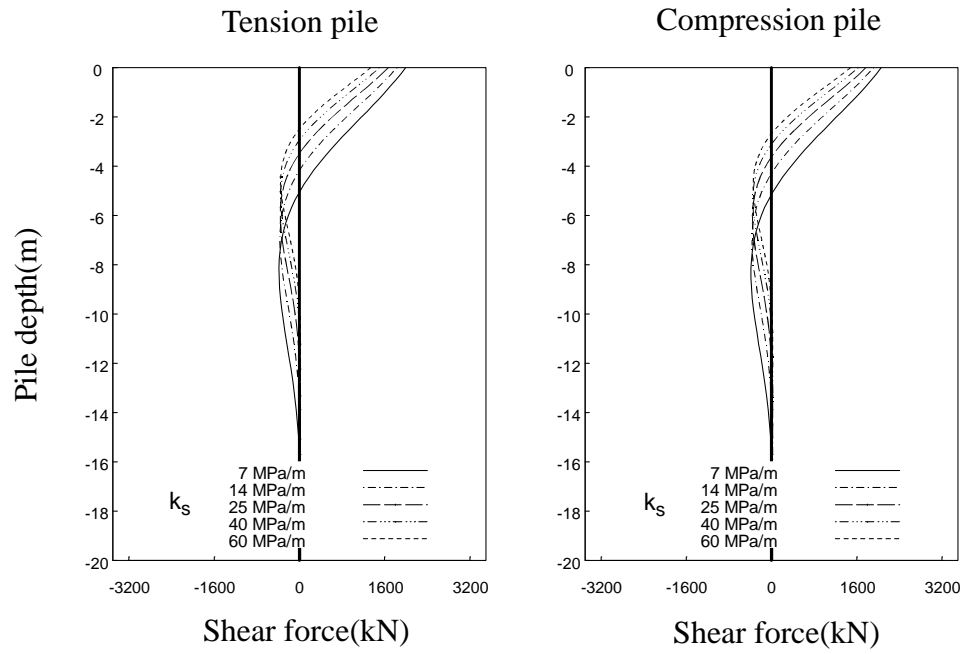
Figure 2.12: Pile shear force of linear analysis(L_c/D_c = 2.5, pilecap restraint)
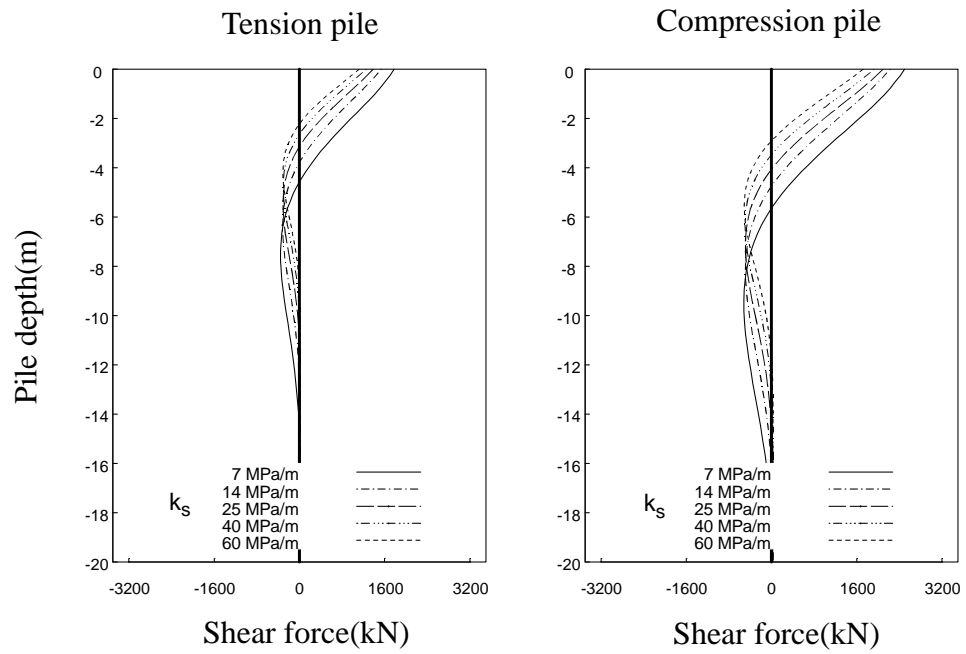
Figure 2.13: Pile shear force of nonlinear analysis(L_c/D_c = 2.5, pilecap restraint)

Tension pile   Compression pile
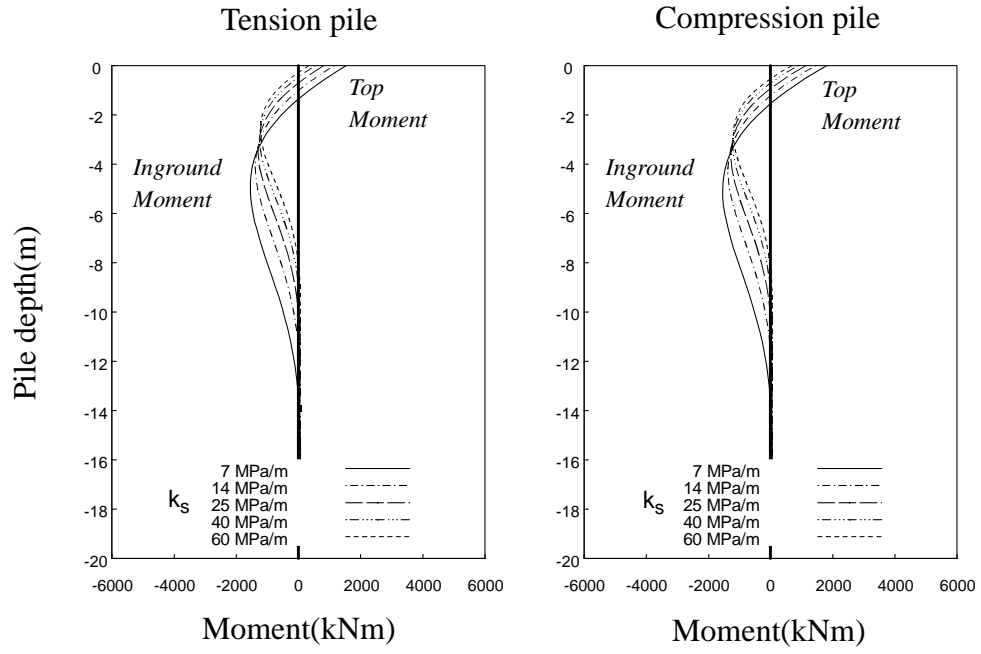
Figure 2.14: Pile moment of linear analysis($L_c/D_c = 5.0$, no pilecap restraint)

Tension pile   Compression pile
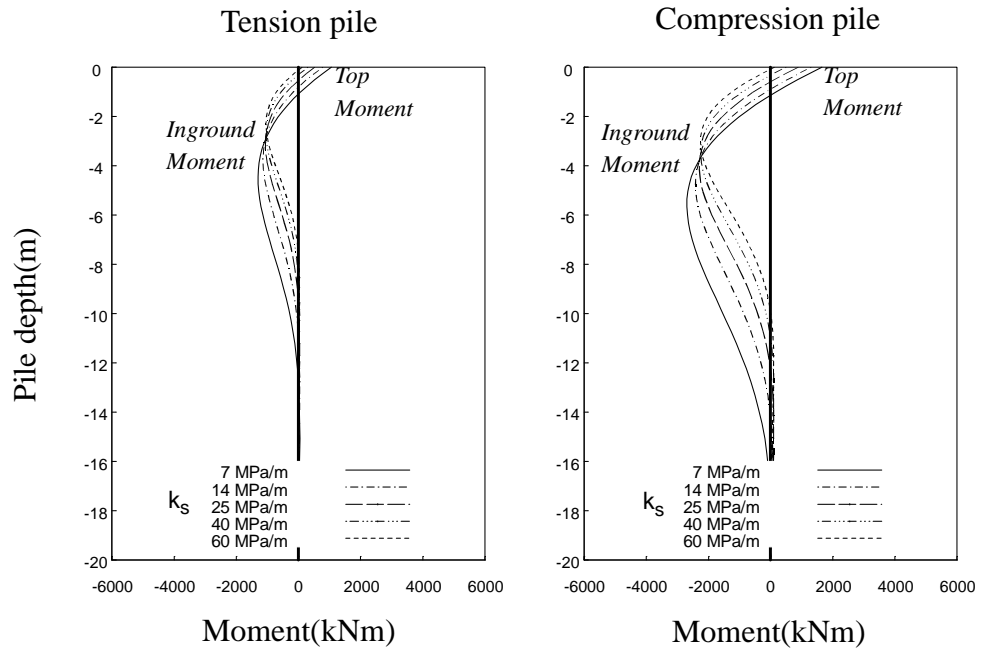
Figure 2.15: Pile moment of nonlinear analysis($L_c/D_c = 5.0$, no pilecap restraint)
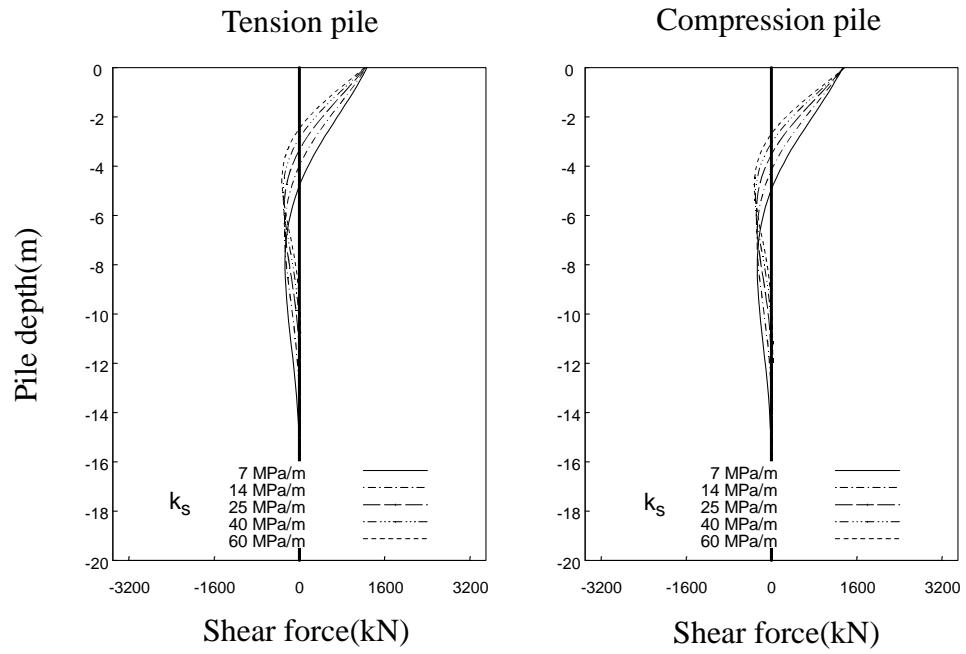
Figure 2.16: Pile shear force of linear analysis($L_c/D_c = 5.0$, no pilecap restraint)
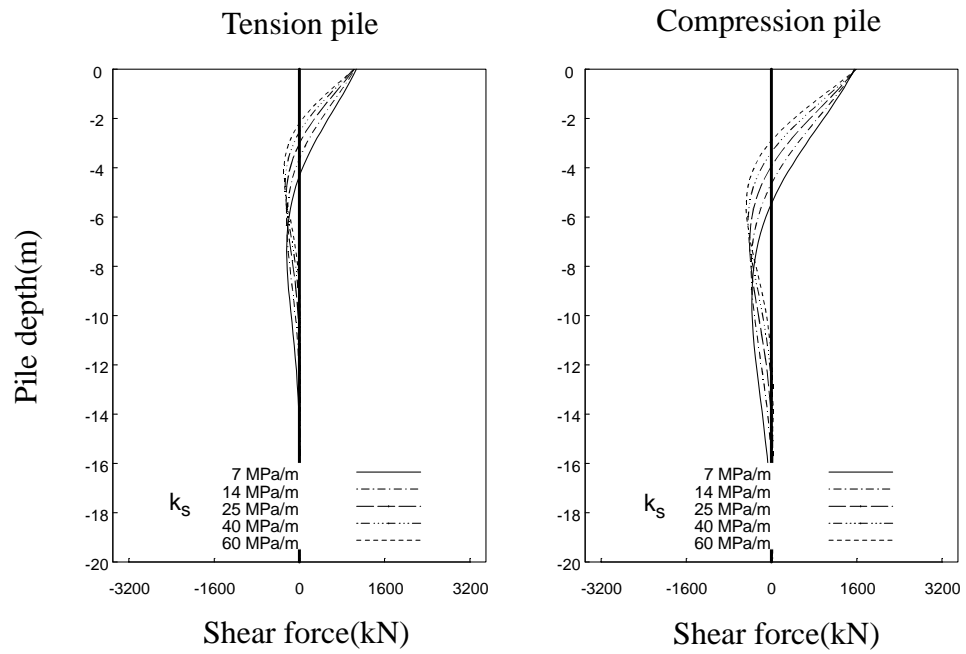
Figure 2.17: Pile shear force of nonlinear analysis($L_c/D_c = 5.0$, no pilecap restraint)

Tension pile   Compression pile
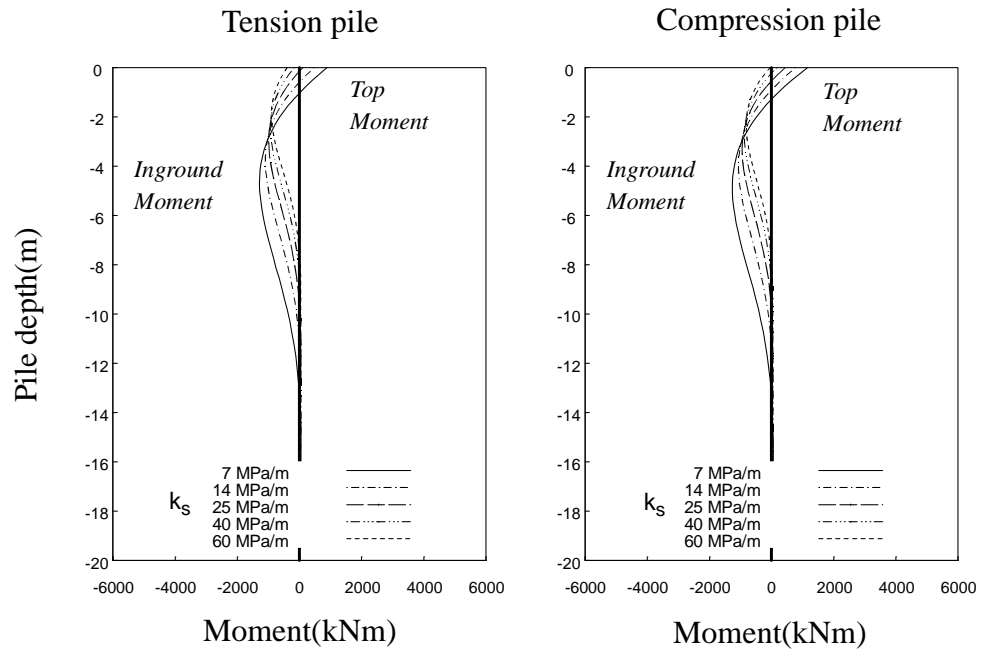
Figure 2.18: Pile moment of linear analysis($L_c/D_c = 5.0$, pilecap restraint)

Tension pile   Compression pile
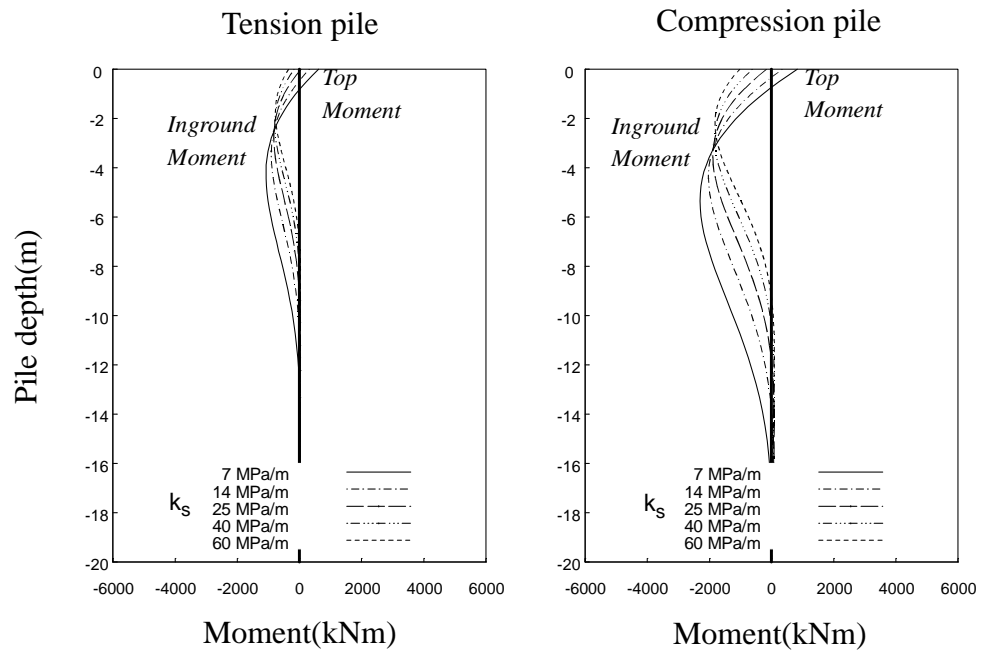
Figure 2.19: Pile moment of nonlinear analysis($L_c/D_c = 5.0$, pilecap restraint)

Tension pile

Compression pile
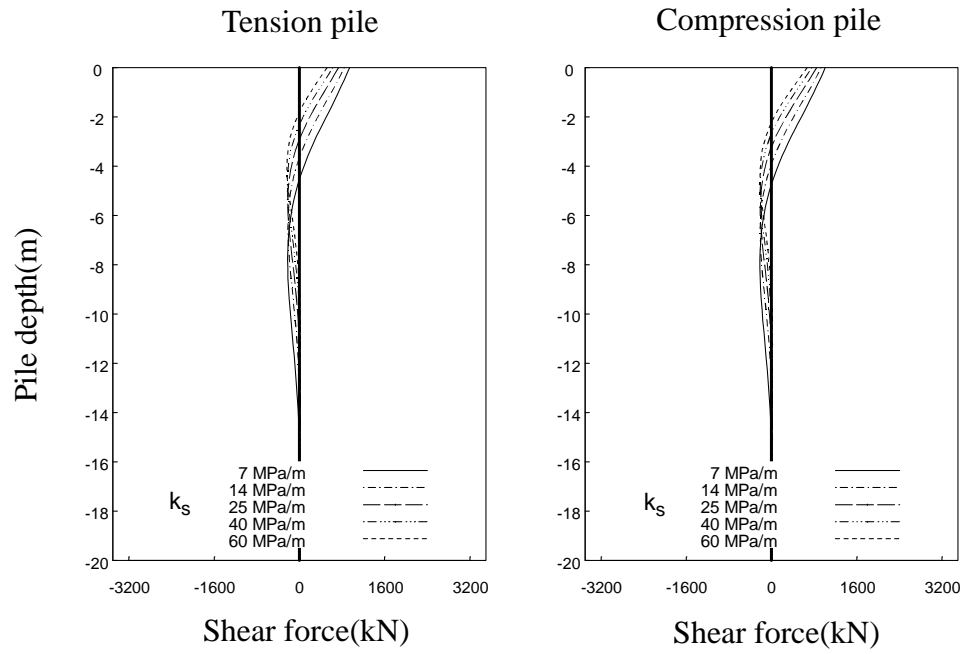
Figure 2.20: Pile shear force of linear analysis(L_c/D_c = 5.0, pilecap restraint)

Tension pile

Compression pile
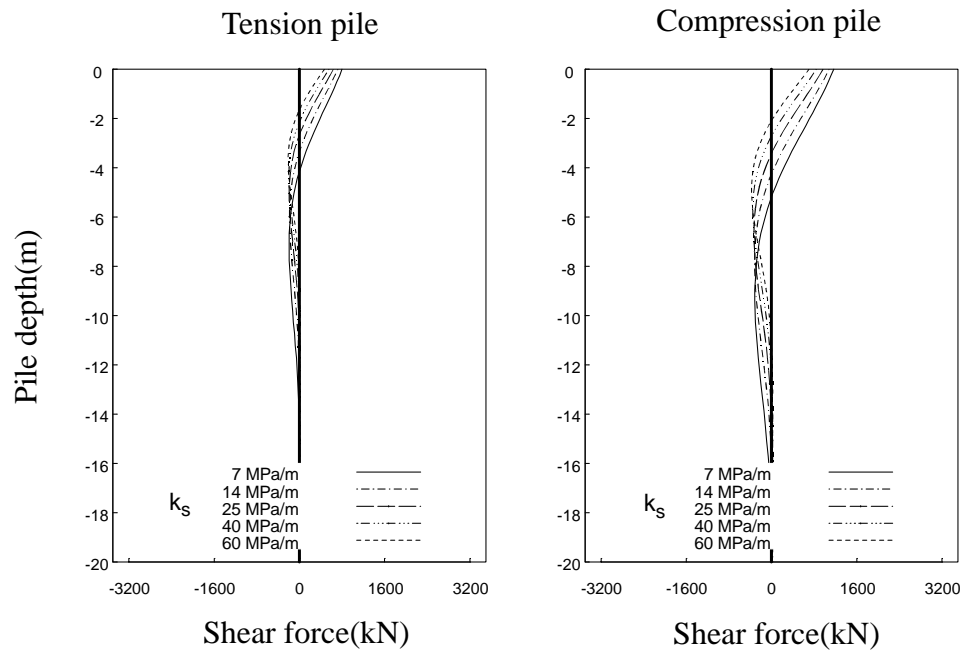
Figure 2.21: Pile shear force of linear analysis(L_c/D_c = 5.0, pilecap restraint)

Tension pile

Compression pile
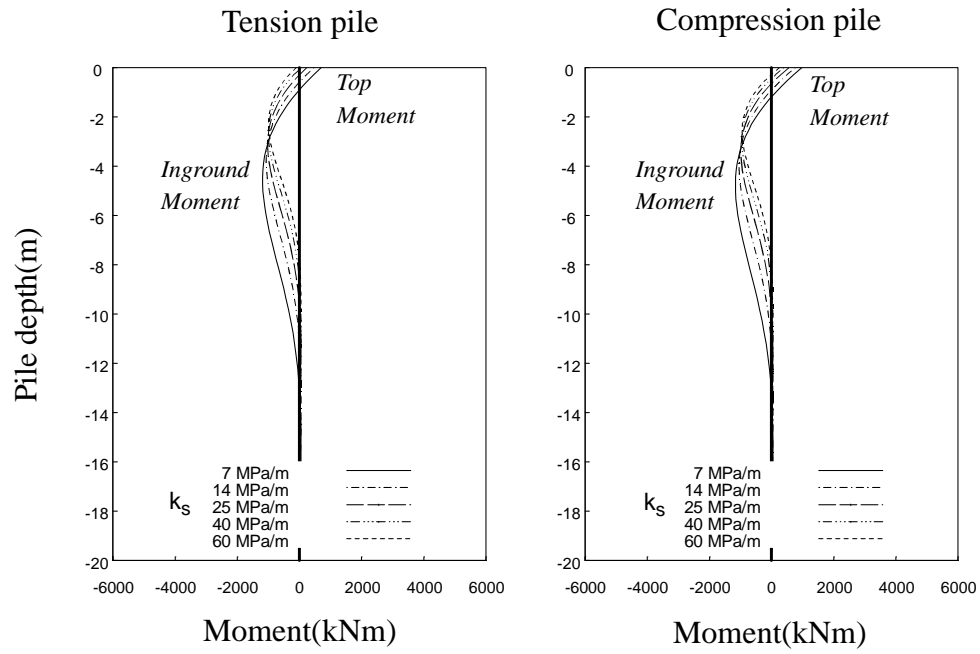
Figure 2.22: Pile moment of linear analysis($L_c/D_c = 7.5$, no pilecap restraint)

Tension pile

Compression pile
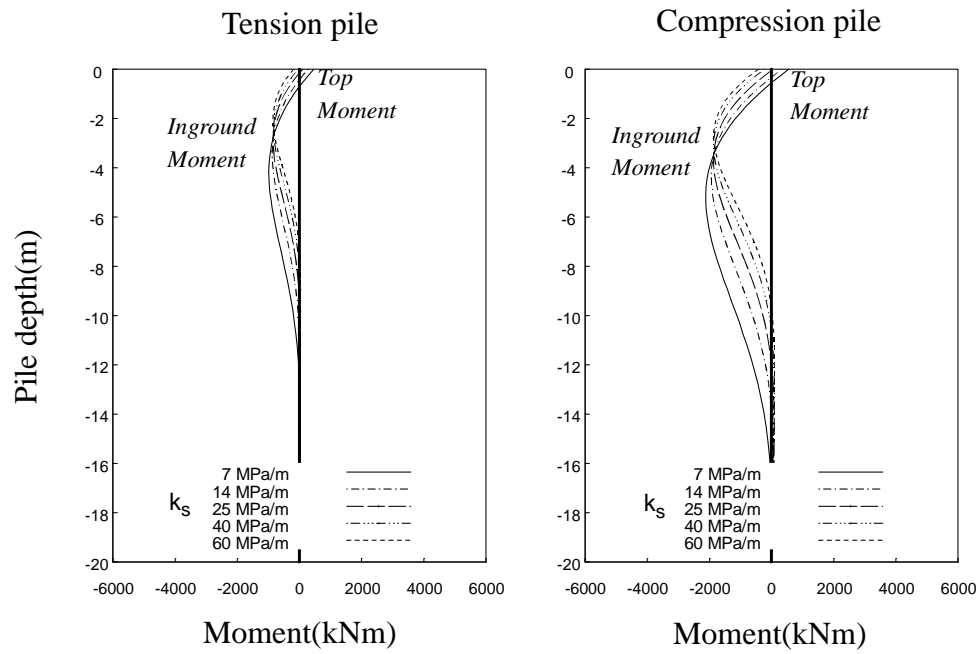
Figure 2.23: Pile moment of nonlinear analysis($L_c/D_c = 7.5$, no pilecap restraint)

Tension pile   Compression pile
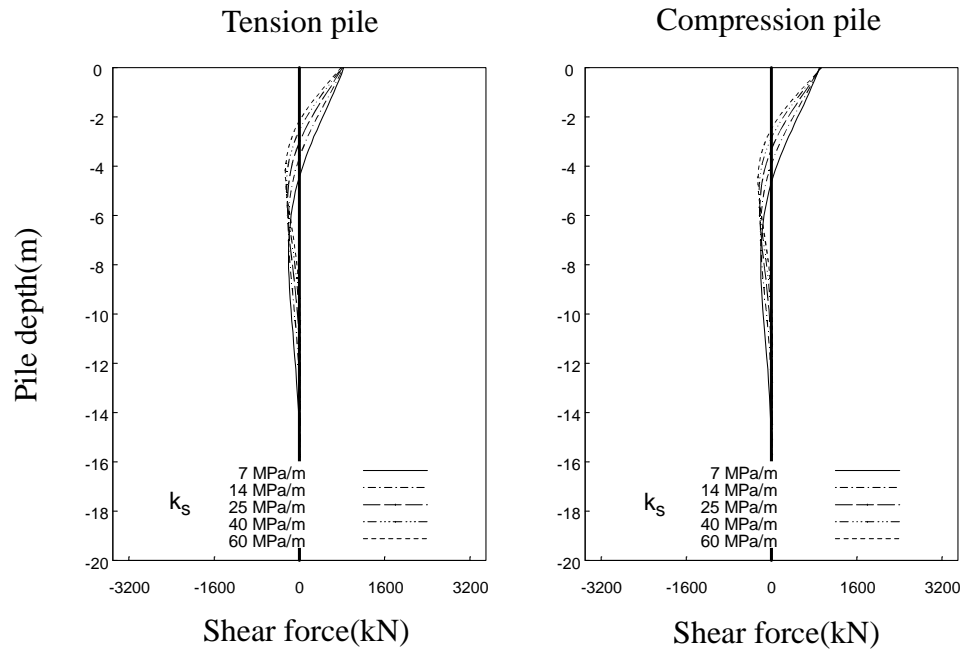
Figure 2.24: Pile shear force of linear analysis(L_c/D_c = 7.5, no pilecap restraint)

Tension pile   Compression pile
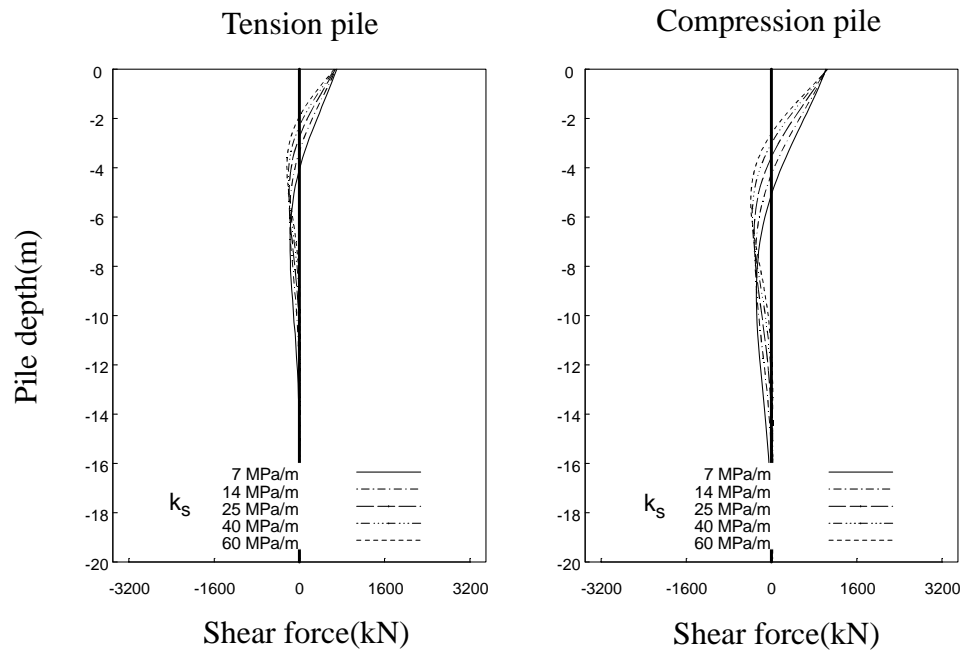
Figure 2.25: Pile shear force of nonlinear analysis(L_c/D_c = 7.5, no pilecap restraint)

Tension pile   Compression pile
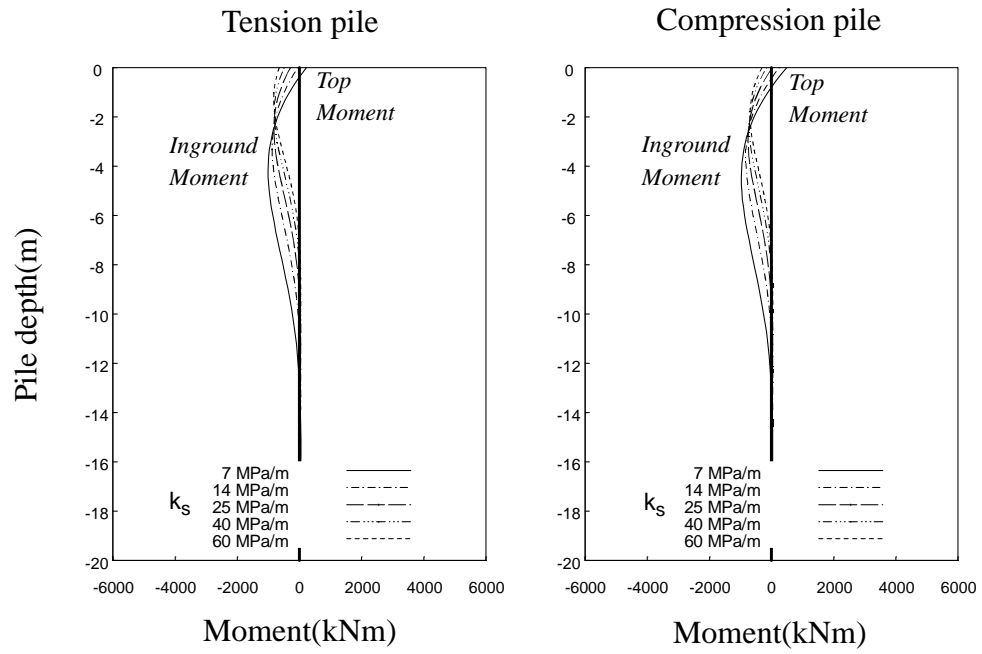
Figure 2.26: Pile moment of linear analysis(L_c/D_c = 7.5, pilecap restraint)

Tension pile   Compression pile
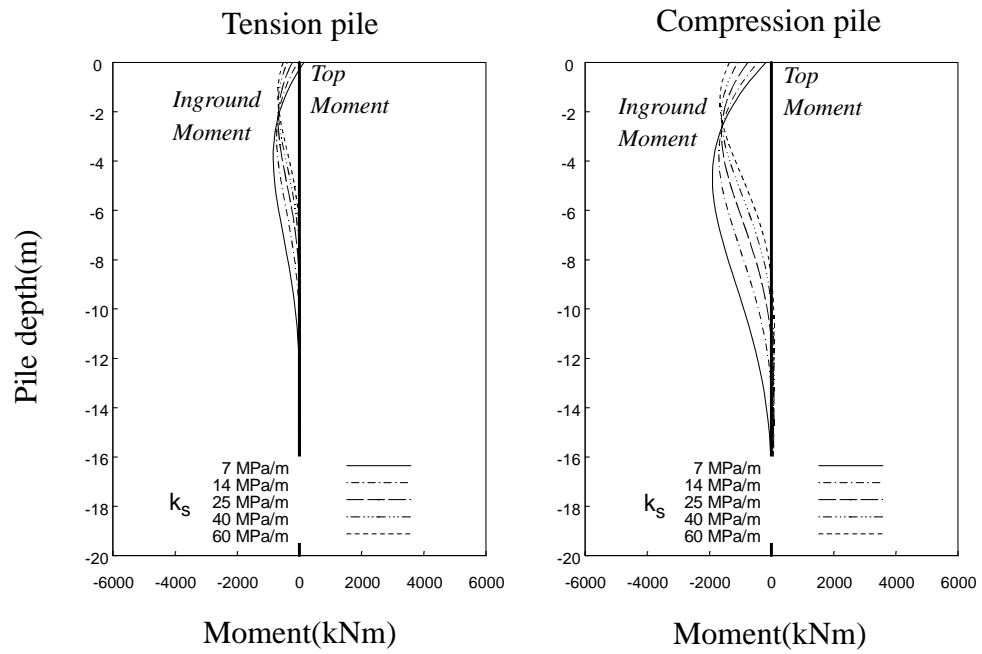
Figure 2.27: Pile moment of nonlinear analysis(L_c/D_c = 7.5, pilecap restraint)

Tension pile
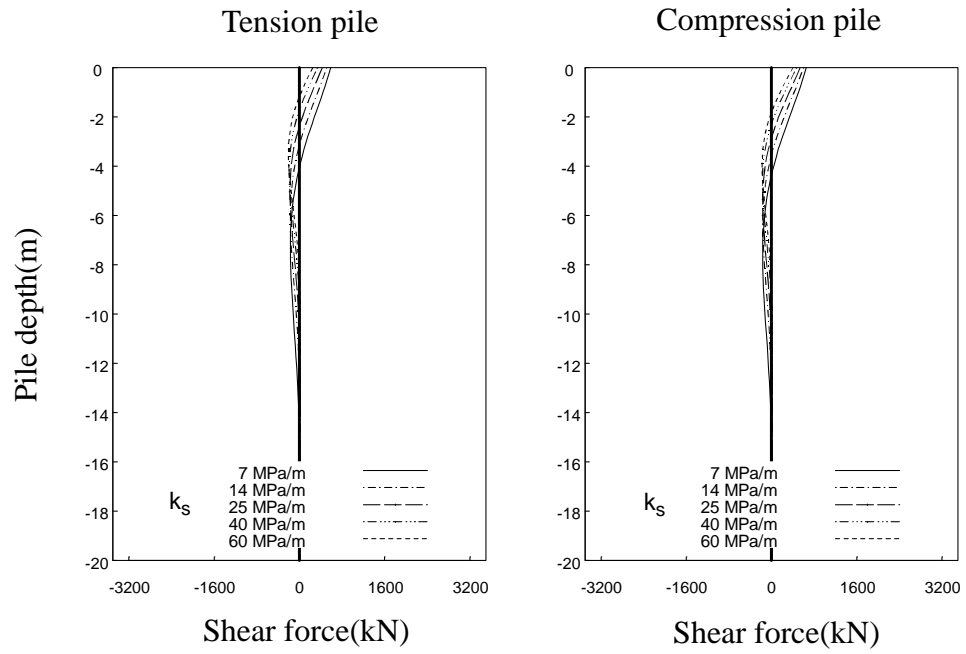
Compression pile

Figure 2.28: Pile shear force of linear analysis(L_c/D_c = 7.5, pilecap restraint)

Tension pile
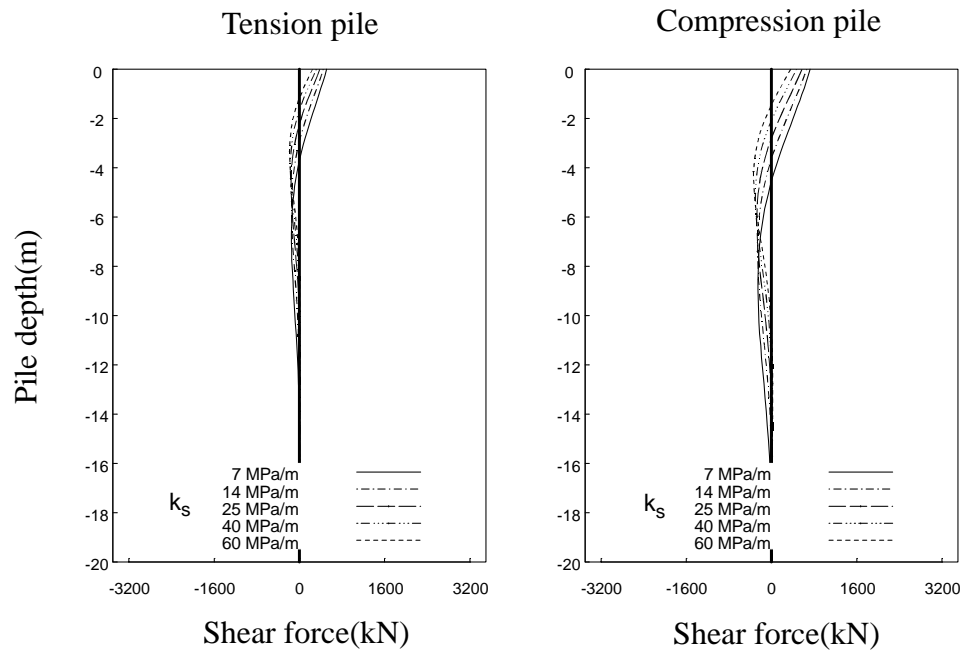
Compression pile

Figure 2.29: Pile shear force of nonlinear analysis(L_c/D_c = 7.5, pilecap restraint)

41
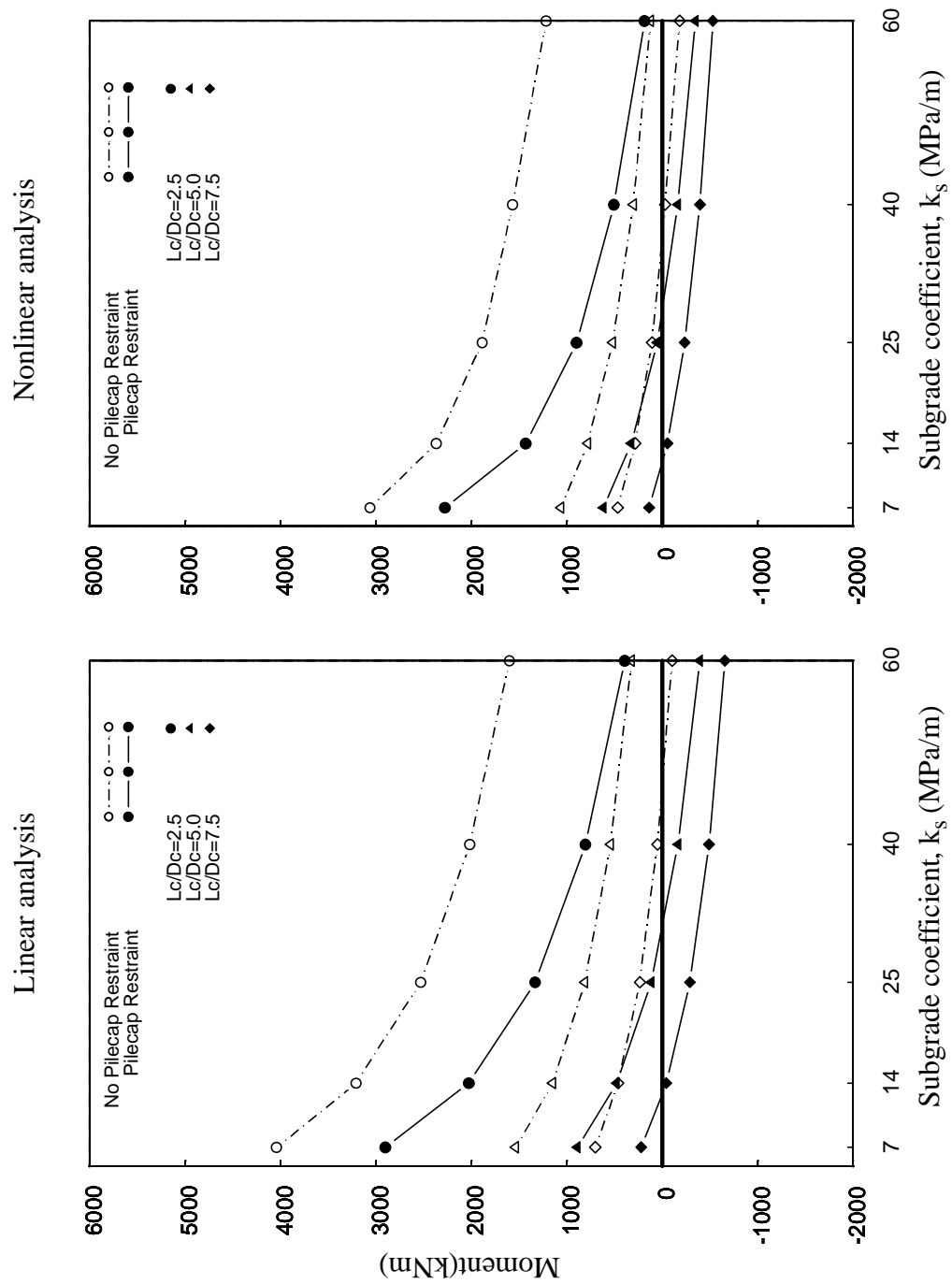
Figure 2.30: Tension pile top moment
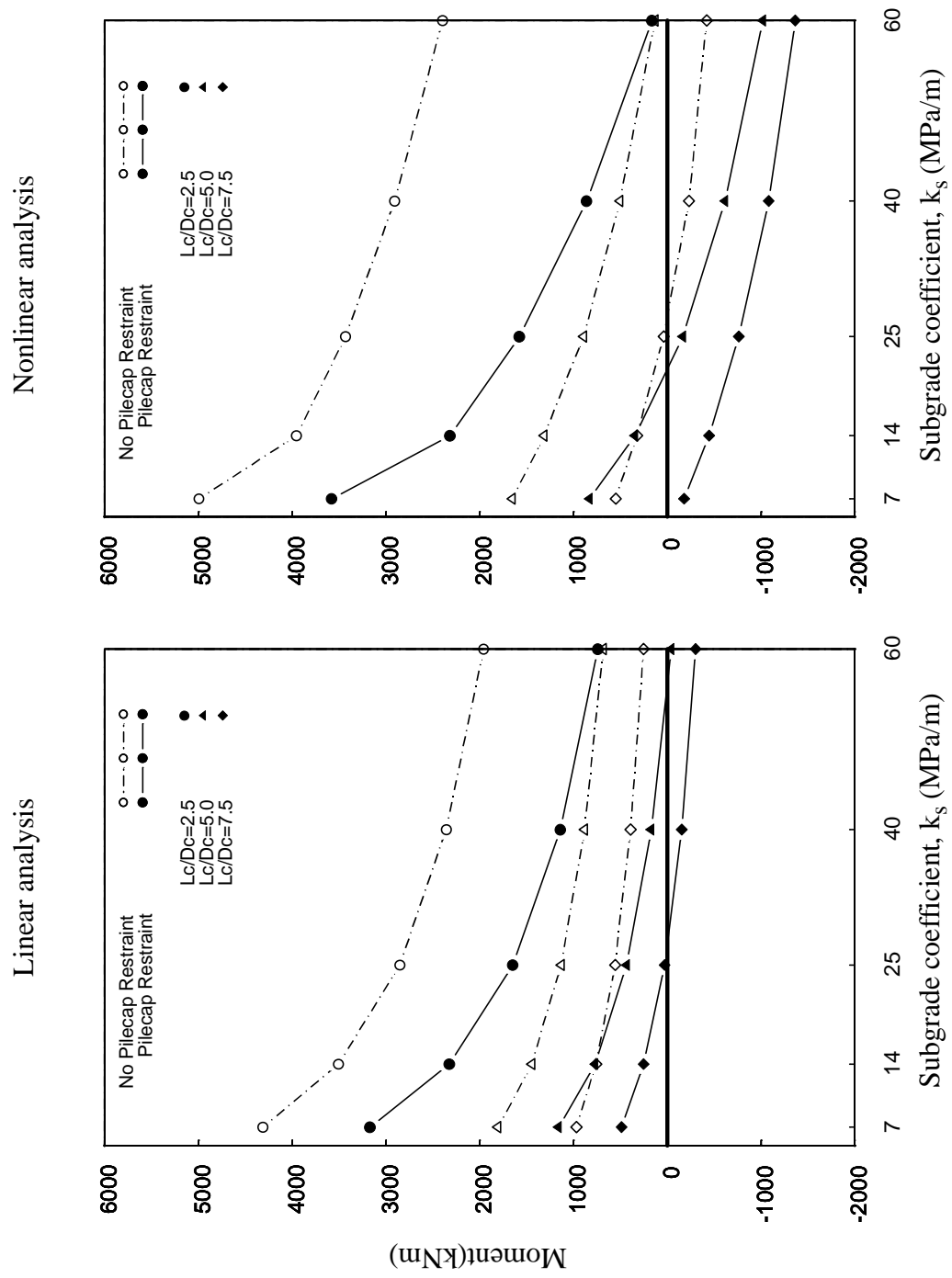
Figure 2.31: Compression pile top moment
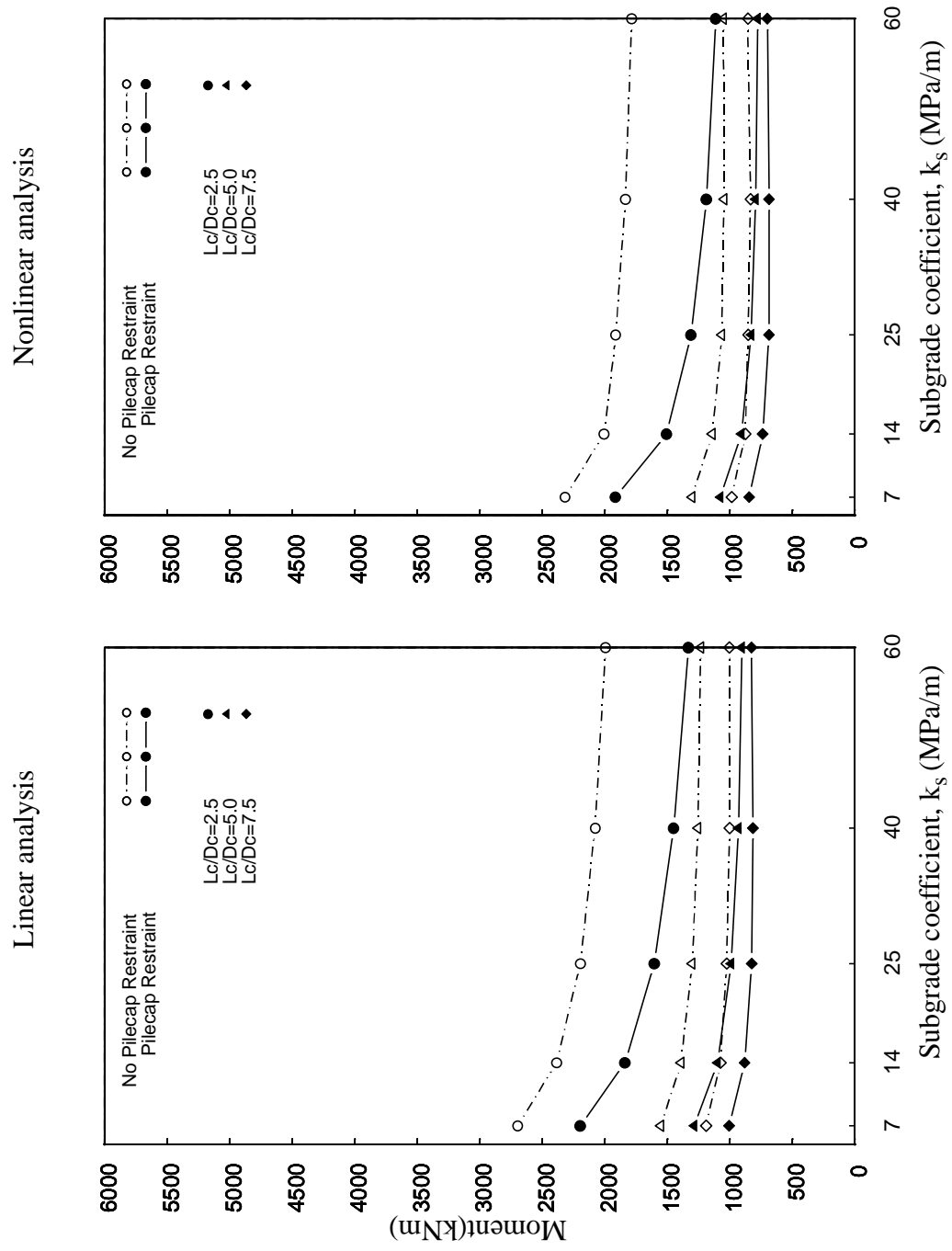
Figure 2.32: Tension pile maximum In-Ground moment
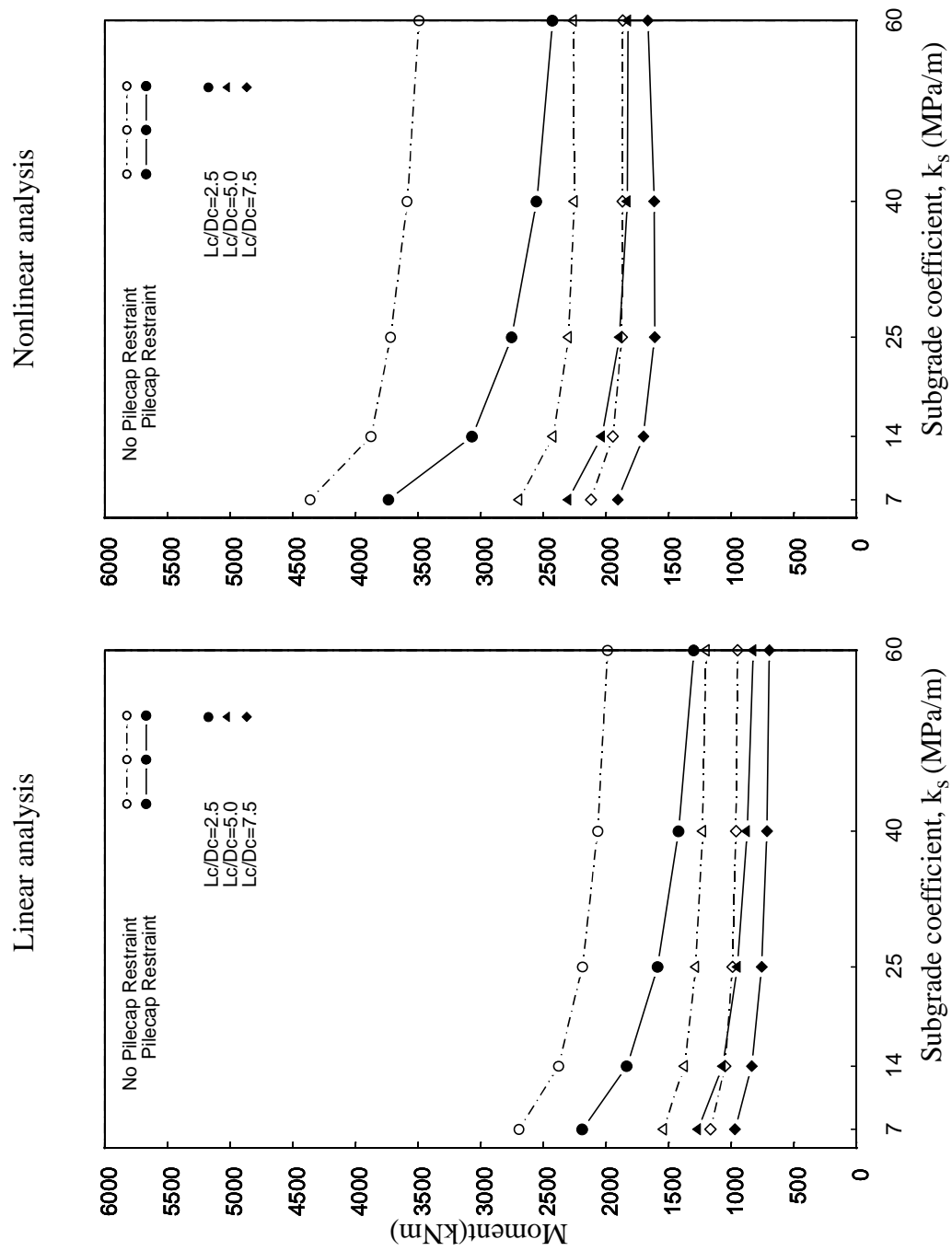
Figure 2.33: Compression pile maximum In-Ground moment
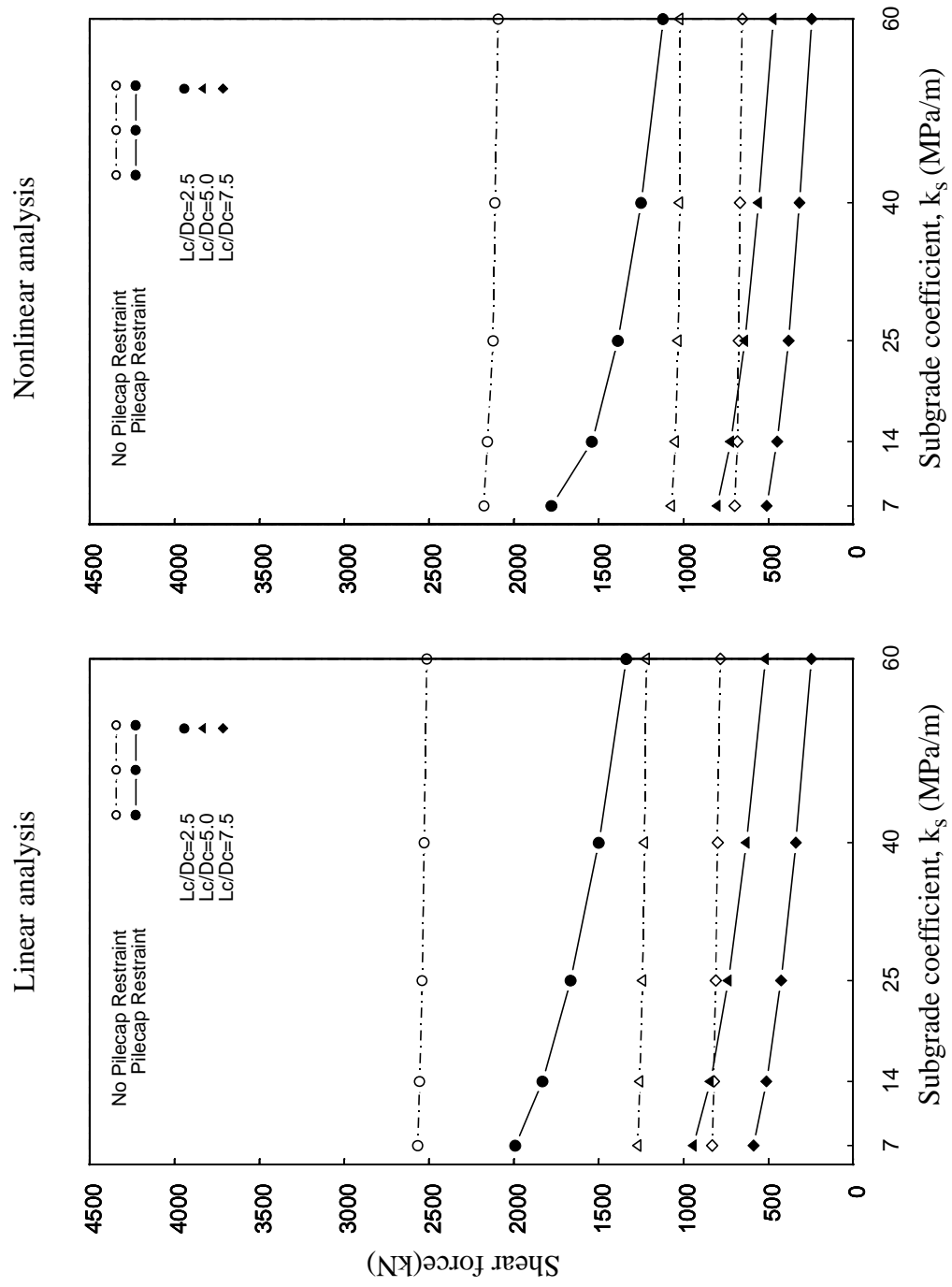
Figure 2.34: Tension pile top shear force

46
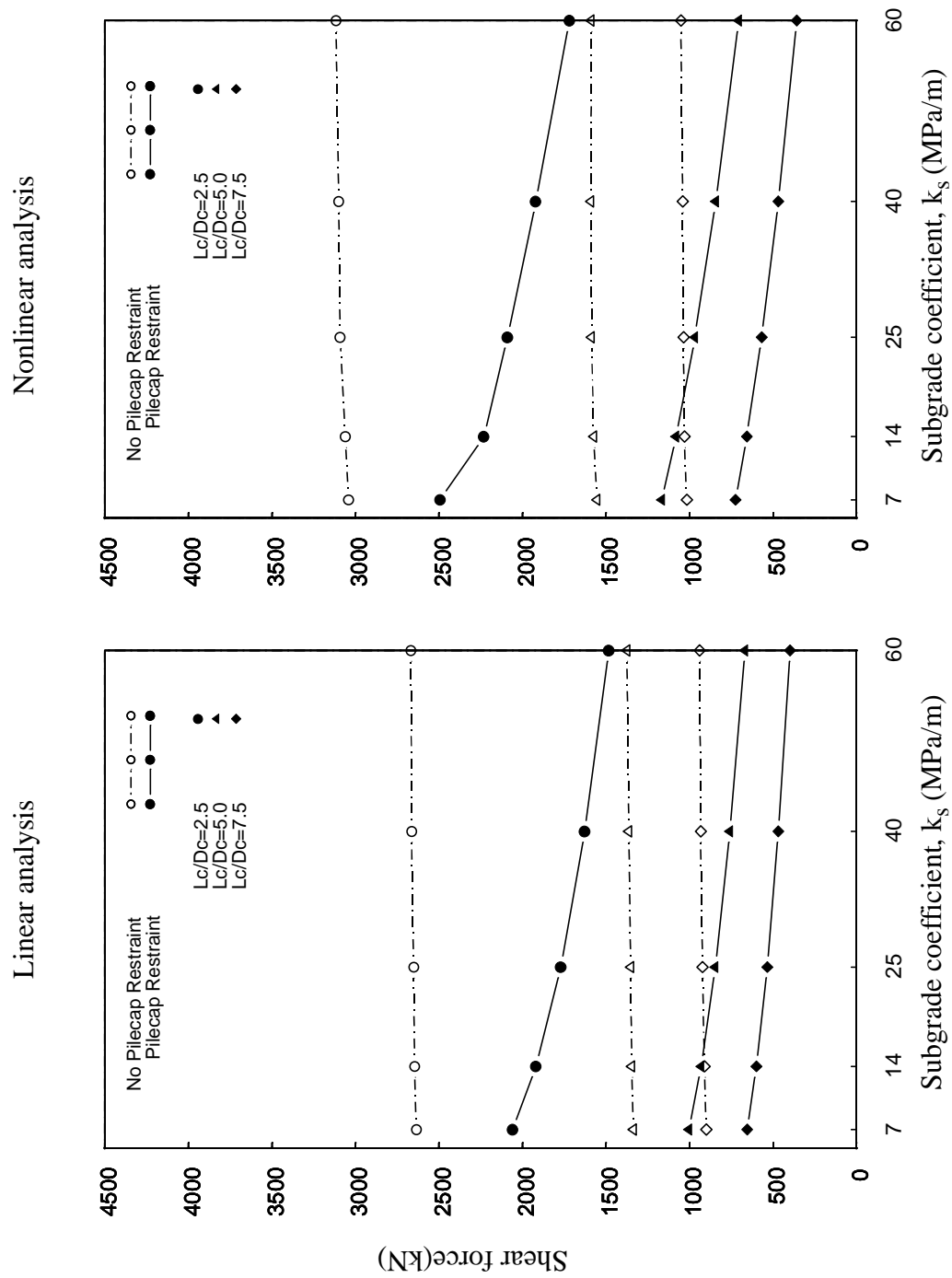
Figure 2.35: Compression pile top shear force
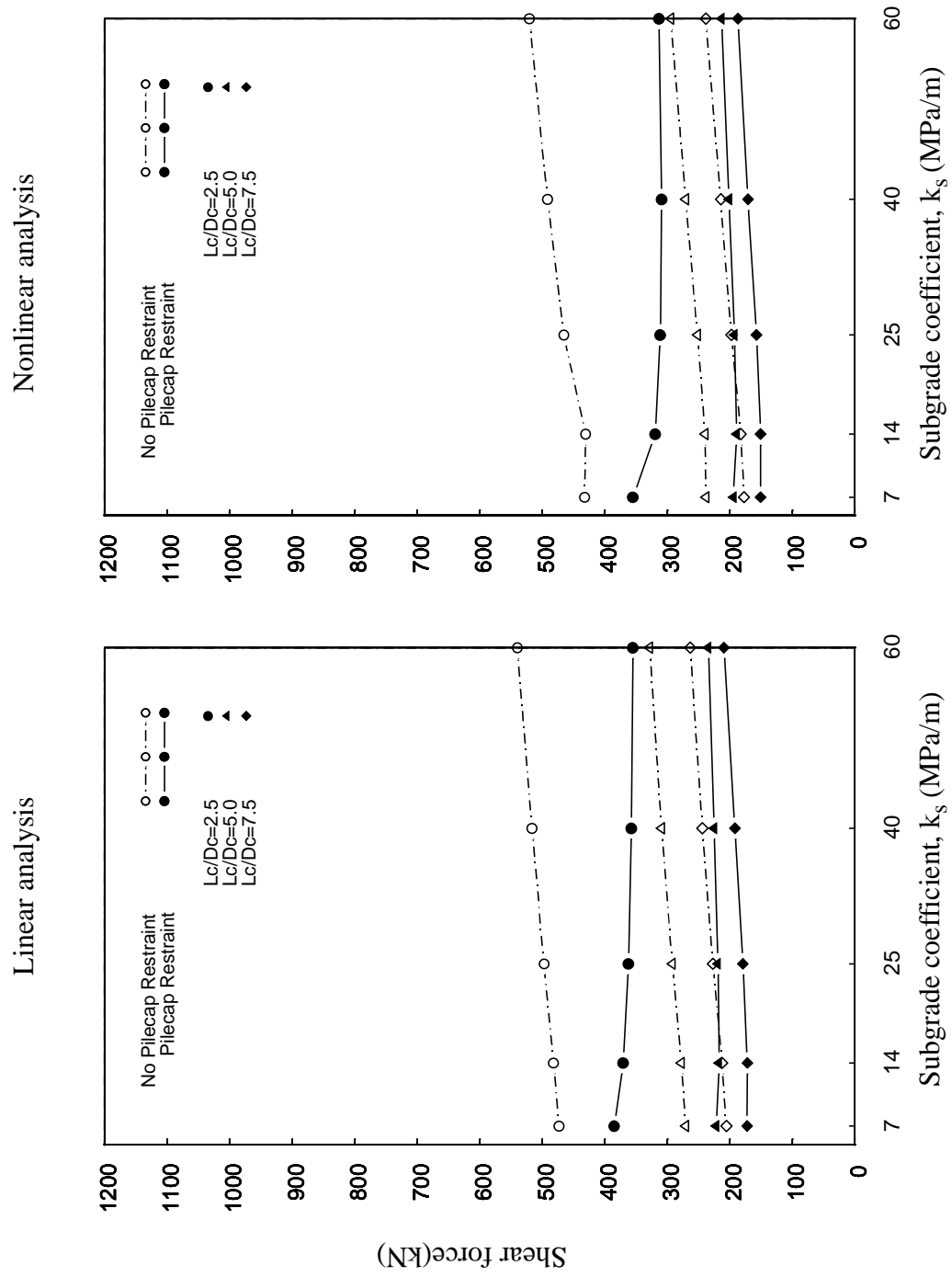
Figure 2.36: Tension pile maximum In-Ground shear force
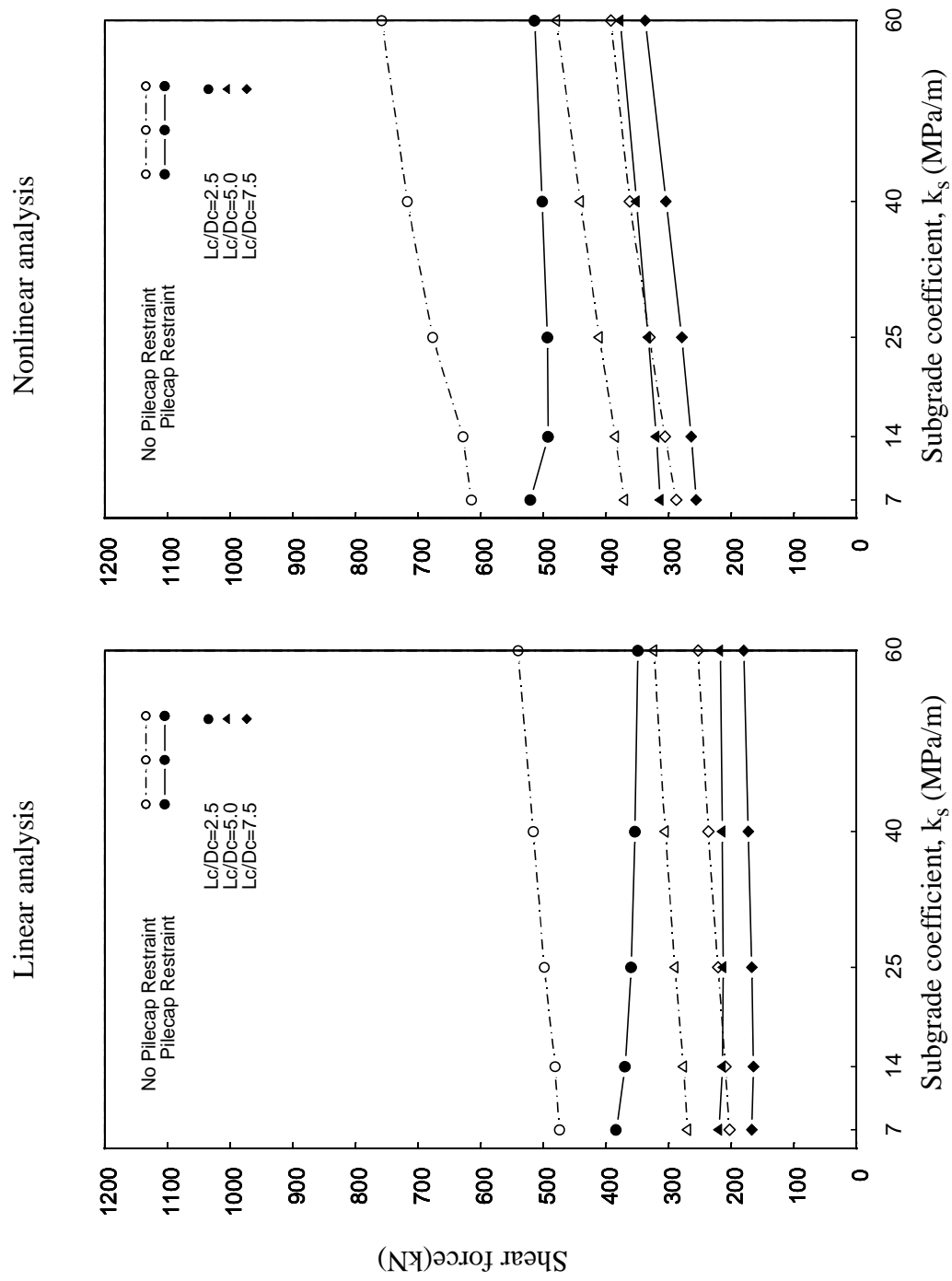
Figure 2.37: Compression pile maximum In-Ground shear force

49
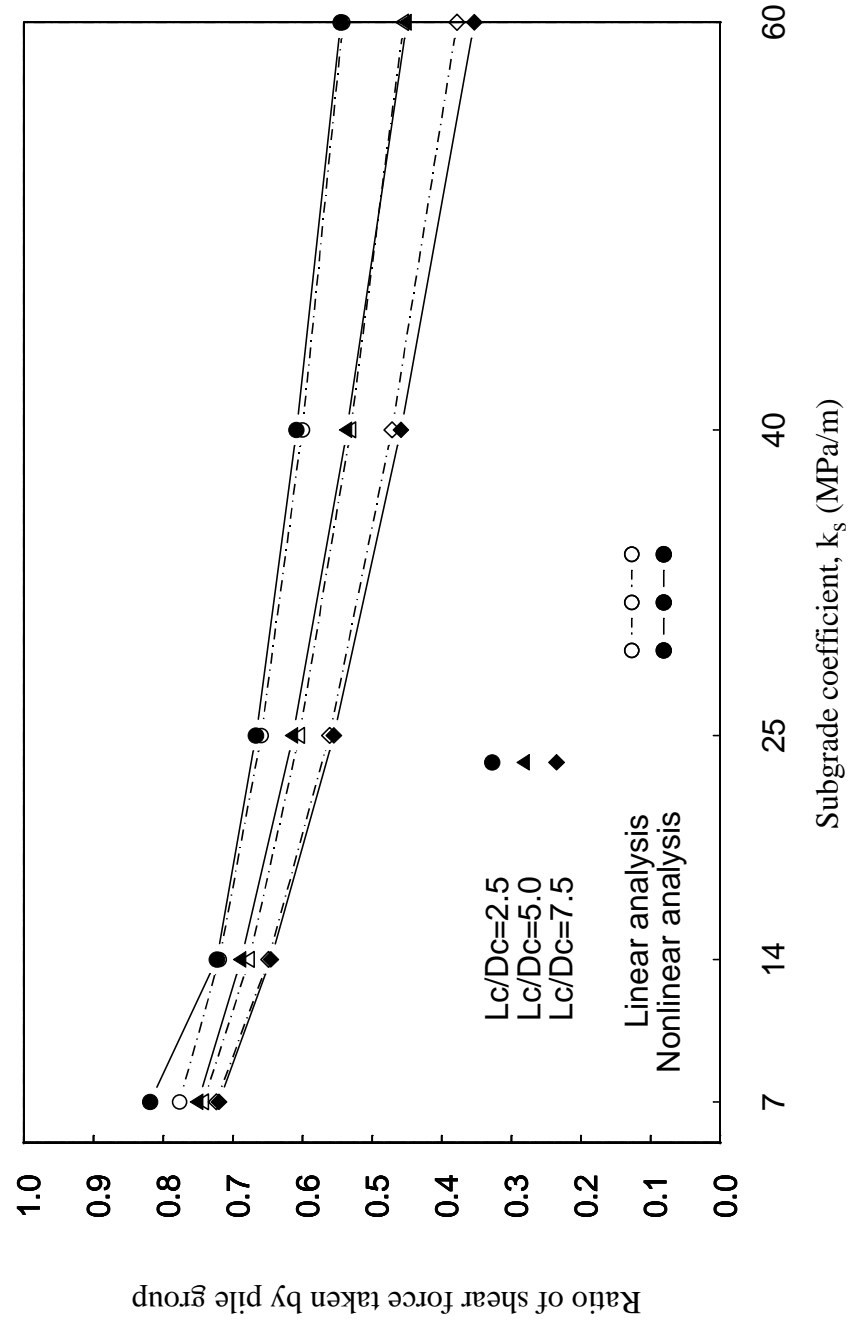
Figure 2.38: Effect of pilecap passive soil pressure on pile shear force

Chapter 3: Design Procedure for Test Units

3.1 Introduction

The modeling, design and test set-up for the experimental testing of units CFPS1 and CFPS2 conducted as part of this research are presented in this chapter. The main difference between these two units was the reinforcement type and amount. The first unit, CFPS1, was designed with conventional deformed bars for reinforcement. The second unit, CFPS2, differed from CFPS1 in that headed deformed bars were used as reinforcement except for the column and pile transverse reinforcement.

The aims of the experimental program were to examine :

1) The distribution of force between compression and tension piles

2) The response with an elastic pile system

3) The response with an inelastic pile system

4) The design concepts for column/footing and pile/footing joints

5) The design concepts for pilecap reinforcement

The differences between 2) and 3) were obtained by testing the units first with pilecap restraint, which reduced the shear force and the moments in the piles. Later the units were tested without pilecap restraint, which increased the pile moments to the extent that pile plastic hinge formation was expected.
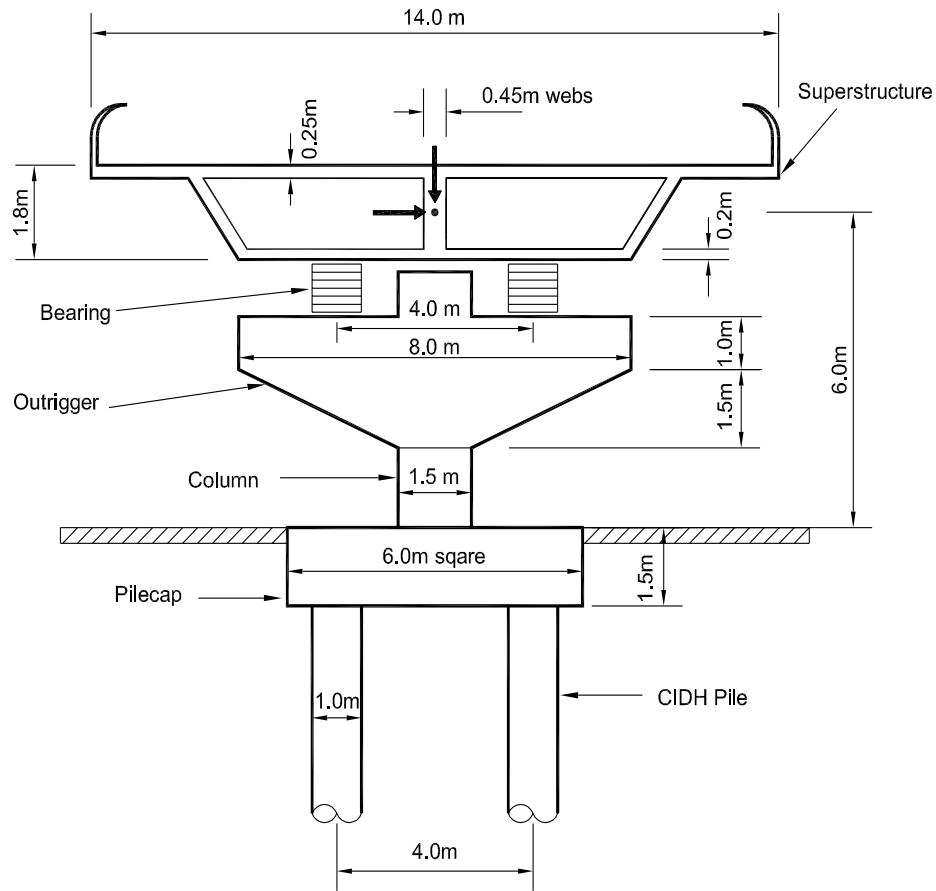
Figure 3.1: Prototype of Test Units

3.2 Prototype Structure

The pier shown in Figure 3.1 was chosen as the prototype structure for building the test units. This prototype had been set as an example for comparative analysis at the 2nd International Workshop on Seismic Design of Bridges[19]. The prototype consisted of four CIDH piles, a pilecap, a single column and a superstructure. The reinforcement details of the prototype were not utilized in the design of the test units.

3.3 Laboratory Test Model

In order to examine the seismic performance of a CIDH pile supported footing under laboratory conditions, the test specimens were built at one-half scale and without the superstructure. Although the overall dimensions of the prototype structure were considered in modeling the test units, several modifications were necessary to achieve the objective of the research study. The following modifications to the prototype were considered.

6) The superstructure was removed. To emulate the gravity load in the superstructure, both test units were post-tensioned through the column and footing to the strong floor.

7) The bent cap at the top of the column was also removed. The column was designed as a prismatic member to the load stub.

The modifications described above and the dimensions of the laboratory model are shown in Figures 3.2 and 3.3.

3.4 Test Set-Up

When establishing a suitable test set-up under the laboratory conditions, the following considerations were taken.

A gravity load of 2002 kN was applied to the test units by means of post-tensioning tendons which were anchored at the top of the load stub and ran vertically through a duct embedded at the center of the column and footing. The other ends were anchored to the test base which was tied down to the strong floor for unit CFPS1. Fifteen - ϕ15 mm strands were used for post-tensioning. To achieve the target post-tensioning force on the
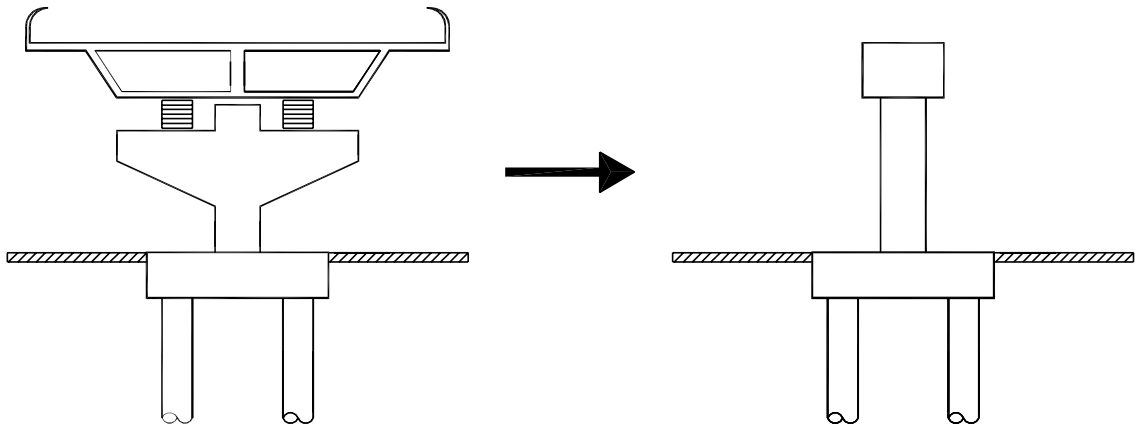
Figure 3.2: Modification of the Prototype Structure

day of testing, the post-tensioning was carried out in two steps. First, 20% of the target

force was applied for the lock-off of the tendons to the anchorage device and the full

target force was applied at the begining of the test. The applied force was monitored

during the test and adjusted whenever necessary to keep it within a reasonable margin of

the target force.

To simulate the horizontal seismic forces for the orthogonal and diagonal directions

with respect to the pilecap configuration in plan view, two servo-controlled hydraulic

actuators were mounted on the two perpendicular sides of the load stub at the column

head and force was applied cyclically by directional combinations of actuator forces as

was shown in Figure 3.4.
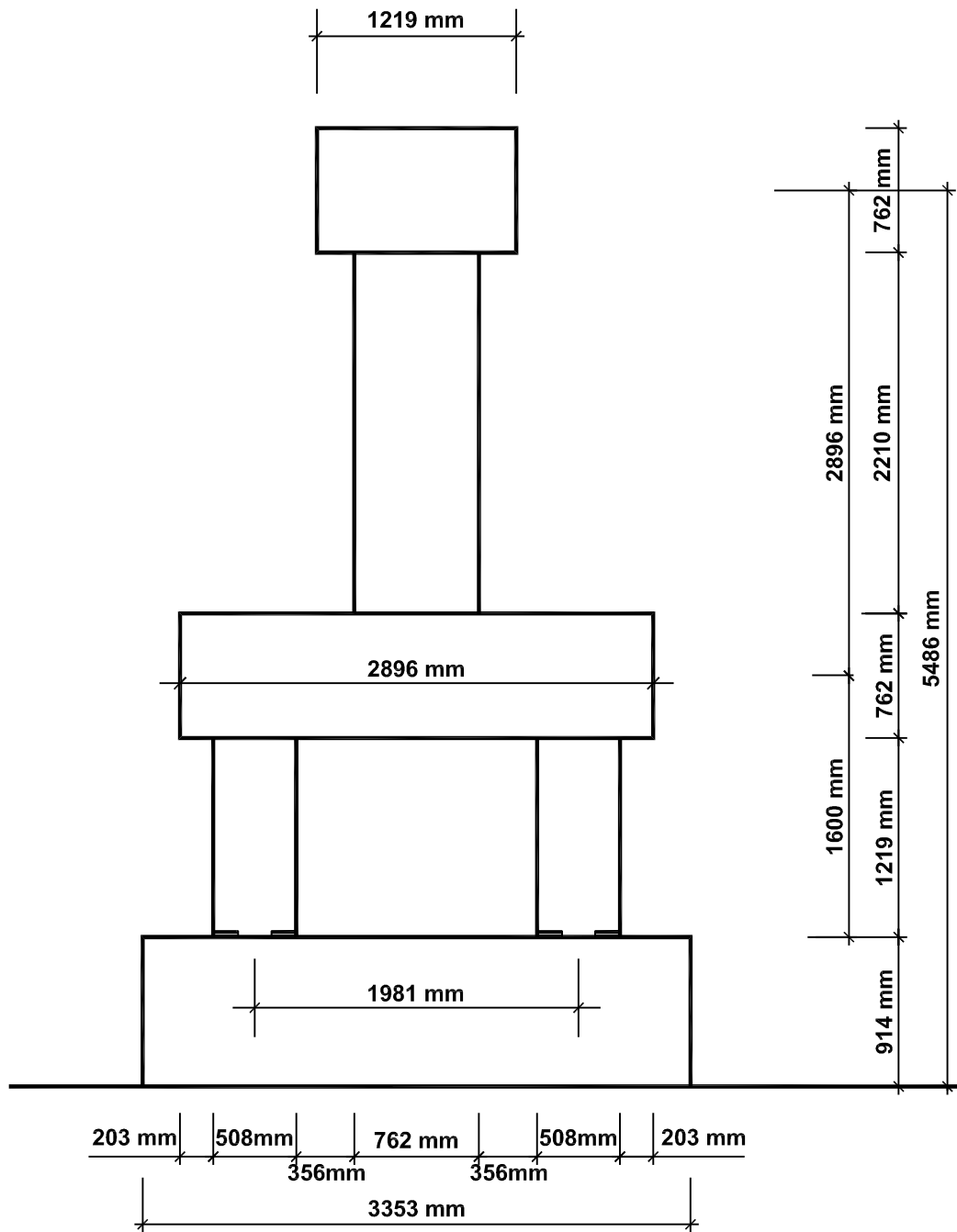
Figure 3.3: Laboratory model dimension of unit CFPS1
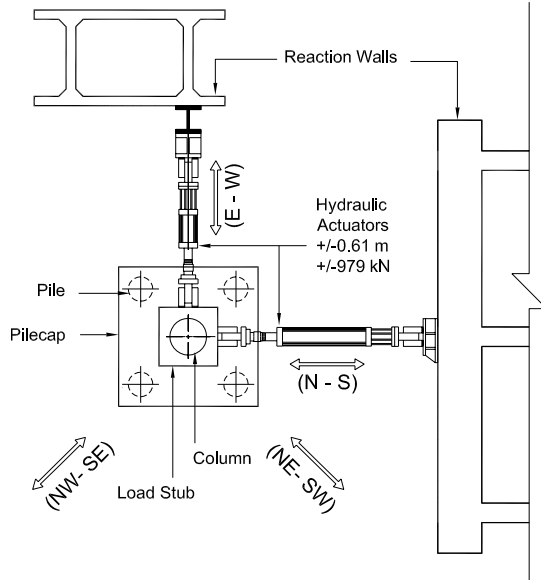
Figure 3.4: Plan view
of column top actuators
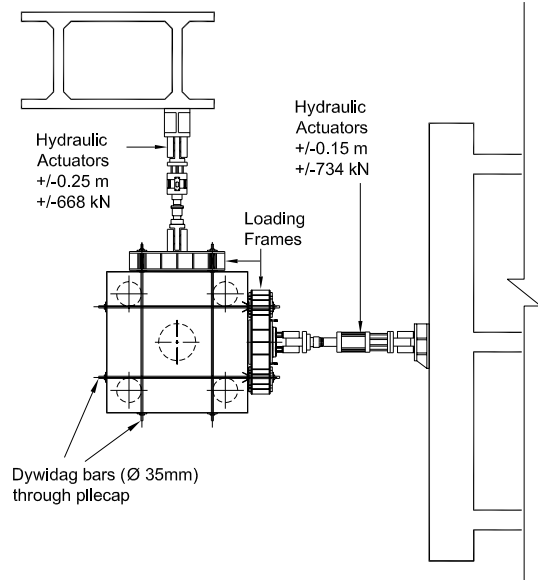
Figure 3.5: Plan view
of pilecap actuators

It was also necessary to emulate a passive restraint mechanism on the pilecap sides to study the effect of the passive soil pressure on the pilecap. To do this, two additional actuators were mounted on the two pilecap sides which were also perpendicular to each other in same configuration with the actuators on the column load stub as illustrated in Figure 3.5. The soil passive pressure on the pilecap sides in the opposite direction to the seismic load was modeled by a two point load representing the resultant force of soil passive pressure. This was achieved by four Dywidag bars running through the pilecap. One end of the Dwidag bars was end-plated using two pieces of steel plate at the loading points of the resultant force of soil passive pressure and the other ends were connected to the loading beams which were attached to the pilecap actuators. For the push directional loading, the resultant force of passive soil pressure on the opposite sides of the pilecap was activated by the pilecap actuators pulling the Dywidag bars endplated at the

resultant points of soil passive pressure. Likewise, the resultant force of passive soil pressure on the pilecap sides of actuators was activated by the pilecap actuators pushing the two steel plates at the points of the two resultant forces of soil passive pressure through the loading beams which were attached to the pilecap actuators.

To model the long piles embedded in the ground, the piles terminated at the theoretical position of contra-flexure points in pin details as described in section 3.5.5. To emulate the vertical stiffness of the tension pile-soil structure interaction, 60mm diameter mild steel rods with lengths of 600mm were embedded in the piles. The dimensions of the rod were determined by converting the vertical stiffness of the pile-soil structure interaction estimated by analytical work into the axial stiffness of the steel rod using the formula of axial stiffness, EA/L where E is the Young's modulus of steel, A and L are the sectional area and the length of the rod. The numerical calculation for this is given in section 3.5.5. The rod was debonded by applying grease on its surface and end-plated for anchoring with 200mm diameter and 25.4mm thick steel plate disk ribbed with four pieces of 25.4mm thick steel. For the compression piles no specific modelling was done for the vertical stiffness of the compression pile-soil structure interaction due to the difficulty of emulating the pile endbearing stiffness. Hence, the piles in the compression side were supported by the test base directly considering the large magnitude of the vertical stiffness of the compression pile-soil structure interaction.

Table 3.1: Critical loading conditions for the design of actions

Structural member actions to be designed	Critical loading phase : Loading direction / Pilecap restraint condition	Max. applicable lateral load
Pilecap Negative Bending	Loading Phase 2 : Orthogonal / No Pilecap Restraint	845 kN
Pilecap Positive Bending	Loading Phase 1 : Diagonal / Pilecap Restraint	934 kN
Pilecap Shear Transfer	Loading Phase 1 : Orthogonal / Pilecap Restraint	934 kN
Pile - Pilecap Joint	Loading Phase 2 : Diagonal / No Pilecap Restraint	801 kN
Pile Bending, Shear and Confinement	Loading Phase 2 : Diagonal / No Pilecap Restraint	801 kN
Pile-Test Base Pin Connection	Loading Phase 2 : Diagonal / No Pilecap Restraint	801 kN

3.5 Design of The Test Units

In designing the test units state-of-the-art design procedures were adopted[26]. For desirable seismic response the units were designed so that a plastic hinge would develop at the bottom of the column. Using capacity design principles, the pilecap and joints were designed for the maximum possible forces that would develop in the column plastic hinge, considering potential strain hardening and uncertainties in material strengths. With assumed material strengths f'_{ce} = 27.6 MPa and f_{ye}= 455.1 MPa which corresponds to $1.1f_y$ in accordance with the recommendations given by Priestley [26], the test units were designed so that the piles would remain elastic in Loading Phase 1 which is the loading case with pilecap resistance and would perform inelastically at Loading Phase 2 which is the loading case without pilecap resistance. Since there were orthogonal and diagonal loading directions with two conditions of pilecap restraints in each loading direction, four loading cases were considered for the design of the test units. Table 3.1 shows the critical loading phase for each structural member action to be considered. Loading Phases 1 and 2 are defined for the loadings with and without pilecap restraint, respectively. Pilecap positive flexural design and the checking of the direct shear transfer of the pilecap were done for Loading Phase 1. Corresponding maximum applicable

lateral load, 934 kN, is the load required to form a plastic hinge of the column which is carefully designed considering the capacity of the actuators, 979 kN, mounted on the column load stub. The critical loading condition for the pilecap negative bending was determined as orthogonal direction loading without pilecap restraint. The design of unit CFPS1 was done first. Unit CFPS2 was designed after the test on unit CFPS1 had been completed. This unit incorporated minor modifications except pilecap reinforcement, based primarily on the experience gained from testing the first unit, and used headed reinforcement to improve anchorage of reinforcement. The design of unit CFPS2 is described in Section 5.2.

3.5.1 Column design

a) **Longitudinal Reinforcement**

Since the maximum load capacity of the actuators at the top of the column was 979 kN, the column longitudinal reinforcement ratio of $\rho_l = 2.57\%$ provided by 23 bars of 25.4mm diameter was determined so that the corresponding maximum shear force of the column would not exceed this value. In determining the column longitudinal reinforcement ratio, the gravity load of 2002 kN corresponding to the column axial load ratio of 0.16 was arbitrarily assumed. The maximum shear force resulting from the moment at the development of the flexural overstrength of the column plastic hinge was :

$$V_c^{\circ} = 934 \text{kN} \tag{3.1}$$

which was about 5% less than the maximum load capacity of the actuators at the top of the column.

b) Confinement

When determining the appropriate quantity of transverse reinforcement, it was ensured that an adequate lateral confinement was provided in the plastic hinge region of the column so that a dependable ductile performance could be obtained for the units. The volumetric confinement ratio, ρ_s, used for the circular columns conformed with the seismic design requirements for California bridges[2] :

$$\rho_s = 0.16\frac{f'_{ce}}{f_{ye}}\left[0.5 + \frac{1.25P}{f'_{ce}A_g}\right] + 0.13(\rho_l - 0.01) \tag{3.2}$$

where f'_{ce} is the expected unconfined concrete compressive strength, f_{ye} is the expected yield strength of column longitudinal reinforcment, P is the axial load at the column plastic hinge region, A_g is the gross area of the section of the column and ρ_l is the column longitudinal reinforcement ratio. The value of $\rho_s = 0.0112$ provided by 12.7mm diameter spiral with 63.5mm spacing exceeded the value of $\rho_s = 0.0089$ obtained from Eq. (3.2). With the provided transverse reinforcement in the plastic hinge region, the displacement ductility capacity of the column was 10.3.

c) Anti-Buckling Considerations

To ensure adequate transverse reinforcement is provided to avoid premature buckling of the longitudinal reinforcement, the buckling mode over several layers of transverse reinforcement was checked by Eq. (3.3) according to the design requirement as recommended in references[2, 26].

$$\rho_{s, min} = 0.0002n = 0.0046 < \rho_s = 0.0089 \tag{3.3}$$

$$V_c = k\sqrt{f'_{ce}}\ A_e$$
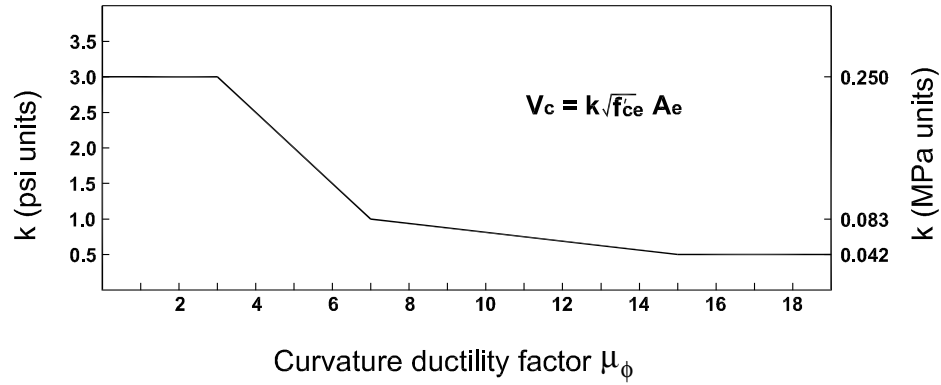
Figure 3.6: Design strength of concrete shear based on section curvature ductility

where n is the number of longitudinal column bars, which in the column in unit CFPS1 equaled n = 23.

An explicit check for the bar buckling between adjacent transverse reinforcement was not carried out because this bar buckling mode is already accounted for in Eq. (3.2).

d) Shear Requirements

In order to avoid undesirable shear failure in the column, the column's shear strength was checked with the transverse reinforcement provided for confinement using a recently developed approach[26]. In this method the three independent and additive mechanisms contribute to the nominal shear strength, namely the concrete shear resisting mechanism, the steel truss mechanism and the axial load :

$$V_n \ = \ V_c + V_s + V_p \tag{3.4}$$
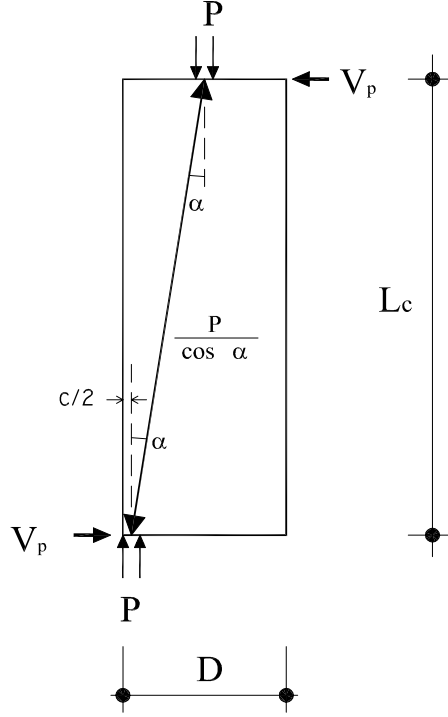
Figure 3.7: Contribution of axial force to shear strength in single curvature columns[26]

where V_n is the nominal shear resistance, V_c is the concrete component, V_s is the resistance from the truss mechanism by transverse reinforcement, and V_p is the contribution of the axial compression.

V_c is considered a function of curvature ductility, see Figure 3.6, and represented as Eq.(3.5).

$$V_c = k\sqrt{f'_{ce}}A_e \tag{3.5}$$

where A_e is the effective shear area(assumed to be $0.8A_g$), and k is an empirical value that depends on the member curvature ductility μ_ϕ. The magnitude of k was conservatively set as the minimum value 0.042 and the corresponding minimum V_c was 80 kN.
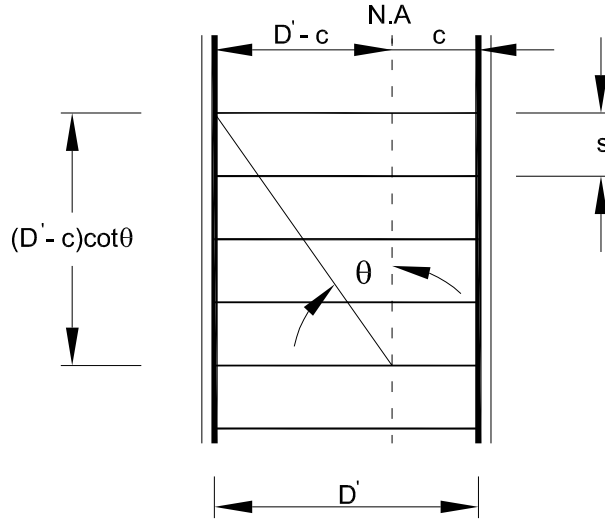
Figure 3.8: Model for shear resistance due to a truss mechanism

The shear strength from the axial load contribution was estimated based on the recommendation [26] that the V_p component be obtained in accordance with Eq.(3.6) as shown in Figure 3.7.

$$V_p = 0.85P \cdot \tan\alpha \qquad (3.6)$$

For a member of single curvature such as the column of the test units, α is the angle formed between the column axis and the strut from the point of load application to the point of compressive stress resultant at the critical section of the column plastic hinge, see Figure 3.7. The point of compressive stress resultant can be approximated to be c/2 where c is the depth of compression stress block. In the above expression, the factor 0.85 accounts for the scatter observed [36]. The contribution to the shear strength due to axial load, calculated using Eq. (3.6), was 169 kN.

The truss mechanism component V_s by column spiral was calculated using Eq. (3.7), which reflects the truss contribution shown in Figure 3.8.

$$V_s = \frac{\pi}{2} \times \frac{A_h f_{yh}(D' - c)}{s} \cot\theta \qquad (3.7)$$

where, D' is the core dimension, from center to center of the spiral reinforcement. A_h and f_{yh} are the sectional area and yield stress of the spiral reinforcement, respectively. In Eq. (3.7), the angle of the inclined shear cracking to the column axis was taken as $\theta = 35^o$ according to the recommendations given by Priestley et al. [26]. The development of cracking angles steeper than the $\theta = 45^o$ assumed by Caltrans' standard shear equation[6] is well observed in experimental results[26]. The shear strength of the truss mechanism from the transverse reinforcement provided for confinement was 885 kN.

From Eq. (3.4), the nominal shear capacity of the column was :

$$V_n = 80 + 169 + 885 = 1134 \text{kN} \qquad (3.8)$$

This is greater than the required shear strength given by Eq. (3.9) using shear strength reduction factor, $\phi_s = 0.85$:

$$\frac{V_c^{\circ}}{\phi_s} = \frac{934}{0.85} = 1099 \text{kN} \qquad (3.9)$$

which associated with the development of flexural overstrength at column plastic hinge.

3.5.2 Pile design

The piles of the two units were designed for the worst possible scenario which is loading in the diagonal direction without restraint being provided by the passive pressure

mechanism of lateral force resistance. Under this condition, pile plastic hinging was expected.

1) Longitudinal reinforcement and axial loads in piles

First, a longitudinal reinforcement ratio of 0.89% was determined so that piles would remain elastic in Loading Phase 1. This reinforcement ratio was determined through an iterative process, considering all possible loading scenarios assuming that lateral loading, when applied in the diagonal direction, resulted in no additional axial force being developed in the mid-piles. Thus, with this assumption the overturning moment is resisted by the extreme piles, which developed an axial force given by Eq. (3.10) :

$$T \ = \ C \ = \ \frac{F(L_c + h_f + L_p)}{L_f \sqrt{2}} \tag{3.10}$$

where T and C are the axial tension and compression force, respectively, developed in the piles from the lateral load only, F is the applied lateral load, L_c is the column height, h_f is the depth of the pilecap, L_p is the cantilevered pile length and L_f is the distance between piles which was 1.981m. Because the tension capacity of the longitudinal reinforcement in the piles was 818 kN, based on f_{ye}= 455.1 MPa, the maximum tension force in the piles, T_{max}, was limited to 756 kN when considering the moment induced in the pile at the pilecap face. Hence, from Eq.(3.10), the maximum possible lateral force at the column top that did not cause the piles to yield in tension was :
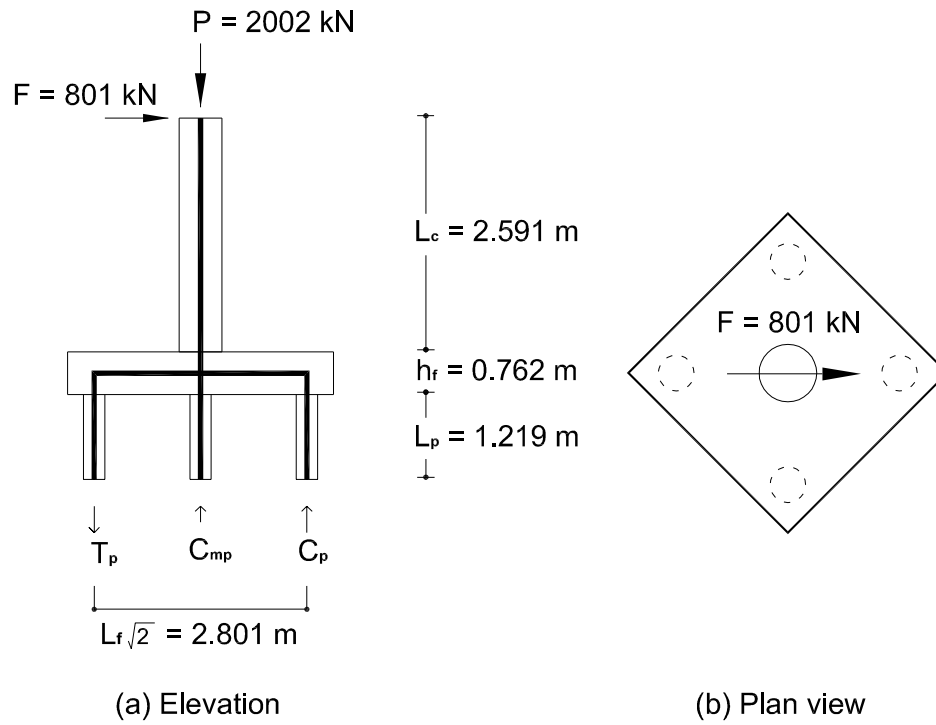
Figure 3.9: Diagonal direction loading without pilecap resistance for pile design
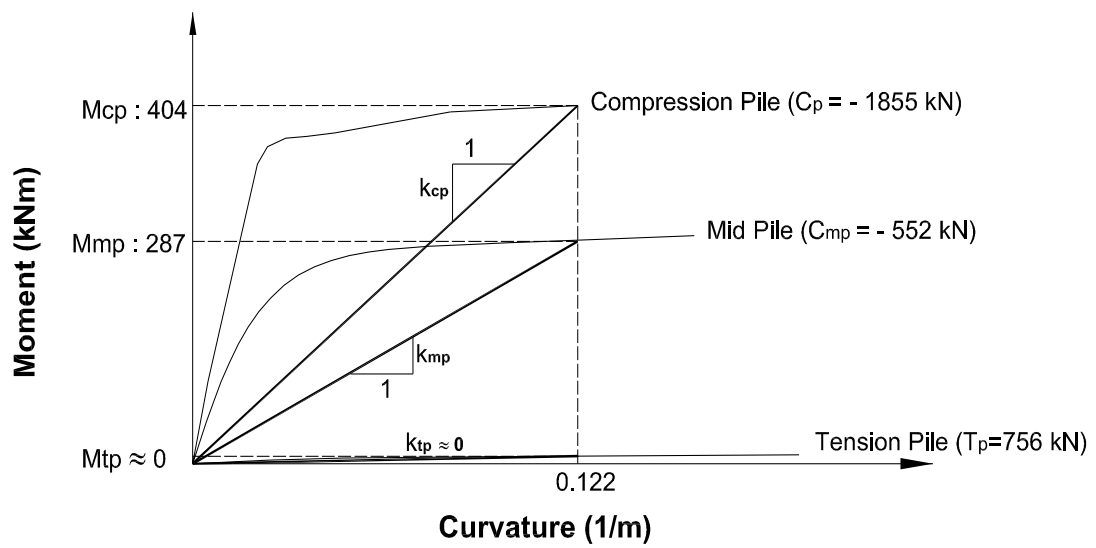
Figure 3.10: Partial moment-curvature responses for piles

66

$$F_{max} = \frac{(P_v + T_{max}) \times L_f \sqrt{2}}{(L_c + h_f + L_p)} = \frac{(552 + 756) \times 1.981 \sqrt{2}}{(2.591 + 0.762 + 1.219)} = 801 \text{kN} \qquad (3.11)$$

where, $P_v = P/4$ was the average axial force in the piles due to gravity load. This is illustrated in Figure 3.9. Therefore, solving Eq (3.10) with the value of Eq (3.11), the maximum pile compression force was :

$$C_p = P_v + \frac{F_{max}(L_c + h_f + L_p)}{L_f \sqrt{2}} \qquad (3.12)$$

$$= 552 + \frac{801(2.591 + 0.762 + 1.219)}{1.981 \sqrt{2}} = 1859 \text{kN}$$

2) Shear reinforcement

Removal of the pilecap lateral force resisting mechanism, emulating the passive soil pressure on the pilecap vertical face, was envisioned for Loading Phase 2 of the experimental program. The removal of this mechanism meant that lateral forces applied at the top of the column had to be resisted entirely by the piles. In this situation the mechanism of plastic deformation was expected in the piles since the ratio of the yield strength of the pile group to the maximum applicable lateral load was 0.84 for both orthogonal and diagonal direction loadings. The Moment-curvature analyses of the piles, under different axial forces corresponding to the maximum applicable lateral loads as shown in Table 3.1, revealed that the yield strengths of the pile group for orthogonal and diagonal direction loadings were 712kN and 676kN, respectively. Consequently, the piles were detailed for ductility to enable the development of plastic hinges immediately below the pilecap face. Transverse reinforcement with rs = 0.0087 was provided by 9.52mm diameter spiral with 70mm spacing to satisfy Eq. (3.2).

Table 3.2: Contribution of the shear strength mechanism for the mid and compression piles

Shear Component	Mid Piles	Compression Pile
V_c [Eq.(3.5)] with k=0.042	31 kN	31 kN
V_p [Eq.(3.6)]	76 kN	205 kN
V_s [Eq.(3.7)] with θ=35°	325 kN	258 kN
$\phi_s V_n$ [Eq.(3.4)]	432 kN	494 kN

If it is assumed that the plastic hinge length is independent from axial force, see Eq. (A.19), and that the curvature distribution in the piles is also independent from axial force, the lateral force applied at the top of the column is distributed in the piles in proportion to the secant flexural rigidity, providing that the length of the piles to the point of inflection is the same. This concept is depicted in Figure 3.10 and formally derived in Eq. (3.13) when maximum curvature reaches 0.122 m-1.

Shear was critical in the mid and compression piles as Table 3.2 shows. The shear demand in tension pile was small enough to be neglected. The value of k for V_c components for both the mid and compression piles was considered, conservatively, to be the minimum shown in Figure 3.6. With a shear strength reduction factor of $\phi_s = 0.85$, the shear capacity still greatly exceeded the demand :

$$V_{cp} = \frac{M_{cp}}{M_{cp} + 2 \times M_{mp} + M_{tp}} \times F = \frac{404}{404 + 2 \times 287 + 0} \times 801 = 331 \text{ kN}$$

$$V_{mp} = \frac{M_{mp}}{M_{cp} + 2 \times M_{mp} + M_{tp}} \times F = \frac{287}{404 + 2 \times 287 + 0} \times 801 = 236 \text{ kN} \quad (3.13)$$

$$V_{tp} = \frac{M_{tp}}{M_{cp} + 2 \times M_{mp} + M_{tp}} \times F = \frac{0}{404 + 2 \times 287 + 0} \times 801 = 0 \text{ kN}$$

where, V_{cp}, V_{mp} and V_{tp} are the shear demands for compression, mid and tension piles, respectively. And M_{cp}, M_{mp} and M_{tp} are the moments at the curvature, 0.122 m^{-1}, of compression, mid and tension piles, respectively.

3) Anti-buckling reinforcement

Considering the number of longitudinal bars provided in the pile, it was found that Eq. (3.3) required $\rho_s \geq 0.0018$ to ensure adequate resistance against buckling of the longitudinal reinforcement in the pile. The transverse reinforcement ratio provided in the piles was $\rho_s = 0.0087$, which was significantly greater than that required for resisting buckling of the pile bars.

3.5.3 Pilecap design

The design of the pilecap was based only on the actions of the compression side since they were of greatest significance.

1) Negative moment

The critical condition for the design of the pilecap for negative bending moment was loading along the principal axis during Loading Phase 2(see Figure 3.11 and Table 3.1).

Since the total shear capacity of the piles at the ultimate curvature of the compression pile was 845 kN, the applicable lateral force was reduced from 934 kN. Under the combined gravity and lateral loads, the induced axial tension and compression forces in the piles were 422 kN and 1526 kN, respectively.

Based on the moment-curvature analyses for the piles with different axial forces, the moments in each piles at the curvature of 0.134 m^{-1}, corresponding to equal

P = 2002 kN

F = 845 kN

L_c = 2.591 m

h_f = 0.762 m

L_p = 1.219 m

2V_{tp} = 226 kN

2V_{cp} = 622 kN

T_p = 423 kN

C_p = 1526 kN

L_f = 1.981 m

(a) Elevation

F = 845 kN

(b) Plan view
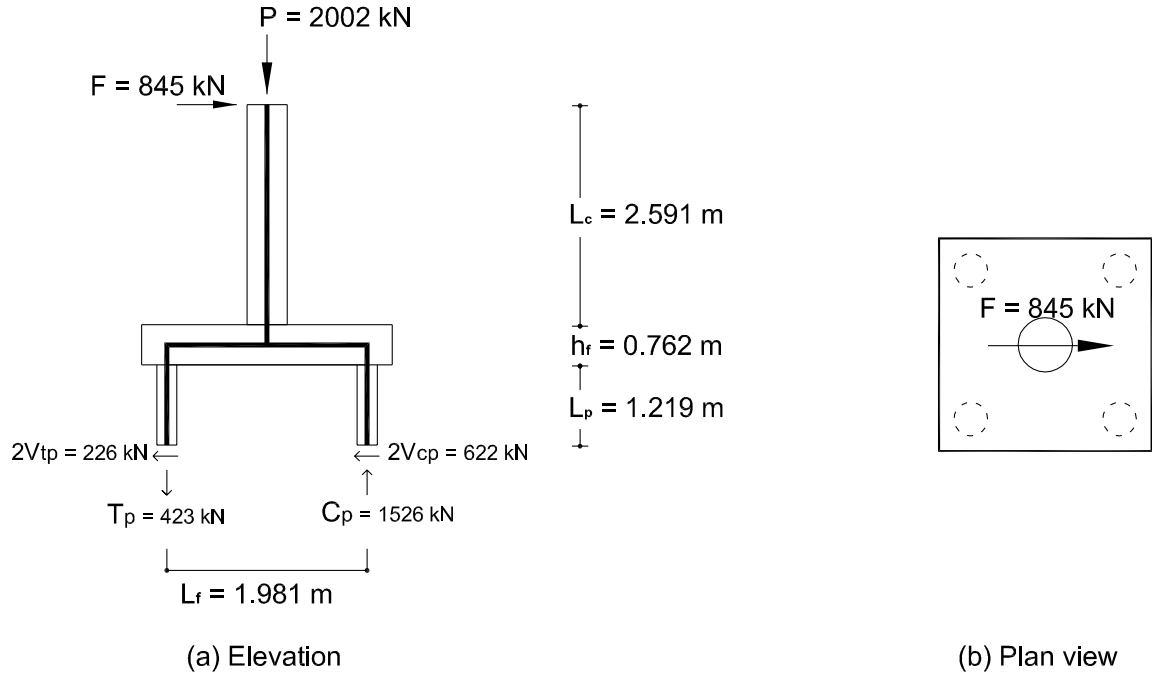
Figure 3.11: Orthogonal direction loading without pilecap resistance
for pilecap negative bending

displacements of piles were M_{cp} = 383 kNm and M_{tp} = 140 kNm(see Figure 3.12).

Accordingly, the individual pile shear forces are :

$$2V_{cp} = \frac{M_{cp}}{M_{cp} + M_{tp}} \times F = \frac{383}{383 + 140} \times 845 = 622 \text{ kN}$$

$$2V_{tp} = \frac{M_{tp}}{M_{cp} + M_{tp}} \times F = \frac{140}{383 + 140} \times 845 = 226 \text{ kN}$$

(3.14)

Although current design practice recommends the line (see section A-A in Figure 3.13) with the pile face as a critical section for the pilecap negative bending moment, the design pilecap negative bending moment, M_{fn}, was obtained conservatively at the centerline of the piles from equilibrium considerations shown in Figure 3.13-(a). This resulted in :
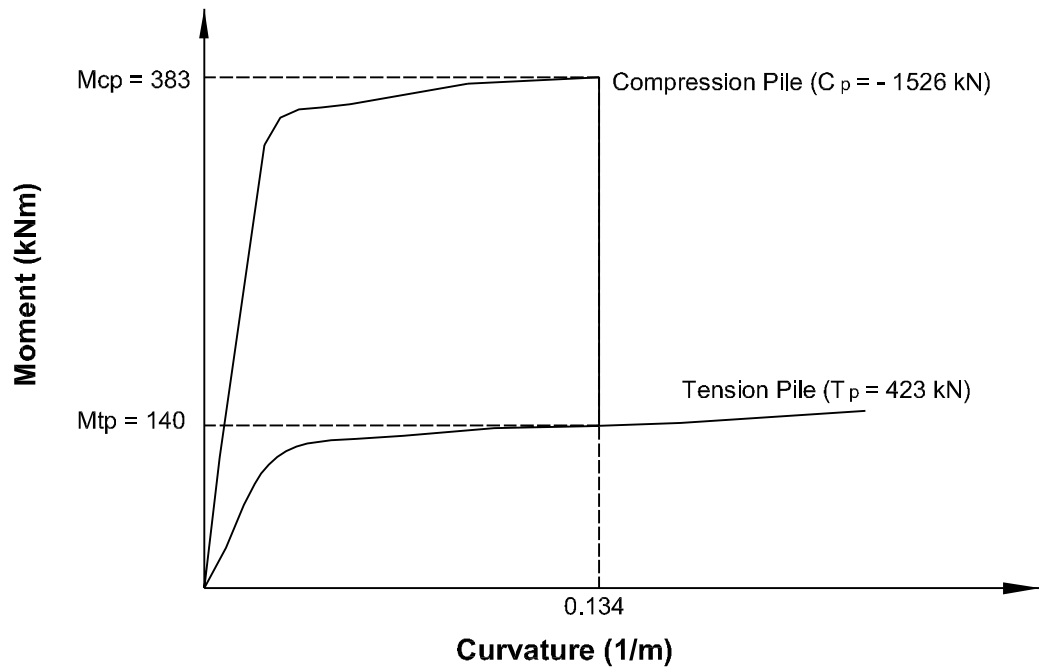
Figure 3.12: Moment-curvature response of piles for determining the pilecap actions

(a) Design actions   (b) Bending moment diagram
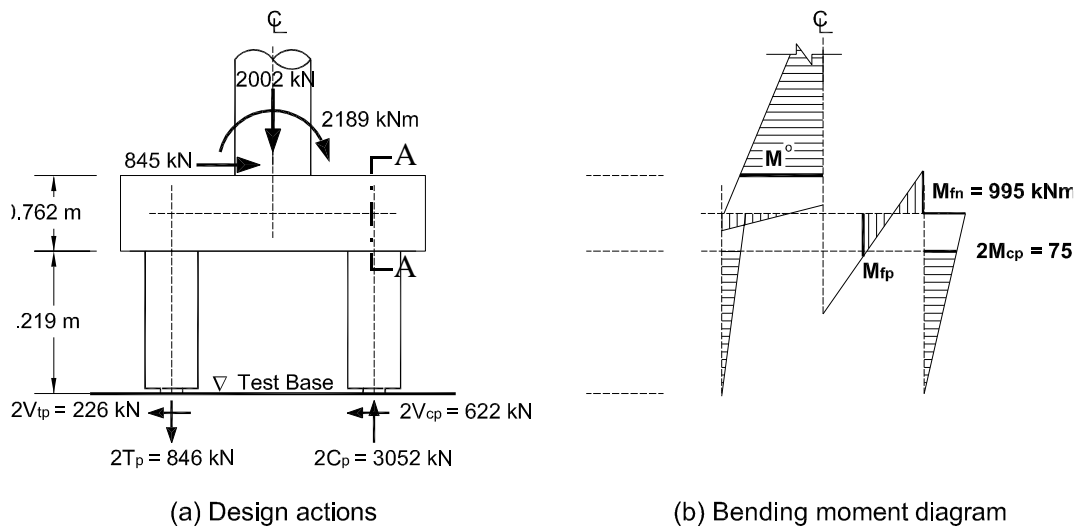
Figure 3.13: Critical moments for the negative bending of the pilecap

71

(a) Negative bending   (b) Positive bending

Figure 3.14: Pilecap effective widths for flexure design[26]

(a) Elevation   (b) Plan view

Figure 3.15: Diagonal direction loading with pilecap resistance
for the design pilecap positive moment

$$M_{fn} = 622\text{kN} \times (1.219 + 0.762/2)\text{m} = 995\text{kNm} \tag{3.15}$$

for which,

$$M_n \geq \frac{M_{fn}}{\phi_f} = \frac{995}{0.9} = 1106 \text{ kNm} \tag{3.16}$$

where, the strength reduction factor for flexure ϕ_f is :

$$\phi_f = 0.9 \tag{3.17}$$

Although Caltrans does not use a factor of safety due to cost considerations, It is clearly more consistent to adopt an appropriate flexural strength reduction factor for capacity protected actions when there is any uncertainty associated with the ideal strength.

Tests on column-pilecap connections[36,37] have indicated that to ensure the pilecap reinforcement remains elastic, the flexural reinforcement must be placed within an effective width of b_{eff} given by[26] :

$$b_{eff} = D_p + 2d_f \tag{3.18}$$

where D_p is the diameter of the column and d_f is the effective depth of the pilecap. This design criteria is illustrated in Figure 3.14. As shown in Figure 3.14-(a), the effective width of the pilecap at the compression pile inner face was $2b_{eff}$ of 2.9 m according to Eq. (3.18) as D = 0.762m and df = 0.71m. Since the effective width for negative bending was almost same as the entire pilecap width, the negative reinforcement was detailed as #5[dia. 15.9mm] at 152mm centers in both orthogonal directions. For anchorage, this reinforcement had 90° hooks at each end, extending down the vertical face to 254mm from the pilecap soffit.
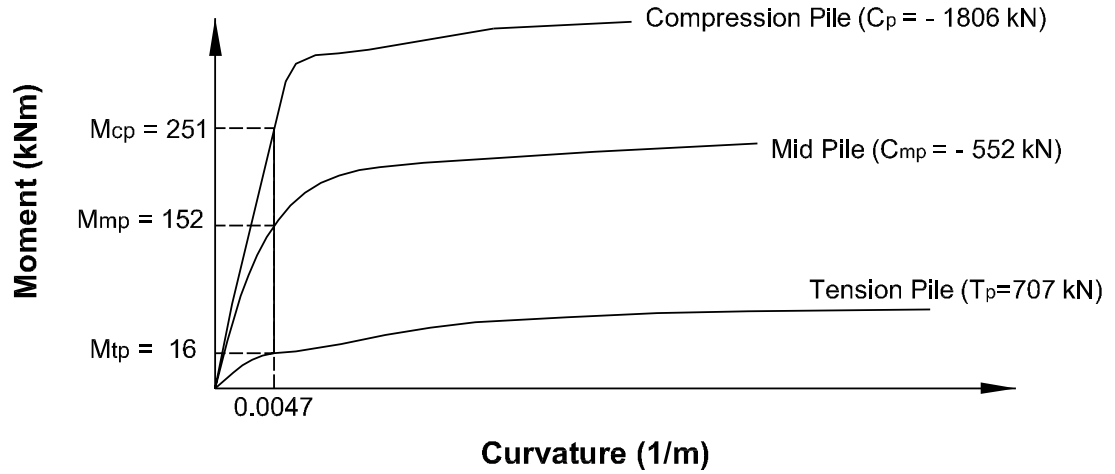
Figure 3.16: Partial moment-curvature responses of piles for Pilecap Positive Bending

2) Positive moment

The critical loading condition for the design of the pilecap positive bending was loading in the diagonal direction in Loading Phase 1 as shown in Figure 3.15 and Table 3.1. Unlike the case of pilecap negative bending, the applicable maximum load was 934 kN corresponding to the moment capcity of the column plastic hinge since 50% of the applied shear force was resisted by the actuators mounted on the pilecap sides. Assuming no axial force development in the mid piles under lateral loading, the axial tension and compression forces in the extreme piles needed to resist the overturning moment is :

$$
T = C = \frac{F(L_c + h_f + L_p) - 0.5F\left(\frac{h_f}{2} + L_p\right)}{L_f\sqrt{2}} = 1259 \text{kNm} \tag{3.19}
$$

Under the combined seismic and gravity loads, the induced axial forces in the piles were 707 kN in the tension pile, 552 kN in the mid piles and 1810 kN in the compression

(a) Design actions   (b) Bending moment diagram
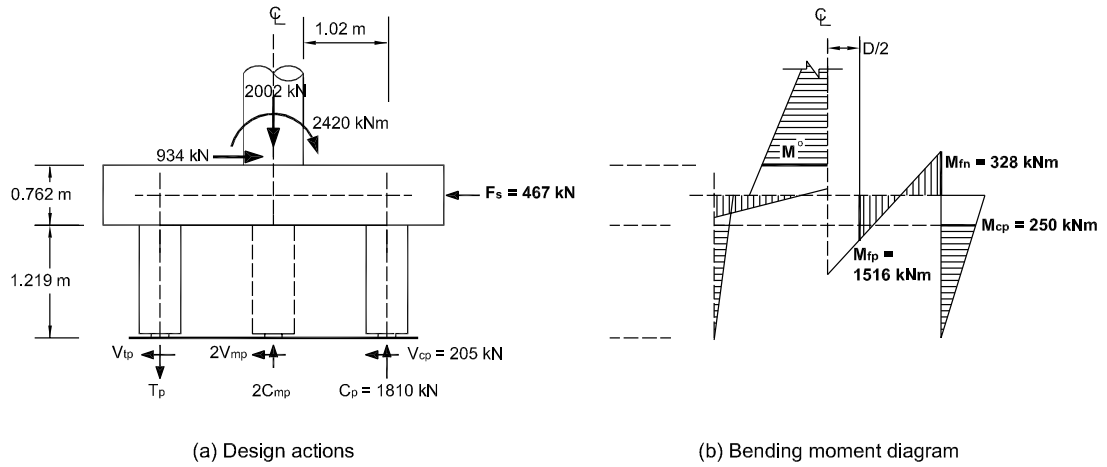
Figure 3.17: Critical Moments for the Positive Bending of the Pilecap

pile. The moment-curvature analyses for these piles with three different axial forces yielded the moments of each piles as $M_{tp} = 16 kNm$, $M_{mp} = 152$ kNm and $M_{cp} = 251 kNm$ at the curvature of $0.0047 m^{-1}$ as shown in Figure 3.16. The shear forces in the compression pile was therefore :

$$V_{cp} = \left(\frac{0.5F \times M_{cp}}{M_{cp} + 2M_{mp} + M_{tp}}\right) = \left(\frac{467 \times 251}{251 + 2(152) + 16}\right) = 331 \text{ kN} \tag{3.20}$$

The design pilecap positive moment, M_{fp}, obtained from equilibrium considerations, see Figure 3.17, was :

$$M_{fp} = C_p \times \left(\frac{L_f \sqrt{2} - D}{2}\right) - M_{fn} = 1810 \times \left(\frac{2.800 - 0.762}{2}\right) - 328 \tag{3.21}$$

$$= 1516 kNm$$

75
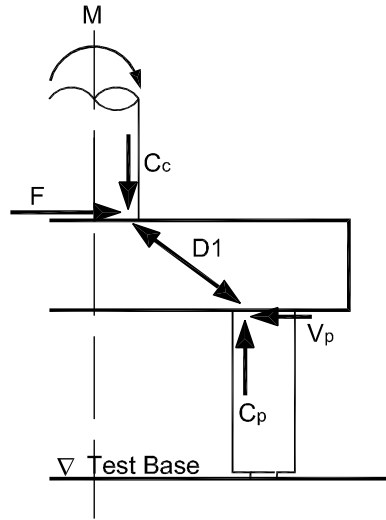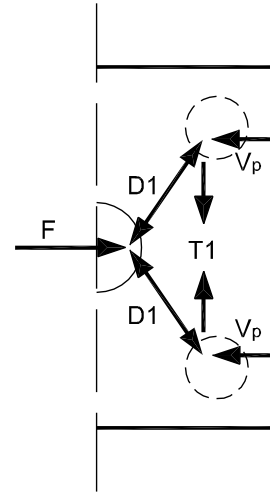
(a) Vertical View	**(b) Plan View (Orthogonal Loading)**

Figure 3.18: Pilecap Shear Transfer by direct compression struts in Loading Phase 2

However, a fraction on the resisting bending moment is due to the passive presure force, F_p, and its eccentricity with respect to the resultant compression force. Thereby, the moment resisted by the reinforcement can be approximated to be :

$$M_n \geq \frac{M_{fp}}{\phi_f} - 0.5F\left(\frac{h_f - a}{2}\right) = \frac{1516}{0.9} - 467\left(\frac{0.762 - 0.05}{2}\right) = 1518 \text{ kNm} \qquad (3.22)$$

Hence, the reinforcement detail with #5[dia. 15.9 mm]+#6[dia. 19.1 mm] at 152 mm centers was obtained by considering the effective width of 2184 mm, which is based on Eq. (3.18), and provided in both orthogonal directions over the entire pilecap width.

It was assumed, as is common design practice, that the critical moment occur in line with the column face. This is non-conservative, as demonstrated by the test performance

(a) Vertical View   **(b) Plan View (Orthogonal Loading)**
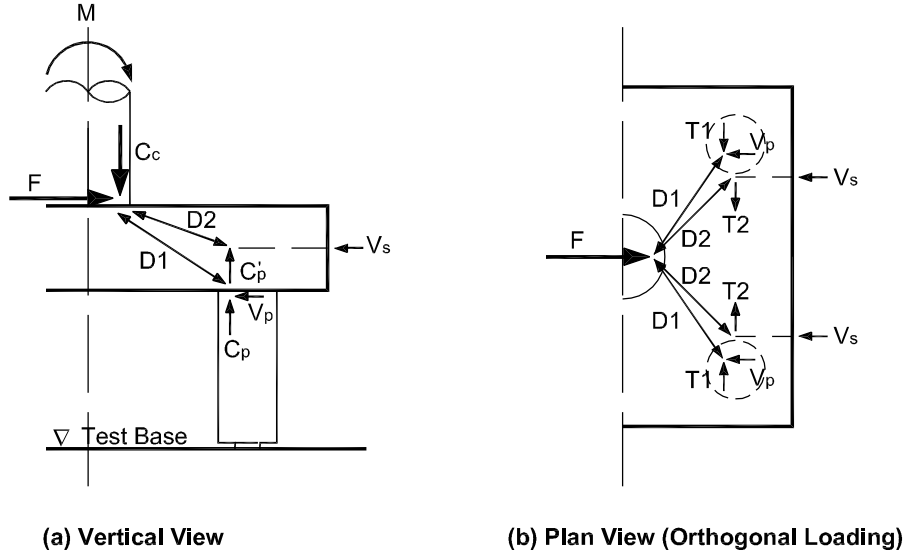
Figure 3.19: Pilecap Shear Transfer at the orthogonal direction loading with pilecap restraint

of unit CFPS1, and that modification was made for unit CFPS2, as discussed subsequently.

3) Shear transfer of the Pilecap

Since the applied shear force, F, could be transferred by a diagonal compression strut formed inside the pilecap directly[26] as seen in the Figure 3.18 for both orthogonal and diagonal direction loadings, shear reinforcement of the pilecap was not needed. Particularly, in the case of orthogonal direction loading [Figure 3.18-(b)], a horizontal tension force, T1, which is perpendicular to the direction of the applied shear, F, is required to balance this compression strut. In the vertical plane [Figure 3.18-(a)], D1 is equilibriated by the compression pile shear force, V_p, and part of the pile compression force, C_p. In the horizontal plan [Figure 3.18-(b)], it is seen that the strut, D1, consists of two 45° components, spreading from the column to the piles. Furthermore, there

should be another pair of diagonal compression struts D2 inside the pilecap carrying the part of the applied shear force in case of the orthogonal direction loading with the pilecap restraint, due to the passive soil pressure in opposite direction[Figure 3.19]. In Figure 3.19-(a), the strut, D2, is balanced vertically by the resultant force of soil passive pressure and part of the pile compression force C'_p. Horizontally [Figure 3.19-(b)], struts D2 are seen to be a fan spreading to the full width of the pilecap. Resolving the passive pressure into two equal resultants V_s, a second tension force T2 is needed. Assuming that the reinforcement perpendicular to the direction of the applied shear force was not to be utilized for flexure, the flexural reinforcement was checked for the horizontal tenstion force, T(= T1+T2), of the critical case of orthogonal direction loading with pilecap restraint. However, it was found from this research that both directional reinforcement for flexure should be mobilized against the pilecap bending even though the seismic force is applied in orthogonal direction. This will be discussed further in Chapter 7.

With 0.5F of lateral pilecap resistance in opposite direction to the applied shear force, F, the remaining shear of 0.5F was distributed among the piles in proportion to their stiffnesses. Based on the moment-curvature analyses of the piles with different axial forces[Figure 3.20], the moment of compression pile at the curvature of 0.00013^{-1}, which yielded equal displacements of piles, was $M_{cp} = 236$ kNm. Hence, the distributed compressive pile shear forces was :

$$V_{cp} = M_{cp}/L_p = 236/1.219 = 194 \text{ kN} \qquad (3.23)$$
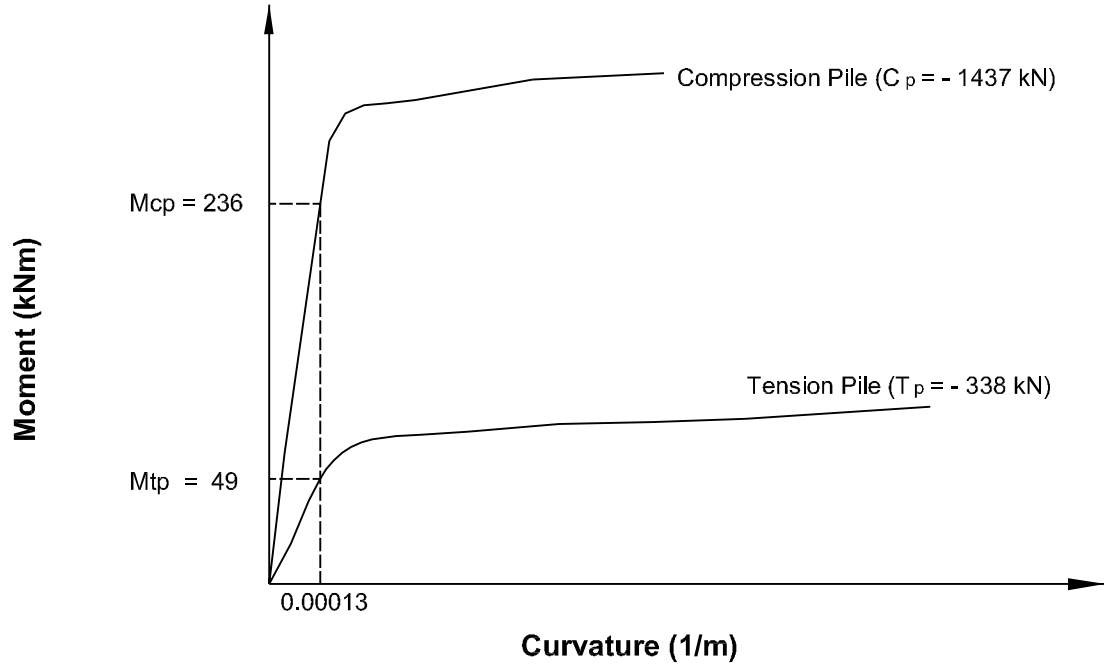
Figure 3.20: Partial moment-curvature responses of piles
at orthogonal direction loading with pilecap restraint

The required tension force, T1, for the strut D1 was thus 194 kN with $\theta = 45^o$ and the second tension force, T2, for the strut D2 was :

$$T_2 = \frac{0.5F}{2} \times \frac{0.25b_f}{0.5W_p} = 169 \text{ kN} \qquad (3.24)$$

Therefore, a total tension force of 363 kN was needed over the outer 914 mm of effective width. The available tensile capacity of the steel provided for the positive moment in this effective width was 600 kN which greatly exceeded the demand.

When piles are in tension, the direct compression strut can not be relied on to transmit shears from the tension piles, which must use the conventional combination of concrete and transverse reinforcement shear-resisting mechanisms. Since the pilecap

shear force on the tension side is $2T_p = 0.676$ MN, with a pilecap effective width of 2.18m based on Eq. (3.18), this corresponds to an average shear stress of

$$v_f = \frac{2T_p}{d_f \times b_{eff}} = \frac{0.676}{0.71 \times 2.18} = 0.437 \, \text{MPa} \tag{3.25}$$

corresponding to a stress ratio of $0.083\sqrt{f_c'}$ MPa. This implies that a minimum amount of shear reinforcement satifying Eq. (3.26), with spacing between the vertical legs of not more than $0.5h_f$, is sufficient.

$$\rho_v = \frac{0.35}{f_y} \, \text{(MPa)} \tag{3.26}$$

3.5.4 Pilecap joints design

The pilecap joints of the test units were designed with reduced amounts of reinforcement by explicitly identifying an internal force flow. The joint principal tensile stress, p_t, was calculated to determine whether the joint reinforcement was needed to transfer joint forces [26,35] :

The average principal tensile stresses of the joints at the ultimate limit state were estimated to be $0.52\sqrt{f_c'}$ [MPa] and $0.09\sqrt{f_c'}$ [MPa] for the column-pilecap and the pilecap-pile joints, respectively. When comparing these values to the joint design threshold values described above, it was concluded that only the column-pilecap joint should be detailed to ensure appropriate force transfer mechanism for satisfactory internal force flow through the joint. Because $p_t \leq 0.29\sqrt{f_c'}$ [MPa] for the pilecap-pile joint, joint shear cracking is not expected, and only nominal joint reinforcement satisfying Eq.(B.11) was provided in the form of spirals.

The area of external vertical stirrups required by Eq. (B.7) was 7948 mm^2, which was equivalent to 62 sets of #4[dia. 12.7 mm] stirrups. The stirrups were placed within 381mm distance from the face of the column (Figure 4.6). The amount of internal vertical stirrups obtained from Eq. (B.8) was 1000 mm^2, requiring 8 legs of #4[dia. 12.7 mm] stirrups. The volumetric ratio of the horizontal hoop joint reinforcement required according to Eq. (B.10) was 1.12 %, which was represented by #4 [dia. 12.7 mm] spirals at 63.5 mm spacing. In addition to the above details for the joint force transfer mechanism, the pilecap top longitudinal reinforcement area was increased by 1000 mm^2 to be consistent with Eq. (B.12). The longitudinal column bars were extended into the joint as close to the bottom pilecap reinforcement as possible. The embedment length of the column bars was 711 mm, which was almost the minimum required anchorage length obtained for #8 [dia. 25.4 mm] bars from Eq. (B.9).

3.5.5 Pin connection between the piles and the test base

In the test units the piles were connected to the test base using a pin detail. The pin connection between the piles and the test base was achieved by terminating all the longitudinal column reinforcement just above the test base, reducing gross area of the pile circular section from 508 mm to 203 mm at the interface of pile and test base, and by providing a plain round steel rod at the centers of the piles. The area of the piles was reduced by placing expansion joint pads around the pin concrete perimeter. The thickness of the pad at the pile base was decided considering the maximum expected rotation of 0.04 radians at the pile base assuming pilecap rigid body translation. This corresponds to a gap of about 10 mm between the pile and test base at the extreme pile

fiber. Considering a flexibility of the pilecap, a 38mm thick pad of expansion joint material was provided conservatively so that a maximum lateral displacement could be accommodated without any damage to the pile and pile base. No significant force transfer was expected through the pads and, thus, pin capacities were estimated ignoring any force transfer through the expansion joint pads.

It is believed that the behavior of the pile supported foundation system is also influenced by the pilecap rigid body rotation which depends on the vertical stiffness of soil-pile interaction. Because the vertical stiffness of compression pile is usually much larger than that of tension pile due to end bearing, no emulation was done for the vertical stiffness of the compression pile. The vertical stiffness of soil-floating pile interaction, was calculated by dividing the axial force by the corresponding vertical displacement at the top of the pile. To calculate the vertical displacement at the top of the tension pile, the differential equation governing its behavior was solved assuming elastic shear stress at the interface of pile and soil. The equation is derived in Section 2.2.4.

The selected increase rate of soil Young's modulus was 40 MPa/m. Besides, Poisson's ratio of soil, ν_s, was assumed to be 0.3 and $l_p/D_p= 25$ corresponding to the scaled pile length of 12.7m was adopted. The results of Eq. (2.25) with applied force at the top of pile, 800 kN, was shown in Figure 3.21 and the vertical displacement at the top of pile was 1.12mm. The vertical stiffness of soil-pile interaction was obtained dividing the vertical diplacement by the pile force at the top of pile. Accordingly, vertical stiffnesses at the top of tension pile, k_{tp}, were 714 MN/m and the rod was designed based on this value. Since the maximum axial force in the tension pile was 756 kN as shown in
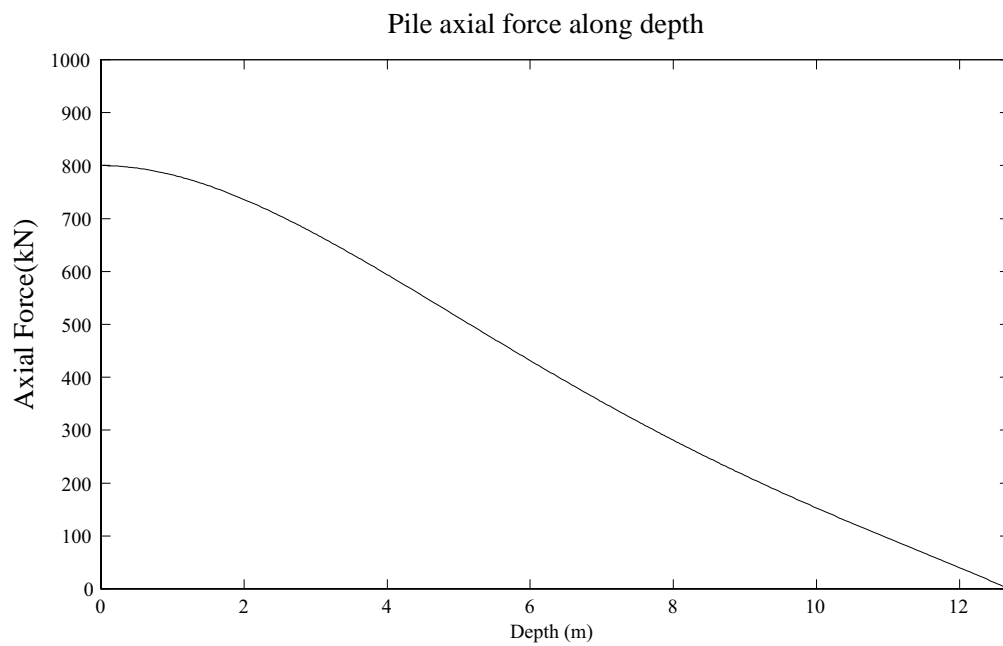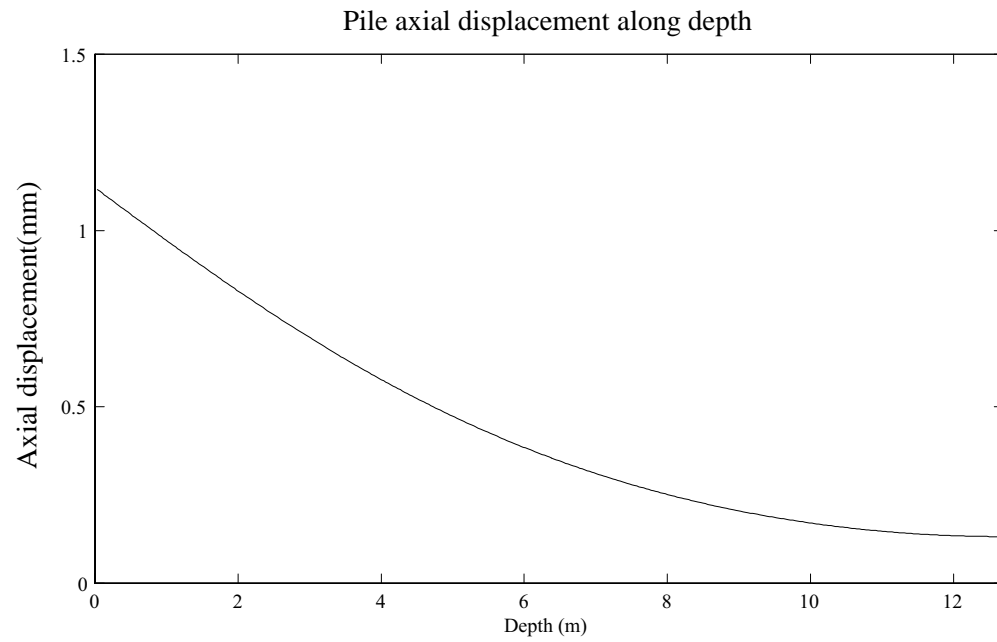
Figure 3.21: Distribution of vertical deflection and force of pile along depth
for applied tension force of 800kN

37.5mm thick
expansion
joint filler

spiral
#4[dia.12.7mm]
@38mm

305 mm

711mm

2 - # 8
[dia.25.4mm]

Ø57mm
rod with
Grease
Coating

Fillet
Welding

50.8 mm
25.4 mm

711 mm

914 mm

203 mm

203 mm

(a) Pile-Test Base Pin Connection Detail   (b) Steel Rod Detail
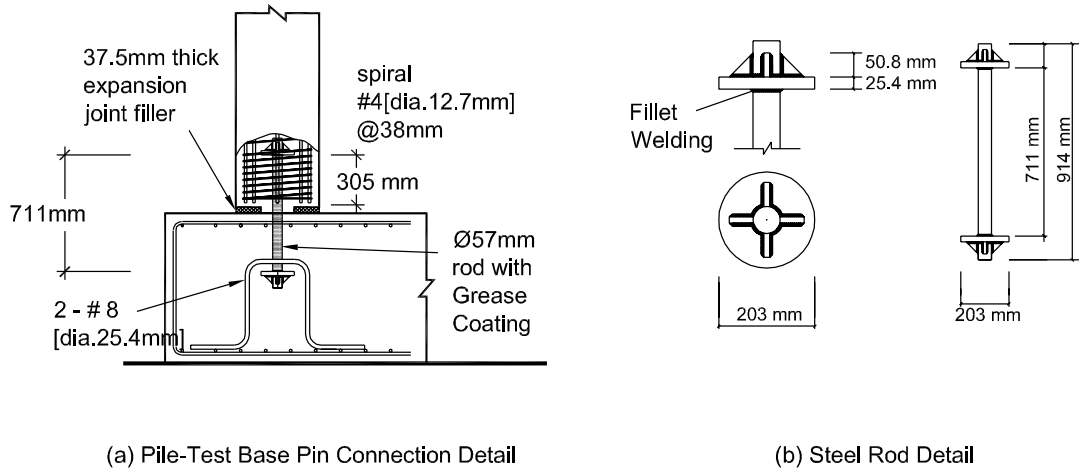
Figure 3.22: Details of the pile-test base pin connection

Figure 3.10 and the yield strength of the steel rod was 545 MPa, the sectional area of the steel rod, A_R, was selected to be 0.00255 m^2. This ensured that the steel rod with a strength of 1.39 MN would not yield under the demand of tension pile, 756kN. The length of the steel rod, l_R, was determined by the following equation in order to ensure that it maintained the same stiffness as the tension pile. The length of 0.711m was used for the test unit.

$$l_R = \frac{E_s A_R}{k_{tp}} = \frac{200000(\mathrm{MN/m^2}) \times 0.00255(\mathrm{m^2})}{714(\mathrm{MN/m})} = 0.714(\mathrm{m}) \qquad (3.27)$$

The bottom of the piles were confined with #4[dia. 12.7mm] at 38mm spacing to avoid pulling out of the rod . The rods were debonded by the application of the grease on the surface of the rod and anchored in the pile and in the test base with 25.4 mm thick

84

steel disks as anchor plates at both ends. The pin connection detail is illustrated in Figure 3.22 without the stirrups in the test base for clarity.

In addition, the following design checks were performed to ensure that the above details adopted for the pin connection would be sufficient and failure would not occur during the test. In these calculations, the forces estimated for the design of the test unit CFPS1 were considered since the force levels induced in the pins of the unit CFPS2 were expected to be similar.

- Axial compression stress in the concrete key

Assuming a uniform stress distribution through the key, the maximum average concrete stress was expected as follows:

$$\sigma = \frac{C_p - C_R}{\pi(r_p - r_R)^2} = \frac{(1859 - 1240) \times 10^3}{\pi \times (101.6^2 - 28.6^2)} = 20.7 \text{MPa} = 0.75 f_c' \quad (3.28)$$

where f_c' = 27.6 MPa was assumed and C_p and C_R were the maximum compression force in the piles and the compression force to be transferred through the steel rod. Higher stresses should be expected in the extreme compression fiber of the pin concrete because the moment capacities of the pins would be fully developed. As the concrete key is likely to be well confined by the adjacent concrete of the pile and of the test base, a compressive strength as high as $2f_c'$ is expected for the key [22]. On this basis, it was believed that crushing of concrete at the key would not occur due to axial force transfer.

- Axial tension force transfer

  The axial tension force from the pile to the pin was transferred by the steel rod placed at the center of the pile. The axial tension capacity of the steel rod was estimated as 1240 kN, which was greater than the pile axial tension capacity of 756 kN.

- Shear transfer

  A shear friction mechanism was relied upon for shear transfer between the pile and test base. Assuming a friction coefficient $\mu_f = 1.0$ consistent with the recommendation in reference [2], the maximum shear transfer V_{SF} for compression pile obtained using Eq. (3.29) [2,22,35], was significantly greater than the maximum shear force, $V_{c,max}$, expected to develop in the compression pile :

  $$V_{SF} = \mu_f C_p = 1.0 \times 1859 = 1859 \text{ kN} \geq V_{c,\,max} = 329 \text{ kN} , \qquad (3.29)$$

  where A_{sv} is the total area of the steel rod in the pin and f_{ye} is the expected yield strength of the steel rod. In the above calculations, it was assumed that the yield strength was developed in the steel rod. Shear transfer at the pin of the tension pile was not checked noting a small magnitude of the shear force developed in the tension pile against the large capacity of the shear transfer by the dowel action of the steel rod which was 1240 kN.

3.5.6 Test base

Test base dimensions of 3.353m x 3.353m x 0.914m was chosen and the test base was tied down to the strong floor with 22-Dywidag bars with 667kN each of post-tension force. For ease of dismantling, the test base was composed of three blocks of concrete.
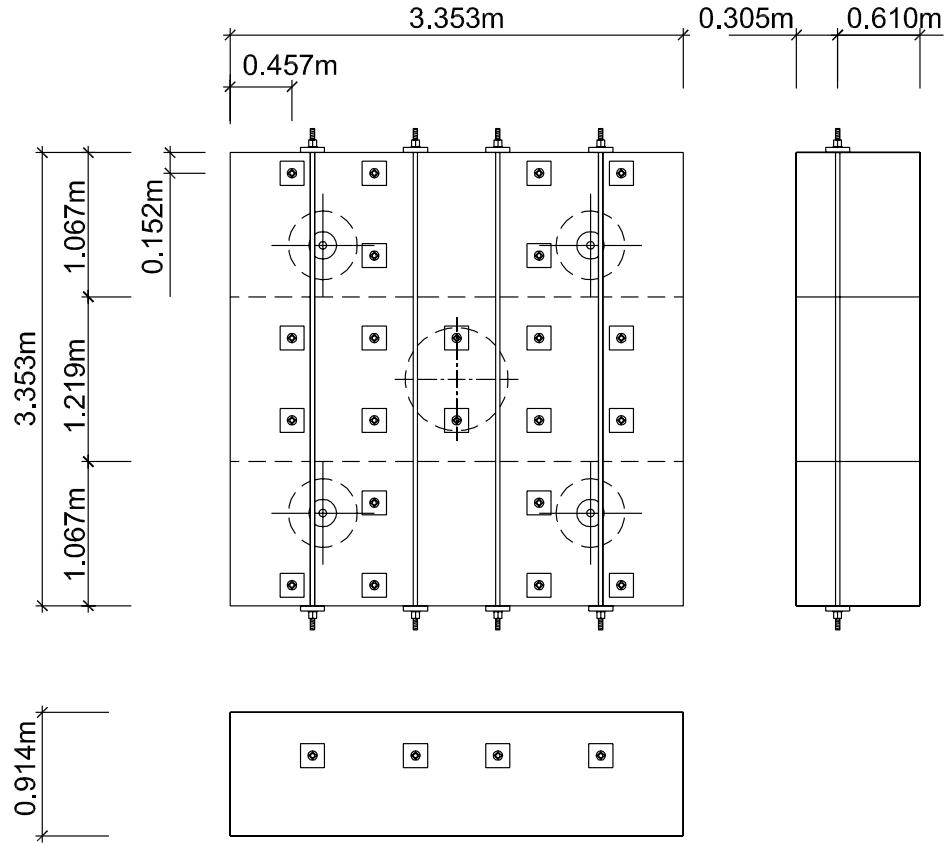
Figure 3.23: Post-tensioning of the Test Base

Those concrete blocks were tied together with 4 numbers of Dywidag bars with 890 kN of post tensioning. In detailing the footings, minimum reinforcement quantities were found to be sufficient. A longitudinal steel ratio of 0.8% was provided with at least 60 legs of #4 [dia. 12.7 mm] J-hooks.The dimensions of the test base are shown in Figure 3.23.

3.6 Construction

The test units were constructed at the Charles Lee Powell Strucutures Research Laboratory at UCSD. Prior to the construction of the test units, the steel reinforcement

was instrumented with electrical resistance strain gauges. Following the application of the strain gauges, the steel reinforcement cages for the piles and the column were prefabricated. The test base was then constructed. The top surface area of the test base providing the pin connection was roughened. After placing the expansion joint material, the prefabricated pile reinforcement cages were placed in positions with paper tubes as formworks. On top of the pile cages, the pilecap reinforcement cage was built with the prefabricated column reinforcement cage. The piles and the pilecap were cast in a single pour using standard concrete mix with a target compressive strength of 27.6 MPa at the age of 28 days. The construction of the unit was completed by casting the column and a load stub. Construction photos of test units are shown in Appendices H and J.

Chapter 4: Test Details and Results of CFPS1 (Conventional Reinforcement)

4.1 Geometry and Reinforcement Details of Unit CFPS1

The geometry and general reinforcement details of CFPS1 are shown in Figure 4.1.
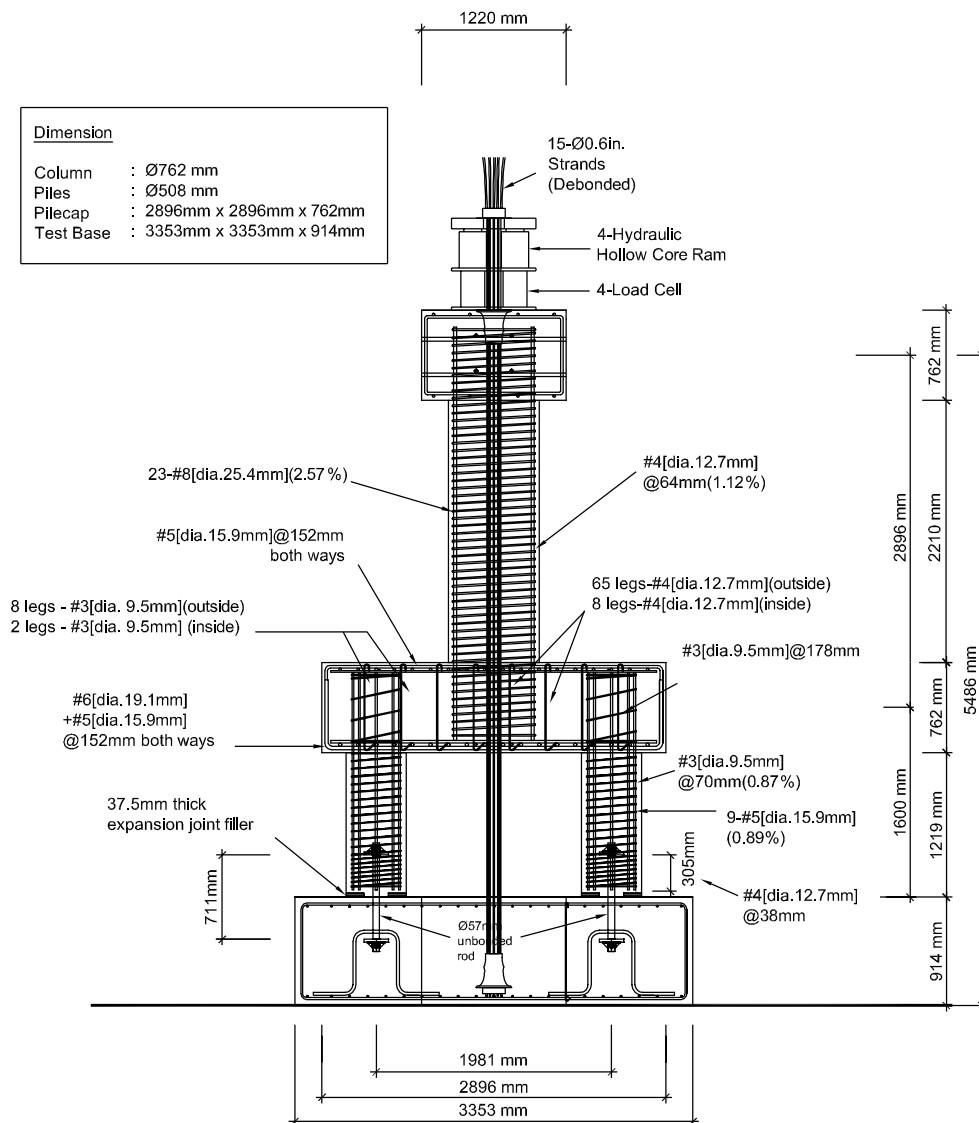
Figure 4.1: Reinforcement Details of CFPS1

4.2 Test Set-Up

The complete test setup before testing is shown in Figure 4.2.
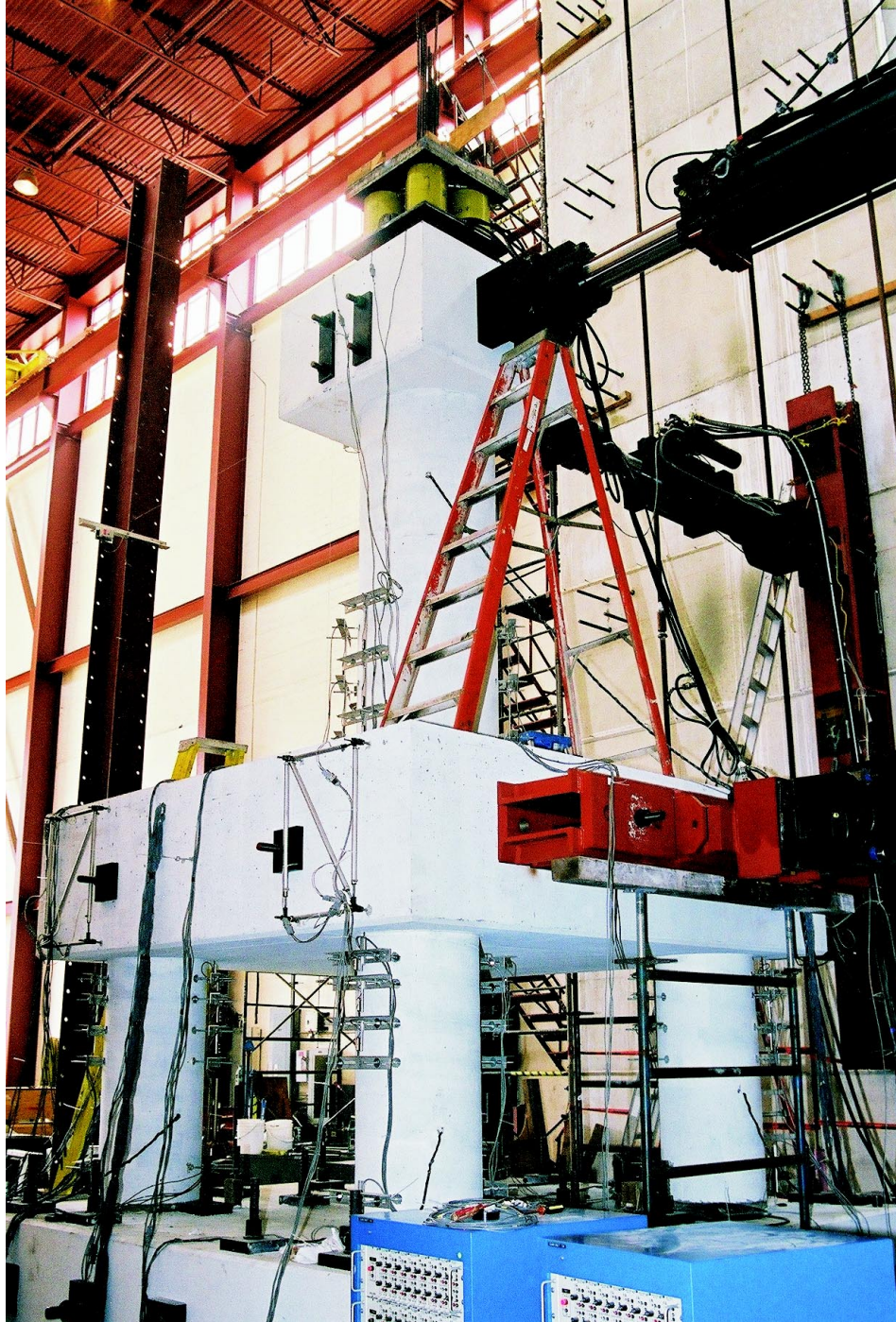
Figure 4.2: Complete test setup of CFPS1

4.3 Instrumentation

4.3.1 External instrumentation

External instrumentation consisting of load cells, linear potentiometers and inclinometers were attached to the test units.

The curvatures were recorded within several segments of the piles and the column using a pair of linear potentiometers placed opposite to each other near the face of the members. Curvature was calculated based on incremental displacement readings along highly strained regions of piles and the column to measure the responses for the orthogonal and diagonal direction loadings independently. The column and beam curvatures were obtained from the displacements measured in one potentiometer with respect to the other :

$$\phi = \frac{\text{rotation}}{\text{gauge length}} = \frac{(\Delta_2 - \Delta_1)/l_w}{l_g} \tag{4.1}$$

where $(\Delta_2 - \Delta_1)$ represents the relative extension within the curvature cell, l_w is the distance between the two linear potentiometers and l_g is the gauge length. When curvature was calculated in the curvature cell adjacent to the supporting member such as pilecap in the test units, a modified gauge length as given in Eq. 3.23 was considered:

$$l'_g = l_{sp} + l_g \tag{4.2}$$

where l_{sp} is the equivalent strain penetration length taken as $0.022f_y d_{bl}$ where f_y is the longitudinal bar yield stress in MPa and d_b is the longitudinal bar diameter in mm. This modification was necessary to account for the base rotation resulting from strain penetration into the joint [25].

91

The lateral displacement histories of the top of the column and the pilecap were recorded with linear potentiometers. Additional linear potentiometers were placed vertically between the load stub and the pilecap, and between the pilecap and the test base. The pile-pilecap joint panel deformation was measured on south and east sides of pilecap joint areas using five linear potentiometers. Rotation devices were also mounted for two directions using angle brackets on the south side of the load stub and the bottom of the pilecap beneath the column to continuously record their inclinations during the test. The external instrumentation is illustrated in Figure 4.3 and 4.4.
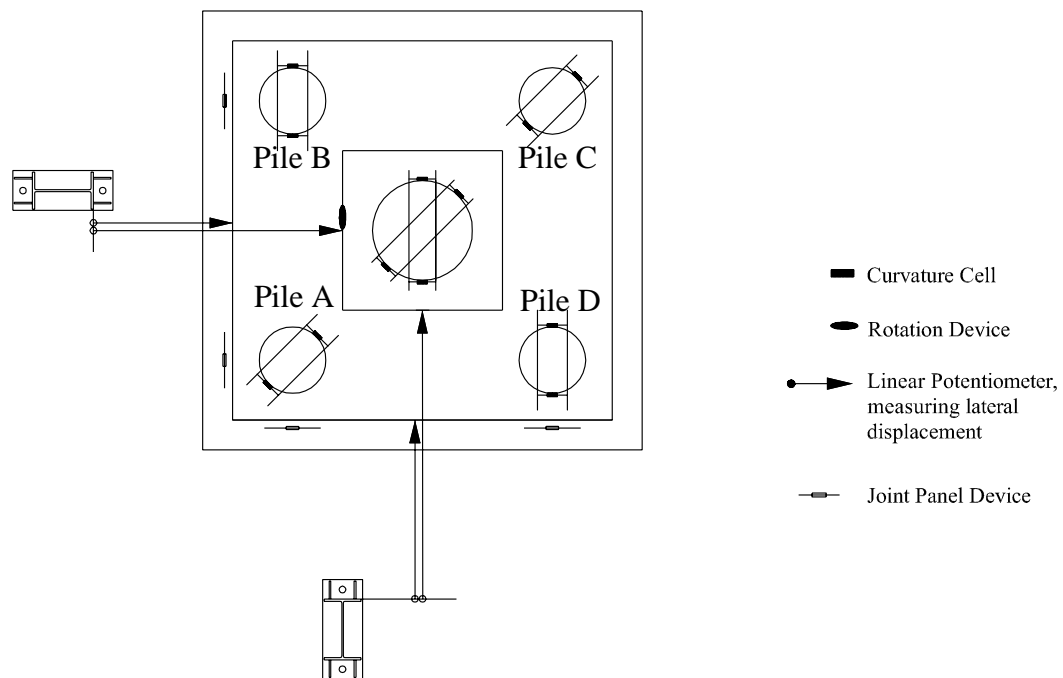
Figure 4.4: Horizontal view of external instrumentation

Curvature Cell,
6" spacing

Rotation Device,
One is to be installed
at the soffit of pile-cap

Linear Potentiometer,
measuring lateral
displacement

Joint Panel Device

305
305
152
152
152

102
102
152
152

203
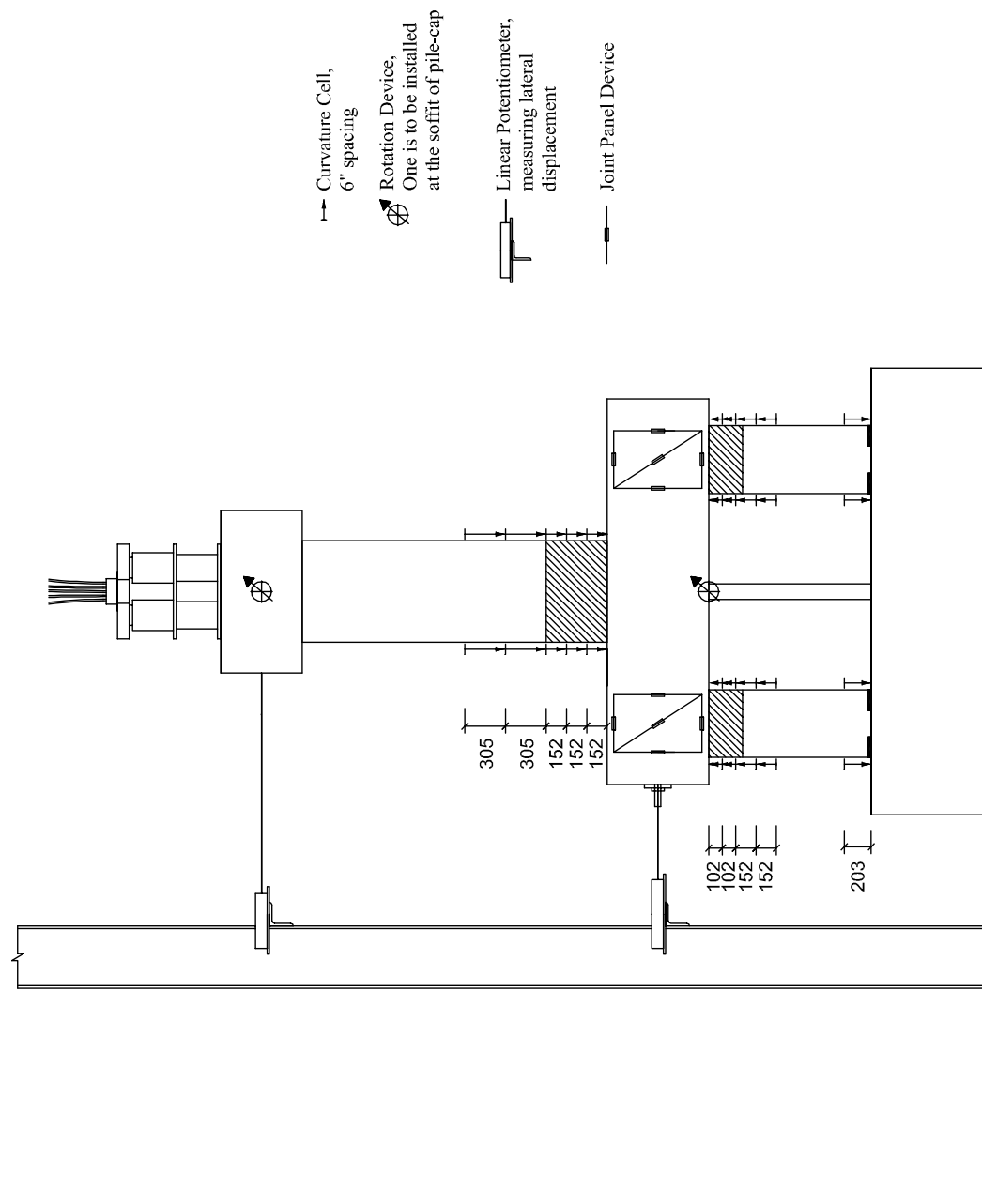
Figure 4.3: Vertical view of external instrumentation (East elevation)

93

4.3.2 Internal instrumentation

Test units were instrumented with electrical resistance strain gauges. Most of strain gauges were mounted on the reinforcing steel of the test unit in the pilecap and pilecap joint regions. The strain gauge with gauge length = 5mm, gauge resistance = 120Ω and gauge factor=2.13 was used. The procedure used for fixing the gauge is described in reference [11]. The major locations of strain gauges are shown in Figures 4.5 and 4.6.

4.4 Material Testing

The concrete and reinforcement properties used in the test unit CFPS1 were established from testing at UCSD's Charles Lee Powell Laboratory. The compression strength of concrete was measured at 7days, 28 days and on the day of testing (D.O.T). Results are listed in Tables 4.1. Each value in this table represents an average strength obtained from three unconfined concrete cylinders (152.4mm diameter x 304.8mm height), which were cast during the concrete pour. Tensile strength of concrete was not experimentally measured.

Uniaxial tensile testing was performed on 914mm long three randomly selected coupons for each bar type and a complete stress-strain relation was obtained for each

Table 4.1: Compressive strengths of concrete used in test unit CFPS1

Structural member	7 days	28 days	Day of Testing
	MPa	MPa	MPa
Test Base (Mid-Block)	26.7	35.6	45.0
Test Base (Side-Blocks)	24.4	32.7	39.8
Pile & Pilecap	23.3	28.6	31.3
Column	23.7	31.9	34.2
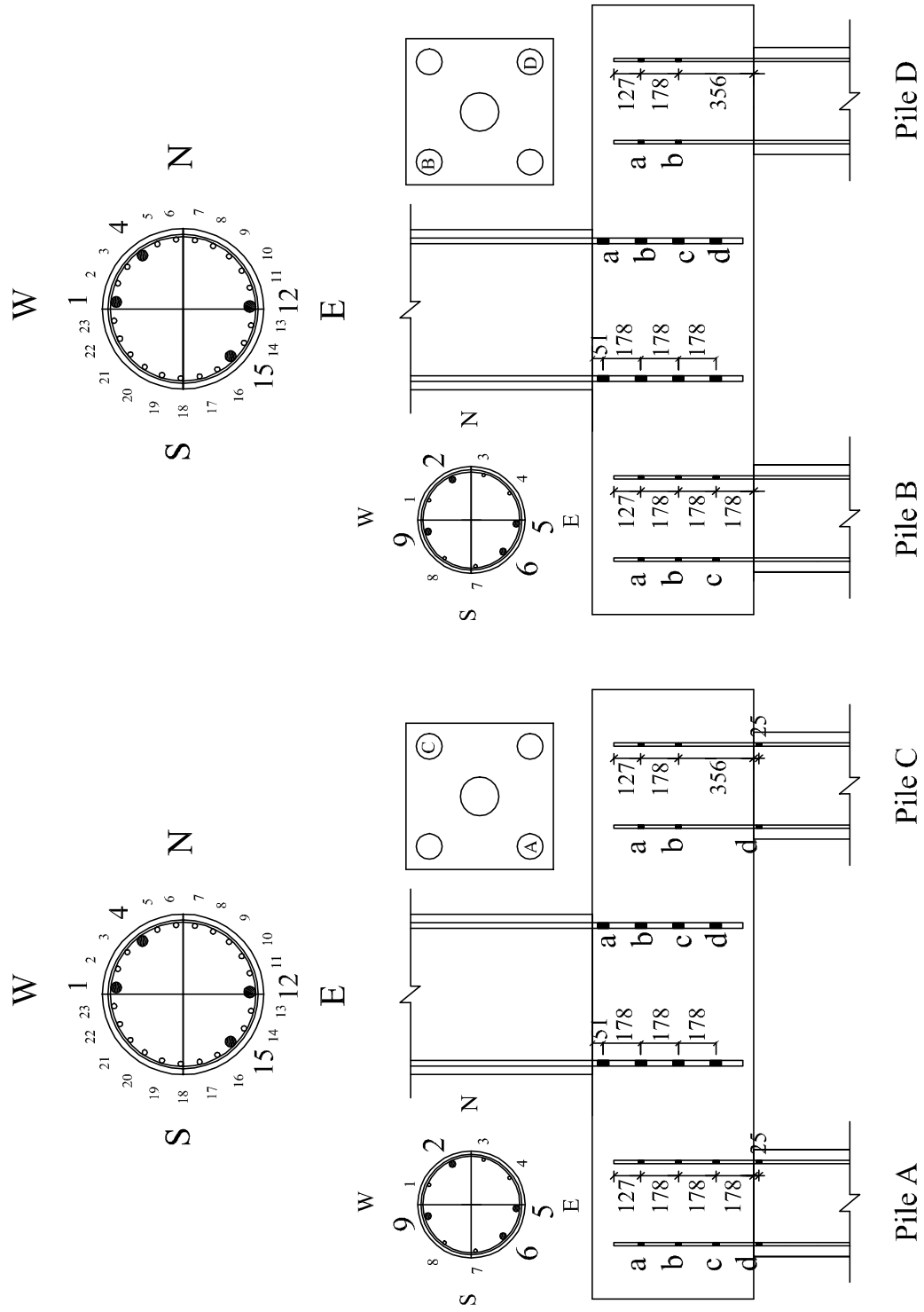
Figure 4.5: Schedule of column and pile longitudinal reinforcement strain gauges

95

North

(b) Shear reinforcement

West   **East**

(a) Flexural reinforcement
(Top & Bottom mat)

South

Figure 4.6: Schedule of pilecap longitudinal(flexural) and stirrup(shear) reinforcement strain gauges

96

coupon until the peak stress was attained. The samples obtained from column and joint spirals did not have clearly defined yield points. This was expected since they were deformed prior to the testing in the process of making spirals. For these reinforcing bars, yield strength was approximated to the stress at a strain of 0.5%, consistent with ASTM specifications. Table 4.2 shows the average yield and ultimate strengths established for all the reinforcement.

Table 4.2: Yield and ultimate strengths of steel used in test unit CFPS1

Description	Bar Size	Yield Strength	Ultimate Strength
	diameter in mm	MPa	MPa
Column longitudinal bars	25.4	433.0	734.3
Column spiral	12.7	452.7	617.6
Pilecap bars in top & bottom mat	15.9	430.8	705.3
Pilecap bars in bottom mat	19.1	453.3	740.6
Pilecap J-bars	12.7	437.8	730.5
Pile longitudinal bars	15.9	483.9	751.8
Pile spirals	9.5	427.2	686.9

4.5 Loading Protocol

4.5.1 Gravity load

A gravity load of 2002kN, which simulated the weight of super structure, was first applied as a concentrated force at the center of the column through post-tensioning tendons. This load was maintained at constant level by the hydraulic jack during the seismic force simulation though there were fluctuations in the load due to the nature of equipment(see Figures 4.7, D.1 and D.2).
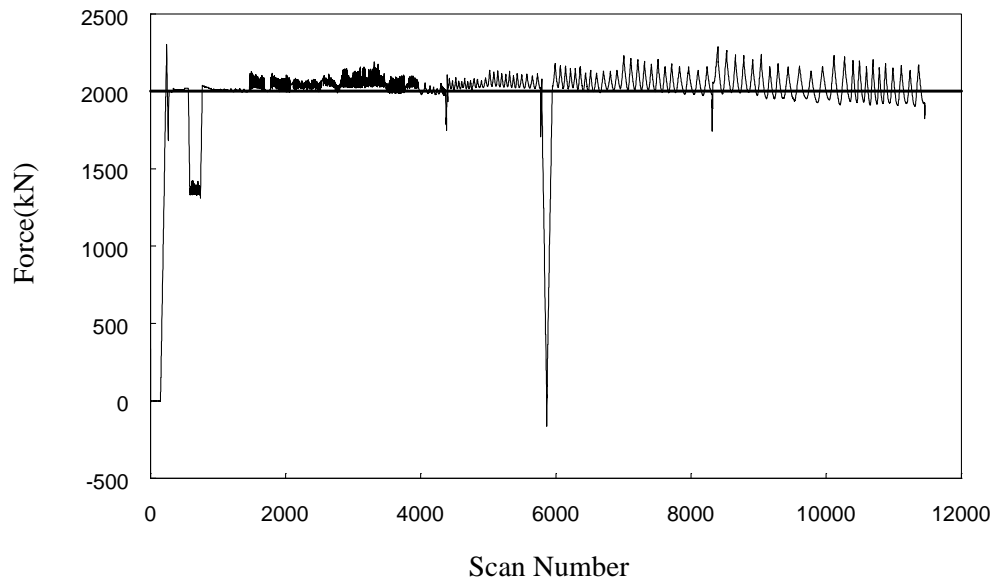
Figure 4.7: Gravity load during the test of CFPS1(Loading Phase 1)

4.5.2 Simulated seismic load

Figures 3.4 and 3.5 show views of the test unit, where lateral load actuators are oriented in two orthogonal directions. The simulated seismic loading of two normal and two diagonal directions were applied cyclically to CFPS1 by directional combinations of loading with two servo-controlled hydraulic actuators. The simulation of passive pilecap soil restraint for each direction was achieved by connecting the two actuators to steel loading frames mounted on two vertical sides of the pilecap. The pilecap actuators were set up to nominally take 50% of the seismic loads applied to the top of column in opposite direction. Each loading frame was linked to two horizontal Dywidag bars end plated on the other side of pilecap for opposite directional loading.

98

The loading protocol for Loading Phases 1 and 2 is shown in Table 4.3

1) **Loading Phase 1 : With pilecap actuators(pilecap passive soil pressure simulated)**

The first part of the seismic loading consisted of force-controlled cycles at 25%, 50%, 75% and 100% of the theoretical first yielding of the longitudinal steel in a column, for a total of four loading steps.

The following loading steps, beyond theoretical first yielding of the longitudinal column bar in the column, were controlled by the lateral displacement of the column head. Using the measured first yield displacements in all the loading directions, an average displacement corresponding to system's displacement ductility, $\Delta_{\mu 1}$, was estimated to be 26.6mm from Eq. (4.3).

$$\Delta_{\mu 1} = \Delta'_{y(ave)} \frac{M_y}{M'_y} \tag{4.3}$$

where $\Delta'_{y(ave)}$ is the average system displacement for all loading directions at the first yield of the column , M'_y is the first yield moment and M_y is the reference yield moment of the column (see section A.1.1).

The displacement used to control the test was increased in steps such to $\mu_\Delta = 1, 1.5, 2, 3, 4, 5$.

The transverse loading was applied to each normal direction with two cycles and each diagonal direction with one cycle at each system displacement ductility level in order that all the structural members experience the same level of loading.

The test was stopped at the system displacement ductility 5 to avoid low cycle fatigue failure of the column steel for further testing at Loading Phases 2 and 3.

2) Loading Phase 2 : Without pilecap actuators(no pilecap passive soil pressure)

The loading sequence was controlled by displacement starting with $\mu_\Delta = 1$ based on the yield displacement derived from the loading Phase 1. Controlling displacement ductilities were $\mu_\Delta = 1, 2, 3, 5$. The test was stopped at $\mu_\Delta = 5$.

3) Loading Phase 3 : With pilecap actuators in phase with column actuators
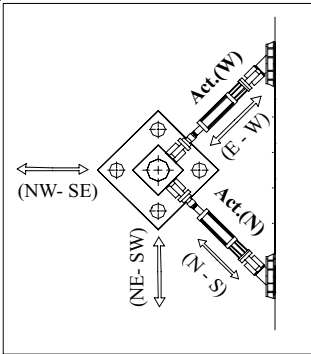
Since pile failure did not occur at the end of Loading Phase 2, an addition loading phase (Loading Phase 3) was carried out to investigate the pile-pilecap joint's behavior at maximum possible forces that would develop in the pile considering potential strain hardening and uncertainties in material strengths.

The loading steps were controlled by displacement of the footing. Pilecap displacement was increased in multiples of 24mm, with column top actuator force set to 2.0 times pilecap actuator force, with both acting in the same direction (as distinct from Loading Phase 1 where the actuator force at column top and pilecap acted in opposition). The system was loaded in two orthogonal and two diagonal directions as in Loading Phases 1 and 2.

4.6 Observations During The Test

Unit CFPS1 was tested under simulated seismic loading using the procedure outlined in section 4.5. The experimental observations of CFPS1 made during the test are summarized below and test photos are shown in Appendix I.

Table 4.3: Loading protocol of CFPS1
(Phases 1 and 2 only)

Actuator Control	Loading Level		Load'g Step	Load'g Direction	# of cycle	Act. (W) kN	Act. (N) kN	Remark
Force(kN) Control	Force Ratio to Fy	25%	1	E - W	1	156		1. Phase 1 :
			2	N - S	1	156		With Pile-Cap Actuator.
			3	NW - SE	1	111	111	
			4	SW - NE	1	111	111	2. Phase 2 :
		50%	5	E - W	1	311		Without Pile-Cap Actuators.
			6	N - S	1	311		Displacement Control Only
			7	NW - SE	1	222	222	
			8	SW - NE	1	222	222	3. Test Model Layout
		75%	9	E - W	1	471		
			10	N - S	1	471		
			11	NW - SE	1	334	334	
			12	SW - NE	1	334	334	
		100%	13	E - W	1	627		
			14	N - S	1	627		
			15	NW - SE	1	445	445	
			16	SW - NE	1	445	445	

Actuator Control	Loading Level		Load'g Step	Load'g Direction	# of cycle	Act. (W) mm	Act. (N) mm.	
Displacement(mm) Control	Ductility Level	1	17	E - W	2	24.9		
			18	N - S	2	24.9		
			19	NW - SE	1	17.6	17.6	
			20	SW - NE	1	17.6	17.6	
		1.5	21	E - W	2	37.4		
			22	N - S	2	37.4		
			23	NW - SE	1	26.4	26.4	
			24	SW - NE	1	26.4	26.4	
		2	25	E - W	2	49.8		
			26	N - S	2	49.8		
			27	NW - SE	1	35.2	35.2	
			28	SW - NE	1	35.2	35.2	
		3	29	E - W	2	74.7		
			30	N - S	2	74.7		
			31	NW - SE	1	52.8	52.8	
			32	SW - NE	1	52.8	52.8	
		4	33	E - W	2	99.6		
			34	N - S	2	99.6		
			35	NW - SE	1	70.4	70.4	
			36	SW - NE	1	70.4	70.4	

4.6.1 Application of gravity load

When the gravity load was applied to the test unit CFPS1, a few flexural cracks of radial direction were observed on bottom of the pilecap and there was no cracking developed in the remainder of the test unit as was expected.

4.6.2 Force control at Loading Phase 1

The seismic force corresponding to the theoretical yield strength was applied to the test unit in four steps. In each step one loading cycle for each direction was applied and the following observations were made:

±0.25 F_y'

There were minor new cracks on the bottom surface of the pilecap in addition to the extensions of cracks which formed at gravity loading.

±0.5 F_y'

The first flexural crack observed at the column-pilecap joint interface and hairline cracks were formed up to 1/2 of column height. On the bottom surface of the pilecap, new flexural cracks also developed and extended up to 2/3 of pilecap depth under positive moments. The previous cracks extended.

±0.75 F_y'

The first cracks were observed at the outer faces of each piles in the diagonal direction loadings. In the normal direction loading, flexural cracks developed newly up to 3/4 of column height and extended.

$\pm\mathbf{F}_\mathbf{y}'$

Flexural cracks reached almost to top of the column. On periperal areas of the pilecap bottom, flexural cracks opened about 0.2 mm ~ 0.5 mm. Additional flexural cracks were observed on the outside faces at pile A and C each.

4.6.3 Displacement control at Loading Phase 1

Using the measured first yield displacements in each directions of loading, an average reference yield displacement, corresponding to $\mu_\Delta = 1$ was estimated to be 26.6mm from Eq. (4.3). The rest of the test was controlled by the column head lateral displacement so that the maximum horizontal displacement of the test unit corresponded to selected displacement ductility levels. Two cycles for two orthogonal directions and one cycle for each diagonal direction were imposed at each displacement ductility.

It was clear that the damage was largely concentrated in the plastic hinge regions of the column as intended in the design of the test unit. The damage at the pilecap did not significantly affect the performance of the test unit.

$\mu_\Delta = \pm 1.0$

In addition to extension of the old cracks, there were first shear cracks in the column. On periperal regions of the bottom of pilecap, flexural cracks widened to be about 0.2mm~1.0mm. In addition, the first crack was observed on top of the pilecap due to the strain penetration of column longitudinal steel into the pilecap. Inclined shear cracks started to form on pilecap side. There were minor extensions of old cracks on piles.

$\mu_\Delta = \pm 1.5$

Crushing of cover concrete was first observed at the column plastic hinge region in the first cycle of the orthogonal direction loading. More shear cracks developed in the column. Two major cracks on each pile cap side widened to be 0.5mm~1.1mm. There were minor crack extensions on piles.

$\mu_\Delta = \pm 2.0$

In the first cycle of the orthogonal direction loading, the first vertical splitting crack developed in the column. Further crushing and spalling of cover concrete occurred at the bottom of the column. On the top surface of the pile cap, flexural cracks were observed. The first cracks were observed on the inside of each four piles in addition to the further extensions of old cracks at the pile cap and piles. The largest crack width on the pile cap side was 1.8mm. This width was greater than expected, and indicates probable yield of bottom mat flexural reinforcement.

$\mu_\Delta = \pm 3.0$

The damage was severe from the crushing and spalling of cover concrete at the column plastic hinge region. Shear cracks were more extended and developed.

$\mu_\Delta = \pm 4.0$

Further crushing and spalling of cover concrete occurred at the column plastic hinge region. More vertical splitting and shear cracks were found in the column. Crack widths at the bottom of pilecap were about 1.0mm ~ 1.2mm and the largest crack width on the pilecap side was 3.0mm. Strain penetration cracks were formed around the column. At this stage, it was noted that concrete had spalled over 508mm length from the critical

section. The column reinforcing bars were well exposed in the hinge regions with no sign of buckling of the longitudinal compression bars. Further crushing and spalling of concrete at the base of the columns were the significant damage observed during the first cycle. The column bars were carefully examined and they did not appear to have subjected any buckling deformation.

$\mu_\Delta = \pm 5.0$

First sign of the pile concrete crushing was observed. More shear cracks were found in the column.

4.6.4 Loading Phase 2

In Loading Phase 2 the damage to the test unit CFPS1 was largely observed in the pilecap bottom face and the piles. This was because the induced force in the piles increased to about twice that of Loading Phase 1 while the maximum column force was almost the same. Damage to the pilecap-pile joints was not observed and the pin connections at the pile bottom were not damaged.

$\mu_\Delta = \pm 1.0$

Minor spalling of the cover concrete was first observed at pile D. No significant changes were observed.

$\mu_\Delta = \pm 2.0$

More inclined cracks developed in the piles. No significant changes were observed except minor crack extensions.

$\mu_\Delta = \pm 3.0$

A vertical crack developed on Pile **C**. Flexural and shear cracks on the piles propagated down the piles. One large crack width of 1.8 mm was found at the top of the Pile C. More crushing of inner cover concrete of piles was observed. Spalling of cover concrete was started at the interface between the inner face of Pile B and the bottom of the pilecap.

$\mu_\Delta = \pm 5.0$

Spalling of cover concrete was started at the interface between the inner faces of each piles and the bottom of the pilecap. Cover concrete of the pilecap soffit were spalled off at several J-stirrup locations indicating straightening of the 90° hooks. A few more inclined cracks were developed and extended on piles.

4.6.5 Loading Phase 3

$\Delta_{\text{pilecap}} = \pm 24\text{mm}$

More inclined cracks developed in the piles. No significant changes were not observed except minor crack extensions.

$\Delta_{\text{pilecap}} = \pm 36\text{mm}$

A vertical crack was developed on Pile C. Flexural and shear cracks on the piles propagated down to the piles. One large crack width of 1.8 mm was found at the top of the Pile **C**. More crushing of inner cover concrete of piles were observed. Spalling of cover concrete was observed at the interface between the inner face of Pile B and the bottom of the pilecap.

$$\Delta_{\text{pilecap}} = \pm 48\text{mm}$$

Spalling of cover concrete was observed at the interface between the inner faces of each piles and the bottom of the pilecap. Cover concrete of the pilecap soffit were spalled off at several J-stirrup locations. A few more inclined cracks were developed and extended on piles.

4.6.6 End of testing CFPS1

The pilecap damage was significant at the end of test. Large flexural cracks developed on bottom of the pilecap near the column peripheral region and onto the vertical sides of pilecap. The maximum crack width reached to 5mm at the end of test. In addition to the large flexural cracking of pilecap, another remarkable damage, which was spalling of cover concrete of pilecap at 90° J-hook locations, was observed at the pilecap. At the end of the test, the cover concrete beneath the column had totally spalled off and damage to the pilecap was significant. It appeared that the column longitudinal reinforcement was slipping in the pilecap joint.

4.7 Force-Displacement Hysteresis Curve.

4.7.1 Loading Phase 1 : With simulated passive soil pressure on pilecap side

The response of the Loading Phase 1 was well predicted as it was dominated by the column's response. The prediction was done by adding the inelastic response of column to the elastic response of footing and of pile group based on the basic analytical methods described in Appendix A. In Figures 4.8 - 4.11, the measured force-displacement response history of CFPS1 is shown along with the predicted response envelope. For the
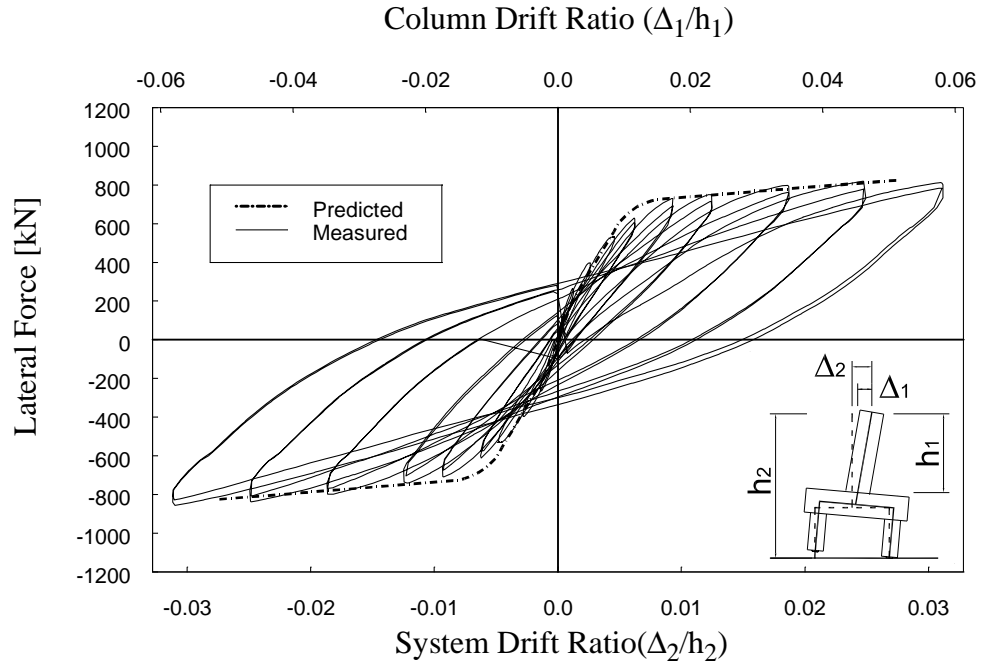
Figure 4.8: Hysteresis loop of orthogonal direction(Eeast-West) loading at Loading Phase 1
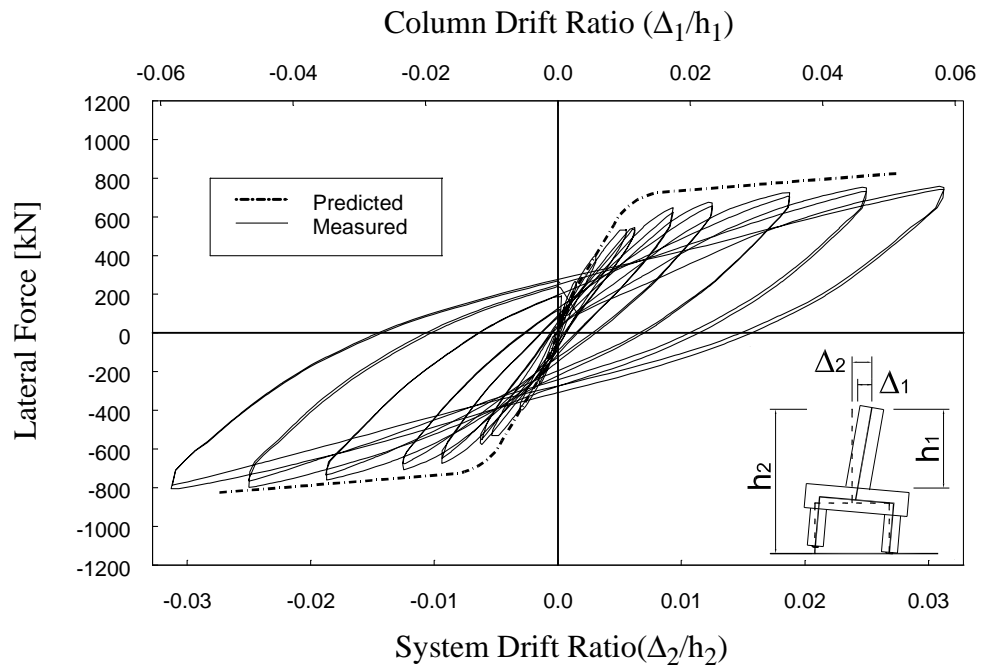
Figure 4.9: Hysteresis loop of orthogonal direction(North-South) loading at Loading Phase 1

108
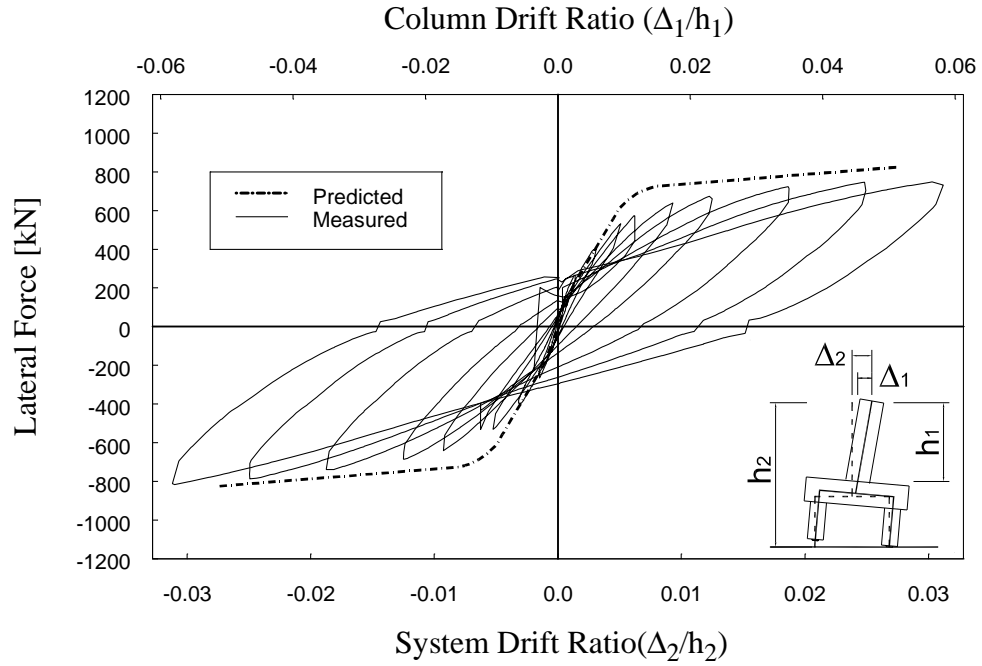
Figure 4.10: Hysteresis loop of diagonal direction(SE-NW) loading at Loading Phase 1
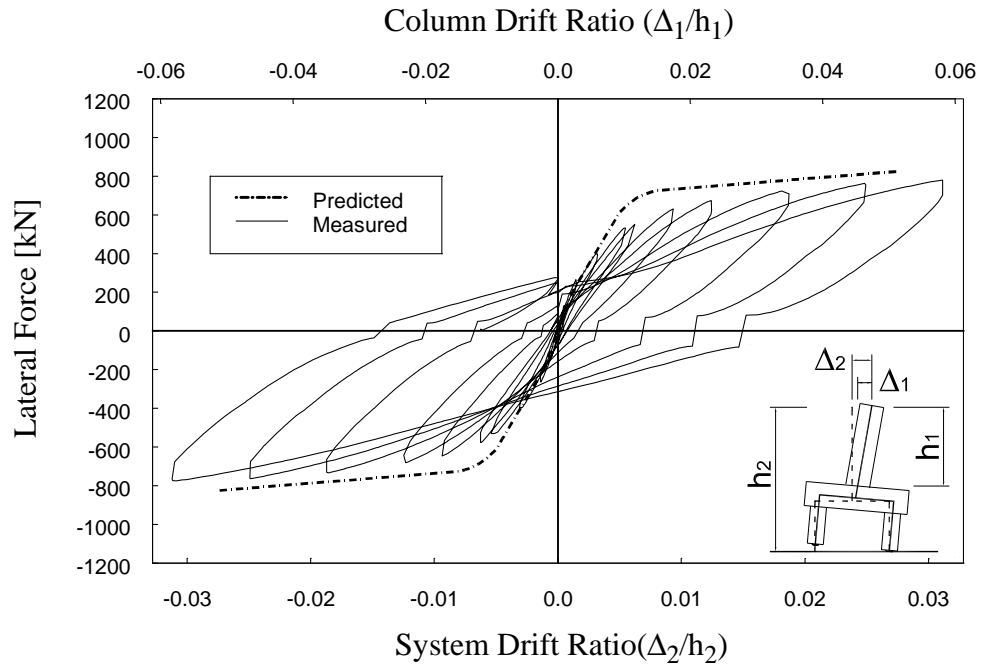
Figure 4.11: Hysteresis loop of diagonal direction(NE-SW) loading at Loading Phase 1
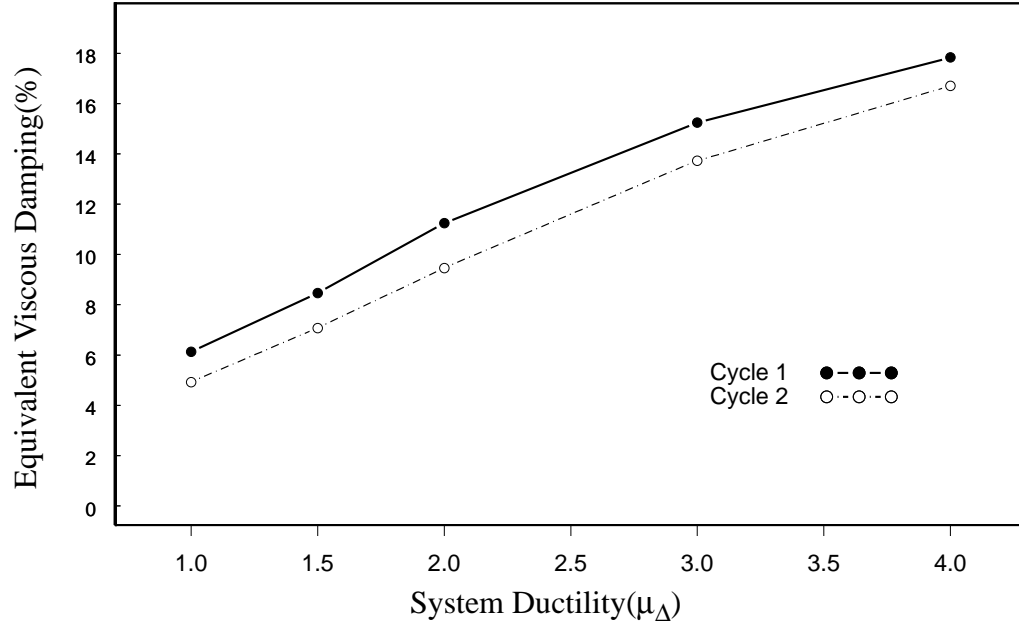
Figure 4.12: Equivalent viscous damping of orthogonal direction loading at loading phase 1

orthogonal direction loading, the predicted and observed envelopes of the force - displacement response are in good agreement, while about 5% of drop in strength occurred in diagonal direction loading due to prior loading in orthogonal direction. Energy absorption capacity of the system, as indicated by the shape and stability of the hysteresis loops, was excellent. There was no strength degradation observed until the system displacement ductility 5, which corresponded to a column drifted about 6.0 %.

The equivalent viscous damping of CFPS1 at different ductilities for the orthogonal direction loading is presented in Figure 4.12. It is seen that the equivalent viscous damping of the system increased from 6% at $\mu_\Delta =1$ to 18% at $\mu_\Delta = 5$. The difference in

the equivalent viscous damping level between the first and second series of cycles was about 1.5%.

4.7.2 Loading Phase 2 : Without simulated passive soil pressure on pile-cap side

In Figures C.1 and C.3 the measured force-displacement response history of each orthogonal and diagonal direction at loading phase 2 is shown. Since the column had been loaded well beyond the elastic range during loading phase 1, the initial stiffness of the unit in the loading phase 2 was much less than the stiffness in the loading phase 1.

4.7.3 Loading Phase 3 : Until pile reinforcement fracture

Since several pile longitudinal rebars fractured at pilecap displacement of 48mm, the test was terminated. Although the strength of CFPS1 dropped to 75% of loading phase 2, there was no sign of further strength degradation in the system as was seen in the hysteresis loops. The measured force-displacement response history of loading phase 3 is shown in Figures C.5 and C.11.

4.8 Strain Data for Pile Bending

In this section the strain data obtained during the test are presented in a reduced form as strain profile plots using the strains recorded at the peak displacements in the first loading cycle at each ductility. Only the data related to the unsymmetric cyclic behavior of pile are reported here and the other strain data on the column-pilecap joint region are presented in Appendix F.

4.8.1 Unsymmetric cyclic behavior of pile

Figures 4.13 - 4.15 and 4.16 - 4.18 are the peak strain profiles of pile longitudinal reinforcement, PAL6 and PAL2, respectively, in the pile-pilecap joint region at diagonal direction loading(SE-NW). Figures 4.13 - 4.15 shows that the strains of PAL6, which is located near the outer face of the pile with respect to the column location, are in tension during the test except $0.25F_y$ of loading in Figure 4.13. However, the strains of PAL2 which is located near the inner face of the pile have subjected to both tension and compression during the test as shown in Figures 4.16 - 4.18. This means that the pile was subjected to unsymmetric cyclic behavior with the critical direction being pile-pilecap closing moment during the test. This behavior is significant because that it implies that the force transfer mechanism of the Knee joint for the bridge bent may not be applied to the design of the pile-pilecap joint for opening moment since the mechanism needs the compressive stress block in the pile section at the interface of the pile-pilecap. This is further discussed in Section 6.3.2.
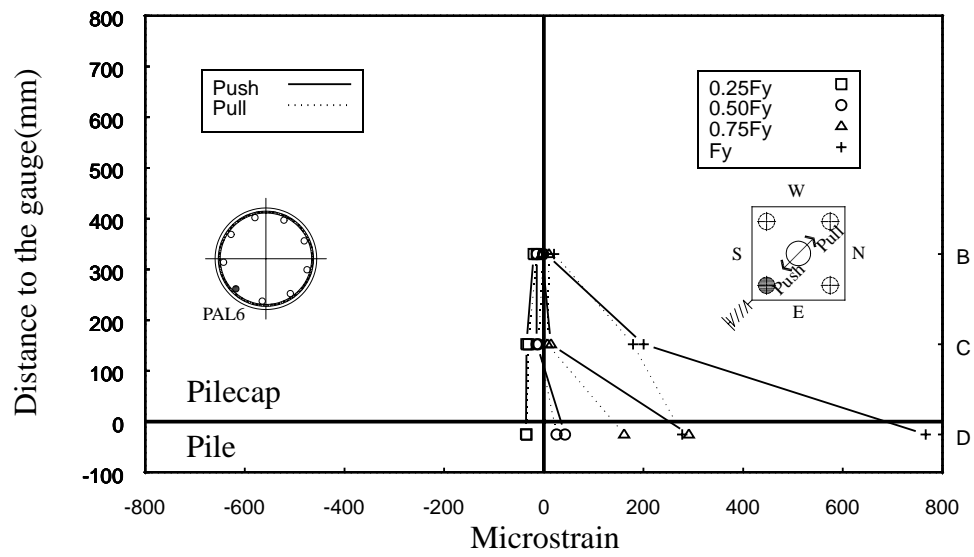
Figure 4.13: Peak strain profiles of pile longitudinal reinforcement(PAL6) in pile A.
At column pre-yield in diagonal direction(SE-NW) loading at Loading Phase 1
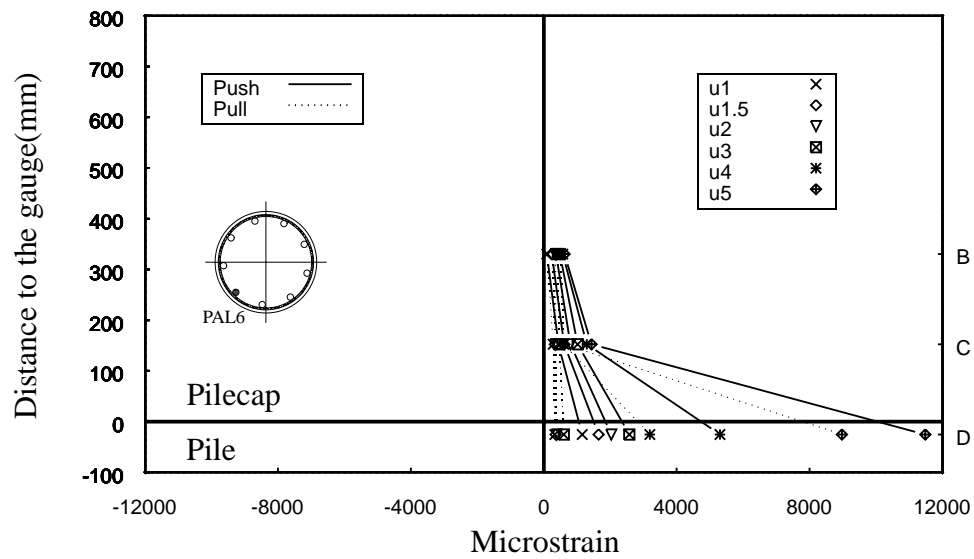
Figure 4.14: Peak strain profiles of pile longitudinal reinforcement(PAL6) in pile A.
At column post-yield in diagonal direction(SE-NW) loading of Loading Phase 1
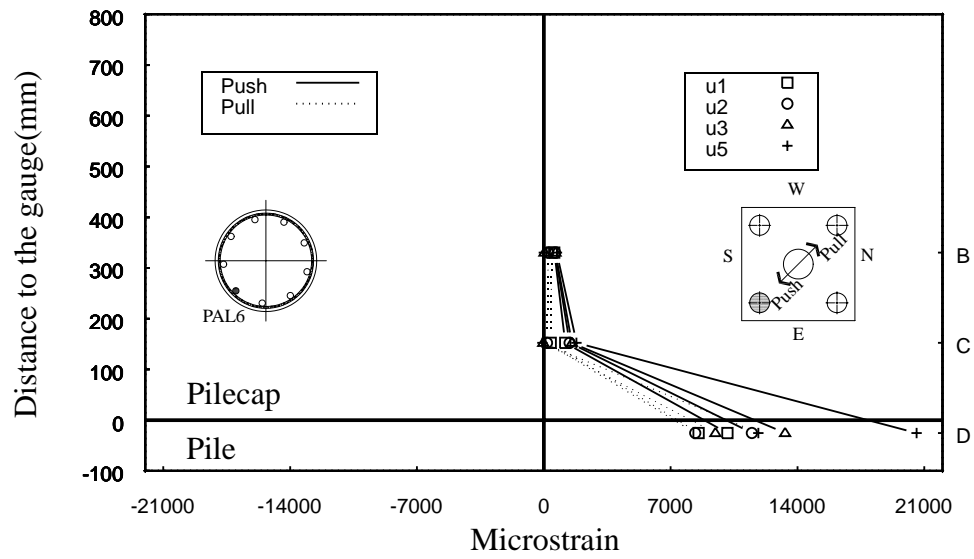
Figure 4.15: Peak strain profiles of pile longitudinal reinforcement(PAL6) in pile A. At column post-yield in diagonal direction(SE-NW) loading of Loading Phase 2
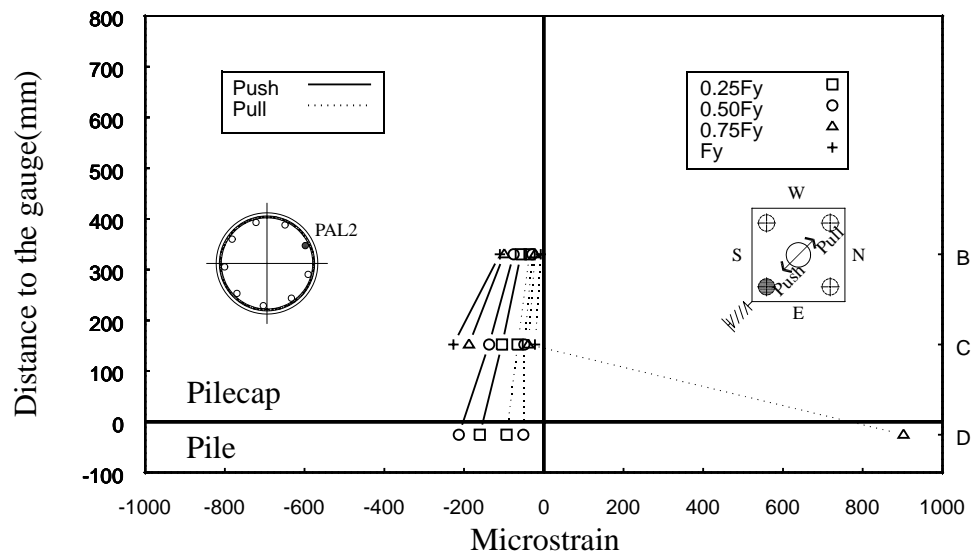
Figure 4.16: Peak strain profiles of pile longitudinal reinforcement(PAL2) in pile A. At column pre-yield in diagonal direction(SE-NW) loading at Loading Phase 1
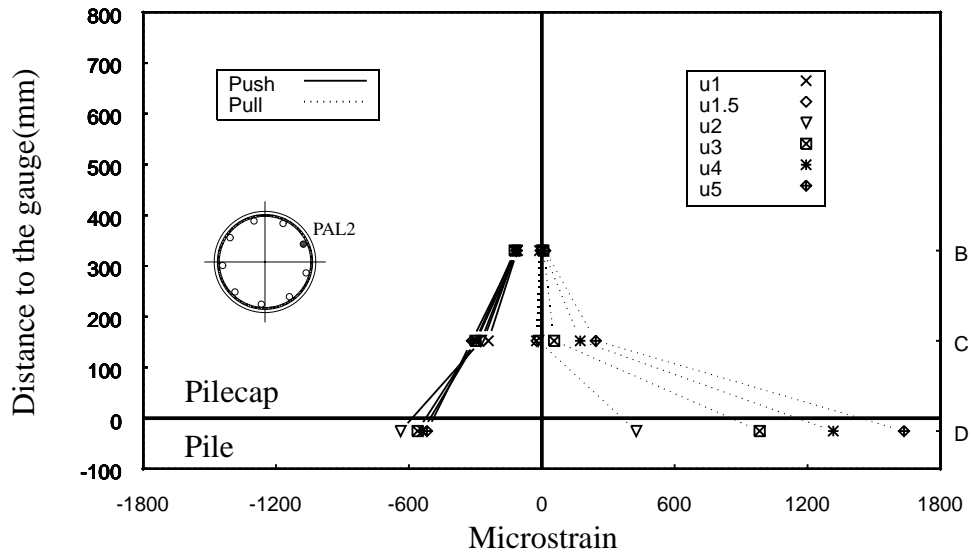
Figure 4.17: Peak strain profiles of pile longitudinal reinforcement(PAL2) in pile A.
At column post-yield in diagonal direction(SE-NW) loading at Loading Phase 1
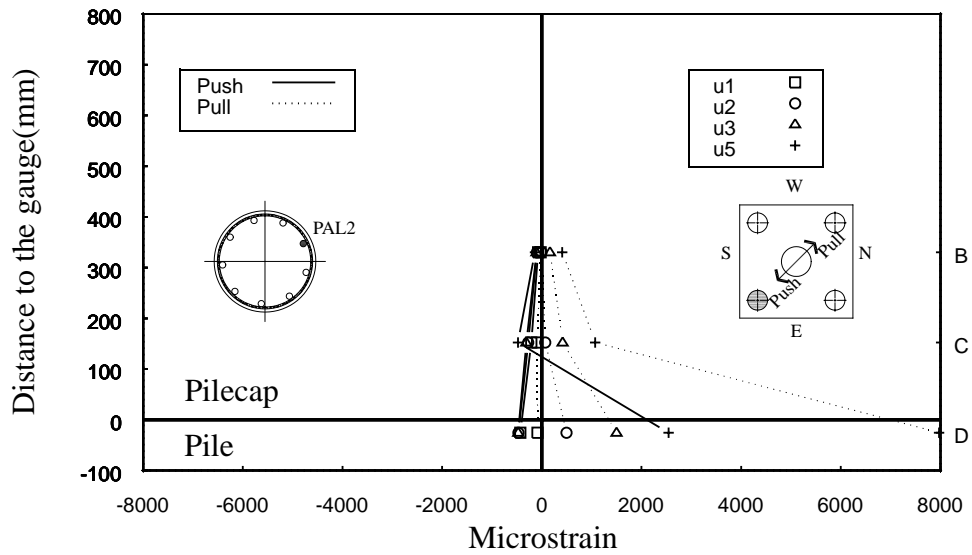
Figure 4.18: Peak strain profiles of pile longitudinal reinforcement(PAL2) in pile A.
At column post-yield in diagonal direction(SE-NW) loading of Loading Phase 2

Chapter 5: Test Details and Results of CFPS2 (Headed Reinforcement)

5.1 Reinforcement Detail of CFPS2

The general dimensions and reinforcement details of CFPS2 are shown in Figure 5.1. Unit CFPS2 was designed after the testing of unit CFPS1. Its design incorporated the experience gained from the first test. All rebar except spirals were provided by headed reinforcement. Larger diameter column bars were used, making anchorage potentially more difficult, if headed rebar had not been used. Headed reinforcement is expected to provide improved anchorage, particularly, of column longitudinal reinforcement, and pilecap stirrups which suffered anchorage failure in test CFPS1.

5.2 Design of Unit CFPS2

Unit CFPS2 was designed based on the experience gained from the test of CFPS1. The same design principle and procedure as those adopted for unit CFPS1 were used. Since CFPS1 did not show full plastic hinge formation at the piles at Loading Phase 2, the column length was reduced by 305mm from that of CFPS1 to increase the shear force to the pile group. This made the maximum lateral load required to form a plastic hinge at the bottom of the column to be the capacity of the actuators, 979 kN, mounted on the column load stub. In addition, the reinforcement ratio of the pile longitudinal rebars were reduced from 0.0089 to 0.0079 by providing 8 bars of 15.9mm diameter to reduce the pile yield moment capacities.

102 mm

Dimension

Column   : Ø762 mm
Piles   : Ø508 mm
Pilecap   : 2896mm x 2896mm x 762mm
Test Base : 3353mm x 3353mm x 914mm

15-Ø0.6in.
Strands
(Debonded)

4-Hydrolic
Hollow Core Ram

4-Load Cell

18-#9[dia.28.7mm](2.55%)

#5[dia.15.9mm]
@102mm(1.09%)

#6[dia.19.1mm]@152mm
both ways

65 legs-#4[dia.12.7mm](outside)
8 legs-#4[dia.12.7mm](inside)

5 legs - #4[dia. 12.7mm](outside)
1 legs - #4[dia. 12.7mm] (inside)

#3[dia.9.5mm]@178mm

#8[dia.25.4mm]@152mm
both ways

#3[dia.9.5mm]
@64mm(0.92%)

37.5mm thick
expansion joint filler

8-#5[dia.15.9mm]
(0.79%)

711mm

305mm

#4[dia.12.7mm]
@38mm

Ø57mm
unbonded
rod

762 mm
1905 mm
2667 mm
762 mm
5182 mm
1219 mm
1600 mm
914 mm

1981 mm
2896 mm
3353 mm

Figure 5.1: Reinforcement details of CFPS2

117

Table 5.1: Critical loading conditions for the design of actions

Structural member actions to be designed	Critical loading phase : Loading direction / Pilecap restraint condition	Max. applicable lateral load
Pilecap Negative Bending	Loading Phase 2 : Orthogonal / No Pilecap Restraint	823 kN
Pilecap Positive Bending	Loading Phase 2 : Diagonal /No Pilecap Restraint	817 kN
Pilecap Shear Transfer	Loading Phase 1 : Orthogonal / Pilecap Restraint	979 kN
Pile - Pilecap Joint	Loading Phase 2 : Diagonal / No Pilecap Restraint	817 kN
Pile Bending, Shear and Confinement	Loading Phase 2 : Diagonal / No Pilecap Restraint	817 kN
Pile-Test Base Pin Connection	Loading Phase 2 : Diagonal / No Pilecap Restraint	817 kN

Table 5.1 shows the critical loading phase for each structural member action to be considered for the design of CFPS2.

5.2.1 Column design

1) Longitudinal Reinforcement

Although the column length is reduced by 305mm from that of CFPS1 to increase the shear force, the reinforcement ratio of CFPS1(rl = 2.57%), is maintained as much as possible by providing 18 bars of 28.7mm diameter which made the column longitudinal reinforcement ratio, rl = 2.55%. Under the same gravity load of 2002 kN as that of CFPS1, the maximum shear force resulting from the moment at the development of the flexural overstrength of the column plastic hinge was :

$$V_c^\circ = 979\text{kN} \tag{5.1}$$

This was the maximum load capacity of the actuators at the top of the column.

2) Confinement

The ratio of transverse reinforcement, rs = 0.0109 provided by 15.9mm diameter bar with 102mm spacing in the form of spiral, was determined. The provided reinforcement

ratio of CFPS2 was similar to that of CFPS1 ($\rho_s = 0.0112$) and exceeded the value of ρ_s = 0.0084 obtained from Eq. (3.2).

3) Anti-Buckling Considerations

The minimum transverse reinforcement ratio against the buckling mode over several layers of transverse reinforcement was 0.0036 by Eq. (3.3) with n=18.

An explicit check for the bar buckling between adjacent transverse reinforcement was not carried out because this buckling mode is already accounted for in Eq. (3.2).

4) Shear Requirements

In accordance with Eqs. (3.5)-(3.7),

$$V_c = 0.042 \times \sqrt{27.6} \times \left(0.8 \times \frac{\pi \cdot 0.762^2}{4} \right) = 80\text{kN} \tag{5.2}$$

$$V_p = 0.85 \times 2002 \times \frac{(381 - 127)}{2286} = 189\text{kN} \tag{5.3}$$

$$V_s = \frac{\pi}{2} \times \frac{0.0002 \times 413.7 \times (0.724 - 0.127)}{0.102} \times \cot 35 = 1086\text{kN} \tag{5.4}$$

From Eq. (3.4), the nominal shear capacity of the column was :

$$V_n = 80 + 189 + 1086 = 1355\text{kN} \tag{5.5}$$

This is greater than the required shear strength given by Eq. (5.6) using the shear strength reduction factor, $\phi_s = 0.85$:

$$\frac{V_c^\circ}{\phi_s} = \frac{979}{0.85} = 1151\text{kN} \tag{5.6}$$

which associated with the development of flexural overstrength at column plastic hinge.

5.2.2 Pile design

1) Longitudinal reinforcement and axial loads in piles

First, a longitudinal reinforcement ratio of the pile was reduced to 0.0079 from 0.0089 of CFPS1 so that piles would fail in Loading Phase 2. This reinforcement ratio was determined through an iterative process as had been done in the design of unit CFPS1.

From the moment equilibrium condition under diagonal direction loading without passive pilecap restraint, the axial forces developed in the extreme piles is given by Eq. (3.10).

Because the tension capacity of the longitudinal reinforcement in the piles, $T_{s,max}$, was :

$$T_{s,\,max} \;=\; 8 \times 0.0002 \times \frac{455.1}{1000} \;=\; 728 \text{kN} \tag{5.7}$$

based on f_{ye}= 455.1 MPa, the maximum tension force in the piles, T_{max}, was assumed to be 95% of $T_{s,max}$, which is 692kN considering the moment induced at the pile-pilecap interface. Hence, from Eq. (3.11), the maximum lateral force at the column top to avoid the tensile yield of piles was :

$$F_{max} \;=\; \frac{(552 + 692) \times 1.981 \sqrt{2}}{(2.286 + 0.762 + 1.219)} \;=\; 817 \text{kN} \tag{5.8}$$

This is illustrated in Figure 5.2. Therefore, from Eq (3.12), the maximum pile compression force was :

$$C_p \;=\; 552 + \frac{817(2.286 + 0.762 + 1.219)}{1.981 \sqrt{2}} \;=\; 1796 \text{kN} \tag{5.9}$$

$$P = 2002 \text{ kN}$$

$$F = \textbf{817} \text{ kN}$$

$$L_c = \textbf{2.286} \text{ m}$$

$$h_f = 0.762 \text{ m}$$

$$L_p = 1.219 \text{ m}$$

$$F = \textbf{817} \text{ kN}$$

T_p C_{mp} C_p

$$L_f \sqrt{2} = 2.801 \text{ m}$$

(a) Elevation   (b) Plan view
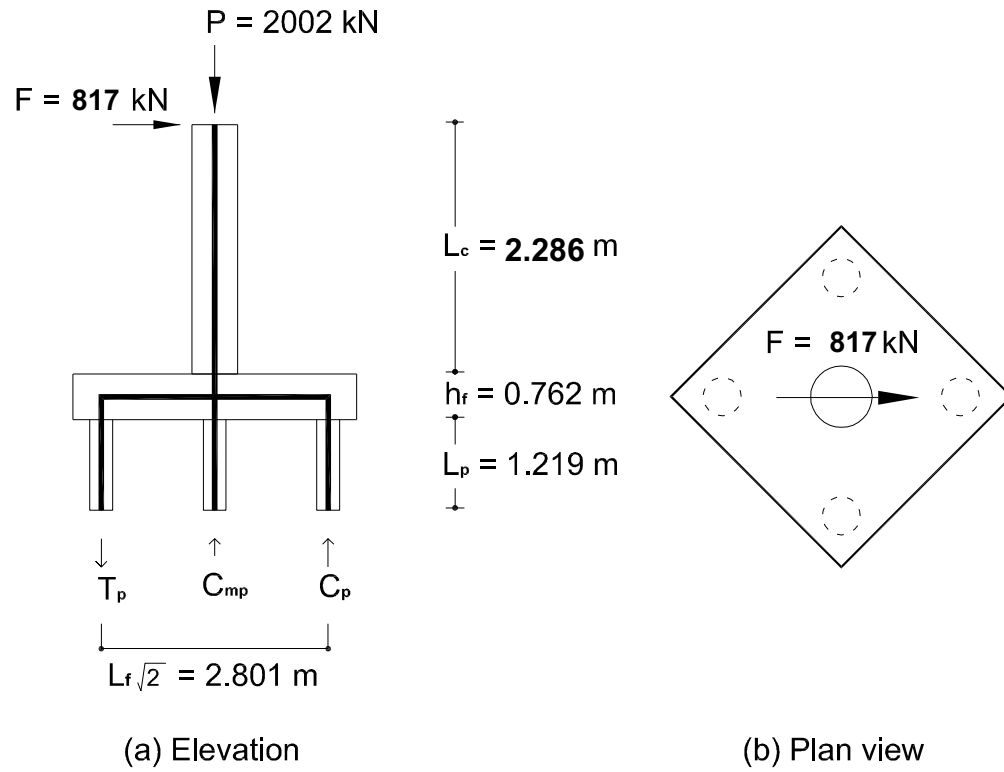
Figure 5.2: Diagonal direction loading without pilecap resistance for pile design
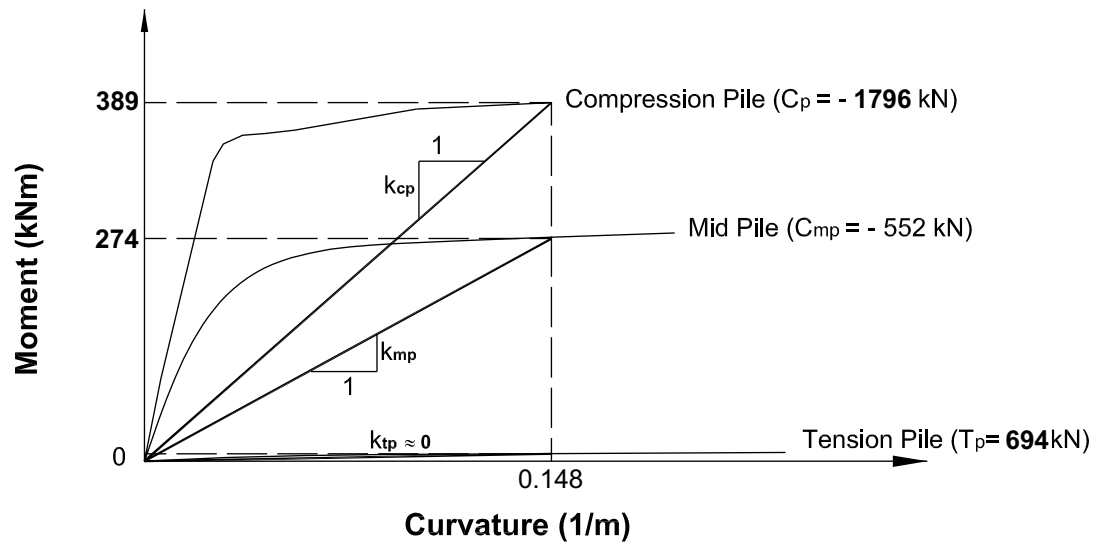
Figure 5.3: Partial moment-curvature responses for piles

2) Shear reinforcement

Without the passive pilecap restraint, the moment-curvature analyses of the piles showed that the yield strengths of the pile group for the orthogonal and diagonal direction loadings were 683kN and 703kN, respectively. The ratios of these yield strengths to the maximum lateral loads for the orthogonal and diagonal direction loading were 0.83 and 0.88, respectively. Accordingly, the piles were detailed for ductility to enable the development of plastic hinges immediately below the pilecap face. Transverse reinforcement of 9.52mm diameter spiral with 64mm spacing (ρ_s = 0.0097) was provided to satisfy Eq. (3.2).

Shear was critical in the mid and compression piles as Table 5.2 shows. The shear demand in tension pile was small enough to be neglected. The value of k for V_c components for both the mid and compression piles was considered conservatively to be the minimum, 0.042, shown in Figure 3.6. With a shear strength reduction factor of ϕ_s = 0.85, the shear capacity still greatly exceeded the demand.

Based on the assumption that plastic hinge length and the curvature distribution is independent from axial force, the lateral force distribution among the piles, from Eq (3.13) and Figure 5.3, is:

Table 5.2: Contribution of the shear strength mechanism for the mid and compression piles

Shear Component	Mid Piles	Compression Pile
V_c [Eq. (3.5)] with k=0.042	31 kN	31 kN
V_p [Eq. (3.6)]	76 kN	205 kN
V_s [Eq. (3.7)] with θ=35°	360 kN	294 kN
$\phi_s V_n$ [Eq. (3.4)]	397 kN	451 kN

$$V_{cp} = \frac{389}{389 + 2 \times 274 + 0} \times 817 = 339 \text{ kN}$$

$$V_{mp} = \frac{274}{389 + 2 \times 274 + 0} \times 817 = 237 \text{ kN} \qquad (5.10)$$

$$V_{tp} = \frac{0}{389 + 2 \times 274 + 0} \times 817 = 0 \text{ kN}$$

3) Anti-buckling reinforcement

Considering the number of longitudinal bars provided in the pile, it was found that Eq. (3.3) required $\rho_s \geq 0.0016$ to ensure adequate resistance against buckling of the longitudinal reinforcement in the pile. The transverse reinforcement ratio provided in the piles was $\rho_s = 0.0097$, which was significantly greater than that required for resisting buckling of the pile bars.

5.2.3 Pilecap design

The design of the pilecap was based only on the actions of the compression side since they were of greatest significance.

1) Negative moment

The critical condition for the design of the pilecap for negative bending moment was orthogonal direction loading without passive pilecap restraint (see Figure 5.4 and Table 5.1).

Since the total shear capacity of the piles at the ultimate curvature of the compression pile was 823 kN, the applicable lateral force was reduced from 979 kN. Under the combined gravity and lateral loads, the induced axial tension and compression forces in the piles were 334 kN and 1437 kN, respectively.

P = 2002 kN

F = **823** kN

L_c = **2.286** m

h_f = 0.762 m

L_p = 1.219 m

2Vtp = **223** kN

2Vcp = **600** kN

T_p = **334** kN

C_p = **1437** kN

L_f = 1.981 m

(a) Elevation

F = **823** kN

(b) Plan view
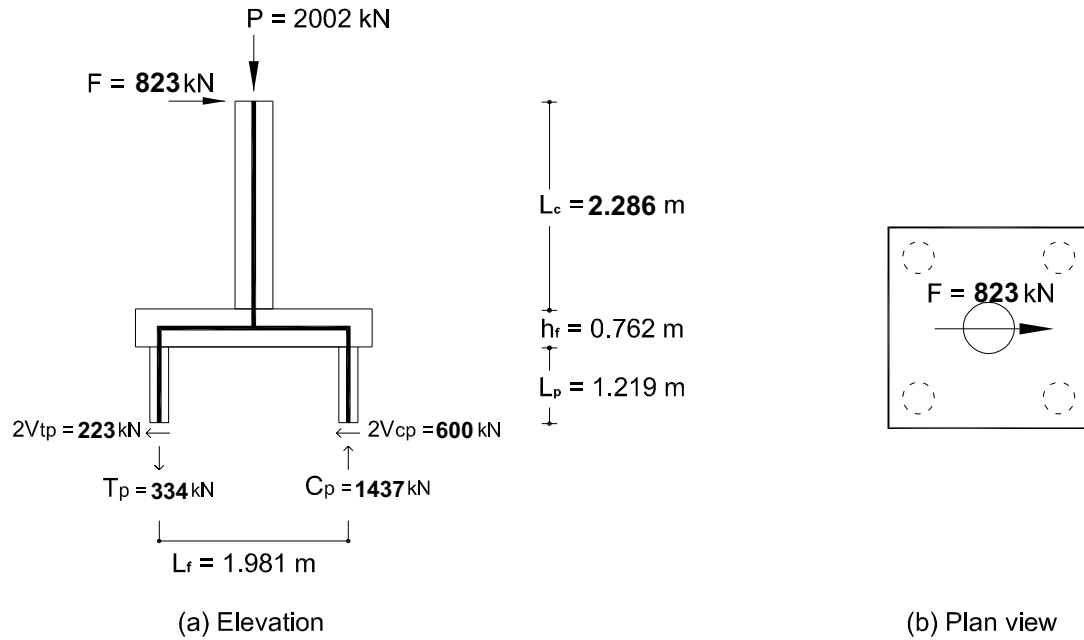
Figure 5.4: Orthogonal direction loading without pilecap resistance
for pilecap negative bending

Based on the moment-curvature analyses for the piles with different axial forces, the moments in each piles at the curvature of 0.163m^{-1}, corresponding to equal displacements of piles were M_{cp} = 366 kNm and M_{tp} = 136 kNm (see Figure 5.5). Accordingly, the individual pile shear forces are :

$$2V_{cp} = \frac{M_{cp}}{M_{cp} + M_{tp}} \times F = \frac{366}{366 + 136} \times 823 = 600 \text{ kN}$$

$$2V_{tp} = \frac{M_{tp}}{M_{cp} + M_{tp}} \times F = \frac{136}{366 + 136} \times 823 = 223 \text{ kN}$$

(5.11)

Although current design practice recommends using the line with the pile face as a critical section for the pilecap negative bending moment, the design pilecap negative
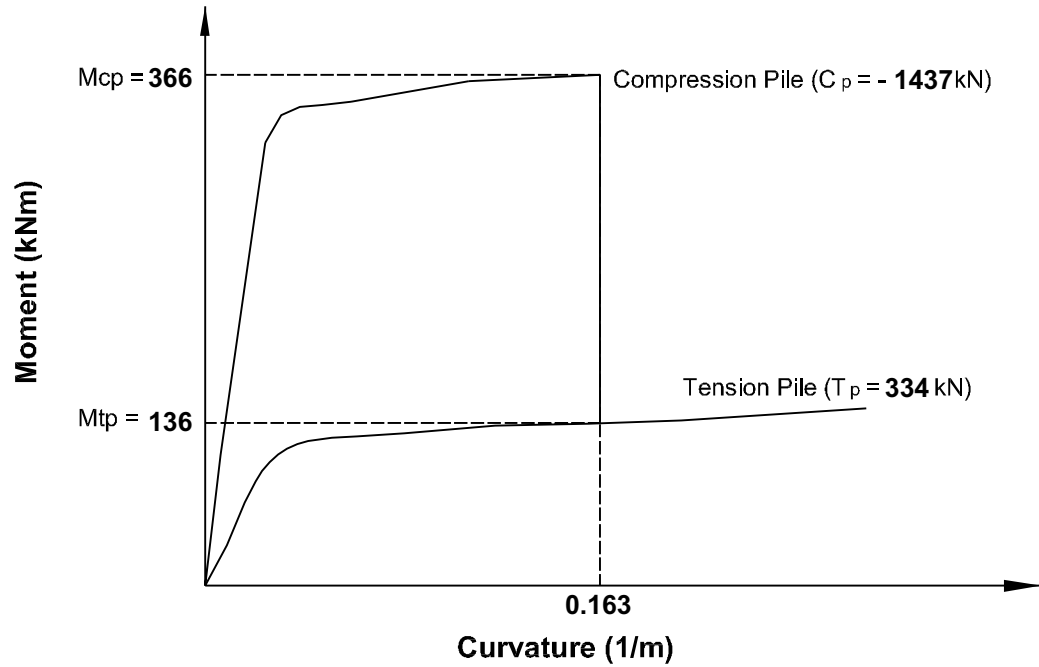
Figure 5.5: Moment-curvature response of piles for determining the pilecap actions

(a) Design actions   (b) Bending moment diagram
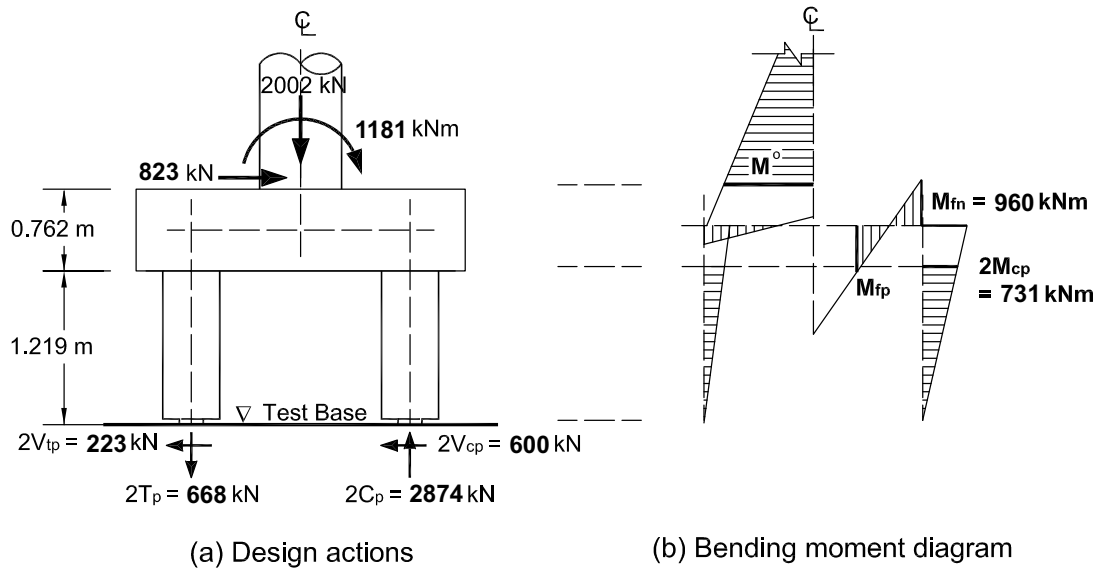
Figure 5.6: Critical moments for the negative bending of the pilecap

125

bending moment, M_{fn}, was obtained conservatively at the centerline of the piles from equilibrium considerations shown in Figure 5.6-(a). This resulted in :

$$M_{fn} = 600 \text{kN} \times (1.219 + 0.762/2)\text{m} = 960 \text{kNm} \qquad (5.12)$$

for which,

$$M_n \geq \frac{M_{fn}}{\phi_f} = \frac{960}{0.9} = 1066 \text{ kNm} \qquad (5.13)$$

where the strength reduction factor for flexure ϕ_f is :

$$\phi_f = 0.9 \qquad (5.14)$$

To ensure the pilecap reinforcement remains elastic, the flexural reinforcement must be placed within an effective width of $2b_{eff} = 2.9$m, as given by Eq. (3.18) and shown in Figure 3.14-(a).

Although reinforcement of #5[dia. 15.9mm] at 152mm centers in both orthogonal directions satisfied the required amount, #6[dia. 19.1mm] was used conservatively ensuring elastic behavior for the pilecap negative bending.

2) Positive moment

The critical loading condition for the design of the pilecap positive bending was loading in the diagonal direction in Loading Phase 1 as shown in Figure 5.7 and Table 5.1. Unlike the case of pilecap negative bending, the applicable maximum load was 979 kN corresponding to the moment capcity of the column plastic hinge since 50% of the applied shear force was resisted by the actuators mounted on the pilecap sides. Assuming

P = 2002 kN

F = **979** kN

L_c = **2.286** m

0.5F

h_f = 0.762 m

L_p = 1.219 m

← V_{tp} ← $2V_{mp}$ ← V_{cp}

T_p C_{mp} C_p

$L_f\sqrt{2}$ = 2.801 m

(a) Elevation

F = **979** kN

0.5F

(b) Plan view
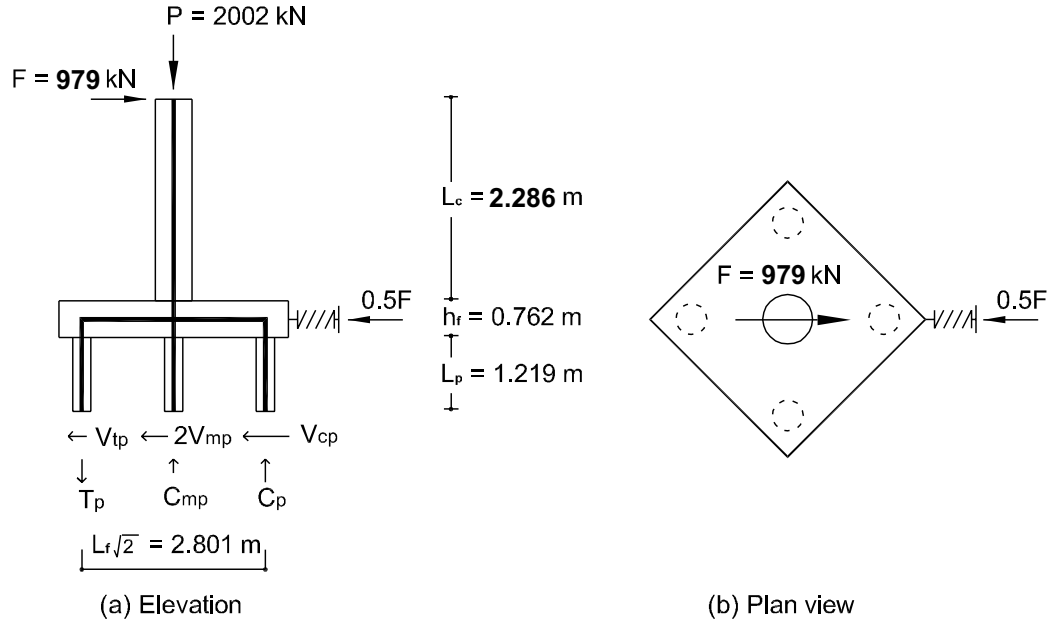
Figure 5.7: Diagonal direction loading with pilecap resistance
for the design pilecap positive moment

no axial force development in the mid piles under lateral loading, the axial tension and compression forces in the extreme piles needed to resist the overturning moment, from Eq. (3.19), is :

$$T = C = \frac{979(2.286 + 0.762 + 1.219) - 0.5 \times 979\left(\frac{0.762}{2} + 1.219\right)}{1.981\sqrt{2}} \qquad (5.15)$$

$$= 1211 \text{kNm}$$

Under the combined seismic and gravity loads, the induced axial forces in the piles were 658 kN in the tension pile, 552 kN in the mid piles and 1761 kN in the compression pile. The moment-curvature analyses for these piles with three different axial forces yielded the moments of each piles as $M_{tp} = 0$ kNm, $M_{mp} = 273$ kNm and $M_{cp} = 389$ kNm

127
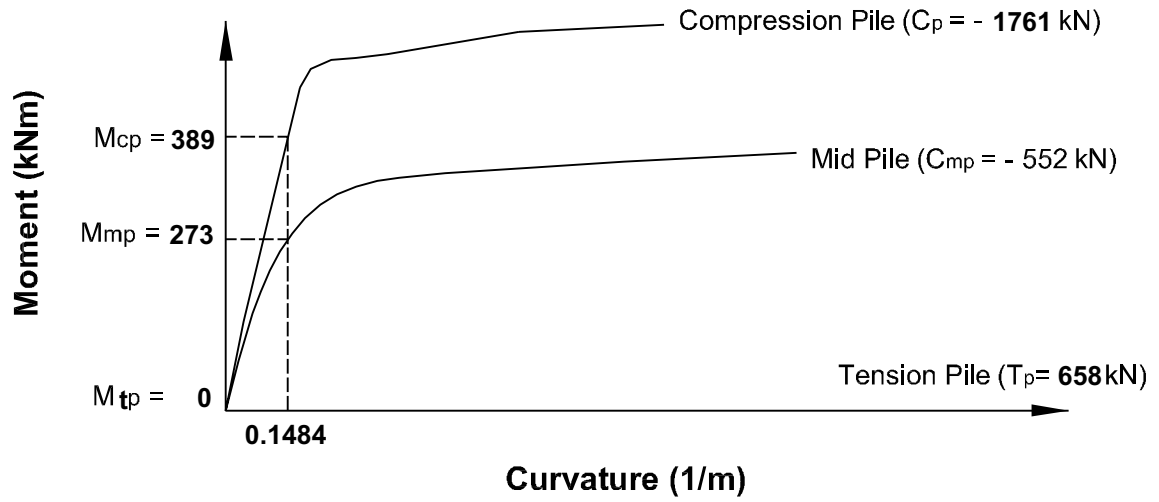
Figure 5.8: Partial moment-curvature responses of piles for Pilecap Positive Bending

at the curvature of 0.1484m^{-1} as shown in Figure 5.8. Therefore, the shear forces in the compression pile, from Eq. (3.20), was :

$$V_{cp} = \frac{389}{389 + 2 \times 273 + 0} \times 489 = 203 \text{ kN} \tag{5.16}$$

The design pilecap positive moment, M_{fp}, obtained from equilibrium considerations (see Figure 5.9) was :

$$M_{fp} = C_p \times \left(\frac{L_f\sqrt{2} - D_c + c}{2} \right) - M_{fn} \times \left(\frac{D_c - c}{L_f\sqrt{2}} \right) \tag{5.17}$$

$$= 1761 \times \left(\frac{2.801 - 0.762 + 0.257}{2} \right) - 325 \times \left(\frac{0.762 - 0.257}{2.801} \right)$$

$$= 1964 \text{kNm}$$

128

(a) Design actions   (b) Bending moment diagram
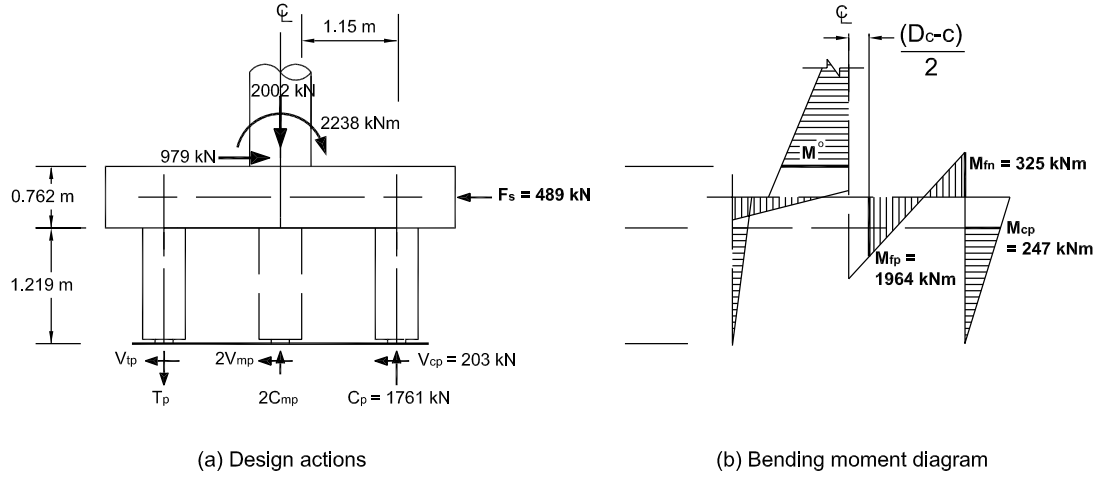
Figure 5.9: Critical Moments for the Positive Bending of the Pilecap

However, a fraction on the resisting bending moment is due to the passive presure force, F_p, and its eccentricity with respect to the resultant compression force. Thereby, the moment resisted by the reinforcement can be approximated to be :

$$M_n \geq \frac{M_{fp}}{\phi_f} - 0.5F\left(\frac{h_f - a}{2}\right) = \frac{1964}{0.9} - 489\left(\frac{0.762 - 0.1}{2}\right) = 2020 \text{ kNm} \qquad (5.18)$$

Hence, the reinforcement detail with #8[dia. 25.4 mm] at 152 mm centers was obtained by considering the effective width of 2184 mm, which is based on Eq. (3.18), and provided in both orthogonal directions over the entire pilecap width.

Since unit CFPS1 showed severe pilecap damage due to the yield of pilecap bottom reinforcement when the design was based on the critical moment in line with the column face, the design moment of the pilecap positive bending for unit CFPS2 was taken at the point of the column compressive stress resultant as discussed in section 6.2.2.

129

3) Shear transfer of the Pilecap

With 0.5F of lateral pilecap resistance in opposite direction to the applied shear force, F, the remaining shear of 0.5F was distributed among the piles in proportion to their stiffnesses. Based on the moment-curvature analyses of the piles with different axial forces[Figure 5.10], the distributed shear force of compression pile, V_{cp}, was 200kN from Eq. (5.19) :

$$2V_{cp} = \frac{M_{cp}}{M_{cp} + M_{tp}} \times 0.5F = \frac{180}{180 + 40} \times 489 = 400 \text{ kN} \tag{5.19}$$

The required tension force, T1, for the strut D1 was thus 200 kN with $\theta = 45^o$ and the second tension force, T2, for the strut D2 was :

$$T2 = \frac{0.5F}{2} \times \frac{0.25b_f}{0.5(L_f - c)} = \frac{0.5 \times 979}{2} \times \frac{0.25 \times 2.896}{0.5(1.981 - 0.254)} = 205 \text{ kN} \tag{5.20}$$

Therefore, a total tension force of 405kN (T1+T2) was needed over the outer 914 mm of effective width. The available tensile capacity of the steel provided for the positive moment in this effective width was 1265kN which greatly exceeded the demand.

5.2.4 Pilecap joints design

The pilecap joints of the test units were designed with reduced amounts of reinforcement by explicitly identifying an internal force flow. The average principal tensile stresses of the joints at the ultimate limit state were estimated to be $0.54\sqrt{f'_c}$ [MPa] and $0.06\sqrt{f'_c}$ [MPa] for the column-pilecap and the pilecap-pile joints,
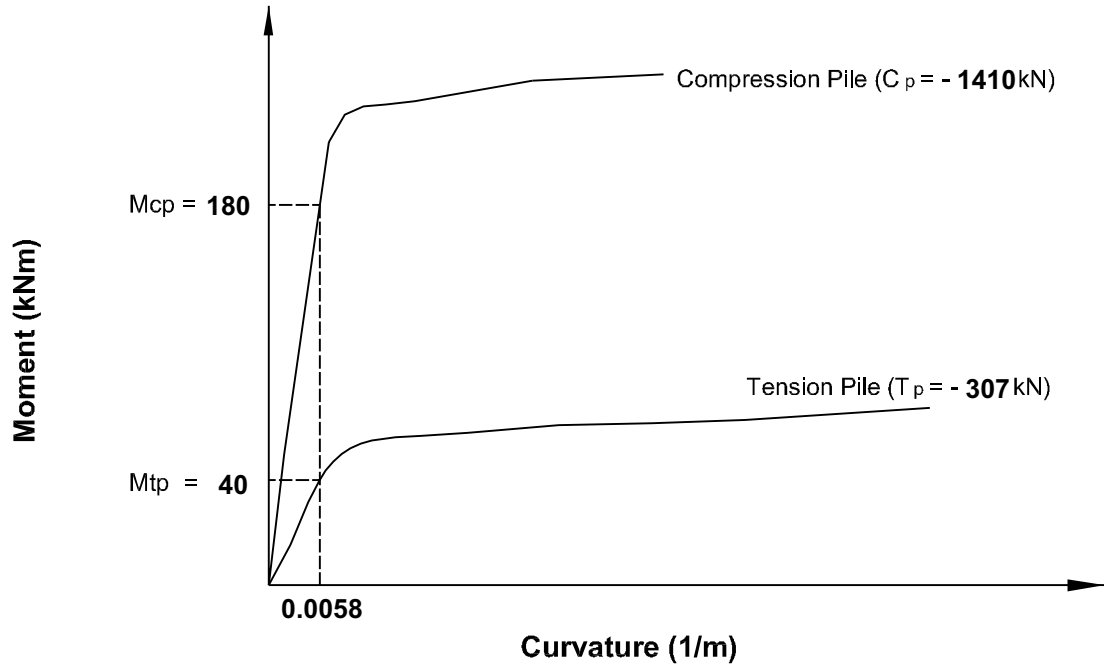
Figure 5.10: Partial moment-curvature responses of piles
at orthogonal direction loading with pilecap restraint

respectively. When comparing these values to the joint design threshold values described above, it was concluded that only the column-pilecap joint should be detailed to ensure appropriate force transfer mechanism for satisfactory internal force flow through the joint. Because $p_t \leq 0.29 \sqrt{f'_c}$ [MPa] for the pilecap-pile joint, joint shear cracking is not expected, and only nominal joint reinforcement satisfying Eq.(B.11) was provided in the form of spirals.

The area of external vertical stirrups required by Eq. (B.7) was 8303mm^2, which was equivalent to 65 sets of #4[dia. 12.7 mm] stirrups. The stirrups were placed within 381mm distance from the face of the column (Figure 5.17). The amount of internal vertical stirrups obtained from Eq. (B.8) was 1039 mm^2, requiring 8 legs of #4[dia. 12.7 mm] stirrups. The volumetric ratio of the horizontal hoop joint reinforcement required

according to Eq. (B.10) was 0.89%, which was provided by #5 [dia. 15.9 mm] spirals at 102mm spacing. In addition to the above details for the joint force transfer mechanism, the pilecap top longitudinal reinforcement area was increased by 1038mm^2 to be consistent with Eq. (B.12). The longitudinal column bars were extended into the joint as close to the bottom pilecap reinforcement as possible. The embedment length of the column bars was 711 mm although there is no minimum development length requirement for the headed rebars.

5.2.5 Pin connection and the test base

The same detail of the pin connection between the piles and the test base as used in Unit CFPS1 was adopted for Unit CFPS2. The test base of Unit CFPS2 was also same as that of Unit CFPF1.

5.3 Test Set-Up

Unlike unit CFPS1, which used two independent reaction walls oriented perpendicularly, the unit CFPS2 used a single reaction wall by constructing the test unit with a 45° rotation to the wall. The actuators were mounted on the reaction wall using 45° angled mounting fixtures. Because the actuator reaction force should be resisted with a 45° angle, there was the possibility of slip of the mounting plate to the reaction wall. To prevent this, the mounting plates which were attached to the reaction wall were connected to each other with 25.4mm thick and 305mm wide steel plates which were tied back on the reaction wall. This was so that the reduced friction resistance between the mounting plate and the reaction wall of one actuator in tension could be compensated by the increased friction resistance of the other mounting plate in compression. In addition,

Figure 5.11: Complete test setup of CFPS2

a steel reaction beam, which was tied down to the strong floor through the hole of the test base, was used for anchoring the post tensioning tendons due to the malfunction of the anchorage device embedded in the test base as shown in Figures 5.1 and 5.11.

5.4 Instrumentation

5.4.1 External instrumentation
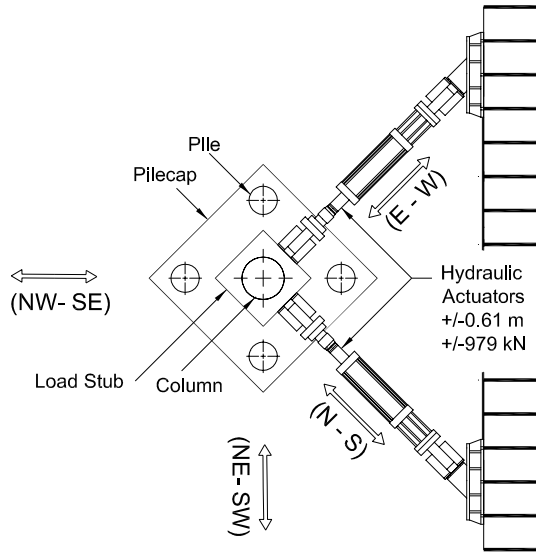
Figure 5.12: Plan view
of column top actuators
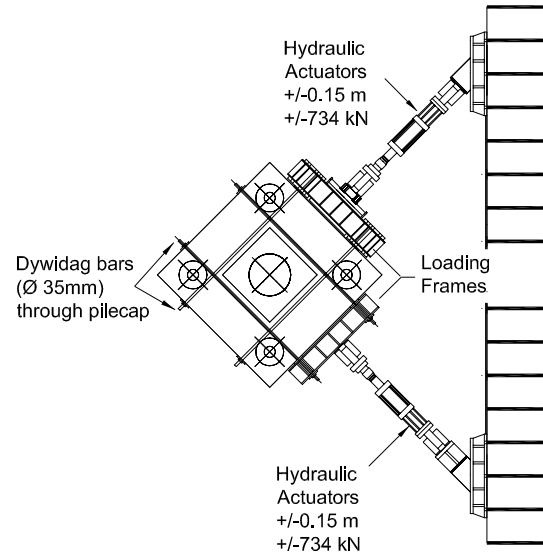
Figure 5.13: Plan view
of pilecap actuators

The external instrumentation of CFPS2 was identical to that of CFPS1 except for the linear potentiometers on piles. Unlike CFPS1, linear potentiometers on piles were installed on piles A and C only. For these piles, those linear potentiometers were instrumented in cross configuration to investigate the directions of the shear force acting on the piles. The external instrumentation is illustrated in Figures 5.14 and 5.15.

5.4.2 Internal instrumentation

CFPS2 was instrumented with strain gauges mounted in the column/pilecap and pile/pilecap joint regions. The locations of strain gauges on reinforcement were same as those of CFPS1 except that addtional strain gauges were placed on top and bottom reinfocement of pilecap in diagonal direction. These strain gauges enabled the study of
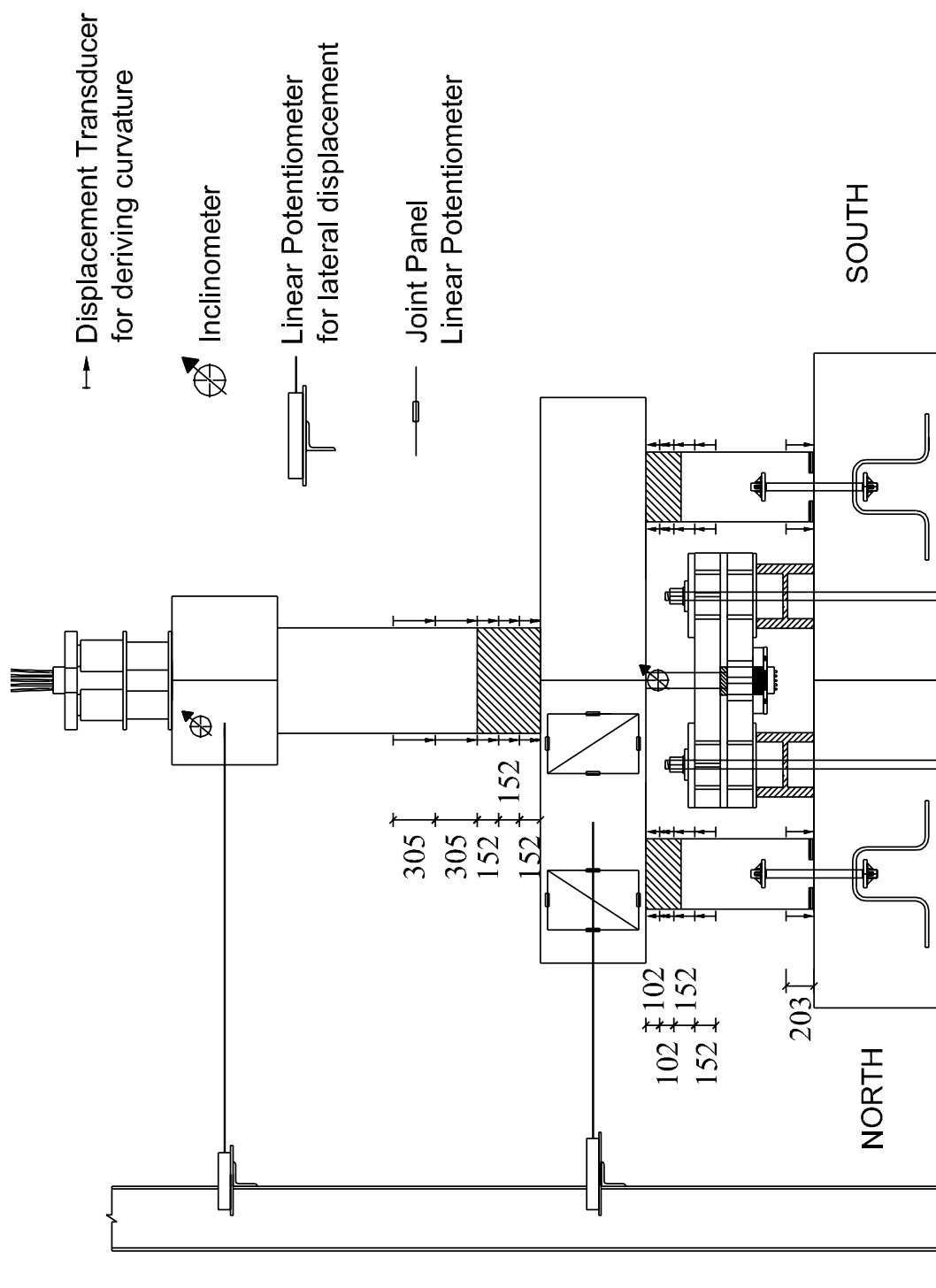
Figure 5.15: Unit CFPS2 vertical view of external instrumentation (Northeast elevation)

135
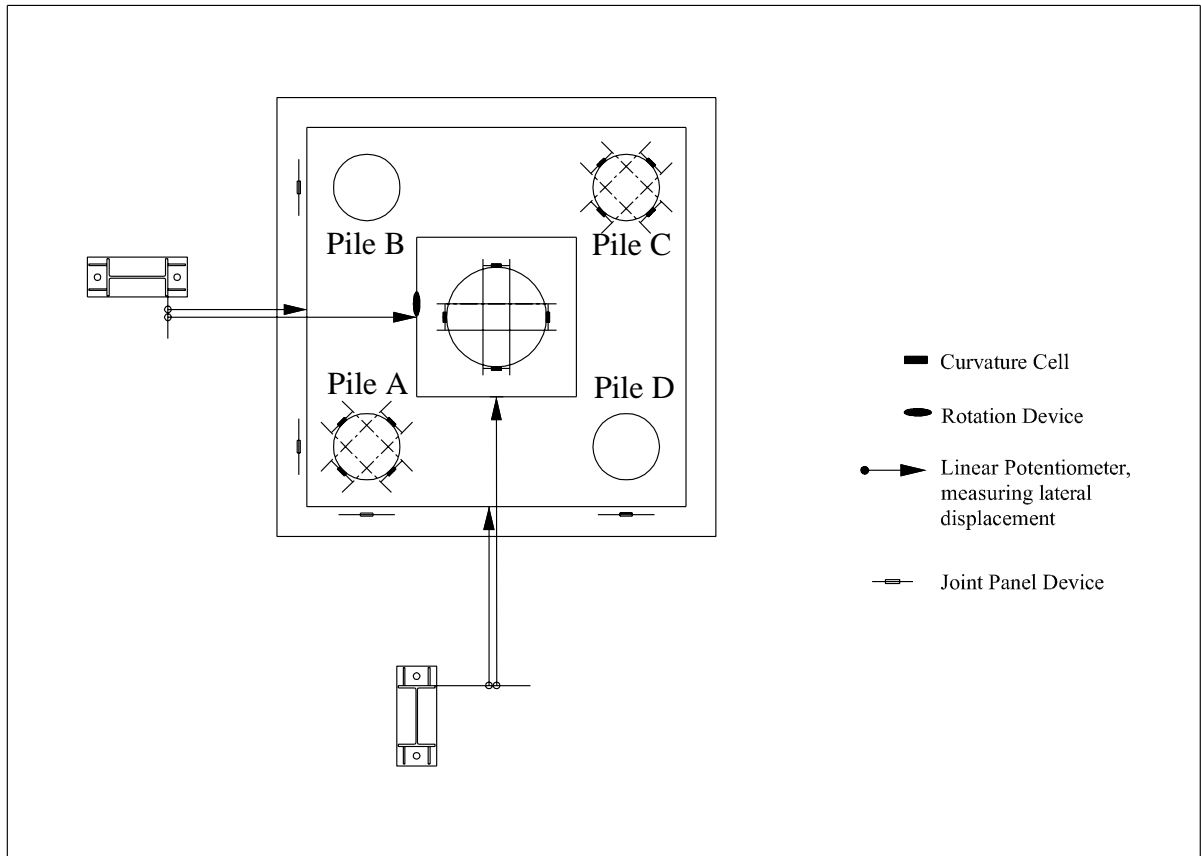
Figure 5.14: Horizontal view of external instrumentation

the force transfer path of 4-CIDH pile supported pilecap at orthogonal direction loading. The major locations of strain gauges are shown in Figures 5.16 and 5.17.

5.5 Material Testing

The material properties of concrete and reinforcement used in the test unit CFPS2 were determined as described in section 4.4. Tables 5.3 shows the compressive strengths of the concrete at different ages. Table 5.4shows the properties of the steel reinforcement used in unit CFPS2.
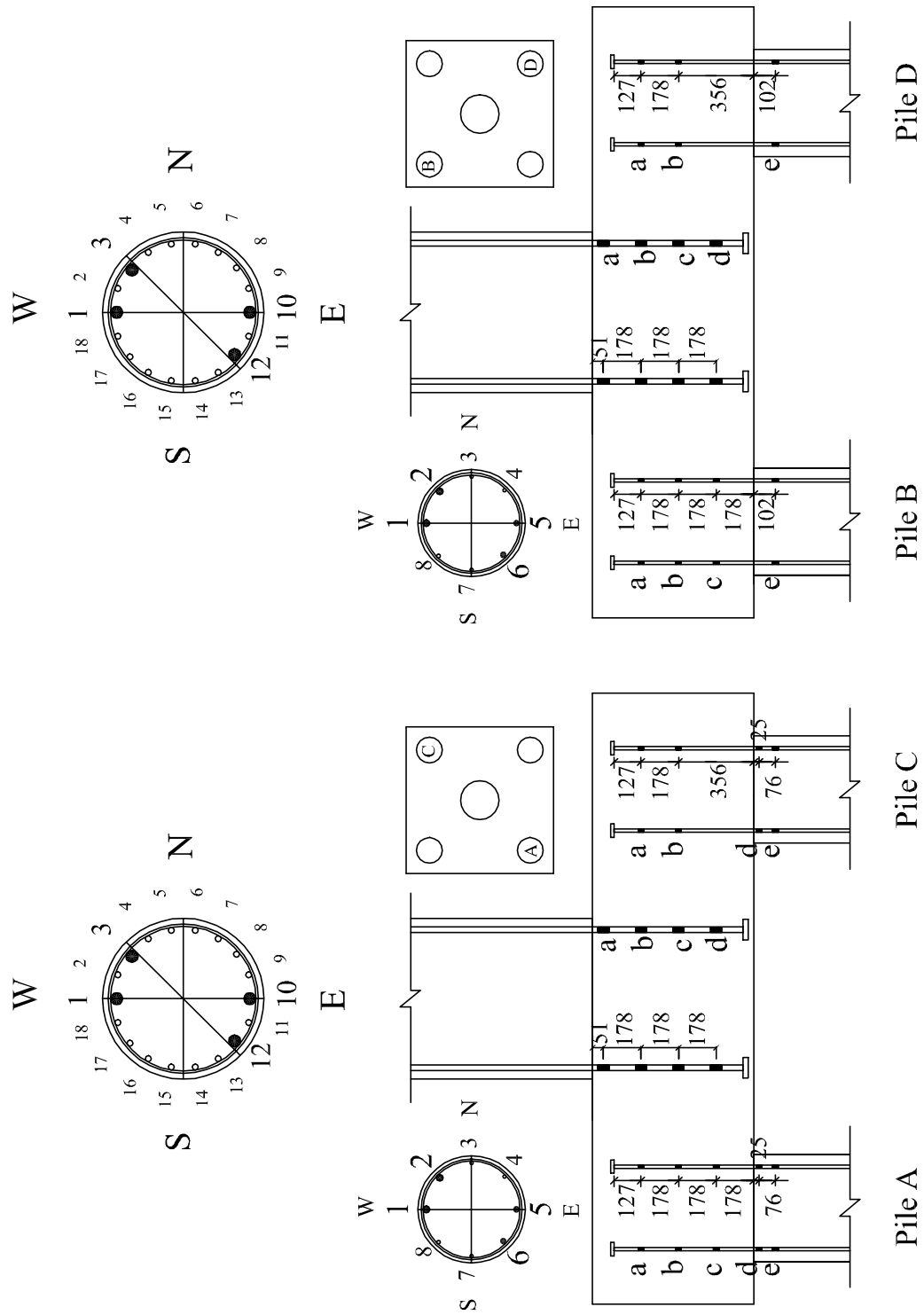
Figure 5.16: Schedule of longitudinal reinforcement strain gauges

137

(a) Flexural reinforcement

(b) Shear reinforcement
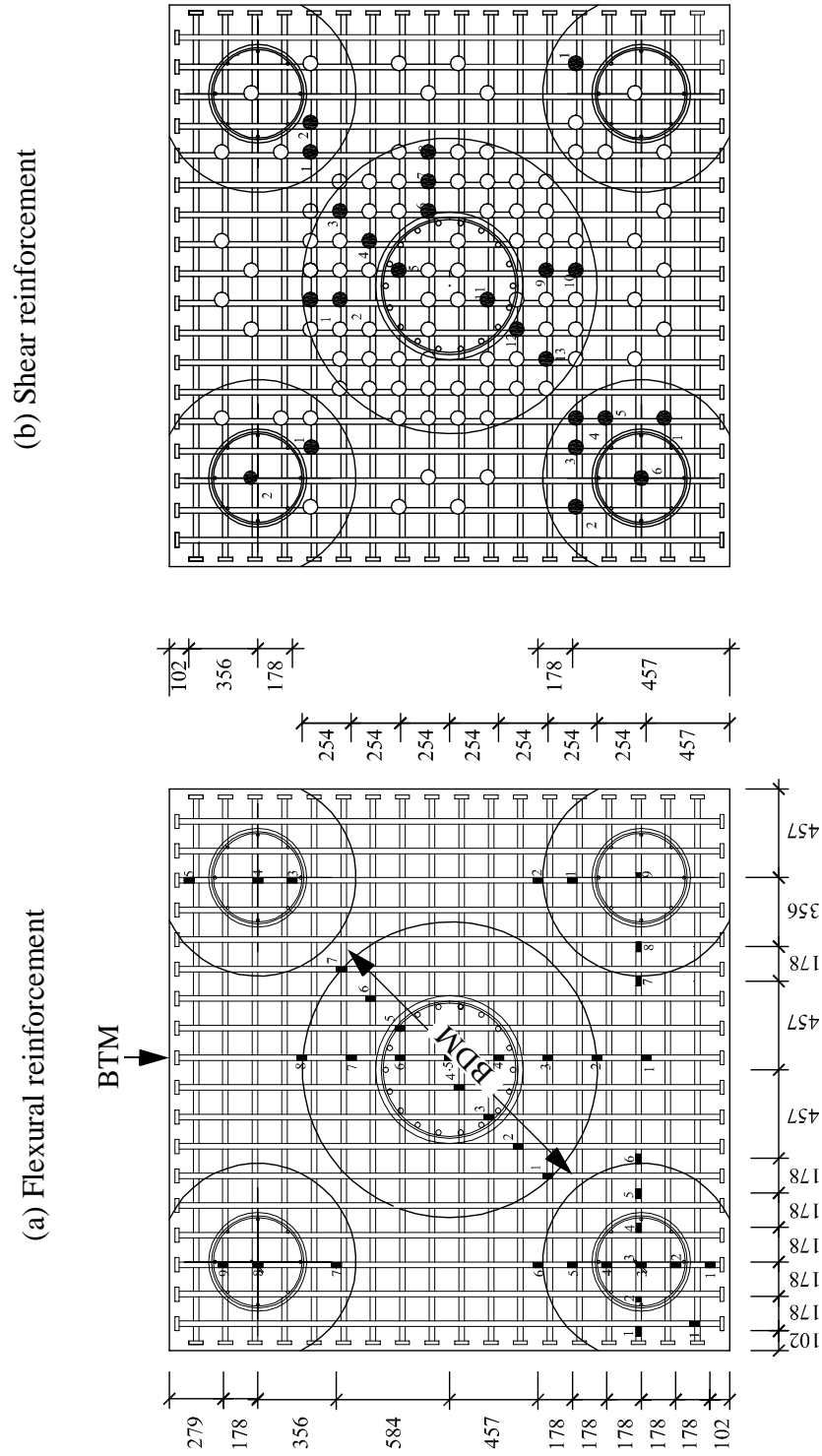
Figure 5.17: Schedule of pilecap transverse and stirrup reinforcement strain gauges

138

Table 5.3: Compressive strengths of concrete used in test unit CFPS2

Structural member	7 days	28 days	Day of Testing
	MPa	MPa	MPa
Test Base (Side-Blocks)	28.5	36.8	44.6
Pile & Pilecap	21.3	29.3	31.8
Column	18.1	24.8	28.8

Table 5.4: Yield and ultimate strengths of steel used in test unit CFPS2

Description	Bar Size	Yield Strength	Ultimate Strength
	diameter in mm	MPa	MPa
Column longitudinal bars	28.7	497.8	697.3
Column spiral	15.9	480.6	720.5
Pile spirals	9.5	379.4	670.6

5.6 Loading Protocol

5.6.1 Gravity load

The gravity load of 2113kN simulating the scaled weight of super structure was slightly larger than the design gravity load of 2002kN. This load was first applied as a concentrated force at the center of column through post-tensioning. This load was maintained at a constant level by the hydraulic jack until $\mu_\Delta = 1$ at Loading Phase 1 though there were slight fluctuations in the load due to the nature of the equipment(see Figures 5.18). However, this load was increased to $(2180 \pm 111)\,\text{kN}$ after $\mu_\Delta = 1$. Particularly, the gravity load at $\mu_\Delta = 3$ was increased up to $(2380 \pm 67)\,\text{kN}$ due to the malfunction of the hydraulic pump and the gravity load was maintained $(2180 \pm 111)\,\text{kN}$ manually at $\mu_\Delta = 4$. During Loading Phase 2, the gravity load was maintained at 2475kN until $\mu_\Delta = 2$ with slight fluctuations. The gravity load was then increased to $(2202 \pm 89)\,\text{kN}$ and maintained to the end of Loading Phase 2(see Figure D.3).
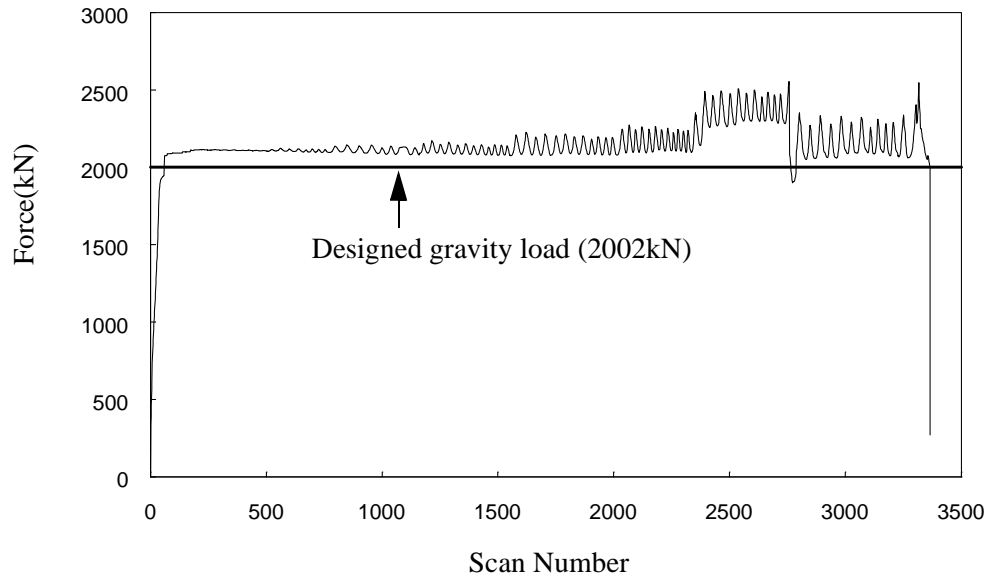
Figure 5.18: Applied gravity load during the test of CFPS2(Loading Phase 1)

5.6.2 Simulated seismic load

Figures 5.12 and 5.13 show a plan view of the test unit, where lateral load actuators are oriented in two orthogonal directions. The simulated seismic loading of two normal and two diagonal directions were applied cyclically to CFPS2 by directional combinations of loading with two servo-controlled hydraulic actuators. The simulation of passive pilecap soil restraint for each direction was achieved by connecting the two actuators to steel loading frames mounted on two vertical sides of the pilecap. The pilecap actuators were set up to nominally take 50% of the seismic loads applied to the top of column in opposite direction. Each loading frame was linked to two horizontal Dywidag bars end plated on the other side of pilecap for opposite directional loading.

The loading protocol for Loading Phases 1 and 2 is shown in Table 5.5.

1) **Loading Phase 1 : With pilecap actuators**
(pilecap passive soil pressure simulated)

The first part of the seismic loading consisted of force-controlled cycles at 25%, 50%, 75% and 100% of the theoretical first yielding of the longitudinal bar in the column for a total of four loading steps.

The following loading steps, beyond theoretical first yielding of the longitudinal steel in the column, were controlled by the lateral displacement of the column head. Using the measured first yield displacements in all the loading directions, an average displacement corresponding to system's displacement ductility $\mu_\Delta = 1$ was estimated to be 24.9mm. The displacement used to control the test was increased in steps such to $\mu_\Delta = 1, 1.5, 2, 3, 4$.

The transverse loading was applied to each normal direction with two cycles and each diagonal direction with one cycle at each system displacement ductility level in order that all the structural members experience the same level of loading.

Loading Phase 1 had been planned so that loading would be stopped at $\mu_\Delta = 5$ to be consistent with CFPS1. However, failure in the control system meant that such ductility level could not be achieved.
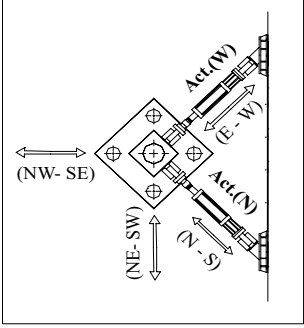
2) **Loading Phase 2 : Without pilecap actuators (no pilecap passive soil pressure)**

The loading sequence was controlled by displacement starting with $\mu_\Delta = 1$ based on the yield displacement derived from the loading Phase 1. Controlling displacement

ductilities were μ_Δ = 1, 1.5, 2, 3, 4. The test was stopped at μ_Δ = 4 due to the decrease of column strength more than 80%.

Table 5.5: Loading protocol of CFPS2

Actuator Control	Loading Level		Load'g Step	Load'g Direction	# of cycle	Act. (W) kN	Act. (N) kN	Remark
Force(kN) Control	Force Ratio to Fy	25%	1	E - W	1	156		1. Phase 1 :
			2	N - S	1	156		With Pile-Cap Actuator.
			3	NW - SE	1	111	111	
			4	SW - NE	1	111	111	2. Phase 2 :
		50%	5	E - W	1	311		Without Pile-Cap Actuators.
			6	N - S	1	311		Displacement Control Only
			7	NW - SE	1	222	222	
			8	SW - NE	1	222	222	3. Test Model Layout
		75%	9	E - W	1	471		
			10	N - S	1	471		
			11	NW - SE	1	334	334	
			12	SW - NE	1	334	334	
		100%	13	E - W	1	627		
			14	N - S	1	627		
			15	NW - SE	1	445	445	
			16	SW - NE	1	445	445	
Actuator Control	Loading Level		Load'g Step	Load'g Direction	# of cycle	Act. (W) mm	Act. (N) mm.	
Displacement(mm) Control	Ductility Level	1	17	E - W	2	24.9		
			18	N - S	2	24.9		
			19	NW - SE	1	17.6	17.6	
			20	SW - NE	1	17.6	17.6	
		1.5	21	E - W	2	37.4		
			22	N - S	2	37.4		
			23	NW - SE	1	26.4	26.4	
			24	SW - NE	1	26.4	26.4	
		2	25	E - W	2	49.8		
			26	N - S	2	49.8		
			27	NW - SE	1	35.2	35.2	
			28	SW - NE	1	35.2	35.2	
		3	29	E - W	2	74.7		
			30	N - S	2	74.7		
			31	NW - SE	1	52.8	52.8	
			32	SW - NE	1	52.8	52.8	
		4	33	E - W	2	99.6		
			34	N - S	2	99.6		
			35	NW - SE	1	70.4	70.4	
			36	SW - NE	1	70.4	70.4	

3) **Loading Phase 3 : With pilecap actuators in phase with column actuators**

To investigate the pile-pilecap joint behavior at ultimate forces, the loading was controlled by displacement of the pilecap with the load ratio of 0.5 between the pilecap loading and the column loading in same direction. However, since the stiffness of the column was reduced greatly from column bar ruptures during the East-West direction loading at 24mm of pilecap target displacement, the ratio of the pilecap actuator load over the colum load was increased from 0.5 to 0.75 after reaching -250mm of column head displacement without reaching -24mm of pilecap displacement. Even this did not make the footing reach the target displacement of -24mm, so the actuator load on the pilecap was increased independently while the column head displacement was held fixed.

For the other direction loading of 24mm of pilecap displacement, the column actuator force was increased, maintaining the force ratio of 0.75 until either the pilecap displacement reached the desired target level or until the top displacement reached a maximum. In the latter case, the pilecap actuator load was independently increased until the pilecap displacement reached the desired target value.

After loading the pilecap to 24mm of displacement, the top actuators were completely disconnected. The pilecap actuators were put into displacement controlled to apply the desired pilecap lateral displacement for the loading of 36mm pilecap displacement. However, the pilecap actuator capacity was inadequate to reach the target displacement for orthogonal(E-W, N-S) directions, so only diagonal direction loading was applied for 36mm of pilecap displacement to the end.

The loading of 48mm pilecap displacement could not be applied due to the lack of pilecap actuator capacity and the test of CFPS2 was finished.

5.7 Observations During The Test

Unit CFPS2 was tested under simulated seismic loading using the procedure outlined in section 5.6. The experimental observations of CFPS2 made during the test are summarized below and test photos are shown in Appendix K.

5.7.1 Application of gravity load

When the gravity load was applied to the test unit CFPS2, only one hairline crack was observed on bottom of the pilecap in N-S(North-South) direction.

5.7.2 Force control of Loading Phase 1

The seismic force corresponding to the theoretical yield strength was applied to the test unit in four steps. In each step one loading cycle for each direction was applied and the following observations were made:

±0.25 F_y'

There were minor new cracks on the bottom surface of the pilecap. The crack which formed at gravity load extended to the pilecap vertical sides.

±0.5 F_y'

The flexural hairline cracks were developed up to 3/4 of column height. On the bottom surface of the pilecap, new flexural cracks also developed and extended up to 1/2 of pilecap depth. The first flexural crack was observed at the inner interface of pile C and pilecap. The previous cracks extended.

±0.75 F_y'

First cracks were observed at the pile-pilecap outer interfaces of each piles. Flexural cracks developed farther up to 4/5 of column height and the previous cracks extended.

±1.0 F_y'

New flexural cracks were observed on outer faces of piles. The cracks on vertical sides of pilecap extended the whole pilecap depth. First inclined cracks and vertical splitting cracks were observed on the column. In addition, the first crack was observed on top of the pilecap due to the strain penetration of column longitudinal steel into the pilecap. On periperal areas of the pilecap bottom, the maximum flexural crack width was about 0.3 mm. An additional flexural crack was observed on piles.

5.7.3 Displacement control of Loading Phase 1

Using the measured first yield displacements in each directions of loading, an average reference yield displacement, corresponding to $\mu_\Delta = 1$, was estimated to be 24.9mm from Eq. (A.16), about 6.4% less than for unit CFPS1. The rest of the test was controlled by column head displacement so that the maximum horizontal displacement of the test unit corresponded to selected displacement ductility levels. Two cycles for two orthogonal directions and one cycle for each diagonal direction were imposed at each displacement ductility.

In the figures of Appendix K, the observations of unit CFPS2 during the test are shown. It was clear that the damage was largely concentrated in the plastic hinge regions of the column as intended. The pilecap-pile joints were not damaged.

$\mu_\Delta = \pm1.0$

Crushing of cover concrete was initiated at the column-pilecap interface in the first cycle of the orthogonal direction loading. On periperal regions of the bottom of pilecap, maximum flexural crack width was about 0.6mm which is significantly less compared to unit CFPS1. The first inclined crack was observed on the vertical side of pilecap. There were extensions of old cracks as well as new cracks.

$\mu_\Delta = \pm1.5$

First spalling of the column cover concrete was observed in diagonaldirection loading. On the top surface of the pile cap, flexural cracks were observed.

$\mu_\Delta = \pm2.0$

Further crushing and spalling of cover concrete occurred at the bottom of the column up to 150 mm from the column-pilecap interface. Further extensions of strain penetration cracks on top face of pilecap. The largest crack width on the pile cap side was 0.8mm.

$\mu_\Delta = \pm3.0$

The damage was severe from the crushing and spalling of cover concrete at the column plastic hinge region, up to 300 mm from the column-pilecap interface. Strain pentraion cracks were formed around the column. Hairline cracks were observed at pile-pilecap joint region. Shear cracks were more extended and developed on column.

$\mu_\Delta = \pm4.0$

Further crushing and spalling of cover concrete occurred at the column plastic hinge region and most of the column bars were exposed. More vertical splitting and shear cracks were found in the column. Maxiumn crack width on the bottom of pilecap beneath the column was about 1.2mm. At this stage, it was noted that concrete had spalled over 450mm length from the column-pilecap interface.

$$\mu_\Delta = \pm 5.0$$

The loading at this ductility level was stopped during the first cycle of E-W direction loading due to the failure in the control system. This controller failure caused excessive column displacement and the data at this stage is not valid.

5.7.4 Loading Phase 2

In Loading Phase 2 the damage to the test unit CFPS2 was largely confined to the piles. This was because the induced force in the piles increased to about twice that of Loading Phase 1 while the maximum column force was almost the same as that of the loading Phase 1. Damage to the pilecap-pile joints was not observed and the pin connections at the pile bottom were not damaged.

$$\mu_\Delta = \pm 1.0$$

Inclined and vertical cracks were observed at piles. No significant changes were observed.

$$\mu_\Delta = \pm 1.5$$

Three column rebars started to buckle. This premature buckling of column rebars was believed to be from the excessive column displacement at $\mu_\Delta = \pm 5.0$ of Loading Phase 1. These bars were thought to have suffered excessive tensile strains.

$\mu_\Delta = \pm 2.0$

Pile cracks propagated farther down to 3/5 of pile length.

$\mu_\Delta = \pm 3.0$

Flexural and shear cracks on the piles propagated down to the piles. First signs of cover concrete crushing were observed at the interface of Pile A, D and the bottom of the pilecap. A fourth bar buckled.

$\mu_\Delta = \pm 4.0$

A fifth bar was buckled and three bars were ruptured. Spalling of cover concrete initiated at pile D.

5.7.5 End of testing CFPS2

No significant damage such as large flexural deformations, nor the straightening of 90° J-hook of the stirrups in the pilecap, which occurred previously during the test of CFPS1 was observed. The greatly reduced damage at the pilecap of CFPS2 was thought to be due to the use of headed reinforcement as stirrups, and modifications to accomodate the flexural moment demands taken into account in the footing design of CFPS2. No damage in the joint region was observed either. Figure K.25 shows the bottom surface of

the pilecap of CFPS2 at the end of the test which exhibited only minor damage compared to the bottom surface of CFPS1 as shown Figure I.15.

5.8 Force-Displacement Hysteresis Curve.

5.8.1 Loading Phase 1 : With simulated passive soil pressure on pilecap side

The response of the Loading Phase 1 was predicted as it was dominated by column response. In Figures 5.19 - 5.22, the measured force-displacement response history of CFPS2 is shown along with the predicted response envelope. The response was good although the strength of CFPS2 was slightly below the predicted one. For the diagonal direction loading, a drop of about 5% in strength occurred. Energy absorption capacity of the system, as indicated by the shape and stability of the hysteresis loops, was excellent.

The equivalent viscous damping of CFPS2 at different ductilities for the orthogonal direction loading is presented in Figure 5.23. It is seen that the equivalent viscous damping of the system increased from 5% at $\mu_D =1$ to 20 % at $\mu_D = 4$. The difference in the equivalent viscous damping level between the first and second series of cycles was about 1.0%.

5.8.2 Loading Phase 2 : Without simulated passive soil pressure on pilecap side

In Figures C.9 and C.11 in Appendix C, the measured force-displacement response history of each orthogonal and diagonal direction at loading phase 2 is shown. Since the column had been loaded well beyond the anticipated range during loading phase 1, the
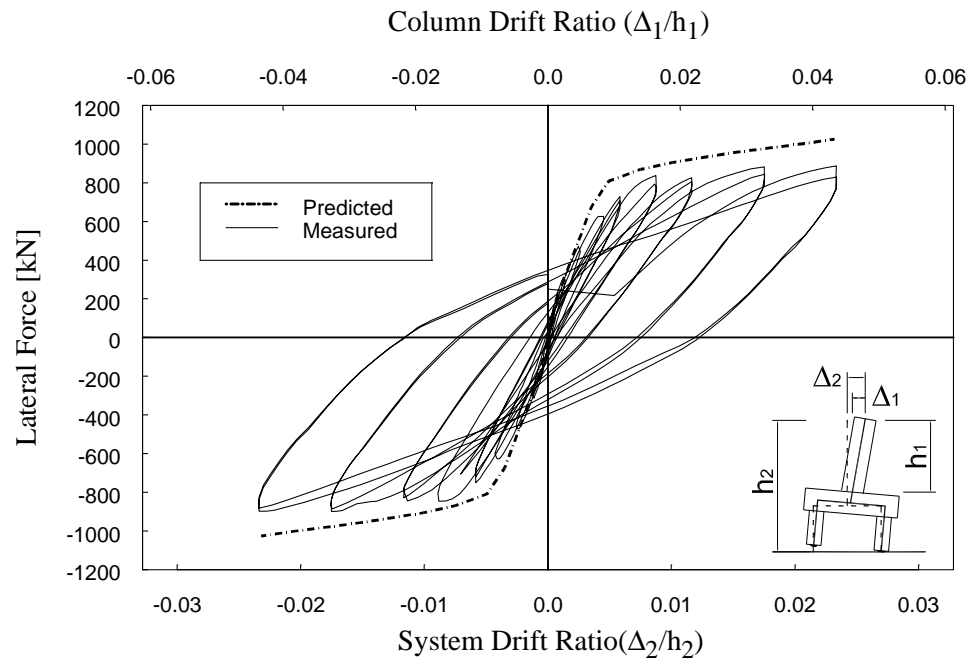
Figure 5.19: Hysteresis loop of orthogonal direction(East-West) loading at loading phase 1
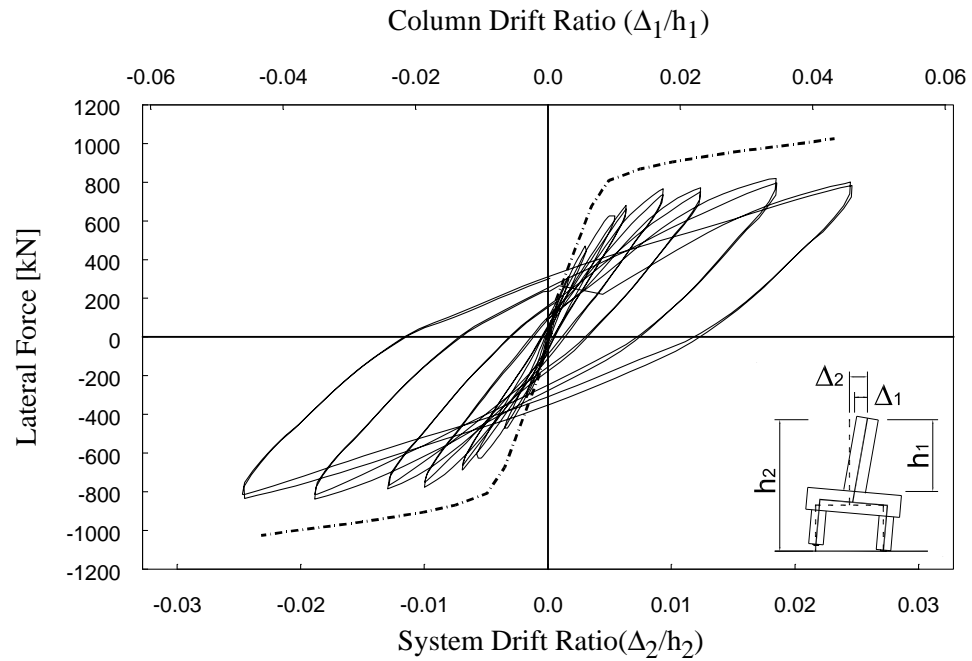
Figure 5.20: Hysteresis loop of orthogonal direction(North-South) loading at loading phase 1

150
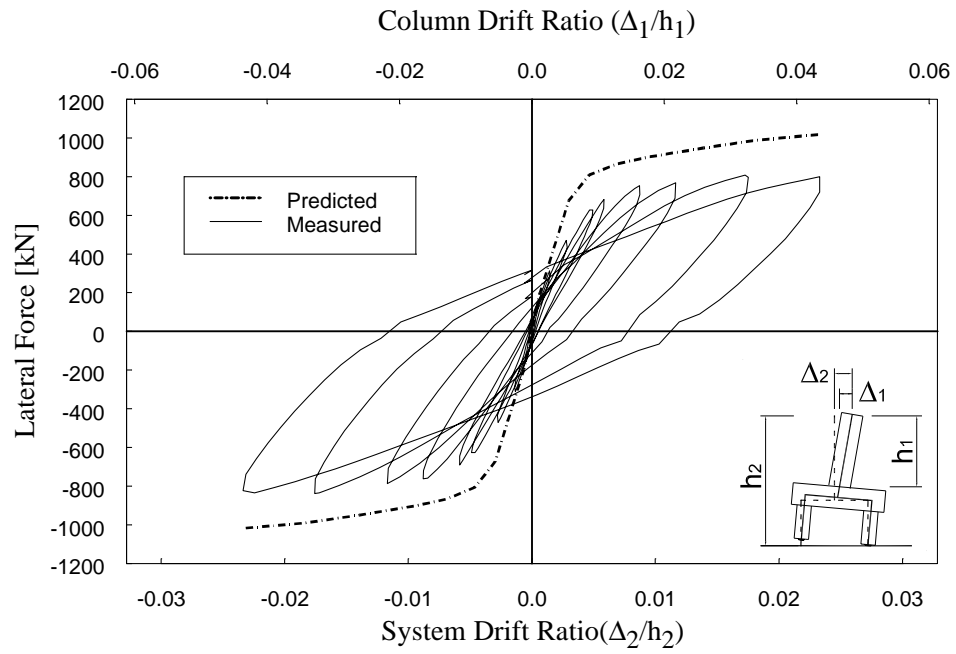
Figure 5.21: Hysteresis loop of diagonal direction(SE-NW) loading at loading phase 1
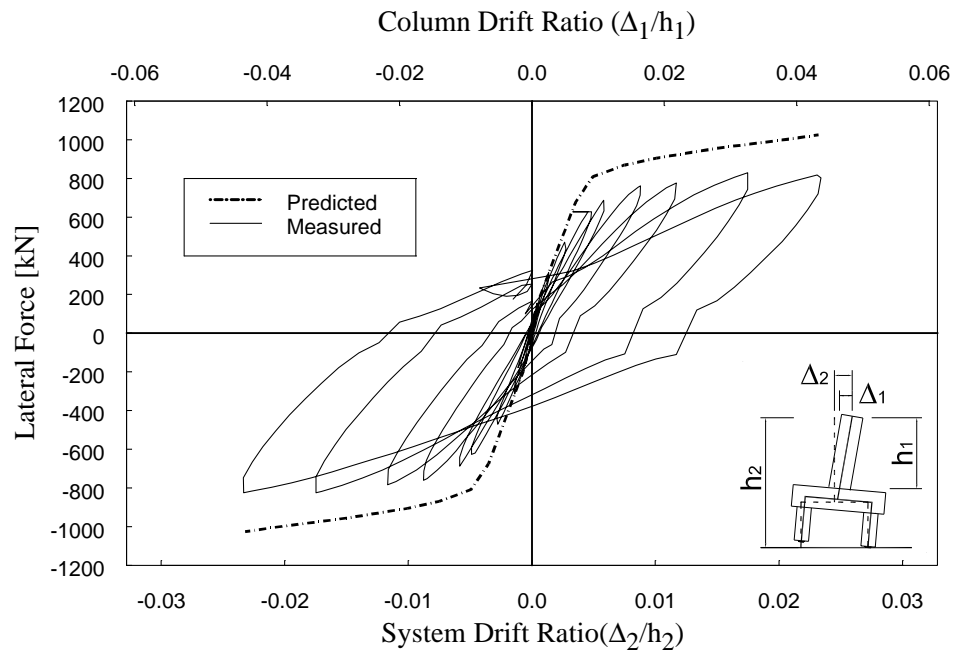
Figure 5.22: Hysteresis loop of diagonal direction(SW-NE) loading at loading phase 1
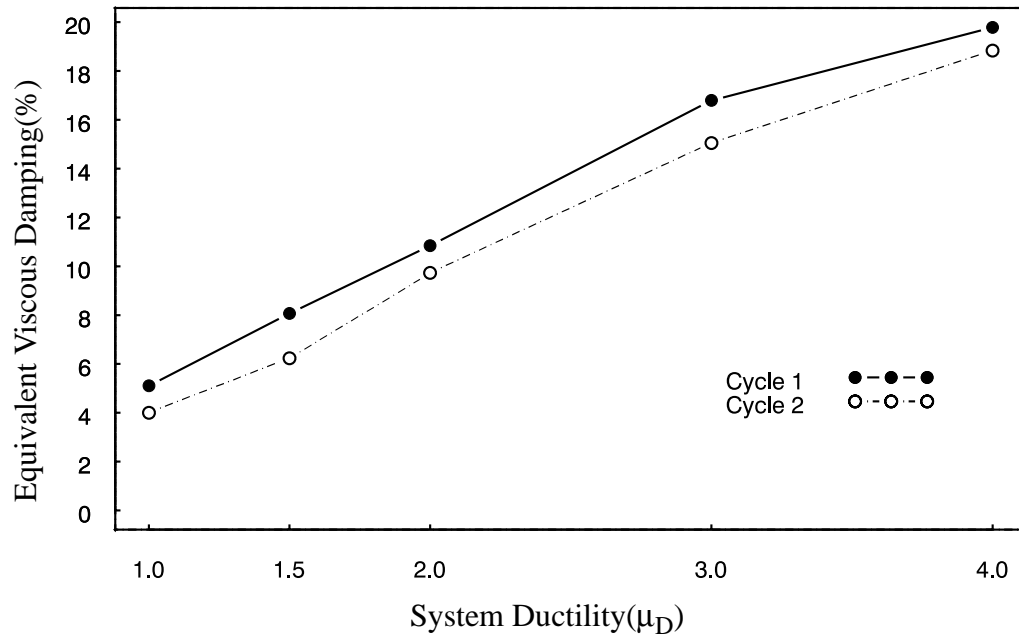
Figure 5.23: Equivalent viscous damping of orthogonal direction loading at loading phase 1

initial stiffness of the unit in the Loading Phase 2 was much less than the stiffness in the

Loading Phase 1. Energy absorption capacity of the system, however, was satisfactory.

5.9 Pile Moments and Principal Direction of Pile Shear

Instrumentation data of piles in unit CFPS1 indicated that the principal direction of

the pile resistance might not coincide with the direction of the seismic load application

at the column head.

5.9.1 Analysis procedure

To study this issue and to calculate the induced moment and shear forces at the pile

top, curvature potentiometers were mounted in a cross configuration at Piles A and C on
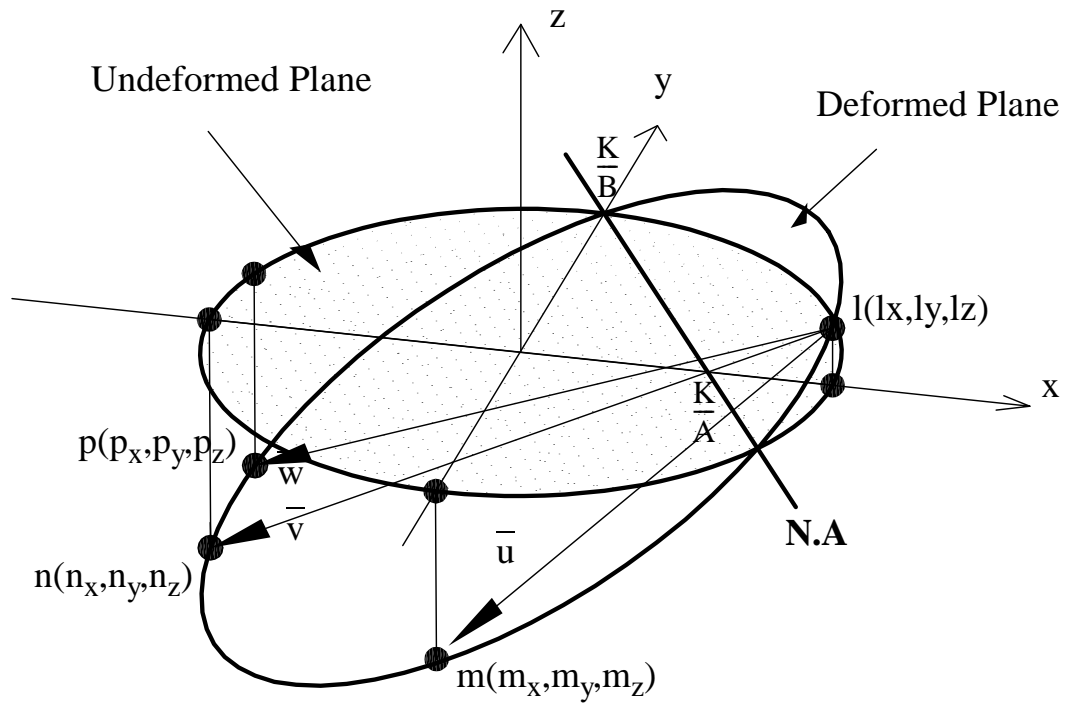
Figure 5.24: Neutral axis as a intersecting line between deformed and undeformed pile planes

unit CFPS2 as shown in Figure 5.14. With three deformation quantities measured from these potentiometers, the equation of the plane of the deformed pile section was determined. Since three displacements on a plane of pile section should be known to set up the equations of planes in three dimensional space, the linear potentiometers were installed in a cross configuration for the convenience of instrumentation, although one deformation of potentiometer out of four is redundant. The direction of pile shear force was determined by locating the intersecting line of a deformed and a undeformed plane of the pile top section as illustrated in Figure 5.24. This was based on the assumption of bending theory that a plane section remains plane before and after bending.

153
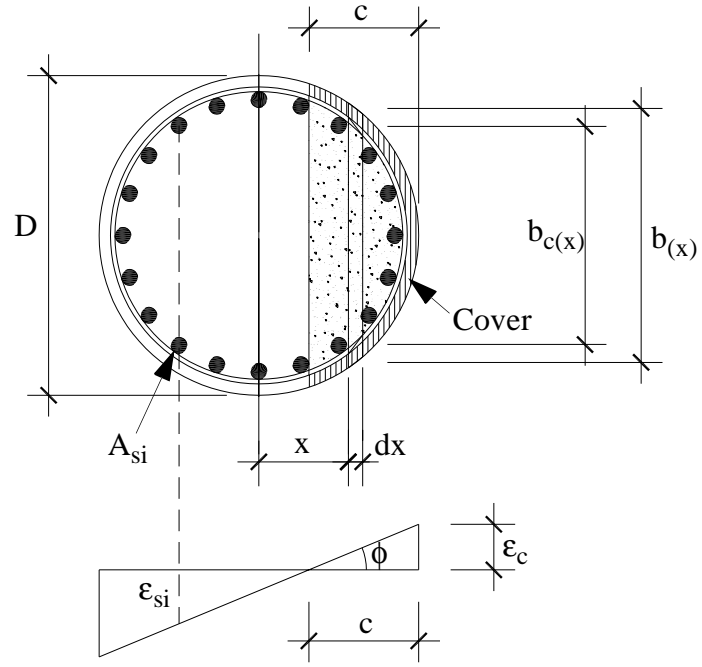
Figure 5.25: Strain profile of circular section at moment equilibrium[26]

Determination of the direction of pile shear force was, then, followed by the evaluation of the induced moment and coresponding shear in the compression pile based on the strain profile at equilibrium state of the pile top section(see Figure 5.25).

Refering to Figure 5.25, the pile moment, M_p, and shear force, V_p, are :

$$M_p = \int_{x = (D/2) - c}^{D/2} [b_{c(x)} f_c(\varepsilon_x) + (b_{(x)} - b_{c(x)}) f_{cu}(\varepsilon_x)] x dx \qquad (5.21)$$

$$+ \sum_{i = 1}^{n} A_{si} f_c(\varepsilon_x) x_i$$

$$V_p = M_p / L_p \qquad (5.22)$$

where $f_c(\varepsilon)$, $f_{cu}(\varepsilon)$ and $f_s(\varepsilon)$ are the stress-strain relationships for confined concrete, unconfined concrete and reinforcing steel, respectively, and A_{si} is the area of a reinforcing bar with distance x_i from the centroidal axis.[26]

With the angle, α, of the shear force direction, the shear force component which is parallel to the applied lateral force was obtained. The shear force of the tension pile in orthogonal direction was then obtained by subtracting the shear force of the compression pile in orthogonal direction from the applied lateral load. These shear forces at each loading level are shown in Figure 5.29.

The strain profile across the pile section was established by finding the equation of the intersecting circles (in this study, the ellipse was approximated by a circle because of the small curvatures) between the pile cylinder and the deformed plane of pile section as depicted in Figure 5.26. Combining with the angle, α, of principal direction of the moment, the maximum strains of compression and tension were calculated as shown in Figure 5.27.

This calculation was done with the data from the potentiometers at second level from the pilecap soffit because the deformations of the potentiometers at first level included the additional displacement due to the tensile reinforcement strain penetration into the pilecap which causes additional deformation of the plane of pile top section.

For determination of the principal direction of pile resistance and induced forces, the following steps were used along with Figures 5.24, 5.26 and 5.27.
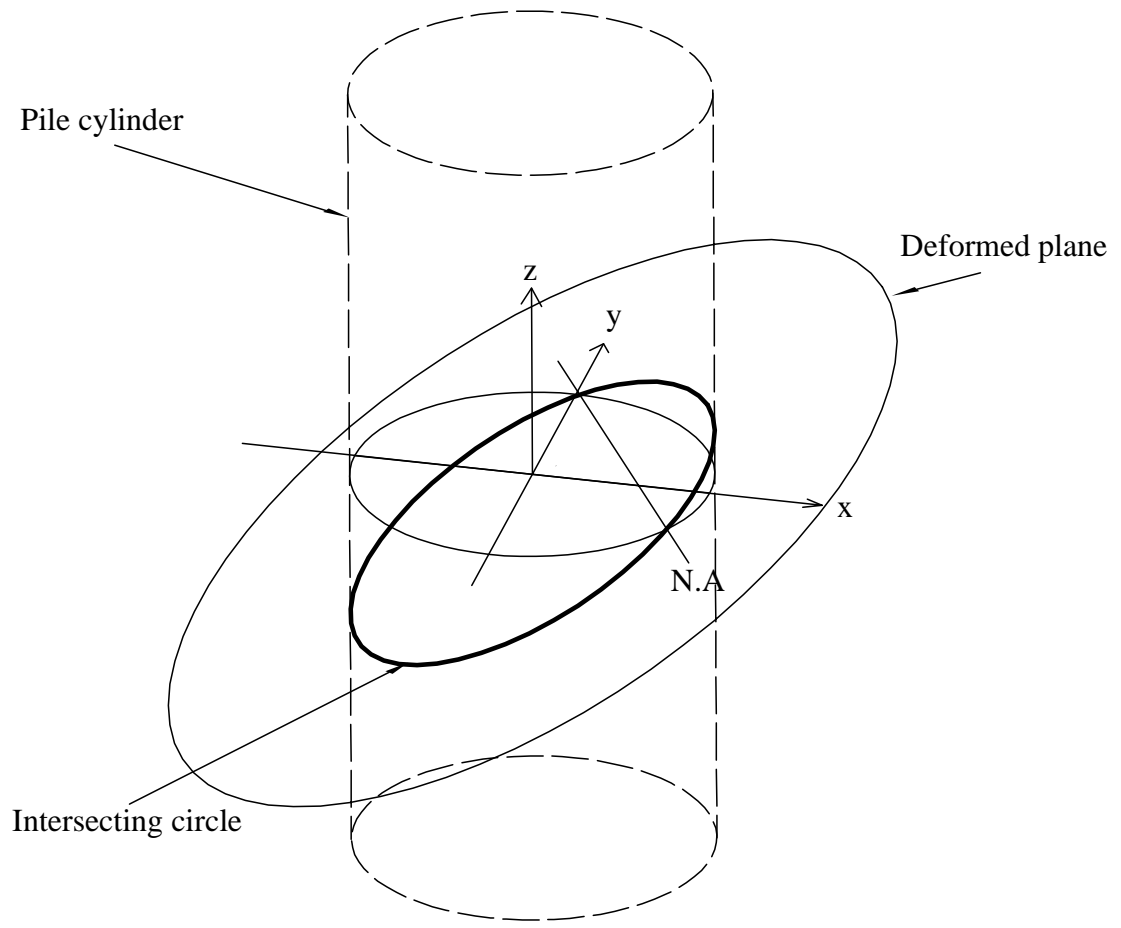
Figure 5.26: Determination of deformed pile section boundary
by intersecting deformed plane and pile cylinder

1) The equation of the plane of undeformed pile section was set up in three dimensional

space.

$$a_o x + b_o y + c_o z = k_o \qquad (5.23)$$

where a_o, b_o, c_o, k_o are constant.

2) Determine the coordinates of the three points using the three calculated strains at pile

surface on the plane of the deformed pile section and a arbitrary point, p. The x and y
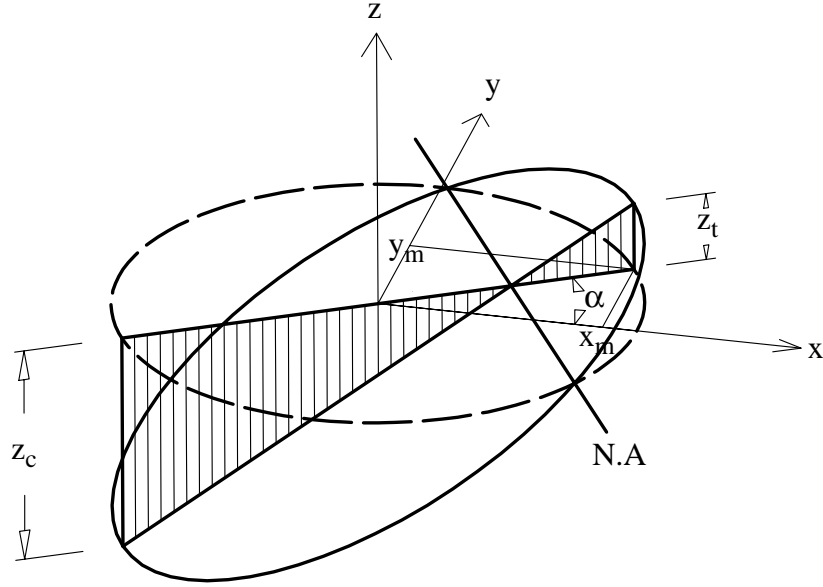
Figure 5.27: Maximum bending strain profile
obtained with a angle of pile shear force direction, α

components of each point define the location of the point on undeformed x,y plane of

the pile section and the z-component of each point is the strain in z-direction on that

point.

$$
\begin{aligned}
&l \; (l_x \quad, l_y \quad, l_z) \\
&m \; (m_x \;, m_y \;, m_z) \\
&n \; (n_x \quad, n_y \quad, n_z) \\
&p \; (x \quad\;, y \quad\;, z)
\end{aligned}
\tag{5.24}
$$

3) Three vectors were set up by pairing three points with the point, p.

$$
\begin{aligned}
\vec{u} &= \overrightarrow{lm} = (m_x - l_x)\vec{e_i} + (m_y - l_y)\vec{e_j} + (m_z - l_z)\vec{e_k} \\
\vec{v} &= \overrightarrow{ln} = (n_x - l_x)\vec{e_i} + (n_y - l_y)\vec{e_j} + (n_z - l_z)\vec{e_k} \\
\vec{w} &= \overrightarrow{lp} = (x - l_x)\vec{e_i} + (y - l_y)\vec{e_j} + (z - l_z)\vec{e_k}
\end{aligned}
\tag{5.25}
$$

4) The normal vector to the plane of deformed pile section was found.

$$\vec{u} \times \vec{v} \; = \; \begin{vmatrix} \vec{e_i} & \vec{e_j} & \vec{e_k} \\ (m_x - l_x) & (m_y - l_y) & (m_z - l_z) \\ (n_x - l_x) & (n_y - l_y) & (n_z - l_z) \end{vmatrix} \; = \; a\vec{e_i} + b\vec{e_j} + c\vec{e_k} \qquad (5.26)$$

where

$$a \; = \; (m_y - l_y)(n_z - l_z) - (n_y - l_y)(m_z - l_z)$$
$$b \; = \; (m_x - l_x)(n_z - l_z) - (n_x - l_x)(m_z - l_z) \qquad (5.27)$$
$$c \; = \; (m_x - l_x)(n_y - l_y) - (n_x - l_x)(m_y - l_y)$$

5) The equation of the plane of the deformed pile section is then :

$$(\vec{u} \times \vec{v}) \cdot \vec{w} \; = \; a(x - l_x) + b(x - l_x) + c(x - l_x) \; = \; 0 \qquad (5.28)$$

$$ax + by + cz \; = \; k \qquad (5.29)$$

where

$$k \; = \; al_x + bl_y + cl_z \qquad (5.30)$$

6) The equation of the intersecting line between a deformed and an undeformed plane of

the pile section, as shown in Figure 5.24, was found by solving Eqs. (5.23) and (5.30)

simultaneously. The intersecting line is the neutral axis of the pile moment.

$$Ax + By \; = \; K \qquad (5.31)$$

where

$$A = \left(a_o - \frac{c_o}{c}a\right), \; B = \left(b_o - \frac{c_o}{c}b\right), \; K = \left(k_o - \frac{c_o}{c}k\right) \tag{5.32}$$

7) The direction of the neutral axis of the pile resistance was then found by an inner product of two vectors, which are a normal vector of the neutral axis, $\vec{n}$, and a unit vector of x-axis, $\vec{e_i}$.

Since the inner product of the vector of the neutral axis and the normal vector to it is zero,

$$\vec{n} \cdot \overrightarrow{XY} = 0 \tag{5.33}$$

where

$$\vec{n} = (n_1, n_2) \tag{5.34}$$

$$\overrightarrow{XY} = \left(-\frac{K}{A}, \frac{K}{B}\right) \tag{5.35}$$

From Eqs. (5.33) - (5.35) :

$$\frac{n_2}{n_1} = \frac{B}{A} \tag{5.36}$$

From the inner product of the normal vector of the neutral axis, $\vec{n}$, and a unit vector of the x-axis, $\vec{e_i}$, the direction of the neutral axis of the pile top moment, α, is :

$$\alpha = \mathrm{acos}\frac{\vec{n} \cdot \vec{e_i}}{|\vec{n}|} = \mathrm{acos}\frac{n_1}{\sqrt{n_1^2 + n_2^2}} = \mathrm{acos}\frac{A}{\sqrt{A^2 + B^2}} \tag{5.37}$$

8) The equation of the intersecting circle of the pile cylinder and the deformed plane of pile section was found.

The equation of the pile cylinder is,

$$x^2 + y^2 = r^2, z = z \tag{5.38}$$

From Eq. (5.29),

$$z = \frac{1}{c}(k - ax - by) \tag{5.39}$$

By solving the Eqs.(5.38) and (5.39) simultaneously, the equation of the intersecting circle of the pile cylinder and the deformed plane of pile can be determined.

$$x^2 + y^2 = r^2 \ , \ z = \frac{1}{c}(k - ax - by) \tag{5.40}$$

9) The maximum strains of compression and tension and their locations on the pile section were found in Eq.(5.43) by solving Eqs.(5.37), (5.40) and (5.41).

$$\tan\alpha = \frac{y_m}{x_m} \Rightarrow y_m^2 = x_m^2 (\tan\alpha)^2 \tag{5.41}$$

$$x^2 + y^2 = r^2 \Rightarrow x^2 [1 + (\tan\alpha)^2] = r^2 \tag{5.42}$$
$$\Rightarrow x^2 = r^2 (\cos\alpha)^2$$

$$\begin{aligned} x &= \pm r \cdot \cos\alpha \\ y &= \pm r \cdot \sin\alpha \\ z &= k \mp (ra)\cos\alpha \mp (rb)\cos\alpha \end{aligned} \tag{5.43}$$

160

(a) Magnified view of neutral axes of pile A   (b) Loading direction
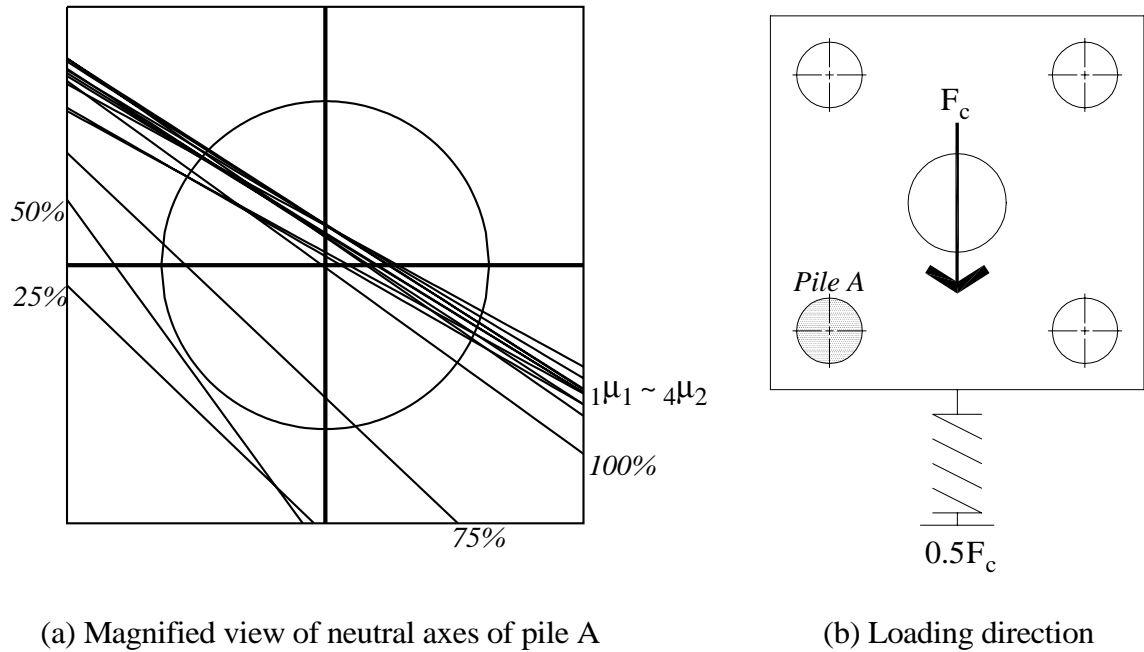
Figure 5.28: Neutral axes locations of pile A in orthogonal direction loading at Loading Phase 1

5.9.2 Neutral axis locations of pile

The neutral axis locations of compression pile A at different level of orthogonal direction loading was found using the analysis procedure described in Section 5.9.1 as shown in 5.28. These neutral axes indicate the direction of shear force at the pile-pilecap joint. As seen in the figure, the direction of the pile shear force at peak loading is approximately 55° with respect to the column loading direction. This behavior is believed mainly due to the flexural deformation of the footing caused by the resultant force of the column compressive stress, resulting from the column moment. Misalignment of the neutral axis with the applied shear force implies that two dimensional frame analysis which results in forces parallel to the loading direction will
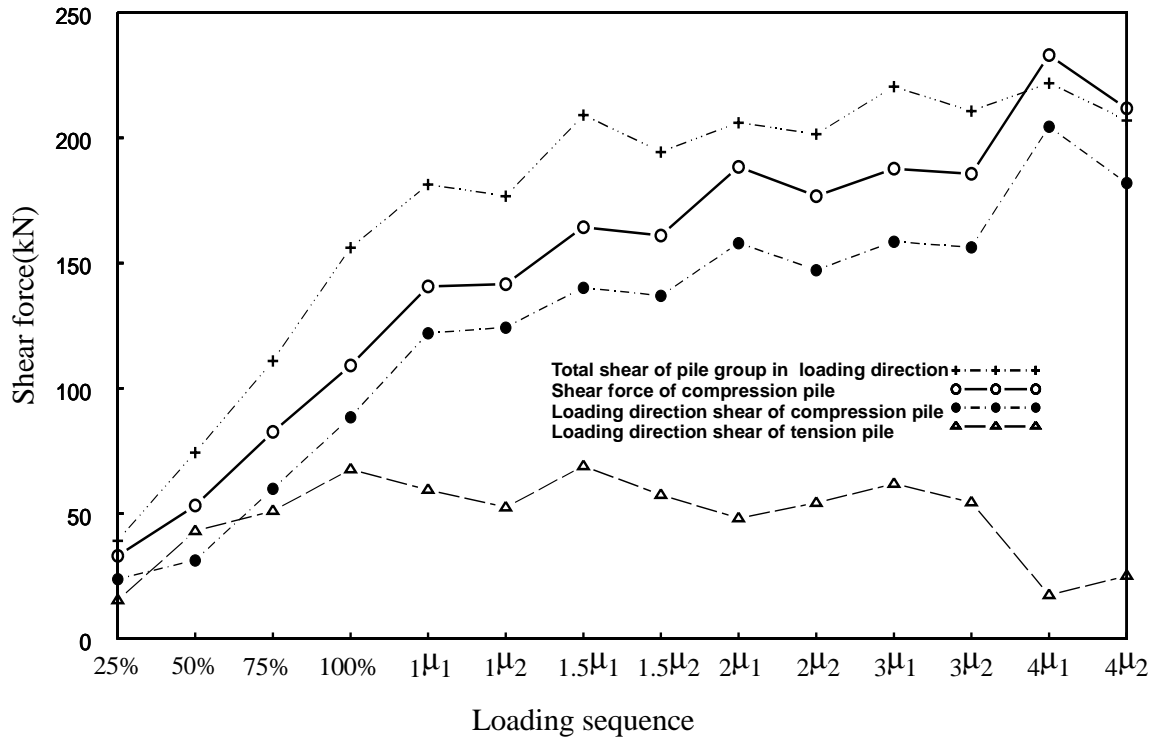
Figure 5.29: Shear force distribution between compression and tension pile
in orthogonal direction loading at Loading Phase 1

not capture the response of a pile supported footing system. Further discussion on this
issue is in Chapter 6.

5.9.3 Shear distribution between compression and tension piles

Figure 5.29 shows the shear forces of compression and tension piles. In this figure
the component of shear force in the loading direction of the compression pile is about
two times greater than that of tension pile after loading level of $_1\mu_1$. This behavior is
significant because it means that applied shear force to the pile supported foundation is
not distributed evenly between the compression and tension piles. Moreover, the shear
force in the compression pile is greater than the sum of components of the shear force in

the direction of loading. This difference results from the angle formed by the neutral axis of pile and loading direction as shown in Figure 5.28. Further discussion about the issue is in Chapter 6.

5.10 Strain data for pilecap bending

In this section the strain data obtained during the test are presented in a reduced form as strain profile plots using the strains recorded at the peak displacements in the first loading cycle at each ductility. Only the data related to the research topics, maximum strain beyond column face and critical loading direction for the pilecap, are reported here and the other strain data on the column-pilecap joint region are presented in Appendix G.

5.10.1 Maximum strain beyond column face

Figures 5.30 - 5.33 show peak strain profiles of bottom reinforcement(see BDM in Figure 5.17) in the column-pilecap joint region in Loading Phase 1. Figures 5.30 and 5.31 are for the orthogonal direction(E-W) loading and Figures 5.32 and 5.33 are for the diagonal direction of loading. In these figures it is shown that maximum strain occurs inside the column face. This implies that the moment taken at the column face for the design of pilecap positive bending, which is the method of current design practice, may be underestimated since the induced maximum moment developed beyond the column face is not recognized by designers. This topic is covered more deeply in Chapter 6.

5.10.2 Critical loading direction for pilecap

Figures 5.34 - 5.35 depict the peak strain profiles measured on the bottom reinforcement(see BTM in Figure 5.17) in the column-pilecap joint region at othogonal
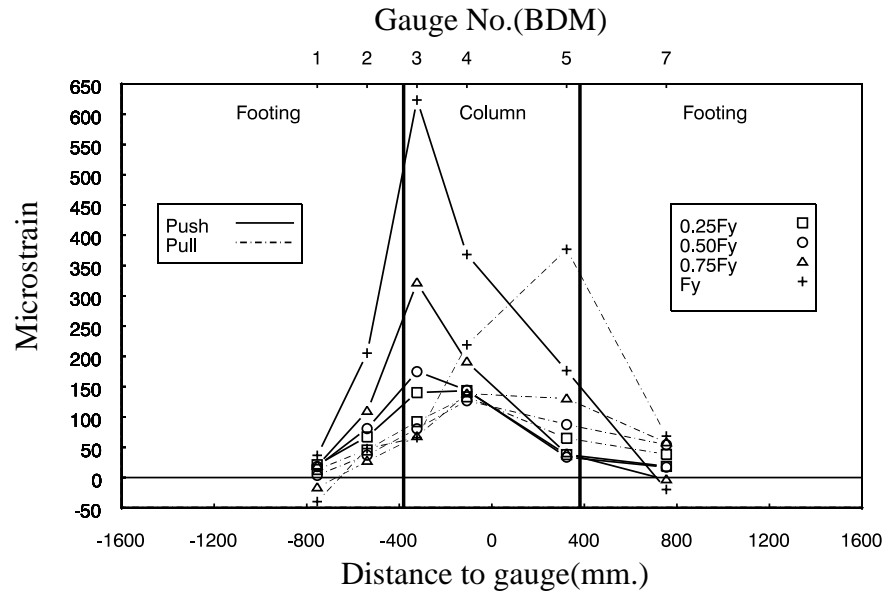
Figure 5.30: Peak strain profiles of bottom reinforcement(BDM) in column-pilecap joint region. Orthogonal direction(E-W) loading at column pre-yield in Loading Phase 1.
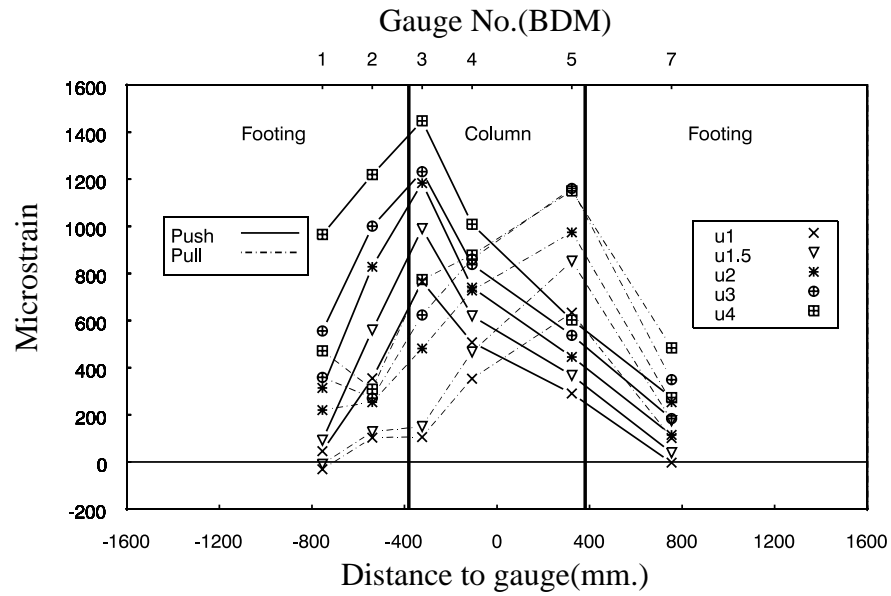
Figure 5.31: Peak strain profiles of bottom reinforcement(BDM) in column-pilecap joint region. Orthogonal direction(E-W) loading at column post-yield in Loading Phase 1.
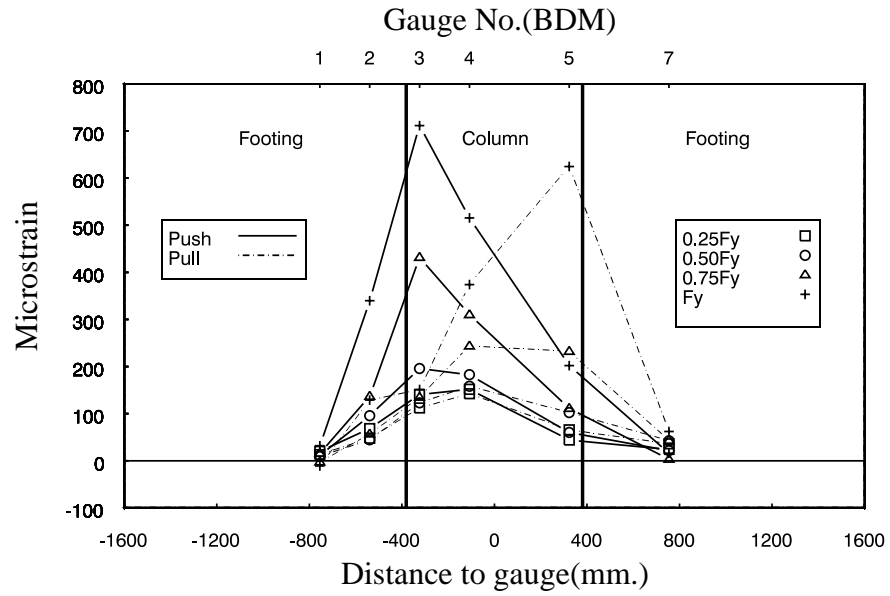
Figure 5.32: Peak strain profiles of bottom reinforcement(BDM) in column-pilecap joint region. Diagonal direction(SE-NW) loading at column pre-yield in Loading Phase 1.
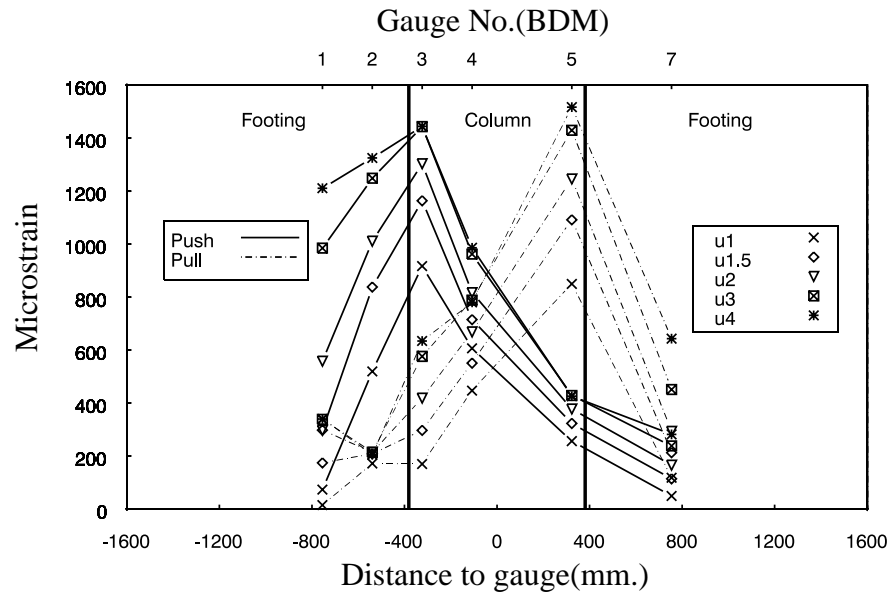
Figure 5.33: Peak strain profiles of bottom reinforcement(BDM) in column-pilecap joint region. Diagonal direction(SE-NW) loading at column post-yield in Loading Phase 1.

165

direction loading during Loading Phase 1. By comparing the peak strains of BDM1 in Figure 5.31 to those of BTM2 in Figure 5.35, which is located at same distance from the column face, it is shown that the strain levels of BDM1 are much greater than those of BTM2 at a given loading condition. However, the strains of BDM7 in Figure 5.31 and BTM8 in Figure 5.35, which are also located at same distance from the column face, are very similar. Although the strains of BDM7 and BTM8 are of similar order, the reinforcement in the diagonal direction suffers higher force than the reinforcement in the orthogonal direction at orthogonal direction loading since the force of the rebar corresponding to the strain of BDM7 is only the orthogonal component of the diagonally transferred force. This implies that the force is transferred to the piles directly through a diagonal load path and is explained by the use of the equivalent diagonal portal frame discussed in Chapter 6.
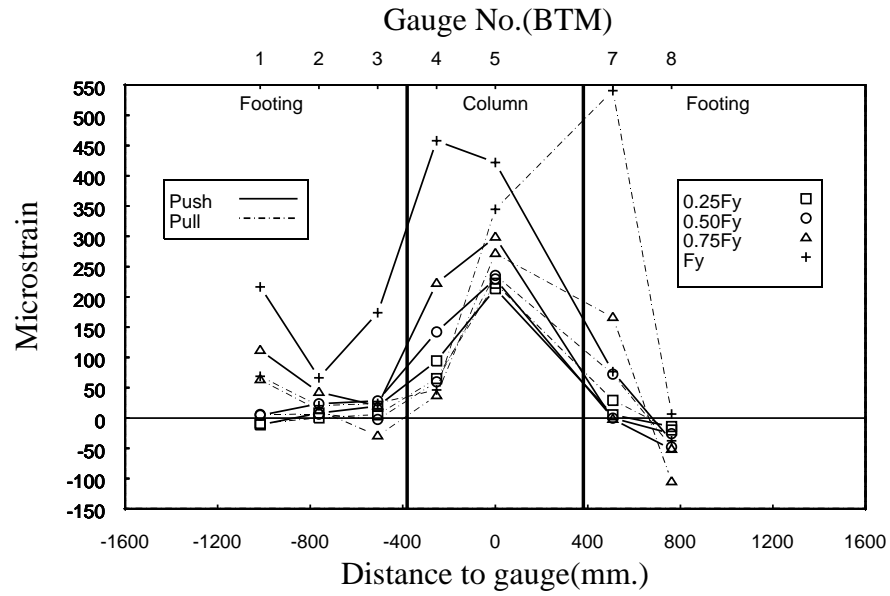
Figure 5.34: Peak strain profiles of bottom reinforcement(BTM) in column-pilecap joint region. Orthogonal direction(E-W) loading at column pre-yield in Loading Phase 1.
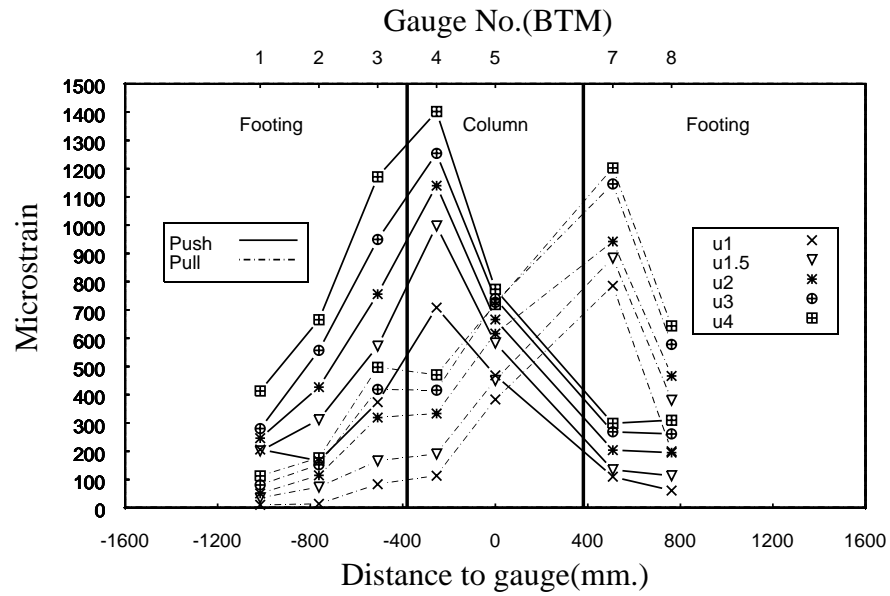
Figure 5.35: Peak strain profiles of bottom reinforcement(BTM) in column-pilecap joint region. Orthogonal direction(E-W) loading at column post-yield in Loading Phase 1.

Chapter 6: Discussion of Results

This chapter is dedicated to the theoretical study of the phenomena observed in the testing program. For the piles, the force distribution between compression and tension piles, which is observed from the test result of CFPS2 and described in Section 5.9.3, is studied. And the principal direction of pile resistance under orthogonal direction loading, which is also observed from the test result of CFPS2 and described in Section 5.9.2, is investigated. Since the three dimensional geometry of the foundation system influences the shear direction of the elastic pile, a parameter study was performed to investigate the combined effect of axial force and shear force direction of the piles. For the parameter study, a simplified foundation model similar to the test units was adopted and four distinctive parameters were used, which are representative of gravity load, column length, soil property and the relative stiffness of pile. Since the damage of the pilecap of unit CFPS1 is significant, a pilecap force transfer mechanism is investigated and the critical loading direction and the estimation of the design moment for the pilecap flexural design is studied. For the study of the pile-pilecap joints, the difference of the pile-pilecap joints and the Knee joints of the bridge bent is compared with respect to the closing and opening moments.

6.1 Piles

6.1.1 Moment distribution between compression and tension piles

For a given member section, elastic bending stiffness depends on the axial force level acting on the member. Axial compression increases the bending stiffness. The effect of this is that in a pile group, the compression piles attract greater shear force than the tension piles, as plotted in Figure 5.29. To study the axial load effect on 4-CIDH pile foundation, pile stiffness enhancement factors, β_{cp} and β_{tp} for compression and tension piles, respectively, are introduced. Factors β_{cp} and β_{tp} are defined, from Figure 6.1, as :

$$\beta_{cp} = \frac{k_{cp}}{k_{po}} = \frac{M_{cp}}{M_{po}} = \frac{M_{po} + \Delta M_{cp}}{M_{po}} \tag{6.1}$$

$$\beta_{tp} = \frac{k_{tp}}{k_{po}} = \frac{M_{tp}}{M_{po}} = \frac{M_{po} - \Delta M_{tp}}{M_{po}} = 1 - \frac{T_p}{M_{po}}\left(\frac{M_{po} - M'_{tp}}{T'}\right) \tag{6.2}$$

where M_{po} is the pile moment when $P = 0$ and ΔM_{cp} and ΔM_{tp} are the change in bending moment in the compression and tension piles, respectively, due to induced pile axial forces. The moment, M'_{tp}, is the reference moment which corresponds to any arbitrary tension load, T'.

The axial loads induced in a compression pile, C_p, and in a tension pile, T_p, are illustrated in Figure 6.2 and expressed by the following equations. :

$$C_p = C_{p1} + C_{p2} + C_{p3} = \frac{P}{4} + \frac{M_c^{\circ}}{2L_f}\left[1 + \frac{(1 - \zeta)L_p}{L_c}\right] \tag{6.3}$$

$$T_p = T_{p1} + T_{p2} + T_{p3} = -\frac{P}{4} + \frac{M_c^{\circ}}{2L_f}\left[1 + \frac{(1 - \zeta)L_p}{L_c}\right] \tag{6.4}$$

where ζ is the ratio of the shear force taken by the soil adjacent to pilecap vertical face.
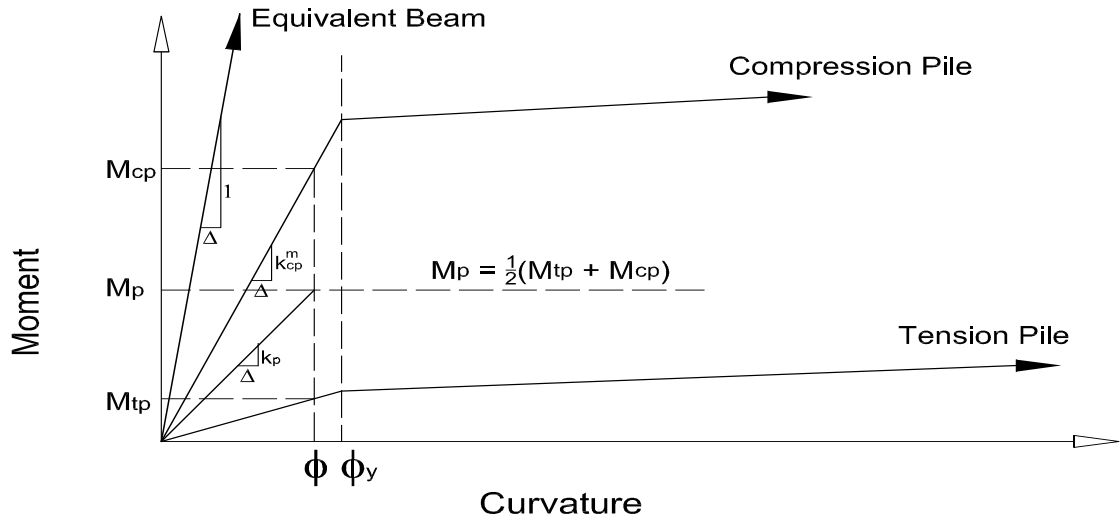
Figure 6.1: Graphical representation of the axial load effects
on the stiffness and moment distribution
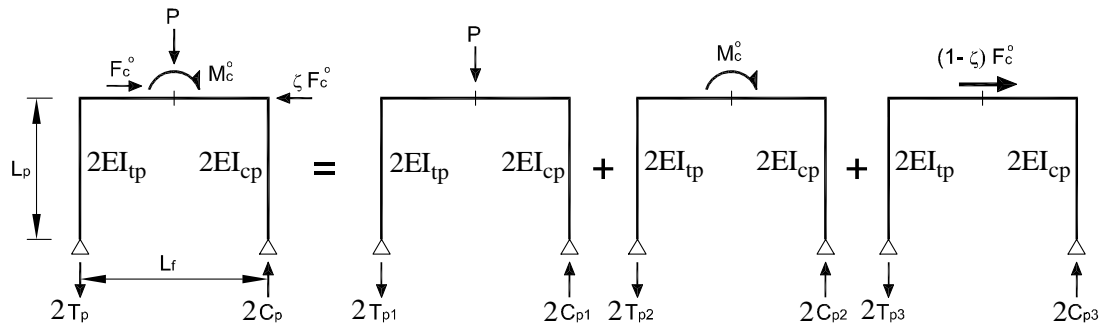
Figure 6.2: Axial reaction forces in a 4-CIDH pile foundation

Although axial force in the pile changes, the pile bending stiffnesses and accordingly the distribution of the total moment of the pile group among piles, the axial force in the pile also changes the moment capacity of the pile in the same ratio. This is

170

based on the assumption of equal curvatures in the tension and compression piles due to equal displacement of piles of equal lengths to the inflection point.

6.1.2 Principal direction of pile resistance under orthogonal direction loading

The neutral axis location of pile A, shown in Figure 5.28, indicates that the direction of pile shear force, which acts perpendicular to the neutral axis, does not coincide with the direction of applied lateral force. This is due to the three dimensional behavior of a multiple pile supported foundation, which exists inherently in the footing system, particularly, if the piles remain elastic. In two-dimensional frame analysis, the forces and the deformations are always in-plane and no three-dimensional behavior of the structure can therefore be captured.

In this section, the three-dimensional effect of a 4-CIDH pile supported footing is discussed by investigating the individual behavior of the system in the x and the y directions in horizontal plan. To discuss this issue, the development of pile moments is investigated in three parts. The pile moment due to the gravity load, P, is introduced first and the study with respect to the y-axis followed by the study with respect to the x-axis under the lateral loading in positive x-axis. If piles are designed to remain elastic, as is intended in current design practice, the moment vectors at the top of the piles can be obtained by combining the individual moments in the x and the y directions. Considered in the study is the effect of pilecap boundary conditions, which are the lateral passive soil stiffness on the pilecap vertical side and the vertical stiffnesses at the pile locations, which results from the soil-pile interactions. Further, sensitivity of pile moments and

171

(a) Plan view

(b) Y_{tp} - Y'_{tp}

(c) X - X'

(d) Y_{cp} - Y'_{cp}
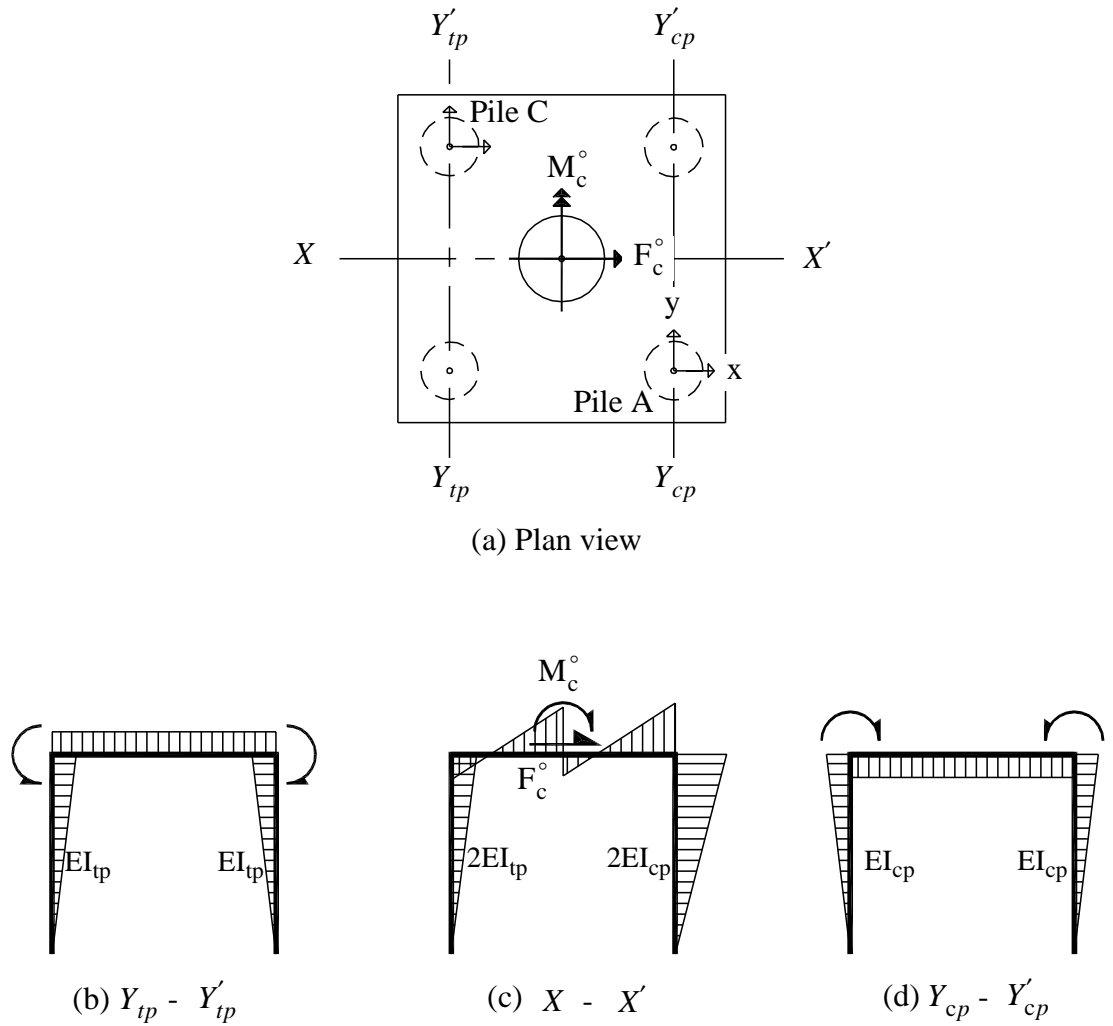
Figure 6.3: Moment profiles under seismic loads

their directions was investigated via a parametric study in section 6.1.3 and the results are shown in section 6.1.5.

1) Pile moment due to gravity load, P

To quantify the moment at the top of the piles due to gravity load, P, the equivalent portal frame method was adopted. see Figure 6.4.

<table>
</table>

(a) Plan view of equivalent two portal frames   (b) Moment profile of section A-A under gravity load, P
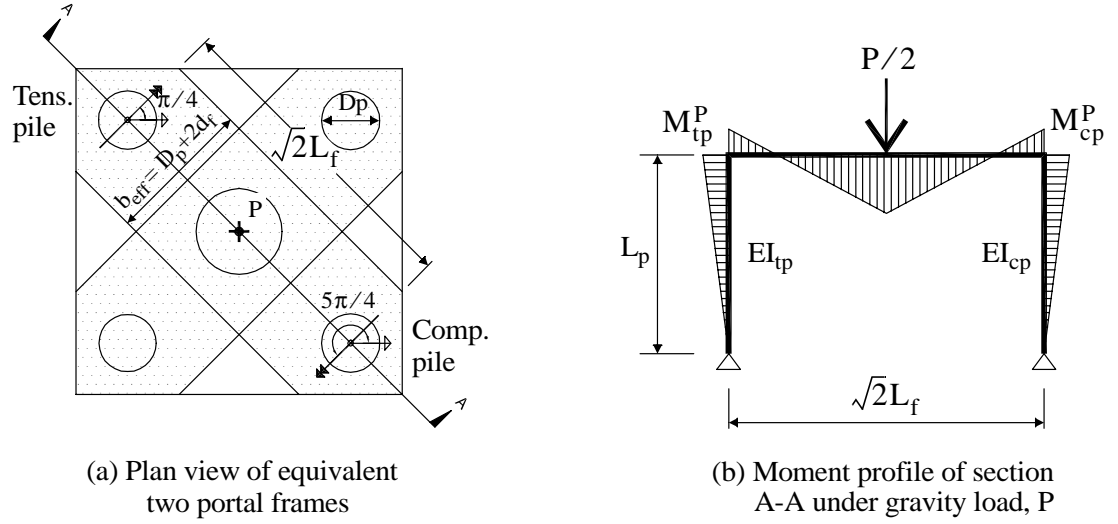
Figure 6.4: Moment and its direction due to gravity load, P

If M_{cp}^P is defined as the moment at the top of the compression pile due to the gravity load, P,

$$M_{cp}^P = \frac{\sqrt{2}}{16} \cdot P \cdot L_f \cdot \left(\frac{\beta_{cp} K_p}{\alpha K_f + \beta_{cp} K_p} \right) = \frac{\sqrt{2}}{16} \cdot P \cdot L_f \cdot \left(\frac{\beta_{cp} k_p}{\alpha + \beta_{cp} k_p} \right) \tag{6.5}$$

where, $K_p = 3EI_p/L_p$ and $K_f = 4EI_f/(\sqrt{2}L_f)$ are the rotational bending stiffnesses for the piles and for the equivalent beam, respectively. The effective bending stiffness ratio of compression pile, k_p, is :

$$k_p = \frac{K_p}{K_f} = \left(\frac{3EI_p}{L_p} \right) \Big/ \left(\frac{4EI_f}{\sqrt{2}L_f} \right) = \frac{3\sqrt{2}}{4} \left(\frac{L_f}{L_p} \right) \frac{EI_p}{EI_f} \tag{6.6}$$

In Eq. (6.5), K_f was multiplied by the pilecap stiffness modification factor, α, to consider the original pilecap stiffness in the equivalent portal frame method. Factor, α,

can be obtained using r_θ, which is defined as the ratio of the pilecap-pile joint rotations, θ/θ', between the equivalent portal frame modeling and full pilecap modeling. If M is the given moment at the pile-pilecap joint, the ratio of rotations, r_θ, is :

$$r_\theta = \frac{\theta}{\theta'} = \frac{M/(K_f + K_p)}{M/(\alpha K_f + K_p)} = \frac{\alpha + k_p}{1 + k_p} \tag{6.7}$$

From Eq. (6.7), α is :

$$\alpha = r_\theta + k_p(r_\theta - 1) \tag{6.8}$$

The ratio of rotation, r_θ, is obtained from the analyses results of full pilecap modeling and equivalent portal frame modeling. Assuming equal effective stiffness ratio, $\xi = EI_p/E_cI_p = EI_f/E_cI_f$, for both pile and beam in equivalent portal frame after cracking, EI_p/EI_f in Eq. (6.6) is calculated as follows :

$$\frac{EI_p}{EI_f} = \frac{\xi E_c I_p}{\xi E_c I_f} = \frac{I_p}{I_f} = \left(\frac{\pi D_p^4}{64}\right) \Big/ \left[\frac{(2\sqrt{2}D_p) \cdot (\gamma D_p)^3}{12}\right] = 0.208 \cdot \gamma^{-3} \tag{6.9}$$

where, I_p and I_f are the second moment of inertias of the gross section of the pile and beam in equivalent portal frame, respectively, and γ is the ratio of pilecap depth, h_f, over the pile diameter, D_p.

$$\gamma = \frac{h_f}{D_p} \tag{6.10}$$

For the piles that will be subjected to tension upon the application of lateral loading, the moment due to gravity load, P, is obtained by using β_{tp} instead of β_{cp} in Eq. (6.5) as :

$$M_{tp}^P = \frac{\sqrt{2}}{16} \cdot P \cdot L_f \cdot \left(\frac{\beta_{tp} k_p}{\alpha + \beta_{tp} k_p} \right) \tag{6.11}$$

It is ovbious that the direction of pile shear forces due to gravity load, P, only, is in the diagonal direction pointing toward the column vertical axis. Thus, the angles, α_{cp}^P of M_{cp}^P and α_{tp}^P of M_{tp}^P, between positive x-axis and the moment are $5\pi/4$ and $\pi/4$, respectively, as shown in Figure 6.4-(a).

Hence,

$$
\begin{aligned}
M_{cp, x}^P &= M_{cp}^P \cos\frac{5\pi}{4} = -\frac{M_{cp}^P}{\sqrt{2}} \\
M_{cp, y}^P &= M_{cp}^P \sin\frac{5\pi}{4} = -\frac{M_{cp}^P}{\sqrt{2}}
\end{aligned}
\tag{6.12}
$$

and,

$$
\begin{aligned}
M_{tp, x}^P &= M_{tp}^P \cos\frac{\pi}{4} = \frac{M_{tp}^P}{\sqrt{2}} \\
M_{tp, y}^P &= M_{tp}^P \sin\frac{\pi}{4} = \frac{M_{tp}^P}{\sqrt{2}}
\end{aligned}
\tag{6.13}
$$

2) Response of pile-pilecap joints with respect to y-axis

The pile supported foundation under column overstrength moment, M_c° and shear force F_c°, shows the combined response of rigid body rotation and lateral translation. The rigid body rotation of the pilecap, θ_f, depends on the vertical stiffnesses at the pile locations which result from the soil - pile interaction. The lateral translation of pilecap, Δ_f, depends on the lateral stiffness of soil on the pilecap vertical side. The direction of
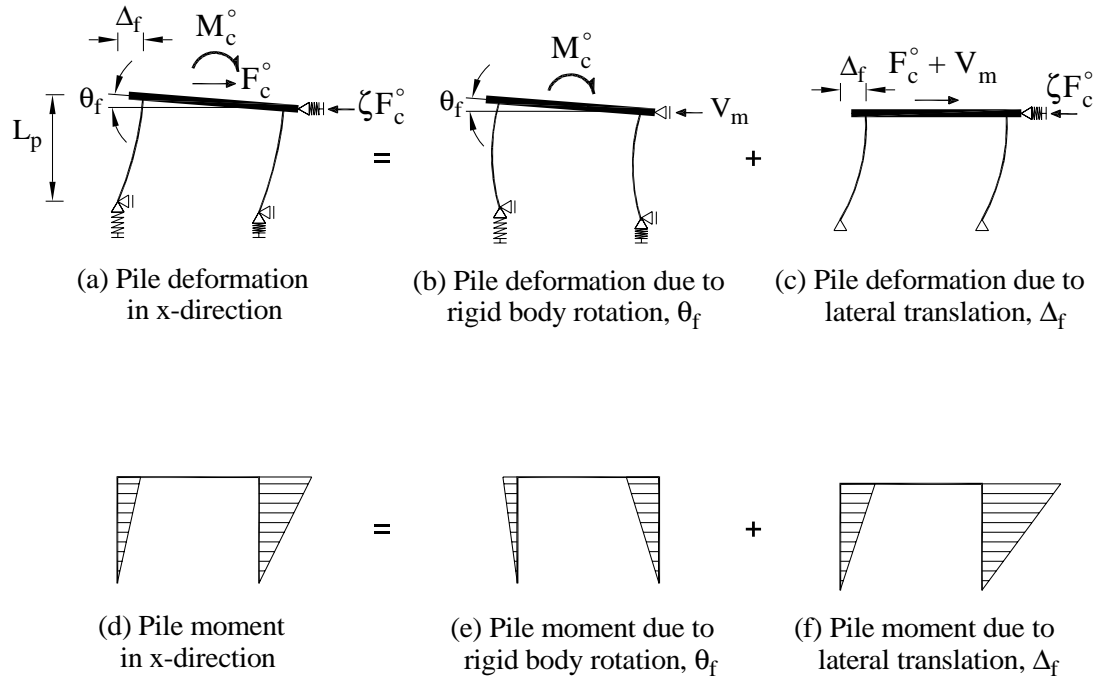
Figure 6.5: Modes of pilecap deformations under seismic load
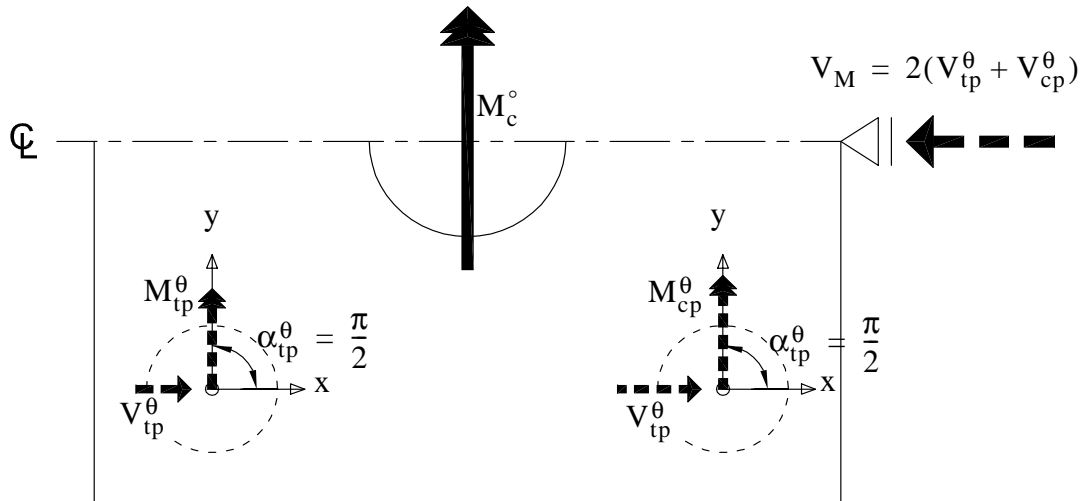
Figure 6.6: Pile top moment and its direction due to the rigid body rotation of the foundation
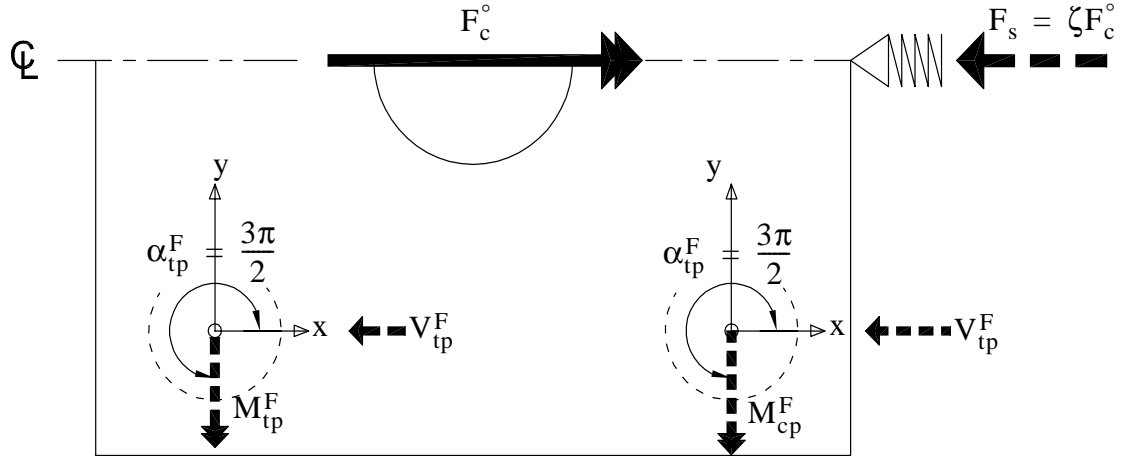
Figure 6.7: Pile top moment and its direction due to the lateral translation of the foundation

the pile shear force due to these two modes of foundation behavior is parallel to the column overstrength shear force, F_c° as shown in Figure 6.6.

If M_{cp}^y, α_{cp}^y and M_{tp}^y, α_{tp}^y are defined as the moments and their directions with respect to the y-axis at the top of the compression and tension piles, respectively, these can be quantified via *the force method* using *the principle of virtual work*. Figure 6.8 shows the decomposition of the system into the released structure and the redundant forces. To use this method, it was assumed that the center of rotation is at the tip of the compression pile because the vertical soil-pile interaction stiffness of the compression pile is much greater than that of the tension pile. The vertical stiffness of the compression pile is composed of soil-pile friction and end bearing, while the stiffness of the tension pile relies only on the friction between pile and soil.
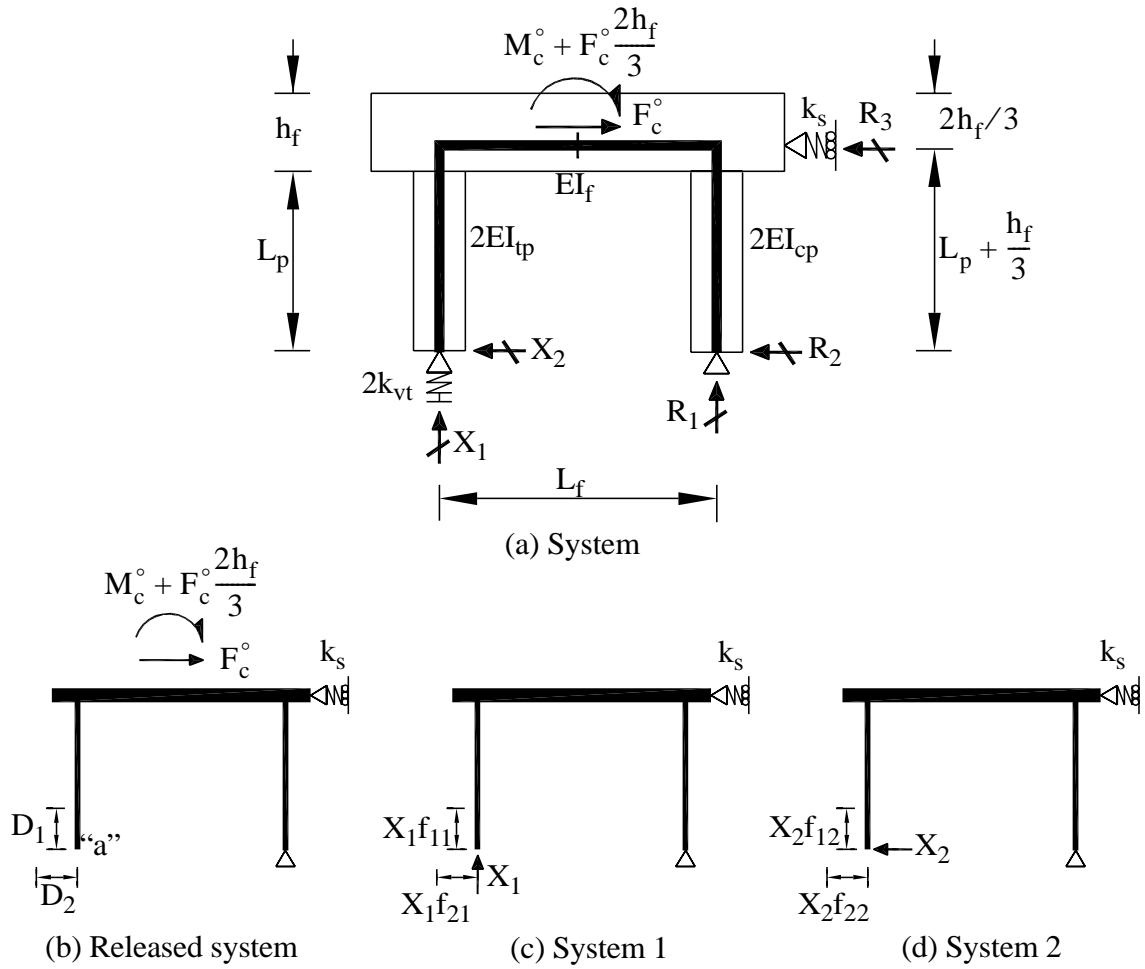
Figure 6.8: Decomposition of the system
under orthogonal direction loading for the force method

In Figure 6.8 the depth of the point where pilecap passive soil pressure acts is assumed $2h_f/3$ from the soil surface assuming linearly increased soil Young's modulus with depth. In addition, the skeletal frame of the pilecap is aligned with the lateral stiffness of pilecap passive soil. Accordingly, the moment acting on the skeletal frame of the foundation system is $M_c^\circ + F_c^\circ(2h_f/3)$. The vertical and horizontal displacements at

the joint "a" of released structure is represented as D_1 and D_2, respectively. The f_{ij} (i = 1, 2 and j = 1, 2) are the flexibility coefficients representing the displacement at the coordinate i due to a unit force at the coordinate j. The compatibility condition states that the final vertical and horizontal translations at "a" are $X_1/(2k_{vt})$ and 0, respectively. Thus, the compatibility condition at joint "a" is expressed in matrix form as follows :

$$\begin{Bmatrix} D_1 \\ D_2 \end{Bmatrix} + \begin{bmatrix} f_{11} + 1/(2k_{vt}) & f_{12} \\ f_{21} & f_{22} \end{bmatrix} \begin{Bmatrix} X_1 \\ X_2 \end{Bmatrix} = \begin{Bmatrix} 0 \\ 0 \end{Bmatrix} \tag{6.14}$$

where

$$D_1 = \frac{3}{8EI_f} M_c^\circ L_f^2 + \frac{2M_c^\circ L_f L_p^3}{3\beta_{cp}EI_p(L_p + h_f/3)^2} + \left(F_c^\circ + \frac{M_c^\circ}{L_p + h_f/3}\right)\left(\frac{L_f}{L_p + h_f/3}\right)\frac{1}{k_s}$$

$$D_2 = \frac{1}{2EI_f} M_c L_f L_p + \frac{2M_c^\circ L_p^3}{3\beta_{cp}EI_p(L_p + h_f/3)}$$

$$f_{11} = \frac{L_f^3}{3EI_f} + \frac{2L_f^2 L_p^3}{3\beta_{cp}EI_p(L_p + h_f/3)^2} + \left(\frac{L_f}{L_p + h_f/3}\right)^2 \frac{1}{k_s}$$

$$f_{21} = \frac{1}{2EI_f} L_f^2 L_p + \frac{2L_f L_p^3}{3\beta_{cp}EI_p(L_p + h_f/3)}$$

$$f_{12} = \frac{1}{2EI_f} L_f^2 L_p + \frac{2L_f L_p^3}{3\beta_{cp}EI_p(L_p + h_f/3)}$$

$$f_{22} = \frac{2}{3\beta_{tp}EI_p} L_p^3 + \frac{1}{EI_f} L_f L_p^2 + \frac{2}{3\beta_{cp}EI_p} L_p^3$$

After solving Eq. (6.14) on the redundant forces, X_1 and X_2, the reactions of the released structure, R_1, R_2 and R_3, can be obtained by the ordinary methods of statics as follows :

$$R_1 = -X_1$$

$$R_2 = F_c^\circ - R_3 - X_2$$

$$R_3 = \frac{1}{(L_p + h_f/3)}\left[\left(M_c^\circ + F_c^\circ \frac{2h_f}{3}\right) + F_c^\circ(L_p + h_f/3) + X_1 L_f\right]$$

(6.15)

Therefore, M_{cp}^y and M_{tp}^y with respect to y-axis at the pile-pilecap joints are :

$$M_{cp}^y = \left(\frac{R_2}{2}\right)L_p$$

$$M_{tp}^y = \left(\frac{X_2}{2}\right)L_p$$

(6.16)

The stiffness enhancement factor of the compression pile, β_{cp}, can be based on the axial load obtained using the original pile stiffnesses in the system since the influence of the pile bending stiffness on the vertical reaction of the system is negligibly small.

The angles, α_{cp}^y of M_{cp}^y and α_{tp}^y of M_{tp}^y, between positive x-axis and the moment are $\pm \pi/2$ as a combination of the two response modes as shown in Figures 6.5 - 6.7.

3) Pile moment with respect to x-axis

Because the lateral force, which is applied in the orthogonal direction, should be resisted by two pairs of diagonally aligned piles as shown in Figure 6.42, M_c° is divided into two components of $M_c^\circ/\sqrt{2}$ on each diagonal direction as illustrated in Figure 6.9-(a). Accordingly, the moments and the corresponding rotations develop at the joints of pile - pilecap. Since the y-component of these moments are already considered in the response with respect to the y-axis, which is described in previous section, the response about the x-axis is discussed here.
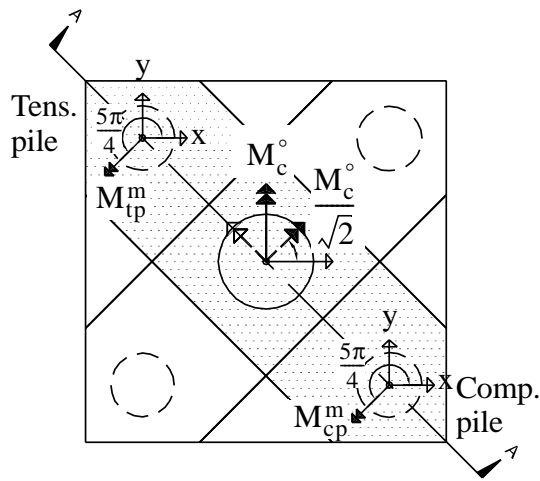
(a) Plan view of moments
on an equivalent portal frame
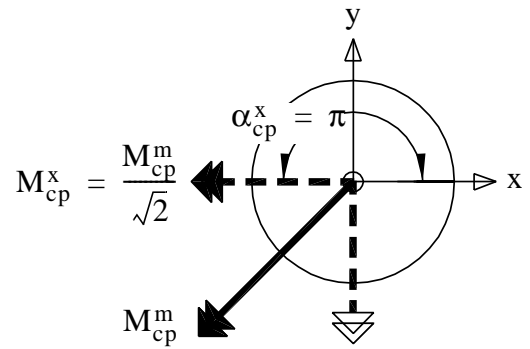
(b) X-component of
compression pile Moment
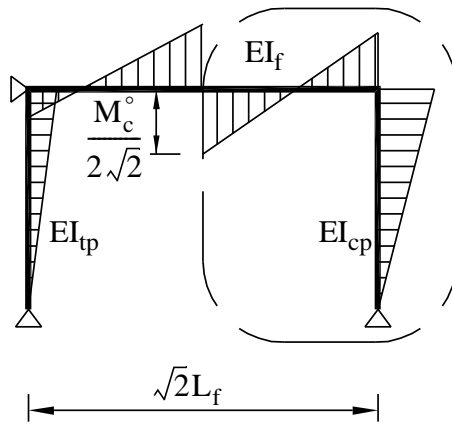
(c) Moment profile of an equivalent
portal frame(section A-A)
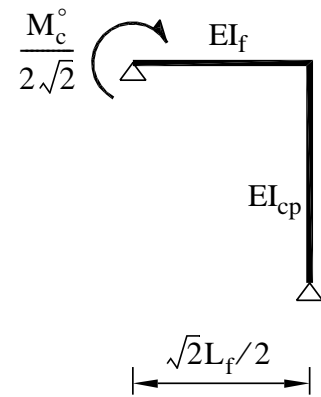
(d) Eqivalent structure of
the part in dashed line of (c)

Figure 6.9: Grapical presentation of the pile moment with respect to x-axis due to M_c°
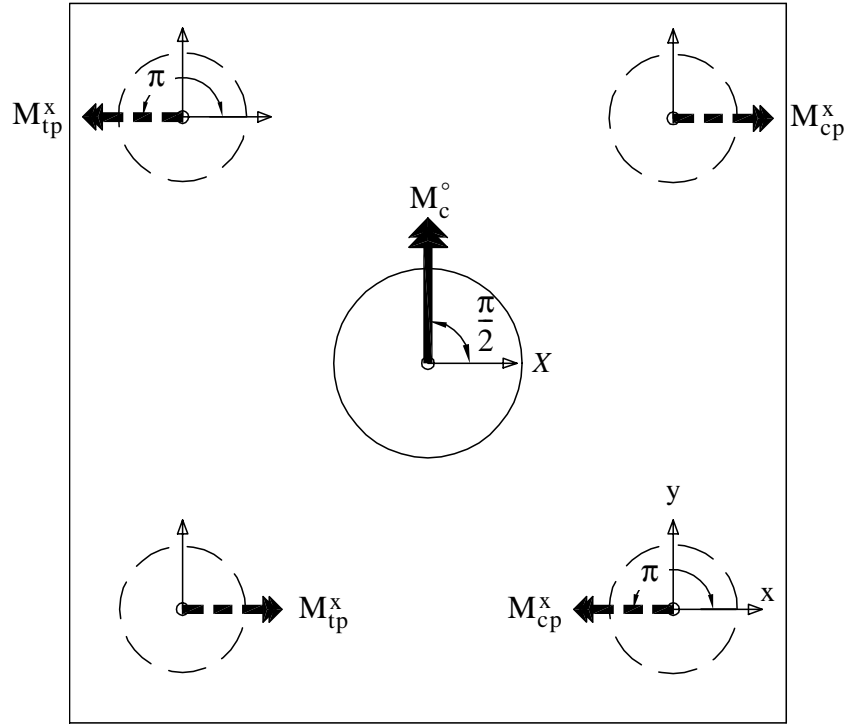
Figure 6.10: Pile moments with respect to x-axis under applied M_c°

If M_{cp}^m is defined as the induced moment at the top of compression pile due to $M_c^\circ / \sqrt{2}$ as shown in Figures 6.9-(a) and 6.9-(b), M_{cp}^m can be expressed, from Figures 6.9-(c) and 6.9-(d), as :

$$
M_{cp}^m = \frac{M_c^\circ}{4\sqrt{2}} \cdot \left(\frac{\beta_{cp} K_p}{\frac{3\alpha}{4} K_f + \beta_{cp} K_p} \right) = \frac{M_c^\circ}{4\sqrt{2}} \cdot \left(\frac{\beta_{cp} k_p}{\frac{3\alpha}{4} + \beta_{cp} k_p} \right) \tag{6.17}
$$

However, only the x-component of this moment, M_{cp}^m, contributes to the response with respect to x-axis. Thus, M_{cp}^x, the x-component of M_{cp}^m, is obtained as $M_{cp}^m / \sqrt{2}$ and

182

illustrated in Figure 6.9-(b). M_{cp}^x causes positive bending of pilecap as depicted in Figure 6.3-(d).

$$M_{cp}^x = \frac{M_{cp}^m}{\sqrt{2}} = \frac{M_c^\circ}{8} \cdot \left(\frac{\beta_{cp}k_p}{\frac{3\alpha}{4} + \beta_{cp}k_p} \right) \tag{6.18}$$

The direction of M_{cp}^x is π, which is perpendicular to the column overstrength moment, M_c°, as depicted in Figure 6.10 - (c).

In the same way, the corresponding moment at the top of tension pile, M_{tp}^x, is :

$$M_{tp}^x = \frac{M_c^\circ}{8} \cdot \left(\frac{\beta_{tp}k_p}{\frac{3\alpha}{4} + \beta_{tp}k_p} \right) \tag{6.19}$$

The direction of the moment, M_{tp}^x, is π and the moment cause the negative bending of pilecap as illustrated in Figure 6.3-(b).

4) The magnitudes of M_{cp}, M_{tp} and their direction α_{cp}, α_{tp}

The x and y components of the pile top moment can be calculated using vectorial addition of the moment components which are obtained in previous stages **1) - 3)**.

From the Eqs. (6.12) , (6.16) and (6.18) :

$$\begin{aligned} M_{cp,x} &= M_{cp,x}^P + M_{cp}^x \\ M_{cp,y} &= M_{cp,y}^P + M_{cp}^y \end{aligned} \tag{6.20}$$

Thus, the magnitude of moment, M_{cp}, and its direction, α_{cp}, at the joint of the pilecap and the compression pile is :

$$M_{cp} = \sqrt{M_{cp,x}^2 + M_{cp,y}^2} \tag{6.21}$$

$$\alpha_{cp} = \text{atan}\left(\frac{M_{cp,y}}{M_{cp,x}}\right) \tag{6.22}$$

Likewise, the magnitude of moment, M_{tp}, and its direction, α_{tp}, at the joint of the pilecap and the tension pile is :

$$M_{tp} = \sqrt{M_{tp,x}^2 + M_{tp,y}^2} \tag{6.23}$$

$$\alpha_{tp} = \text{atan}\left(\frac{M_{tp,y}}{M_{tp,x}}\right) \tag{6.24}$$

where

$$\begin{aligned} M_{tp,x} &= M_{tp,x}^P + M_{tp}^x \\ M_{tp,y} &= M_{tp,y}^P + M_{tp}^y \end{aligned} \tag{6.25}$$

6.1.3 Parameter study for principal direction of pile resistance

1) Design of foundation system

To investigate the sensitivity of the moments at the top of piles and their directions, a parameter study was done for a four pile supported foundation system. The foundation system was carefully designed for piles to remain elastic through whole ranges of variables. The column and pile diameters were identical to those of the test unit CFPS2, that is, 762mm and 508mm, respectively. The column and pile reinforcement ratio were 1.98% and 1.56%, respectively.
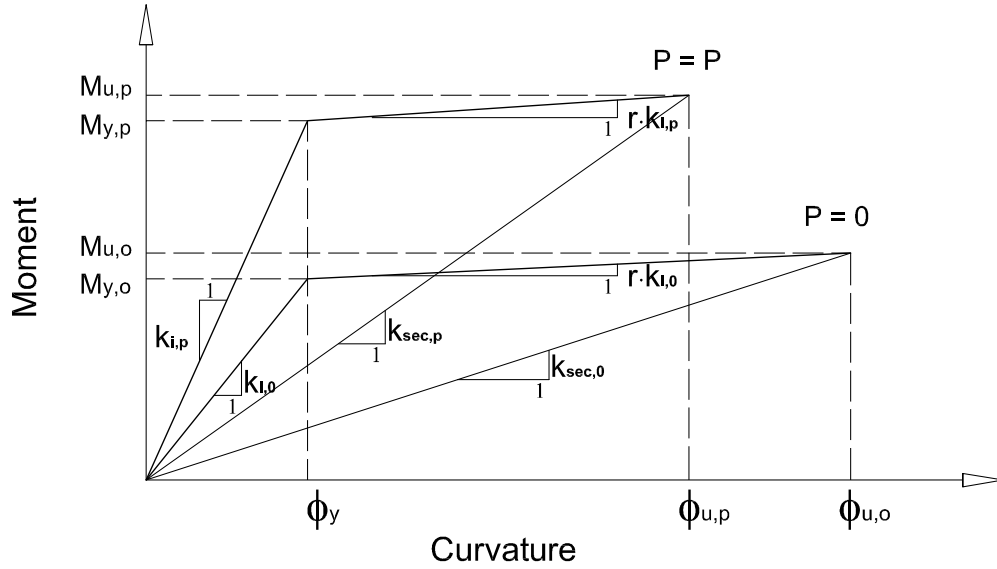
Figure 6.11: Bilinear moment-curvature curves for different axial loads

2) Parameters and their ranges

A total of four parameters were chosen for the study : the column axial load ratio, $P/(f_c' A_g)$, the nondimensional column length, L_c/D_c, the ratio of pilecap depth over pile diameter, h_f/D_p, the soil subgrade modulus, E_{s1}(MPa/m).

- Axial load ratio : $P/(f_c' A_g)$

This variable was chosen to see the effect of gravity load on the foundation response. The capacity of column overstrength moment and shear capacities, M_c° and F_c° , which act on the foundation as seismic loads, is a function of the column axial load, P. The enhancement of M_c° and F_c° due to applied gravity load, P, can be explained as follows.

From the idealized bilinear moment-curvature curve of P = 0 in Figure 6.11, The column overstrength moment capacity, $M_{u,o}$, can be obtained as :

185

$$M_{u,o} = M_{y,o} + (M_{u,o} - M_{y,o}) = k_{i,o}[\phi_y + (\phi_{u,o} - \phi_y) \cdot r] \tag{6.26}$$

where $M_{y,o}$ is the yield moment capacity, $k_{i,o}$ is the elastic stiffness, ϕ_y is the yield curvature which is approximately $2.45\varepsilon_y/D$ [26] in columns with circular section, $\phi_{u,o}$ is the ultimate curvature and r is the ratio of post-yield stiffness over elastic stiffness. Dividing Eq. (6.26) by ϕ_y, the secant stiffness, $k_{sec,o}$, is obtained as :

$$k_{sec,o} = \frac{k_{i,o}(1 + \mu_{\phi,o}r_o - r_o)}{\mu_{\phi,o}} \tag{6.27}$$

where $\mu_{\phi,o}$ is the curvature ductility of the section when P = 0. Similarly, $k_{sec,p}$ which is the secant stiffness for the bilinear moment-curvature curve with axial load, P, can be obtained as :

$$k_{sec,p} = \frac{k_{i,p}(1 + \mu_{\phi,p}r_p - r_p)}{\mu_{\phi,p}} \tag{6.28}$$

where $k_{i,p}$ is the elastic stiffness, $\mu_{\phi,p}$ is the curvature ductility and r_p is the ratio of post-yield stiffness over elastic stiffness of the section with axial load P. From Eqs. (6.27) and (6.28), the ratio, β_c, representing the increased overstrength moment capacity due to an increase in axial load, P, with respect to the overstrength moment capacity when P = 0, can be obtained as :

$$\beta_c = \frac{M_{u,p}}{M_{u,o}} = \left(\frac{k_{i,p}}{k_{i,o}}\right) \cdot \left(\frac{1 + \mu_{\phi,p}r_p - r_p}{1 + \mu_{\phi,o}r_o - r_o}\right)\left(\frac{\mu_{\phi,o}}{\mu_{\phi,p}}\right) \tag{6.29}$$

Because, in Figure 6.11:

$$\frac{k_{i,p}}{k_{i,o}} = \frac{M_{y,p}}{M_{y,o}} \tag{6.30}$$

186

Eq. (6.30) indicates that axial load influences yield moment capacity and flexural stiffness by the same ratio.

Eq. (6.29) becomes :

$$\beta_c = \left(\frac{M_{y,p}}{M_{y,o}}\right) \cdot \left(\frac{1 + \mu_{\phi,p}r_p - r_p}{1 + \mu_{\phi,o}r_o - r_o}\right)\left(\frac{\mu_{\phi,o}}{\mu_{\phi,p}}\right) \tag{6.31}$$

The range of the axial load ratio was chosen from 5% to 30% with 5% increment, which are the typical axial load ratios in bridge columns.

- Nondimensional column length : L_c/D_c

The variation of column length, L_c, causes the different overstrength column shear force, F_c° for a given overstrength moment capacity at column plastic hinge, M_c°, by the equation :

$$F_c^{\circ} = \frac{M_c^{\circ}}{L_c}. \tag{6.32}$$

To make a column length, L_c, as a nondimensional quantity, it is divided by the diameter of column, D_c (= 762mm)

The range of the nondimensional column length, L_c/D_c, was arbitrarily determined from 3.0 to 13.0 with 2.0 increments.

- Ratio of pilecap depth and pile diameter : h_f/D_p

The moment at the top of pile depends on the relative pile bending stiffness ratio which is determined by the pilecap depth, h_f, for a given pile section. For the foundation

(a) partial plan view of beam
in equivalent portal frame

(b) partial section view of A-A
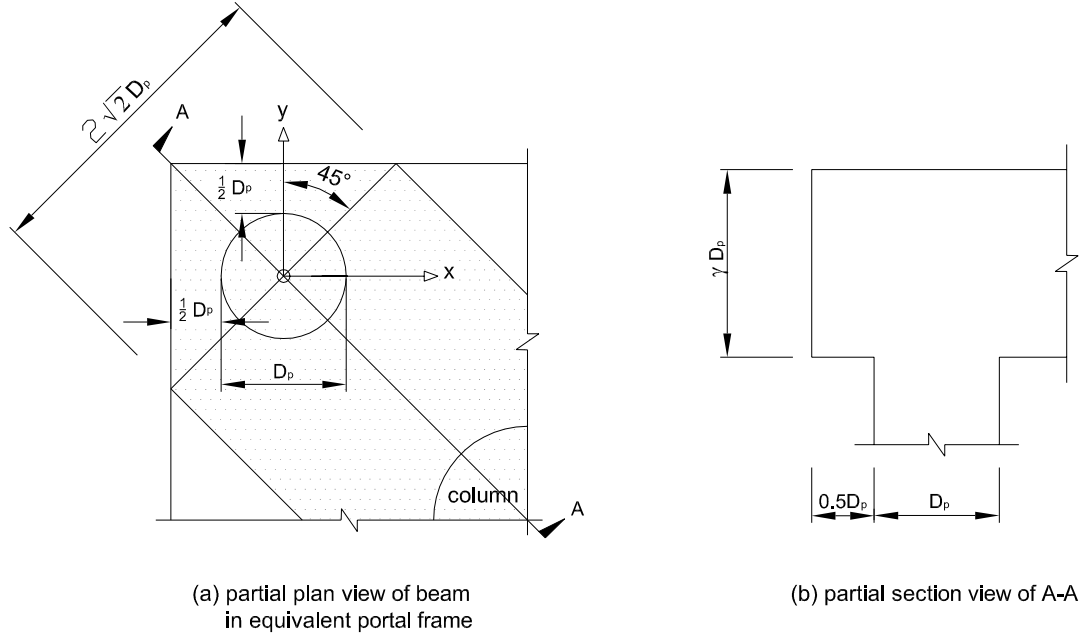
Figure 6.12: Effective width of the beam in equivalent diagonal portal frame

system which is simplified to the two equivalent portal frames diagonally oriented, the effective beam width of equivalent portal frame, b_{eff}, is limited to $2\sqrt{2}D_p$ adopting b_{eff} = $D_p + 2h_f$ as shown in Figure *6.4*, by the protruded length of the pilecap stub of approximately $0.5D_p$ as recommended in reference[26]. This is based on the assumption that the pilecap depth is greater than $(\sqrt{2} - 0.5)D_p$ with a $45°$ spreading of stress from the boundary of pile in all direction. The influence of the pilecap flexibility, which is the reverse of pilecap stiffness, on the lateral stiffness of the foundation system may also be studied through the chosen variable, h_f/D_p. The range of the variable was 1.0 to 2.0 with 0.2 increments.

- <u>Variation of the soil elastic modulus with depth</u> : $E_{s1}(MPa/m)$

It was mentioned in Section 6.1.2 that the pile moment and its direction are influenced by the pilecap rigid body rotation, which depends on the vertical stiffness of soil-pile interaction and the passive soil stiffness adjacent to pilecap. The interactive vertical stiffness of the tension pile was calculated by dividing the applied tension force by the resulting pile top displacement. To calculate the displacement at the top of tension pile, the differential equation was solved using the shear stress at the face of the pile. The derivation of the equation is described in Section 2.2.4 - 2). If k_s is assumed to be a linear function of z in Eq. (2.25), which is one of the typical cases in sands, k_s can be expressed as :

$$k_s = k_{s1} \cdot z = \frac{G_{s1} \cdot z}{4(D_p/2)(1 - v_s)} = \frac{E_{s1} \cdot z}{4D_p(1 - v_s^2)} \tag{6.33}$$

where

$$k_{s1} = \frac{G_{s1}}{4(D_p/2)(1 - v_s)} \tag{6.34}$$

$$G_{s1} = \frac{E_{s1}}{2(1 + v_s)} \tag{6.35}$$

Substituting Eqs. (6.34) and (6.35) into Eq. (2.25) :

$$E_p A_p \frac{dw^2}{dz^2} - \frac{E_{s1} S w}{4D_p(1 - v_s^2)} \cdot z = 0 \tag{6.36}$$

The necessary boundary conditions to solve Eq. (6.36) with respect to the pile deflection, *w*, were Eqs (2.26) and (2.27).

Therefore, the vertical stiffness at the top of the tension pile due to soil - pile interaction can be obtained with the pile force :

$$F_p = E_p A_p \frac{dw^2}{dz^2} \tag{6.37}$$

For the parameter study three types of soil, Loose Sand, Medium Sand and Dense Sand, were selected. The variation of the soil elastic modulus with depth was taken as 7 MPa/m, 25 MPa/m and 60 MPa/m. Poisson's ratio of soil , ν_s, was assumed constant and equal to 0.3 and a pile length of 20m was adopted. The results of Eq. (6.37) with applied vertical tension force at the top of pile, 800 kN, is shown in Figure 6.13. The vertical stiffness of soil-pile interaction was obtained dividing the diplacement by the pile force at the top of the pile. The vertical stiffness at the top of the pile were 300 kN/m, 596 kN/m and 830 kN/m for each soil type.

The lateral stiffness of passive soil on pilecap vertical sides also has a great influence on the demand of the pile shear force by reacting part of the overstrength column shear. The lateral stiffness of passive soil on pilecap side was determined by the following equation.

$$k_s(z) = k_h(z) \cdot B_f \cdot h_f \tag{6.38}$$

where $k_h(z)$ is the coefficient of horizontal subgrade reaction at depth, z, which is the soil spring location, B_f and h_f are the width and the depth of the pilecap, respectively. The coefficient of horizontal subgrade reaction, $k_h(z)$, was obtained from the following equation.

(a) Pile vertical displacement along depth

7MPa/m

25MPa/m

60MPa/m

(b) Pile axial force along depth

7MPa/m

25MPa/m

60MPa/m
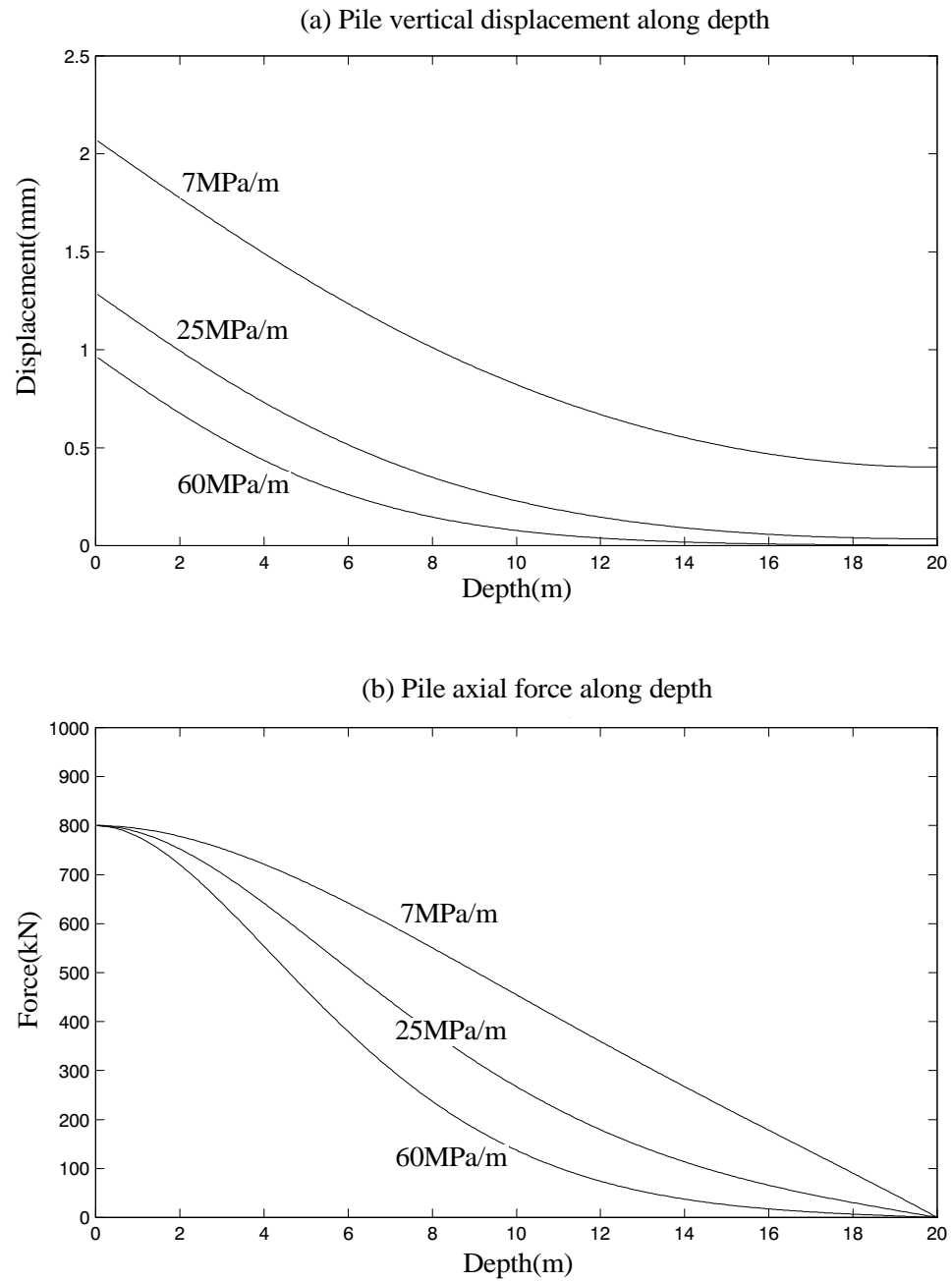
Figure 6.13: Distribution of vertical deflection and force of pile along depth for applied tension force of 800kN, with different soil stiffnesses

$$k_h(z) = \frac{E_{s1} \cdot z}{D^*} \tag{6.39}$$

where E_{s1} is the increase rate of soil Young's modulus and D^* is the reference pile diameter, 1.83m.[7]

6.1.4 Moment at the top of piles under diagonal loading

Because the parameter study is on the pile moment under orthogonal direction loading, the result is compared with the diagonal direction loading cases. The pile top moment under diagonal direction loading can be obtained using the same method which is adopted for the cases under orthogonal direction loading. However, the direction of pile moment is obviously $5\pi/4$ from the x-axis shown in Figure 6.3-(a).

1) Pile top moment, M_{cp}^P, and M_{tp}^P, due to gravity load, P.

The moments induced at the top of the piles due to gravity load, P, can be expressed as before, by Eqs. (6.5) and (6.11).

2) Pile top moments, M_{cp}^R and M_{tp}^R, due to a combined rigid body rotation, θ_f, and lateral translation of pilecap, Δ_f.

The pile top moments, M_{cp}^R and M_{tp}^R, due to a combined rigid body rotation, θ_f, and lateral translation of pilecap, Δ_f, can be found via *the force method* using *the principle of virtual work*. However, under diagonal direction loading, it is important to note that the width of the pilecap varies along the local x_1 and x_2 axes and accordingly, the second moment of inertia of the pilecap, I_f, is a function of x_1 and x_2, respectively, as illustrated in Figure 6.14. Thus, the width of the pilecap, $B_f(x_1)$ and $B_f(x_2)$, are :
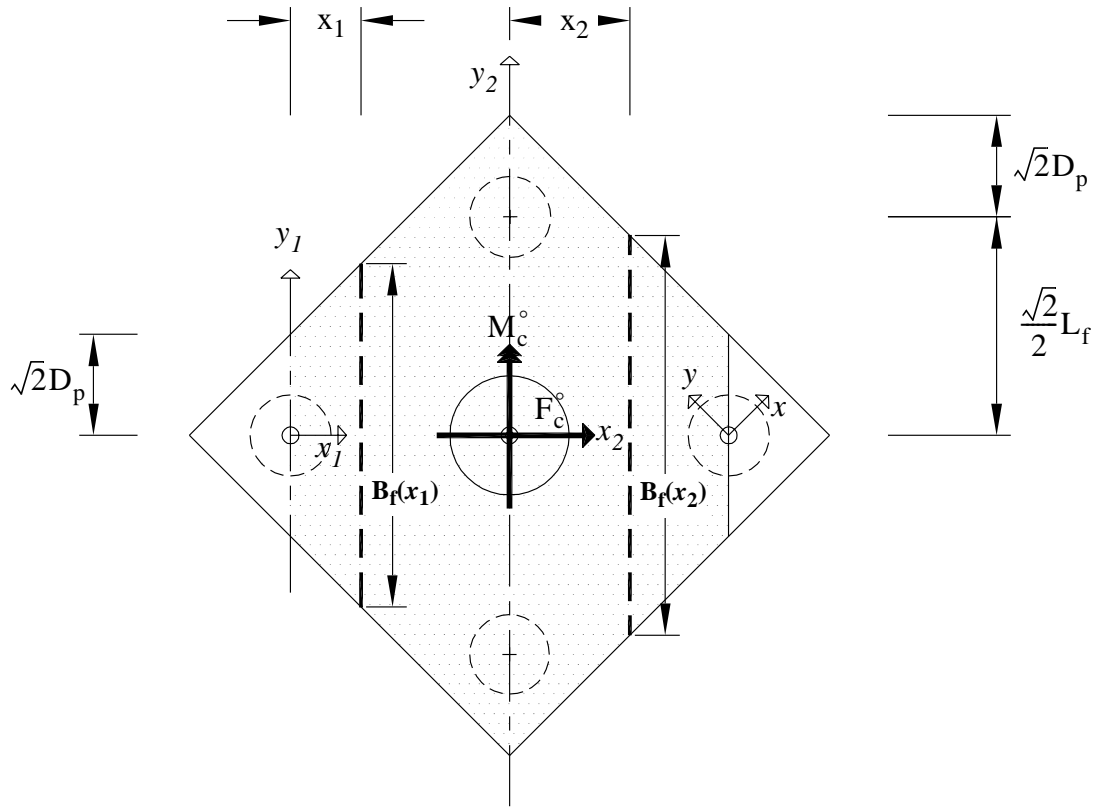
Figure 6.14: Varying pilecap width along x_1 and x_2 axes

$$B_f(x_1) = 2(\sqrt{2}D_p + x_1)$$

$$B_f(x_2) = 2\left(\sqrt{2}D_p + \frac{\sqrt{2}L_f}{2} - x_2\right)$$

(6.40)

Another difference from the case under orthogonal direction loading is that the lateral passive stiffness of soil on the pilecap vertical side is $\sqrt{2}\,k_s$ since the effective width of the pilecap, which mobilize the passive soil pressure, is $\sqrt{2}\,B_f$.

The released structure and the redundant forces are shown in Figure 6.15. The approximation is reasonably made that the center of rotation is assumed to be at the tip

193

$$\sqrt{2}L_f$$

$$M_c^\circ + F_c^\circ \frac{2h_f}{3}$$

$$F_c^\circ$$

$$\sqrt{2}k_s$$

$$R_3$$

$$EI_f(x_1) \quad EI_f(x_2)$$

$$L_p$$

$$EI_{tp} \quad 2EI_{mp} \quad EI_{cp}$$

$$K_{vt} \quad X_2 \quad X_4 \quad R_2$$

$$2K_{vt}$$

$$X_1 \quad X_3 \quad R_1$$

(a) system

$$M_c^\circ + F_c^\circ \frac{2h_f}{3}$$

$$F_c^\circ$$

$$\sqrt{2}k_s$$

$$D_2 \quad D_4$$

$$D_1 \quad D_3$$

(b) released system

$$\sqrt{2}k_s$$

$$X_1f_{11} \quad X_1f_{31}$$

$$X_1$$

$$X_1f_{21} \quad X_1f_{41}$$

(c) system 1

$$\sqrt{2}k_s$$

$$X_2f_{12} \quad X_2f_{32}$$

$$X_2$$

$$X_2f_{22} \quad X_2f_{42}$$

(d) system 2

$$\sqrt{2}k_s$$

$$X_3f_{13} \quad X_3f_{33}$$

$$X_3$$

$$X_3f_{23} \quad X_3f_{43}$$

(e) system 3

$$\sqrt{2}k_s$$

$$X_4f_{14} \quad X_4f_{34} \quad X_4$$

$$X_4f_{24} \quad X_4f_{44}$$
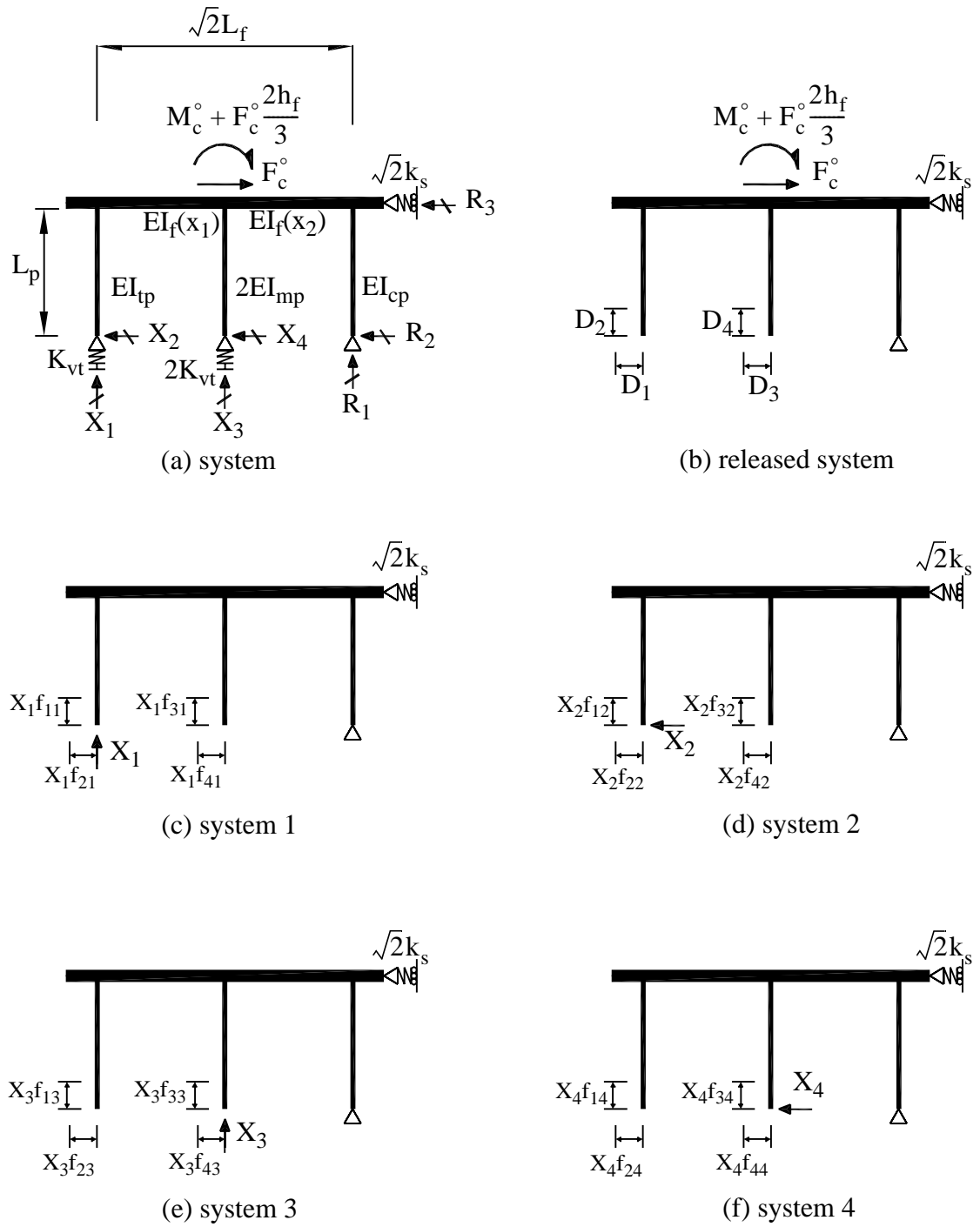
(f) system 4

Figure 6.15: Decomposition of the system
under diagonal direction loading for the force method

194

of the compression pile because the ratio of vertical soil-pile interaction stiffnesses between tension and compression piles is so large.

The compatibility condition in matrix form is :

$$
\begin{Bmatrix} D_1 \\ D_2 \\ D_3 \\ D_4 \end{Bmatrix} + \begin{bmatrix} f_{11} + 1/k_{vt} & f_{12} & f_{13} & f_{14} \\ f_{21} & f_{22} & f_{23} & f_{24} \\ f_{31} & f_{32} & f_{33} + 1/2k_{vt} & f_{34} \\ f_{41} & f_{42} & f_{43} & f_{44} \end{bmatrix} \begin{Bmatrix} X_1 \\ X_2 \\ X_3 \\ X_4 \end{Bmatrix} = \begin{Bmatrix} 0 \\ 0 \\ 0 \\ 0 \end{Bmatrix} \quad (6.41)
$$

After obtaining the redundants, X1 - X4, by solving Eq. (6.41), the reactions of the released structure, R1, R2 and R3, are :

$$
\begin{aligned}
R_3 &= \left[\left(M_c^\circ + \frac{2h_f}{3} \right) + F_c^\circ (L_p + h_f/3) + \sqrt{2} X_1 L_f + \frac{\sqrt{2}}{2} X_3 L_f \right] / (L_p + h_f/3) \\
R_2 &= F_c^\circ - R_3 - X_2 - X_4 \\
R_1 &= -(X_1 + X_3)
\end{aligned} \quad (6.42)
$$

Therefore, M_{cp}^R and M_{tp}^R due to a combined rigid body rotation, θ_f, and lateral translation of pilecap, Δ_f, are :

$$
\begin{aligned}
M_{cp}^R &= R_2 L_p \\
M_{tp}^R &= X_2 L_p
\end{aligned} \quad (6.43)
$$

The flexibility coefficients for this method are presented in Appendix E.

3) The magnitudes of M_{cp}, M_{tp}

From the Eqs. (6.5), (6.11) and (6.43) :

$$M_{cp} = M_{cp}^P + M_{cp}^R$$
$$M_{tp} = M_{tp}^P + M_{tp}^R$$

(6.44)

6.1.5 Results of parameter study

The result of the parameter study is shown in this section using polar, 2-D and 3-D graphical presentations. Referring to Figure 6.16, polar graphs can be interpreted. Analysis of the results under orthogonal direction loading is followed by the comparison with the result under diagonal direction loading. Lastly, the sensitivity of the moment direction and the normalized magnitude along with the individual variable is investigated.
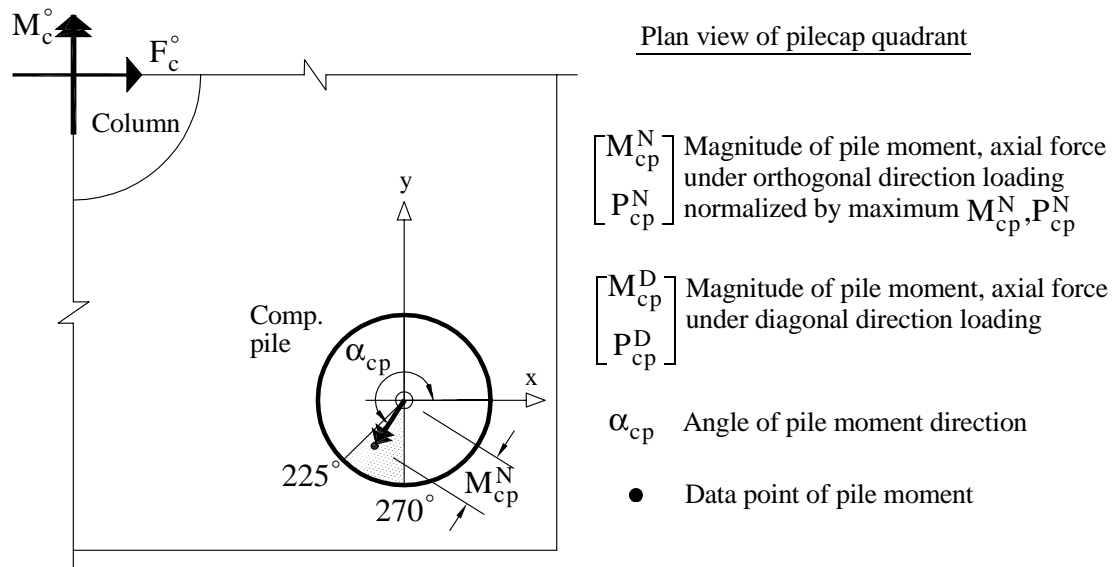
Figure 6.16: Interpretation of graph in polar coordinates

Max. (1.00, 256$^{\mathrm{o}}$)

$P/(f_c^{'}A_g) = 0.3$

$L_c/D_c = 3.0$

$h_f/D_p = 1.0$

$E_{s1} = 7\mathrm{MPa}/\mathrm{m}$

Min. (0.025, 249$^{\mathrm{o}}$)

$P/(f_c^{'}A_g) = 0.05$

$L_c/D_c = 13.0$

$h_f/D_p = 2.0$

$E_{s1} = 60\mathrm{MPa}/\mathrm{m}$
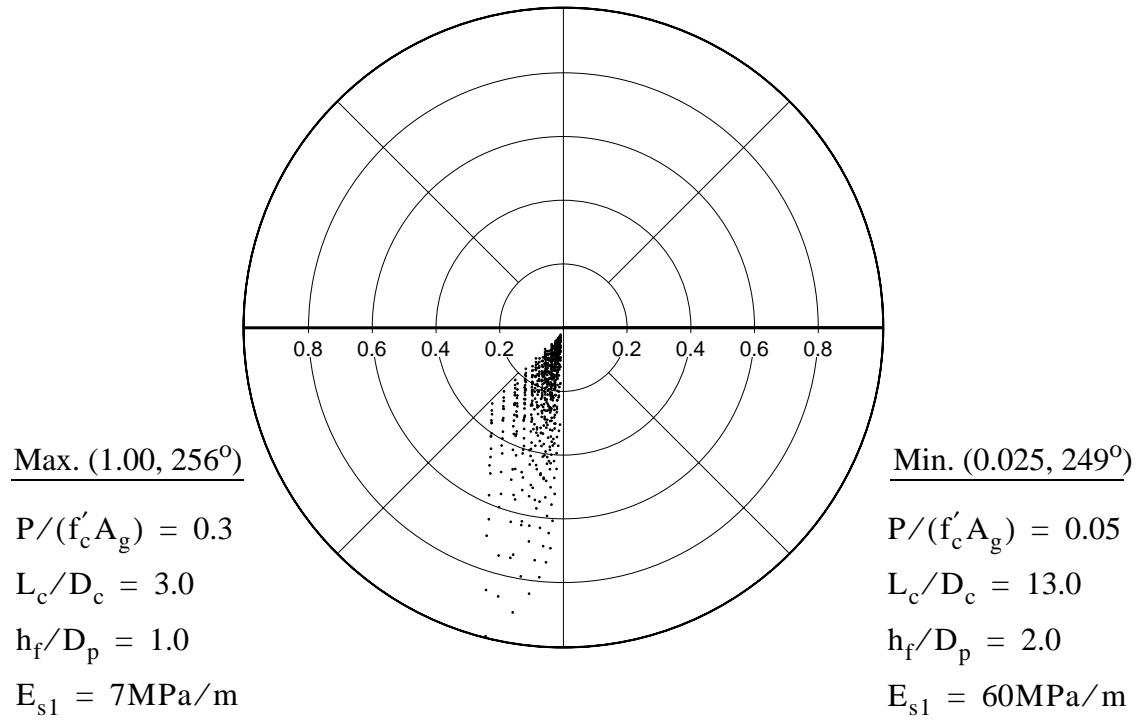
Figure 6.17: Moment and direction at compression pile-pilecap joint
under orthogonal direction loading
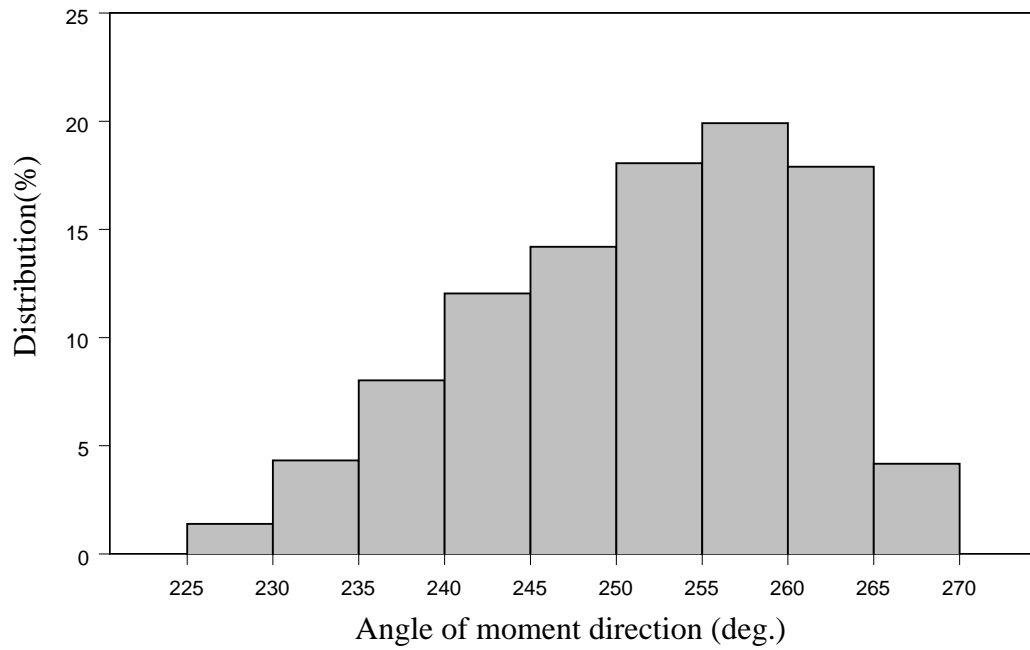
Figure 6.18: Histogram of moment direction

Max. (1.00, 267°)

$P/(f'_c A_g) = 0.3$

$L_c/D_c = 3.0$

$h_f/D_p = 2.0$

$E_{s1} = 7MPa/m$

Min. (0.22, 249°)

$P/(f'_c A_g) = 0.05$

$L_c/D_c = 13.0$

$h_f/D_p = 2.0$

$E_{s1} = 60MPa/m$
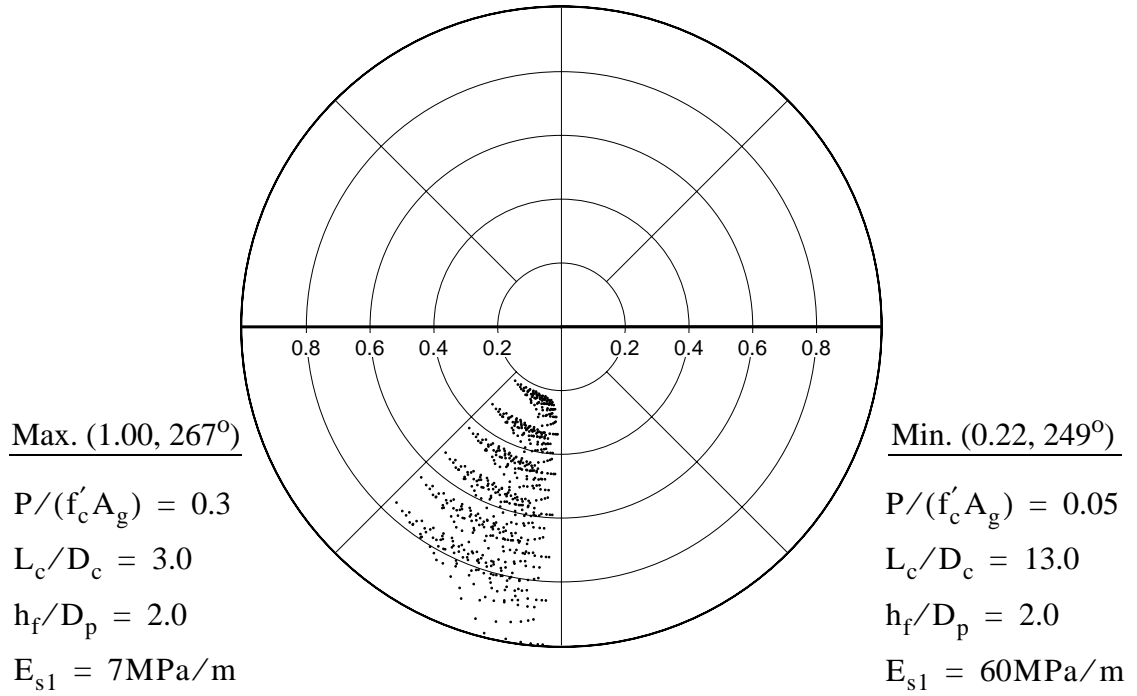
Figure 6.19: Axial force in compression pile under orthogonal direction loading

1) Distribution of data points with respect to principal directions of pile shear

The angles of the compression pile moment directions under orthogonal direction loading are in the range of $227°$ and $268°$ as shown in Figures 6.17 - 6.19. The distribution of the data points along with the angle of moment direction is shown in Figure 6.18. The distribution ratio gradually increases from $227°$ and peaks at 20% in the range of $255° \sim 260°$. The distribution ratio of data points is, then, drastically reduced past peak. The magnitudes of corresponding moments and axial loads, which are normalized by respective maximum values, are also shown.

2) Axial load effect on pile moment

Figure 6.20 shows the ratio of the moments with respect to y-axis, which is obtained by dividing the moment, based on enhanced pile bending stiffness due to axial force in the pile, with the moment based on original bending stiffness. It is seen that the axial load effect on the pile moment is significant. The ratio of the increased shear force due to the axial force effect is from 1.13 to 1.36.

3) Increase of pile moment due to three-dimensional behavior of foundation

The three dimensional geometry which is inherent in the four-CIDH-pile supported foundation system develops pile moment about x-axis. Combined with the y-component which has been previously discussed, the pile is subjected to greater moment than that predicted by two dimensional analysis. The increase of the pile moment due to this behavior can be seen in Figure 6.21. The ratio of moment increase is $1/\sin(\alpha_{cp})$ and the maximum reached to 1.37.

4) Combined effect of axial force and three-dimensional behavior of foundation on pile moment

Total moment increase in the compression pile was compared to the moment obtained via two-dimensional analysis without consideration of axial load effect as shown in Figure 6.22. The ratio 1.13 ~ 1.77 indicates that use of conventional two dimension analysis for the moment-resisting pile foundation underestimates pile moment significantly. Therefore, it is recommended that modified pile bending stiffness, based on axial load in the pile, be used in the analysis of the moment-resisting pile

Max. (1.36, 261°)

$P/(f'_c A_g) = 0.3$

$L_c/D_c = 3$

$h_f/D_p = 2.0$

$E_{s1} = 60 MPa/m$

Min. (1.13, 240°)

$P/(f'_c A_g) = 0.05$

$L_c/D_c = 13$

$h_f/D_p = 1.0$

$E_{s1} = 7 MPa/m$
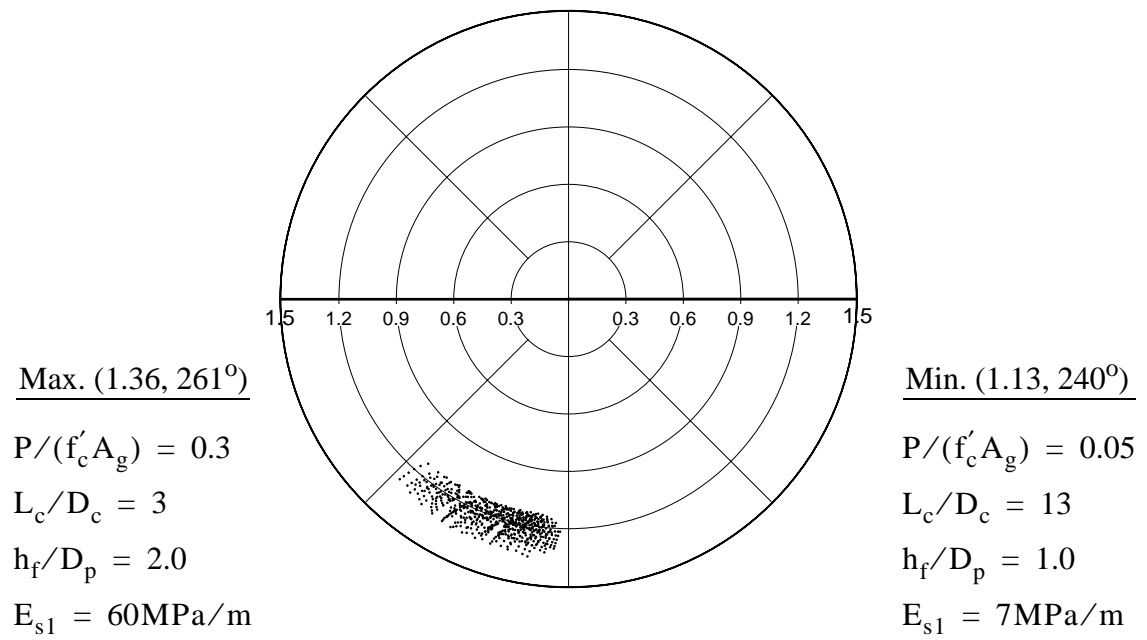
Figure 6.20: Moment increase in compression pile due to axial load
under orthogonal direction loading

Max. (1.37, 227°)   Min. (1.00, 269°)
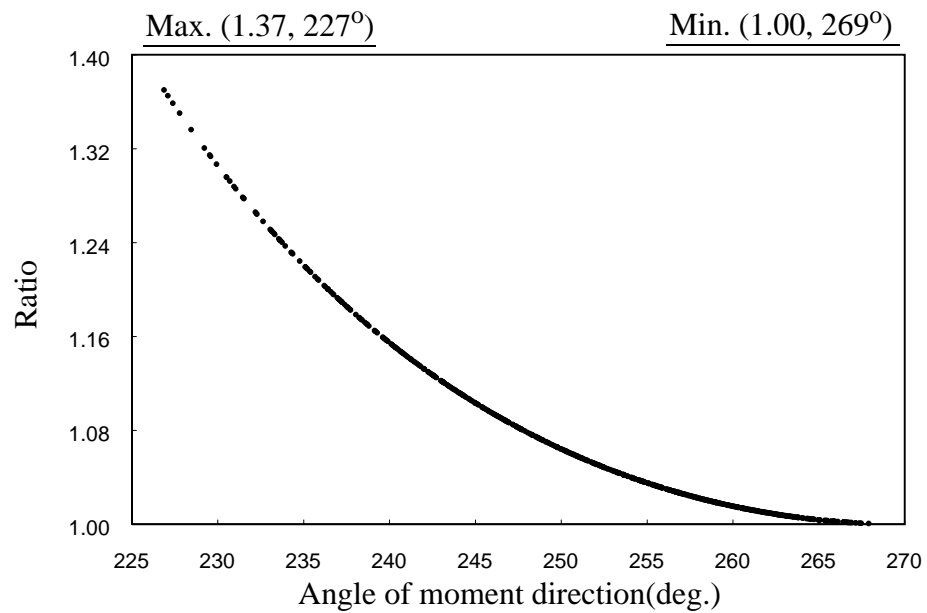
Figure 6.21: Moment increase in compression pile due to the rotations of moment direction
under orthogonal direction loading

Max. $(1.77, 227^{o})$

$P/(f_{c}^{'}A_{g}) = 0.3$
$L_{c}/D_{c} = 13$
$h_{f}/D_{p} = 1.0$
$E_{s1} = 60MPa/m$

Min. $(1.15, 262^{o})$

$P/(f_{c}^{'}A_{g}) = 0.05$
$L_{c}/D_{c} = 13$
$h_{f}/D_{p} = 2.0$
$E_{s1} = 7MPa/m$

1.6   1.2   0.8   0.4   0.4   0.8   1.2   1.6

Min. $(1.15, 262^{o})$

Max. $(1.77, 227^{o})$
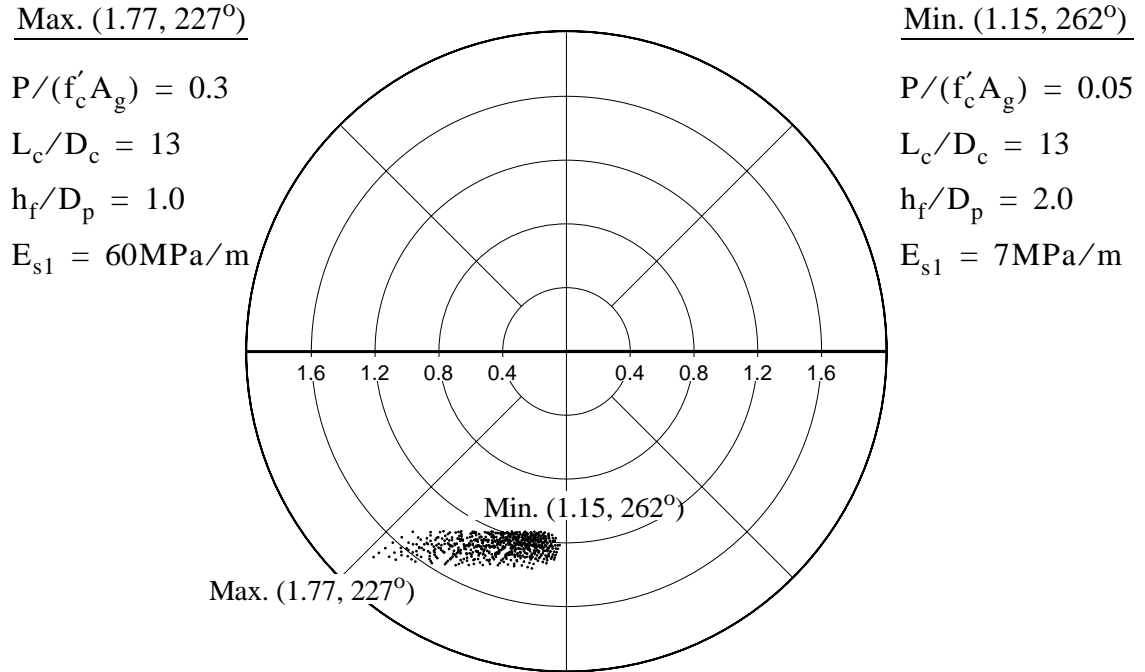
Figure 6.22: Moment increase in compression pile due to combined effect
of axial force and moment directions under orthogonal direction loading

foundation. In addition, three dimensional behavior of the foundation should be considered in the analysis and design.

5) Sensitivity of the moment magnitude and direction vs. variables

The sensitivity of the pile moment for individual varibles are discussed in this section with the 3-D graphical presentations as shown in Figures 6.23 - 6.34. Since the total number of variables are more than two, the maximum number which is required to plot the 3-D graph, two variables are selected in a graph and investigated while the other two variables are fixed at an arbitrary value in their range.

201

- <u>Column length</u> : L_c

The column length impacts the ratio of the moment over the shear force. Besides, the column moment influences the x-component of pile moment as discussed in section 6.1.2, while the column shear force develops only the y-component of pile moment. Accordingly, the increase in the column length makes the weight of the x-component in the pile moment grow. This is noted in Figures 6.23, 6.25 and 6.33 which reveal that the angle of the pile moment direction reduces by increasing the x-component of the pile moment as column length increases. In Figures 6.23, 6.25 and 6.33, it is also shown that the reduction of the angle of moment direction escalates with the decrease of pilecap flexibility and the increases of the soil density and column axial load ratio.

The magnitude of the pile moment decreases with increasing column length as shown in Figures 6.24, 6.26 and 6.34. This is because the shear force of the column decreases as the column length increases, although the column moment, which depends on the column section, remains constant for a given column. The high rate of decrease, observed in the range for short columns, dwindles as column length increases.

- <u>Ratio of pilecap depth and pile diameter</u> : h_f/D_p

The ratio of pilecap depth over pile diameter is a measure of the relative pilecap stiffness over pile stiffness. As briefly mentioned above, it is shown in Figures 6.23, 6.29 and 6.31 that the angle of the pile moment direction reduces as the ratio of pilecap depth over pile diameter decreases. Since the decrease of the angle indicates the reduction of the weight of the y-component in the pile moment, the y-component of the pile moment

reduces as the pilecap becomes more flexible due to the rotation of the pile-pilecap joint for a given lateral loads. This effect intensifies as the column gets longer as shown in Figure 6.23. It is also shown in Figures 6.24, 6.30 and 6.32 that, as the ratio of pilecap depth over pile diameter increases, the magnitude of the pile moment decreases because the relative stiffness of the pile reduces.

- Increased rate of soil elastic modulus with depth : E_{s1}(MPa/m)

Figures 6.25, 6.27 and 6.31 exhibit that the angle of the pile moment direction reduces as soil gets stiffer although the decrease of the angle is not great. The soil property effects the lateral displacement of the pilecap, which cause the y-component of the pile moment, as well as the pilecap rigid body rotation, which lessens the y-component of pile moment. Therefore, the soil effect on the direction of pile moment is not significant because respective influences on the y-component of pile moment work against each other. However, the decrease of the angle of pile moment along with the increase of soil stiffness implies that the effect of the soil property on the lateral displacement of the pilecap is more substantial rather than the influence on the rigid body rotation of the pilecap.

The magnitude of the pile moment also reduces as soil gets stiffer as shown in Figures 6.26, 6.28 and 6.32.

- Axial load ratio : $P/(f_c' A_g)$

Although it is not significant, Figure 6.27, 6.30 and 6.33 show the effect of column axial load ratio on the angle of pile moment direction. The increase in the column gravity

load enhances the capacity of the overstrength moment of plastic hinge and shear force of the column together for a given column length. Since the column moment effects the x-component of pile moment, and the column shear force influences the y-component of pile moment, the angle change of pile moment direction becomes minor by cancelling out the respective influences. In Figures 6.27, 6.30 and 6.33, the angle of pile moment decreases, as column axial load ratio increses. This indicates that the column moment effects the direction of the pile moment more than the column shear force does.

It is obvious that the magnitude of pile moment pile moment increases as column axial load ratio increases as is seen in Figures 6.28, 6.30 and 6.34.

6) Regression analysis of pile moment direction

To investigate the contribution of each variable to pile moment direction, regression analysis was carried out via the Nonlinear Least-Square-Fit method. The relationship between the pile moment direction and each variable is approximated as :

$$\alpha_{cp}^R \ = \ 274 \times \frac{\Gamma^{0.096}}{P^{0.012}H^{0.047}\Sigma^{0.017}} \tag{6.45}$$

where α_{cp}^R is the moment direction of the compression pile under orthogonal direction loading, $\Gamma(=h_f/D_p)$ is the ratio of pilecap depth to pile diameter, P is the column axial load ratio, $H(=L_c/D_c)$ is the nondimensional column length and Σ(MPa/m) is the increasing rate of soil elastic modulus.

It is known from Eq. (6.45) that the ratio of pilecap depth to pile diameter, Γ, has the greatest influence to the pile moment direction since it has the greatest power. Figure

6.35 shows the ratio of the moment direction for each data point, calculated using Eq. (6.45) to the exact solution calculated using Eq. (6.22). From Figure 6.35, it is known that Eq. (6.45) which is the approximated solution yields good agreement with the exact solution. The maximum and minimum errors of the regression analysis were - 2% to + 4%. Further, Eq. (6.45) enables the presentation of the sensitivity of the compression pile moment to the individual variables, which is similar to that described in section 5), in 2-D graphs as shown in Figures 6.36 - 6.39.

Since there is a total of four variables, each variable is selected in a graph while the other three variables are fixed at an arbitrary value in their range.

7) Critical diagonal direction loading

Since the results of the parameter study which are discussed above are only under orthogonal direction loading, the magnitudes of the moment and the axial force of the pile are compared with those under diagonal direction loading. The magnitudes of moments and axial loads, which are normalized by the values under diagonal direction loading, are provided in Figures 6.40 and 6.41, respectively. The range of the ratios for the compression pile moment is from 0.40 to 0.68 and that of axial force is from 0.56 to 0.76. The higher axial load and therefore the higher moment of the compression pile under diagonal direction loading is theoretically explained in Section 6.2.1. Therefore, it is recommended that the pile should be designed under diagonal direction loading. Figures 6.40 and 6.41 also provide important information for the design of the pilecap which is discussed in section 6.2.   .   .
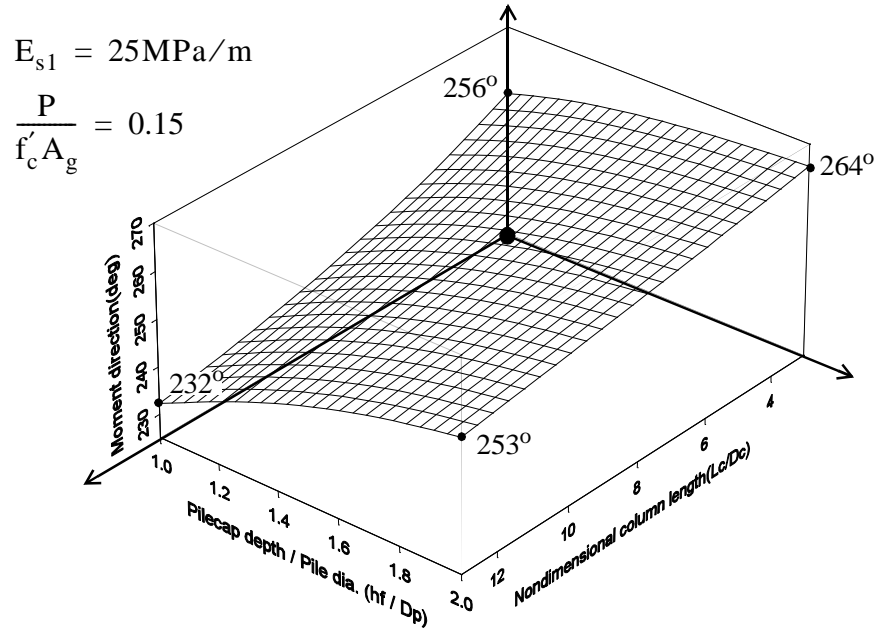
205

Figure 6.23: Moment direction vs. ratio of pilecap depth/pile diameter(h_f/D_p)
and nondimensional column length(L_c/D_c)
for soil Young's modulus(E_{s1})=25MPa/m and column axial load ratio $(P/f_c'A_g) = 0.15$
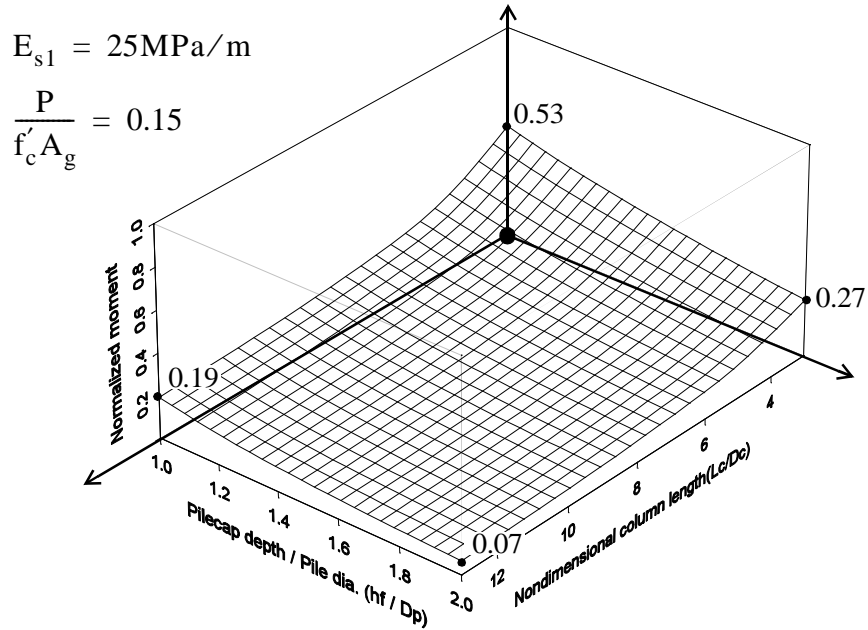

Figure 6.24: Moment magnitude vs. ratio of pilecap depth/pile diameter(h_f/D_p)
and nondimensional column length(L_c/D_c)
for soil Young's modulus(E_{s1})=25MPa/m & column axial load ratio $(P/f_c'A_g) = 0.15$

206

Figure 6.25: Moment direction vs. nondimensional column length(L_c/D_c) and soil Young's modulus(E_{s1}) for column axial load ratio, $P/(f'_c A_g) = 0.15$ and ratio of pilecap depth/pile diameter(h_f/D_p) = 1.4

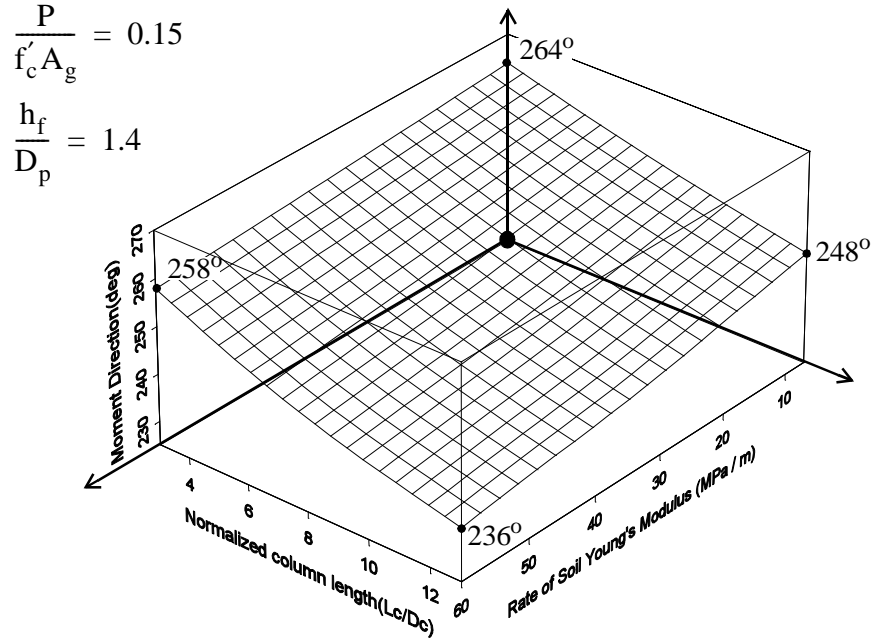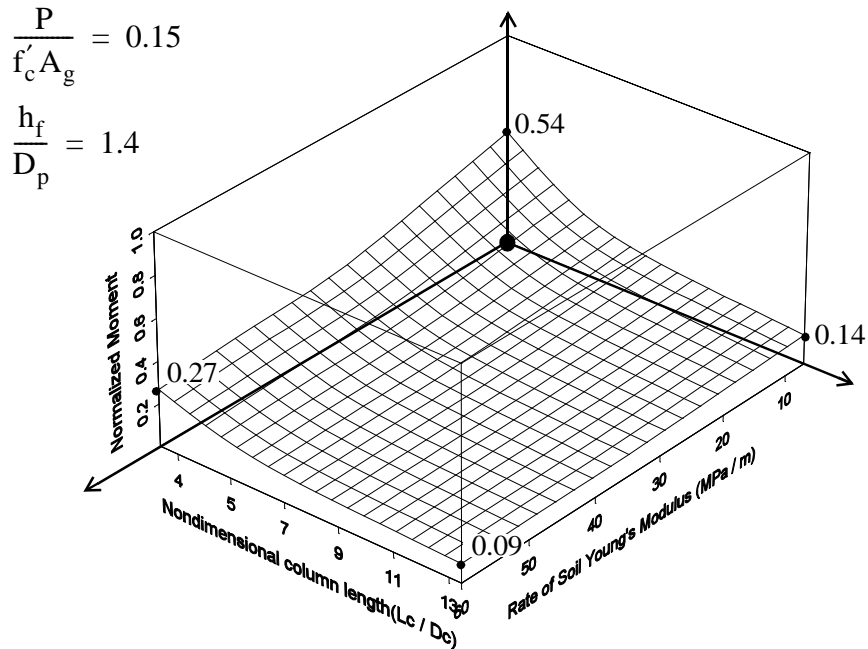Figure 6.26: Moment magnitude vs. nondimensional column length(L_c/D_c) and soil Young's modulus(E_{s1}) for column axial load ratio, $P/(f'_c A_g) = 0.15$ and ratio of pilecap depth/pile diameter(h_f/D_p) = 1.4

Figure 6.27: Moment direction vs. column axial load ratio, $P/(f_c' A_g)$
and soil Young's modulus(E_{s1}) for the ratio of pilecap depth/pile diameter(h_f/D_p) = 1.4
and nondimensional column length(L_c/D_c) = 9
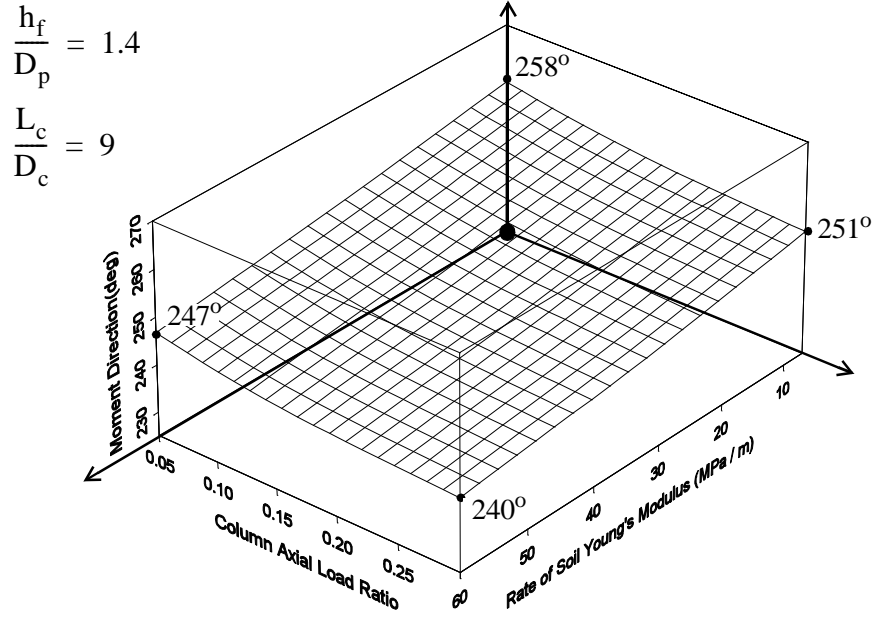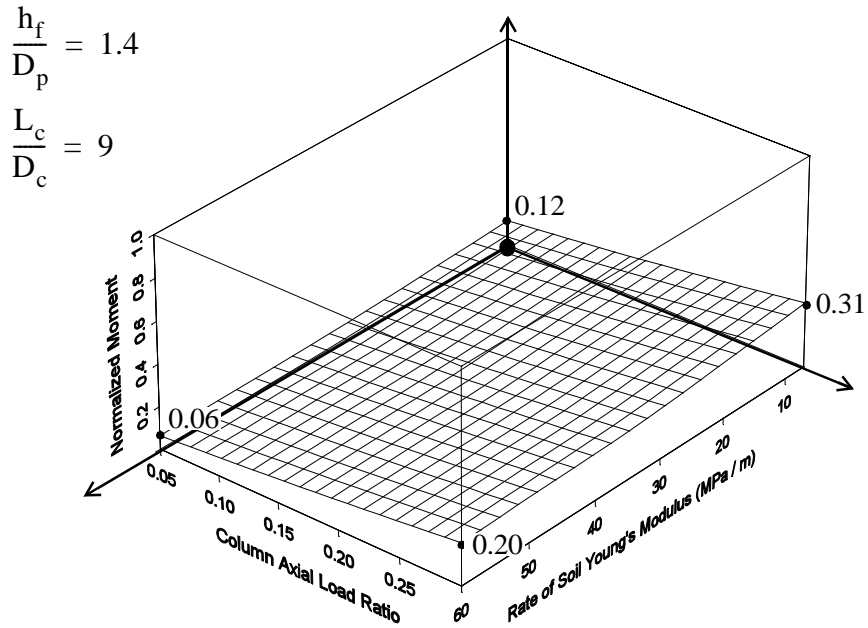

Figure 6.28: Moment magnitude vs. column axial load ratio, $P/(f_c' A_g)$
and soil Young's modulus(E_{s1}) for ratio of pilecap depth/pile diameter(h_f/D_p) = 1.4
and nondimensional column length(L_c/D_c) = 9

Figure 6.29: Moment direction vs. ratio of pilecap depth/pile diameter(h_f/D_p) and column axial load ratio, $P/(f'_c A_g)$ for soil Young's modulus(E_{s1})=25MPa/m and nondimensional column length(L_c/D_c) = 9

Figure 6.30: Moment magnitude vs. ratio of pilecap depth/pile diameter(h_f/D_p) and column axial load ratio, $P/(f'_c A_g)$ for soil Young's modulus(E_{s1})=25MPa/m and nondimensional column length(L_c/D_c) = 9
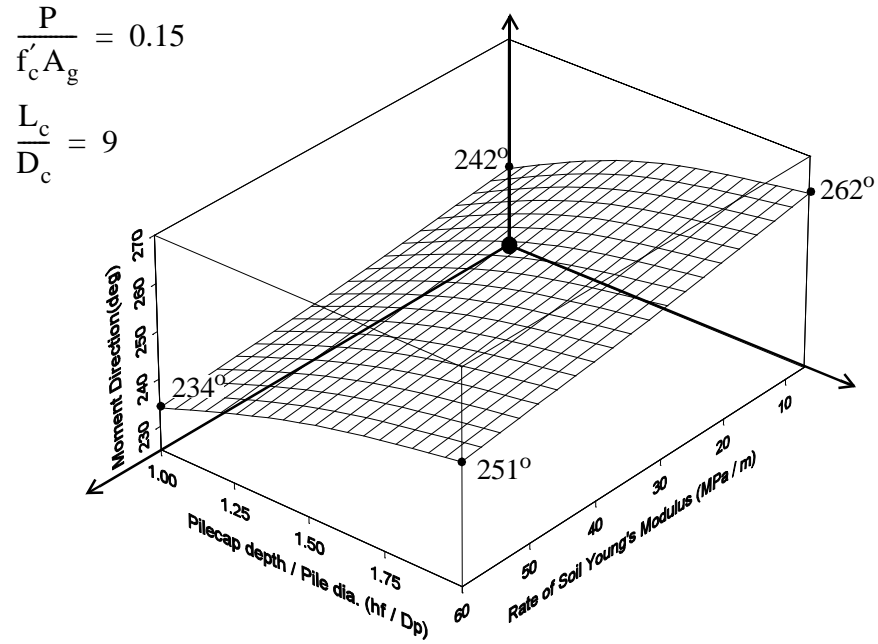
Figure 6.31: Moment direction vs. ratio of pilecap depth/pile diameter(h_f/D_p) and soil Young's modulus(E_{s1}) for column axial load ratio $(P/f'_c A_g) = 0.15$ and nondimensional column length(L_c/D_c) =9
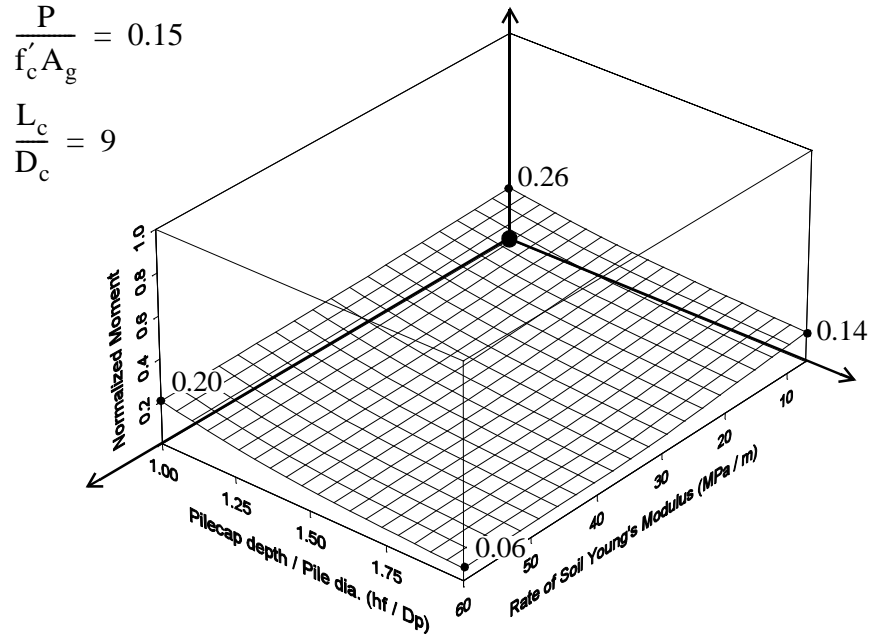
Figure 6.32: Moment magnitude vs. ratio of pilecap depth/pile diameter(h_f/D_p) and soil Young's modulus(E_{s1}) for column axial load ratio $(P/f'_c A_g) = 0.15$ and nondimensional column length(L_c/D_c) =9

$E_{s1} = 25MPa/m$

$\dfrac{h_f}{D_p} = 1.4$
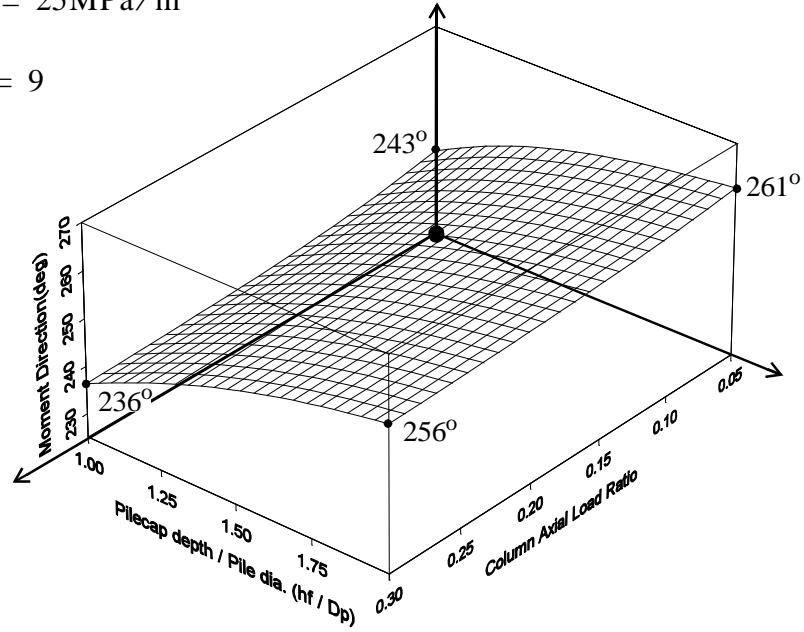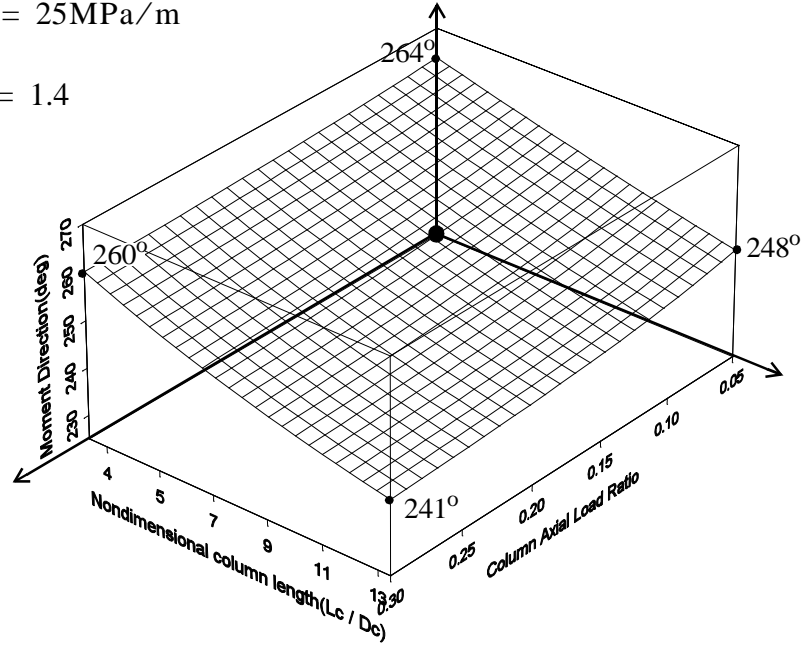
Figure 6.33: Moment direction vs. nondimensional column length(L_c/D_c) and column axial load ratio $(P/f'_c A_g)$ for soil Young's modulus(E_{s1}) = 25MPa/m and ratio of pilecap depth/pile diameter(h_f/D_p) = 9

$E_{s1} = 25MPa/m$

$\dfrac{h_f}{D_p} = 1.4$
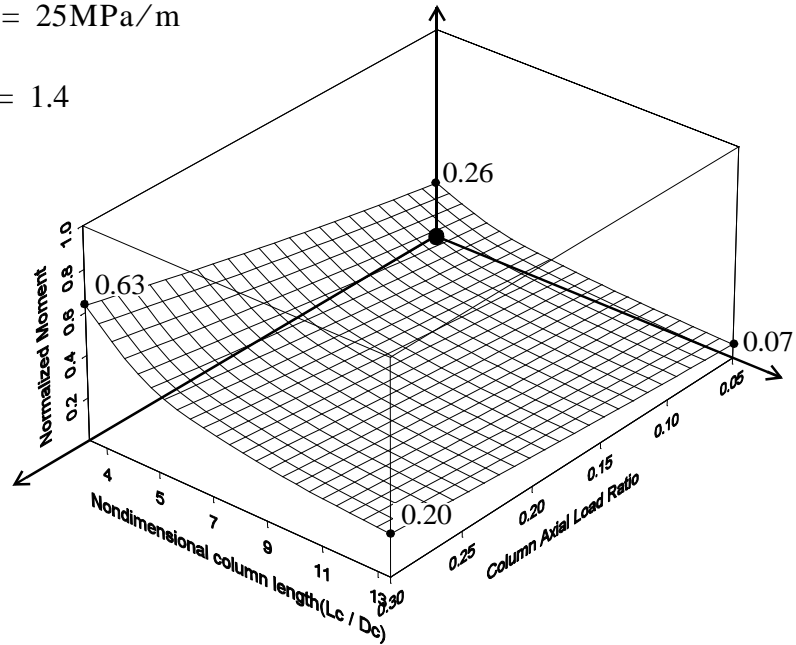
Figure 6.34: Moment magnitude vs. nondimensional column length(L_c/D_c) and column axial load ratio $(P/f'_c A_g)$ for soil Young's modulus(E_{s1}) = 25MPa/m and ratio of pilecap depth/pile diameter(h_f/D_p) = 9
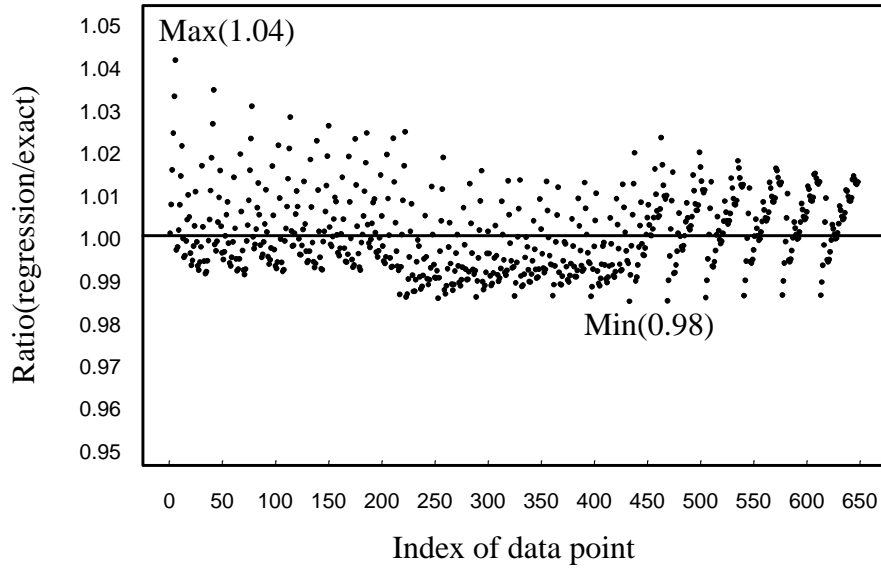
Figure 6.35: Ratio of the moment directions(regression solution/ exact solution)

$$L_c/D_c = 9, E_{s1} = 25(MPa/m), P/(f_c'A_g) = 0.15$$
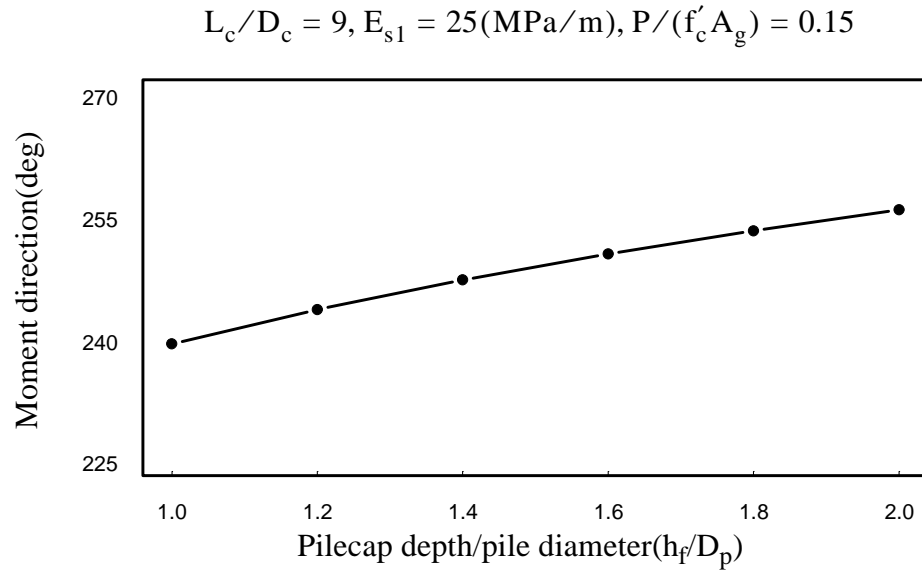
Figure 6.36: Moment direction vs. ratio of pilecap depth/pile diameter(h_f/D_p)
for nondimensional column length(L_c/D_c)=9,
soil Young's modulus(E_{s1})=25MPa/m and column axial load ratio $(P/f_c'A_g) = 0.15$

$$h_f/D_p = 1.4, E_{s1} = 25(MPa/m), P/(f'_c A_g) = 0.15$$
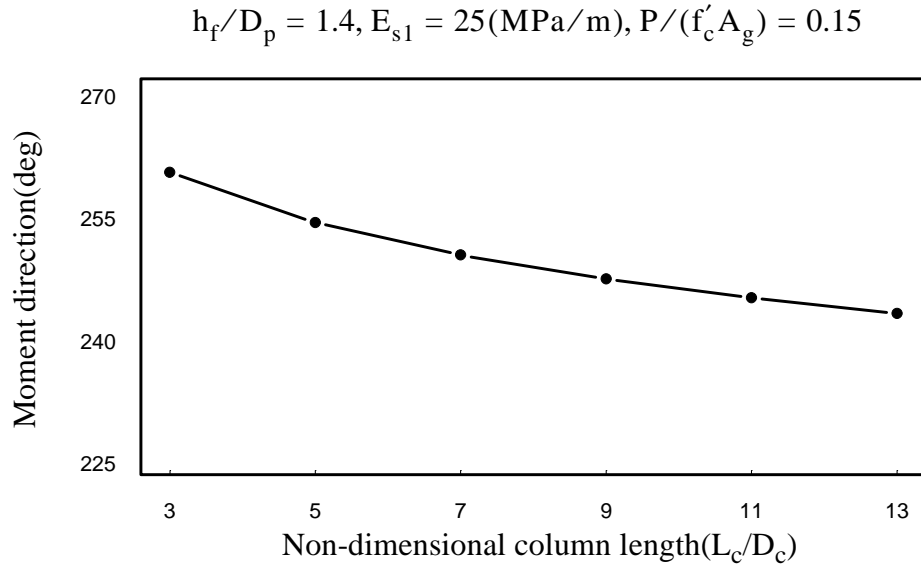
Figure 6.37: Moment direction vs. non-dimensional column length(L_c/D_c) for the ratio of pilecap depth/pile diameter(h_f/D_p)=1.4, soil Young's modulus(E_{s1})=25MPa/m and column axial load ratio $(P/f'_c A_g) = 0.15$

$$L_c/D_c = 9, E_{s1} = 25(MPa/m), h_f/D_p = 1.4$$
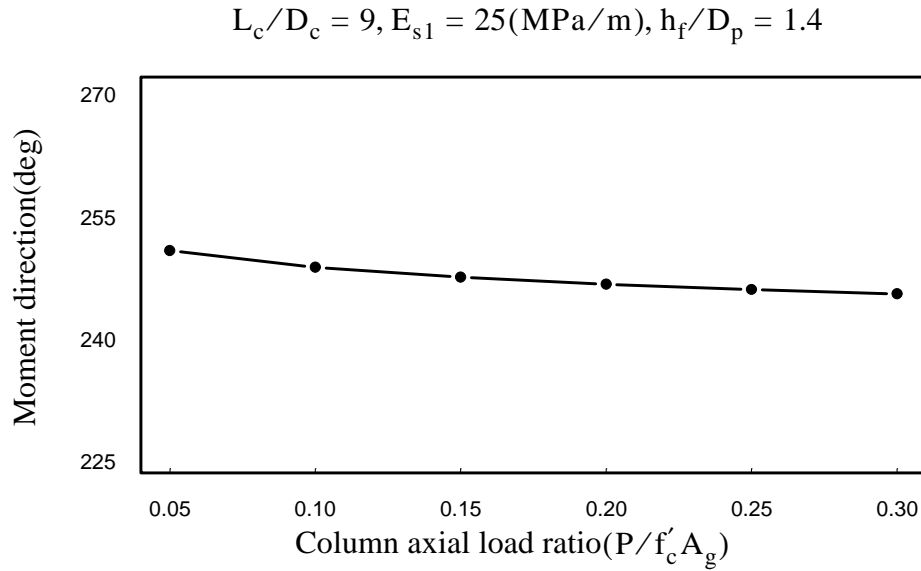
Figure 6.38: Moment direction vs. column axial load ratio $(P/f'_c A_g)$ for nondimensional column length(L_c/D_c)=9, soil Young's modulus(E_{s1})=25MPa/m and ratio of pilecap depth/pile diameter(h_f/D_p)=1.4

$$L_c/D_c = 9, \ h_f/D_p = 1.4, \ P/(f'_c A_g) = 0.15$$
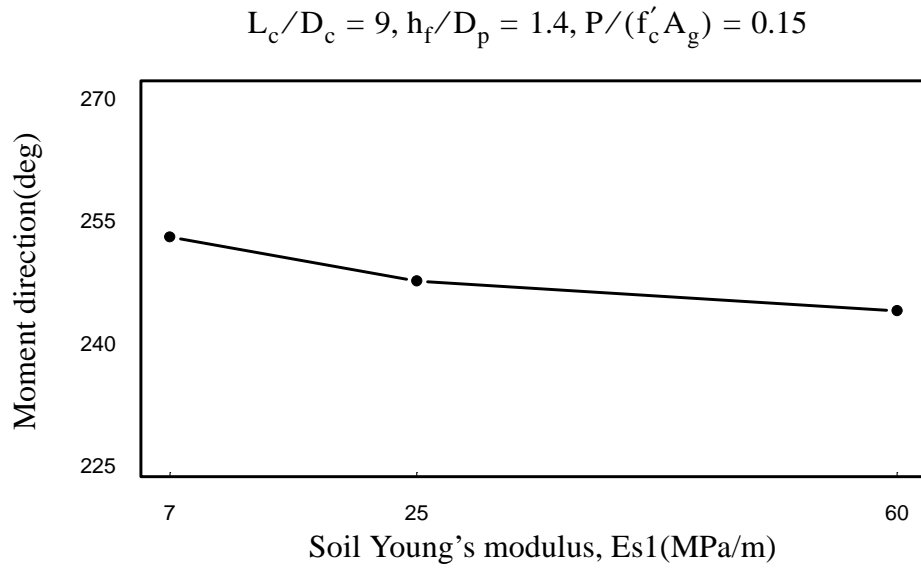
Figure 6.39: Moment direction vs. soil Young's modulus(E_{s1})
for the ratio of pilecap depth/pile diameter(h_f/D_p) =1.4,
nondimensional column length(L_c/D_c)=9 and column axial load ratio $(P/f'_c A_g) = 0.15$

Max. (0.68, 227°)

$P/(f'_c A_g) = 0.3$
$L_c/D_c = 13$
$h_f/D_p = 1.0$
$E_{s1} = 60MPa/M$
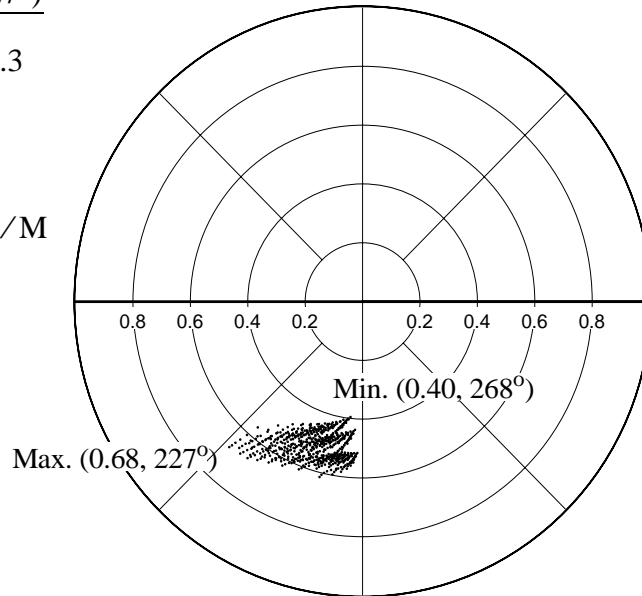
Min. (0.40, 268°)

$P/(f'_c A_g) = 0.05$
$L_c/D_c = 3$
$h_f/D_p = 2.0$
$E_{s1} = 60MPa/M$

Figure 6.40: Compression pile moments under orthogonal direction loading

Max. (0.76, 227°)

$P/(f'_c A_c) = 0.3$
$L_c/D_c = 13$
$h_f/D_p = 1.0$
$E_{s1} = 60MPa/M$

Min. (0.56, 268°)

$P/(f'_c A_c) = 0.05$
$L_c/D_c = 3$
$h_f/D_p = 2.0$
$E_{s1} = 25MPa/M$

0.8 0.6 0.4 0.2   0.2 0.4 0.6 0.8

Min. (0.56, 268°)

Max. (0.76, 227°)
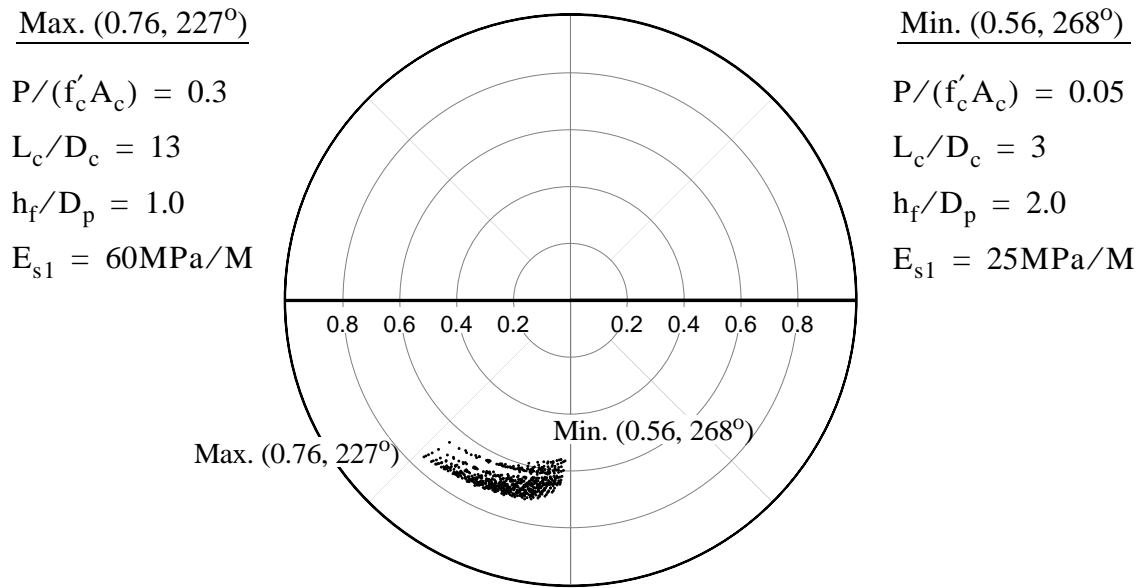
Figure 6.41: Compression pile axial loads under orthogonal direction loading

8) Different consequences of axial load effects on the pile moment and shear

The presence of axial force in the pile changes the bending stiffness and the capacity of the pile. As a result, the moment the pile attracts is proportional to the pile bending stiffness. Thus, the ratio of the demand over capacity of pile moment remains constant regardless of an axial load in the pile. This indicates that the flexural design of the pile can be done based on the average pile shear force which is distributed evenly among piles.

However, as the pile moment increases due to the axial force effect in the pile, the shear force of the pile also increases. Because the axial force in the pile contributes only to the part of the pile shear strength as shown in Section 3.5.1, the increase of shear force demand is greater than the increase in shear strength. Therefore, it is recommended that

the shear design of the pile should be done for the increased shear force demand due to axial force effect.

6.2 Pilecap

6.2.1 Critical diagonal loading direction for the flexural design of pilecap

The maximum pilecap negative moment is calculated by extrapolating the compression pile moment up to the centerline of the pilecap. And the maximum pilecap positive moment is determined by the axial force in the compression pile and the negative moment of the pilecap. The results, shown in Figures 6.40 and 6.41, indicate that the critical loading direction for the pilecap flexural design is diagonal which produces higher axial force and moment in the compression pile. The logic for this results can be explained as follows.

The lateral force applied in the orthogonal direction is resisted by two pairs of diagonally aligned piles as shown in Figure 6.42. In this force transfer mechanism the induced axial force in the compression pile will be $1/\sqrt{2}$ times smaller than that of diagonal direction loading since the shear force taken by pile groups are same. If $C_{P,D}$ and $C_{P,N}$ are defined as the axial forces, under diagonal and orthogonal direction loadings, respectively, :

$$C_{P,D} = \frac{P}{4} + \frac{M_c^\circ + (1-\zeta)F_c^\circ L_p}{\sqrt{2}L_f} \tag{6.46}$$

$$C_{P,N} = \frac{P}{4} + \frac{M_c^\circ + (1-\zeta)F_c^\circ L_p}{2L_f} \tag{6.47}$$

(a) Diagonal direction loading   (b) Orthogonal direction loading
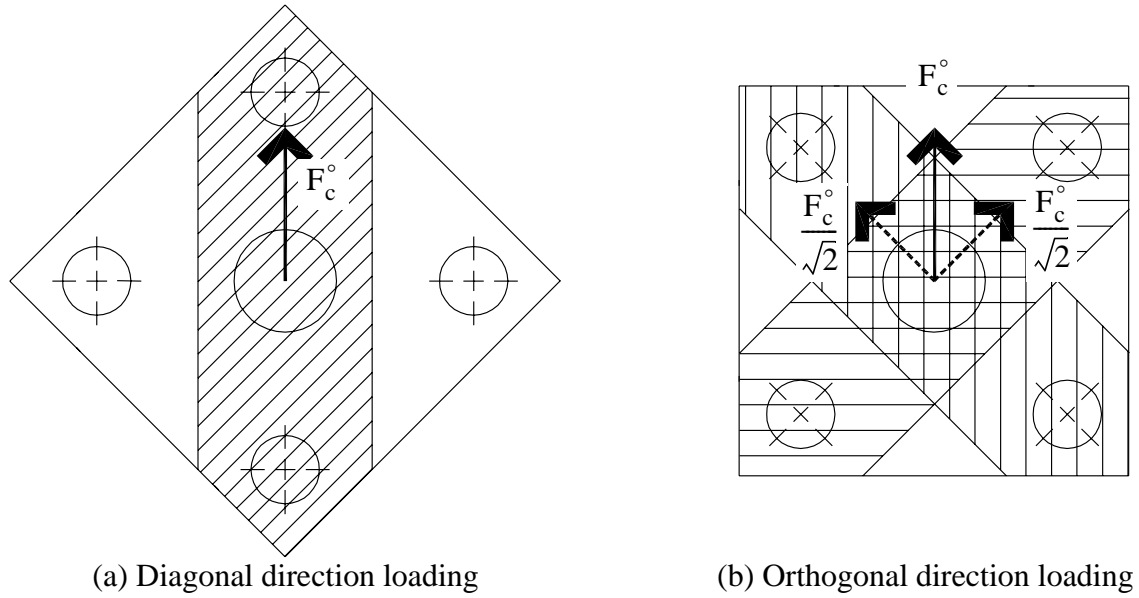
Figure 6.42: Lateral force resisting mechanism of 4-CIDH pile supported foundation

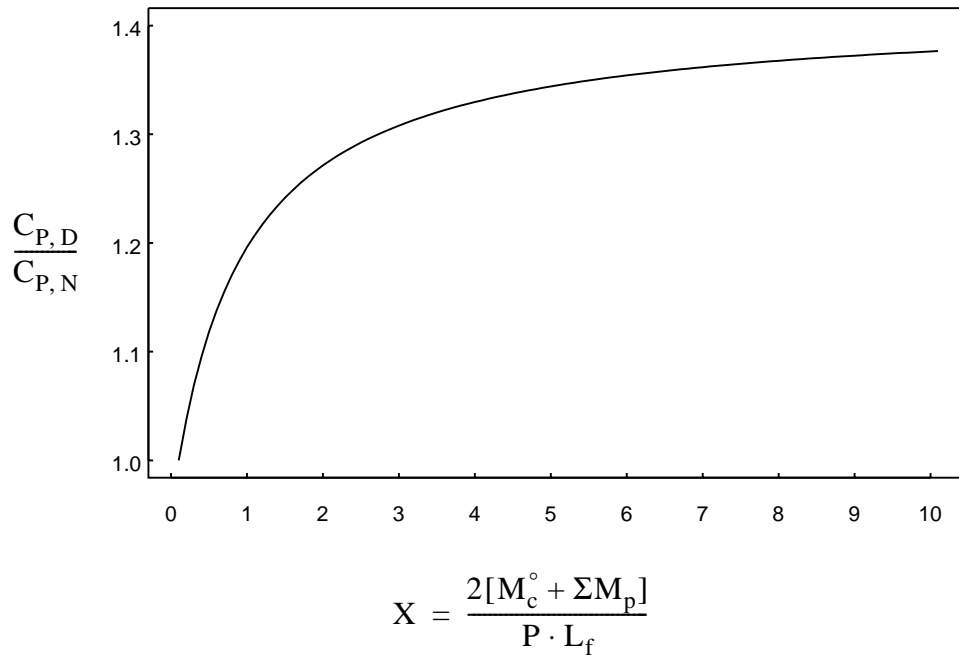

$$X = \frac{2[M_c^{\circ} + \Sigma M_p]}{P \cdot L_f}$$

Figure 6.43: Ratio of the pilecap positive moment demands
between diagonal and orthogonal direction loadings

where P is the gravity load, M_c° and F_c° are the column overstrength moment and shear, respectively, L_f is the distance between the piles in the orthogonal direction and L_p is the pile length from the pilecap to the contraflexure point in the pile. The ratio of $C_{P,D}/C_{P,N}$ indicates the increased demand of pilecap positive bending moment, which develops by the pile axial load, under diagonal direction loading and simply quantified as :

$$\frac{C_{P,D}}{C_{P,N}} = \frac{1 + \sqrt{2}X}{1 + X} \tag{6.48}$$

where X is a constant expressed as :

$$X = \frac{2[M_c^{\circ} + \Sigma M_p]}{P \cdot L_f} \tag{6.49}$$

and plotted in Figure 6.43.

Eqs. (6.48), (6.49) and Figure 6.43 shows that the ratio, $C_{P,D}/C_{P,N}$ approches assymptotically to $\sqrt{2}$ as X increases. This ultimate value means the loading condition without gravity load since the larger X represents the more dominance of the lateral forces over the gravity load.

Because the axial force in the compression pile governs the pilecap positive moment, the critical loading direction for the pilecap positive moment is diagonal.

6.2.2 Design moment for pilecap positive bending

In designing the pilecap of CFPS1, the moment of the pilecap, M_A, which is at the column face, was taken as the design moment for the pilecap positive bending, as shown in Figure 6.44. This is common practice in current designs. However, the induced

(a) Large moment gradient
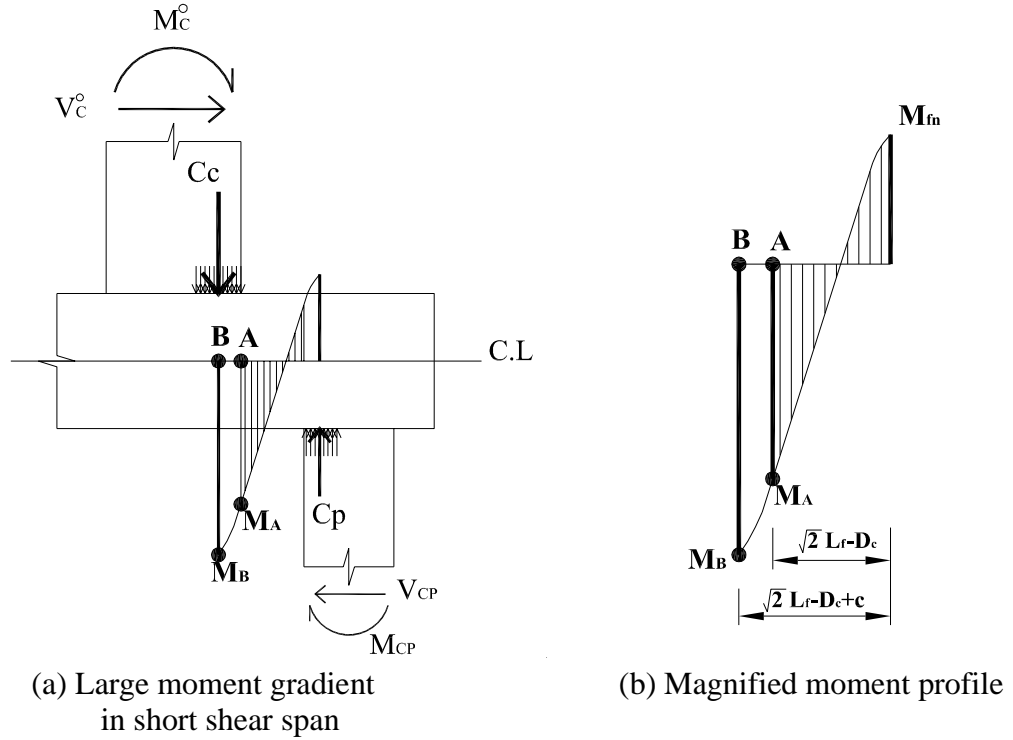in short shear span

(b) Magnified moment profile

Figure 6.44: Moment profile between compression pile and column

positive moment of the pilecap continues to increase beyond point A to M_B at point B

which is the point of column compressive stress resultant C_c. The difference between M_A

and M_B is significant when the shear span is short and the moment gradient is large. This

means that the moment, M_A, which was taken at column face underestimates the design

positive bending moment. Unit CFPS1 suffered pilecap positive moment failure, at least

partly due to this effect, while unit CFPS2, which was designed for the higher moment

M_B, had only minor damage to the soffit of the pilecap.

6.3 Pile - pilecap joint

The pile-pilecap joint was designed following the design recommendations for Knee joints of bridge bent as described in Appendix B. During the test the pile-pilecap joint regions showed no damage. The behavior of pile-pilecap joint is investigated and the characteristics of pile - pilecap joint are discussed in this section.

6.3.1 Different joint shear demand between compression and tension piles

In designing Knee joints in a bridge multi-column bent using an explicit joint shear force transfer mechanism, the joint shear force demand is determined based on the overstrength moment of the bridge column in accordance with the capacity design philosopy. The overstrength moments of the bridge column between opening and closing moment depends on the column axial force as discussed in section 6.1.1. This is also true for the piles. However, the effect of axial force to the overstrength moment may be more pronounced with a pile foundation. This indicates that the difference of the shear force demand of pile-pilecap joint is much more significant between the closing and opening moment than that between bridge tension and compression columns. The joint behavior for the opening and the closing moments are discussed in following sections.

6.3.2 Joint behavior for opening moment

When the pile-pilecap joint is subjected to opening moment, the pile is generally under large axial tension force and therefore small moment. In this condition the whole section of the pile tends to be under tension. If the whole section of a pile is subjected to tension, the joint transfer mechanism of Knee joint of bridge multi-column bent is no longer valid due to the lack of compression block in the pile section. In addition to the

strain profiles presented in Section 4.8, this can also be explained from that closing of the cracks developed outer face of piles was not observed and the crushing of the pile concrete occurred only on inner face of piles during the test. However, it is believed that the anchorage failure which may be possible due to high tension force will not occur since there is a large amount of pilecap bottom transverse reinforcement in two way direction, clamping the splitting cracks developing in the concrete around the reinforcement. For this situation the sleeving failure mode seems more likely and anchorage length in confined condition given in Eq. (6.50)[26] may be adopted.

$$l_{dc} = \frac{0.3d_b f_{ye}}{\sqrt{f_c'}} \tag{6.50}$$

6.3.3 Joint behavior for closing moment

The pile-pilecap joint is subjected to larger shear force demand under closing moment as discussed in Section 6.3.1. However, it is believed that the amount of pilecap top and bottom transverse reinforcement is enough to provide adquate confinement to the longitudinal reinforcement of the pile as long as they are in the form of continuous U-bars, or T-headed bars by the force transfer mechanism shown in Figure B.6. The reason is that the amount of the reinforcement in the pile is still much smaller than that in the pilecap. Therefore, only minimum spiral given in Eq. (6.51)[26] is sufficient for the joint reinforcement for closing moment.

$$\rho_{s, min} = \frac{0.29 \sqrt{f_c'}}{f_{yh}} \tag{6.51}$$

Chapter 7: Conclusions and Recommendations

7.1 Overview

The seismic behavior of four-CIDH-pile-supported-footings is the focus of the investigation. In this foundation system the piles are connected to the pilecap through moment resisting joints, similar to T and knee joints in bridge multi-column bents.

Linear and nonlinear analyses on the soil-structure interaction were performed for the 2-D skeletal frame of four-CIDH-pile supported footings. The soil was modeled as an array of uncoupled spring elements. During the nonlinear analyses, the tangential flexural stiffnesses, which were obtained from the moment-curvature curves, were updated at each load increment recognizing the coupling of the flexural stiffness and axial load. Futhermore, the nonlinear behavior of the soil was also accounted for in the analysis. The study was carried out for five different soil properties and three different column heights.

Following the analytical work on the axial force effect on pile shear distribution, two large-scale 3-D test units, which consisted of a cantilevered column, a pilecap and four piles, were designed and tested under multi-directional simulated seismic loading. The first test unit, CFPS1, was designed with conventional reinforcement while the second unit, CFPS2, contained headed reinforcement. When designing the test units, a state-of-the-art design procedures were used. For the pile to pilecap joint design, the external strut

joint mechanism was used to improve the joint performance and to reduce the requirement of joint reinforcement.

The seismic performance of the test units was satisfactory. However, the pilecap of Unit CFPS1 suffered severe damage at the end of the test as a result of unexpectedly high strains developed in the bottom reinforcement. This damage was investigated immediately and the findings were considered in the design of Unit CFPS2. No significant damage occurred to Unit CFPS2.

Since it was found from the experimental work that the three dimensional geometry of the foundation system influences the shear direction of elastic pile, a parameter study was done to investigate the combined effect of axial force in the piles and resistance direction of the piles. For the parameter study, a simplified model similar to the test units was used. Four distinctive parameters were used, which are representatives of gravity load, column length, soil property and the relative stiffness of pile.

Lastly, the conclusions of the research, and the recommendations for the seismic design of 4-CIDH-pile-supported-foundation, are presented.

7.2 Conclusions

Referring the design method adopted for the test units, the following conclusions have been drawn from the experimental study and the analytical works which investigate the combined effect of axial force and moment direction of piles.

7.2.1 Experimental Investigation

1) The pile/pilecap joints, which were designed using the external strut shear force transfer mechanism, exhibited satisfactory performance when subjected to simulated seismic loading. However, the column/pilecap joint of Unit CFPS1 experienced spalling of the pilecap cover concrete at several J-stirrup locations, indicating straightening of the 90° hooks. Unit CFPS2, which used headed bars for the shear stirrups, showed no damage during the test.

2) The piles showed unsymmetric cyclic behavior during the test. The inner bar of pile, which was located closer to the column, was subjected to both tension and compression. However, the outer bar was only in tension.

3) The principal direction of elastic pile resistance was at an angle to the applied lateral force under orthogonal direction loading. This findings has a notable effect in the design of four-CIDH-pile supported footing system.

4) It was found that the piles in compression attracted greater shear force than tension piles. The compression pile shear force component in the loading direction was much greater than that of tension pile. It is noted that the current analysis procedures, in which the piles are modeled with a unique flexural stiffness value, can greatly underestimate the pile design shear force.

5) The maximum strain of pilecap bottom reinforcement occurred beyond the column face and inside the column in horizontal plan due to the large moment gradient in the short shear span between the column and pile. This should be considered in design.

6) Although the lateral load is applied in the orthogonal direction, the pilecap bottom reinforcement in diagonal direction suffered higher strain than the reinforcement in orthogonal direction.

7) The performance of CFPS2 using headed reinforcement was satisfactory. No damage occurred to the pilecap and joints of CFPS2. Normal minimum embedment length were satisfied in the test using headed rebars.

7.2.2 Analytical study

Finite element analysis of 2-D skeletal frame of 4-CIDH-pile-supported-footing

1) Linear analysis, which is based on the same stiffness for tension and compression piles, yields almost the same moment and shear force in the tension and compression piles.

2) significant differences in the moments and shear forces between tension and compression piles were observed in the nonlinear analysis that used tangential stiffness of pile moment-curvature curve.

3) The decrease of the pile moment and shear force, due to the passive soil pressure on the pilecap, is significant when compared to the cases without pilecap restraint.

4) The reduction of the pile top moments with increasing soil stiffness is highly nonlinear decreasing slope as the soil becomes stiffer.

5) The influence of soil property on pile moment is greater at the top of piles than in ground.

225

6) The maximum inground moment develops at shallower depth as soil gets stiffer and accordingly, the inflection point of the pile also becomes shallower. Particularly, for the piles embedded in stiffer soil, the reversal of pile moment direction occurs.

7) The shear force of the pile is not as sensitive to the soil property as pile moment.

8) The shear force of the piles, without pilecap restraint, are almost constant regardless of soil property.

9) The pile moment and shear force reduce as column length increases.

Parameter study for combined effect of axial force and pile resistance direction under orthogonal direction loading.

1) The direction of pile shear force is not parallel to the direction of applied lateral force under orthogonal direction loading, due to three dimensional behavior of of 4-CIDH pile supported foundation. This behavior exists inherently in the footing system, particularly, if the piles remain elastic. In 2-D frame analysis, three dimensional behavior can not be captured since the forces and the deformations are in plane.

2) The angle of principal pile moment direction to the direction of applied shear force reduces as column length increases.

3) The angle of principal pile moment direction to the direction of applied shear force reduces as soil becomes stiffer.

4) Maximum and minimum axial load and moment in the piles occur under diagonal direction loading.

5) The presence of axial force in the pile changes the bending stiffness which attract the moment proportionately. Thus, the ratio of the demand over capacity of pile moment remains essentially constant regardless of axial load in the pile.

6) The demand of the pilecap moment under loading the diagonal direction is always greater than in the orthogonal direction.

7) The maximum positive and negative pilecap moments occur at the compressive stress resultants of column and of compression pile at a given loading condition. While this finding has a negligible impact in most structural design, it has an appreciable effect in the design of members with steep moment gradient such as pilecaps.

8) The pile-pilecap joint shear demand for the closing moment is always greater than that for the opening moment due to the greater pile moment resulting from axial load effect.

7.3 Design Recommendations

7.3.1 Pilecap design

1) The pilecap design moments should be determined at the points of the resultant of column and pile compression forces, not at the column or pile faces as is the current design practice.

2) The design moment for the positive bending of the pilecap should be estimated for the diagonal direction loading.

3) The required reinforcement should be placed within the effective width of the pilecap, D_c+2d_f. The full width of the footing should not be relied upon for the maximum pilecap moment capacity due to the lag of reinforcement mobilization.

4) Design of pilecap should be carried out using the typical strength reduction factor $\phi_f = 0.9$ in order that pilecap longitudinal reinforcement does not develop stresses beyond yield point according to the capacity design principle.

7.3.2 Pile design

1) To estimate the shear demand of piles, maximum axial force induced in the piles should be considered.

2) If the pile compression force is less than that of the balance point, design of piles in bending may be carried out based on the average moment of piles regardless of pile axial load level. The reason for this is that axial load developed in a pile changes the demand and capacity of pile bending in same ratio.

3) To avoid undesirable shear failure in the piles, the shear reinforcement should be designed using the three component shear model[26] as discussed in section 3.5.1-(d).

4) Although, the piles are designed to remain elastic in accordance with the capacity design philosophy in current practice, the plastic hinge region of CIDH piles should be designed with adequate confinement amounting to Eq. (7.6) to ensure sufficient curvature ductility capacity of piles, particularly if pilecap passive pressure is not utilized in the design.

5) A minimum transverse reinforcement ratio, amounting to Eq (7.7), is ensured in the plastic hinge regions to prevent premature buckling of the pile longitudinal reinforcement.

7.3.3 Pilecap Joint design

1) In 2-dimensional equivalent portal frame, column/pilecap and pile/pilecap joints are essentially the same as inverted T and knee joints, respectively, with greater effective widths. Therefore, pilecap joints detail can be done based on the method described in Section 3.5.4.

2) Pile-pilecap joint design should be carried for different shear demands for each closing and opening moments since the moment capacity of the piles are different between compression and tension piles due to different axial loads developed in the piles.

3) The force transfer mechanism of Knee joint for opening moment may not be applied for the design of pile/pilecap joint due to the lack of the compressive stress block in pile section at the interface of pile and pilecap.

4) If $p_t \leq 0.29\sqrt{f_c'}$ [MPa], joint shear cracking is not expected to occur and no joint reinforcement is required. Only nominal joint reinforcement satisfying following equation should be provided in the form of hoops.[26]

$$\rho_s = \frac{0.29\sqrt{f_c'}}{f_{yh}} \qquad (7.1)$$

5) If $p_t \geq 0.42\sqrt{f_c'}$ [MPa], a complete force transfer mechanism is required to transmit the joint shear forces.[26] Accordingly, joint should be detailed according to the design procedure described in Appendix B.

7.4 Simplified design procedure for 4-CIDH pile supported footing

Design of 4-CIDH-pile-supported-footing system may be carried out using a simple equivalent portal frame in the diagonal direction. A simplified design procedure is proposed here. The areas covered in the design procedure are :

a) Pilecap flexural and shear design

b) Pile flexural and shear design

c) Pilecap joints design

The design issues regarding the formation of In-Ground plastic hinge are not covered here.

- **Pile flexure and shear design**

Step 1. Obtain the distance to inflection point of pile, L_p, from pilecap, axial forces of piles, T_p and C_p by elastic analysis of equivalent portal frame under diagonal direction loading as shown in Figure 7.1. It is recommended that the pilecap width of $\sqrt{2}B_f$ should be considered for the estimation of the stiffness of passive soil on pilecap, k_s.

Step 2. Design pile section with average axial load, P_{av}, and moment, M_{av}, of piles. Ensure C_p is smaller than P_b which is the axial load at balance point.

(a) Plan view   (b) A-A section of skeletal frame
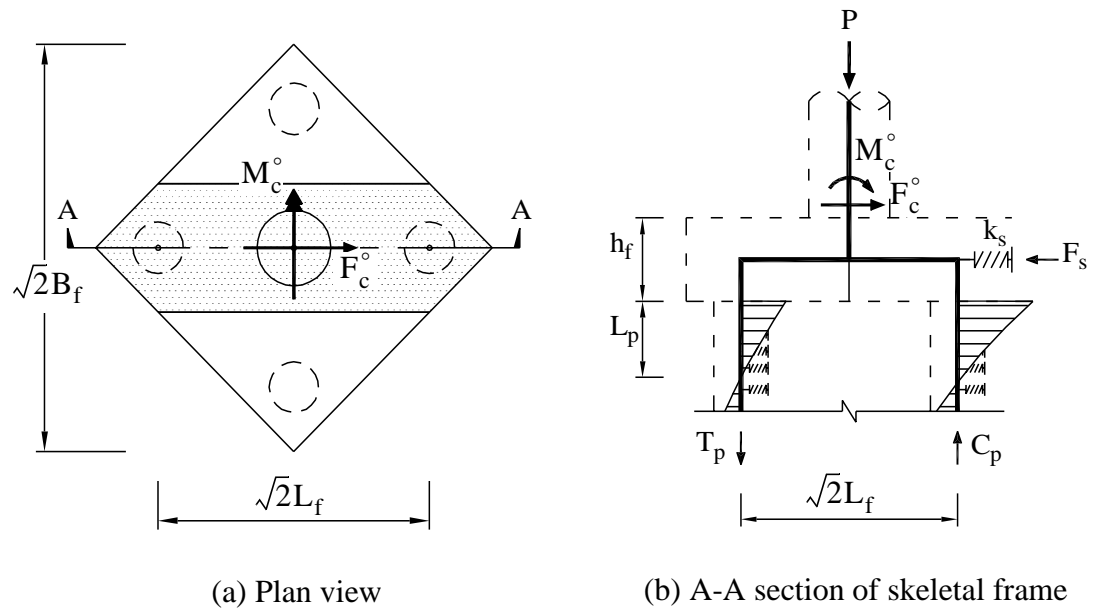
Figure 7.1: Equivalent portal frame under diagonal direction loading
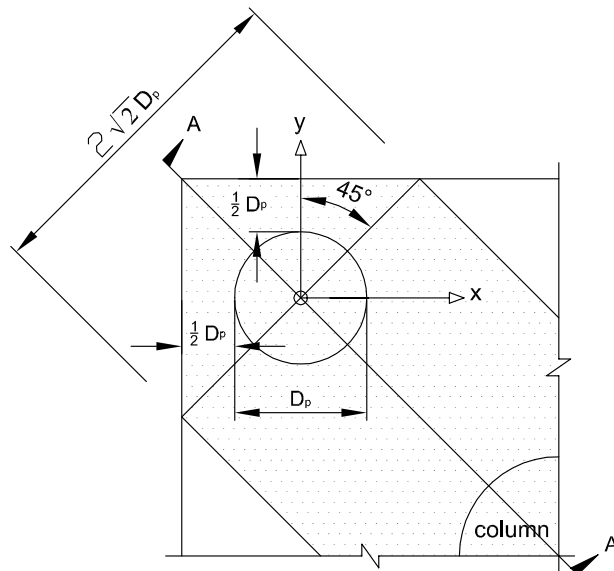
Figure 7.2: Recommended width of equivalent pilecap portal frame

231
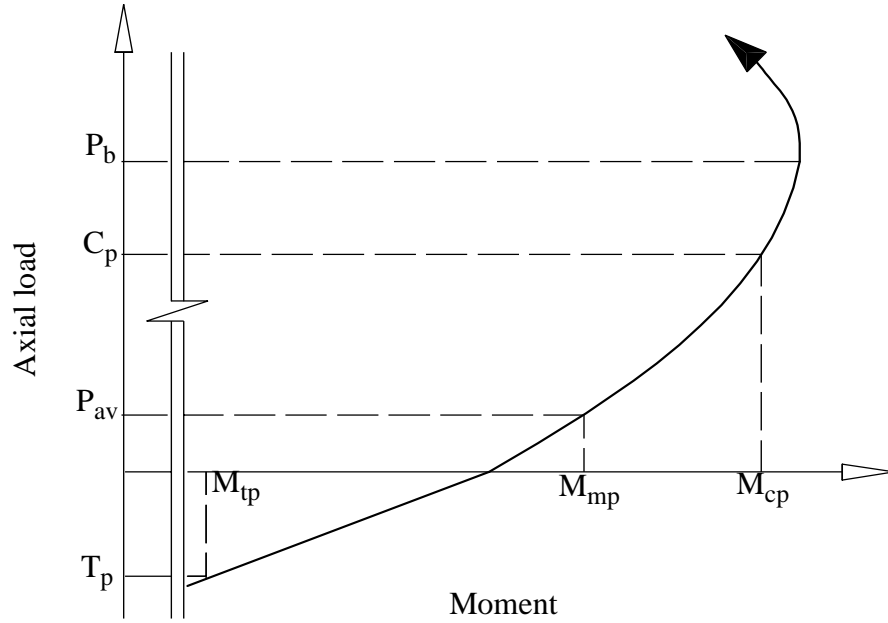
Figure 7.3: Partial M-P curve of pile section

$$P_{av} = \frac{P_G + W_{self}}{4} \tag{7.2}$$

$$M_{av} = \frac{(F_c^\circ - F_s) \cdot L_p}{4} \tag{7.3}$$

Step 3. Obtain the moment of piles, M_{tp}, M_{mp} and M_{cp}, based on the axial forces, T_p, P_{av}

and C_p from the M-P curve of pile section as shown in Figure 7.3.

Step 4. Calculate the shear force of compression pile by distributing the total shear force

of pile group, $(F_c^\circ - F_s)$, to the pile in proportion to M_{cp}.

$$V_{cp} = (F_c^\circ - F_s) \cdot \frac{M_{cp}}{M_{tp} + 2M_{mp} + M_{cp}} \tag{7.4}$$

232

Step 5. Design using the three component shear model[26] as described in Section 3.5.1-

d).

$$V_s = \frac{V_{cp}}{\phi_s} + V_c + V_p = \frac{\pi}{2} \times \frac{A_h f_{yh}(D' - c)}{s} \cot\theta \text{ where, } \theta = 35°$$ (7.5)

Step 6. Ensure that the spiral reinforcement is the greater of :

$$\rho_s = 0.16 \frac{f_{ce}'}{f_{ye}} \left[0.5 + \frac{1.25P}{f_{ce}'A_g} \right] + 0.13(\rho_l - 0.01)$$ (7.6)

and

$$\rho_{s, min} = 0.0002n$$ (7.7)

- **Pilecap flexural design**

Step 7. Calculate the negative moment of pilecap by extrapolating the pile moment up to
the footing centerline.

$$M_{fn} = V_{cp} \cdot (L_p + 0.5h_f)$$ (7.8)

Step 8. Calculate and design the positive moment at the column compressive stress re-
sultant. The following equation is based on the assumption that the shear force
of tension pile is negligible due to large axial force.

$$M_{fp} = C_p \cdot \left(\frac{\sqrt{2}L_f}{2} - \frac{D_c}{3} \right) - \frac{M_{fn}}{\sqrt{2}L_f} \cdot \left(\frac{\sqrt{2}L_f}{2} + \frac{D_c}{3} \right)$$ (7.9)

233

(a) Design actions   (b) Bending moment diagram
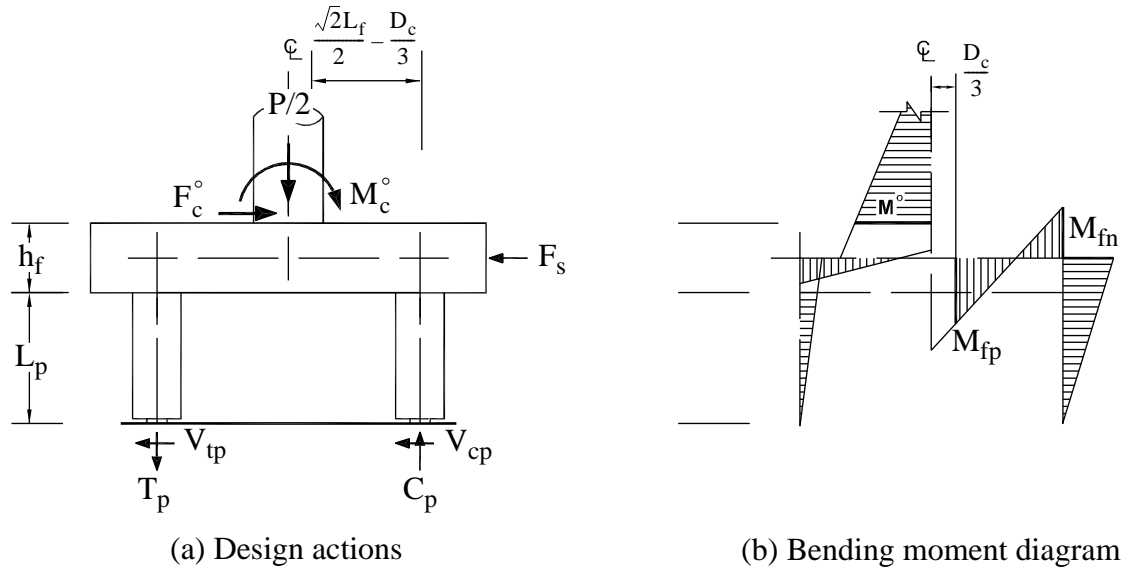
Figure 7.4: Moment diagram of equivalent portal frame

Step 9. Calculate the required pilecap reinforcement. Since the capacity of the pilecap bending within the effective width is same as shown in Figure 7.5, it is recommended that the required reinforcement be placed in two orthogonal directions within effective widths as shown in Figure 7.5-(c), considering construction efficiency and possible inelastic behavior of piles.

$$M_{fN} \geq \frac{M_{fn}}{\phi_f} \text{ for } b_{eff} = 2\sqrt{2}D_p \tag{7.10}$$

$$M_{fP} \geq \frac{M_{fp}}{\phi_f} - (F_c^\circ - F_s) \cdot \left(\frac{h_f - a}{2}\right) \text{ for } b_{eff} = D_c + 2h_f \tag{7.11}$$

234
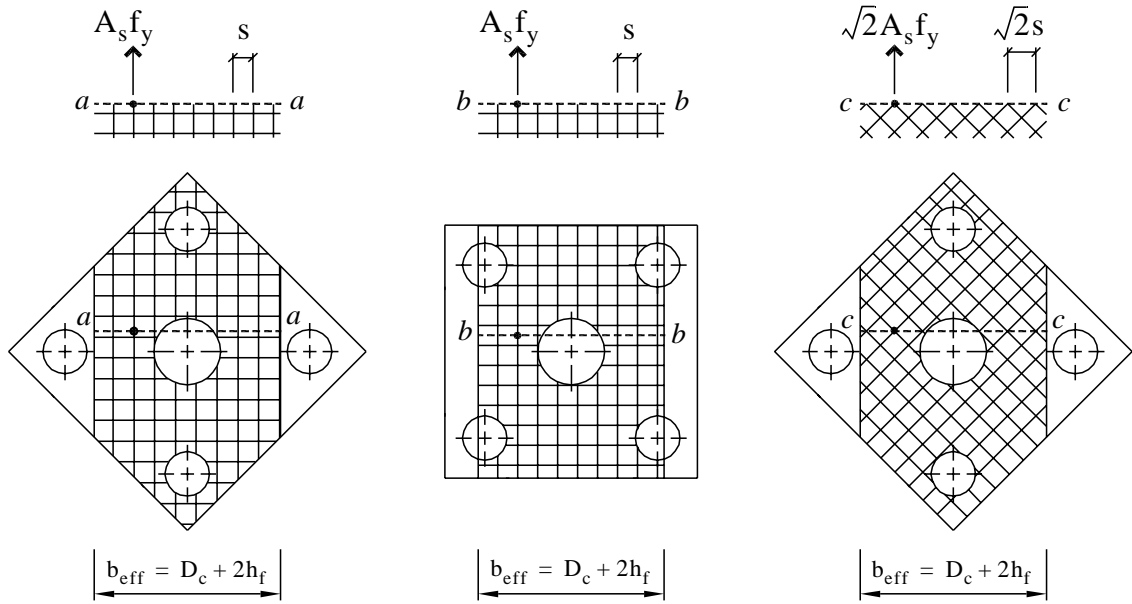
Figure 7.5: Equal capacity of pilecap positive bending within effective width

- **Pilecap shear tansfer**

Step 10. Obtain the axial forces of pile, $T_{p,N}$ and $C_{p,N}$, under orthogonal direction of

loading.

$$C_{p,N} = C_{p1} + C_{p2} + C_{p3} = \frac{P}{4} + \frac{1}{2L_f}[M_c^{\circ} + (F_c^{\circ} - F_s)L_p] \tag{7.12}$$

$$T_{p,N} = T_{p1} + T_{p2} + T_{p3} = -\frac{P}{4} + \frac{1}{2L_f}[M_c^{\circ} + (F_c^{\circ} - F_s)L_p] \tag{7.13}$$

Step 11. Estimate the moment of tension and compression piles, $M_{tp,N}$, $M_{cp,N}$, and,

thereof, shear force of compression pile, $V_{cp,N}$. From the force polygons in Fig-

ure 7.7, T_1 and T_2 can be obtained.

235
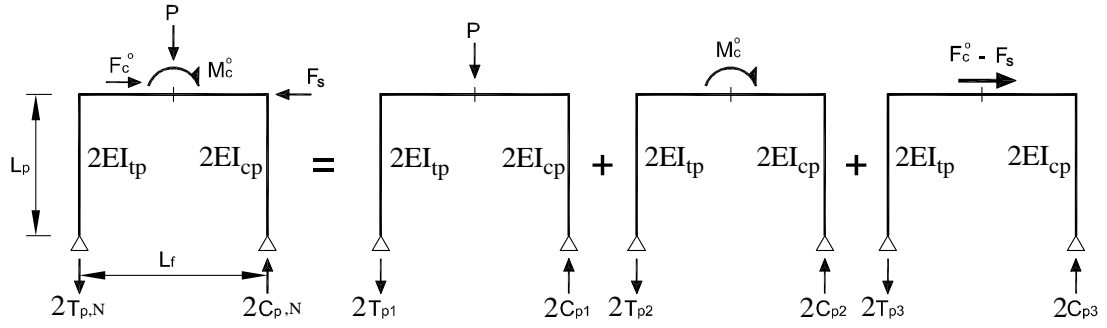
Figure 7.6: Axial reaction forces of pile under orthogonal direction loading

$$C_{p,N} = C_p + C'_p$$
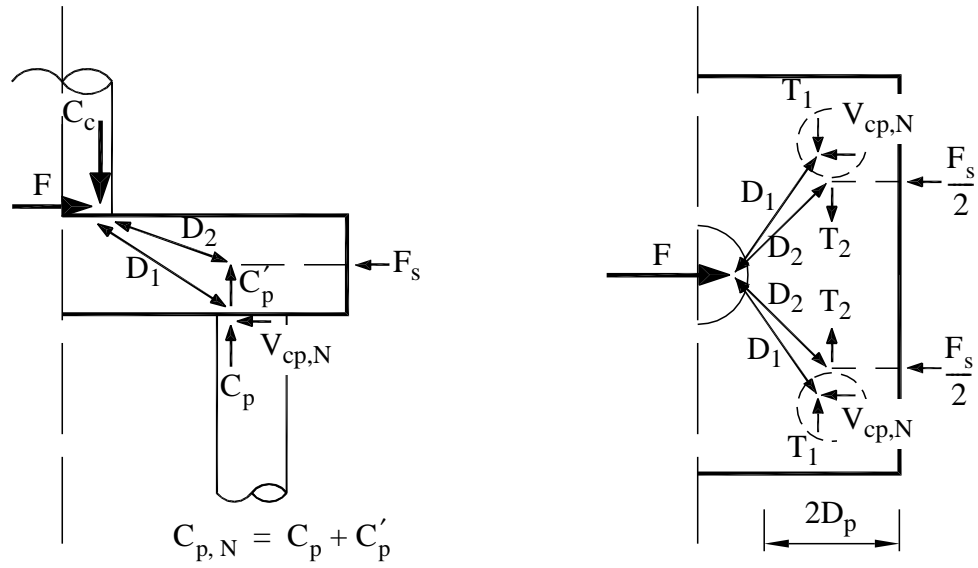
Figure 7.7: Pilecap shear transfer under the orthogonal direction loading

$$T_1 = V_{cp,N} = (F_c^\circ - F_s) \cdot \frac{M_{cp,N}}{M_{tp,N} + M_{cp,N}} \tag{7.14}$$

236

$$T_2 = \frac{F_s}{2} \cdot \frac{0.25b_f}{\left(\dfrac{L_f}{2} + \dfrac{D_c}{3}\right)} \qquad (7.15)$$

Step 12. Ensure tension capacity, T, within the effective width of $2D_p$, is :

$$T \geq T_1 + T_2 \qquad (7.16)$$

- **Pilecap joint design**

Step 13. Place vertical external stirrups in the region shown in Figure 7.8 with a total area

equal to :
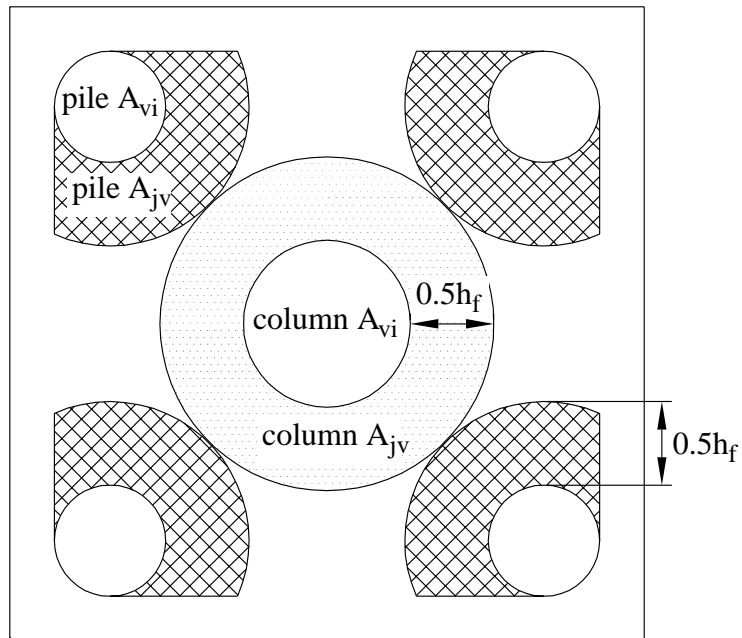
Figure 7.8: Location of vertical stirrups of pilecap

$$A_{jv} = 4T_s = 4 \times 0.125\lambda_o A_{sc}\frac{f_{yc}}{f_{yv}} = 0.5\lambda_o A_{sc}\frac{f_{yc}}{f_{yv}} \text{ for column/pilecap joint} \quad (7.17)$$

$$A_{jv} = 2T_s = 2 \times 0.125\lambda_o A_{sc}\frac{f_{yc}}{f_{yv}} = 0.25\lambda_o A_{sc}\frac{f_{yc}}{f_{yv}} \text{ for pile/pilecap joints} \quad (7.18)$$

Step 14. Place vertical stirrups inside column and piles amounting to :

$$A_{vi} = 0.0625\lambda_\circ A_{sc}\frac{f_{yc}}{f_{yv}} \quad (7.19)$$

Step 15. Put the transverse hoop reinforcement around the column and pile longitudinal

bars equivalent to the greater of Eqs. (7.20) and (7.1).

$$\rho_s = \frac{0.3A_{sc}\lambda_o f_{yc}}{f_{yh}l_a^2} \quad (7.20)$$

7.5 Scope of applicability, and future research

The conclusions and design recommendations drawn in this report are based on the behavior of 4-CIDH-pile-supported-footings. However, there are likely to be foundations which consist of 9 (or 8 which is more common)-CIDH piles and the above conclusions and design recommendations may be applied to these foundation systems. The reason for this is that the behavior of a 9(or 8)-CIDH-pile-supported-foundation will be similar to that of a 4-CIDH-pile-supported-foundation.

Because the soil stress bulb around an individual pile will overlap, as shown in Figure 7.9, it is reasonable to expect that there is unequal distribution of vertical soil-pile interaction stiffness. In other words, the magnitude of vertical soil-pile interaction

(a) Order of vertical stiffness magnitude
due to soil stress bulb overlap

(b) Order of pile axial force magnitude
due to direct force transfer to the nearest piles
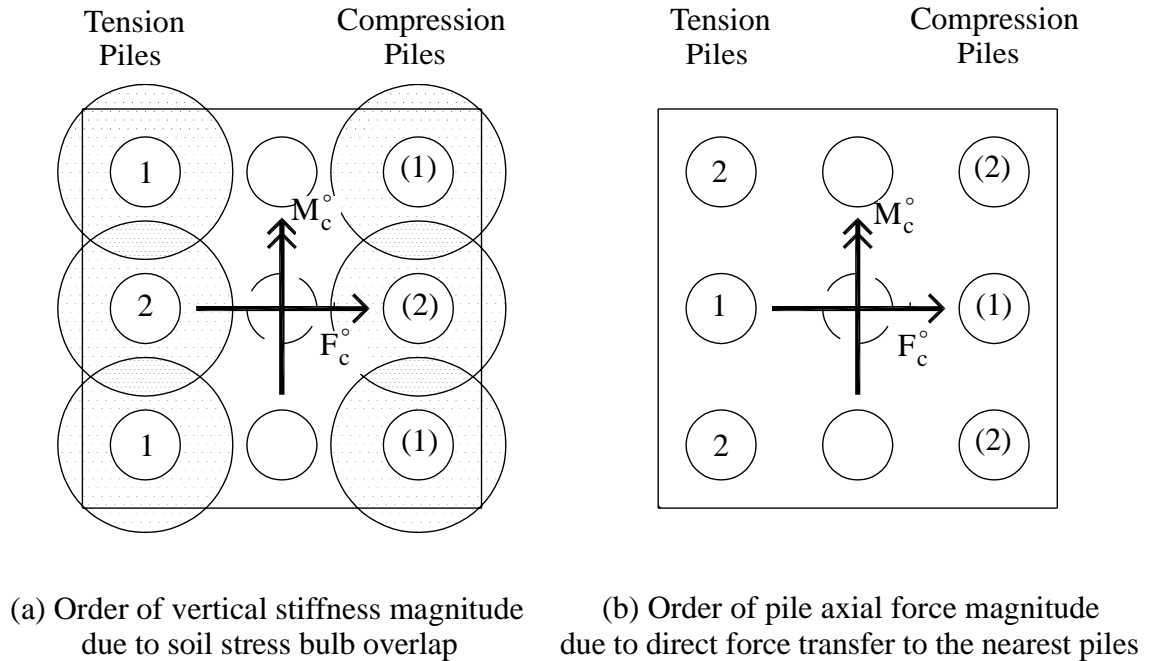
Figure 7.9: Reversed order of magnitudes between the vertical stiffness and axial force of pile

stiffness of each pile depends on the pile location. In Figure 7.9, the vertical stiffness of

the mid-piles in tension or compression is less than that of a corner-pile under orthogonal

direction loading. On the other hand, the vertical force developed in the mid-piles in

tension or compression will be greater than that of corner-piles due to the direct force

transfer to the nearest piles.

Accordingly, vertical displacements of the mid-piles will be greater than those of

corner-piles in tension or compression. Therefore, the pilecap flexural deformation mode

of a 9 (or 8)-CIDH-pile-supported-foundation becomes similar to that of 4-CIDH-pile-

supported-foundation.

These views are only speculation and are outside the scope of the research work. It

is, therefore, recommended that the applicability of the research on 4-CIDH-pile-

239

supported footings be experimentally and analytically explored in future for designs involving 9(or 9)-CIDH-pile-supported footings.

In addition, further simplifications to the design procedure proposed in this report may also be possible. Since the orthogonal direction loading is more familiar to structural engineers than the diagonal direction loading, designing the CIDH-pile-supported-foundation considering only the orthogonal direction loading condition may be possible. If a chart or a table which represents the relationship of the response between orthogonal and diagonal direction loading is constructed, the design force demand under diagonal direction loading may be obtained by multiplying the design force demand under the orthogonal direction loading by an amplification factor. Future research is encouraged in these aspects.

Appendix A: Analytical Tools For Response Of Test Units

The basic analytical methods for evaluating the responses of both test units are described here. Particular emphasis is given here to the moment-curvature evaluation and its integration to obtain displacements. Emphasis is also given to the foundation flexibility and its effect on the evaluation of the system's displacement ductility.

A.1 Moment – Curvature Analysis

A.1.1 General

The structural components tested in this project are mainly composed of elements which are largely influenced by bending or combined axial force and bending. The deformations of these elements can be established from sectional moment - curvature relationships. A typical theoretical moment-curvature relationship of a reinforced concrete section is shown in Figure A.1. The monotonic moment-curvature analysis Program SEQMC[32] was used to determine the theoretical moment-curvature relationship for the elements of the test units. In this program the longitudinal reinforcement in circular section is smeared along the perimeter of the reinforcement cage. The theoretical stress-strain relationship for confined concrete proposed by Mander et al.[14] was used for the analysis.
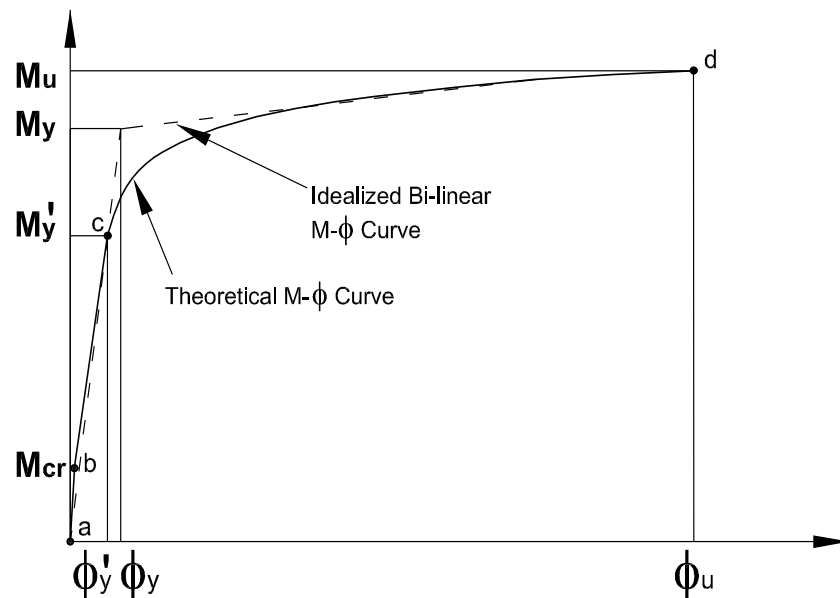
Figure A.1: Typical Moment - Curvature of a R.C section and a theoretical idealization

A theoretical monotonic moment-curvature relationship is characterized by three major regions.

The first region(see line a-b in Figure A.1) describes the response of the section in the uncracked stage. The flexural stiffness, for sections with low or moderate longitudinal steel ratios, can be approximated by E_cI_g, where E_c is the Young's modulus of the reinforced concrete and I_g is the second moment of inertia of the section.

Cracking of the section occurs at point b(see Figure A.1) and results in a reduction in the section's tangent flexural stiffness(see line b-c in Figure A.1).

The onset of significant section's nonlinear response begins at point c, when the outermost longitudinal bar yields in tension or the extreme fiber in compression reaches 0.002 strain, whichever occurs first. This point is defined as the "First" yield point. Yielding and strain hardening of the longitudinal reinforcement in tension and compression as well as the stress-strain relationship of concrete in compression greatly affect the sectional response between points c and d in Figure A.1.

At point d, the section is deemed to have failed. Failure is defined here as when the section's flexural capacity decreases to $0.8\,M_u$ after reaching the ultimate capacity M_u. The latter stage usually occurs when the confined concrete exceeds the ultimate ultimate concrete strain of ε_{cu} associated with hoop fracture, or when several longitudinal bars attain the effective ultimate tensile strain ε_{su}^*, and fracture.

Simple analytical modeling can be done if the theoretical monotonic moment-curvature relationship is idealized by a bilinear relationship. such relationship is depicted

in Figure A.1. The initial portion of the ideal bi-linear relationship passes through the origin and through the "First" yield point and extends to the reference yield point(M_y, ϕ_y). Priestley et al.[26] have found that the references, or ideal yield moment, M_y, can be calculated as that corresponding to an extreme compression fiber strain of 0.004 or a tensile strain of 0.015 in the outermost longitudinal bar in tension, whichever occurs first. The reference yield curvature, ϕ_y, can be calculated by extrapolation to be,

$$\phi_y = \frac{M_y}{M_y'}\phi_y'$$ (A.1)

In the ideal bi-linear moment curvature relationship, the section's curvature ductility capacity is,

$$\mu_\phi = \frac{\phi_u}{\phi_y}$$ (A.2)

where ϕ_u is the ultimate curvature. corresponding to ultimate concrete strain, or maximum permitted reinforcement strain, discussed subsequently.

A.1.2 Reinforcing steel

The behavior of reinforcing steel is characterized by an initial linear elastic portion of the stress-strain relationship with a modulus of approximately 200 GPa, up to the yield stress f_y, followed by a strain plateau up to the strain, ε_{sh}, where the region of strain hardening begins. The Mander et al.[14] model assumed the stain hardening region follows a power curve based on the tangent modulus, E_{sh} at ε_{sh} and proposed the stress-strain relationship in the strain hardening region as :

$$f_s = f_u - (f_u - f_y)\left(\frac{\varepsilon_{su} - \varepsilon_s}{\varepsilon_{su} - \varepsilon_{sh}}\right)^P \quad \text{for } f_s \geq f_y \, , \, \varepsilon_s \geq \varepsilon_{sh} \tag{A.3}$$

where, f_s and ε_s are the stress and corresponding strain, f_u and ε_{su} are the ultimate stress and strain respectively, f_y is the yield stress. P is given by :

$$P = E_{sh}\left(\frac{\varepsilon_{su} - \varepsilon_s}{f_u - f_y}\right) \tag{A.4}$$

After maximum stress is reached, strain softening occurs with deformation concentrating in a local weak spot. In terms of structural response, the strain softening portion of the curve should be ignored, since it imparts little additional ductility to members. In design and analysis a reduced effective ultimate tensile strain, ε_{su}^*, should be adopted, since there is evidence that under cyclic loading involving sequential tensile and compressive strains, the ultimate tensile strain is less than under the monotonic testing. A simple rule of thumb is that the effective ultimate tensile strain should be the monotonic tensile strain at peak stress reduced by the maximum expected compression strain under the reversed direction of seismic response. This is illustrated in Figure A.2. Alternatively, the simpler requirement that $\varepsilon_s \leq 0.75\varepsilon_{su}$ will normally be adequately conservative except for members with high axial compression forces.

The strain hardening of the reinforcing steel is desirable since it spreads plasticity over a reasonable length of the member, ensuring that tensile strains are not excessive at the design ductility limit. However, rapid increase in stress in strain hardening can result in excessive overstrength of plastic hinges, requiring high strengths of capacity protected members.
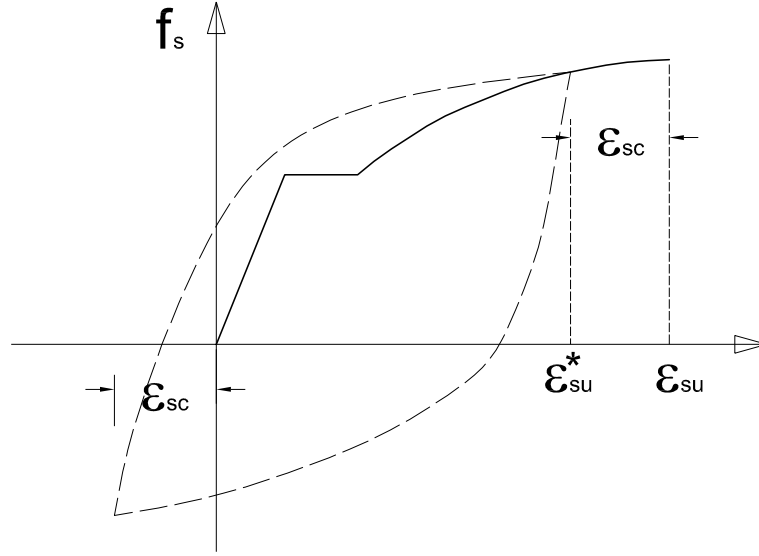
Figure A.2: Effective ultimate tensile strain for reinforcing steel

A.1.3 Compression stress-strain relationships for confined concrete

The stress-strain model for confined concrete which was proposed by Mander et al.[14] was adopted for the moment-curvature analysis. This model is given by,

$$f_c = \frac{f'_{cc} x r}{r - 1 + x} \tag{A.5}$$

where,

$$f'_{cc} = f'_c \left(2.254 \sqrt{1 + \frac{7.94 f'_l}{f'_c}} - \frac{2 f'_l}{f'_c} - 1.254 \right) \tag{A.6}$$

$$x = \frac{\varepsilon_c}{\varepsilon_{cc}} \tag{A.7}$$

$$\varepsilon_{cc} = 0.002 \left[1 + 5 \left(\frac{f'_{cc}}{f'_c} - 1 \right) \right] \tag{A.8}$$
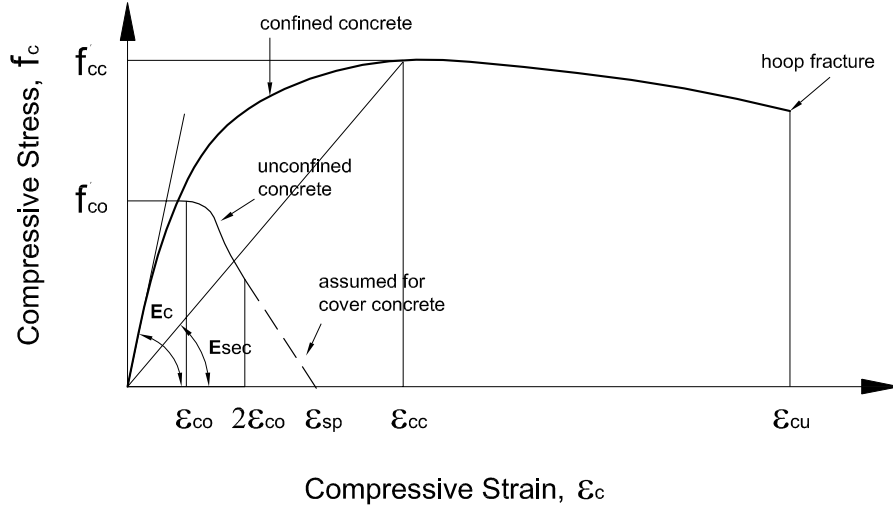
Figure A.3: Stress-Strain Model for concrete in compression

$$r = \frac{E_c}{E_c - E_{sec}} \tag{A.9}$$

$$E_c = 5000\sqrt{f'_c} \tag{A.10}$$

$$E_{sec} = \frac{f'_{cc}}{\varepsilon_{cc}} \tag{A.11}$$

In Eqs. (A.6)-(A.11), ε_{cc} is the concrete strain at peak stress, f'_{cc}, and f'_l is the effective lateral confining stress. f'_c represents the unconfined concrete compressive strength. With $f'_l = 0$, Eqs. (A.6)-(A.11) produce an equation appropriate for unconfined concrete. The effective lateral confining pressure, f'_l, for a circular section is related to the average confining stress of f_l by the expression of

$$f'_l = K_e f_l = 0.95 \times \frac{2 f_{yh} A_h}{D' s} \tag{A.12}$$
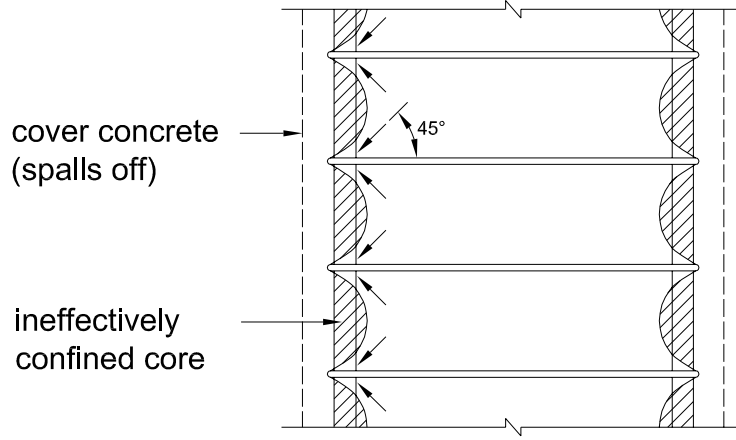
Figure A.4: Arching mechanism of core concrete between hoops

where K_e is the confinement effectiveness coefficient which accounts for the ineffectively confined core concrete and is given by :

$$K_e = A_e / A_{cc} \qquad (A.13)$$

where A_e is the sectional area of effectively confined core concrete and A_{cc} is the sectional area of core concrete. Typically, K_e is taken as 0.95 for circular section [26].

The ultimate compression strain is taken to occur when fracture of transverse steel initiates. This can be estimated conservatively as Eq. (A.14), by equating the strain energy capacity of the transverse reinforcement as it is strained to peak stress f_{uh} to the increase in energy absorbed by the concrete, resulting from confinement.

$$\varepsilon_{cu} = 0.004 + \frac{1.4\rho_s f_{yh}\varepsilon_{su}}{f'_{cc}} \qquad (A.14)$$

where ε_{su} is the transverse steel strain at maximum tensile stress, $\rho_s = 4A_h / (D's)$ is the volumetric ratio of confining steel for a circular section, A_h is the cross sectional

area of spiral, D′ is the diameter of core concrete measured to centerline of spiral, s is the spacing of the transverse reinforcement, f_{yh} is the yield strength of the transverse reinforcement and f_{cc}' is the compressive strength of confined concrete.

A.1.4 Limitation of the monotonic moment-curvature analysis

Under cyclic loading the monotonic stress-strain curves of steel bar may not form an accurate envelope to the inelastic response. Baushinger effects result in nonlinear behavior developing at a strain lower than that of yield stress on unloading from a previous inelastic excursion. Figure A.5 shows the results of two different types of cyclic testing of reinforcing steel [14, 26]. In Figure A.5 the cyclic inelastic excursions are predominantly in the tensile strain range, which is typical of beams or columns with low axial compression. For such a response the monotonic stress-strain curve provides a reasonable envelope to the cyclic response in the tension range but not in the compression range. For columns with high compression stress levels and high reinforcement ratios, reinforcing bars may be subject to strain reversals of almost equal magnitude, implying a neutral-axis position close to the section centroid. As illustrated in Figure A.5, under cyclic response, the stress level for a given strain increases and can substantially exceed the stress indicated by the monotonic stress-strain curves.

Ductile bridge columns typically have low to moderate axial compression levels and are better characterized by the behavior of Figure A.5-(a). Because the columns of the test units have moderate axial load ratio, 15 %, and the piles were subjected to unsymmetrical strain cycles due to the offset between the point of gravity load and the

(a) unsymmetrical strain cycles   (b) symmetrical strain cycles
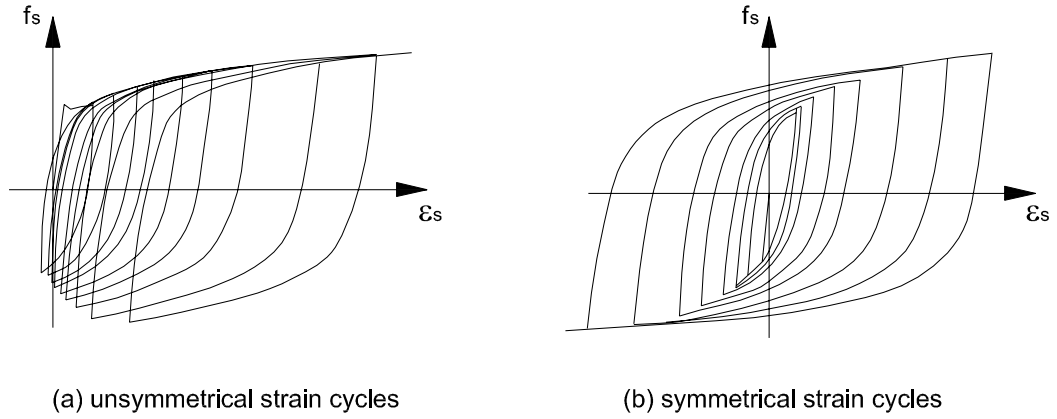
Figure A.5: Cyclic inelastic stress-strain response of reinforcing steel [f_y=380 MPa]

pile location, the monotonic moment-curvature analysis can reasonably be used to determine the response of test units.

A.2 Elastic Deformation

Excluding the additional foundation flexibility effect, which is described in Section A.5, the "First" yield displacement, Δ_y', and the reference yield displacement, Δ_y, of a cantilever column which is fixed at its base, is obtained from the idealized bi-linear monotonic moment-curvature relationship,

$$\Delta_y' = \frac{\phi_y' l_{eff}^2}{3} \tag{A.15}$$

$$\Delta_y = \frac{\phi_y l_{eff}^2}{3} = \frac{M_y}{M_y'}\Delta_y' \tag{A.16}$$

where l_{eff} is the effective length of the cantilever column which is defined as,

$$l_{eff} = L_c + 0.022 f_y d_{bl} \tag{A.17}$$

250

where L_c is the length of the cantilever column measured from critical section to the inflection point and f_y and d_{bl} are the yield stress and the diameter of longidudinal reinforcement, respectively. The second term in Eq. (A.17) makes allowance for the additional rotation at the critical section resulting from the strain penetration of the longitudinal reinforcement into the supporting element[26]. Note that shear deformations are ignored in Eqs. (A.15) and (A.16) considering the comparatively small moment gradient of a single bending member with moderate height.

A.3 Plastic Hinge Length and Plastic Deformation

The plastic deformation, Δ_p, which occurs as a result of yielding at the base of the column is obtained using the plastic curvature, ϕ_p, and a equivalent plastic hinge length, L_p, as described below :

$$\phi_p \ = \ \phi - \frac{M}{M_y}\phi_y \ \text{ when } \phi \geq \phi_y \text{ and } M \geq M_y \tag{A.18}$$

where M and ϕ are the moment and corresponding curvature respectively. The use of an equivalent plastic hinge length, L_h, requires, by definition, a constant plastic curvature. The integration of the plastic curvature over the equivalent plastic hinge length results in the plastic rotation θ_p. The reasonable estimate for the plastic hinge length is represented empirically and analytically as,

$$L_h \ = \ (0.08L_c + 0.022f_y d_{bl}) \geq 0.044f_y d_{bl} \tag{A.19}$$

A minimum plastic hinge length of $0.044f_y d_{bl}$ was enforced in Eq. (A.19), as recommended by Priestley et al. [26], to allow strain penetration into the column as well as into the supporting member such as footing. The plastic displacement, Δ_p, beyond the

ideal yield includes the component due to the plastic rotation, θ_p, and additional elastic displacement resulting from the increase in moment from M_y to M which is greater than M_y. This additional elastic displacement occurs from strain hardening of the reinforcement and is given by :

$$\Delta_e' = \left(\frac{M}{M_y} - 1\right)\Delta_y \text{ for } M \geq M_y \tag{A.20}$$

The plastic displacement, Δ_p, was then calculated as,

$$\Delta_p \approx \left(\frac{M}{M_y} - 1\right)\Delta_y + L_h(\phi - \phi_y)L_c \tag{A.21}$$

In the above expression the term L_c was used considering the strain penetration of the longitudinal reinforcement into the supporting member, allowing plastic rotation of the column to be centered close to the critical section [35].

A.4 Member Ductility

For the estimation of the member ductility level considering the expressions given in Eq. (A.15)-(A.21), the total lateral displacement, Δ_t, of a column loaded beyond the elastic limit is,

$$\Delta_t = \Delta_y + \Delta_p = \frac{M}{M_y}\Delta_y + L_h(\phi - \phi_y)L_c \tag{A.22}$$

Hence the member displacement ductility capacity μ_Δ is given by :

$$\mu_\Delta = \frac{\Delta_t}{\Delta_y} = 1 + \frac{\Delta_p}{\Delta_y} = \frac{M}{M_y} + 3(\mu_\phi - 1)\frac{L_h L_c}{l_{eff}^2} \tag{A.23}$$

A.5 Pilecap Flexibility

So far the lateral force-displacement characteristics described in previous sections were derived only for a cantilever column fixed at its base. When the column is connected to a flexible member such as pilecap with piles, the elastic flexibility of the pilecap and piles contributes to the yield displacement of the system (see Figure A.6)

Under the lateral force F, the overturning moment $M_f = F(L_c + h_f)$ causes rotation, θ_f, of the footing. For a pile supported footing, if it is assumed to be flexurally rigid, rigid body rotation of the pilecap is given by :

$$\theta_f = \frac{M_f}{K_f} \tag{A.24}$$

In Eq. (A.24), K_f is the rotational stiffness which can be derived from the axial stiffness and the distribution of the piles to be

$$K_f = \Sigma x_i^2 k_i \tag{A.25}$$

where k_i is the axial stiffness of pile i at a distance x_i from the axis of rotation through the centroid of the pile group. To evaluate the k_i properly, the vertical stiffness of the piles, including soil-pile interaction, must be considered since lateral force results in variations in the pile axial loads, particularly when a moment-resisting connection between pile and pilecap exists [27].

The pile and soil vertical flexibility result in rotation of the pilecap under seismic actions. It is important to recognize that for a moment-resisting pile-pilecap connection, bending moments induced by the pilecap rotation are of opposite sign to those induced by lateral translation of the pilecap.. The consequence is that rotational and translational
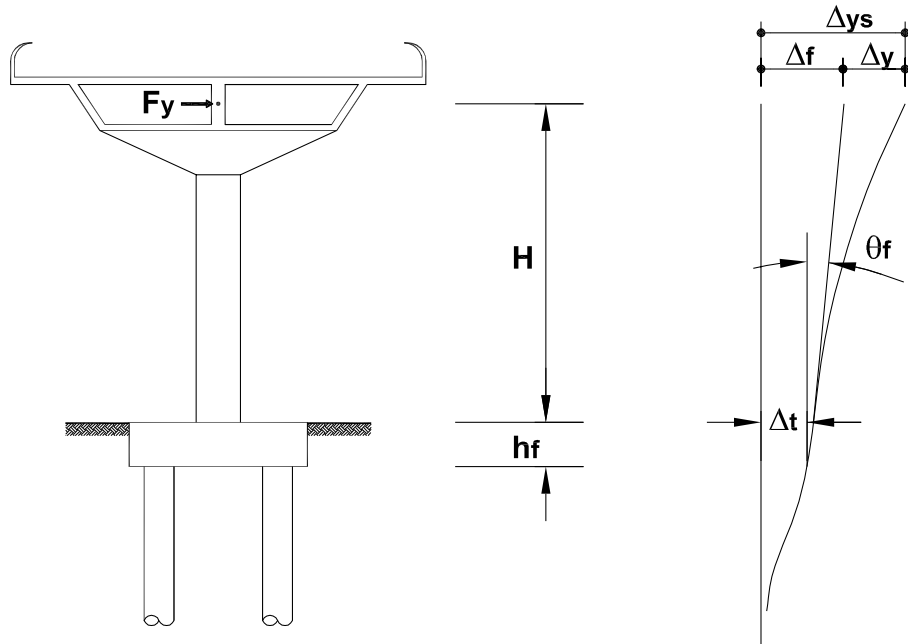
Figure A.6: Influence of Additional Footing Flexibility on Yield Displacement

(a) System   (b) Δ_1 due to pilecap translation   (c) Δ_2 due to pilecap rota
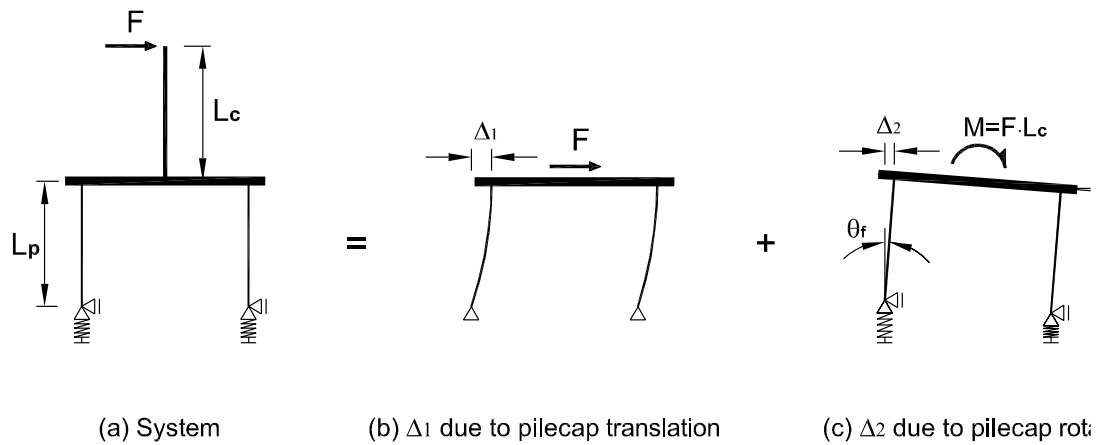
Figure A.7: Influence of Pilecap Rotation on Foundation Lateral Stiffness

stiffness are coupled. This is illustrated in Figure A.7. The lateral translation of moment-resisting pile supported footing, $\Delta_{f,t}$, considering pilecap rigid body rotation is :

$$\Delta_{f,t} = \Delta_1 + \Delta_2 = \frac{FL_p^3}{3(EI)_{pg}} + \theta_f L_p \qquad (A.26)$$

where θ_f is the rigid body rotation of the pilecap, L_p is the pile length from the pilecap to the inflection point and $(EI)_{pg}$ is the stiffness of the pile group. From Eq. (A.26), the equivalent lateral stiffness of the pilecap is :

$$k_\Delta = \frac{F}{\Delta_{f,t}} = \frac{3(EI)_{pg}}{L_p^3}\left(1 - \frac{\theta_f L_p}{\Delta_{f,t}}\right) \qquad (A.27)$$

Thus, the additional elastic deformation at the tip of the column due to foundation compliance is :

$$\Delta_f = \theta_f(L_c + h_f) + \Delta_{f,t} = F\left\{\frac{(L_c + h_f)(L_c + h_f + L_p)}{K_f} + \frac{L_p^3}{3(EI)_{pg}}\right\} \qquad (A.28)$$

The influence of foundation flexibility on the displacement ductility of the structure, which is explained above is based on only the rigid body rotation and translation of pilecap. However, it was found that the flexibility of the pilecap itself is another factor which influences the behavior of the structure and should not always be ignored. This is discussed in Chapter 6 in detail.

A.6 System Ductility

In the previous section it was shown that the pilecap rigid body rotation and translation augment the system's flexibility.

This affects the system's response as :

$$\Delta_{ys} = \Delta_y + \Delta_f \qquad (A.29)$$
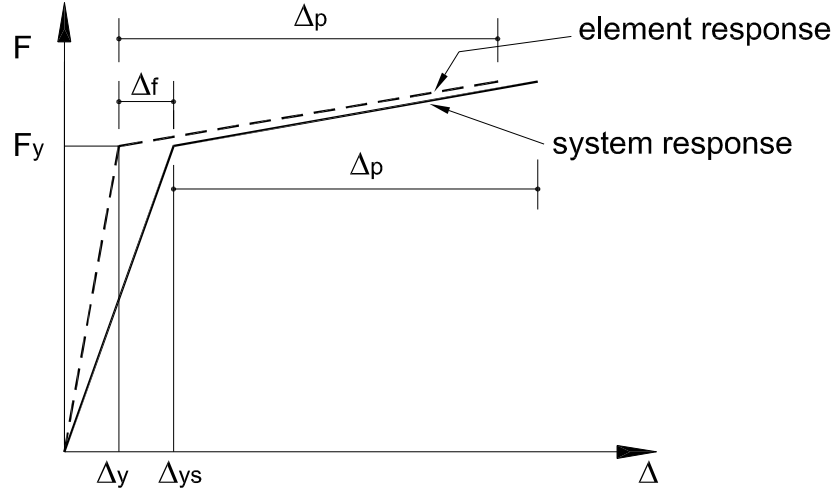
Figure A.8: Force-Displacement Relation caused by Footing Flixiblilty

where Δ_f is the contribution from the flexibility of the pilecap. The total lateral displacement of the test unit is therefore:

$$\Delta_t = \Delta_y + \Delta_f + \Delta_p \tag{A.30}$$

The system displacement ductility, $\mu_{\Delta s}$, considering the effects of the displacement components due to pilecap and bearing flexibility can thus be related to the rigid base ductility $\mu_{\Delta r}$ by :

$$\mu_{\Delta s} = \frac{\Delta_t}{\Delta_{ys}} = \frac{\Delta_y + \Delta_f + \Delta_p}{\Delta_y + \Delta_f} = 1 + \frac{\Delta_p/\Delta_y}{1 + \Delta_f/\Delta_y} = 1 + \frac{\mu_{\Delta r} - 1}{1 + \Delta_f/\Delta_y} \tag{A.31}$$

Since the flexibility of the foundation affects the yield displacement more than the total displacement, the ductility capacity of the system is always smaller than the member ductility capacity. Note that the displacement ductilities referred in this report are system ductilities unless otherwise mentioned.

A.7 Theoretical Response of Test Units

The force-displacement response of each test unit was quantified using estimated material properties. To obtain the force-displacement curve of the cantilever column from the moment-curvature anaysis of the section, Eq. (A.21) was modified in terms of the first yield since it is based on the ideal yield and is valid only beyond the ideal yield moment.

$$\Delta_p = \left(\frac{M}{M_y'} - 1 \right) \Delta_y' + L_h(\phi - \phi_y')L_c \tag{A.32}$$

The analyses of the column and the footing with four piles were done separately. Using Eq. (A.32), the force-displacement relation of the column was obtained from the moment-curvature curve with the applied axial load. The lateral displacement and the rotation at the center of the footing was then obtained applying the forces from the force-displacement relation of the column. The response of the system was then predicted by combining the response of the column and the response of the footing. Nonlinear analysis was done for the column and linear analysis was done for the footing and four piles since these were assumed to be elastic in Loading Phase 1 which is the loading case with pilecap resistance.

Appendix B: Design Tools For Pilecap Joints Of Test Units

It is known that efficient joint reinforcement details can be obtained using force transfer mechanisms when compared to the conventional joint design approach, which is based on the maximum joint shear forces. The shear force transfer mechanism of column-pilecap and pile-pilecap joints of test units and joint design tools, which was proposed by Priestley et al.[26], are described here.

B.1 Joint design criteria

B.1.1 Limit state of principal tension stress in joints

The pilecap joints of the test units can be designed with reduced amounts of reinforcement by explicitly identifying an internal force flow. The joint principal tensile stress, p_t, can be used as threshold values to determine whether the joint reinforcement was needed to transfer joint forces [26,35] :

1) If $p_t \leq 0.29\sqrt{f_c'}$ [MPa], joint shear cracking is not expected to occur. Joint forces are transferred through a tension-compression stress field and no joint reinforcement is required. Only nominal joint reinforcement satisfying Eq.(B.11) should be provided in the form of hoops.

2) If $p_t \geq 0.42\sqrt{f_c'}$ [MPa], a complete force transfer mechanism is required to transmit the joint shear forces. The detailing of the joint reinforcement should be consistent with the force transfer model.

3) For joint principal tensile stresses between the above limits, joint cracking is expected. Failure of the joint is unlikely to occur unless significant ductility levels are achieved within the plastic hinge region. Reduced joint reinforcement may be placed by a linear interpolation of the two reinforcement requirements described above.

The principal tensile stress in a joint is calculated using the average normal and shear stresses given by :

$$p_t = \frac{f_v + f_h}{2} - \sqrt{\left(\frac{f_v - f_h}{2}\right)^2 + v_j^2} \qquad (B.1)$$

(a) Plan View   (a) Section A-A
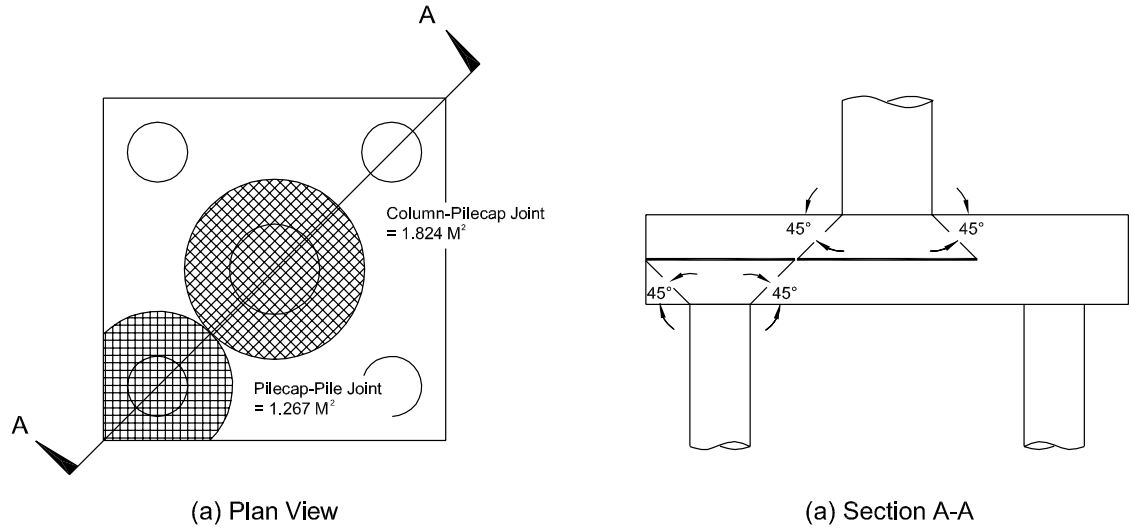
Figure B.1: Effective Joint Area for vertical normal stress f_v

where f_v and f_h are average axial stresses in the vertical and horizontal direcitons; and v_j is the average joint shear stress.

B.1.2 Mean stresses in joints

An average stress, f_v, at midheight of the pilecap due to the column or pile axial force was obtained assuming a 45° spreading of stresses from the boundaries of the column or pile in all directions as shown in Figure. B.1. The horizontal normal stress, f_h, is based on the axial force averaged over the effective pilecap cross sectional area as shown in Figure B.2-(b). Considering that the overstrength flexural capacity develops in the column or pile adjacent to the joint interface, the average joint shear stress was obtained from the joint shear force which may be calculated with adequate accuracy as :

$$V_{jh} = \frac{M_c^o}{h_b} \tag{B.2}$$

260

$A_{eff} = b_{je} \times D$

$A_{eff} = b_{je} \times h_f$

Pilecap-Pile Joint

Column-Pilecap Joint

(a) For horizontal shear stress

(b) For horizontal axial stress
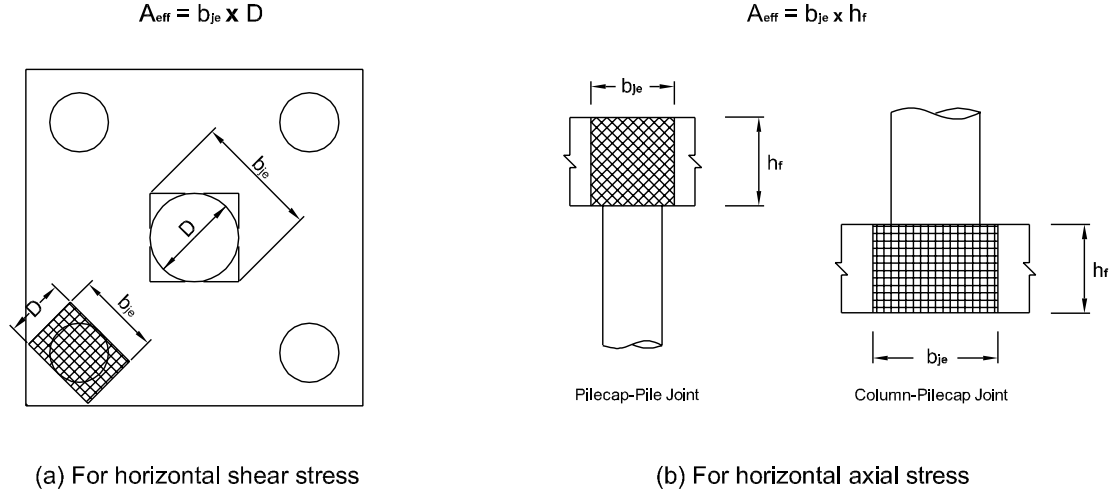
Figure B.2: Effective Joint Area for horizontal shear and axial stresses
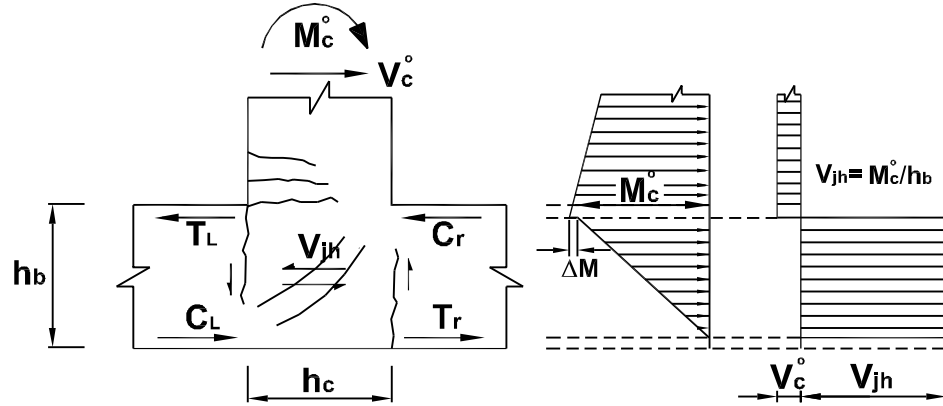
Figure B.3: Column-pilecap joint horizontal shear force

ignoring the incremental moment decrease ΔM(see Fig. B.3) and approximating the lever arm between pilecap stress resultants T and C by h_b, see Figure B.3, B.4. Averaging the shear force over the joint effective area as shown in Figure B.2-(a) and B.5, the joint shear stress was calculated from Eq.(B.3).

$$v_{jh} = \frac{V_{jh}}{b_{je}h_c} \tag{B.3}$$

261
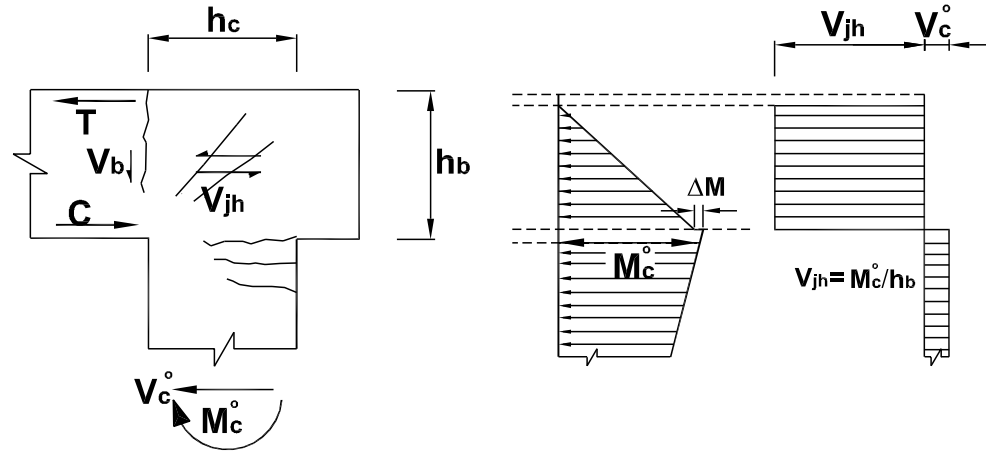
Figure B.4: Pile-pilecap joint horizontal shear force

where $b_{je} = \sqrt{2}\,D$ (D is the column diameter) was assumed as recommended in reference[26].

Since the average shear stress in the joint region should be equal in orthogonal directions, V_{jv} and v_{jv} can be expressed directly as

$$V_{jv} = V_{jh}\frac{h_b}{h_c} \tag{B.4}$$

$$v_{jv} = \frac{V_{jv}}{b_{je}h_b} = \frac{V_{jh}}{b_{je}h_c} = v_{jh} \tag{B.5}$$

B.2 Force tranfer mechanism in joint and design procedure

To describe the force transfer mechanism adopted for designing of the joints, the internal force flow in the joints is illustrated in Figures B.6 and B.7 was used. In this mechanism, it was ensured that the longitudinal column and pile bars could be anchored adequately into the joint with straight bar ends and that the overstrength moment
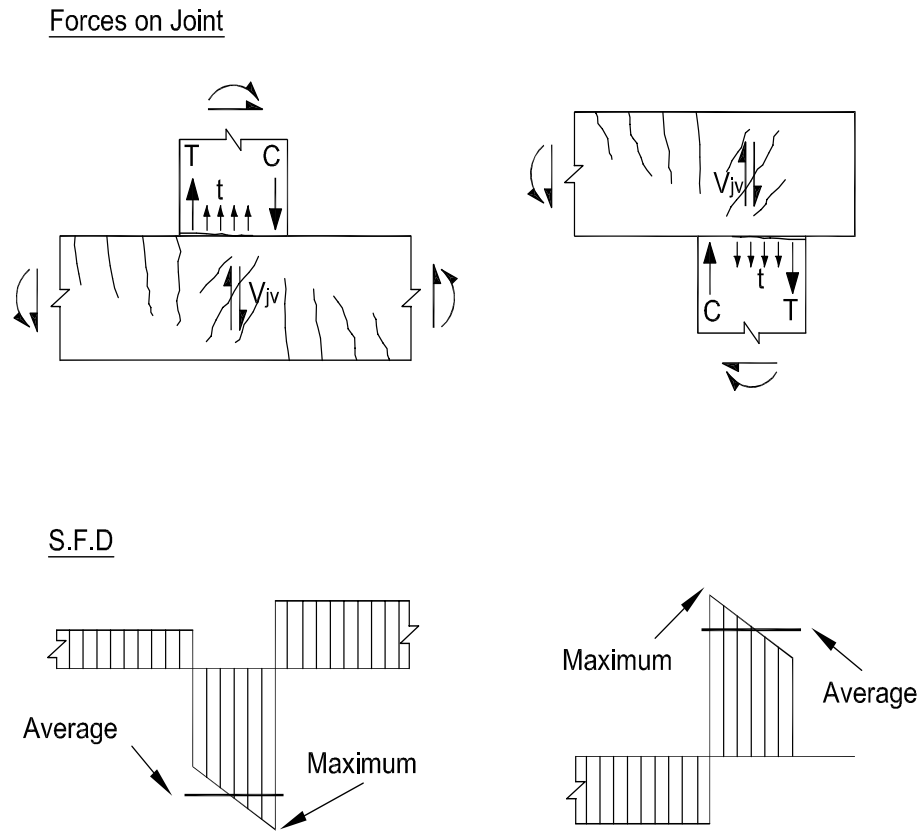
Figure B.5: Average and maximum joint shear forces

capacity of the column and the pile could be developed at the column-pilecap and the pilecap-pile interfaces[24,26,33]. Further, a minimum amount of reinforcement was provided within the joint so that no significant damage would occur in the joint region. The required amount of reinforcement in the column-pilecap joint region was chosen to be consistent with the mechanism as outlined below[26,33].

1) The tension force in a lightly loaded circular column section at its ultimate flexural strength can be approximated as:
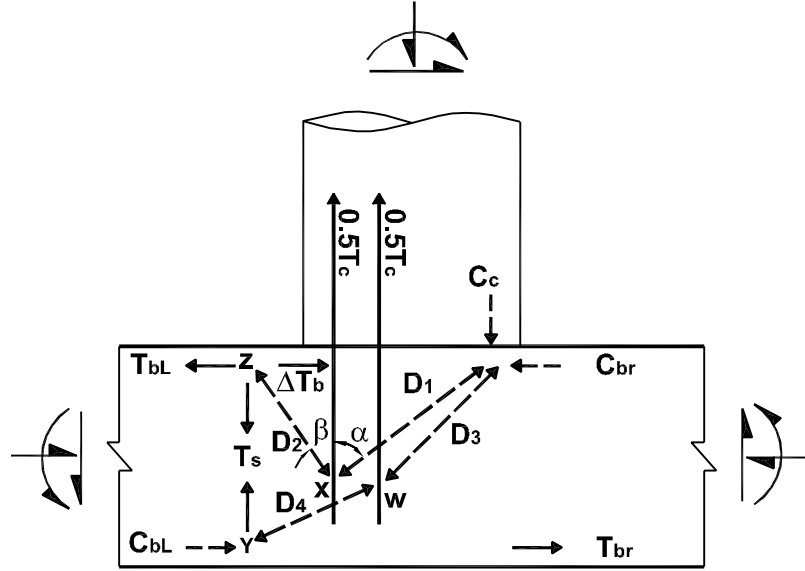
Figure B.6: Column-pilecap joint force transfer mechanism
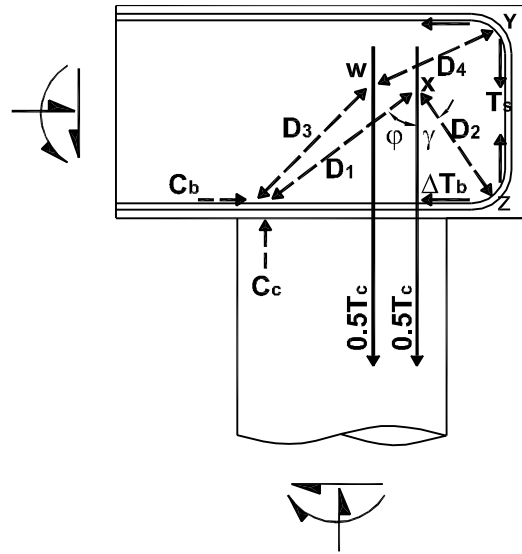
Figure B.7: Pilecap-pile joint force transfer mechanism

$$T_c = 0.5 A_{sc} f_{yc}^{\circ}$$ (B.6)

where A_{sc} is the total area of the column longitudinal reinforcement and f_{yc}° is the overstrength stress in the column longitudinal reinforcement, including yield overstrength and strain hardening.

2) The development length of the column tension bars carrying $0.5T_c$, near the neutral axis of the column section, was assumed to be provided by the main diagonal strut.

3) The remaining $0.5T_c$, which was closest to the face of the column or pile, was likely to have anchorage problems due to large tension forces in the reinforcement and the shallowness of the strut. The anchorage of these bars was provided by struts D_1 and D_2 as shown in Figure B.6. Strut D_1 formed towards the pilecap and column compression resultants C_{bl} and C_c, and strut D_2 formed outward, into the pilecap. In order to support such a mechanism, the vertical component T_s of D_2 was provided by joint external stirrups near the column or pile. Transfer of this tension force to the bottom of the pilecap provided the necessary force to redirect the pilecap compression force C_{br} into the major compression arch D_3 and D_4. Additional top longitudinal reinforcement to resist the horizontal component ΔT_b of D_2 was necessary. This pilecap reinforcement was relatively easy to place and did not cause any construction problems.

4) The vertical components of struts D_1 and D_2 were assumed to be equal and accordingly the magnitude of the vertical component of each strut was $T_s = 0.25T_c$ from Eq.(B.6). However, since the column inelastic action may develop in any direction other than parallel to one of the principal axes of the footing, the required external stirrups for the column-pilecap joint was interpreted as :

$$A_{jv} = 4T_s = 4 \times 0.125\lambda_o A_{sc}\frac{f_{yc}}{f_{yv}} = 0.5\lambda_o A_{sc}\frac{f_{yc}}{f_{yv}} \qquad (B.7)$$

where f_{yv} is the yield strength of the vertical stirrup and λ_o is the overstrength factor. To ensure active participation of the external vertical stirrups in the joint force transfer mechanism, this reinforcement was placed over $h_f/2$ from the joint face, where h_f is the pilecap depth[26,35]. The stirrups were uniformly placed around the column.

5) Although no vertical joint reinforcement was required by the mechanism, to provide assistance in bond transfer, vertical joint reinforcement with an area A_{vi} obtained from Eq.(B.8) was placed inside the column core.

$$A_{vi} = 0.0625\lambda_o A_{sc}\frac{f_{yc}}{f_{yv}} \qquad (B.8)$$

where A_{sc} is the total area and f_{ye} is the yield strength of the column longitudinal reinforcement and f_{yv} is the yield strength of the vertical joint reinforcement.

6) When longitudinal column reinforcement is prematurely terminated within the joint, a poor anchorage condition developed for the bars. This is because the bars can not be effectively clamped into the joint diagonal strut, resulting in bond slip. Thus, the longitudinal column reinforcement with straight bar ends was extended as close to the bottom pilecap reinforcement as possible with a minimum embedment length l_a as suggested in Eq. (B.9).

$$l_a \geq 0.3\lambda_o d_{bl} f_{yc} / \sqrt{f'_c} \qquad (B.9)$$

where d_{bl} is the diameter of longitudinal column reinforcement. The anchorage length requirement given in Eq.(B.9), which assumes an average bond stress of $1.17\sqrt{f'_c}$

over the entire bar length embedded into the joint[26], provides a much smaller development length than that obtained from the current design codes[1,5]. An investigation of the joint performance with such anchorage detail is reported elsewhere[34].

7) Volumetric ratio of the joint horizontal reinforcement, ρ_s, was obtained as follows:

$$\rho_s = \frac{0.3 A_{sc} \lambda_o f_{yc}}{f_{yh} l_a^2} \tag{B.10}$$

This provision was to account for the unbalanced horozontal force induced at node X by struts D_1 and D_2. When deriving the above equation, it was assumed that the unbalanced force at node X would not be greater than 25% of T_c as estimated from Eq. (B.6)[26,35].

8) When a circular column or pile frames into a tee or knee joint, a minimum amount of column spirals or hoops consistent with Eq.(B.11), was ensured within the joint to provide some tensile resistance when cracking occurs in the joint region.

$$\rho_s = \frac{0.29 \sqrt{f'_c}}{f_{yh}} \tag{B.11}$$

where ρ_s is the volumetric ratio of the transverse reinforcement, f_{yh} is the yield strength of the spirals or hoops, and f'_c is the compressive strength of concrete.

9) Strut D_2 imposes additional tension force in the pilecap top flexural reinforcement, as is apparent from equilibrium of forces under D_2 and T_s, see Figure B.6. Since the vertical external joint stirrups were placed over a length $h_f/2$ from the column face, the additional horizontal force to be resisted by the top(bottom for pilecap-pile joint)

pilecap reinforcement was approximated $0.5T_s$. The additional pilecap longitudinal top(bottom for pilecap-pile joint) reinforcement :

$$\Delta A_b = 0.0625\lambda_\circ A_{sc}\frac{f_{yc}}{f_{yv}} \qquad (B.12)$$

was thus provided for the stability of strut D_2 at node Z.

When considering equilibrium at node Y in the force transfer model as shown in Figure B.6, it is obvious that the beam compression force no longer acts horizontally at the pilecap-joint interface. Instead, the tension force T_s redirects the compression force towards node W, forming the compression strut D_4. Further, the remaining $0.5T_c$ could be transferred from the inner bars by increase in the inclination of the diagonal strut, forming the strut D_3 at node W. The change of direction of the strut creates an additional clamping effect for the longitudinal column tension reinforcement, particularly for those bars located away from the extreme tension fiber of the column section.

When determining the appropriate joint reinforcement required for the column-pilecap joint using Eqs.(B.7)-(B.12), equal yield strengths for the reinforcement in the joint (i.e. $f_{ye} = f_{yv} = f_{yh}$) were assumed. The assumed material properties were such that less conservative detailing for the joint region would result.

Appendix C: Hysteresis Loops
at Loading Phases 2 and 3
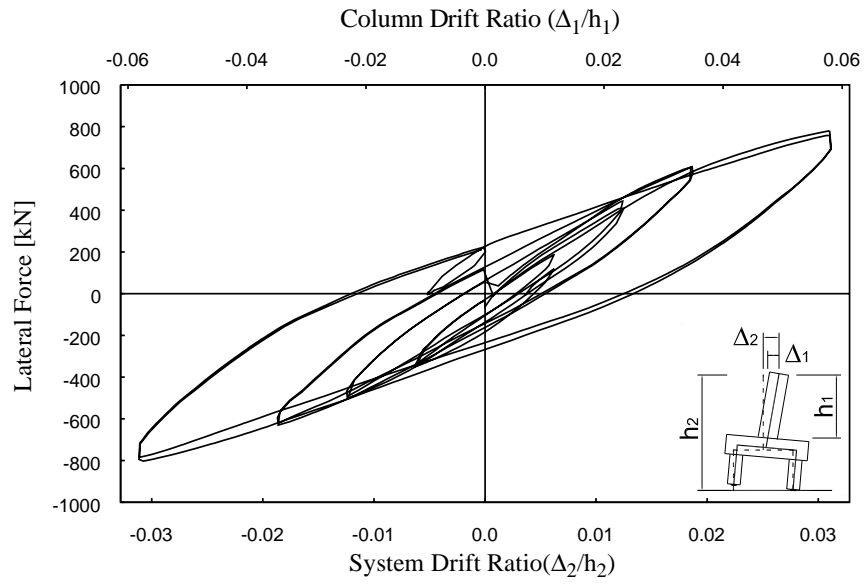
Figure C.1: Unit CFPS1 - orthogonal direction(E-W) loading at loading phase 2
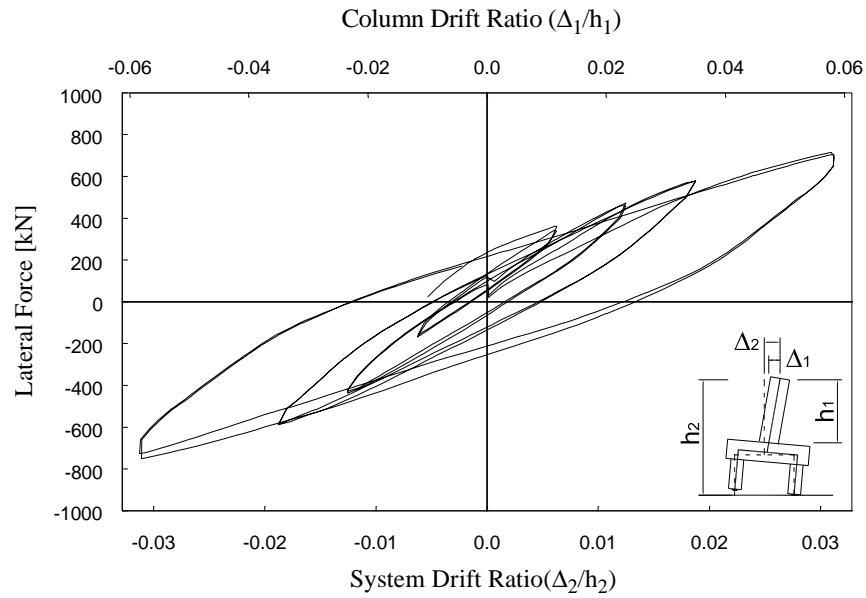
Figure C.2: Unit CFPS1 - orthogonal direction(N-S) loading at loading phase 2
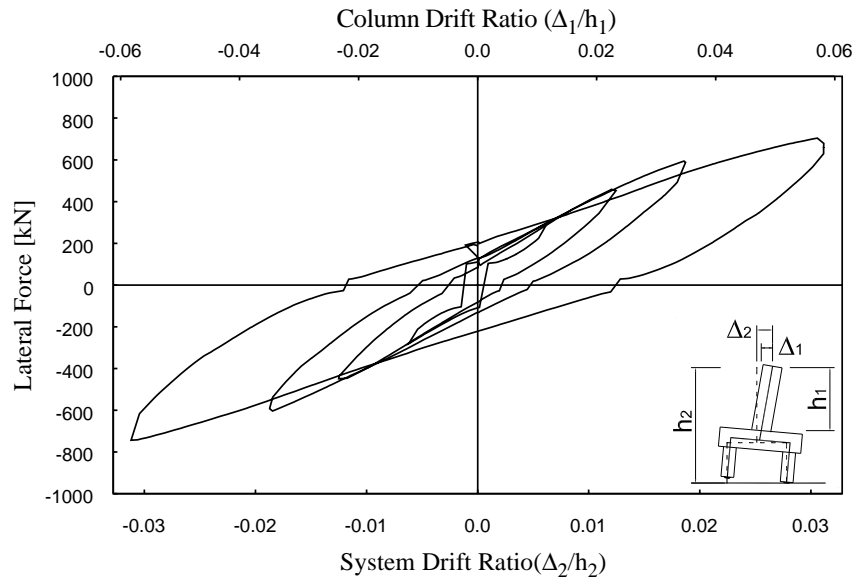
Figure C.3: Unit CFPS1 - diagonal direction(SE-NW) loading at loading phase 2
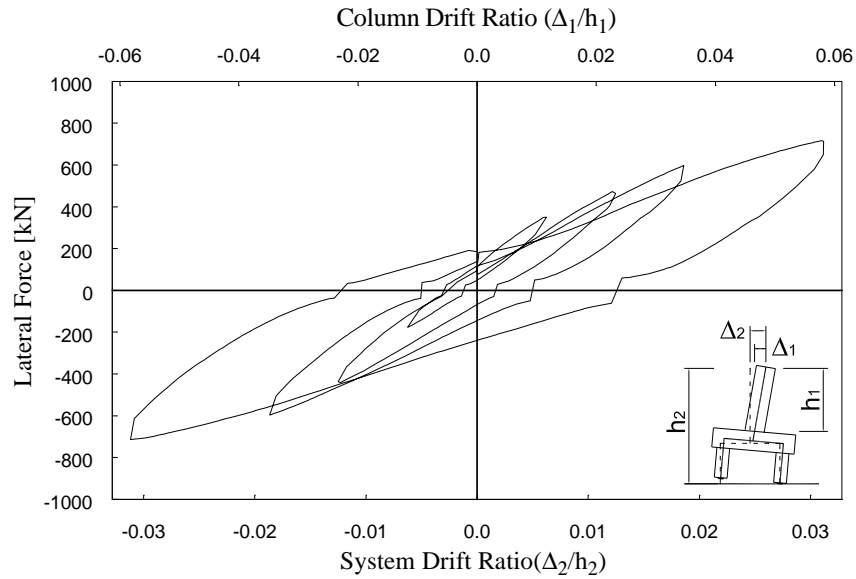
Figure C.4: Unit CFPS1 - diagonal direction(SE-NW) loading at loading phase 2
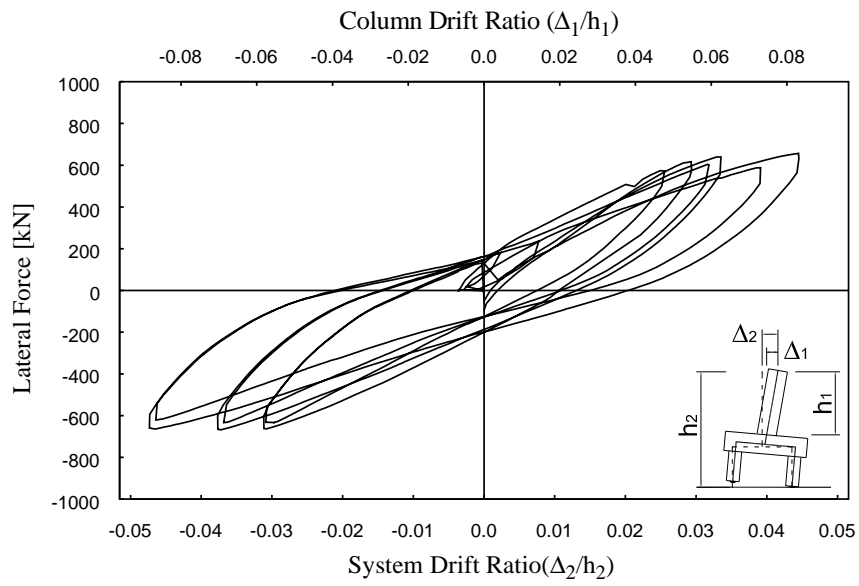
Figure C.5: Unit CFPS1 - orthogonal direction(E-W) loading at loading phase 3
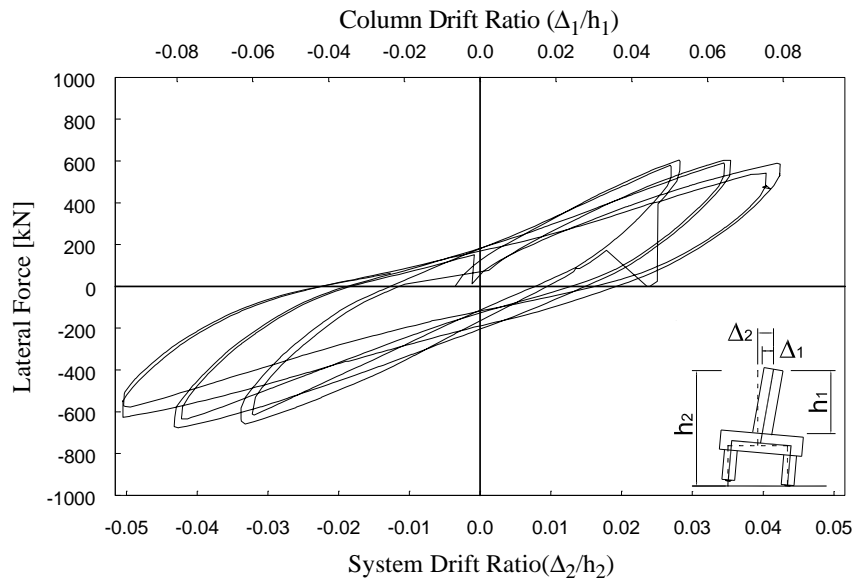
Figure C.6: Unit CFPS1 - orthogonal direction(N-S) loading at loading phase 3

272
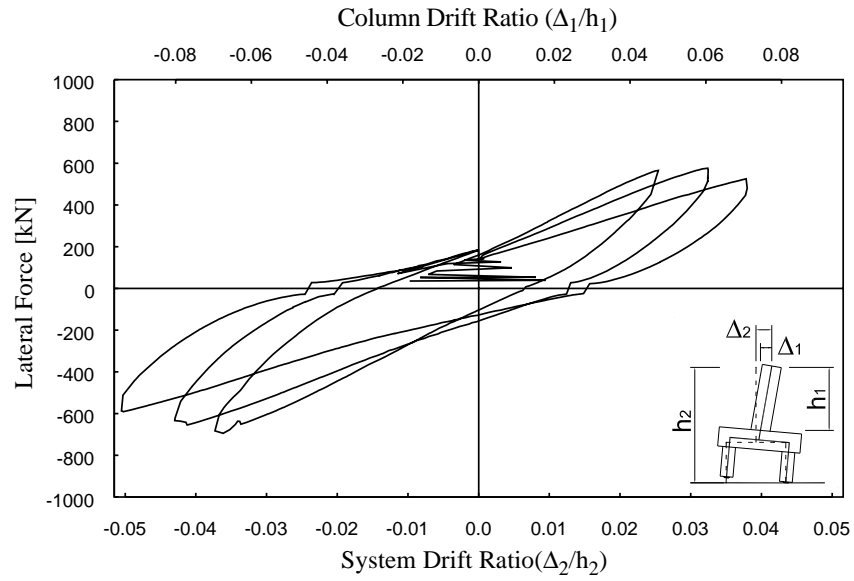
Figure C.7: Unit CFPS1 - diagonal direction(SE-NW) loading at loading phase 3
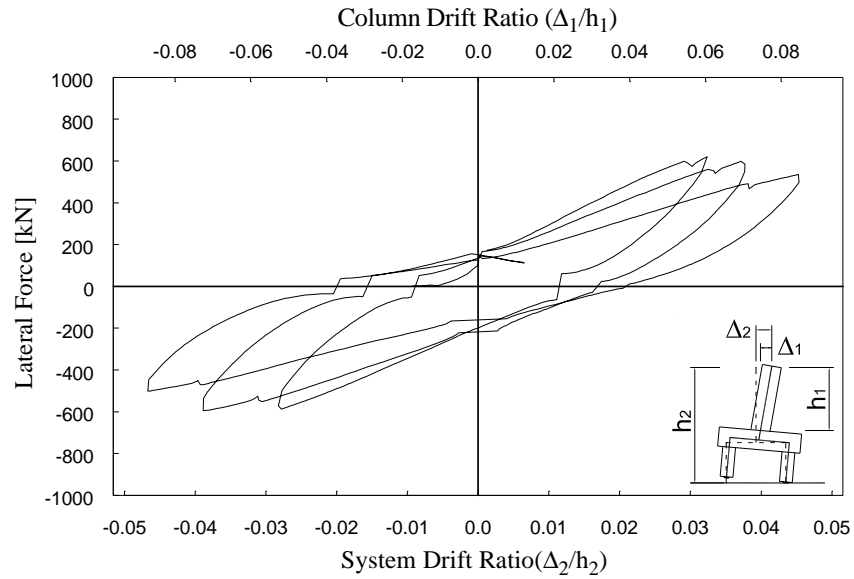
Figure C.8: Unit CFPS1 - diagonal direction(SW-NE) loading at loading phase 3
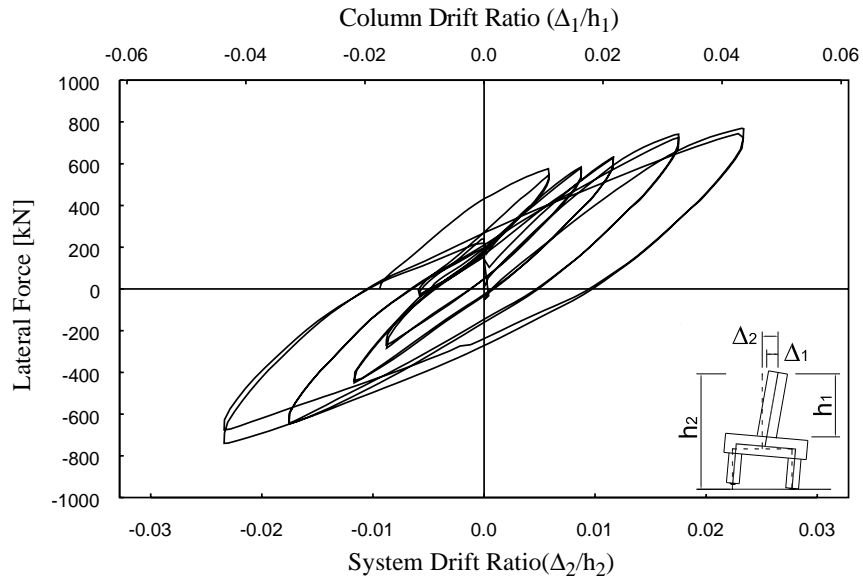
Figure C.9: Unit CFPS2 - orthogonal direction(E-W) loading at loading phase 2
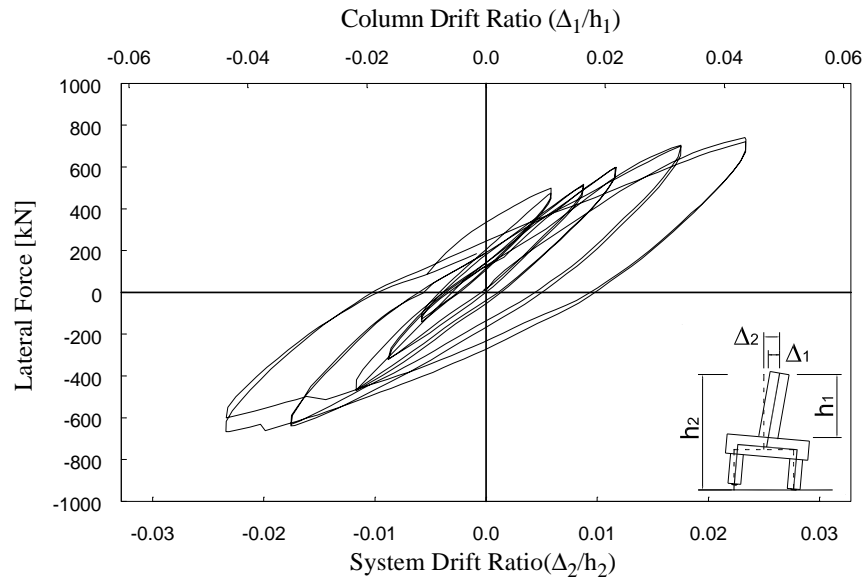
Figure C.10: Unit CFPS2 - orthogonal direction(N-S) loading at loading phase 2
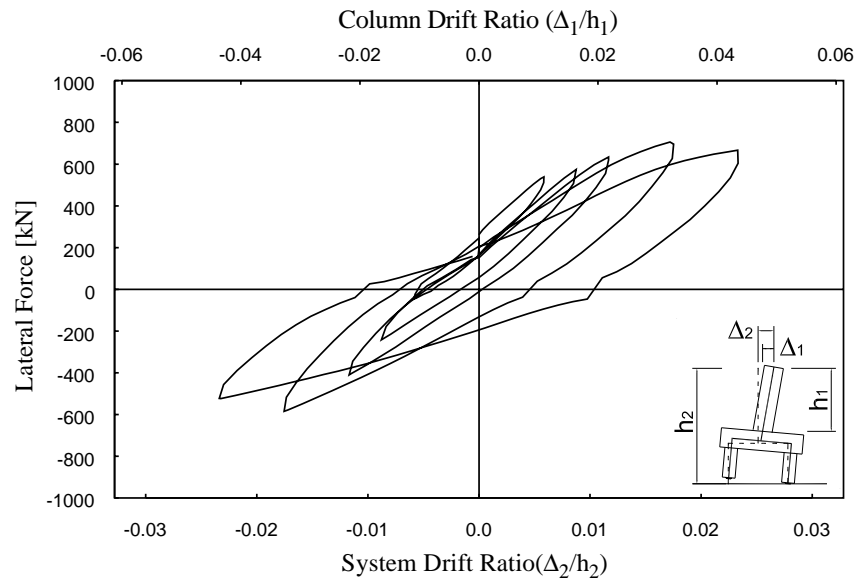
Figure C.11: Unit CFPS2 - diagonal direction(SE-NW) loading at loading phase 2
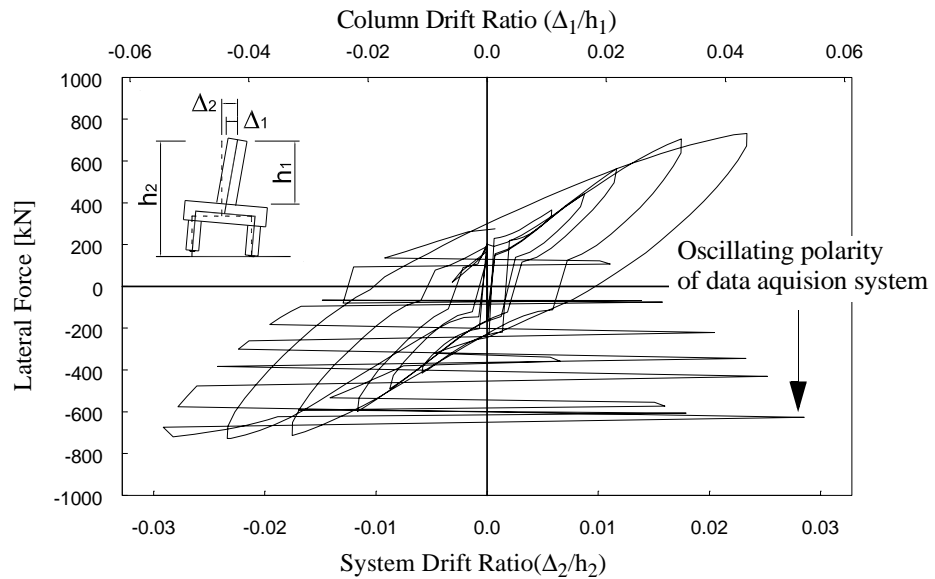
Figure C.12: Unit CFPS2 - diagonal direction(SW-NE) loading at loading phase 2

275

Appendix D: Applied Gravity Load to Test Units During Loading Phases 2 and 3
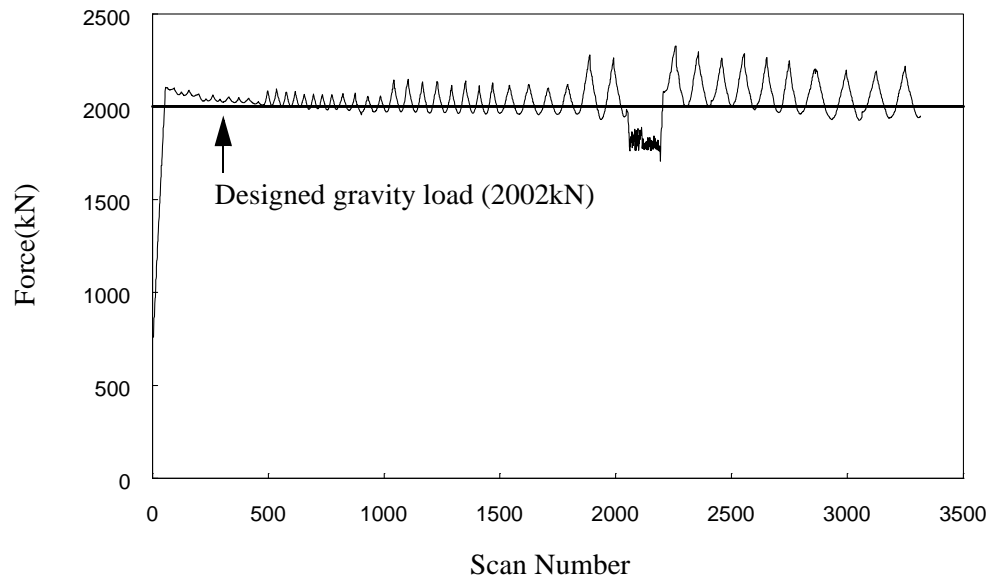
Figure D.1: Applied gravity load during the test of CFPS1 (Loading Phase 2)
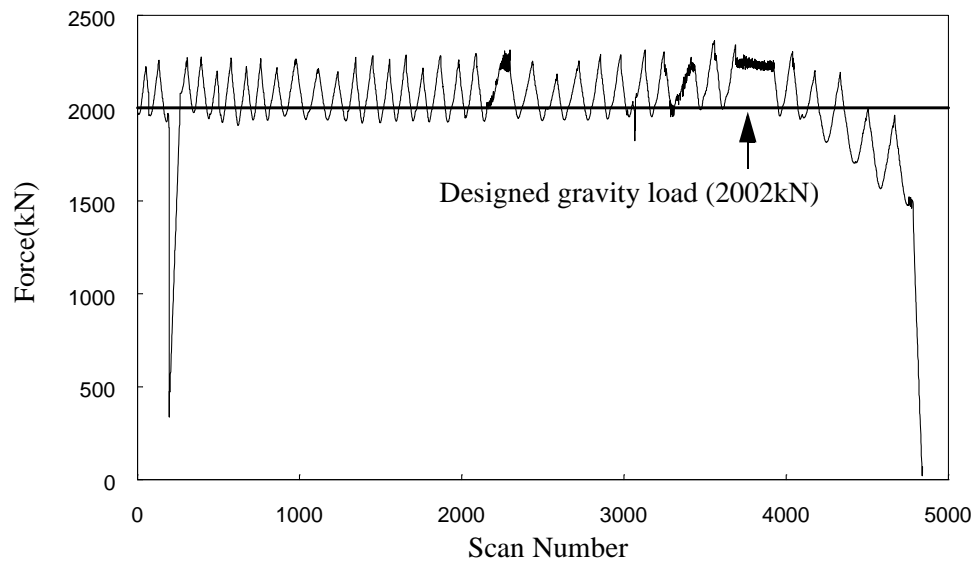
Figure D.2: Applied gravity load during the test of CFPS1 (Loading Phase 3)
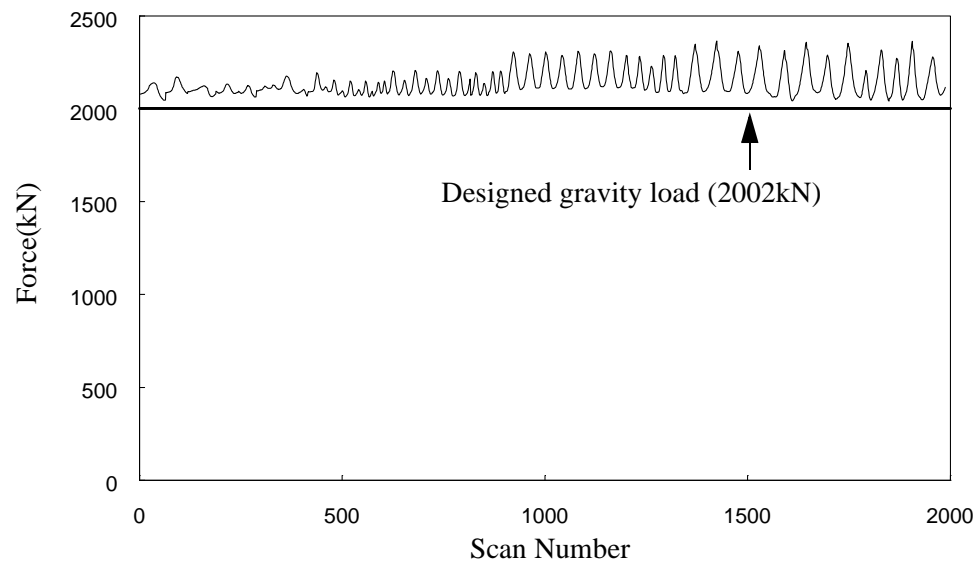
Figure D.3: Applied gravity load during the test of CFPS2 (Loading Phase 2)

Appendix E: Flexibility coefficients for the force method under diagonal direction loading
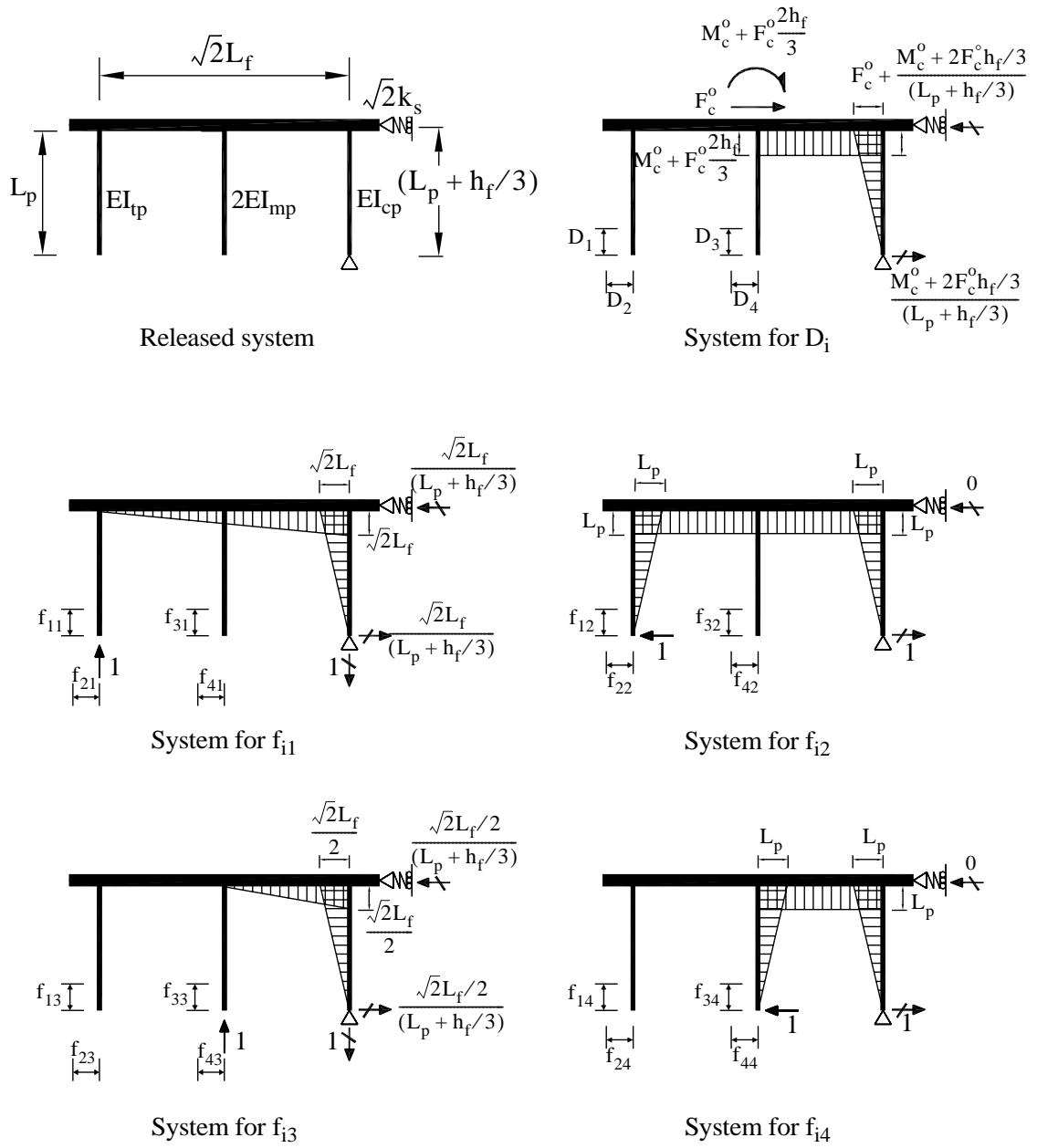
Figure E.1: Bending moment diagrams for flexibility coefficients

$$D_1 = \frac{-\sqrt{2}(3M_c^\circ + 2F_c^\circ h_f)}{E \cdot h_f^3}\left[2(D_p + L_f)\log\left(\frac{2D_p}{2D_p + L_f}\right) + L_f\right]$$

$$+ \frac{\sqrt{2}(3M_c^\circ + 2F_c^\circ h_f)L_f L_p^3}{(3L_p + h_f)^2\beta_{cp}EI_p} + \frac{9(F_c^\circ L_p + F_c^\circ h_f + M_c^\circ)L_f}{(L_p + h_f/3)^2 k_s}$$

$$D_2 = \frac{-2(3M_c^\circ + 2F_c^\circ h_f)L_p}{E \cdot h_f^3}\log\left(\frac{2D_p}{2D_p + L_f}\right) + \frac{(M_c^\circ + 2F_c^\circ h_f/3)L_p^3}{3(L_p + h_f/3)\beta_{cp}EI_p}$$

$$D_3 = \frac{-\sqrt{2}(3M_c^\circ + 2F_c^\circ h_f)}{E \cdot h_f^3}\left[(2D_p + L_f)\log\left(\frac{2D_p}{2D_p + L_f}\right) + L_f\right]$$

$$+ \frac{\sqrt{2}(3M_c^\circ + 2F_c^\circ h_f)L_f L_p^3}{2(3L_p + h_f)^2\beta_{cp}EI_p} + \frac{9(F_c^\circ L_p + F_c^\circ h_f + M_c^\circ)L_f}{2(L_p + h_f/3)^2 k_s}$$

$$D_4 = \frac{-2(3M_c^\circ + 2F_c^\circ h_f)L_p}{E \cdot h_f^3}\log\left(\frac{2D_p}{2D_p + L_f}\right) + \frac{(3M_c^\circ + 2F_c^\circ h_f)L_p^3}{3(3L_p + h_f)\beta_{cp}EI_p}$$

$$f_{11} = \frac{6}{E \cdot h_f^3}\left[(4D_p^2 + 4D_pL_f + 2L_f^2)\log\left(\frac{L_f}{2D_p} + 1\right) - 2D_pL_f - \frac{3L_f^2}{2}\right]$$

$$+ \frac{2L_f^2 L_p}{3\beta_{cp}EI_p} + \left(\frac{L_f}{L_p}\right)^2\frac{\sqrt{2}}{k_s}$$

$$f_{21} = \frac{6\sqrt{2}L_f L_p}{E \cdot h_f^3}\left[\log\left(\frac{L_f}{2D_p} + 1\right)\right] + \frac{\sqrt{2}L_f L_p^2}{3\beta_{cp}EI_p}$$

$$f_{31} = \frac{6}{E \cdot h_f^3}\left[(2D_p^2 + 3D_pL_f + L_f^2)\log\left(\frac{L_f}{2D_p} + 1\right) - D_pL_f - \frac{5}{4}L_f^2\right]$$

$$+ \frac{L_f^2 L_p}{3\beta_{cp}EI_p} + \left(\frac{L_f}{L_p}\right)^2\frac{1}{k_s}$$

$$f_{41} = \frac{6\sqrt{2}L_p}{E \cdot h_f^3}\left[(L_f + D_p)\log\left(\frac{L_f}{2D_p} + 1\right) - \frac{L_f}{2}\right] + \frac{\sqrt{2}L_f L_p^2}{3\beta_{cp}EI_p}$$

$$f_{12} = \frac{6\sqrt{2}L_f L_p}{E \cdot h_f^3}\left[\log\left(\frac{L_f}{2D_p} + 1\right)\right] + \frac{\sqrt{2}L_f L_p^2}{3\beta_{cp}EI_p}$$

$$f_{22} = \frac{12L_p^2}{E \cdot h_f^3}\left[\log\left(\frac{L_f}{2D_p} + 1\right)\right] + \frac{L_p^3}{3\beta_{cp}EI_p}$$

$$f_{32} = \frac{6\sqrt{2}L_p}{E \cdot h_f^3}\left[\left(D_p + \frac{L_f}{2}\right)\log\left(\frac{L_f}{2D_p} + 1\right) - \frac{L_f}{2}\right] + \frac{\sqrt{2}L_fL_p^2}{6\beta_{cp}EI_p}$$

$$f_{42} = \frac{6L_p^2}{E \cdot h_f^3}\left[\log\left(\frac{L_f}{2D_p} + 1\right)\right] + \frac{L_p^3}{3\beta_{cp}EI_p}$$

$$f_{13} = \frac{6}{E \cdot h_f^3}\left[(2D_p^2 + 3D_pL_f + L_f^2)\log\left(\frac{L_f}{2D_p} + 1\right) - D_pL_f - \frac{5}{4}L_f^2\right]$$
$$+ \frac{L_f^2L_p}{3\beta_{cp}EI_p} + \left(\frac{L_f}{L_p}\right)^2\frac{1}{k_s}$$

$$f_{23} = \frac{6\sqrt{2}L_p}{E \cdot h_f^3}\left[\left(D_p + \frac{L_f}{2}\right)\log\left(\frac{L_f}{2D_p} + 1\right) - \frac{L_f}{2}\right] + \frac{\sqrt{2}L_fL_p^2}{6\beta_{cp}EI_p}$$

$$f_{33} = \frac{6}{E \cdot h_f^3}\left[\left(2D_p^2 + 2D_pL_f + \frac{L_f^2}{2}\right)\log\left(\frac{L_f}{2D_p} + 1\right) - D_pL_f - \frac{3}{4}L_f^2\right]$$
$$+ \frac{L_f^2L_p}{6\beta_{cp}EI_p} + \frac{1}{2}\left(\frac{L_f}{L_p}\right)^2\frac{1}{k_s}$$

$$f_{43} = \frac{6\sqrt{2}L_p}{E \cdot h_f^3}\left[\left(\frac{L_f}{2} + D_p\right)\log\left(\frac{L_f}{2D_p} + 1\right) - \frac{L_f}{2}\right] + \frac{\sqrt{2}L_fL_p^2}{6\beta_{cp}EI_p}$$

$$f_{14} = \frac{6\sqrt{2}L_p}{E \cdot h_f^3}\left[(L_f + D_p)\log\left(\frac{L_f}{2D_p} + 1\right) - \frac{L_f}{2}\right] + \frac{\sqrt{2}L_fL_p^2}{3\beta_{cp}EI_p}$$

$$f_{24} = \frac{6L_p^2}{E \cdot h_f^3}\left[\log\left(\frac{L_f}{2D_p} + 1\right)\right] + \frac{L_p^3}{3\beta_{cp}EI_p}$$

$$f_{34} = \frac{6\sqrt{2}L_p}{E \cdot h_f^3}\left[\left(\frac{L_f}{2} + D_p\right)\log\left(\frac{L_f}{2D_p} + 1\right) - \frac{L_f}{2}\right] + \frac{\sqrt{2}L_fL_p^2}{6\beta_{cp}EI_p}$$

$$f_{44} = \frac{6L_p^2}{E \cdot h_f^3}\left[\log\left(\frac{L_f}{2D_p} + 1\right)\right] + \frac{L_p^3}{3EI_p}\left(\frac{2}{\beta_{mp}} + \frac{1}{\beta_{cp}}\right)$$

Appendix F: Strain Profiles of Column-Pilecap Joint of CFPS1 at Loading Phase 1

(b) Shear reinforcement

(a) Flexural reinforcement
(Top & Bottom mat)

Figure F.2: Schedule of pilecap longitudinal(flexural) and stirrup(shear) reinforcement strain gauges

284
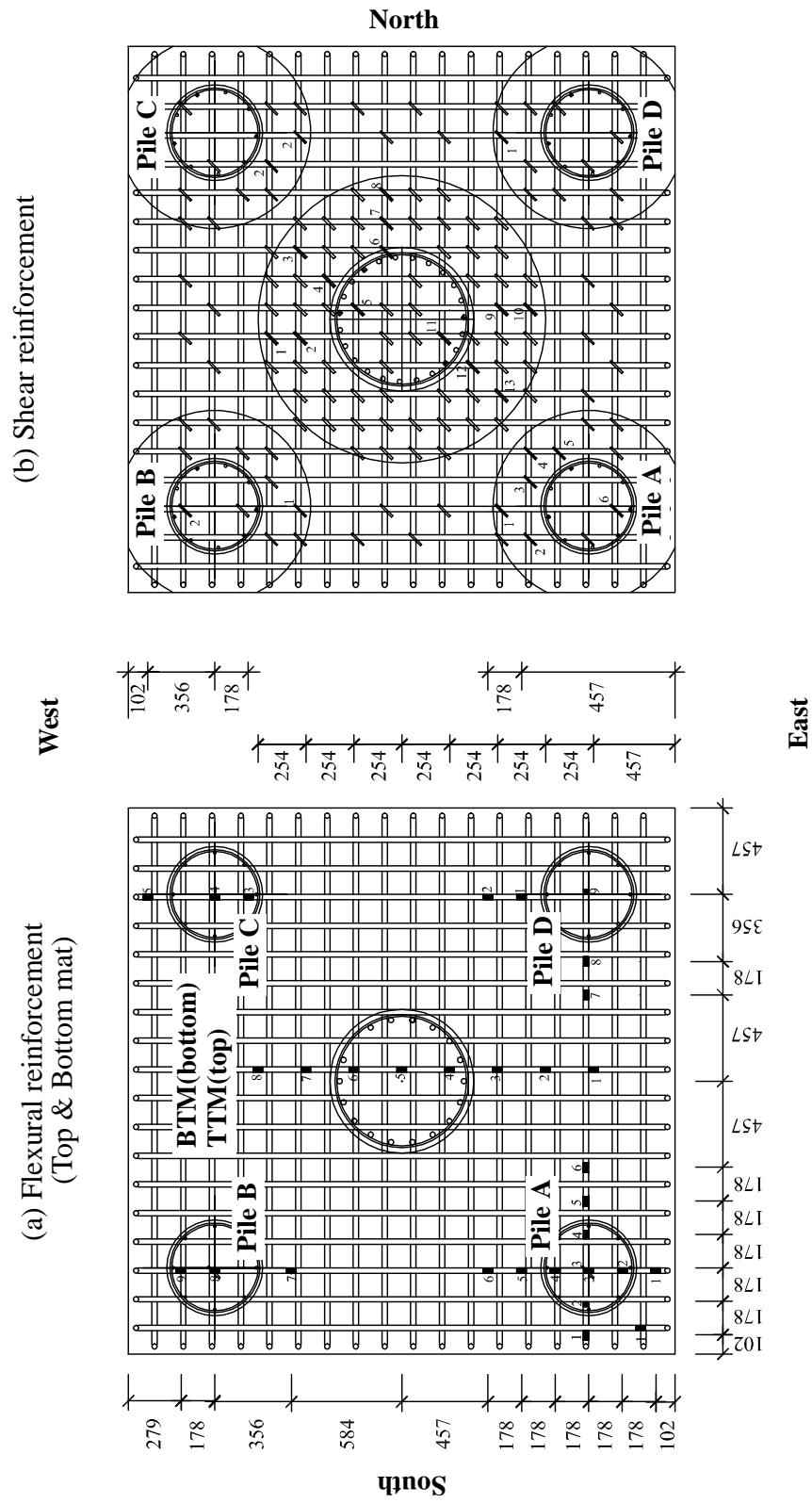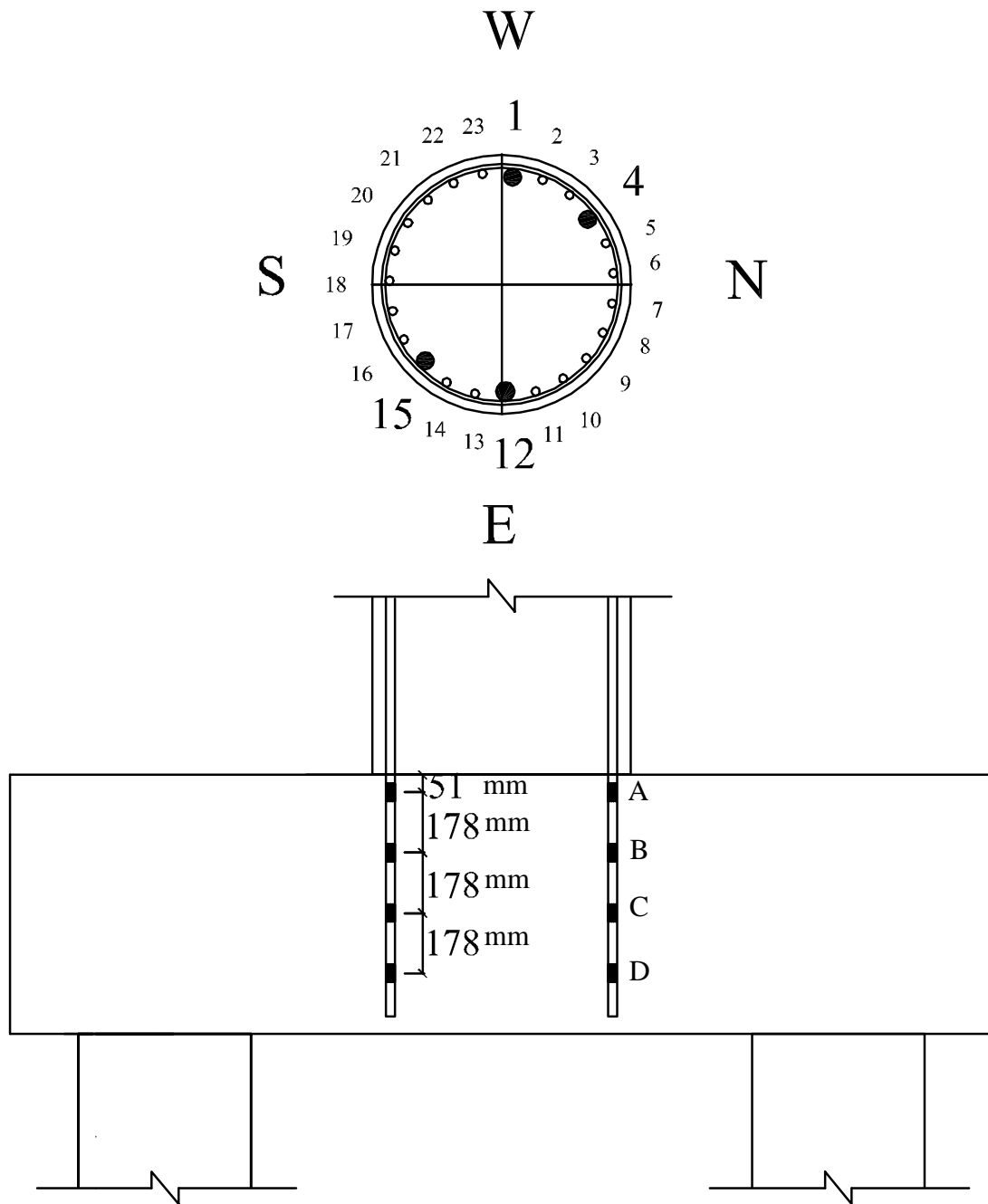
Figure F.1: Strain gauge names and locations on the column longitudinal bar

CSW

CSS — CSN

CSE

L_{ph} = 457mm

4

290mm

3

90mm

190mm

2

190mm

1
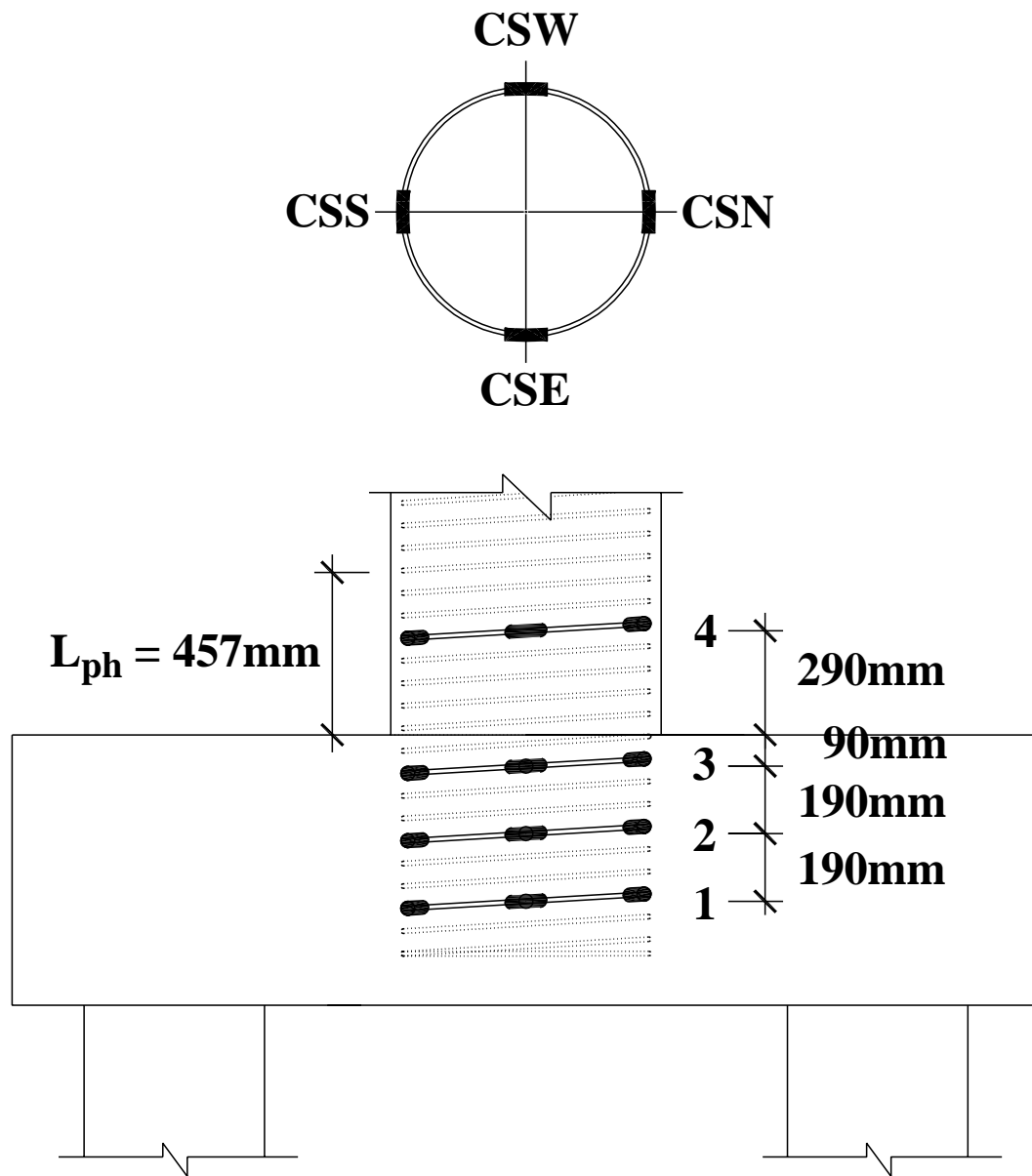
Figure F.3: Strain gauge names and locations on the column spiral bar
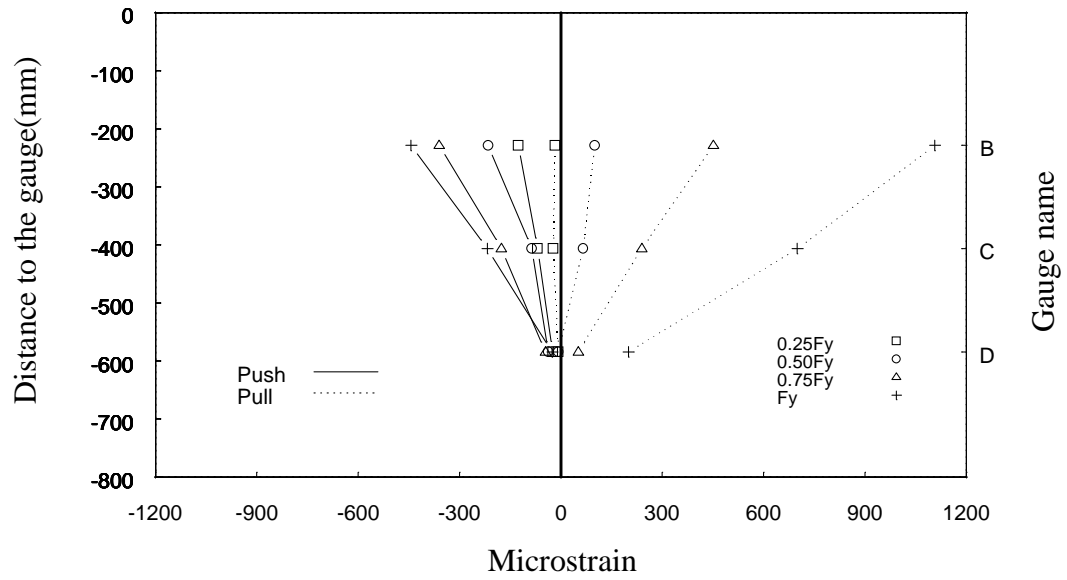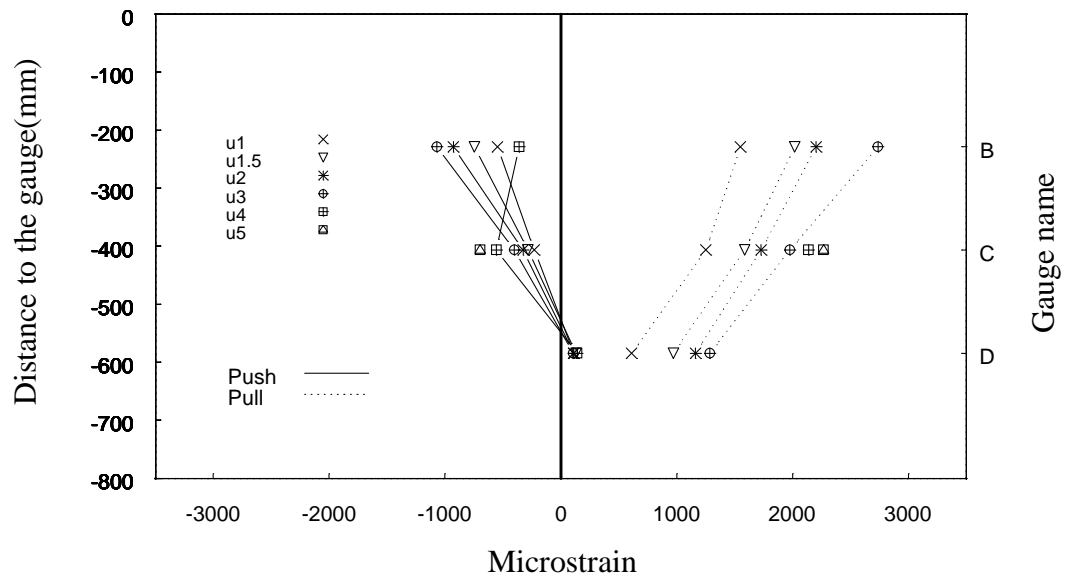
Figure F.4: Strain profile of column longitudinal 1st bar at column-pilecap joint (E-W direction loading at loading phase 1, see Figure F.1)

Initial stages of testing

Final stages of testing
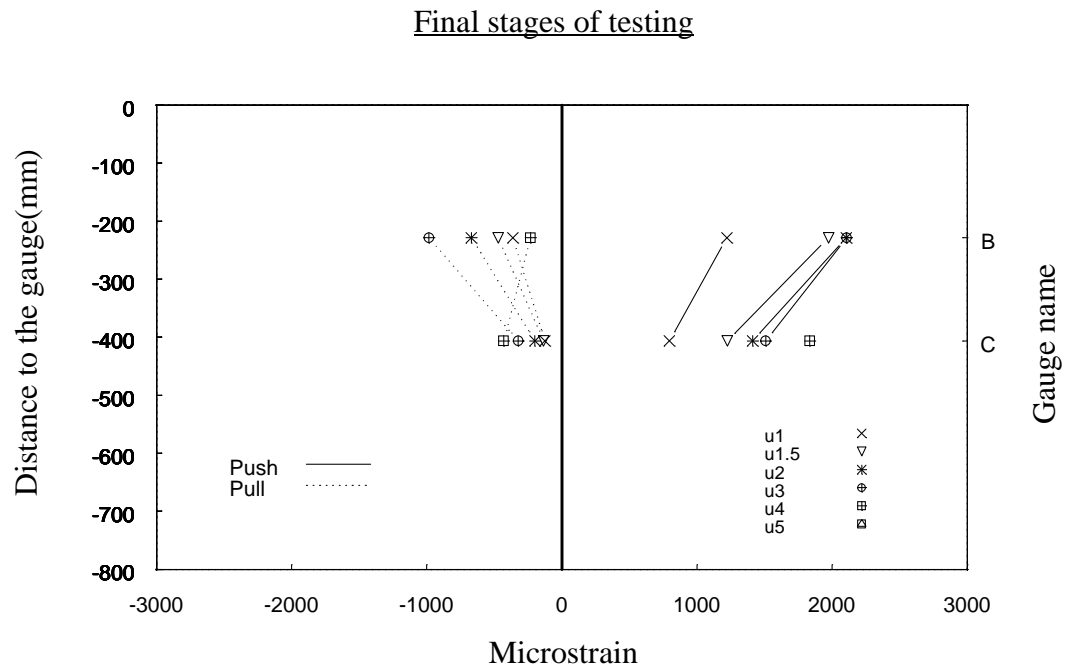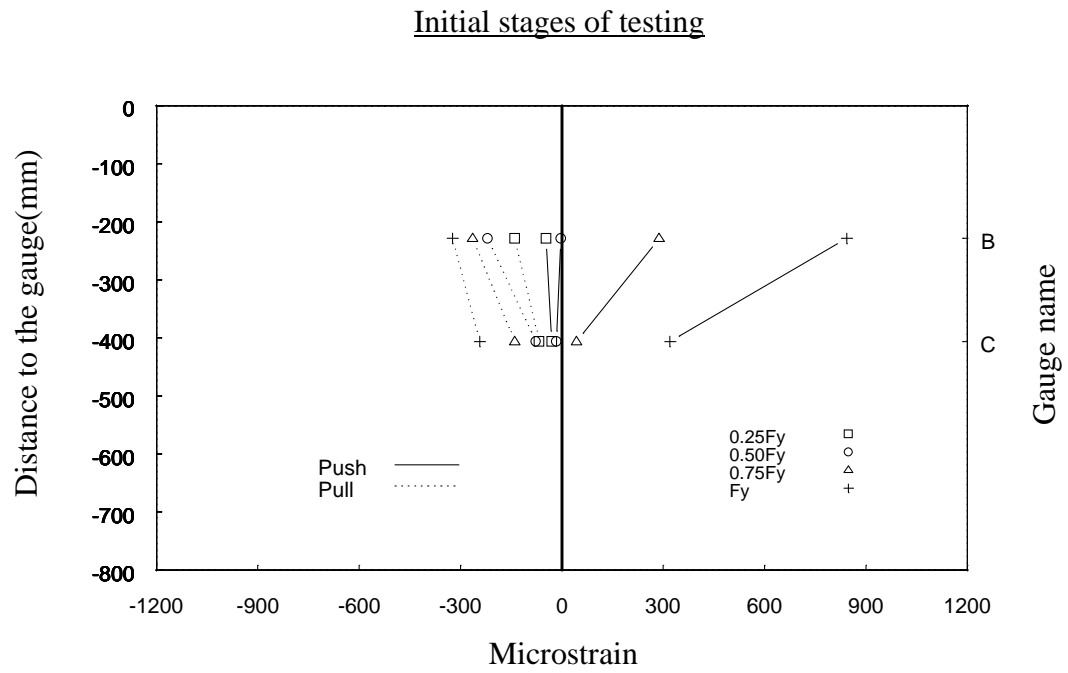
Figure F.5: Strain profile of column longitudinal 12th bar at column-pilecap joint
(E-W direction loading at loading phase 1, see Figure F.1)

288

Initial stages of testing
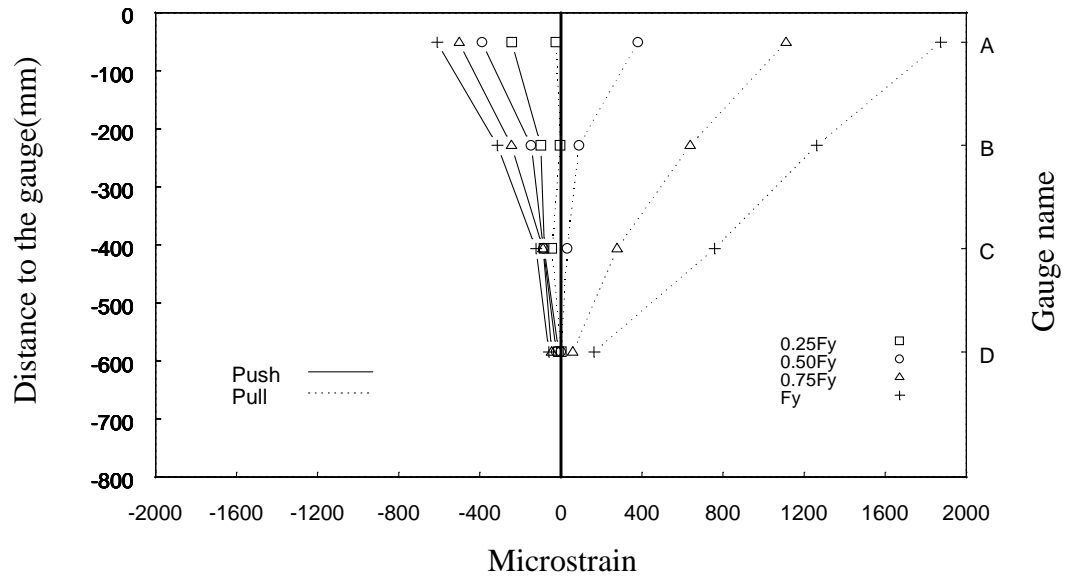
Final stages of testing
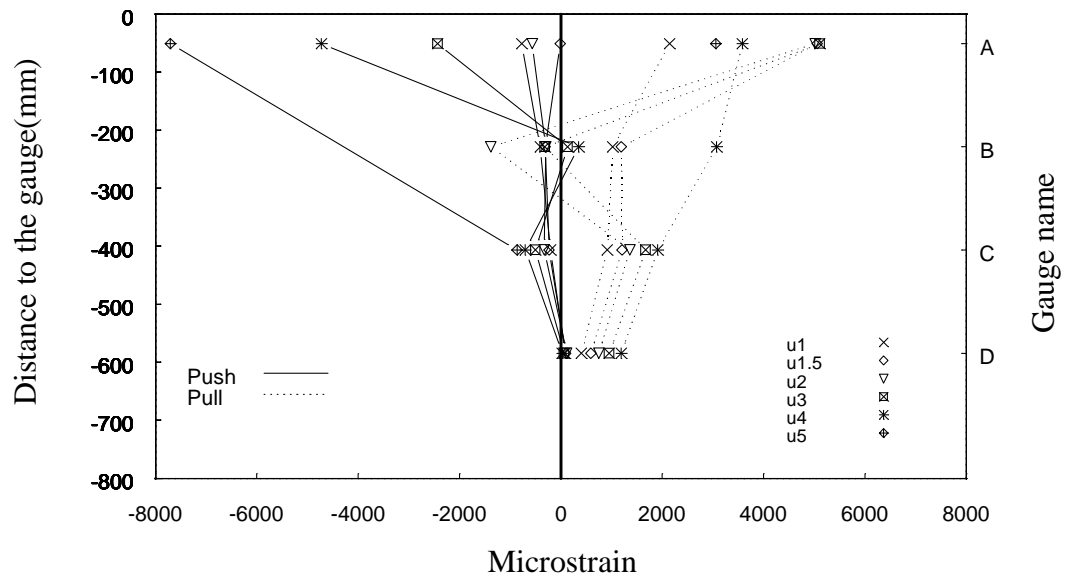
Figure F.6: Strain profile of column longitudinal 4th bar at column-pilecap joint
(SE-NW direction loading at loading phase 1, see Figure F.1)

Initial stages of testing
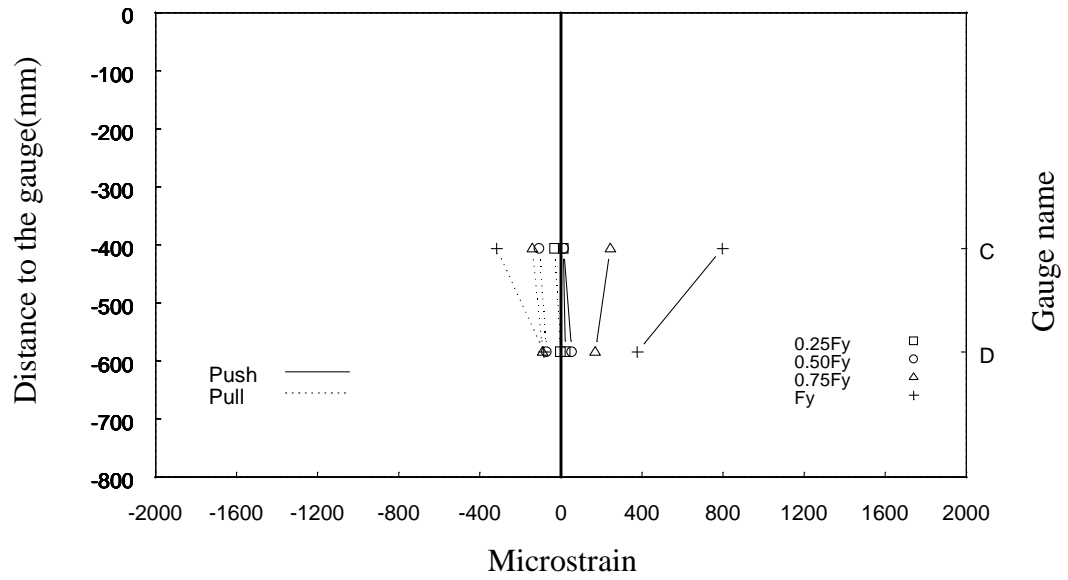
Final stages of testing
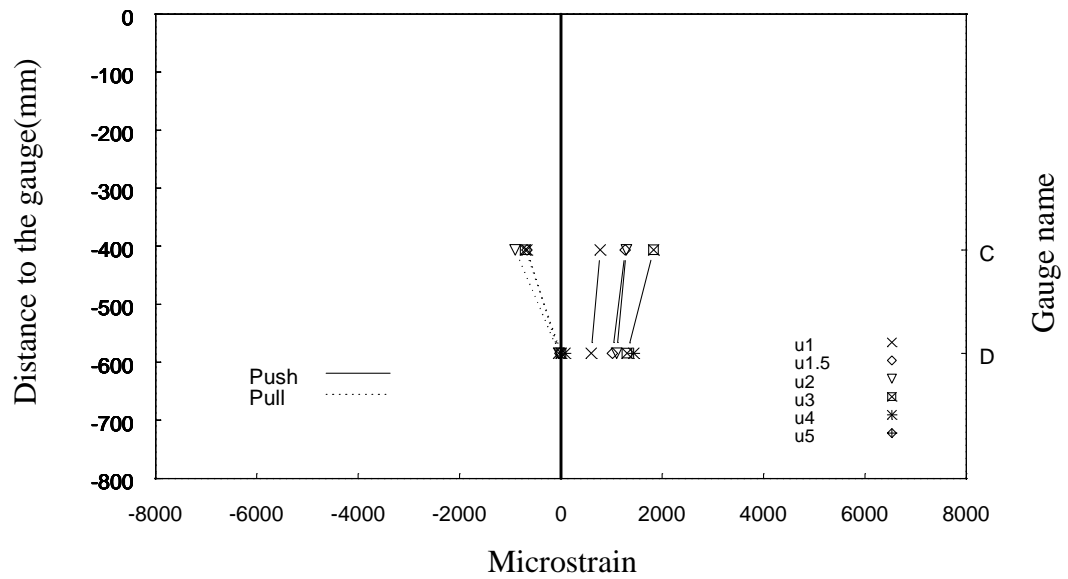
Figure F.7: Strain profile of column longitudinal 15th bar at column-pilecap joint (SE-NW direction loading at loading phase 1, see Figure F.1)

290
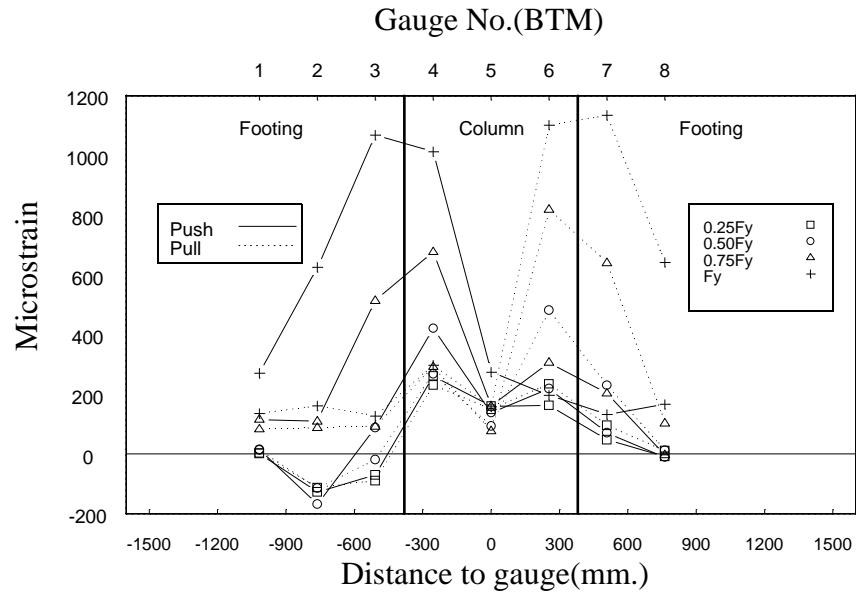
Figure F.8: Peak strain profiles of pilecap bottom reinforcement(BTM)
(E-W direction loading at column pre-yield in loading phase 1, see Figure F.2)
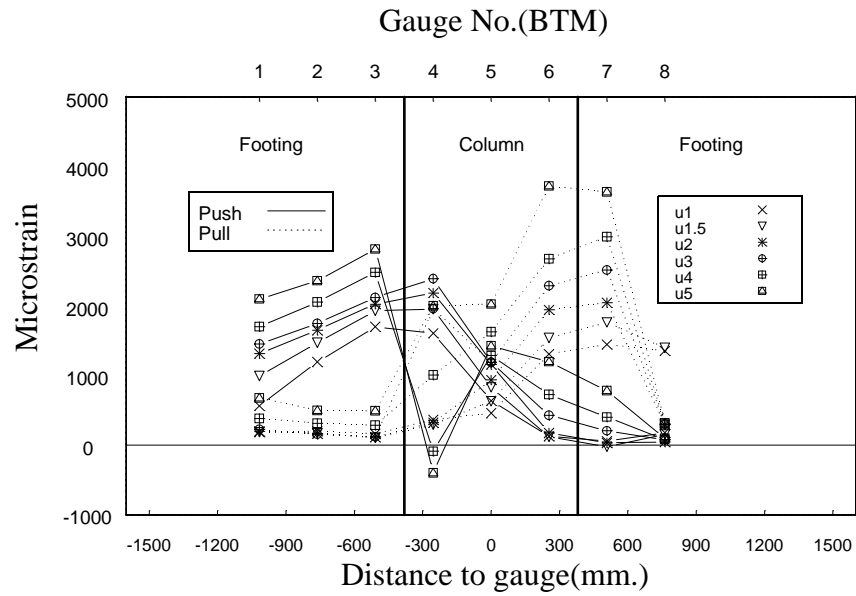
Figure F.9: Peak strain profiles of pilecap bottom reinforcement(BTM)
(E-W direction loading at column post-yield in loading phase 1, see Figure F.2)

Gauge No.(BTM)
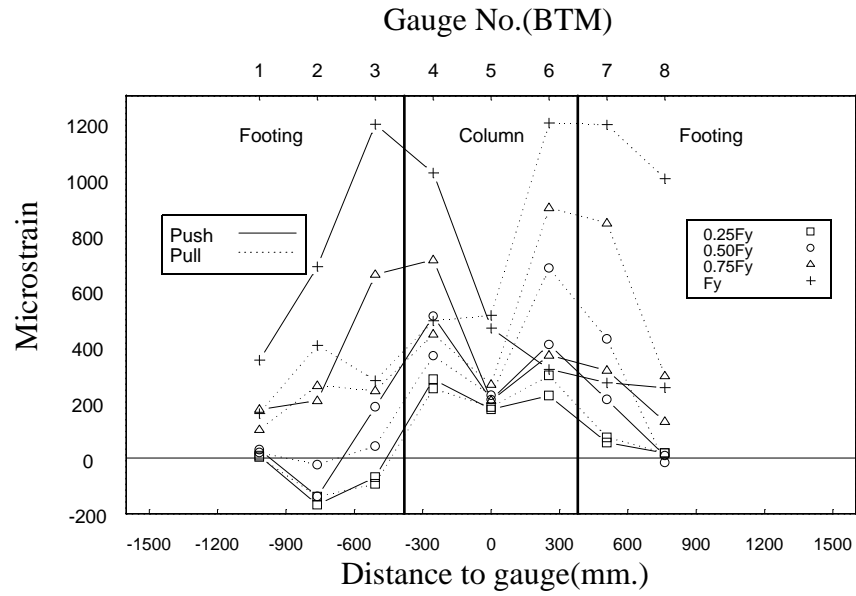
Figure F.10: Peak strain profiles of pilecap bottom reinforcement(BTM)
(SE-NW direction loading at column pre-yield in loading phase 1, see Figure F.2)

Gauge No.(BTM)
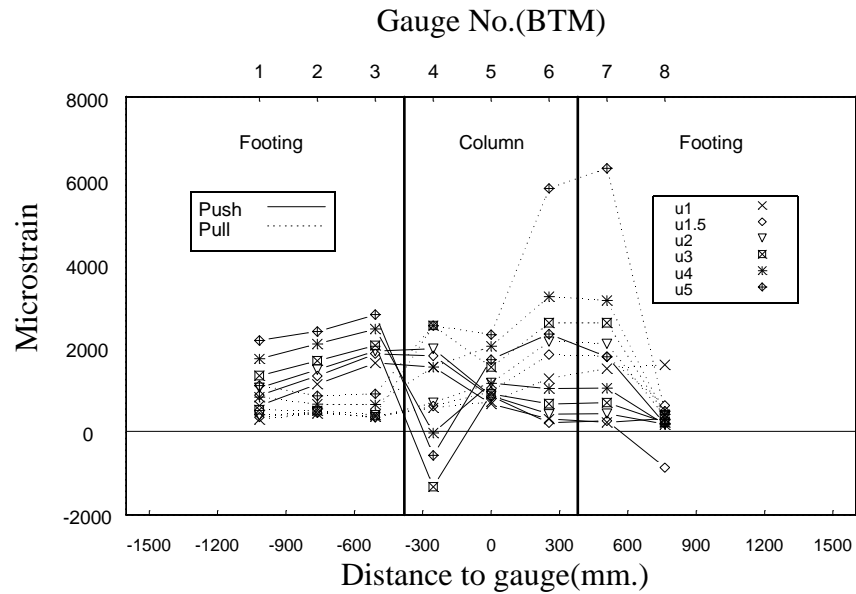
Figure F.11: Peak strain profiles of pilecap bottom reinforcement(BTM)
(SE-NW direction loading at column post-yield in loading phase 1, see Figure F.2)
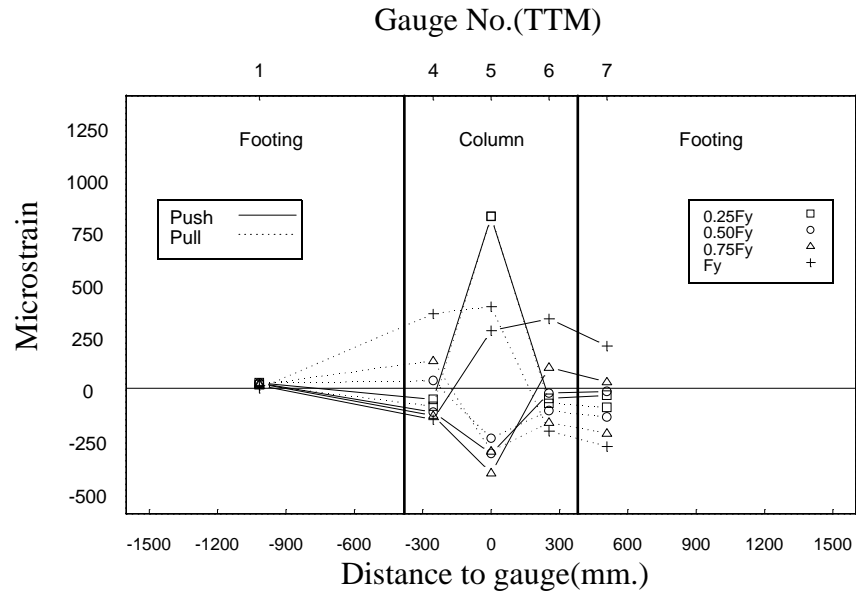
Figure F.12: Peak strain profiles of pilecap top reinforcement(TTM)
(E-W direction loading at column pre-yield in loading phase 1, see Figure F.2)
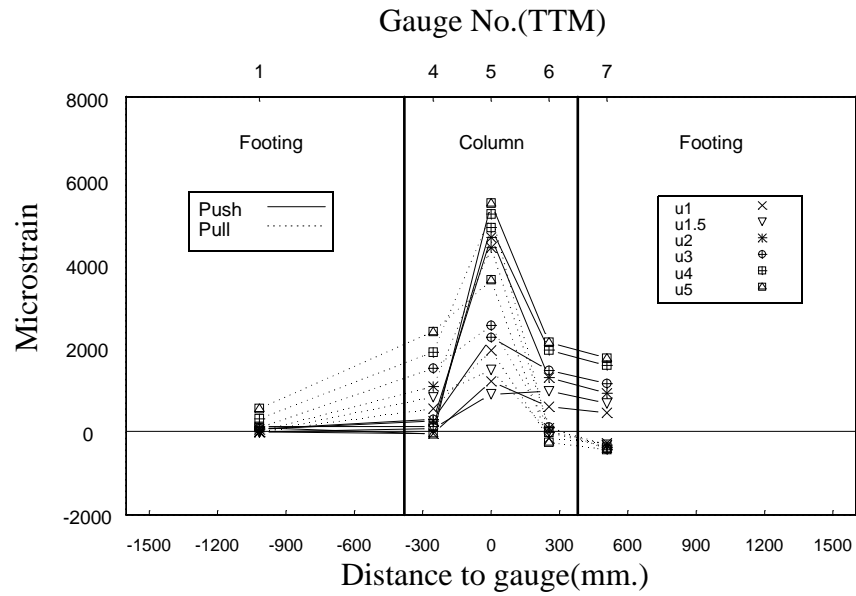
Figure F.13: Peak strain profiles of pilecap top reinforcement(TTM)
(E-W direction loading at column post-yield in loading phase 1, see Figure F.2)

Gauge No.(TTM)
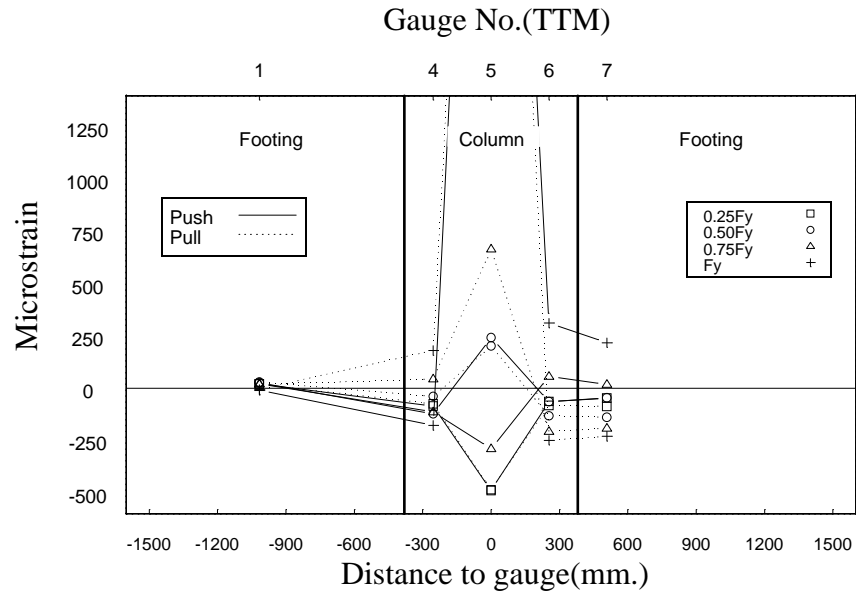
Figure F.14: Peak strain profiles of pilecap top reinforcement(TTM)
(SE-NW direction loading at column pre-yield in loading phase 1, see Figure F.2)

Gauge No.(TTM)
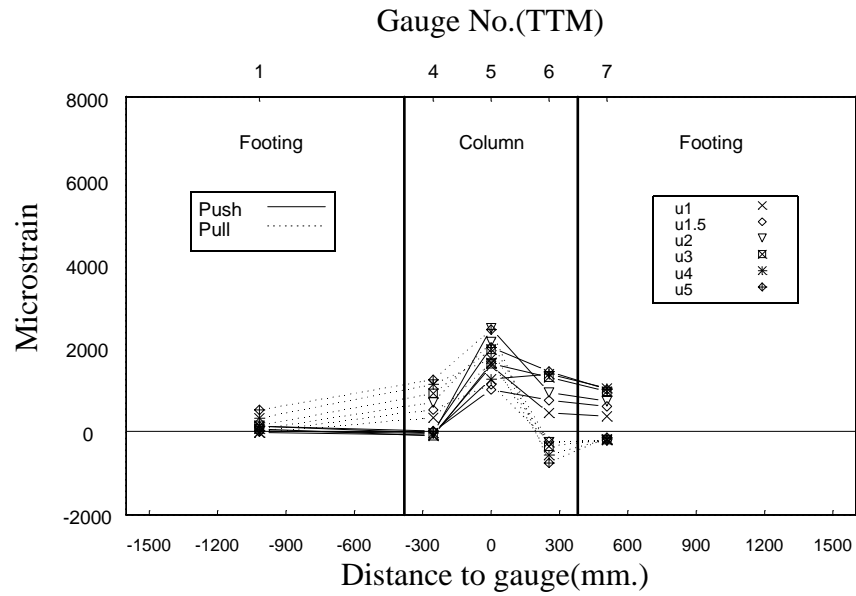
Figure F.15: Peak strain profiles of pilecap top reinforcement(TTM)
(SE-NW direction loading at column post-yield in loading phase 1, see Figure F.2)

Gauge No.(B)
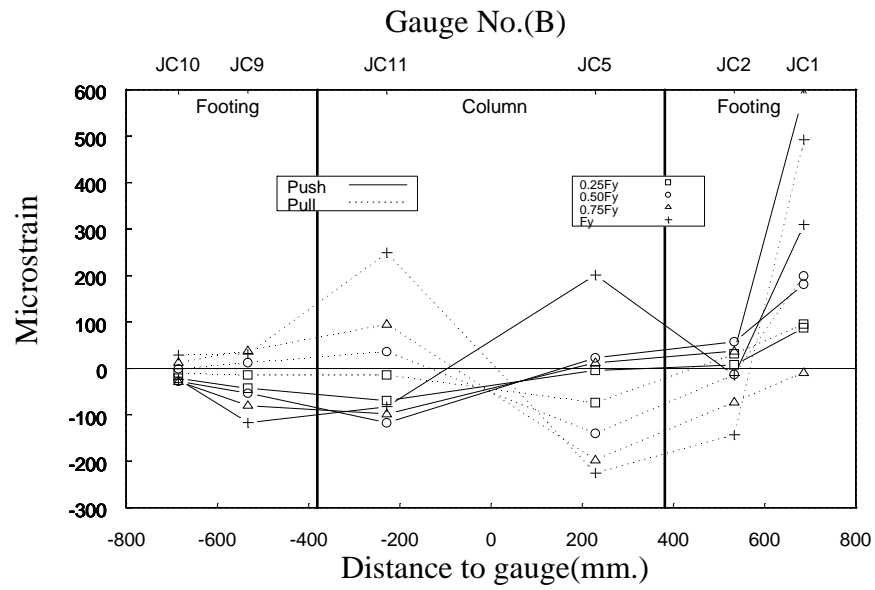
Figure F.16: Peak strain profiles of J-bars at column-pilecap joint
(E-W direction loading at column pre-yield in loading phase 1, see Figure F.2)

Gauge No.(B)
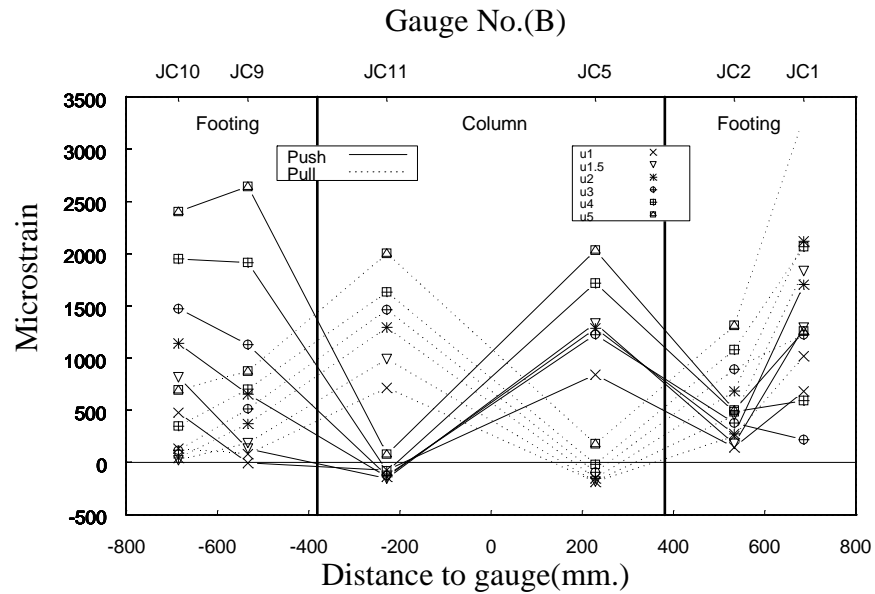
Figure F.17: Peak strain profiles of J-bars at column-pilecap joint
(E-W direction loading at column post-yield in loading phase 1, see Figure F.2)

Gauge No.(B)
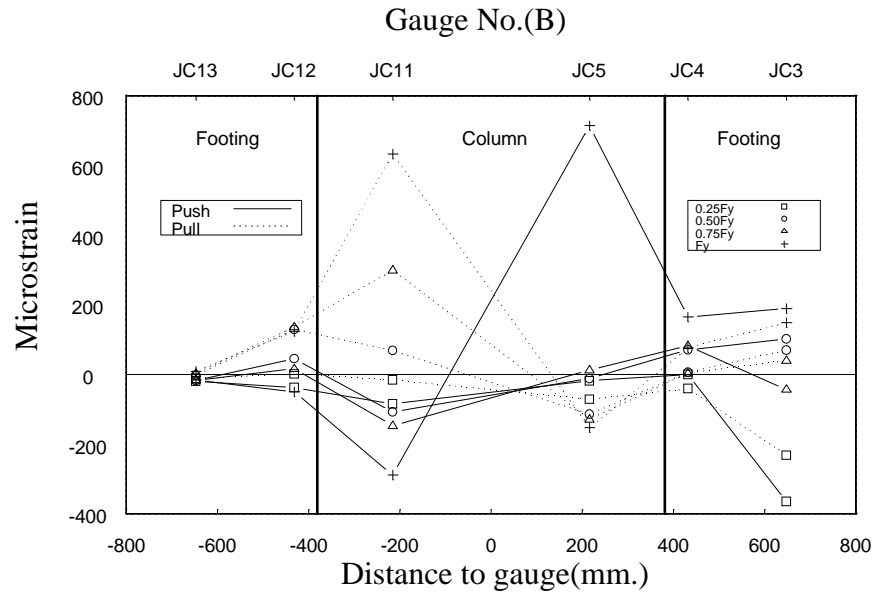
Figure F.18: Peak strain profiles of J-bars at column-pilecap joint
(SE-NW direction loading at column pre-yield in loading phase 1, see Figure F.2)

Gauge No.(B)
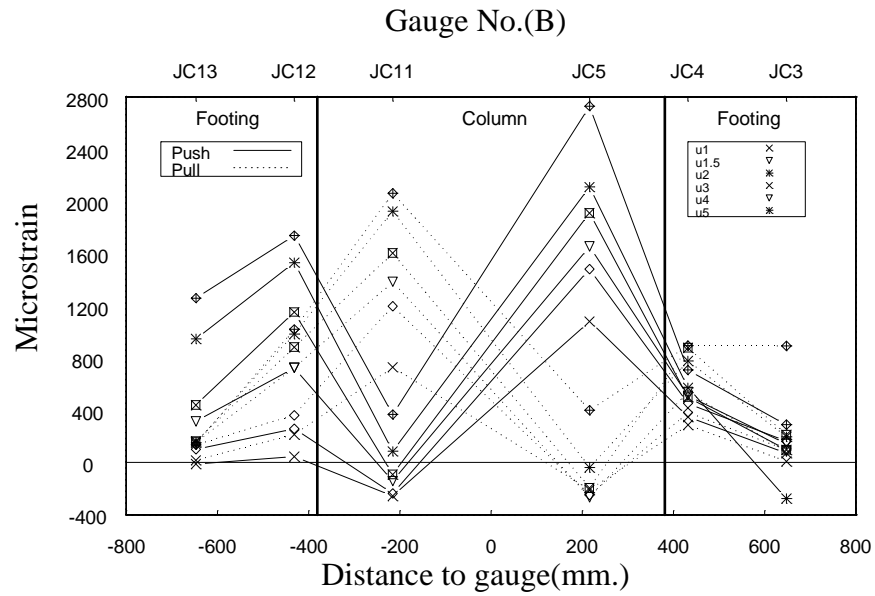
Figure F.19: Peak strain profiles of J-bars at column-pilecap joint
(SE-NW direction loading at column post-yield in loading phase 1, see Figure F.2)
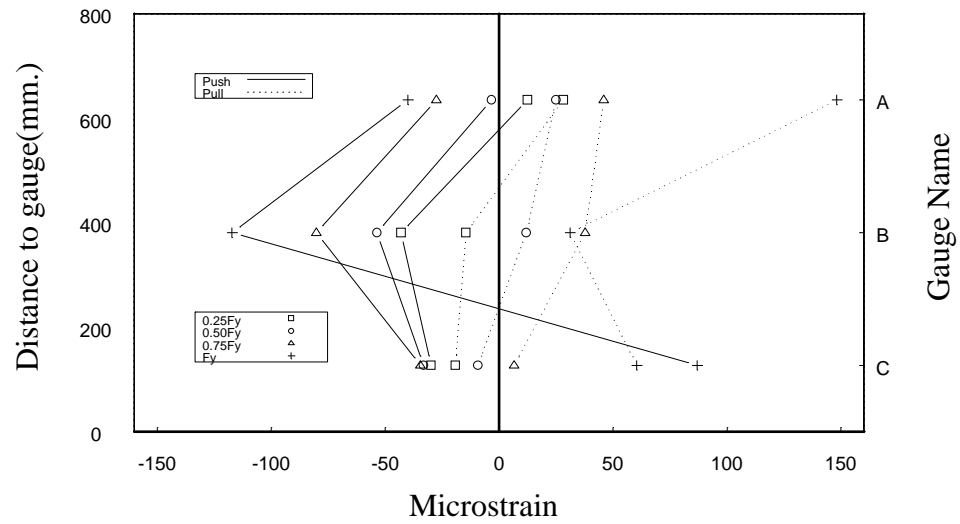
Figure F.20: Peak strain profiles at top, mid, bottom points of 9th J-bar
(E-W direction loading at column pre-yield in loading phase 1, see Figure F.2)
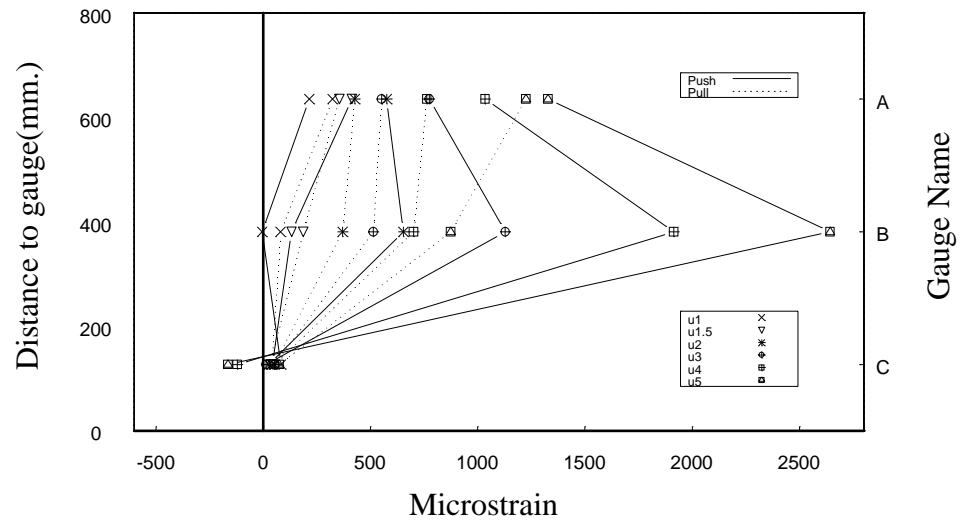
Figure F.21: Peak strain profiles at top, mid, bottom points of 9th J-bar
(E-W direction loading at column post-yield in loading phase 1, see Figure F.2)
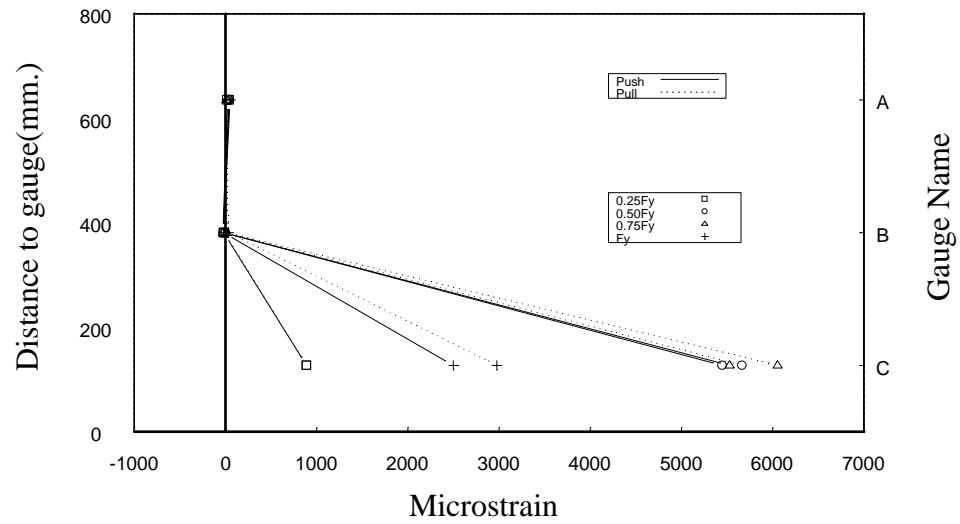
Figure F.22: Peak strain profiles at top, mid, bottom points of 10th J-bar
(E-W direction loading at column pre-yield in loading phase 1, see Figure F.2)
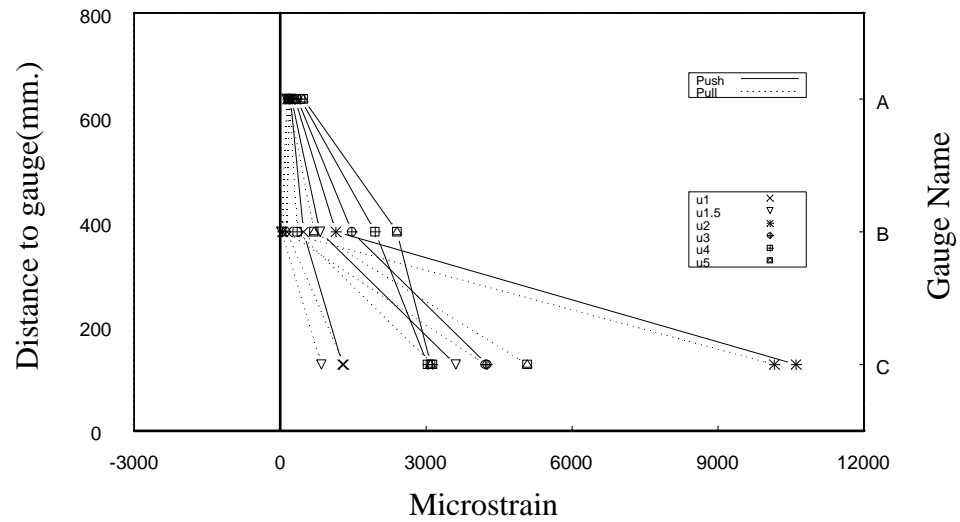
Figure F.23: Peak strain profiles at top, mid, bottom points of 10th J-bar
(E-W direction loading at column post-yield in loading phase 1, see Figure F.2)
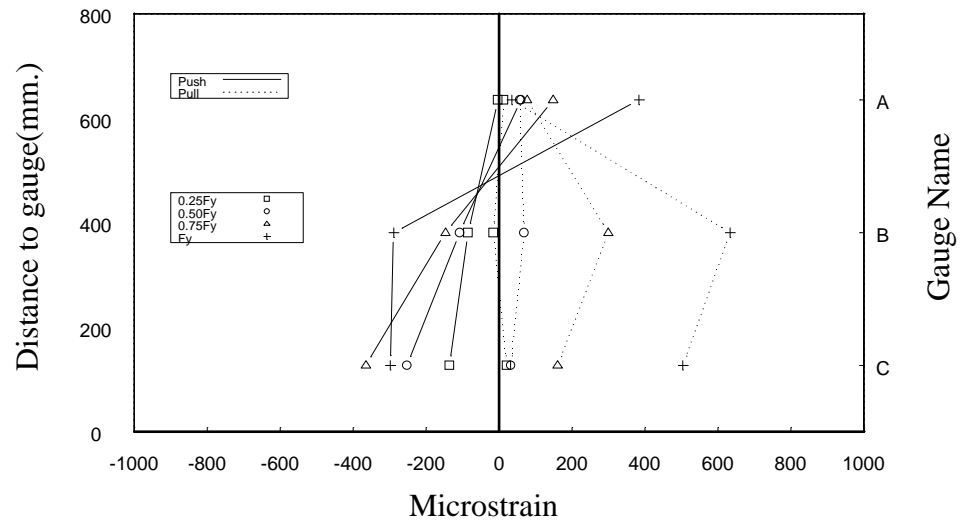
Figure F.24: Peak strain profiles at top, mid, bottom points of 11th J-bar
(SE-NW direction loading at column pre-yield in loading phase 1, see Figure F.2)
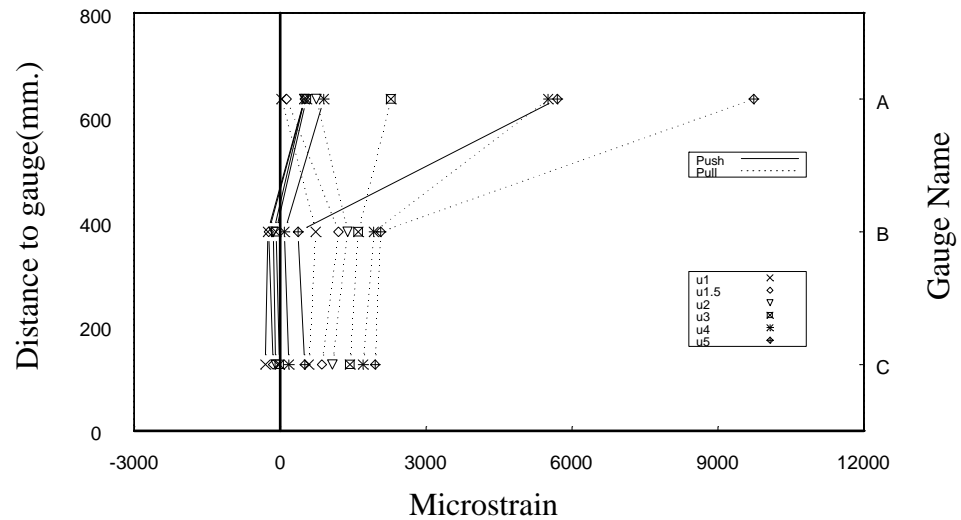
Figure F.25: Peak strain profiles at top, mid, bottom points of 11th J-bar
(SE-NW direction loading at column post-yield in loading phase 1, see Figure F.2)

299
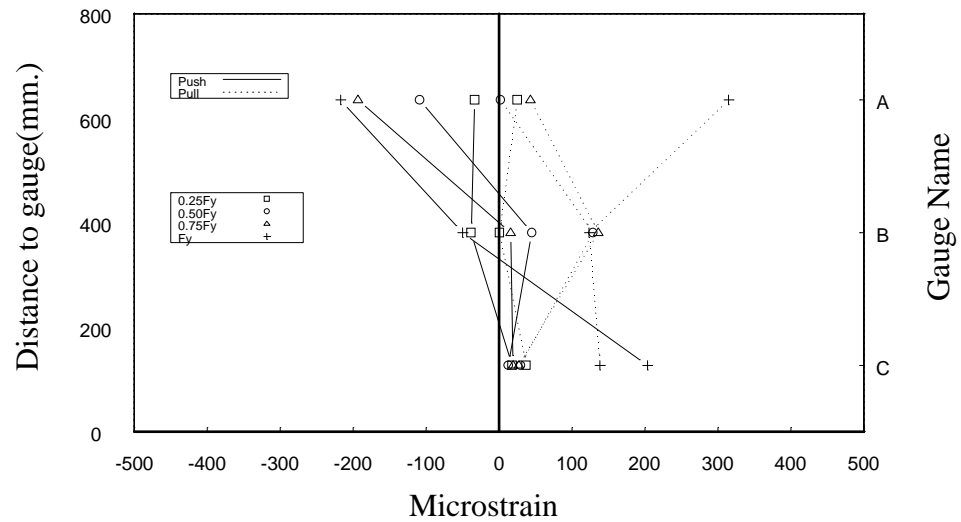
Figure F.26: Peak strain profiles at top, mid, bottom points of 12th J-bar
(SE-NW direction loading at column pre-yield in loading phase 1, see Figure F.2)
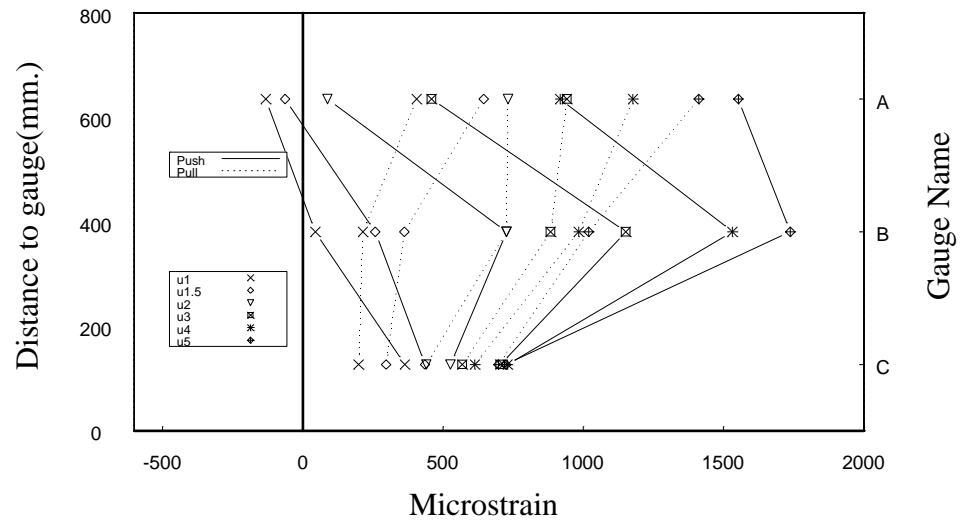
Figure F.27: Peak strain profiles at top, mid, bottom points of 12th J-bar
(SE-NW direction loading at column post-yield in loading phase 1, see Figure F.2)
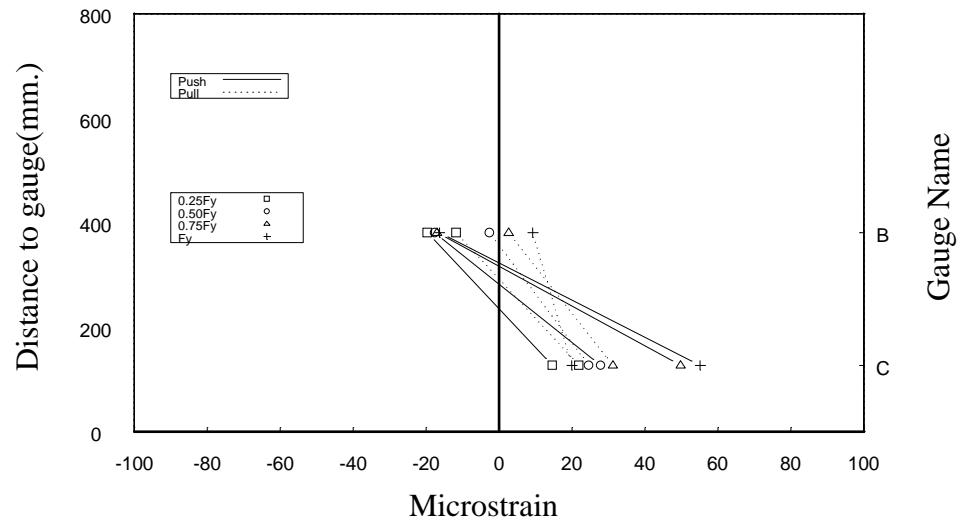
Figure F.28: Peak strain profiles at top, mid, bottom points of 13th J-bar
(SE-NW direction loading at column pre-yield in loading phase 1, see Figure F.2)
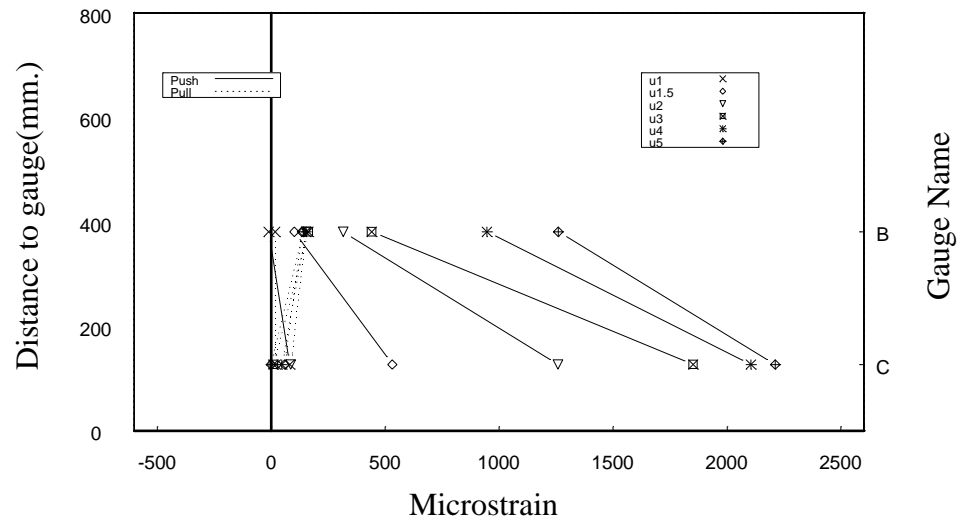
Figure F.29: Peak strain profiles at top, mid, bottom points of 13th J-bar
(SE-NW direction loading at column post-yield in loading phase 1, see Figure F.2)
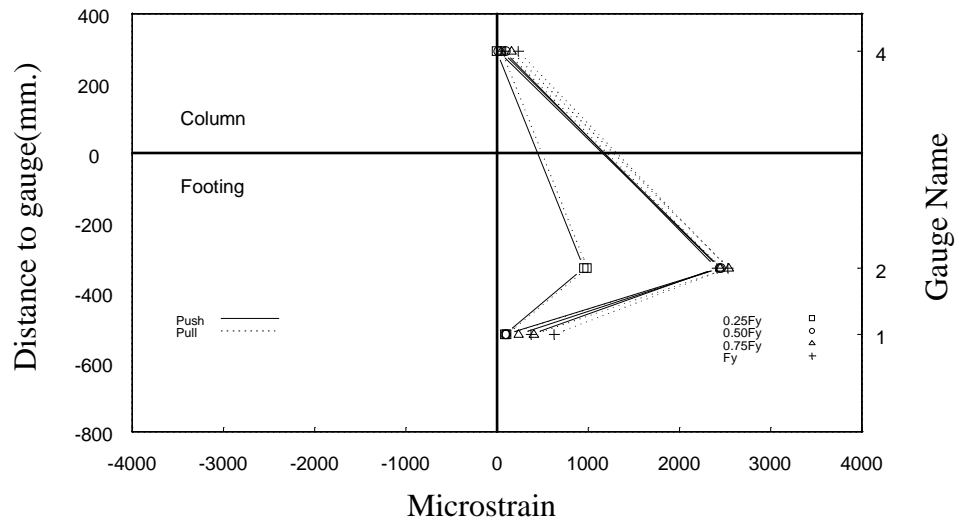
Figure F.30: Peak strain profiles of column spiral at CSW
(E-W direction loading at column pre-yield in loading phase 1, see Figure F.3)
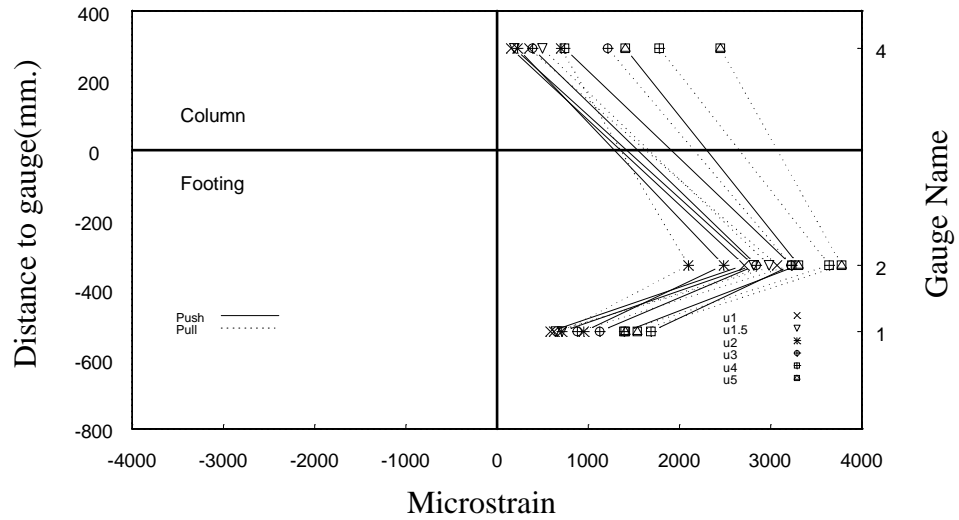
Figure F.31: Peak strain profiles of column spiral at CSW
(E-W direction loading at column post-yield in loading phase 1, see Figure F.3)
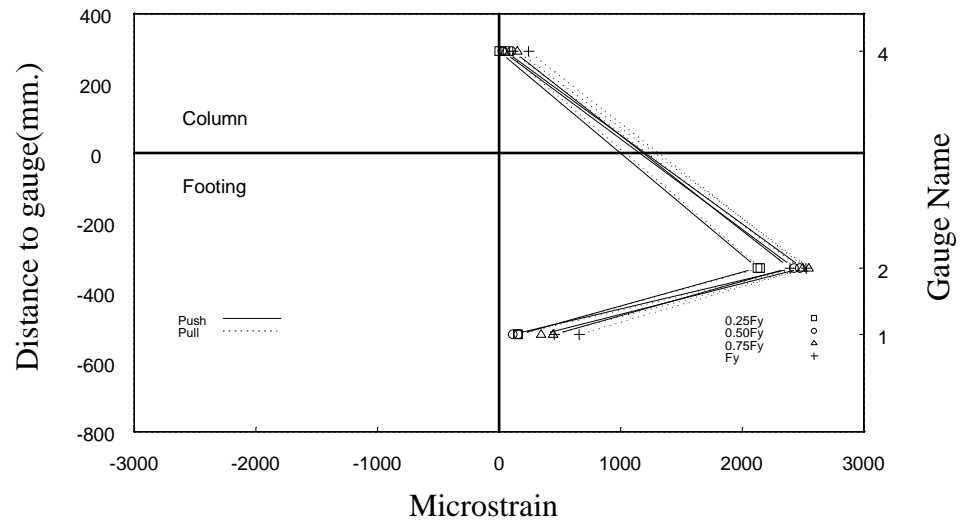
Figure F.32: Peak strain profiles of column spiral at CSW
(N-S direction loading at column pre-yield in loading phase 1, see Figure F.3)
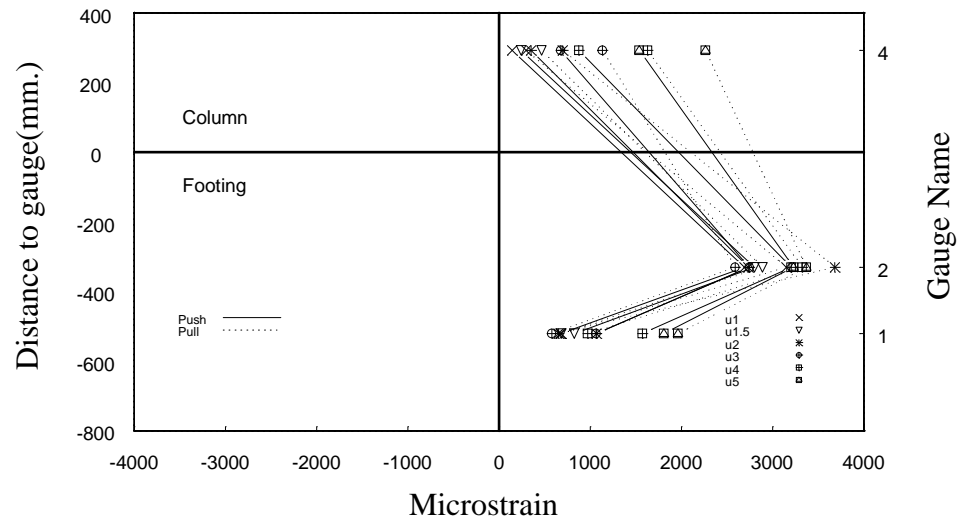
Figure F.33: Peak strain profiles of column spiral at CSW
(N-S direction loading at column post-yield in loading phase 1, see Figure F.3)
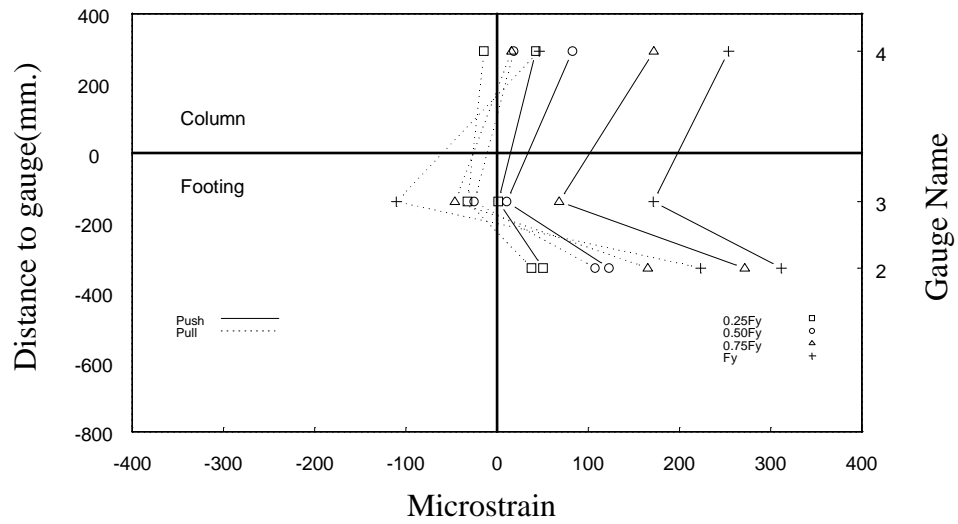
Figure F.34: Peak strain profiles of column spiral at CSE
(E-W direction loading at column pre-yield in loading phase 1, see Figure F.3)
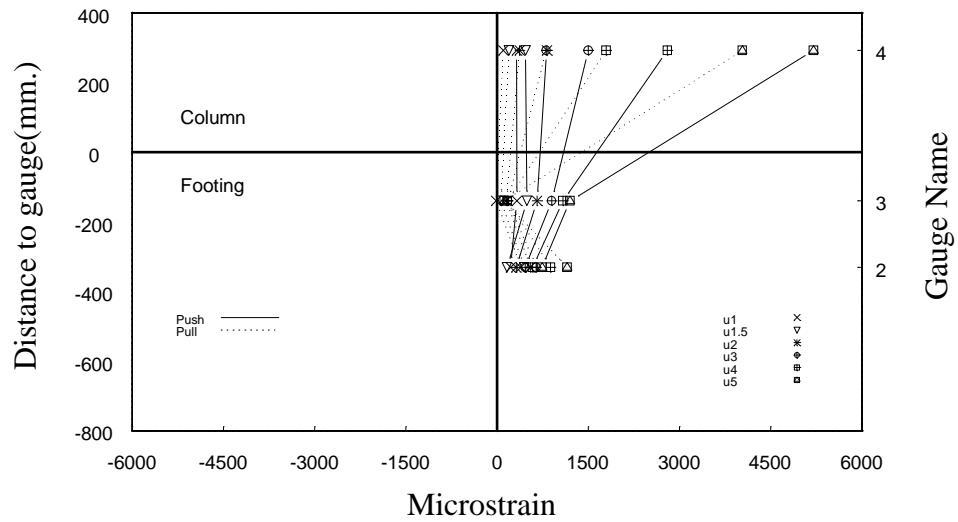
Figure F.35: Peak strain profiles of column spiral at CSE
(E-W direction loading at column post-yield in loading phase 1, see Figure F.3)
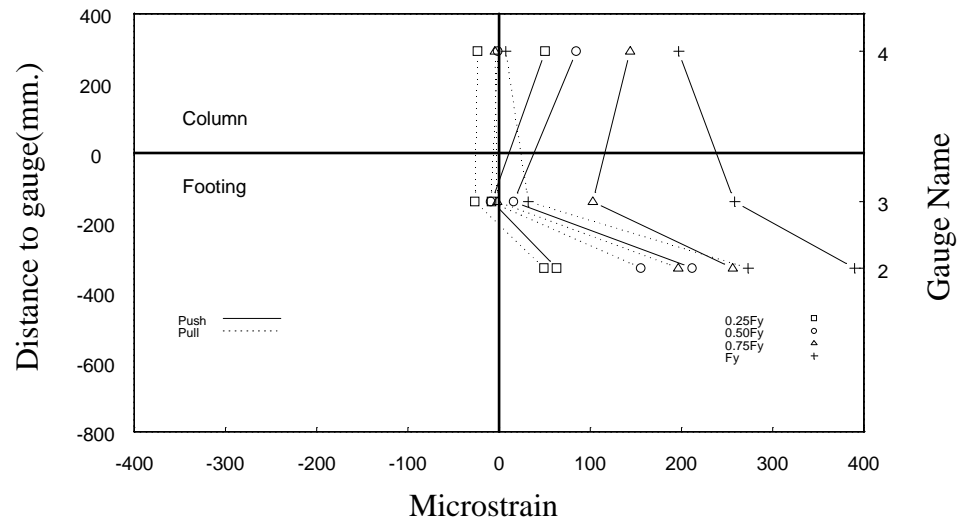
Figure F.36: Peak strain profiles of column spiral at CSE
(N-S direction loading at column pre-yield in loading phase 1, see Figure F.3)
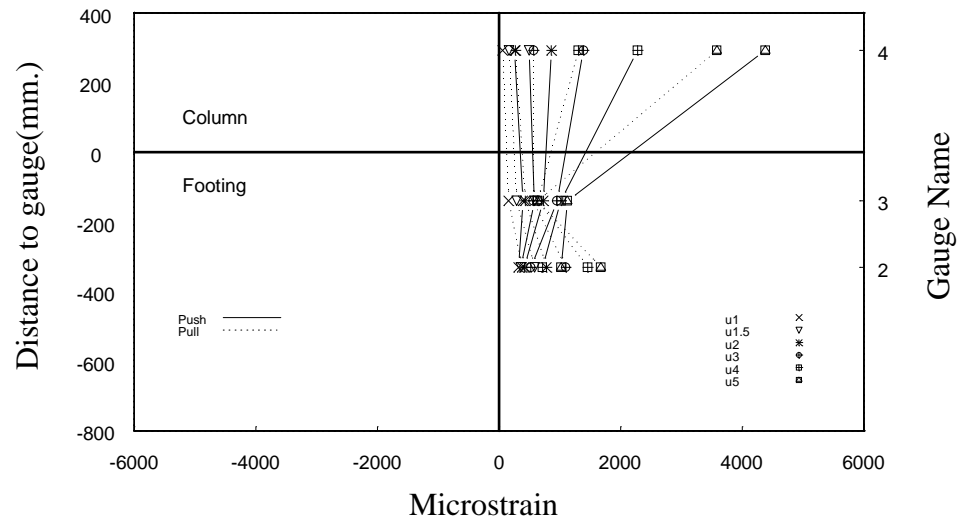
Figure F.37: Peak strain profiles of column spiral at CSE
(N-S direction loading at column post-yield in loading phase 1, see Figure F.3)
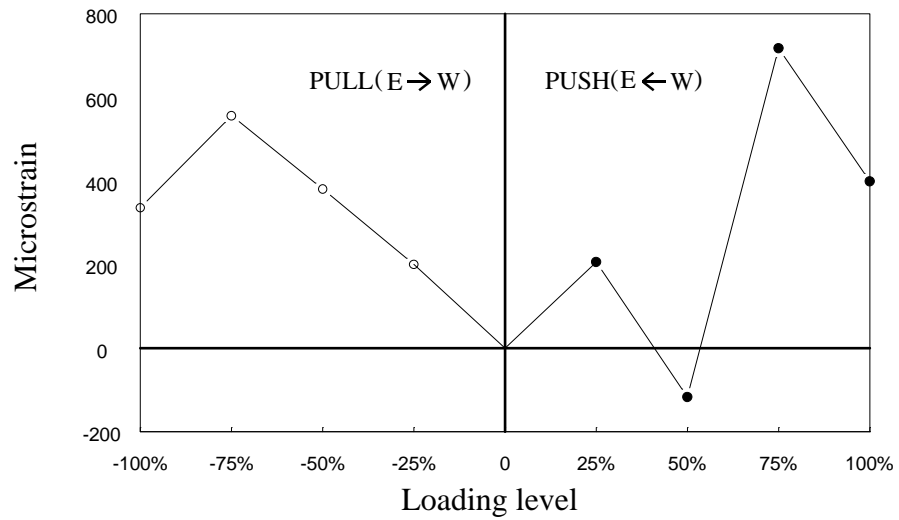
Figure F.38: Peak strains of column spiral at CSN2
(E-W direction loading at column pre-yield in loading phase 1, see Figure F.3)
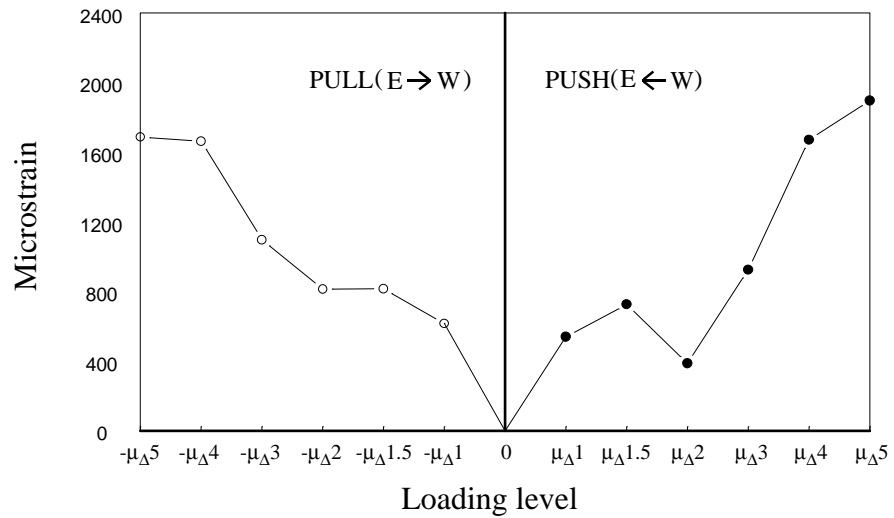
Figure F.39: Peak strains of column spiral at CSN2
(E-W direction loading at column post-yield in loading phase 1, see Figure F.3)
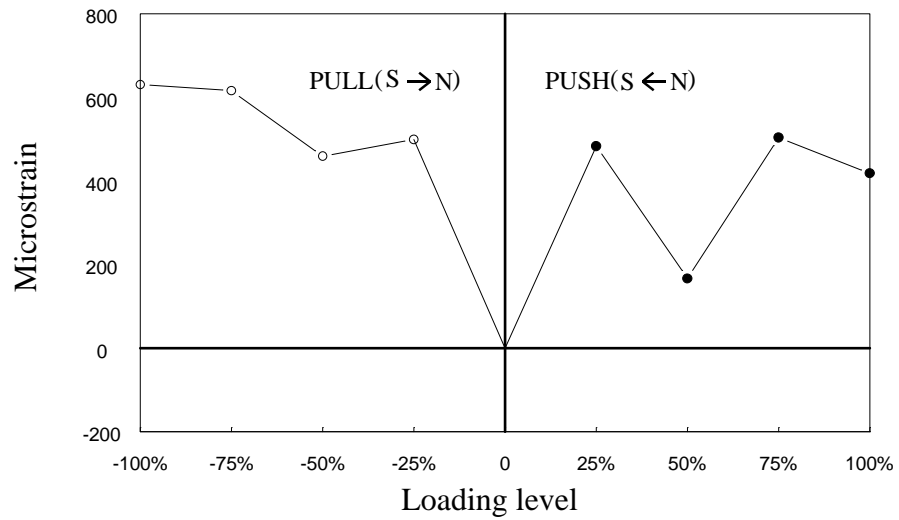
Figure F.40: Peak strains of column spiral at CSN2
(N-S direction loading at column pre-yield in loading phase 1, see Figure F.3)
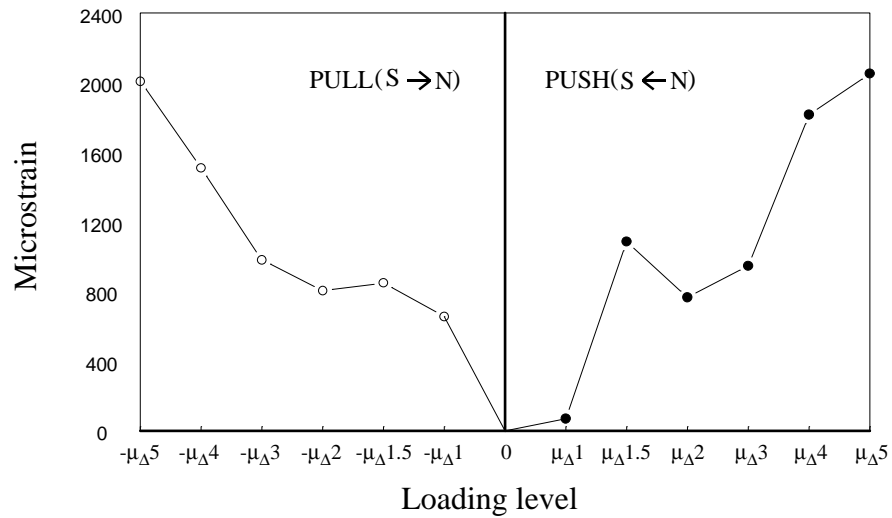
Figure F.41: Peak strains of column spiral at CSN2
(N-S direction loading at column post-yield in loading phase 1, see Figure F.3)
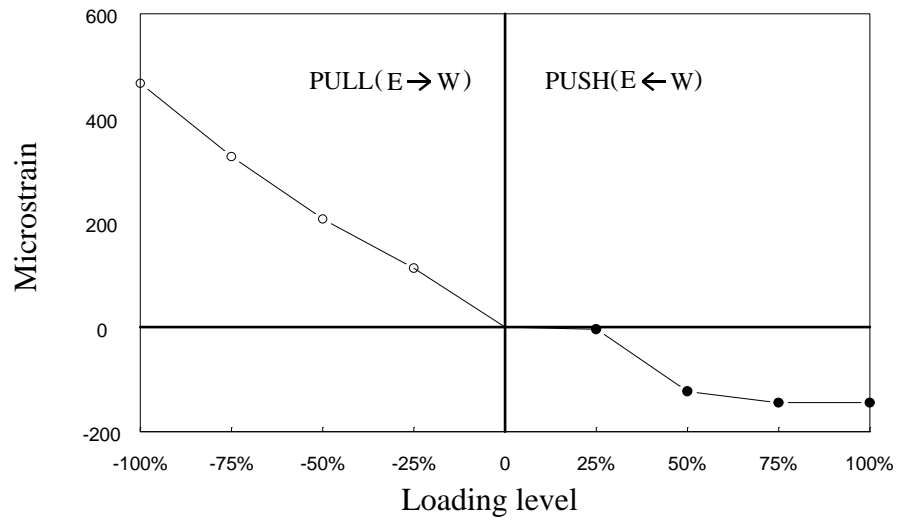
Figure F.42: Peak strains of column spiral at CSS4
(E-W direction loading at column pre-yield in loading phase 1, see Figure F.3)
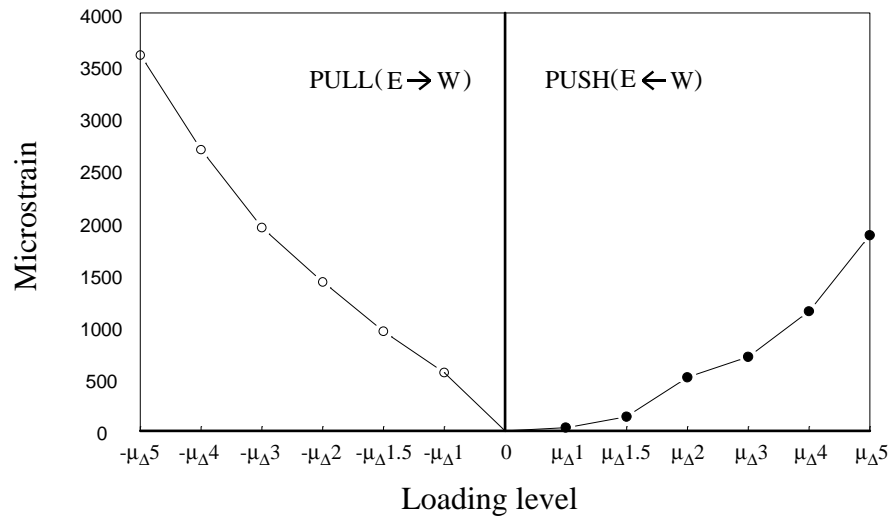
Figure F.43: Peak strains of column spiral at CSS4
(E-W direction loading at column post-yield in loading phase 1, see Figure F.3)
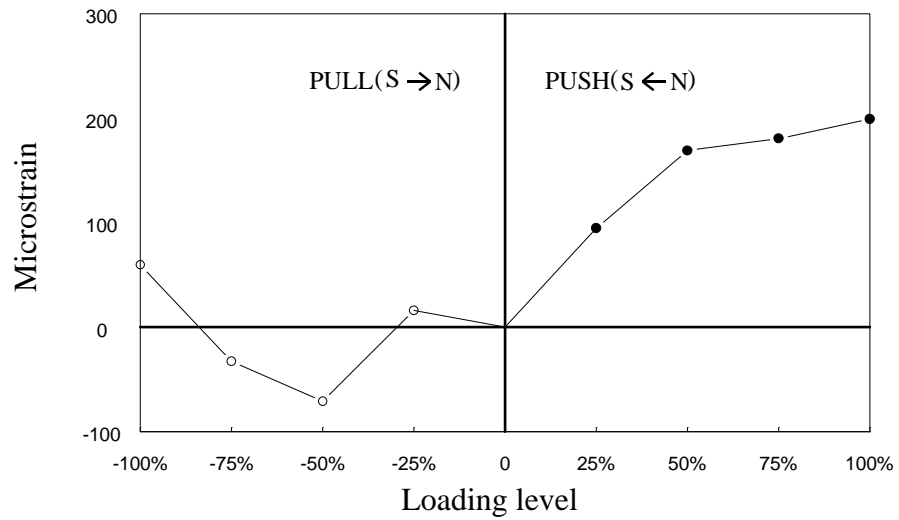
Figure F.44: Peak strains of column spiral at CSS4
(N-S direction loading at column pre-yield in loading phase 1, see Figure F.3)
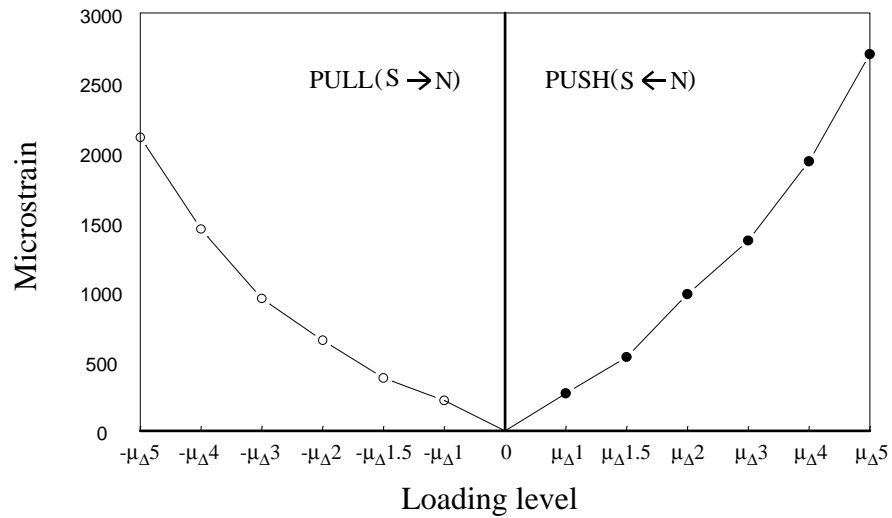
Figure F.45: Peak strains of column spiral at CSS4
(N-S direction loading at column post-yield in loading phase 1, see Figure F.3)

Appendix G: Strain Profiles of Column-Pilecap Joint of CFPS2

North

(b) Shear reinforcement

Pile C

Pile D

Pile B

Pile A

West

102
356
178

178
457

254
254
254
254
254
254
254
457

East

(a) Flexural reinforcement
(Top & Bottom mat)

Pile C

Pile D

BTM(bottom)
TTM(top)

Pile B

Pile A

457
356
178
457
457
178
178
178
178
102

279
178
356
584
457
178
178
178
178
178
102

South
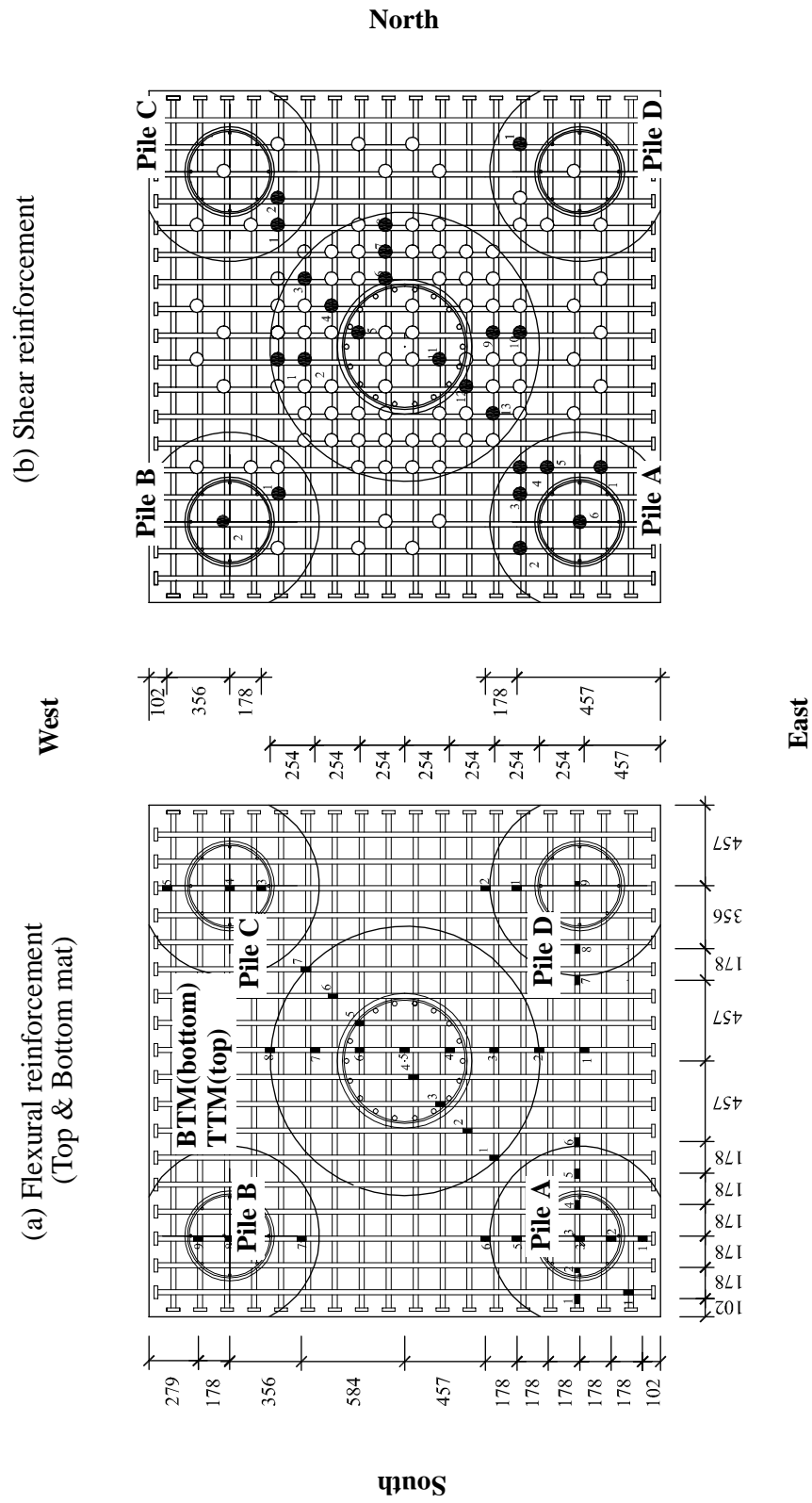
Figure G.2: Schedule of pilecap longitudinal(flexural) and stirrup(shear) reinforcement strain gauges

311
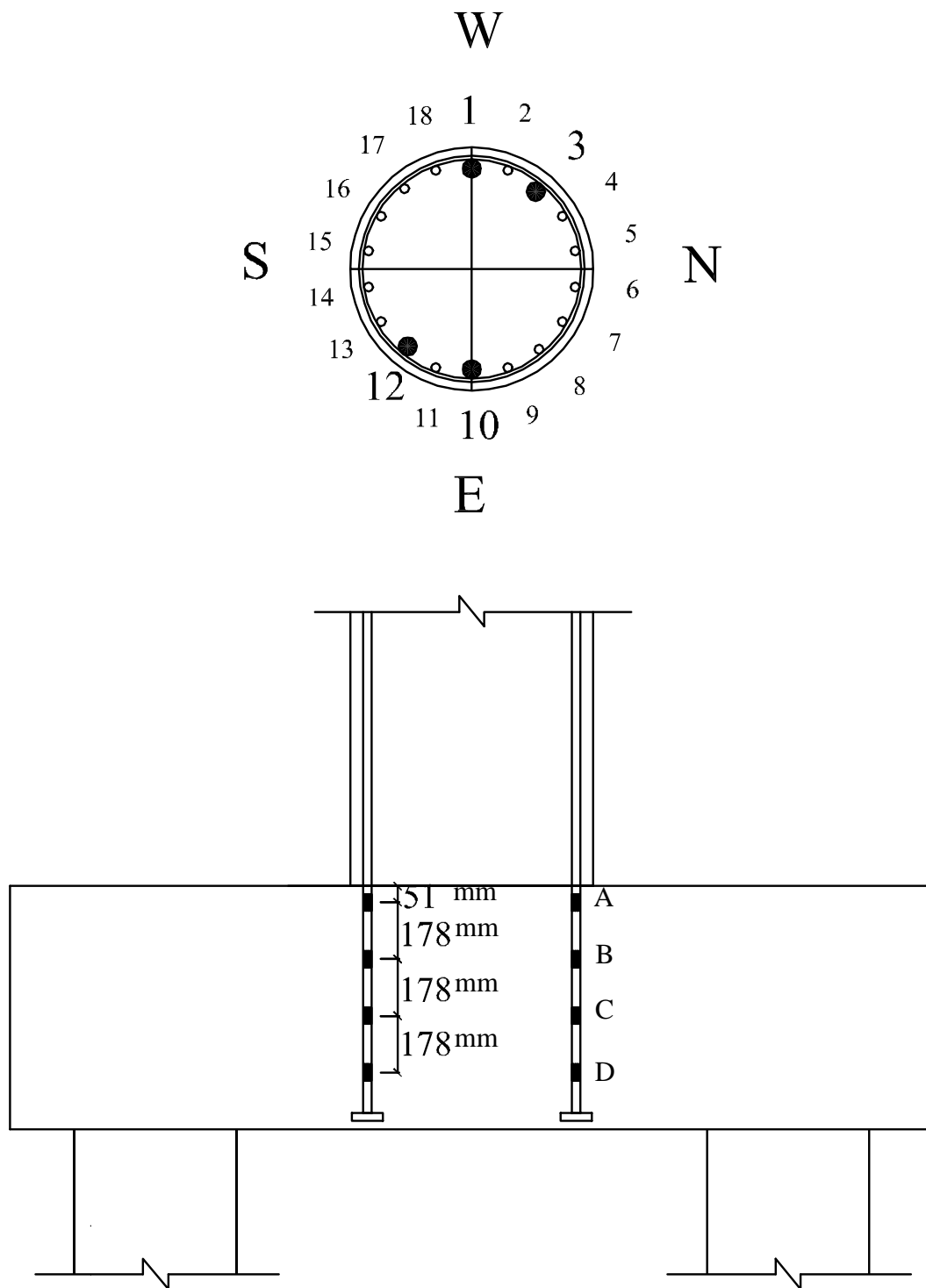
Figure G.1: Strain gauge names and locations on the column longitudinal bar

CSW

CSS | CSN

CSE

L_{ph} = 457mm

4

290mm

3

140mm

190mm

2

190mm

1
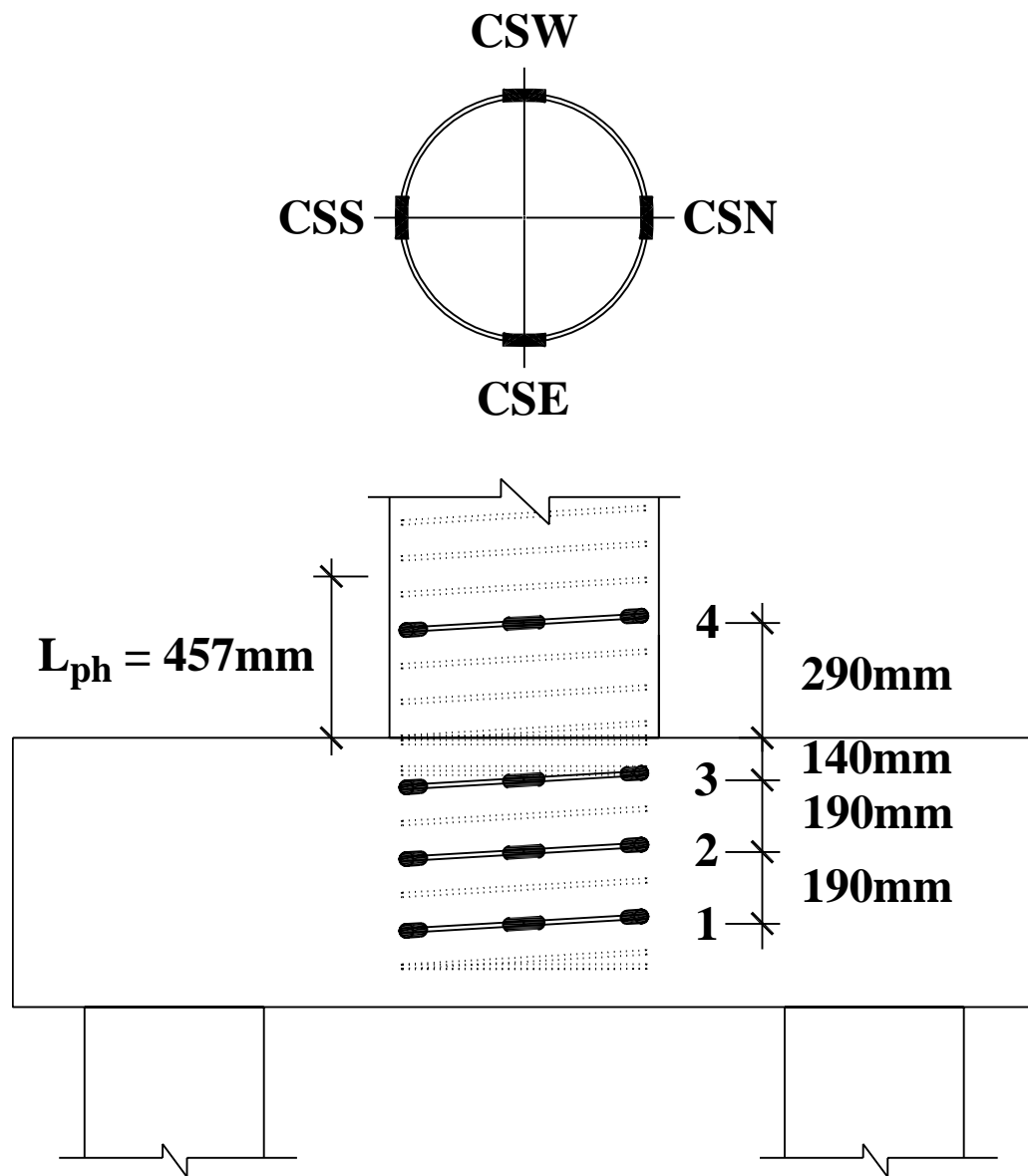
Figure G.3: Strain gauge names and locations on the column spiral bar

Initial stages of testing
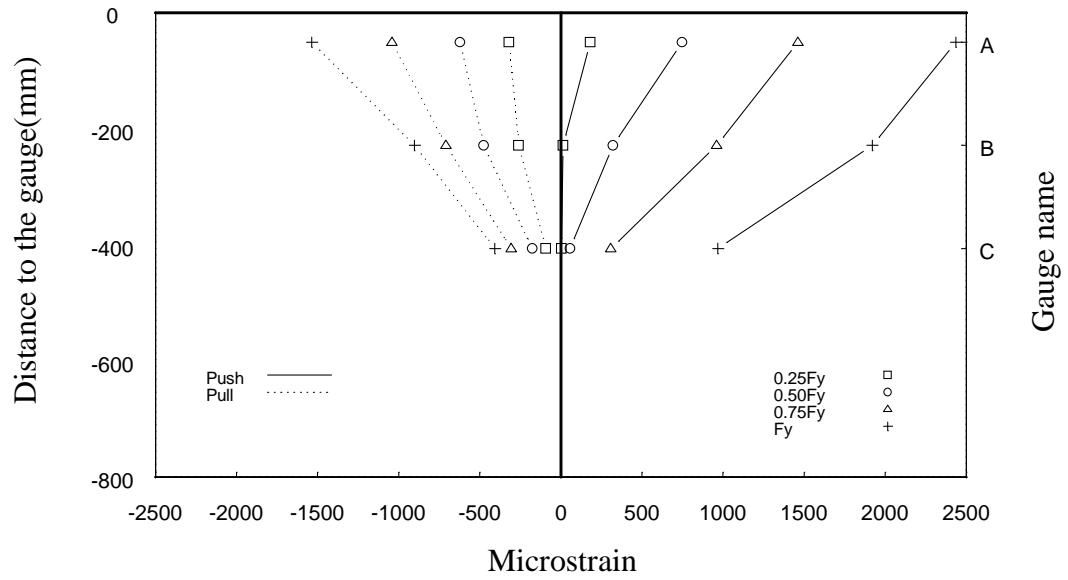
Final stages of testing
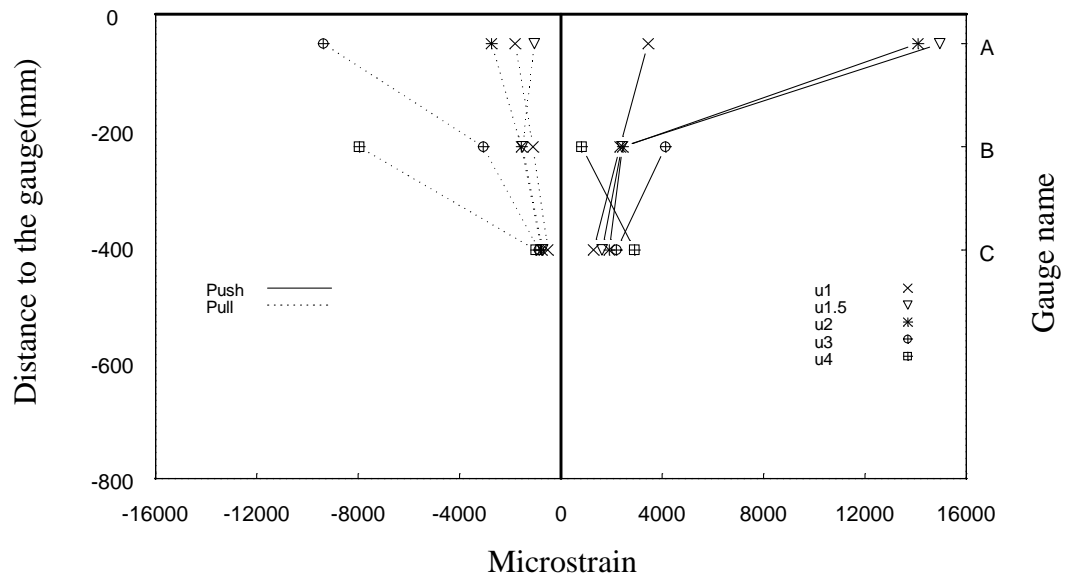
Figure G.4: Strain profile of column longitudinal 1st bar at column-pilecap joint
(E-W direction loading at loading phase 1, see Figure G.1)

Initial stages of testing

Final stages of testing
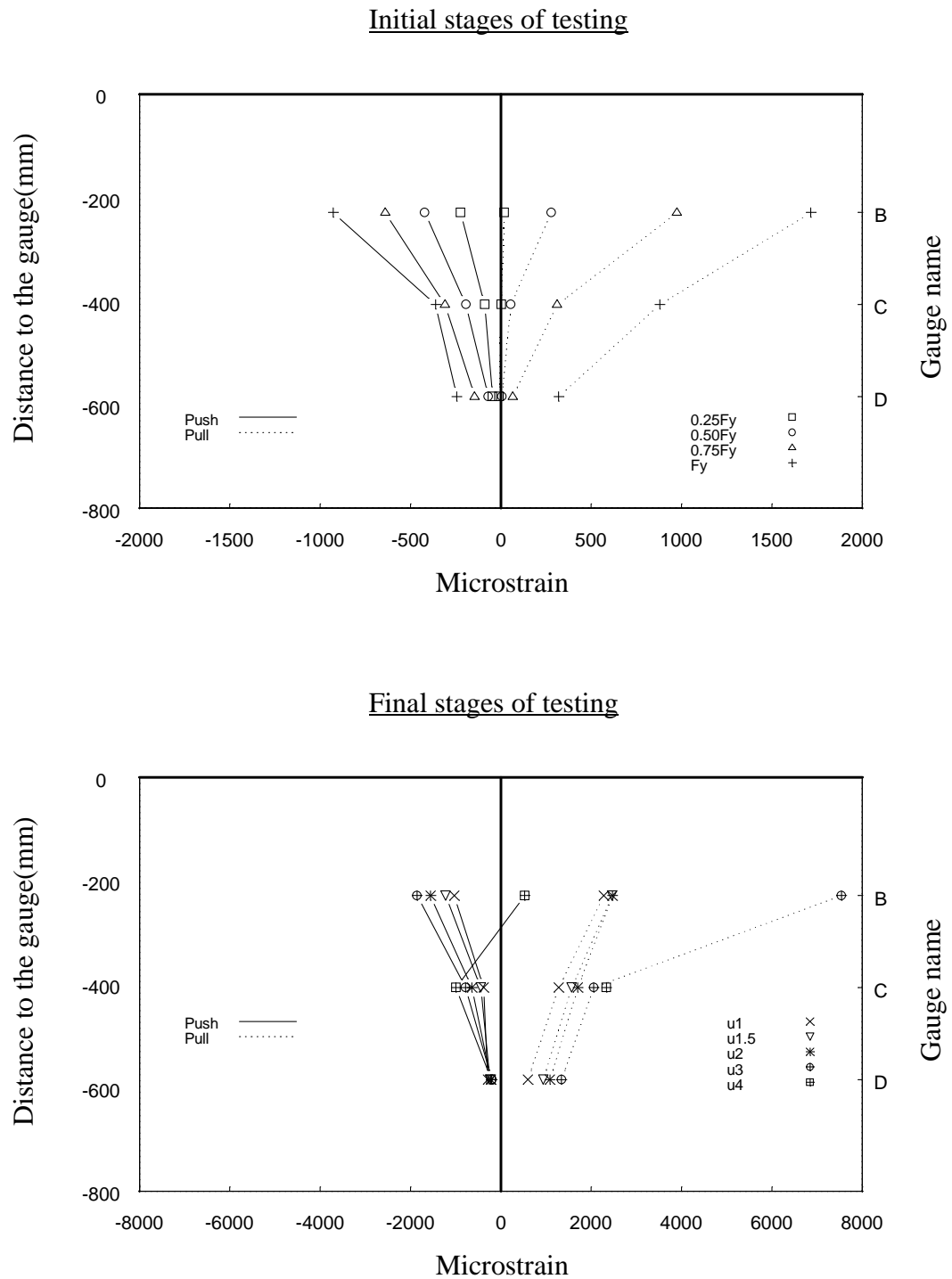
Figure G.5: Strain profile of column longitudinal 10th bar at column-pilecap joint
(E-W direction loading at loading phase 1, see Figure G.1)

315

Initial stages of testing

(Chart: Distance to the gauge(mm) vs Microstrain; Gauge name A, B, C, D)

Push ———
Pull ·······

0.25Fy □
0.50Fy ○
0.75Fy △
Fy +

Final stages of testing

(Chart: Distance to the gauge(mm) vs Microstrain; Gauge name A, B, C, D)

Push ———
Pull ·······

u1 ×
u1.5 ◇
u2 ▽
u3 ⊠
u4 ✳
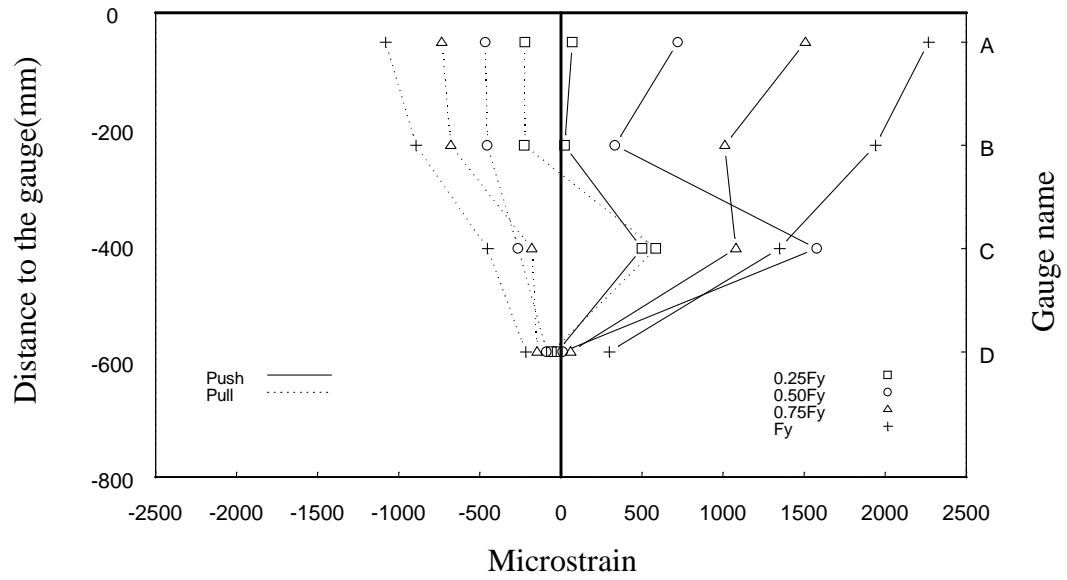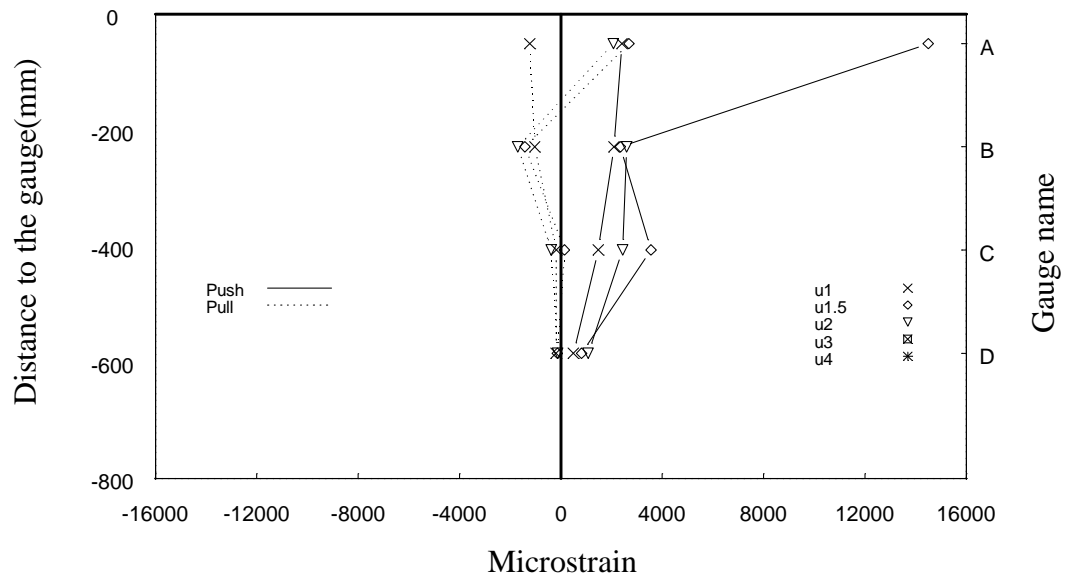
Figure G.6: Strain profile of column longitudinal 3rd bar at column-pilecap joint (SE-NW direction loading at loading phase 1, see Figure G.1)

Initial stages of testing
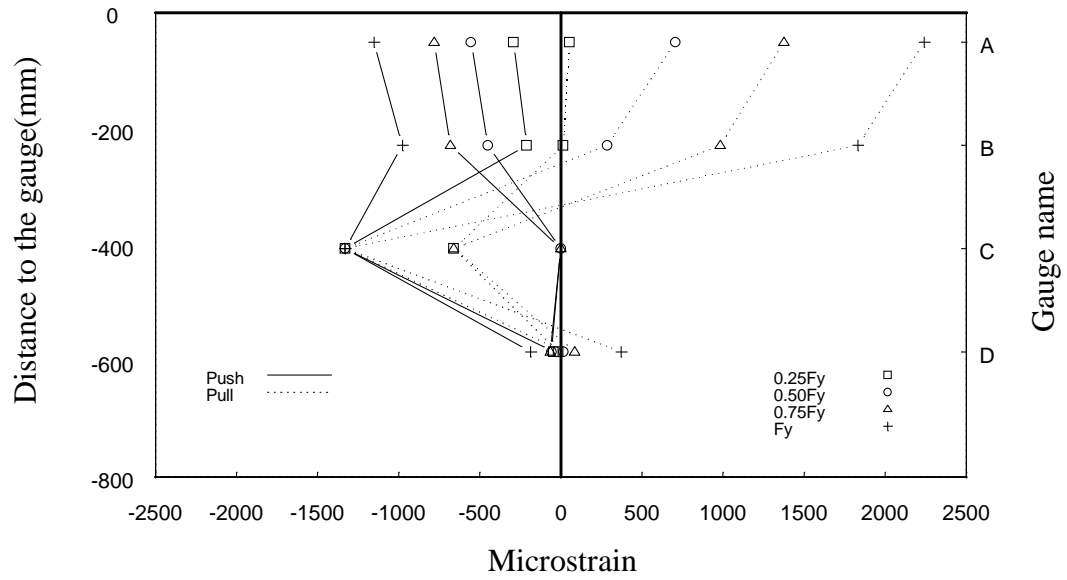
Final stages of testing
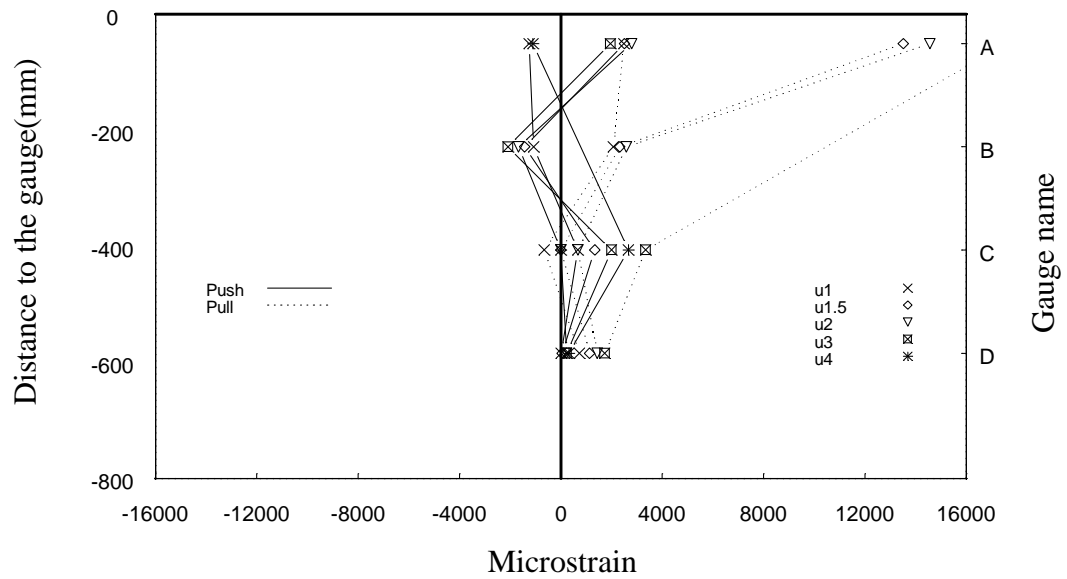
Figure G.7: Strain profile of column longitudinal 12th bar at column-pilecap joint (SE-NW direction loading at loading phase 1, see Figure G.1)

317
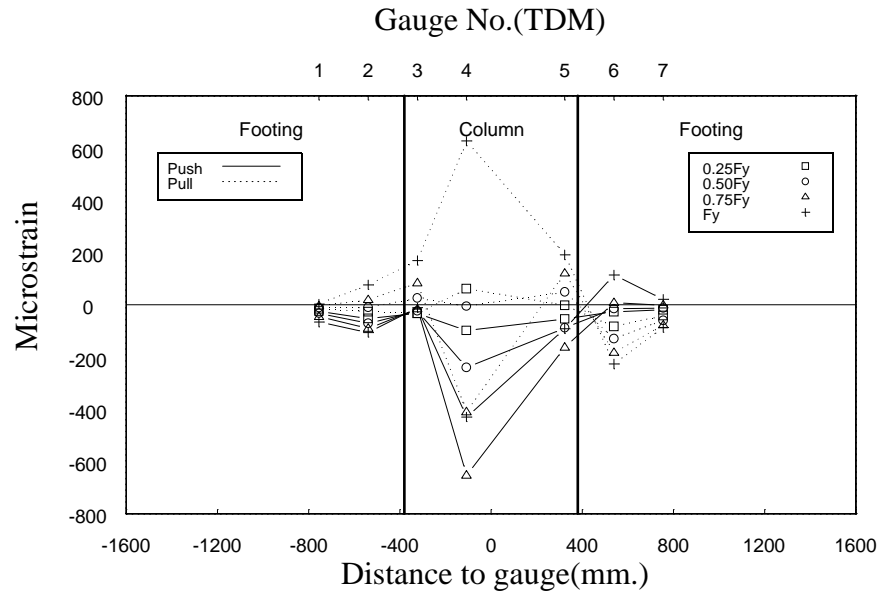
Figure G.8: Peak strain profiles of pilecap top reinforcement(TDM)
(E-W direction loading at column pre-yield in loading phase 1, see Figure G.2)
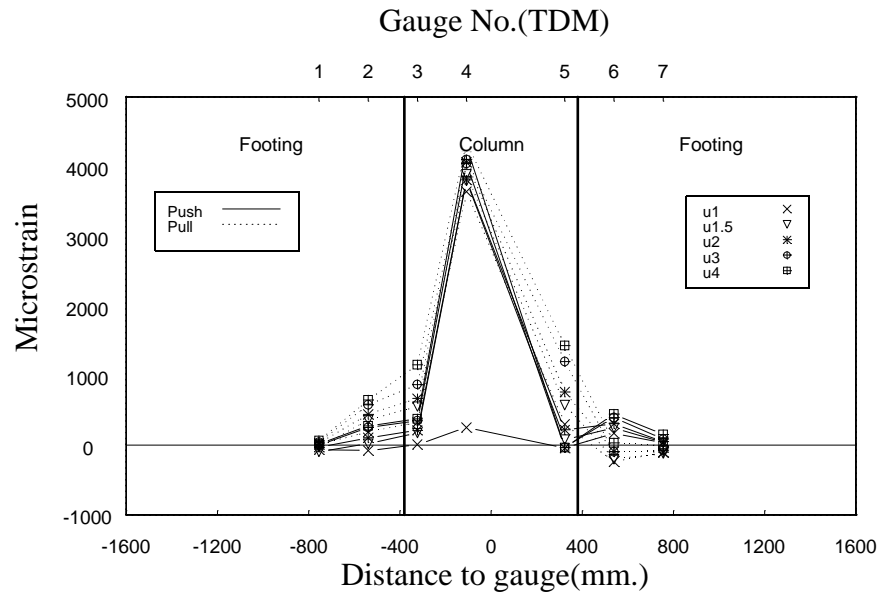
Figure G.9: Peak strain profiles of pilecap top reinforcement(TDM)
(E-W direction loading at column post-yield in loading phase 1, see Figure G.2)

318
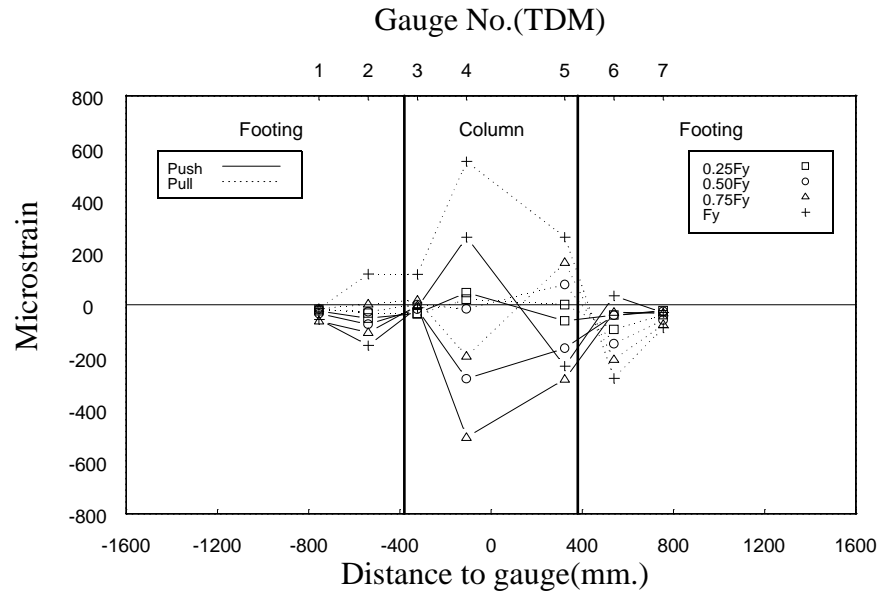
Figure G.10: Peak strain profiles of pilecap top reinforcement(TDM)
(SE-NW direction loading at column pre-yield in loading phase 1, see Figure G.2)
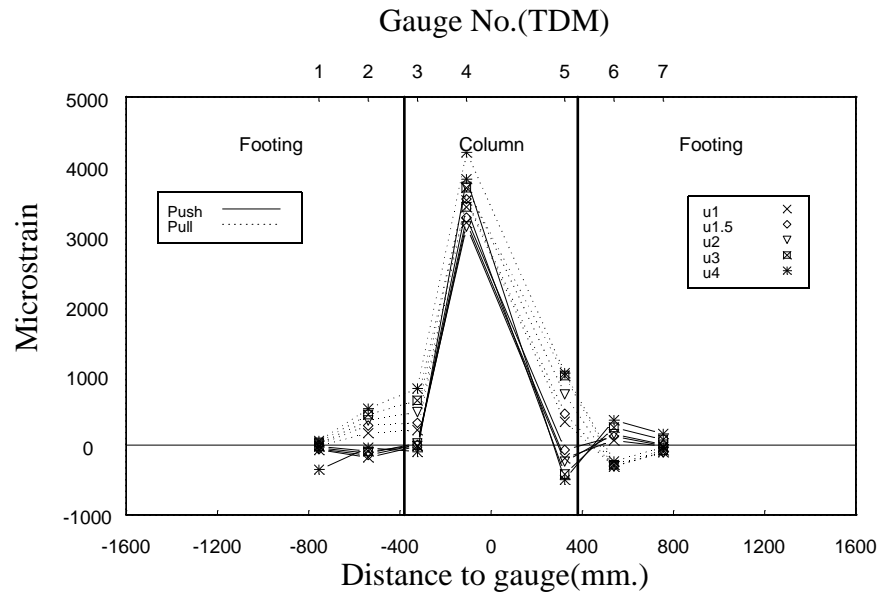
Figure G.11: Peak strain profiles of pilecap top reinforcement(TDM)
(SE-NW direction loading at column post-yield in loading phase 1, see Figure G.2)

319
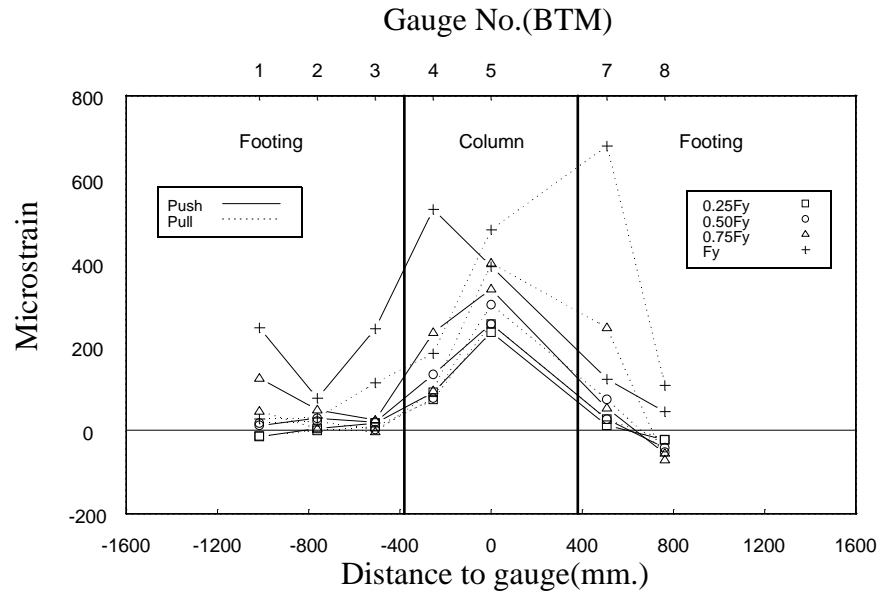
Figure G.12: Peak strain profiles of pilecap bottom reinforcement(BTM)
(SE-NW direction loading at column pre-yield in loading phase 1, see Figure G.2)
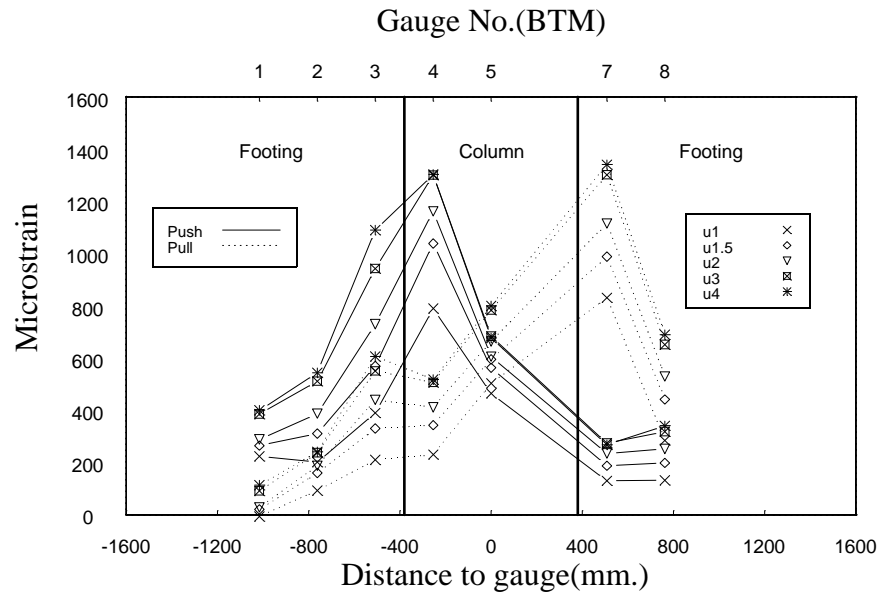
Figure G.13: Peak strain profiles of pilecap bottom reinforcement(BTM)
(SE-NW direction loading at column post-yield in loading phase 1, see Figure G.2)

Gauge No.(TTM)
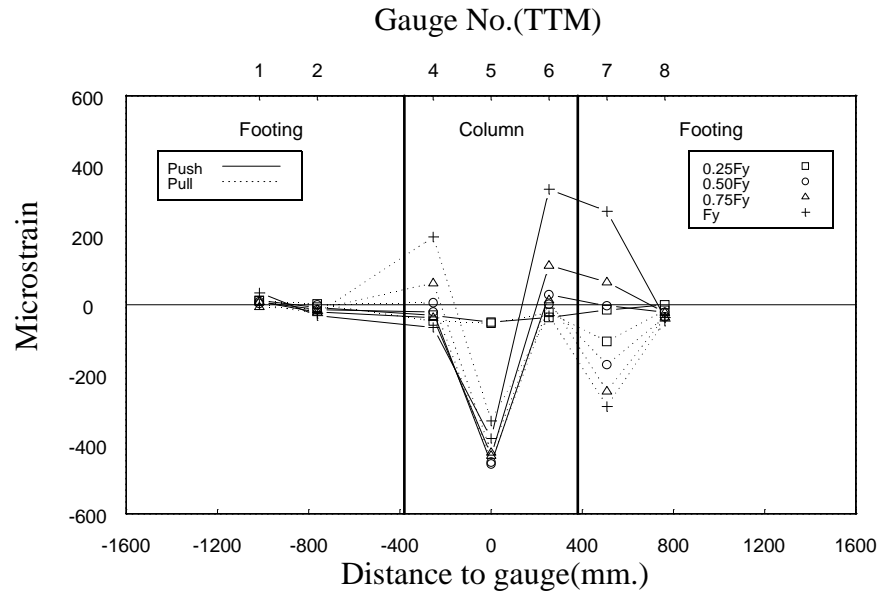
Figure G.14: Peak strain profiles of pilecap top reinforcement(TTM)
(E-W direction loading at column pre-yield in loading phase 1, see Figure G.2)

Gauge No.(TTM)
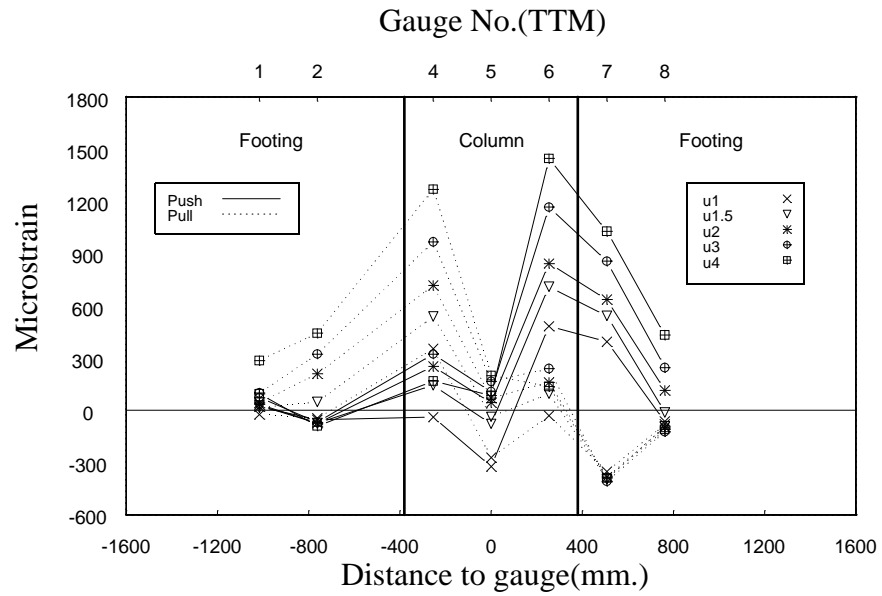
Figure G.15: Peak strain profiles of pilecap top reinforcement(TTM)
(E-W direction loading at column post-yield in loading phase 1, see Figure G.2)
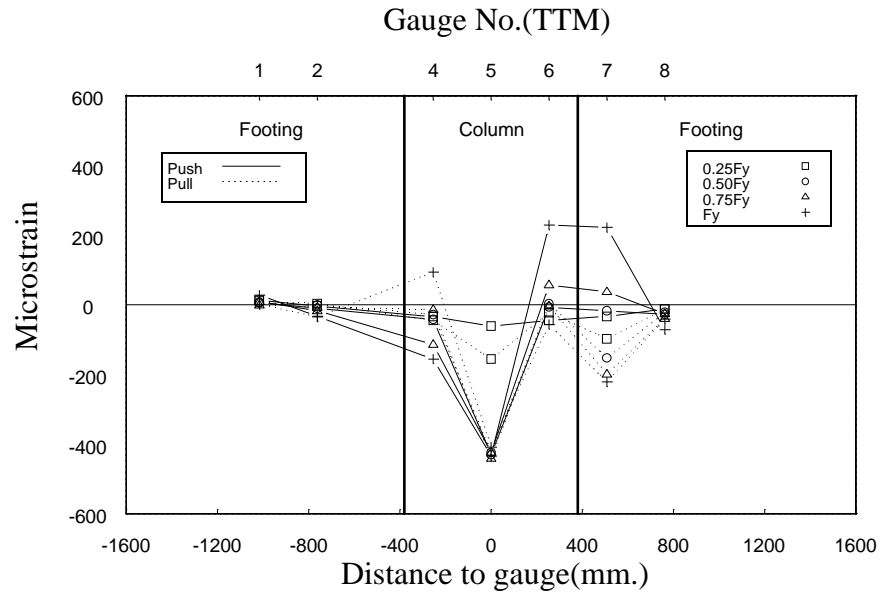
Figure G.16: Peak strain profiles of pilecap top reinforcement(TTM)
(SE-NW direction loading at column pre-yield in loading phase 1, see Figure G.2)
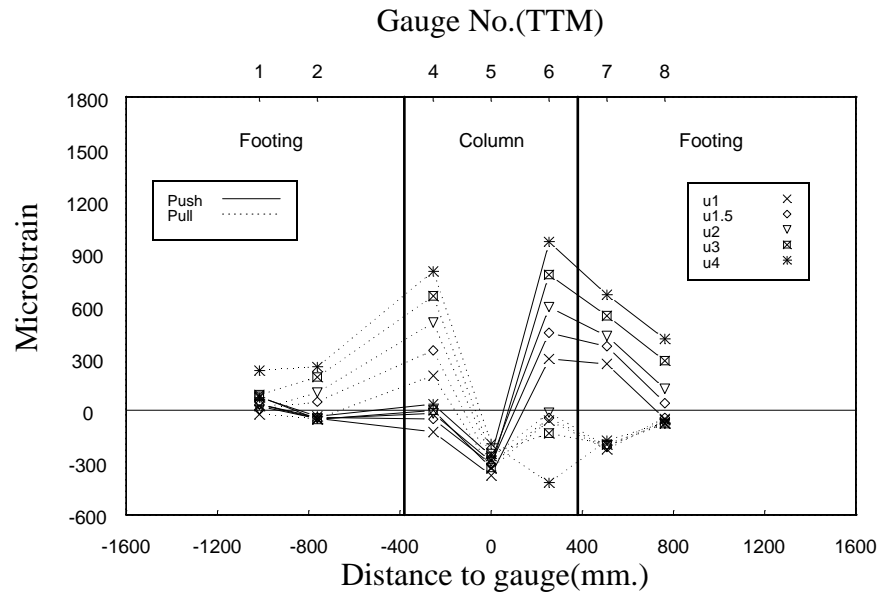
Figure G.17: Peak strain profiles of pilecap top reinforcement(TTM)
(SE-NW direction loading at column post-yield in loading phase 1, see Figure G.2)

Gauge No.(B)
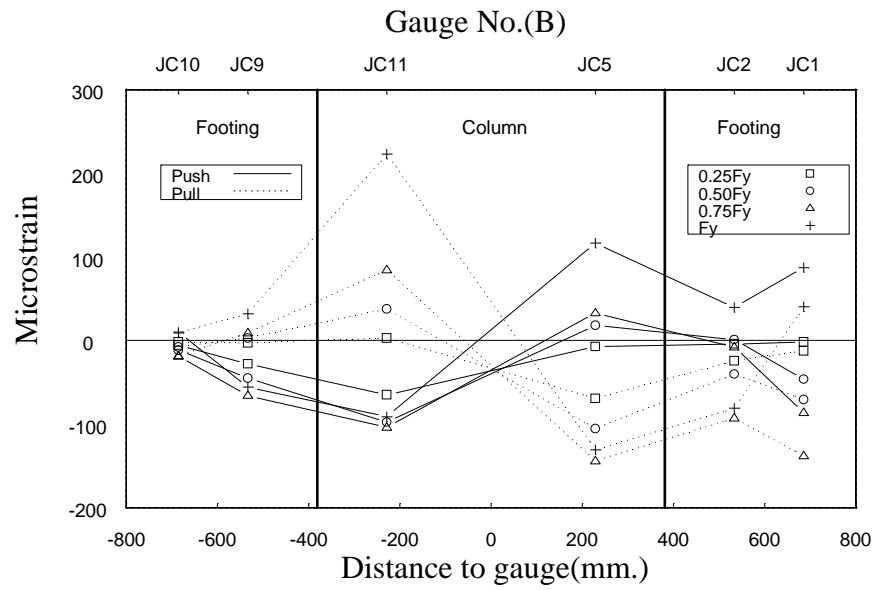
Figure G.18: Peak strain profiles of J-bars at column-pilecap joint
(E-W direction loading at column pre-yield in loading phase 1, see Figure G.2)

Gauge No.(B)
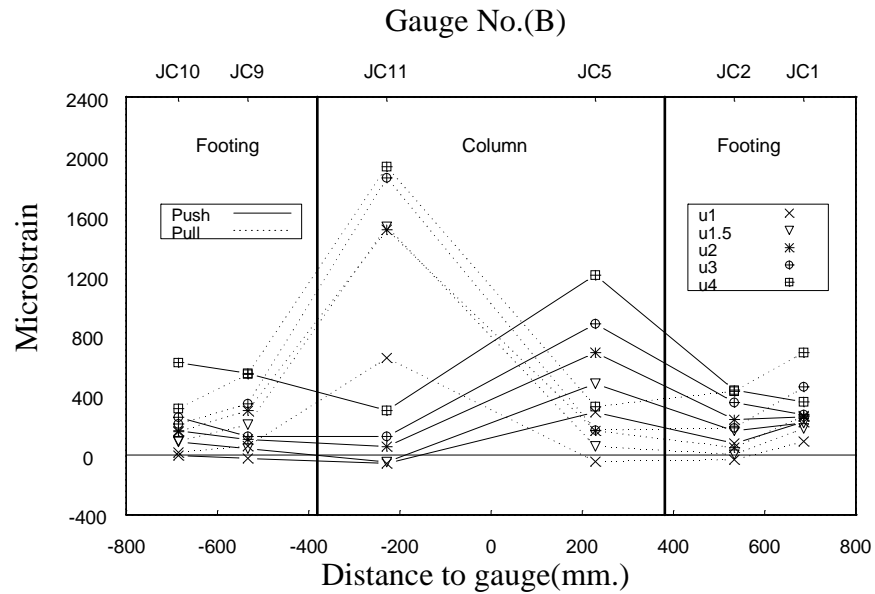
Figure G.19: Peak strain profiles of J-bars at column-pilecap joint
(E-W direction loading at column post-yield in loading phase 1, see Figure G.2)

Gauge No.(B)
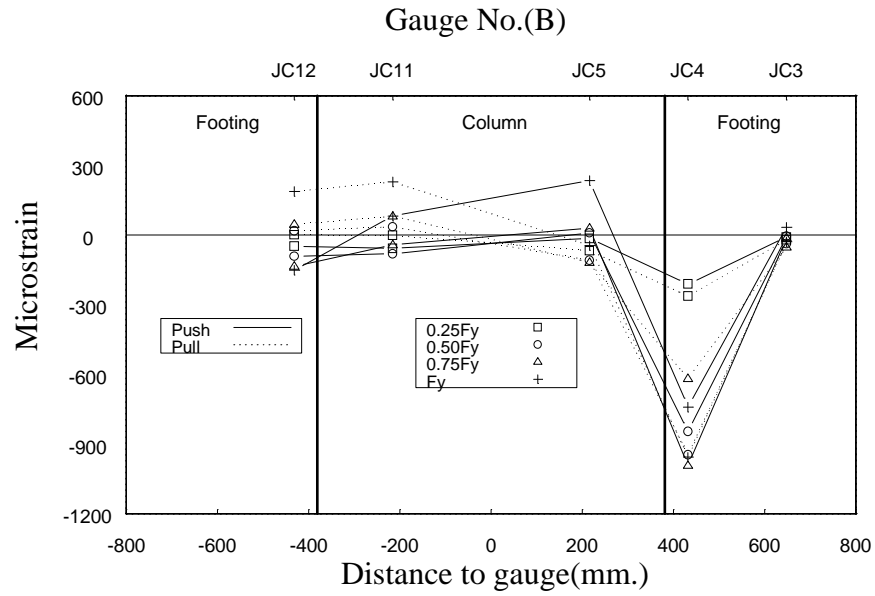
Figure G.20: Peak strain profiles of J-bars at column-pilecap joint
(SE-NW direction loading at column pre-yield in loading phase 1, see Figure G.2)

Gauge No.(B)
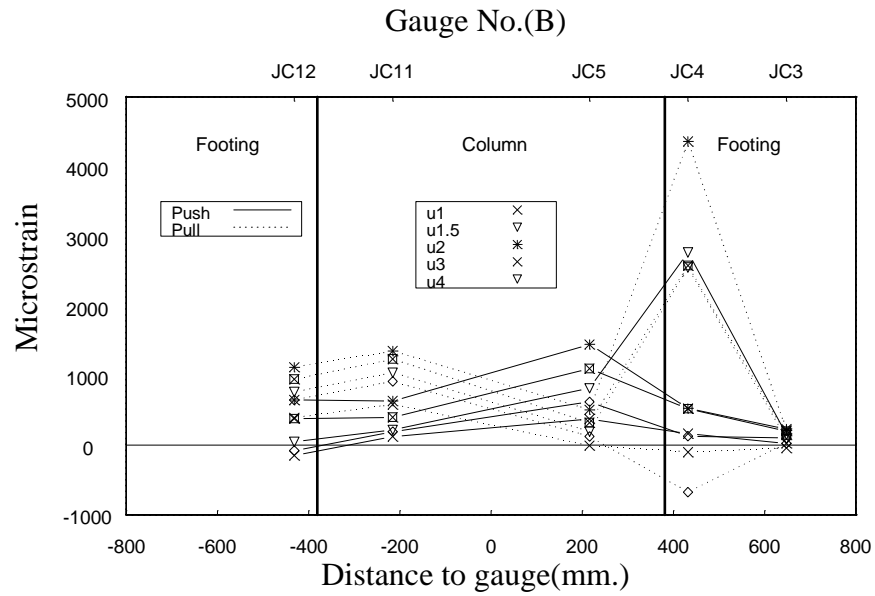
Figure G.21: Peak strain profiles of J-bars at column-pilecap joint
(SE-NW direction loading at column post-yield in loading phase 1, see Figure G.2)

324
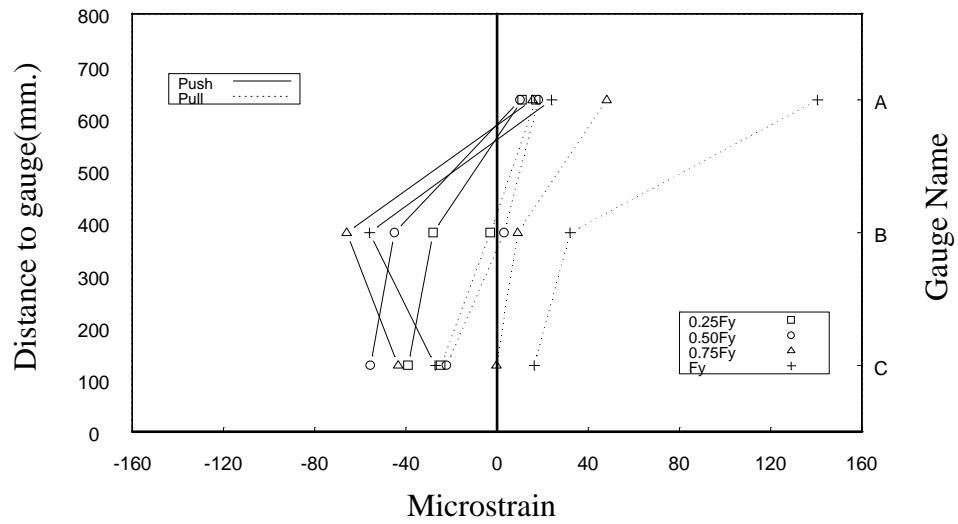
Figure G.22: Peak strain profiles at top, mid, bottom points of 9th J-bar
(E-W direction loading at column pre-yield in loading phase 1, see Figure G.2)
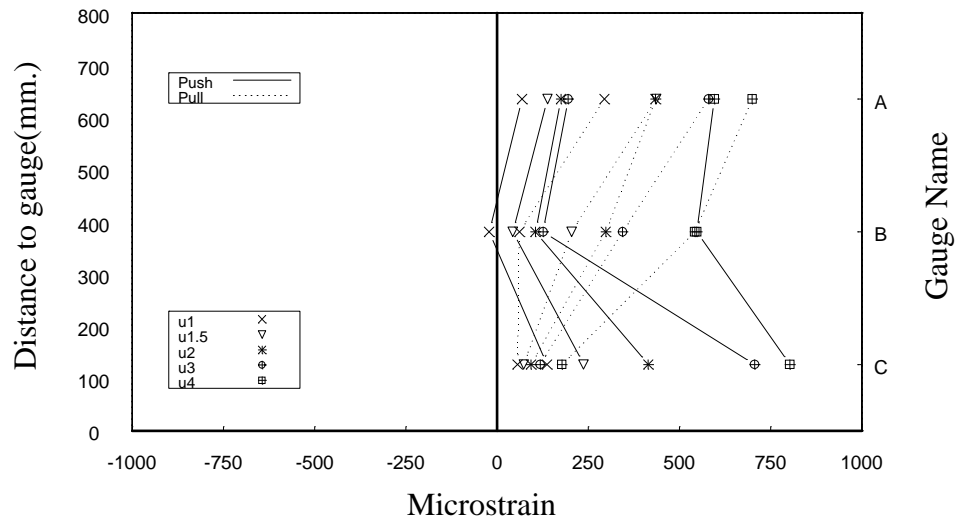
Figure G.23: Peak strain profiles at top, mid, bottom points of 9th J-bar
(E-W direction loading at column post-yield in loading phase 1, see Figure G.2)
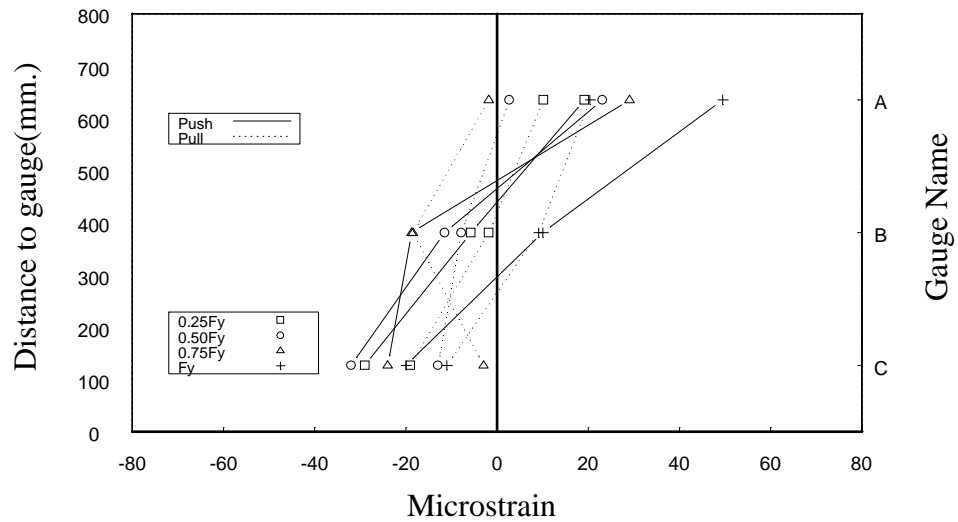
Figure G.24: Peak strain profiles at top, mid, bottom points of 10th J-bar (E-W direction loading at column pre-yield in loading phase 1, see Figure G.2)
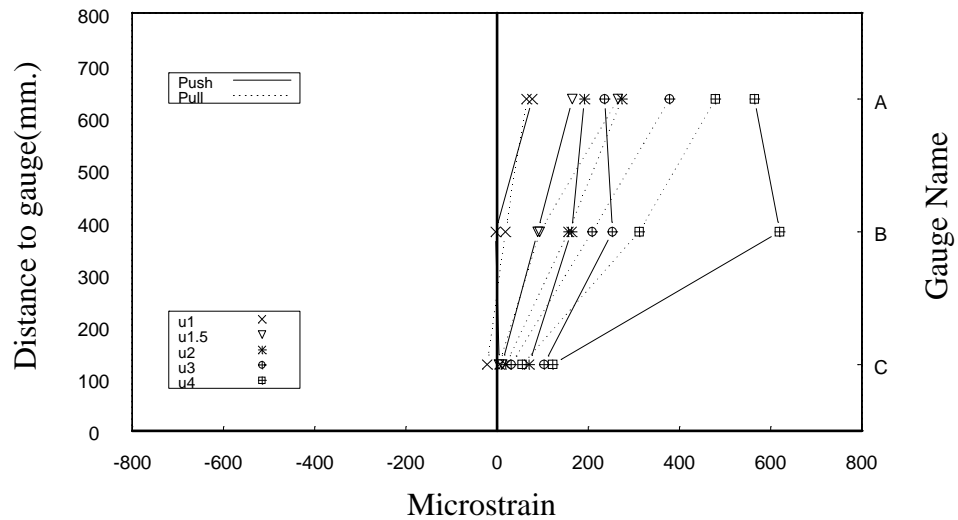
Figure G.25: Peak strain profiles at top, mid, bottom points of 10th J-bar (E-W direction loading at column post-yield in loading phase 1, see Figure G.2)
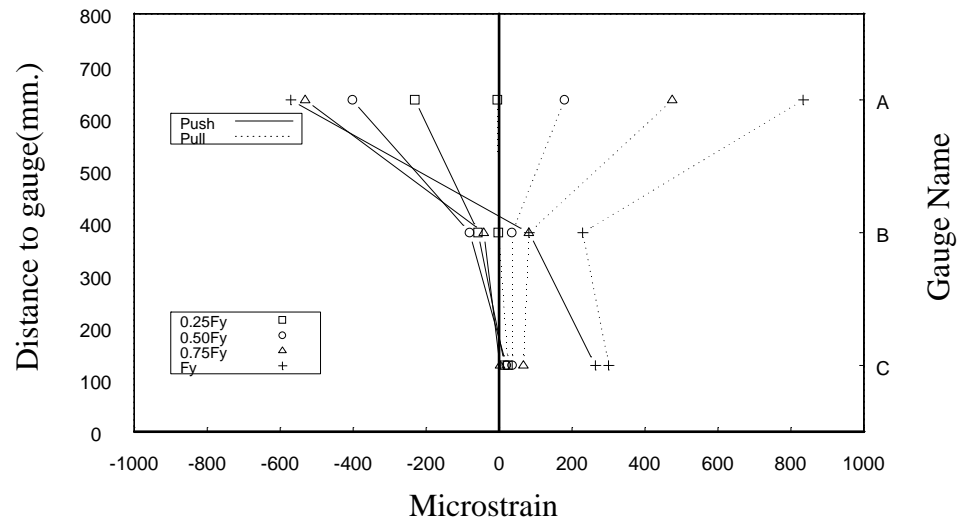
Figure G.26: Peak strain profiles at top, mid, bottom points of 11th J-bar
(SE-NW direction loading at column pre-yield in loading phase 1, see Figure G.2)
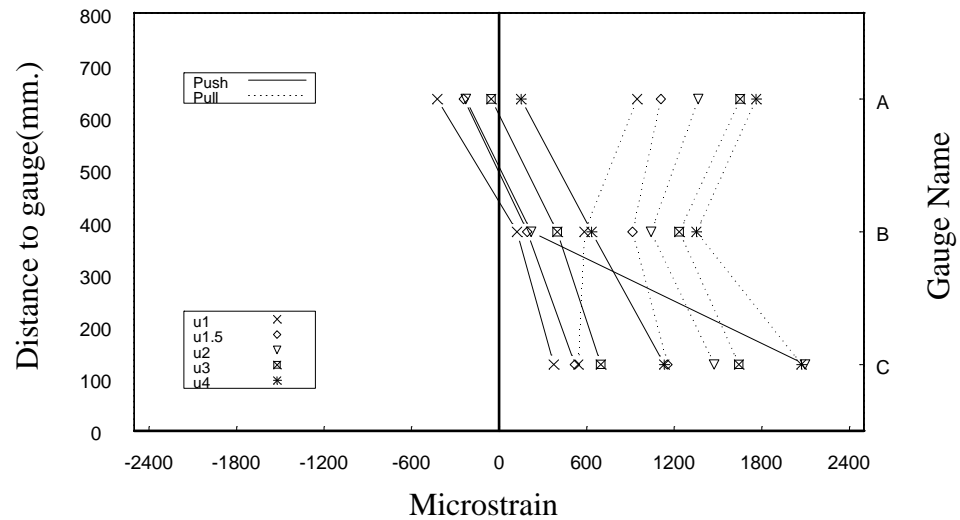
Figure G.27: Peak strain profiles at top, mid, bottom points of 11th J-bar
(SE-NW direction loading at column post-yield in loading phase 1, see Figure G.2)
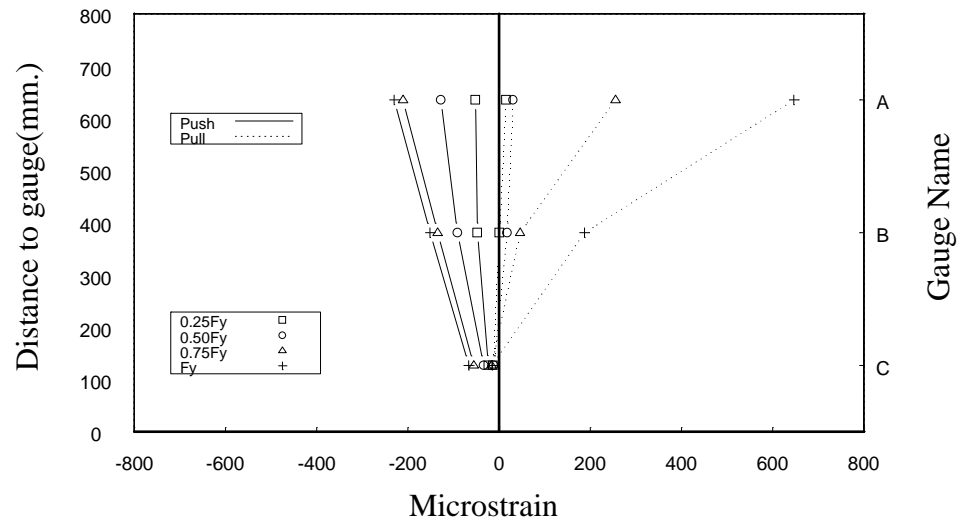
Figure G.28: Peak strain profiles at top, mid, bottom points of 12th J-bar
(SE-NW direction loading at column pre-yield in loading phase 1, see Figure G.2)
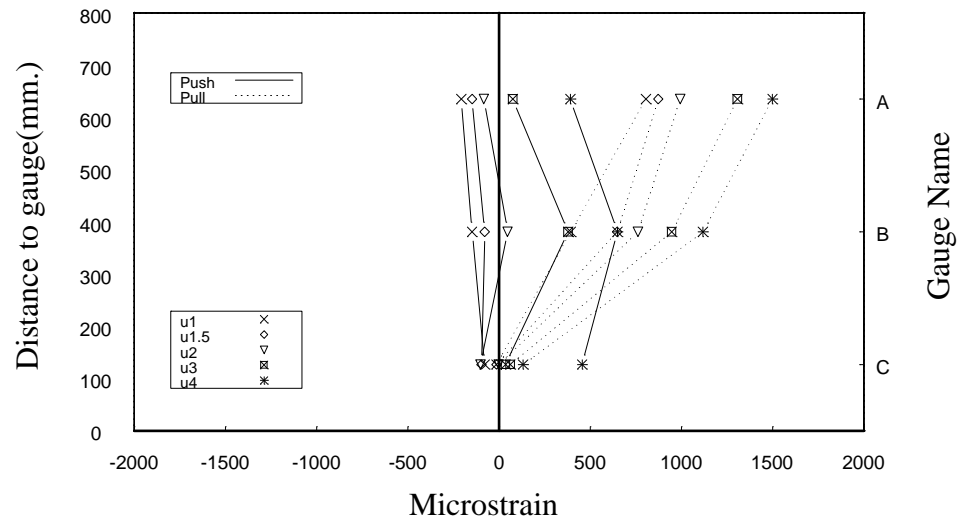
Figure G.29: Peak strain profiles at top, mid, bottom points of 12th J-bar
(SE-NW direction loading at column post-yield in loading phase 1, see Figure G.2)
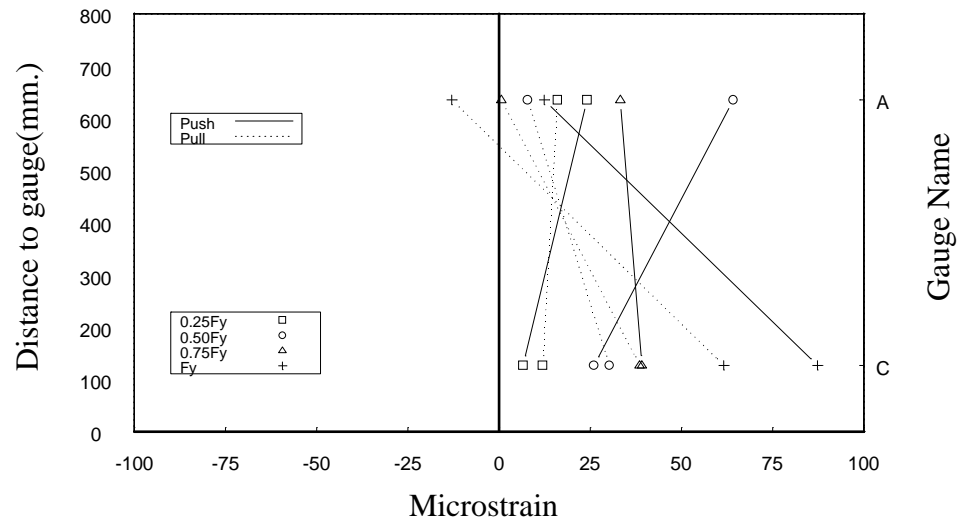
Figure G.30: Peak strain profiles at top, mid, bottom points of 13th J-bar
(SE-NW direction loading at column pre-yield in loading phase 1, see Figure G.2)
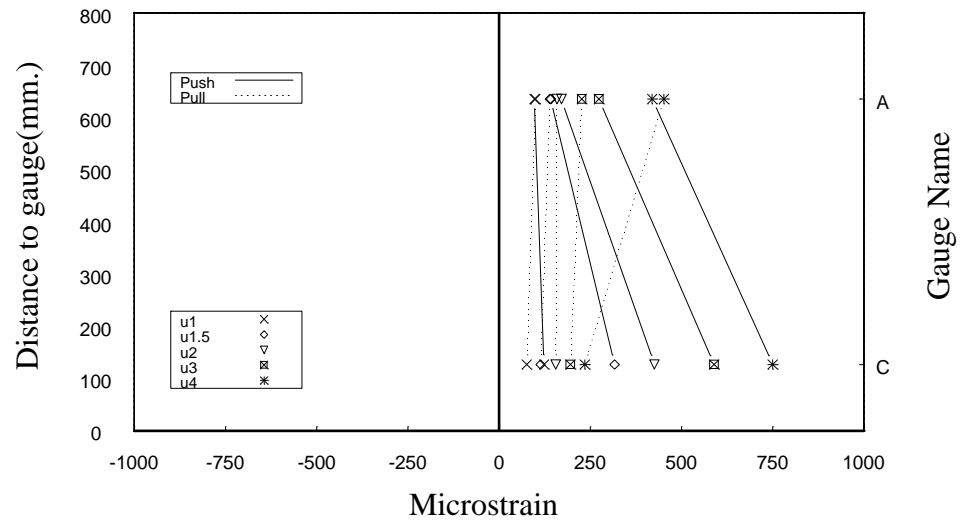
Figure G.31: Peak strain profiles at top, mid, bottom points of 13th J-bar
(SE-NW direction loading at column post-yield in loading phase 1, see Figure G.2)
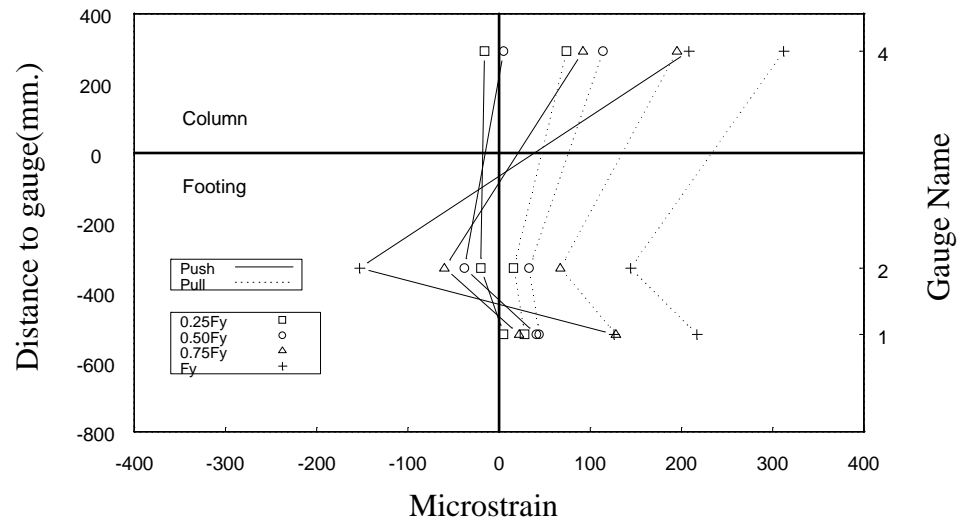
Figure G.32: Peak strain profiles of column spiral at CSW
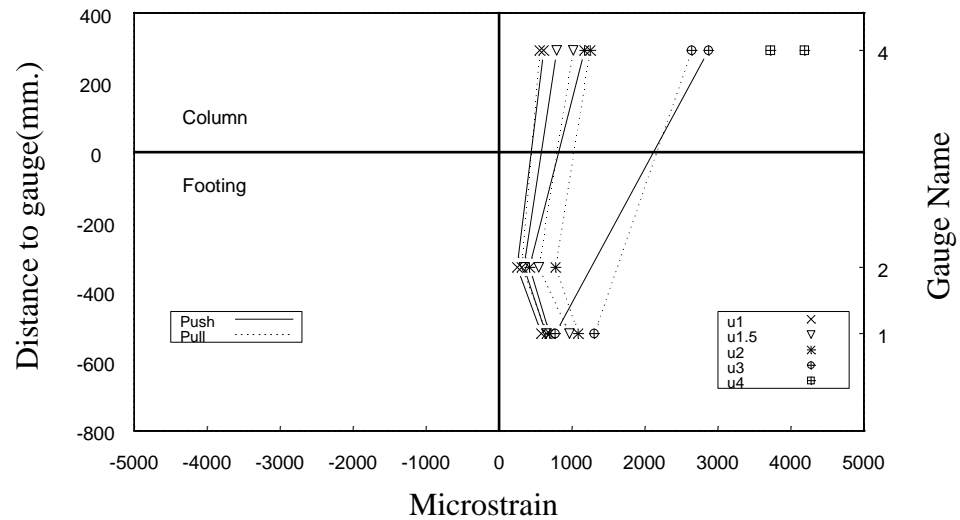(E-W direction loading at column pre-yield in loading phase 1, see Figure G.3)
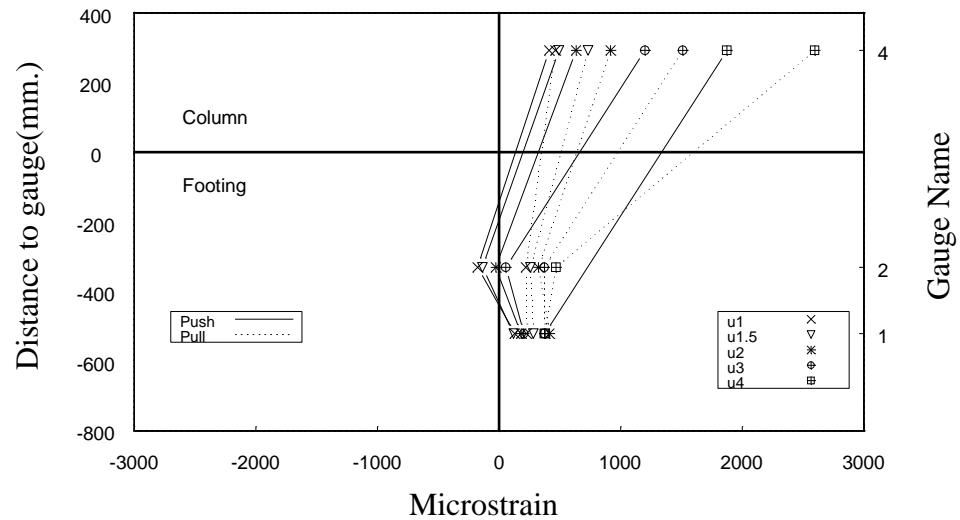
Figure G.33: Peak strain profiles of column spiral at CSW
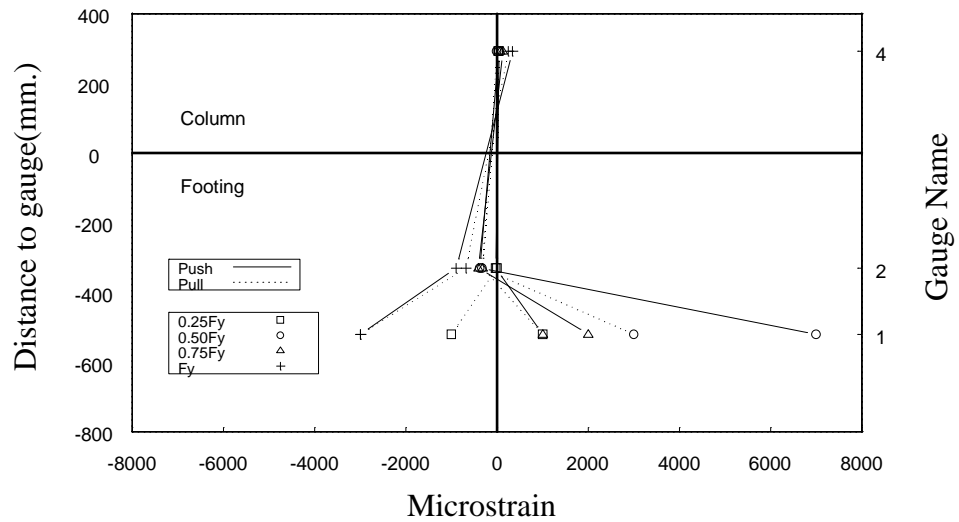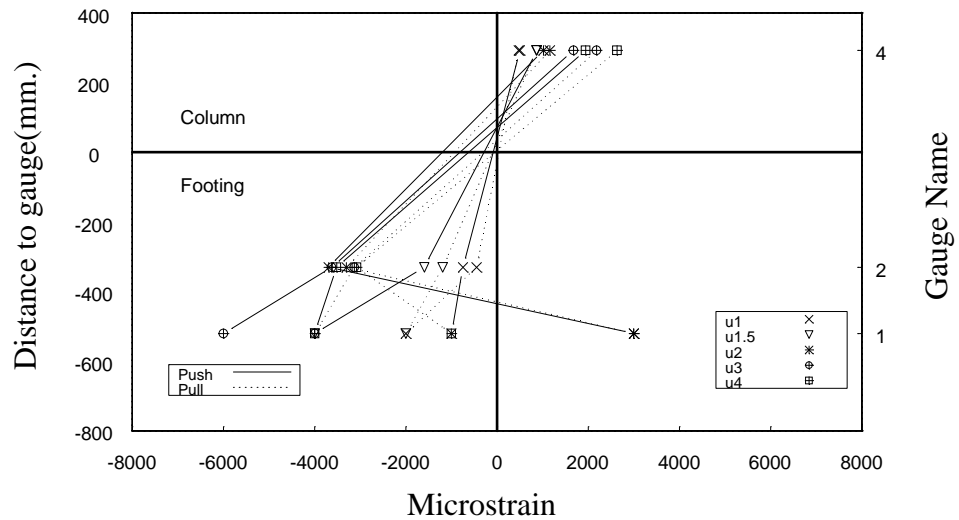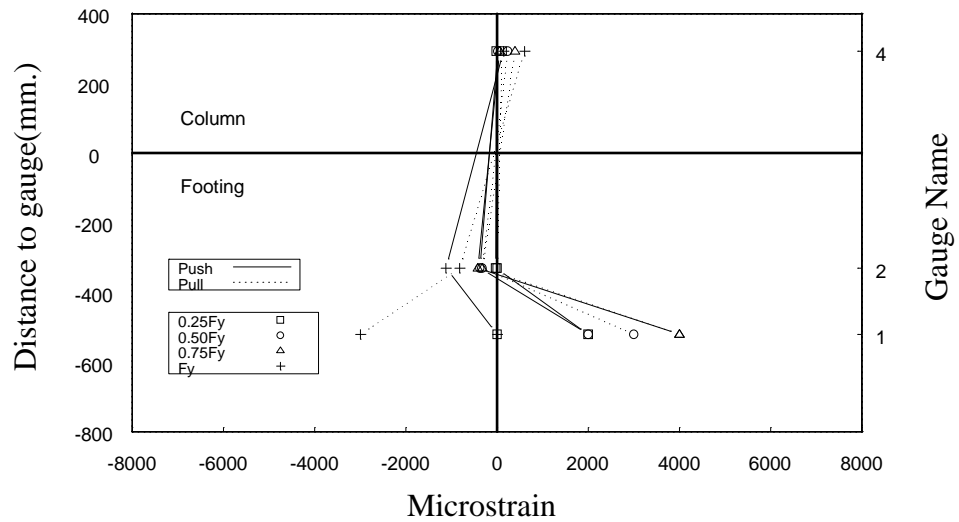(E-W direction loading at column post-yield in loading phase 1, see Figure G.3)

330
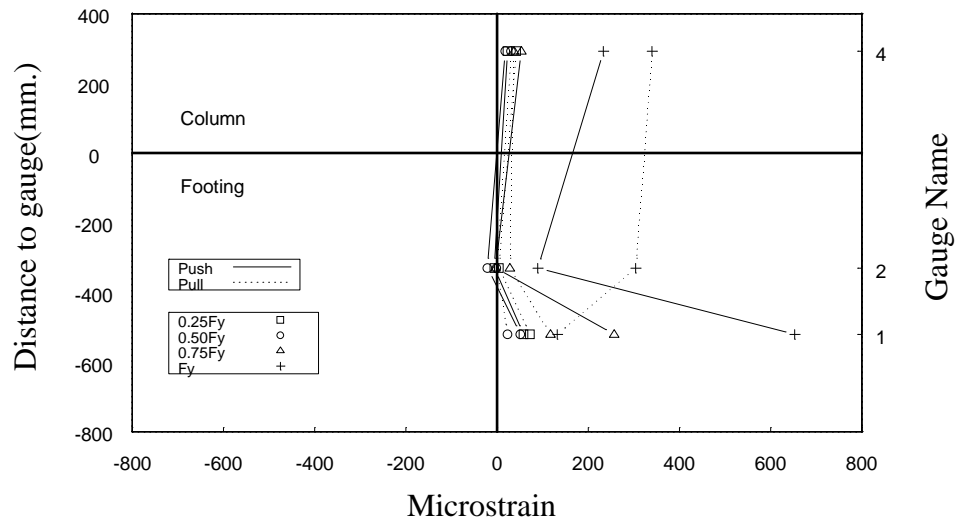
Figure G.34: Peak strain profiles of column spiral at CSW
(N-S direction loading at column pre-yield in loading phase 1, see Figure G.3)
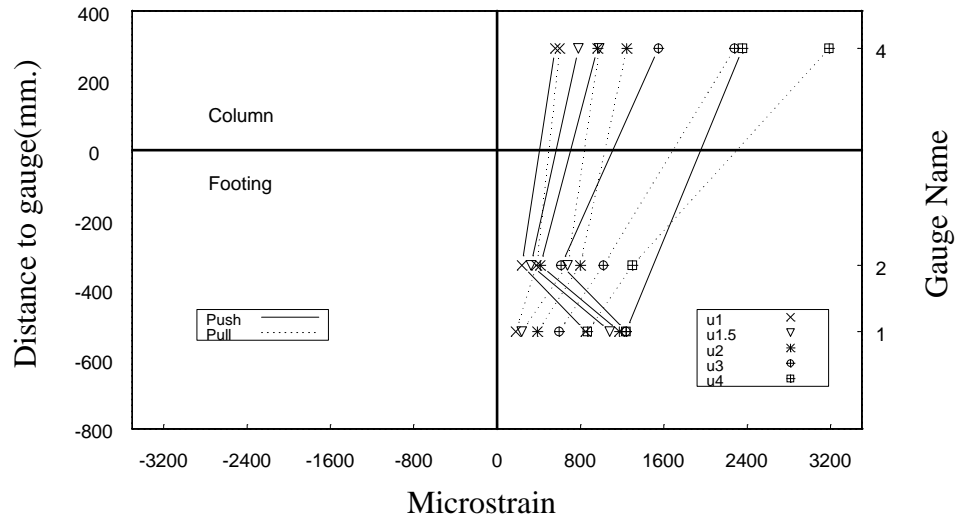
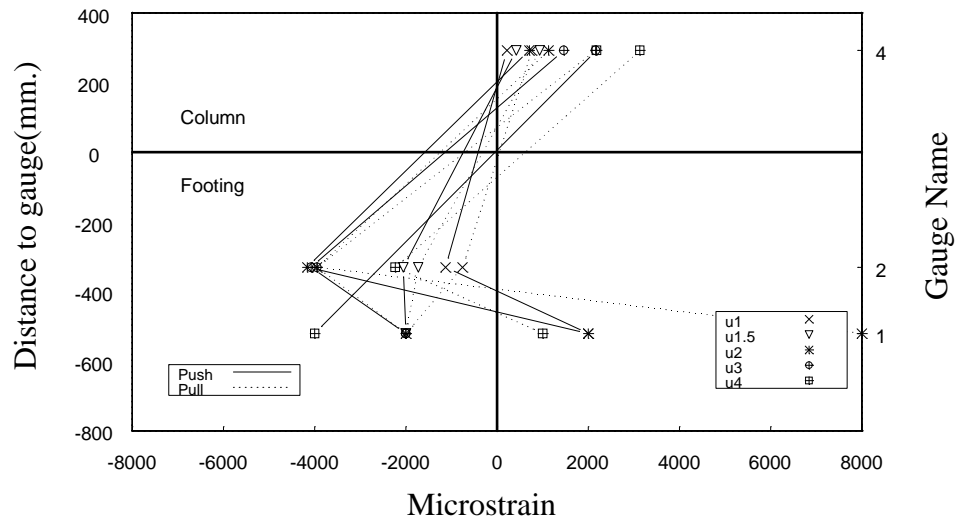Figure G.35: Peak strain profiles of column spiral at CSW
(N-S direction loading at column post-yield in loading phase 1, see Figure G.3)
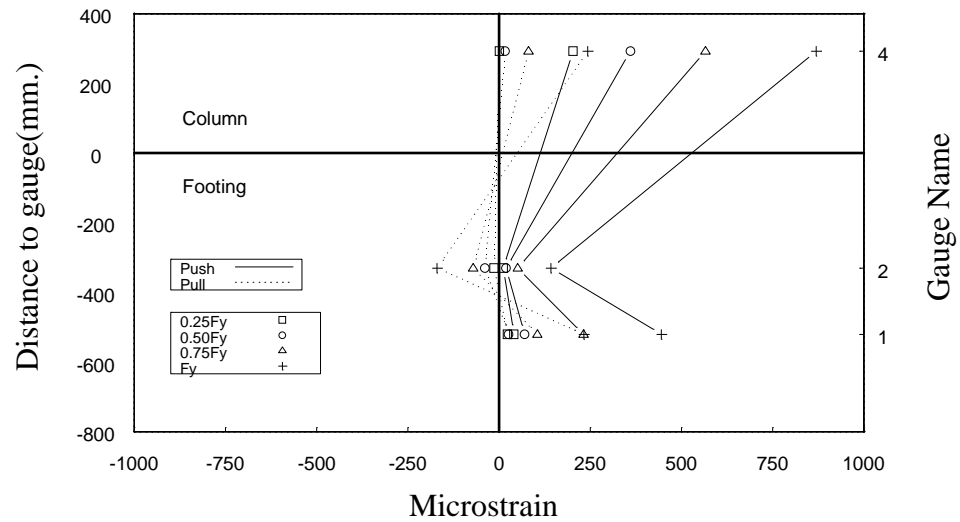
Figure G.36: Peak strain profiles of column spiral at CSE
(E-W direction loading at column pre-yield in loading phase 1, see Figure G.3)
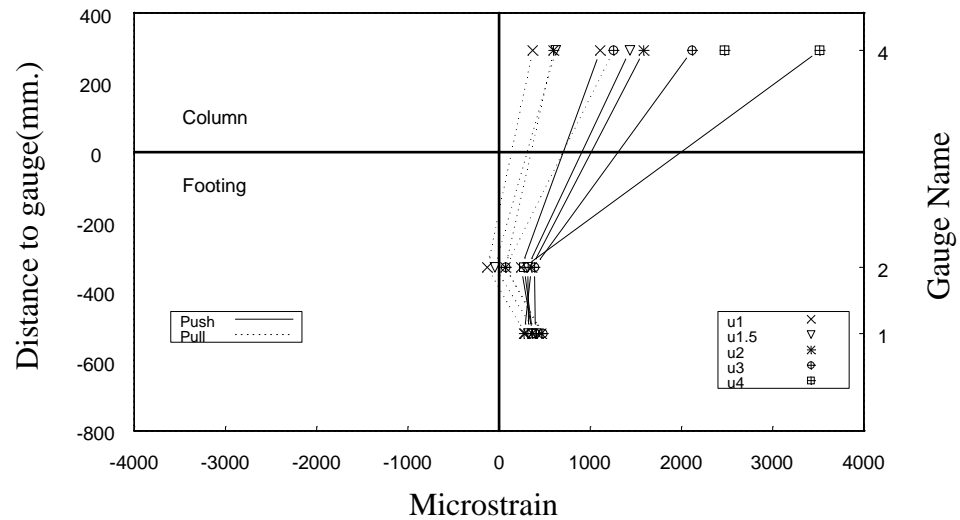
Figure G.37: Peak strain profiles of column spiral at CSE
(E-W direction loading at column post-yield in loading phase 1, see Figure G.3)
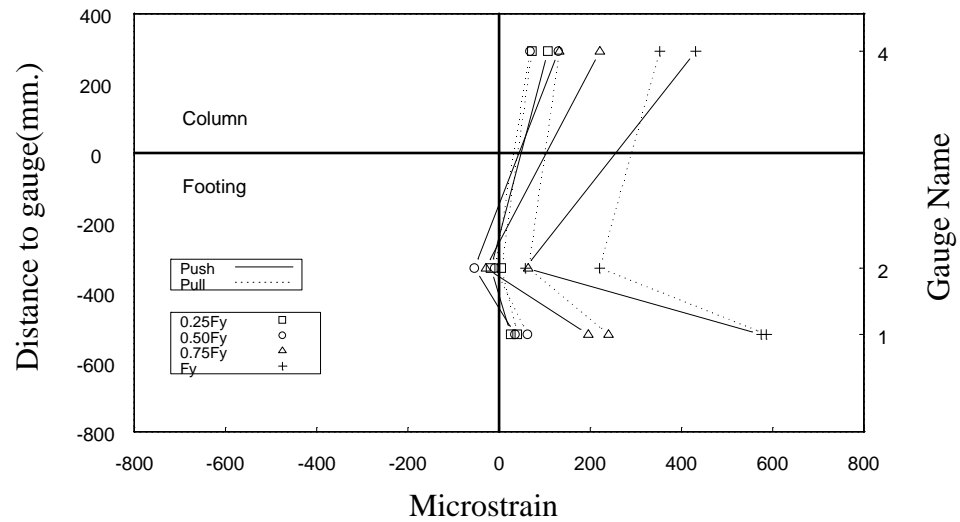
Figure G.38: Peak strain profiles of column spiral at CSE
(N-S direction loading at column pre-yield in loading phase 1, see Figure G.3)

Figure G.39: Peak strain profiles of column spiral at CSE
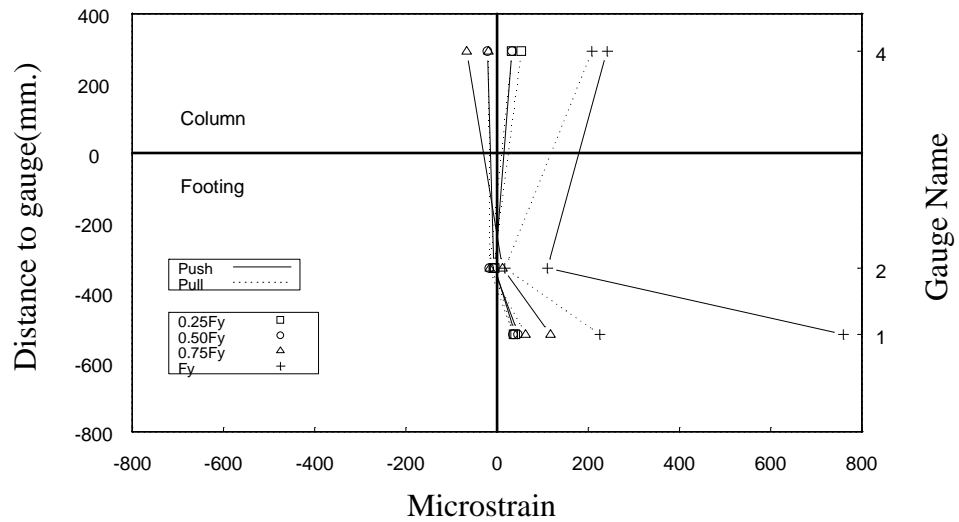(N-S direction loading at column post-yield in loading phase 1, see Figure G.3)

Figure G.40: Peak strains of column spiral at CSN
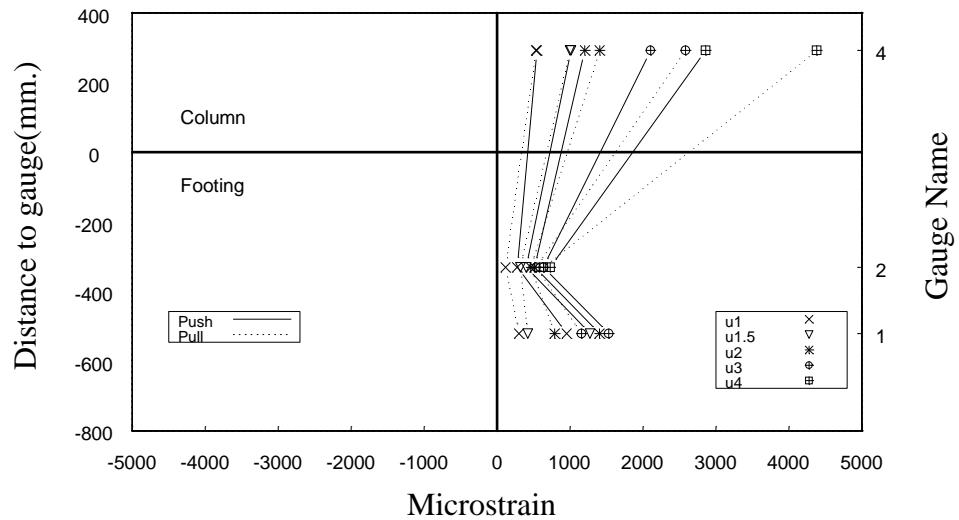(E-W direction loading at column pre-yield in loading phase 1, see Figure G.3)

Figure G.41: Peak strains of column spiral at CSN
(E-W direction loading at column post-yield in loading phase 1, see Figure G.3)
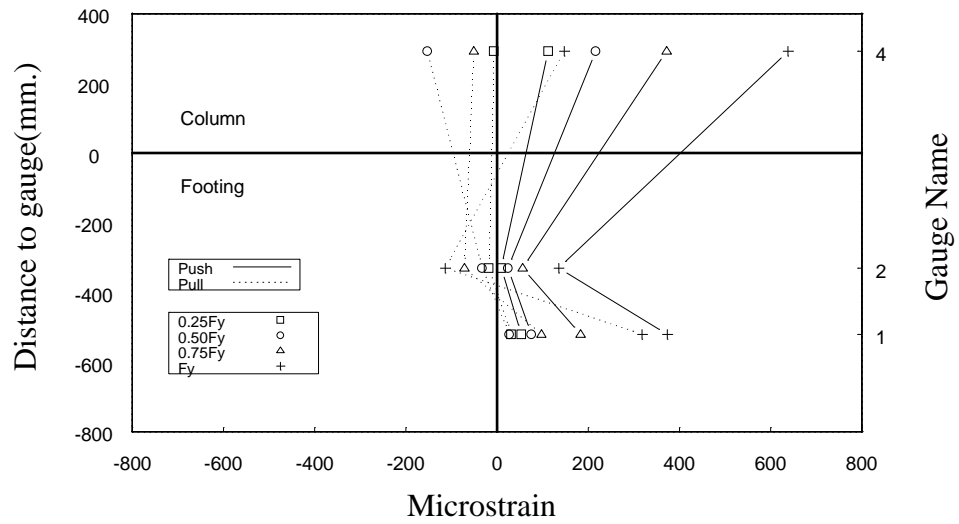
334

Figure G.42: Peak strains of column spiral at CSN
(N-S direction loading at column pre-yield in loading phase 1, see Figure G.3)

Figure G.43: Peak strains of column spiral at CSN
(N-S direction loading at column post-yield in loading phase 1, see Figure G.3)

Figure G.44: Peak strains of column spiral at CSS
(E-W direction loading at column pre-yield in loading phase 1, see Figure G.3)
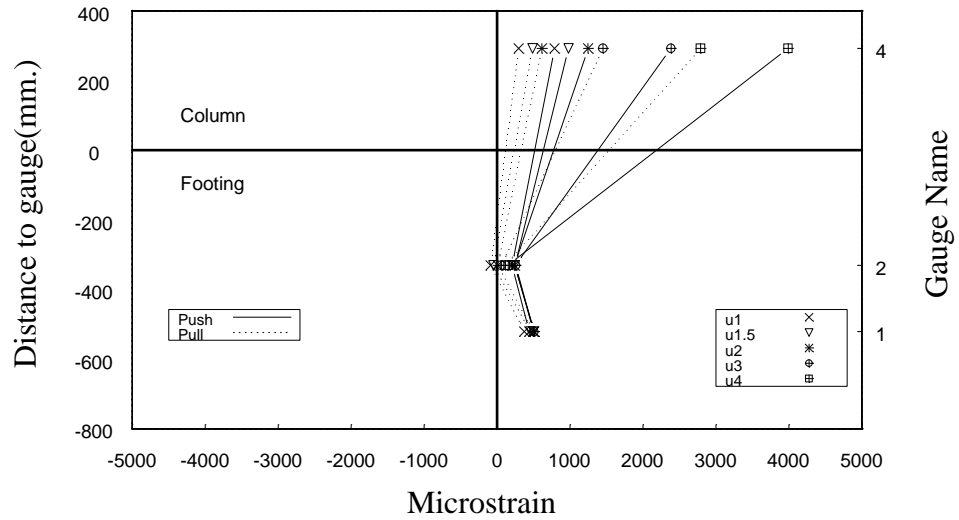

Figure G.45: Peak strains of column spiral at CSS
(E-W direction loading at column post-yield in loading phase 1, see Figure G.3)

336

Figure G.46: Peak strains of column spiral at CSS
(N-S direction loading at column pre-yield in loading phase 1, see Figure G.3)

Figure G.47: Peak strains of column spiral at CSS
(N-S direction loading at column post-yield in loading phase 1, see Figure G.3)

Appendix H: Construction Photos of unit CFPS1

Figure H.1: Prefabricated column cage of CFPS1(I)
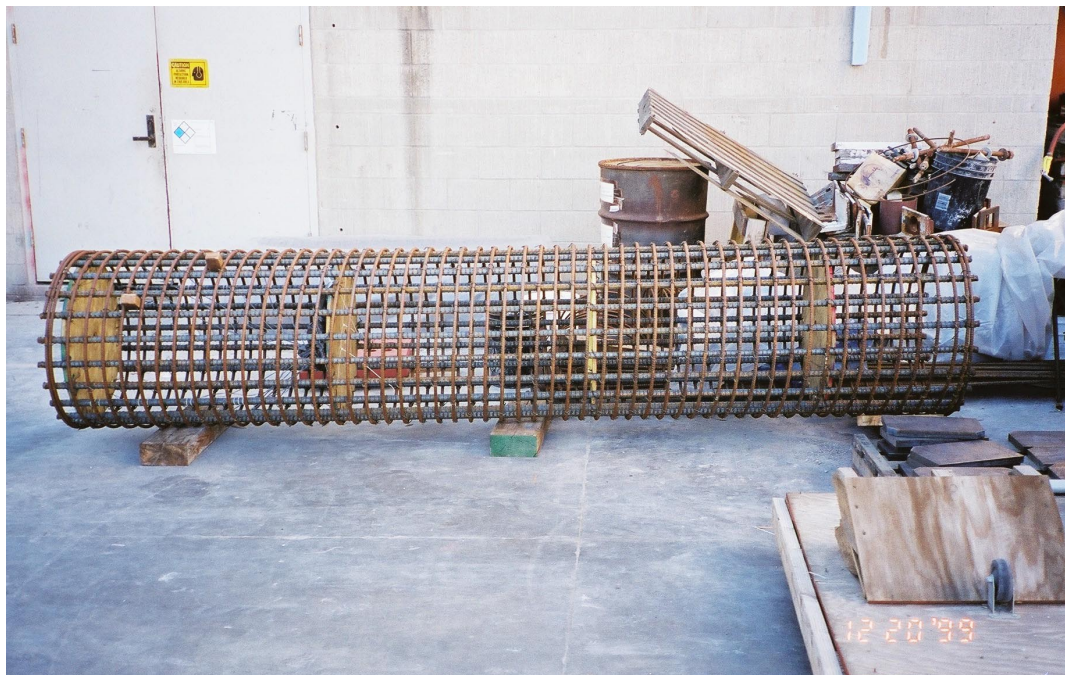
Figure H.2: Prefabricated column cage of CFPS1(II)
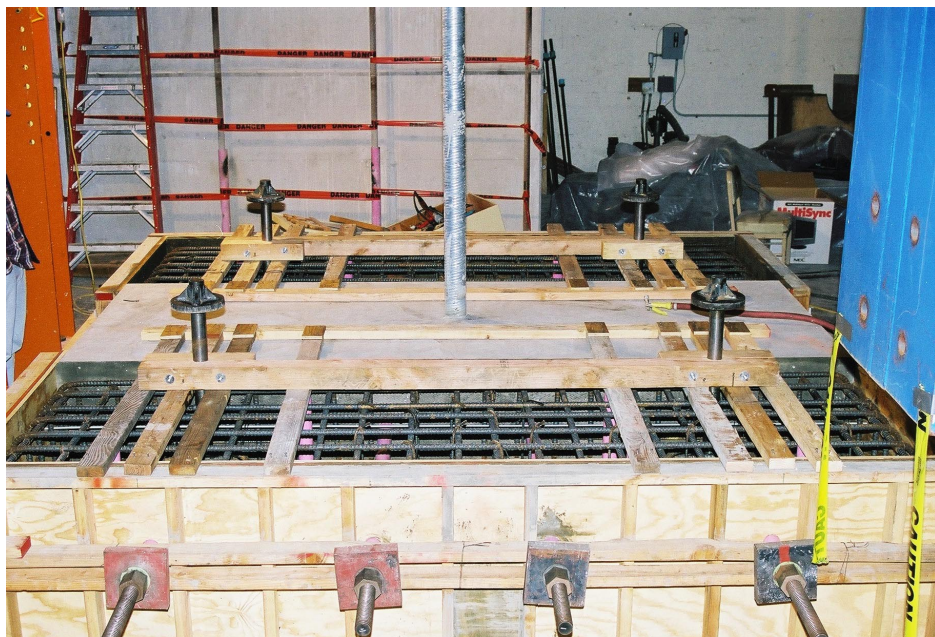
Figure H.3: Solid steel rod for the simulation of vertical soil-pile interaction stiffness

Figure H.4: Construction of test base

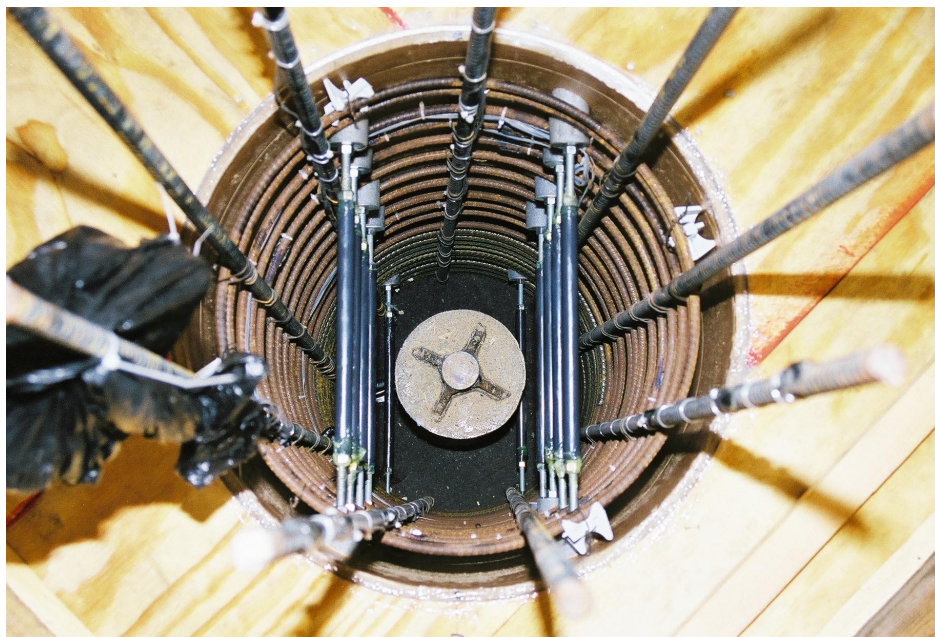Figure H.5: Steel rod embedded in the test base with gap filler between pile and test base

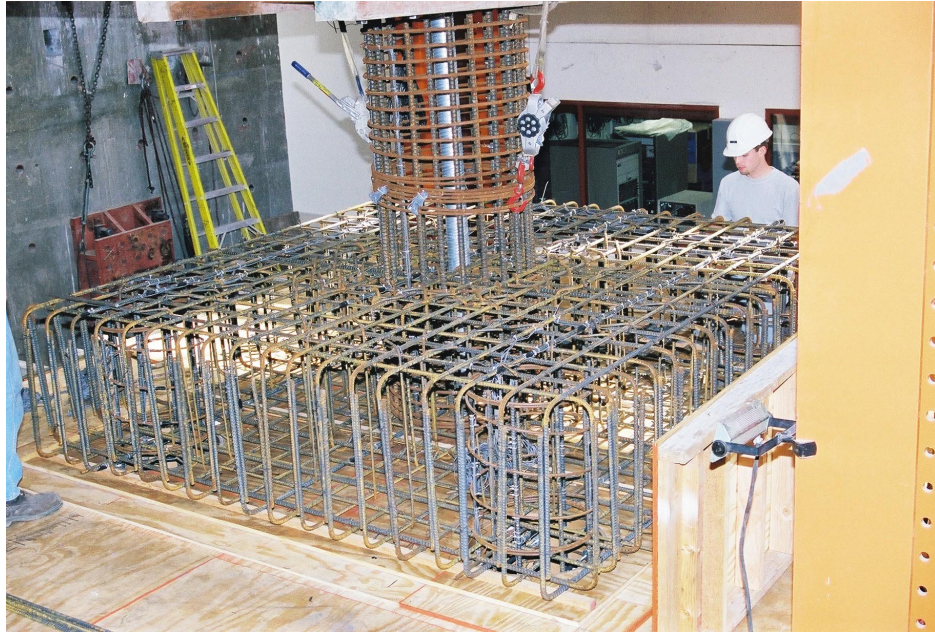Figure H.6: Installation of pile curvature rods
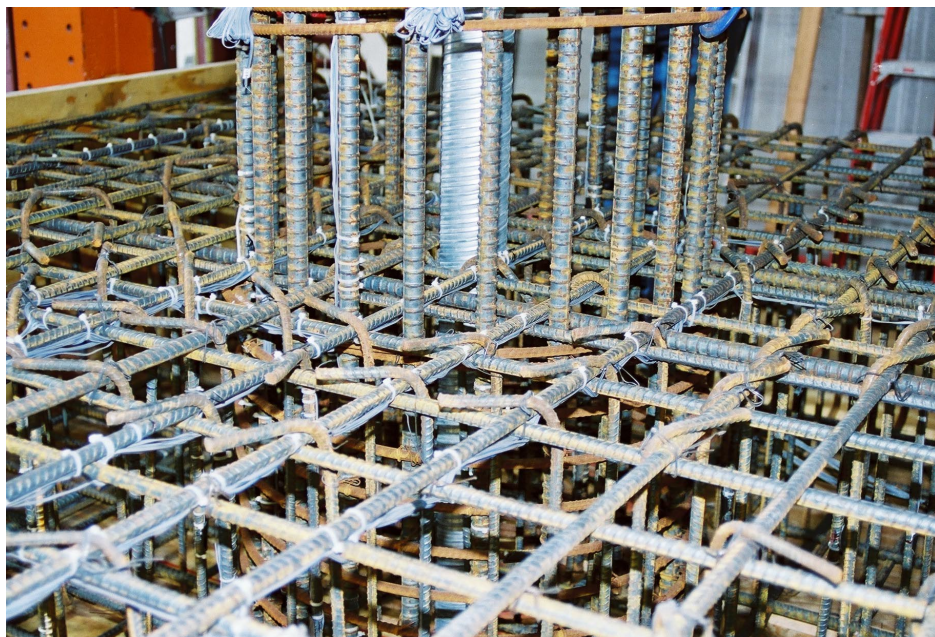
Figure H.7: View of pilecap joints

Figure H.8: Reinforcement of column-pilecap joint region

Figure H.9: Reinforcement of pile-pilecap joint region

Figure H.10: Completed formwork for pilecap

Figure H.11: Overall view of construction of CFPS1
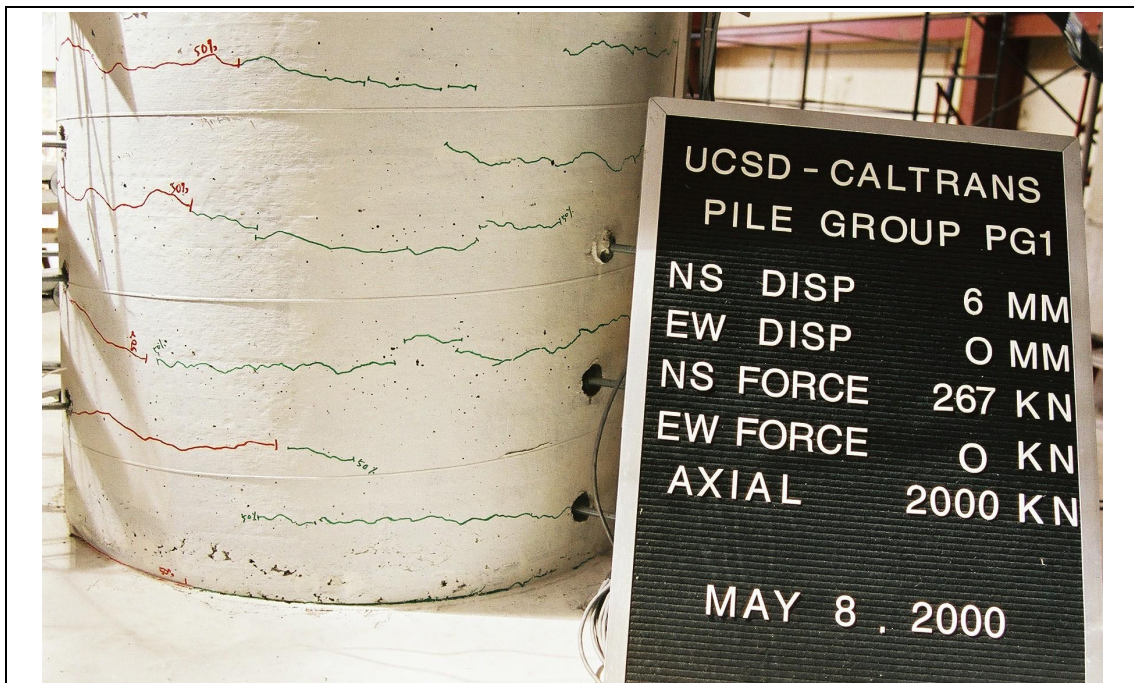
Appendix I: Test Photos of unit CFPS1

Figure I.1: Flexural cracks on column at 0.5F$_y$of Loading Phase 1

Figure I.2: Flexural cracks on pile in diagonal direction loading at 0.75F$_y$ of Loading Phase 1

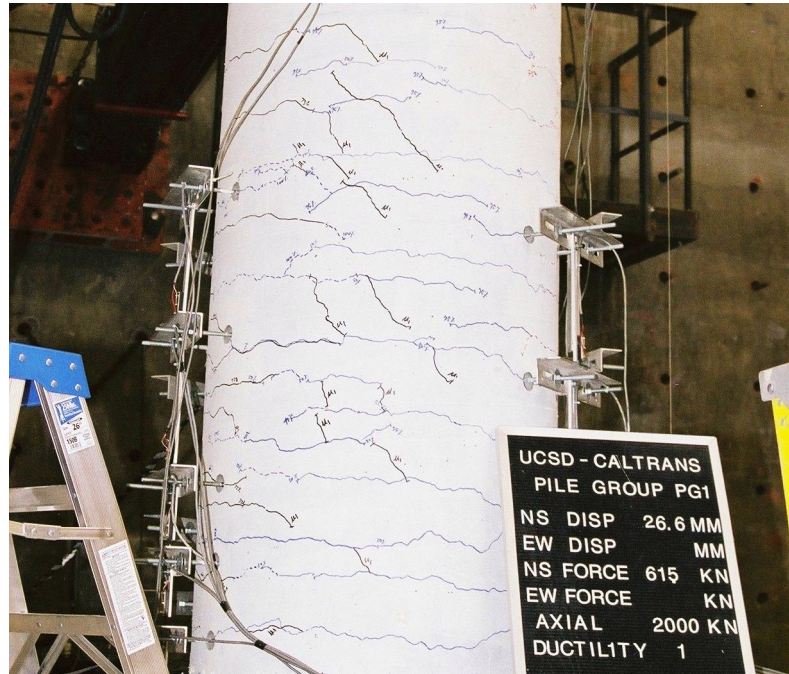Figure I.3: Inclined cracks on column at $\mu_\Delta = 1.0$ of Loading Phase 1

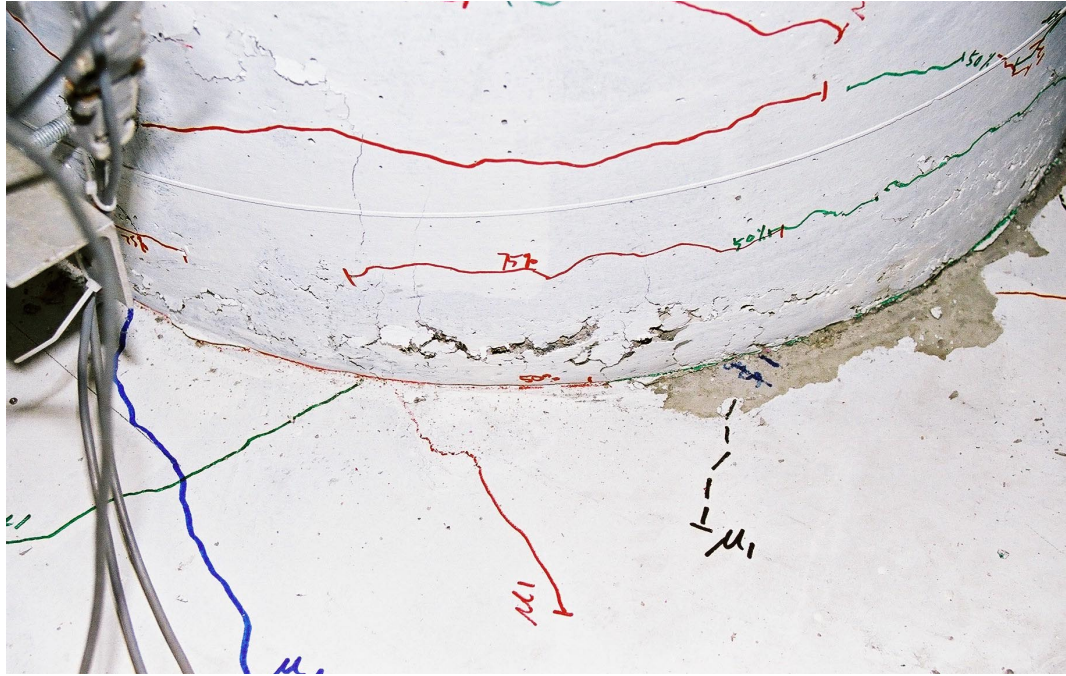Figure I.4: First strain penetration cracks on top of pilecap at $\mu_\Delta = 1.0$ of Loading Phase 1

Figure I.5: Initiation of column cover concrete crushing at $\mu_\Delta = 1.5$ of Loading Phase 1

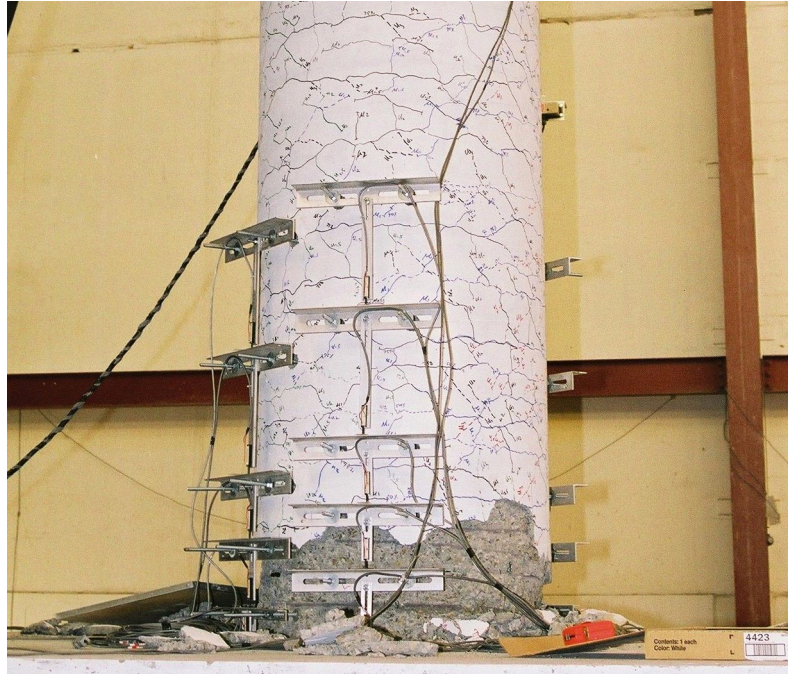Figure I.6: Peripheral crack(t = 1.8mm) of pilecap at $\mu_\Delta = 2.0$ of Loading Phase 1

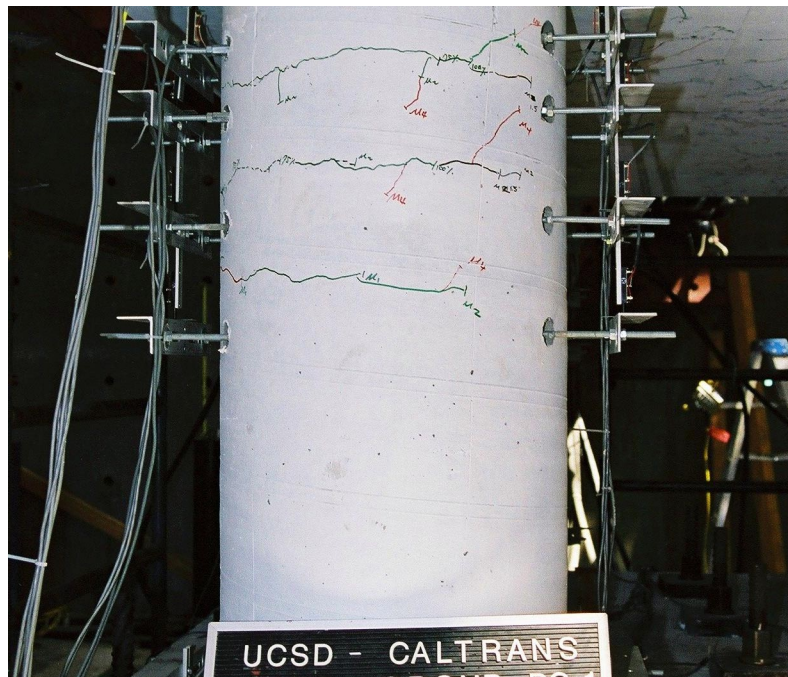Figure I.7: Spalling of column cover concrete at $\mu_\Delta = 3.0$ of Loading Phase 1

Figure I.8: Inclined cracks on pile at $\mu_\Delta = 4.0$ of Loading Phase 1

Figure I.9: Spalling and strain penetration crack of column at $\mu_\Delta = 5.0$ of Loading Phase 1

Figure I.10: Pilecap cover concrete spalling at 90° J-hook locations
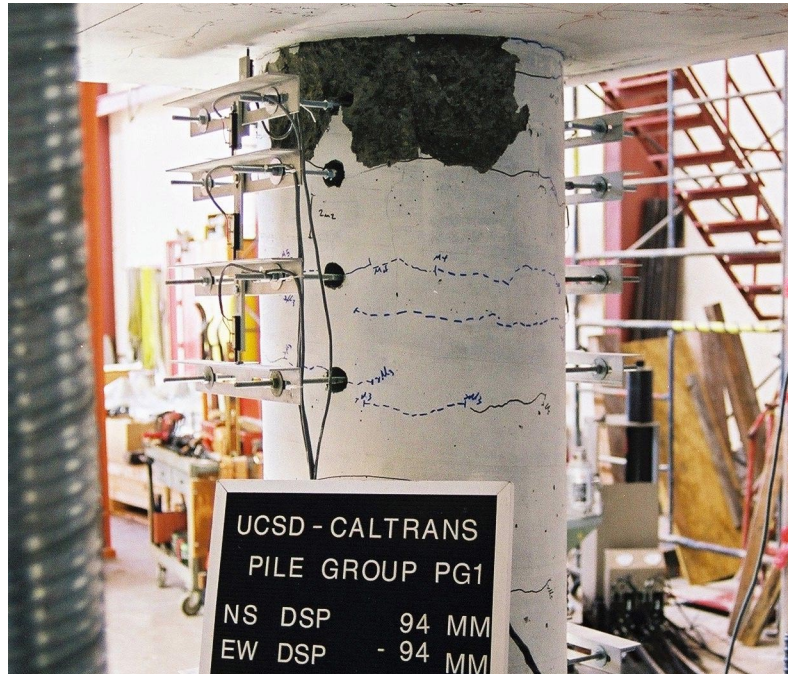($\mu_\Delta = 5.0$ of Loading Phase 2)

350

Figure I.11: Spalling of pile cover concrete ($\mu_\Delta = 5.0$ of Loading Phase 2)

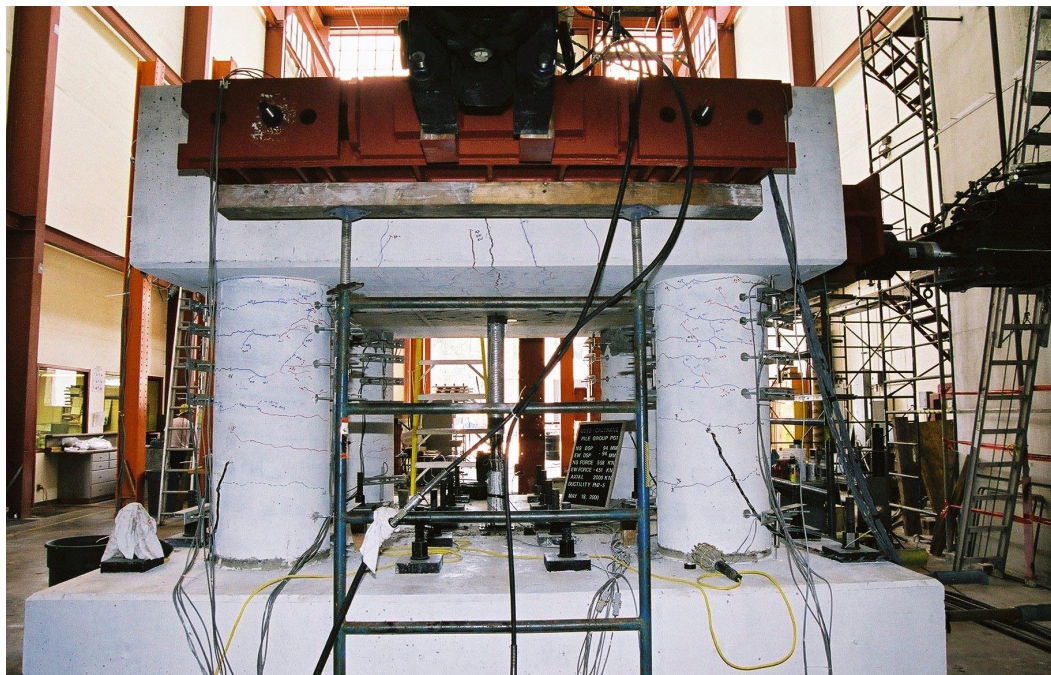Figure I.12: Damage of pilecap and piles ($\mu_\Delta = 5.0$ of Loading Phase 2)

Figure I.13: Damage of column and pilecap ($\Delta_{pilecap}$ = 24mm of Loading Phase 3)

Figure I.14: Buckling of pile longitudinal bar ($\Delta_{pilecap}$ = 24mm of Loading Phase 3)

Figure I.15: Straightening of 90º J-hook at the end of test

353

Appendix J: Construction and Test Setup Photos of unit CFPS2

Figure J.1: Reinforcement of column-pilecap joint region

Figure J.2: Reinforcement of pile-pilecap joint region

Figure J.3: Pilecap transverse reinforcement

Figure J.4: Tee head of column reinforcement

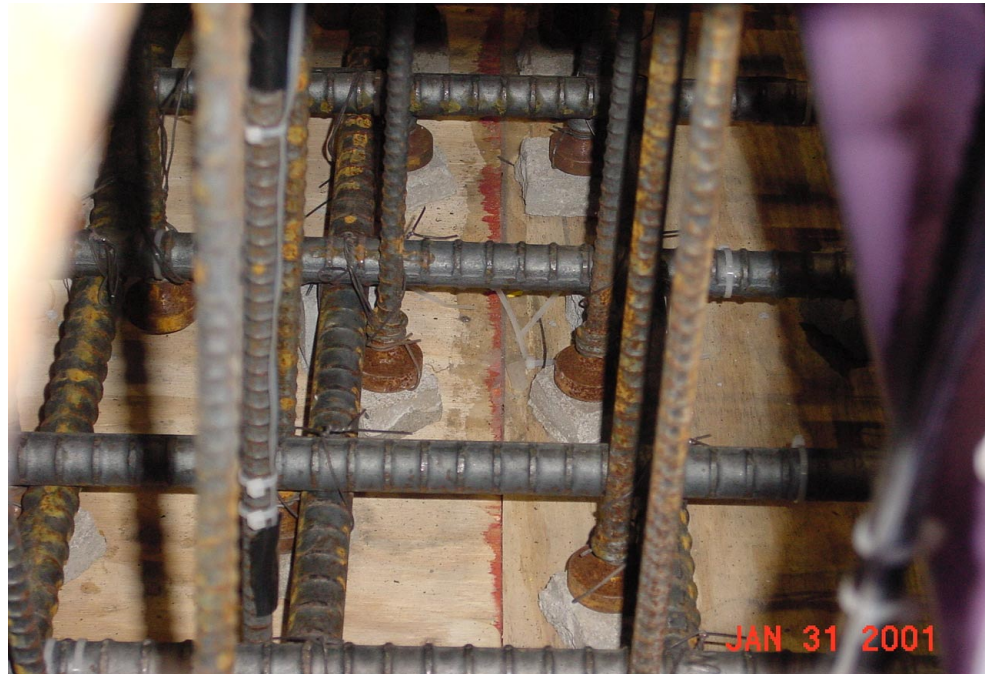Figure J.5: Joint stirrup reinforcement on top of spacers

Figure J.6: Complete reinforcement of CFPS1

Figure J.7: Curvature rods of column in cross configuration
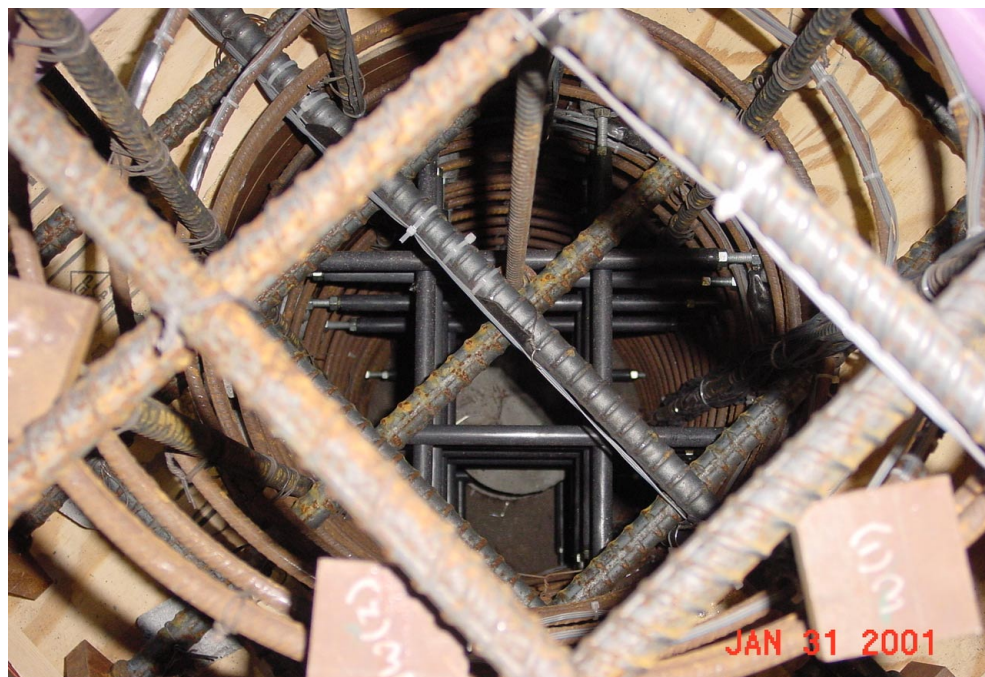
Figure J.8: Curvature rods of pile in cross configuration

Figure J.9: Overall view of construction of CFPS2
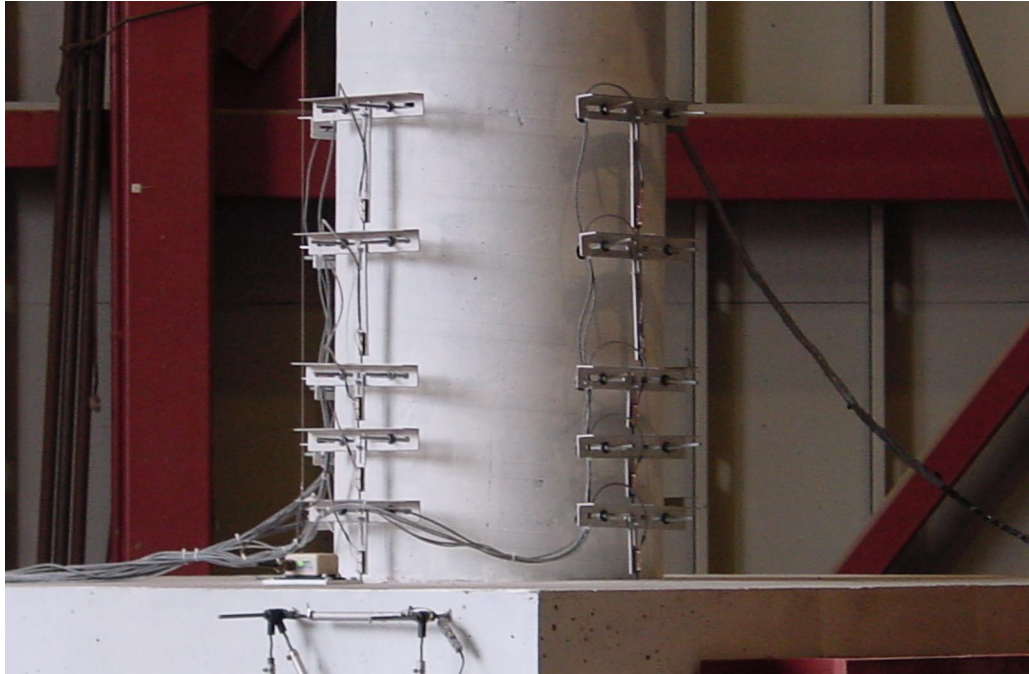
Figure J.10: Potentiometers mounted on column in cross configuration
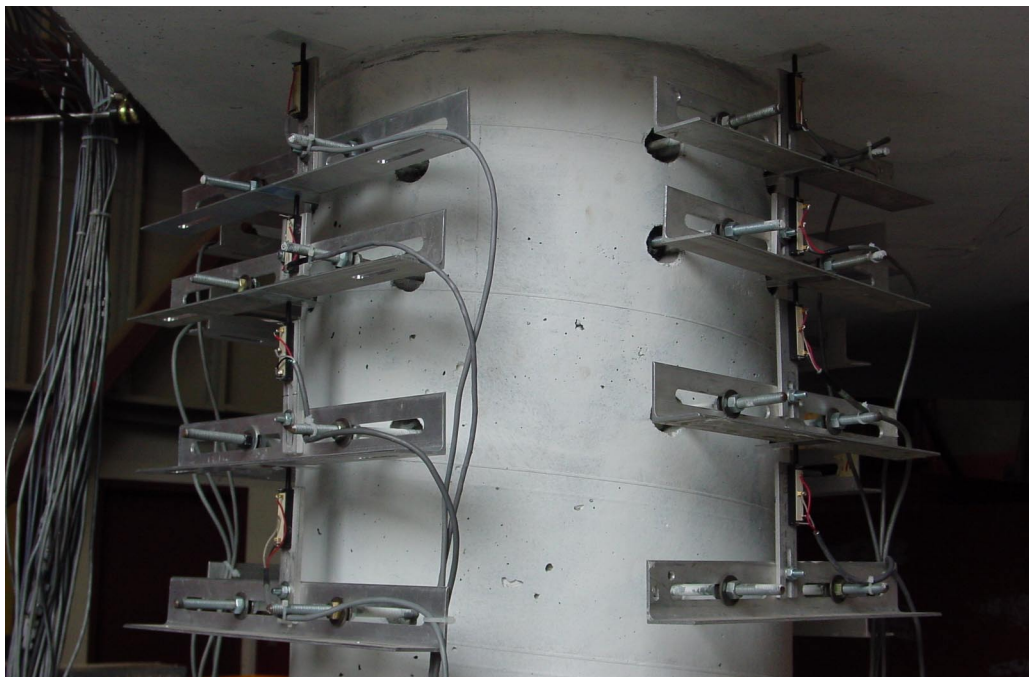
Figure J.11: Potentiometers mounted on pile in cross configuration
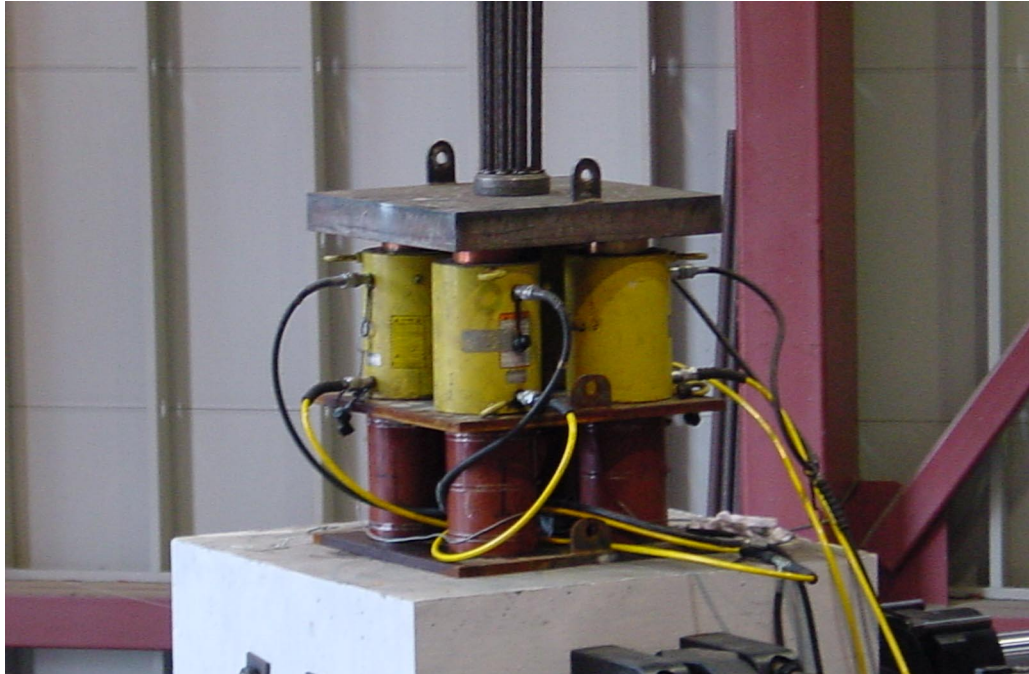
Figure J.12: Hydraulic hollow core ram with load cells for constant gravity load

Figure J.13: Loading Beam on vertical side of pilecap
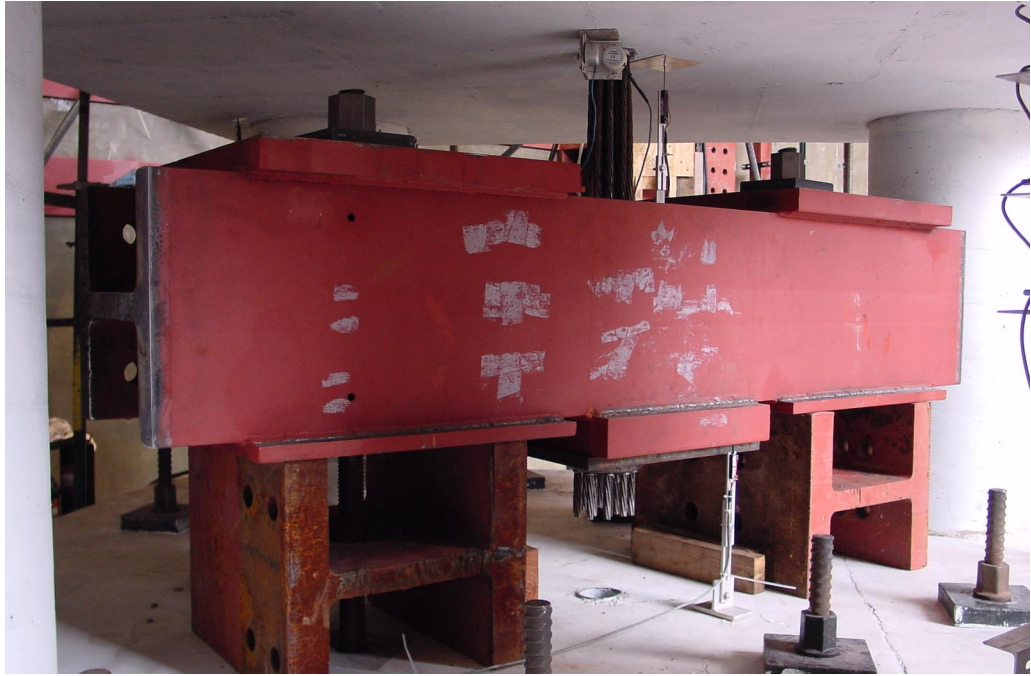
Figure J.14: Reaction beam tied down to strong floor for post tensioning
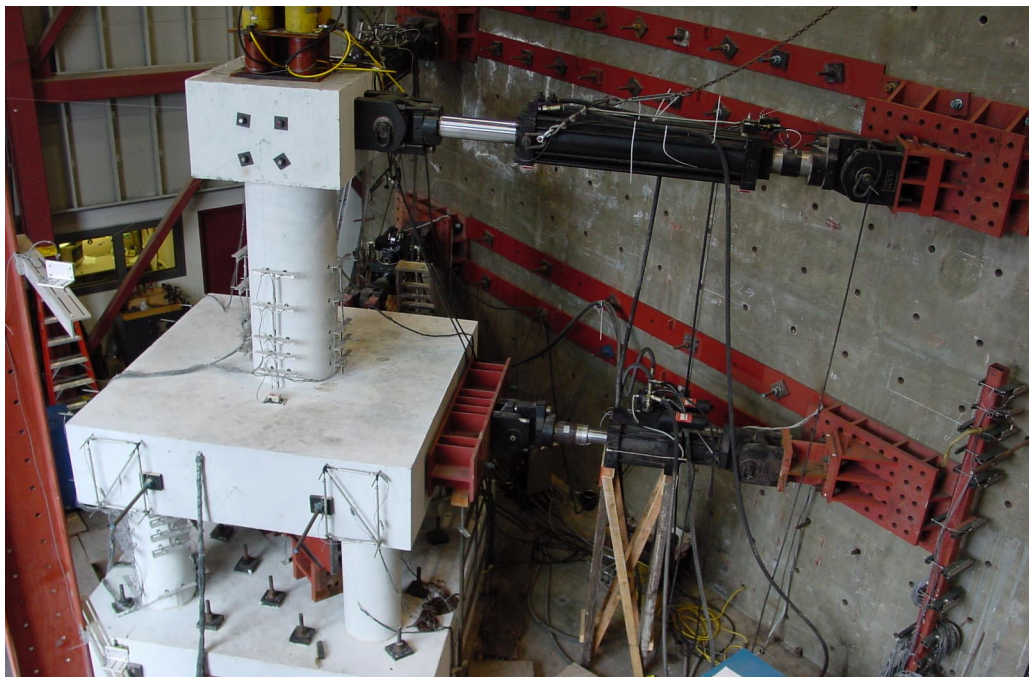
Figure J.15: Complete test setup

Appendix K: Test Photos of unit CFPS2

Figure K.1: Flexural cracks on pilecap bottom at $0.25F_y$ of Loading Phase 1
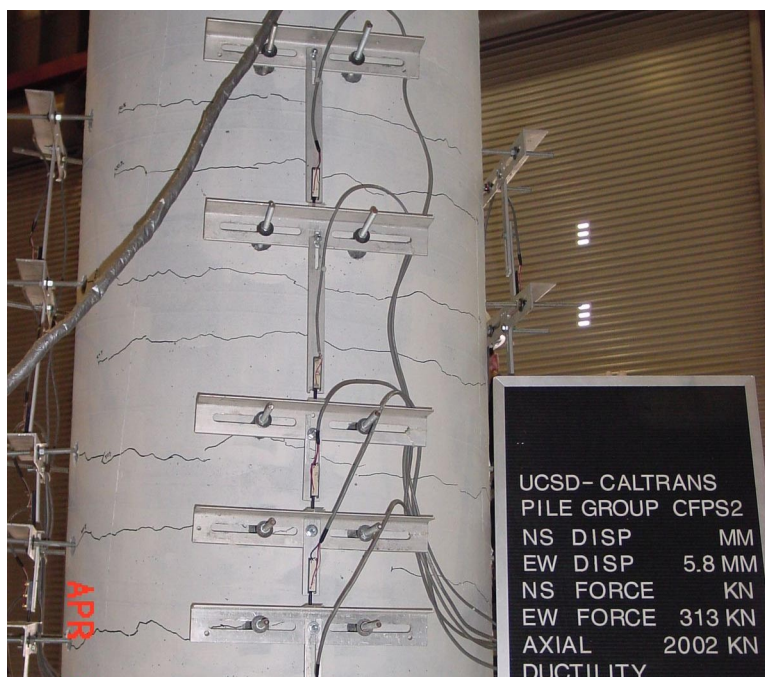
Figure K.2: Flexural cracks on column at $0.5F_y$ of Loading Phase 1
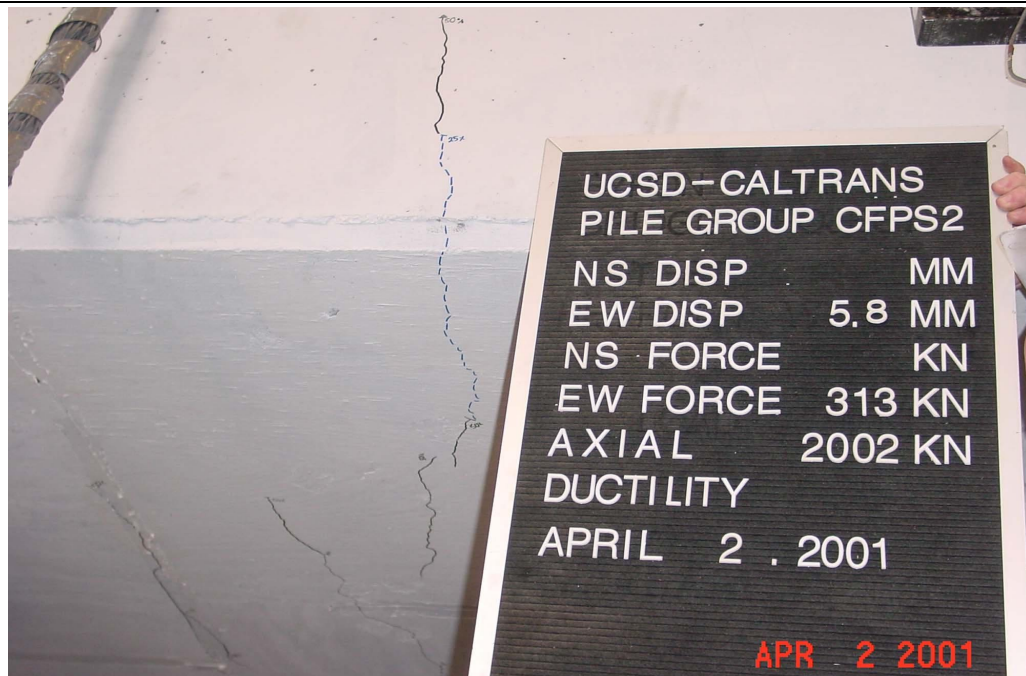
Figure K.3: Flexural cracks on pilecap bottom at $0.5F_y$ of Loading Phase 1

Figure K.4: Flexural cracks on column at $1.0F_y$ of Loading Phase 1

Figure K.5: Flexural cracks on pilecap at 1.0F_y of Loading Phase 1

Figure K.6: Flexural cracks on pile B at 1.0F_y of Loading Phase 1
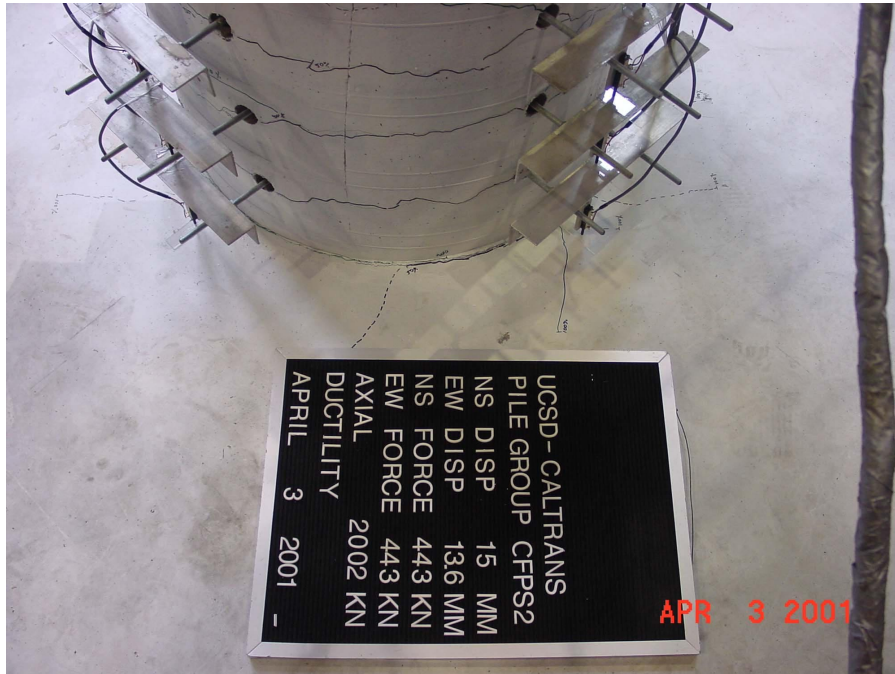
Figure K.7: Strain penetration cracks on pilecap top surface at 1.0F$_y$ of Loading Phase 1

Figure K.8: Initiation of cover concrete crushing at μ_Δ = 1.0 of Loading Phase 1

Figure K.9: Flexural cracks on pilecap at $\mu_\Delta = 1.0$ of Loading Phase 1

Figure K.10: Crushing of column cover concrete at $\mu_\Delta = 1.5$ of Loading Phase 1

Figure K.11: Strain penetration cracks on pilecap top surface at $\mu_\Delta = 1.5$ of Loading Phase 1
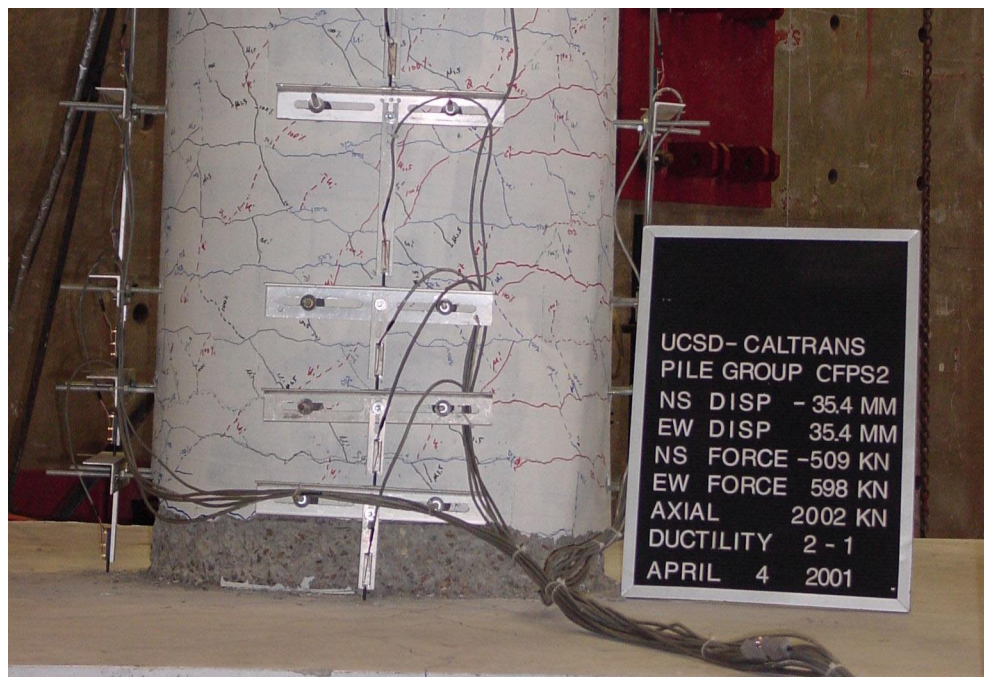
Figure K.12: Spalling of column cover concrete at $\mu_\Delta = 2.0$ of Loading Phase 1
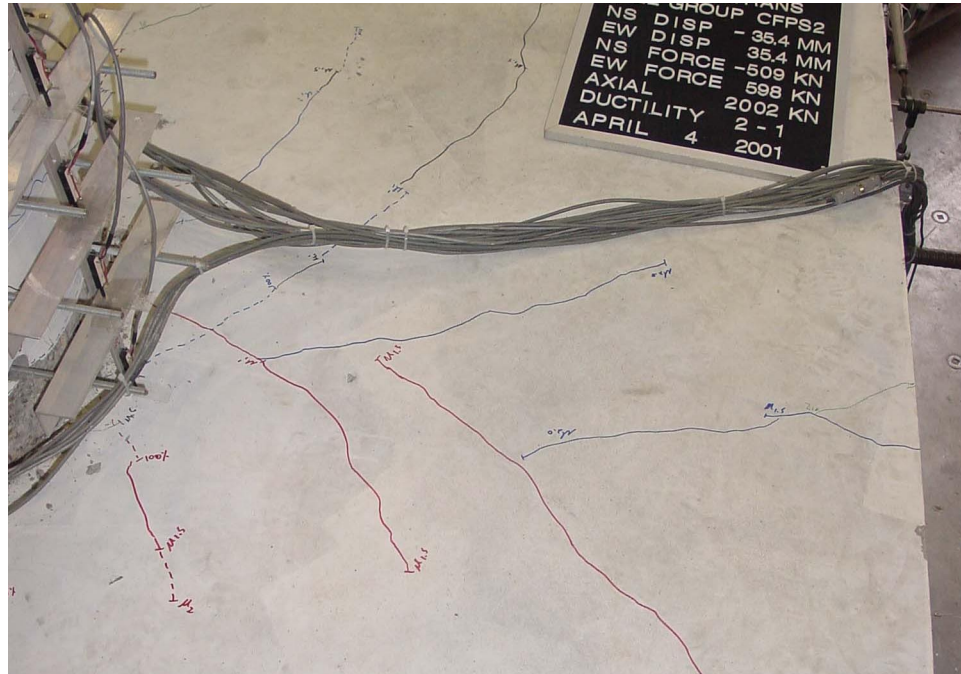
Figure K.13: Strain penetration cracks on pilecap top surface at $\mu_\Delta = 2.0$ of Loading Phase 1

Figure K.14: Flexural cracks on pilecap at $\mu_\Delta = 2.0$ of Loading Phase 1
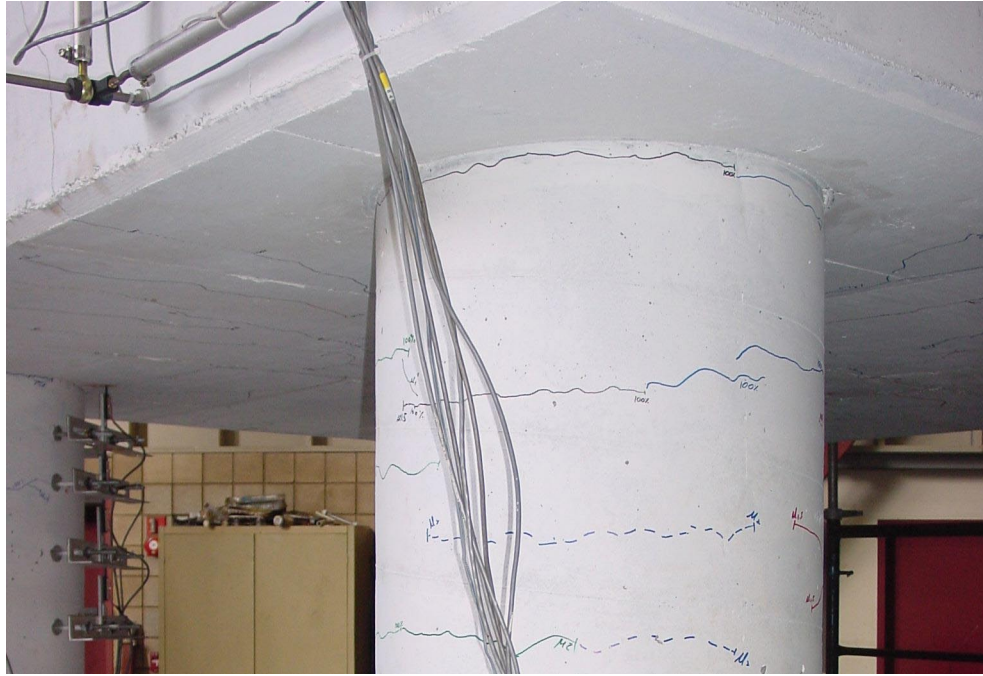
Figure K.15: Flexural cracks on pile D at $\mu_\Delta = 2.0$ of Loading Phase 1

UCSD - CALTRANS
PILE GROUP CFPS2
NS DISP - 52.9 MM
EW DISP   52.9 MM
NS FORCE - 534 KN
EW FORCE 631 KN
AXIAL   2002 KN
DUCTILITY 3 - 1
APRIL 5 2001

Figure K.16: Spalling of column cover concrete at $\mu_\Delta = 3.0$ of Loading Phase 1

Figure K.17: Strain penetration crack around the column at μ_Δ = 3.0 of Loading Phase 1

Figure K.18: Spalling of column cover concrete at μ_Δ = 4.0 of Loading Phase 1
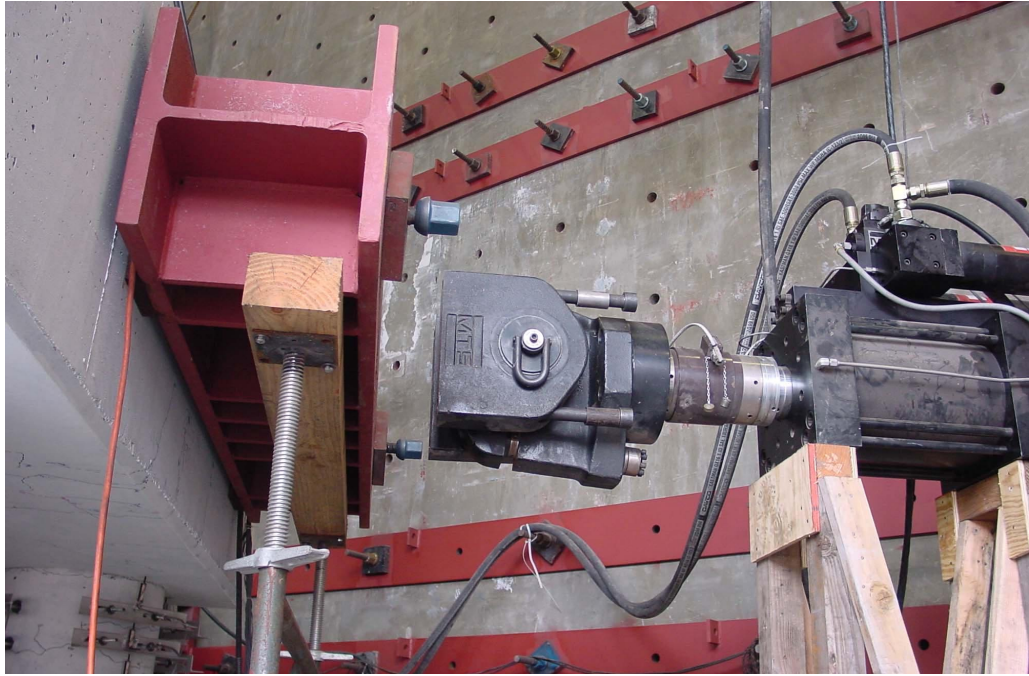
Figure K.19: Detached pilecap actuator for the test of Loading Phase 2

Figure K.20: Initiation of column reinforcement buckling at $\mu_\Delta = 1.5$ at Loading Phase 2

Figure K.21: Flexural cracks on pile C at $\mu_\Delta = 2.0$ of Loading Phase 2

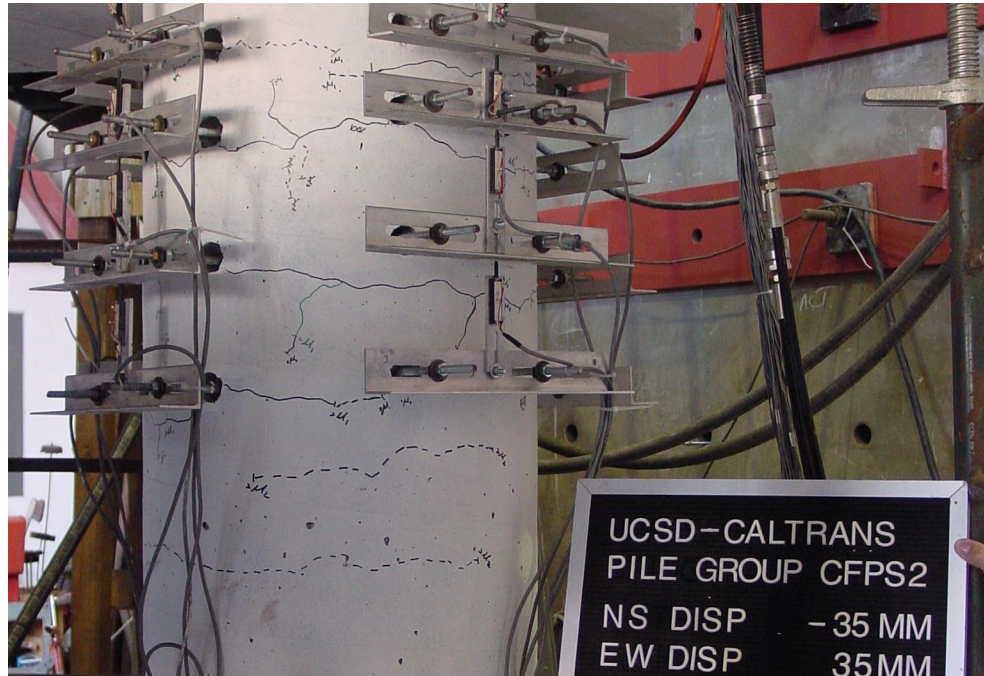Figure K.22: Fracture of column reinforcement at $\mu_\Delta = 4.0$ of Loading Phase 2

Figure K.23: Innner face spalling of pile A at 25mm of pilecap displacement

Figure K.24: Pile damage at the end of the test

Figure **K**.25: Pilecap soffit at the end of test

References

[1]   American Concrete Institute, *Building code Requirements for Structural Concrete(ACI 318-95) and Commentary (ACI 318R-95),* Michigan, 1995.

[2]   Applied Technology Council, *Improved Seismic Design Criteria for California Bridges: Provisional Recommendations.* ATC-32. California, 1996

[3]   Banerjee, P. K., and Davies, T. G., " The behavior of axially and laterally loaded single pile embedded in non-homogeneous soils", Geotechnique, 21(3), 1978.

[4]   Bowles, J. E., *Foundation Analysis and Design*, 5th Ed., McGraw Hill, 1996.

[5]   Caltrans, *Bridge Design Specifications,* California Department of Transportation, State of California, Sacramento, California, 1993.

[6]   Caltrans, *Seismic Design Criteria,* California Department of Transportation, State of California, Sacramento, California, 2001.

[7]   Carter, D. P., "A Non-Linear Soil Model for Predicting Lateral Pile Response", Report No. 359, Department of Civil Engineering, University of Auckland, New Zealand, 1984.

[8]   Desai, C. S., and Appel, G. C., "3-D analysis of laterally loaded structure", Proc., *2nd International Conference on Numerical Methods in Geomechanics*, Blackburg, ASCE, Vol. 1, 1976.

[9]   Gazetas, G., "Foundation vibrations", *Foundation Engineering Handbook,* 2nd Ed., H-Y Fang editor, Van Nostrand Reinold. 1991.

[10]   Heteni, M., *Beams on Elastic Foundations,* The University of Michigan Press, Ann Arbor, Michigan, 1946.

[11]   Ingham, J. M., Priestley M. J. N. and Seible, F., *Seismic Performance of Bridge Knee Joints - Volume I,* Structural Systems Research, Report No. SSRP 94/12, University of California at San Diego, California, June 1994.

[12]   Ingham, J. M., *Seismic Performance of Bridge Knee Joints,* Doctoral Dissertation, Division of Structural Engineering, University of California at San Diego, California, 1996.

[13]   Ling, L. F., "Back analysis of lateral load tests on piles", M. E. Thesis, Department of Civil Engineering, University of Auckland, New Zealand, 1988.

[14]   Mander, J. B., Priestley, M. J. N., Park, R., "Theoretical Stress-Strain Model For Confined Concrete", *Journal of the Structural Division,* ASCE, Vol. 114, No. 8, August 1988, pp. 1804-1826.

[15]   Matlock, H., Foo, S.H.C., and Bryant, L.M., "Simulation of Lateral Pile Behavior Under Earthquake Motion", Speciality Conference on Earthquake engineering, 1978.

[16]   Matlock, H., Reese, L. C., "Generalized Solutions For Laterally Loaded Piles", Journal of the Soil Mchnaics and Foundations Division, ASCE, V. 86, No. SM5, October 1969, pp. 63-91.

[17]   Mindlin, R. D., "Force at a Point in the Interior of a Semi-Infinite Solid", Physics 7, 1936.

[18]   Park, R.J.T., Priestley, M.J.N., and Walpole, W. R., "The Seismic Performance of Steel Encased Reinforced Concrete Bridge Piles", Department of Civil Engineering, University of Canterbury Christchurch, New Zealand, Report No. 82-12, February 1982.

[19]   Park, R., Proceedings, 2nd International Workshop on the Seismic Design of Bridges, Vol.II, Queenstown, New Zealand, August 1994.

[20]   Pauley, T., Priestley, M. J. N., *Seismic Design of Reinforced Concrete and Masonry Buildings,* John Wiley & Son, New York, 1992.

[21]   Pender, M. J., " Aseismic Pile Foundation Design Analysis", Bulletin of the New Zealand National Society for Earthquake Engineering, Vol. 11, No.2, June 1978, pp 49 -160.

[22]   Poulos, H. G., Davis, E. H., " Pile Foundation Analysis and Design", John Wiley & Sons, Inc., New York, 1980.

[23]   Poulos, H. G., "Behavior of Laterally Loaded Piles : I - Single Piles", Proceedings of the American Society of Civil Engineers, Vol. 97, No.SM5, May 1971, pp. 711-731. - Elastic Continum Concept.

[24]   Priestley, M. J. N., *Assessment and Design of Joints for Single-Level Bridges with Circular Columns,* Structural Systems Research, Report No. SSRP 93/02, University of California at San Diego, California, February 1993.

[25]   Priestley, M. J. N., Seible, F., Benzoni, G., *Seismic Performance of Circular Columns with Low Longitudinal Steel Ratios,* Structural Systems Research, Report No. SSRP 94/08, University of California at San Diego, California, 1994.

[26]   Priestley M.J.N., Seible F., Calvi G.M.: *Seismic Design and Retrofit of Bridges*. John Wiley & Sons, New York 1996.

[27]   Priestley M.J.N., Seible F., *Bridge Pile Foundations Under Seismic Loads - Capacity and Design Issues -*. SEQAD Consulting Engineers, Solana Beach, California, 1997.

[28]   Prestley, M. J. N., Budek, A., Benzoni, G., "An Analytical Study of the Inelastic Seismic Response of Reinforced Concrete Pile-Columns in Cohesionless Soil", Department of AMES, University of California San Diego, La Jolla, California, March 1995.

[29]   Pyke, R., Beikae, M., " A New Solution for the Resistance of Single Piles to Lateral Loading", ASTM Commitee D-18 on Soil and Rock, Kansas City, MO, 22 June 1983, pp3-20.

[30] Reese, L. C., Cox, W. R., and Koop, F. D., "Analysis of Laterally Loaded Piles in Sand", *Proceedings, 6th Offshore Technology Conference*, Houston, Texas, 1974.

[31] Scott, R. F., *Foundation Analysis*. Prentice-Hall, Englewood Cliffs, 1981.

[32] SEQMC - *Manual and Program Description,* Seqad Consulting Engineers, Solana Beach, California, 1998.

[33] Sritharan, S., Priestley, M. J. N., Seible, F., *Seismic Response of Column/Cap Beam Tee Connections with Cap Beam Prestressing,* Structural Systems Research, Report No. SSRP 96/09, University of California at San Diego, California, 1996.

[34] Sritharan, S., Ingham, J. M., Priestley, M. J. N., Seible, F., "Bond Slip of Bridge Column Reinforcement Anchored in Cap Beams", *ACI Special Volume on Bond*, American Concrete Institute.

[35] Sritharan, S., Priestley, M. J. N., Seible, F., *Seismic Design and Performance of Concrete Multi-Column Bents for Bridges*, Structural Systems Research Project, Report SSRP-97/03, University of California, San Diego, June 1997.

[36] Xiao, Y., M.J.N. Priestley, F. Seible, "Seismic Assessment and Retrofit of Bridge Column Footings." ACI Structural Journal, Vol. 93 No. 1, January-February 1996, pp. 1-16.

[37] Xiao, Y., M.J.N. Priestley, F. Seible and N. Hamada, *Seismic Assessment and Retrofit of Bridge Footings*, Structural Systems Research Project, Report SSRP-94/11, University of California, San Diego, May 1994, 200 pp.